

A Review on Mesonic Decay of Λ Hypernuclei

E. OSET, P. FERNÁNDEZ de CÓRDOBA,* J. NIEVES,** A. RAMOS***
and L. L. SALCEDO****

*Departamento de Física Teórica and IFIC
Centro Mixto Universidad de Valencia-CSIC, 46100 Burjassot (Valencia)
*Departamento de Matemática Aplicada, Universidad Politécnica de Valencia
Valencia*

***Physics Department, The University Southampton, SO9 5NH*

****Departament d'Estructura i Constituents de la Matèria
Universitat de Barcelona, 08028 Barcelona*

*****Departamento de Física Moderna, Universidad de Granada
18071 Granada*

(Received April 25, 1994)

A review of the present situation of the mesonic decay of Λ hypernuclei is done. The link between the propagator method and the one with wave functions and nuclear matrix elements is established. The lack of links between the mesonic decay and the nucleon occupation number in nuclear matter is also discussed, as well as the effect of the ΛN short range repulsion in the mesonic decay of light hypernuclei. The relevance of the $2p2h$ induced Λ decay channel is also discussed. Finally an overview of the potential use of the process, when systematic measurements over the periodic table are done, is presented at the end.

§ 1. A brief historical introduction

A paper devoted to the memory of our friend Hiroharu Bandō is the right place to recall some interesting events associated with him and the subject of this paper. In 1984 L. L. Salcedo was working in Valladolid for his Ph. D. on the decay of Λ hypernuclei and he surprised me (E. O.) with the results which indicated that the rate for pionic decay of heavy Λ hypernuclei was increased by about two orders of magnitude when a proper medium renormalization of the pion was done. At that time I was still not used to shake every one of the few times that Salcedo would open his mouth, so I told him to check again his program. He did so and came out with the same answer. This time I checked it myself and had to surrender to a reality that was difficult to swallow and worst, I had the feeling it would be difficult to sell. A paper was written and after a few useful corrections suggested by the referee the paper was published.¹⁾ I should thank the generosity of the referee who, probably without believing the results, let it be published. I say that a posteriori because when my selling mission began I could not convince a single colleague of the soundness of the results. To make it short I recall the lapidary sentence of A. Gal: "I do not believe in any renormalization factor of 100".

With this predisposition from my colleagues I presented these results in the hypernuclear Conference at Brookhaven in 1985.²⁾ I went there with clarifying and convincing arguments, with Feynman diagrams, with poles and cuts in the complex plane and Cutkosky rules to separate imaginary parts, and all this heavy artillery that should have crumbled the strongest walls. The result: a lost battle. The whole audience turned against me. Even my friends Gerry Brown and Torlif Ericson showed disbelief in their questions and comments at the end of the talk. But it was Torlif the one who opened my mind to what was happening: I was using an inappropriate language for that audience which was more used to the language of wave functions and matrix elements than to the one of propagators, selfenergies and cuts which I was using. And here came Bandō. I went to him and discussed with him. He was using this alternative language and he should be able to prove the same results using pionic wave functions in the nucleus and evaluating the proper matrix elements. He was the first person to take us seriously and he started to work with his colleagues Motoba and Itonaga on the issue. In Ref. 2), after the experience with the audience and the discussions with Torlif, I wrote a section on “an alternative approach” sketching the way to follow using the language of wave functions and matrix elements, which was the one followed by Bandō and collaborators.

Their work has been very useful.^{3)~5)} It not only confirmed the huge enhancement of the mesonic width found in Ref. 1), but produced detailed and quantitative results in many nuclei, taking into account shell effects, Q values and other details which go far beyond the nuclear matter and local density approach of Ref. 1). Since then the spectacular enhancement of the mesonic width has been universally accepted. Their predictions have been confirmed by the new wave of experiments.^{6),10)}

I came to appreciate Bandō more with this incident. His quiet, flexible and gentle approach to the problems contrasted with my stern and temperamental one, and certainly proved to be much more efficient.

One of the interesting outputs of Refs. 3)~5) is that the mesonic width is quite sensitive to the pion nucleus optical potential, for potentials which fit equally well the pion nucleus scattering data. This information is very useful and should serve as a check for different microscopic models of the pion nucleus interaction. The work done on the mesonic decay and its interconnection with the other Λ decay channels has also been essential to get a unified picture of the Λ decay in nuclei and has generated other interesting developments as we shall see below.

§ 2. Formal derivation of the Λ width in nuclei

— The propagator method —

The starting point is the $\Lambda \rightarrow \pi N$ Lagrangian, accounting for this weak process, which is given by

$$L_{\pi\Lambda N} = G\mu^2 \bar{\psi}_N (A - B\gamma_5) \boldsymbol{\tau} \cdot \boldsymbol{\phi}_\pi \psi_\Lambda + \text{h.c.} \quad (1)$$

with

$$(G\mu^2)^2 / 8\pi = 1.94510^{-15}, \quad A = 1.06, \quad B = 7.10. \quad (2)$$

In Eq. (1) the Λ is assumed to behave as the state $|1/2, -1/2\rangle$ of an isospin doublet with $T=1/2$ and this imposes the $\Delta T=1/2$ rule, which has as a consequence a strength double for the $\Lambda \rightarrow \pi^- p$ channel than for the $\Lambda \rightarrow \pi^0 n$ one. In Eq. (1) the term A violates parity and the term B conserves it.

A practical way to evaluate the Λ width in nuclear matter and introduce the medium corrections is to start from the Λ selfenergy, Σ , associated to the diagram of Fig. 1 and then use the relationship

$$\Gamma = -2\text{Im}\Sigma. \tag{3}$$

The selfenergy is readily evaluated as

$$-i\Sigma(k) = 3(G\mu^2)^2 \int \frac{d^4q}{(2\pi)^4} G(k-q)D(q) \left[S^2 + \left(\frac{P}{\mu}\right)^2 \mathbf{q}^2 \right], \tag{4}$$

where G and D are the nucleon and pion propagators respectively and $P/\mu = B/2M$ with μ, M the pion and nucleon mass. By using the free nucleon and pion propagators, and making the typical nonrelativistic approximation $M/E=1$, one obtains immediately the free Λ width^{(1),(11)}

$$\Gamma_{\text{free}} \equiv \Gamma_\Lambda = 3(G\mu^2)^2 \int \frac{d^3q}{(2\pi)^3} \frac{1}{2\omega(\mathbf{q})} 2\pi\delta(E_\Lambda - \omega(\mathbf{q}) - E_N(\mathbf{k}-\mathbf{q})) \times \left[S^2 + \left(\frac{P}{\mu}\right)^2 \mathbf{q}^2 \right]. \tag{5}$$

In a Fermi sea of nucleons, both the nucleon and pion propagators are changed

$$G(p) = \frac{1 - n(\mathbf{p})}{p^0 - E(\mathbf{p}) - V_N + i\epsilon} + \frac{n(\mathbf{p})}{p^0 - E(\mathbf{p}) - V_N - i\epsilon}, \tag{6}$$

$$D(q) = \frac{1}{q^{02} - \mathbf{q}^2 - \mu^2 - \Pi(q^0, \mathbf{q})}, \tag{7}$$

where V_N is the nucleon potential, $\Pi(q^0, \mathbf{q})$ is the pion selfenergy in the nuclear medium and $n(\mathbf{p})$ is the occupation number in the Fermi sea, $n(\mathbf{p})=1$ for $|\mathbf{p}| \leq k_F$, $n(\mathbf{p})=0$ for $|\mathbf{p}| > k_F$ with k_F the Fermi momentum. The practical way to perform the q^0 integral in Eq. (4) is to perform a Wick rotation as shown in Fig. 2, where the analytical structure of the integrand is shown. The shaded region accounts for the discontinuity of the pion propagator due to $\text{Im} \Pi$. The pole at $\tilde{\omega}(\mathbf{q})$ would correspond to a renormalized pion pole where

$$\tilde{\omega}(\mathbf{q})^2 - \mathbf{q}^2 - \mu^2 - \Pi(\tilde{\omega}(\mathbf{q}), \mathbf{q}) = 0. \tag{8}$$

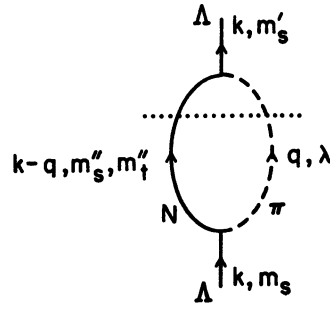


Fig. 1. Feynman graph for the free Λ selfenergy of Eqs. (4) and (5). The $\Lambda \rightarrow \pi N$ “cut” is shown (dotted line).

Missing in the figure is the pole of $G(k-q)$ corresponding to the second term in (6). This pole lies in the lower halfplane of the figure and would contribute in the Wick rotation only when it happens to be in the third quadrant, i.e., $k^0 - E(\mathbf{k}-\mathbf{q}) - V_N < 0$. But this corresponds to $(\mathbf{k}-\mathbf{q})$ very large where $n(\mathbf{k}-\mathbf{q})=0$ and hence this term does not contribute. Thus we obtain for the width^(1),11)

$$\Gamma(k) = -6(G\mu^2)^2 \int \frac{d^3q}{(2\pi)^3} [1 - n(\mathbf{k}-\mathbf{q})] \theta(k^0 - E(\mathbf{k}-\mathbf{q}) - V_N) \times \left[S^2 + \left(\frac{P}{\mu}\right)^2 \mathbf{q}^2 \right] \text{Im} \frac{1}{q^{0^2} - \mathbf{q}^2 - \mu^2 - \Pi(q^0, \mathbf{q})} \Big|_{q^0 = k^0 - E(\mathbf{k}-\mathbf{q}) - V_N} \quad (9)$$

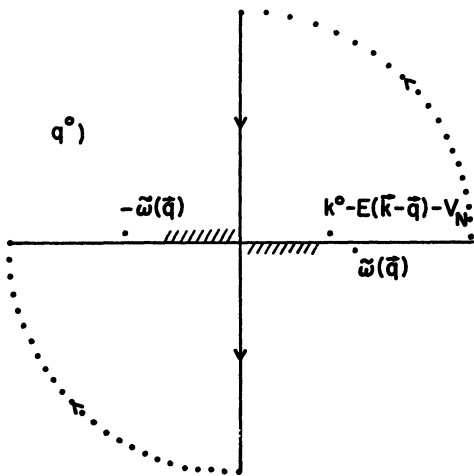


Fig. 2. Analytical structure of the integrand of Eq. (4) in the complex q^0 plane with the nucleon and propagators of Eqs. (6) and (7). The renormalized pion propagator pole $\bar{\omega}(q)$ is shown. The dashed lines close to the real axis indicate the analytical cut from $\text{Im} \Pi(q^0, \mathbf{q})$ related to the nonmesonic Λ decay channel.

In the discussion here we neglect the role of correlations and form factors, which are obviously important and are treated in all detail in Refs. 1) and 11). The simplified formalism will allow us to concentrate on the qualitative aspects of the reaction.

In the first place we observe the Pauli blocking factor, $1-n$, in Eq. (9). Since a Λ with $k=0$ decays into a nucleon and pion with $q \simeq 100$ MeV/c, this momentum is smaller than the Fermi momentum for nuclear matter density, $k_F = 270$ MeV/c, and the decay is forbidden by Pauli blocking, i.e., $1-n(\mathbf{k}-\mathbf{q})=0$. The overlap of the Λ wave function with the nuclear surface in finite nuclei still allows the Λ decay since at some radius the local Fermi momentum will be smaller than 100 MeV/c, and also

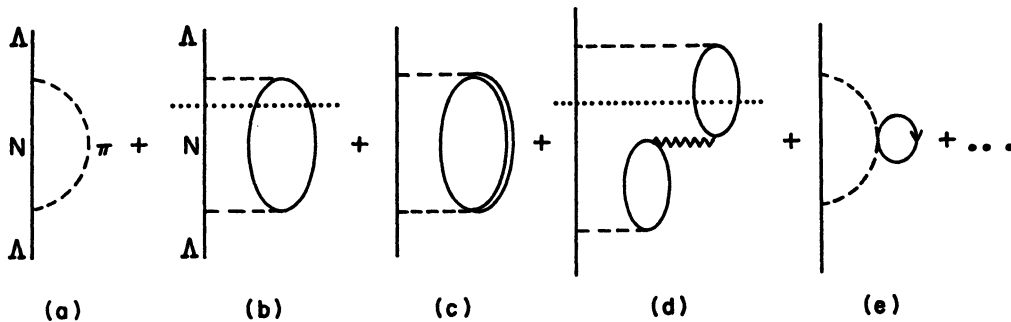


Fig. 3. Λ self-energy diagrams included in Eq. (4) with the nucleon and pion propagators of Eqs. (6) and (7). (a) Free self-energy graph. (b), (c) Insertion of p -wave pion selfenergy at lowest order. (d) Generic RPA graph from the expansion of the pion propagator in powers of the pion selfenergy. (e) s -wave pion selfenergy at lowest order. The cuts represent the nonmesonic decay channel.

because the momentum distribution of the Λ wave function helps a bit in allowing some nucleon momenta in the decay. Nevertheless the Λ mesonic width decreases drastically as a function of the mass number.

The language of propagators which we have used here is the most appropriate in order to provide a unified picture of the Λ nuclear decay. Indeed, Eq. (9) contains not only the modified mesonic channel but also the nonmesonic one. This can be seen diagrammatically by expanding the pion propagator and taking a ph and Δh excitation to account for the pion selfenergy, Π . This is depicted in Fig. 3. The imaginary part of a selfenergy diagram is obtained when the set of intermediate states cut by a horizontal line are placed simultaneously on shell in the intermediate integration. In Fig. 3 we observe a source corresponding to placing on shell a nucleon and the ph of the pion selfenergy. This corresponds to a channel where there are no pions and only nucleons in the final state. The physical process which has occurred is $\Lambda N \rightarrow NN$ and this is the nonmesonic channel. Technically it would be obtained by substituting in Eq. (9)

$$\text{Im} \frac{1}{q^{02} - \mathbf{q}^2 - \mu^2 - \Pi} \rightarrow \frac{\text{Im} \Pi_{ph}}{|q^{02} - \mathbf{q}^2 - \mu^2 - \Pi|^2}, \tag{10}$$

where Π_{ph} is the pion selfenergy due to the $1p1h$ excitation. There is no overlap between $\text{Im} \Pi_{ph}(q^0, q)$ and the pion pole in the propagator of Eq. (9) and thus the separation is clear.

The mesonic channel would correspond to a different cut, the one where the N and the π are placed on shell. This is shown diagrammatically in Fig. 4. The terms in Fig. 4(b), and further iterations contained in (9), lead to a renormalization of the mesonic width, and an appreciable one, as it was shown in Ref. 1).

Technically the mesonic width can be calculated from the total width, Eq. (9), subtracting the nonmesonic width, or equivalently by obtaining the pion pole contribution in Eq. (4) from the renormalized pion pole given in Eq. (8).

The qualitative reason on why the mesonic width is so drastically changed is given in Refs. 1) and 11): The attractive character of the pion selfenergy leads to a larger pion momentum for the same pion energy and thus, to a larger nucleon momentum by momentum conservation. Thus, the nucleon has more chances to have a momentum bigger than the Fermi momentum, therefore increasing the mesonic

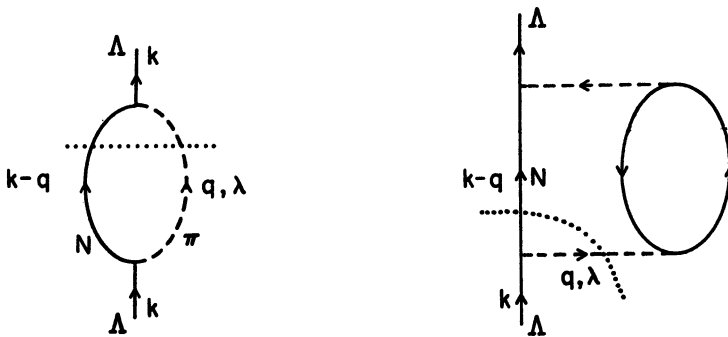


Fig. 4. Free and lowest order Λ selfenergy graph. The dotted cuts represent the mesonic decay channel.

width.

The width in finite nuclei is obtained in Ref. 1) via the local density approximation

$$\Gamma = \int d^3r |\phi_A(\mathbf{r})|^2 \Gamma(k, \rho(\mathbf{r})), \quad (11)$$

where ϕ_A is the A wave function. A further average over the momentum distribution of the A wave function is also done in Ref. 1).

§ 3. Finite nuclei approach to the mesonic width

— *The wave function method* —

This approach was sketched in Ref. 2) and carried out in detail in Ref. 3). The mesonic width is given, in analogy to Eq. (5) by

$$\begin{aligned} \Gamma^{(a)} = & \frac{1}{2} C^{(a)} (G\mu^2)^2 \sum_{N \notin F} \int \frac{d^3q}{(2\pi)^3} \frac{1}{2\omega(\mathbf{q})} 2\pi \delta(E_A - \omega(\mathbf{q}) - E_N) \\ & \times \left\{ S^2 \left| \int d^3x \phi_A(\mathbf{x}) \phi_{\pi^{(-)}}(\mathbf{q}, \mathbf{x})^* \phi_N^*(\mathbf{x}) \right|^2 \right. \\ & \left. + \left(\frac{P}{\mu} \right)^2 \left| \int d^3x \phi_A(\mathbf{x}) \nabla \phi_{\pi^{(-)}}(\mathbf{q}, \mathbf{x})^* \phi_N^*(\mathbf{x}) \right|^2 \right\}, \quad (12) \end{aligned}$$

where ϕ_N is the wave function of the nucleon states and $\phi_{\pi^{(-)}}^*$ corresponds to an outgoing solution of the Klein-Gordon equation normalized to a plane wave asymptotically (e^{-iqr}). The index a stands now for π^-p or π^0n decay, with $C^{(p)}=4$, $C^{(n)}=2$, which one separates here since due to shell effects these channels can depart drastically from the elementary $\Delta T=1/2$ rule.

The sum in Eq. (12) runs only over non occupied nucleon states in the shell model. On the other hand the effects of using for $\phi_{\pi^{(-)}}^*$ a solution of the Klein-Gordon equation with a proper optical potential (or pion selfenergy, $\Pi=2\omega V_{\text{opt}}$, V_c Coulomb potential), i.e.,

$$[-\nabla^2 + \mu^2 + 2\omega V_{\text{opt}}(\mathbf{x})] \phi_{\pi^{(-)}}(\mathbf{q}, \mathbf{x})^* = [\omega - V_c(\mathbf{x})]^2 \phi_{\pi^{(-)}}(\mathbf{q}, \mathbf{x})^*, \quad (13)$$

instead of a plane wave are rather drastic and increase the mesonic width in about two orders of magnitude in heavy nuclei,^{3),5)} in qualitative agreement with the nuclear matter results of Ref. 1).

The arguments for the renormalization are expressed now in the alternative language as follows: the attraction caused by the pion selfenergy increases the pion momenta in the pion wave function. As a consequence the matrix element of the A wave function (in a $1s_{1/2}$ ground state of the A nucleus potential) and the nucleon wave function is considerably enhanced. Note that if the A and N potentials were the same, the A and $N \notin F$ states are orthogonal and the matrix elements of (12) would be zero for $q=0$. The matrix elements thus necessarily increase with q , for the moderately small values of q involved in the present process. In the two languages the physical consequences are the same: an increased probability of reaching the

unoccupied states and thus an enhancement of the mesonic width.

§ 4. Equivalence of the propagator and wave function methods

The discussion above has shown that the physical and numerical results of the pion renormalization are the same. Yet, technically the two approaches look different. In this section we establish the equivalence of the two methods and the approximations implicit in them.

Let us start from the pion propagator in finite nuclei written in coordinate space

$$D(\mathbf{x}, \mathbf{y}, \omega) = \sum_n \frac{\varphi_n(\mathbf{x})\varphi_n^*(\mathbf{y})}{\omega^2 - \epsilon_n^2 + i\eta}, \quad (14)$$

where $\varphi_n(\mathbf{x})$ are the pion wave functions in the nucleus and ϵ_n their corresponding energies. Ignoring pionic bound states, which do not play a role in our problem, we can identify the pionic wave functions by the asymptotic momentum \mathbf{q} . Hence their energy is given by $\omega(\mathbf{q}) = (\mathbf{q}^2 + \mu^2)^{1/2}$. The sum over the index n is then replaced by an integral over \mathbf{q} as given below

$$D_\pi(\mathbf{x}_1, \mathbf{x}_2, E_\pi) = \int \frac{d^3q}{(2\pi)^3} \frac{\phi_\pi(\mathbf{q}, \mathbf{x}_1)\phi_\pi^*(\mathbf{q}, \mathbf{x}_2)}{E_\pi^2 - \omega(\mathbf{q})^2 + i\eta}. \quad (15)$$

For simplicity in the derivation we shall take the s -wave part of the width (the one providing the largest contribution) and will not distinguish between π^0 or π^- decay. Hence, from Eq. (12) we obtain

$$\begin{aligned} \Gamma_s &= 3(G\mu^2)^2 S^2 \sum_{N \notin F} \int \frac{d^3q}{(2\pi)^3} \frac{1}{2\omega(\mathbf{q})} 2\pi\delta(E_\Lambda - E_N - \omega(\mathbf{q})) \\ &\times \left| \int d^3x \phi_\Lambda(\mathbf{x})\phi_\pi^*(\mathbf{q}, \mathbf{x})\phi_N^*(\mathbf{x}) \right|^2, \end{aligned} \quad (16)$$

which can be rewritten as

$$\begin{aligned} \Gamma_s &= 3(G\mu^2)^2 S^2 \sum_{N \notin F} \int d^3x_1 \int d^3x_2 \phi_\Lambda^*(\mathbf{x}_1)\phi_\Lambda(\mathbf{x}_2) \\ &\times \phi_N(\mathbf{x}_1)\phi_N^*(\mathbf{x}_2) \int \frac{d^3q}{(2\pi)^3} \frac{1}{2\omega(\mathbf{q})} 2\pi\delta(E_\Lambda - E_N - \omega(\mathbf{q}))\phi_\pi(\mathbf{q}, \mathbf{x}_1)\phi_\pi^*(\mathbf{q}, \mathbf{x}_2) \end{aligned} \quad (17)$$

or by virtue of Eq. (15) as

$$\begin{aligned} \Gamma_s &= 3(G\mu^2)^2 S^2 \sum_{N \notin F} \int d^3x_1 d^3x_2 \phi_\Lambda^*(\mathbf{x}_1)\phi_N(\mathbf{x}_1)(-2) \\ &\times \text{Im}D_\pi(\mathbf{x}_1, \mathbf{x}_2; E_\pi = E_\Lambda - E_N)\theta(E_\Lambda - E_N)\phi_\Lambda(\mathbf{x}_2)\phi_N^*(\mathbf{x}_2). \end{aligned} \quad (18)$$

Now, in order to connect with Eqs. (9) and (11) one makes a local density approximation. In the first step one evaluates Γ for a slab of infinite nuclear matter and in the second step one replaces the width in the infinite slab by an integral over the nuclear volume assuming slabs of matter in each d^3r of the nucleus with local density $\rho(\mathbf{r})$ and with a probability of finding the Λ particle given by $|\phi_\Lambda(\mathbf{r})|^2$. This

last step is implemented by means of Eq. (11). Hence we should see how we reproduce now Eq. (9) when we assume in Eq. (18) a slab of infinite nuclear matter. For this purpose we have to substitute for the nucleon sector

$$\begin{aligned}
 N &\rightarrow \mathbf{p}, \\
 \sum_{N \notin F} &\rightarrow V \int \frac{d^3 p}{(2\pi)^3} (1 - n(\mathbf{p})), \\
 \phi_N(\mathbf{x}) &\rightarrow \frac{1}{\sqrt{V}} e^{i\mathbf{p}\mathbf{x}}, \\
 E_N &\rightarrow E(\mathbf{p}) - V_N
 \end{aligned} \tag{19}$$

and for the Λ wave function

$$\phi_\Lambda(\mathbf{x}) \rightarrow \frac{1}{\sqrt{V}} e^{i\mathbf{k}\mathbf{x}}. \tag{20}$$

Now in the infinite slab of nuclear matter the pion propagator of Eq. (15) is substituted by

$$D_\pi(\mathbf{x}_1, \mathbf{x}_2, E_\pi) \rightarrow \int \frac{d^3 q}{(2\pi)^3} \frac{e^{i\mathbf{q}(\mathbf{x}_1 - \mathbf{x}_2)}}{E_\pi^2 - \omega(\mathbf{q})^2 - \Pi(E_\pi, \mathbf{q})}, \tag{21}$$

where $\Pi(E_\pi, \mathbf{q})$ is the pion selfenergy, which is a function of ρ . Note that for values of $\mathbf{x}_1, \mathbf{x}_2$ far away from the nucleus Eqs. (15) and (21) are equivalent since there $\rho=0$ and Π (in the local density approximation) will be zero. At other densities, Π will be different of zero and the integral of Eq. (21) gives rise to other momentum components, modulating the plane wave of the numerator and providing a kind of WKB approximation to the wave functions of the numerator of Eq. (15). The local density approximation gives rise to a variable local momentum and hence a distorted pion wave.

By substituting Eqs. (19)~(21) in Eq. (18) we obtain:

$$\begin{aligned}
 \Gamma_s &= -6(G\mu^2)^2 S^2 \int \frac{d^3 p}{(2\pi)^3} \int \frac{d^3 q}{(2\pi)^3} (1 - n(\mathbf{p})) \text{Im} D_\pi(q) \theta(q^0) |_{q^0 = E_\Lambda - E(\mathbf{k} - \mathbf{q}) - V_N} \\
 &\times \int d^3 x_1 d^3 x_2 \frac{1}{V} e^{i\mathbf{p}(\mathbf{x}_1 - \mathbf{x}_2)} e^{i\mathbf{q}(\mathbf{x}_1 - \mathbf{x}_2)} e^{-i\mathbf{k}(\mathbf{x}_1 - \mathbf{x}_2)}
 \end{aligned} \tag{22}$$

with $D_\pi(q)$ given by Eq. (7). Finally, by means of the relationship $(2\pi)^3 \delta^3(0) = \int d^3 x = V$ we can cast Eq. (22) as

$$\Gamma_s = -6(G\mu^2)^2 S^2 \int \frac{d^3 q}{(2\pi)^3} (1 - n(\mathbf{k} - \mathbf{q})) \text{Im} D_\pi(q) \theta(q^0) |_{q^0 = E_\Lambda - E(\mathbf{k} - \mathbf{q}) - V_N}, \tag{23}$$

which coincides with the s -wave contribution to Γ from Eq. (9). This establishes the equivalence between the two methods within the local density approximation which we have done in the case of the propagator method.

§ 5. The mesonic width and the occupation number

We have seen that Pauli blocking is the major factor in the small mesonic width of heavy Λ hypernuclei. It was suggested that because real interacting nuclei have the “occupied” states partly unoccupied, the mesonic width should be enhanced with respect to a calculation with fully occupied Fermi levels.¹⁴⁾ In the nuclear matter approach of § 2 this is easily visualized by recalling a realistic picture of the occupation number of the Fermi sea,¹⁵⁾ which is depicted in Fig. 5.

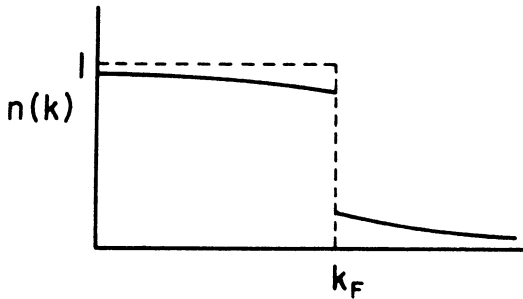


Fig. 5. Schematic representation of the nucleon occupation number for an interacting Fermi sea.

For the states below the Fermi energy the level of occupancy is of the order of 85% and by assuming that in the Λ decay the nucleons can occupy the 15% vacancy of these states we would guess that the mesonic width would stabilize at the level of about 10% of the free width for heavy nuclei (taking into account pion absorption in the way out of the pions). If this were the case the mesonic width could serve as a measure of the occupation number in the Fermi sea. The argument is very appealing and intuitive, however, it is incorrect and leads to an overestimate of the width in about three orders of magnitude in heavy nuclei.

The detailed discussion of this problem was done in Ref. 16). The fallacy in the argumentation lies in the fact that

$$\frac{1 - n_1(\mathbf{k})}{k^0 - E(\mathbf{k}) + i\epsilon} + \frac{n_1(\mathbf{k})}{k^0 - E(\mathbf{k}) - i\epsilon}, \tag{24}$$

where $n_1(\mathbf{k})$ is the realistic occupation number in nuclear matter, *is not* an improvement over the propagator in Eq. (6). The realistic N propagator for an interacting Fermi sea is given in terms of the spectral functions by

$$G(k^0, k) = \int_{-\infty}^{\mu} d\omega \frac{S_n(\omega, k)}{k^0 - \omega - i\epsilon} + \int_{\mu}^{\infty} d\omega \frac{S_p(\omega, k)}{k^0 - \omega + i\epsilon} \tag{25}$$

with μ the chemical potential.

When performing the calculations of the mesonic width with this N propagator one obtains the factor

$$\int_{\mu}^{\infty} d\omega S_p(\omega, \mathbf{k} - \mathbf{q}) 2\pi \delta(k^0 - \omega - \omega(\mathbf{q})) \tag{26}$$

replacing the factor

$$[1 - n(\mathbf{k} - \mathbf{q})] 2\pi \delta(k^0 - E(\mathbf{k} - \mathbf{q}) - \omega(\mathbf{q})) \tag{27}$$

in Eq. (5), when the Pauli blocking factor of Eq. (9) is implemented. Equations (26) and (27) bare some intuitive resemblance because

$$\int_{\mu}^{\infty} d\omega S_p(\omega, \mathbf{k}-\mathbf{q}) = 1 - \int_{-\infty}^{\mu} d\omega S_h(\omega, \mathbf{k}-\mathbf{q}) = 1 - n_1(\mathbf{k}-\mathbf{q}). \quad (28)$$

However, in the presence of the δ function of Eq. (26), the integral of Eq. (28) cannot be factored out because the δ function in Eq. (26) has ω in the argument. Furthermore because of restrictions of the phase space (energy and momentum conservation) the range of values of ω allowed are very small compared to the range (μ, ∞) needed in Eq. (28) to obtain $1 - n_1(\mathbf{k}-\mathbf{q})$ of the interacting Fermi sea. In physical terms we can interpret it in the following way: the occupation number $n_1(\mathbf{k}-\mathbf{q})$ is an integral for all the energies of the nucleon, ω , of the probability of finding a nucleon with momentum $\mathbf{k}-\mathbf{q}$ and an energy ω , which is given by the spectral function $S_h(\omega, \mathbf{k}-\mathbf{q})$. However, in a physical decay process we have conservation of energy and momentum and hence there are severe restrictions to the values of the energies that the nucleon can have. This is why the occupation number $n_1(\mathbf{k}-\mathbf{q})$ cannot be factored out.

The actual calculations carried out in Ref. 16) showed that for light and medium nuclei the use of the spectral representation for the nucleon propagator, Eq. (25), instead of the one of the noninteracting Fermi sea, Eq. (6), has negligible consequences in the mesonic width (of the order of 6% corrections in ^{16}O). The corrections can be of the order of 50% in heavy nuclei, but in all cases, when the pionic renormalization is taken into account, one can disregard these effects.

These findings have been of relevance in showing similar problems in the study of other physical processes, like in the contribution of the pion cloud to K^+ nucleus scattering where one can show¹⁷⁾ that one cannot relate the effect of the pion cloud to the pion excess number in the nucleus as assumed in Refs. 18) and 19).

§ 6. Results for the mesonic width

In Refs. 3)~5) one can find abundant results in different nuclei which are rather realistic. These results have been recently improved¹³⁾ by a more accurate description of the energy balance in the particular reactions, taking into account transitions to the bound and continuum N states and using a pion nucleus optical potential which has been derived theoretically and leads to a good description of the data of pionic atoms and to elastic, reaction and absorption cross sections in the scattering processes.²⁰⁾ The potential allows the separation of its imaginary part into two terms related to pion absorption and quasielastic scattering. In Ref. 13) the pion quasielastic events are not removed from the pion flux, as it corresponds to the actual experimental observation, while the use of a full distortion of the pion with the total optical potential, as done in Refs. 3)~5), inevitably removes the pion quasielastic events, together with the pion absorption events. Though conceptually important, this refinement turns out to be of little practical relevance in the present problem given the small energy that the pions carry and the very small phase space for quasielastic collisions.¹³⁾ However, other considerations, particularly the energy balance in the reactions makes the widths in heavy nuclei for π^- -decay about one order of magnitude smaller than those of Ref. 5).

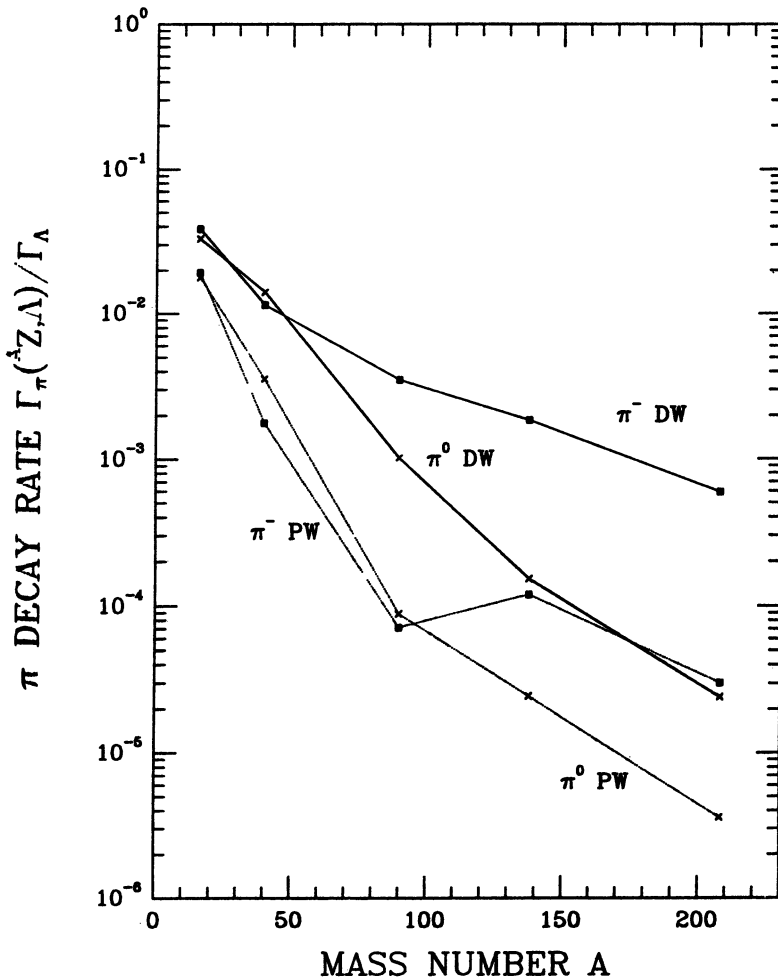


Fig. 6. Pionic decay rate for π^0 and π^- as a function of the mass number (of the host nucleus, ^{16}O , ^{40}Ca , ^{90}Zr , ^{138}Ba and ^{208}Pb). The two lower lines show the calculation with plane waves for the pion and the two upper lines the results with pion distorted waves.

In Fig. 6 we show the prediction of Ref. 13) for different nuclei and for π^0 and π^- decay, with plane waves and the renormalized pion wave function. The drastic effects of the pion renormalization are seen there and are a bit smaller than in former works because the energy balance makes the pions come out with smaller energies than in the previous approaches and the attractive effects of the p -wave part of the optical potential are then diminished.

Of particular relevance are the results in ^{12}C . One obtains the following:

	$\Gamma_{\pi^0}/\Gamma_\Lambda$	$\Gamma_{\pi^-}/\Gamma_\Lambda$	$\Gamma_{\pi^0}/\Gamma_{\pi^-}$
Ref. 13)	0.159	0.086	1.86
Ref. 5)	0.13	0.098	1.32
exp	$0.217 \pm 0.084^{10)}$	$0.052 \pm 0.033^9)$	

Although with large errors the experimental results confirm these striking theoretical predictions which show a large violation of the $\Delta T=1/2$ in nuclei ($\Gamma_{\pi^0}/\Gamma_{\pi^-}$ should be 0.5 under this rule) due mostly to nuclear shell effects.

Another interesting finding is seen in very light nuclei. The mesonic width of ${}^5\Lambda\text{He}$ has attracted particular attention. There, in addition to the pion renormalization, the repulsive character of the ΛN interaction and the relatively weaker medium range attraction, compared to the NN interaction, has as an effect the pushing of the Λ to the surface of the nucleus, weakening the Pauli blocking effect and thus enhancing the mesonic decay.^{21),22)} The experimental numbers clearly favour potentials with a repulsive ΛN core. One should note that such a repulsion automatically appears in quark based models of the ΛN interaction. A recent study of the ${}^5\Lambda\text{He}$ decay using a quark model based hypernuclear wave function²³⁾ leads to the following results:

	$\Gamma_{\pi^-}/\Gamma_{\Lambda}$	$\Gamma_{\pi^0}/\Gamma_{\Lambda}$	$\Gamma_{\text{tot}}/\Gamma_{\Lambda}$
Ref. 23)	0.431	0.239	0.670
exp	$0.44 \pm 0.11^9)$	$0.18 \pm 0.20^9)$	$0.59 \pm 0.31^4)$

These theoretical results are also in good agreement with those of Ref. 24) when a Λ wave function from the modified YNG ΛN interaction of Ref. 25), which has a strong repulsion at short distances, is used.

§ 7. The $2p2h$ induced decay around the pion branch

One of the interesting findings concerning the pionic decay was done in Ref. 26). The idea of this work, expressed in a different way, is the following: A real pion in a nuclear medium has a large width because of the coupling to $2p2h$ components which lead to pion absorption. This means that the strength of the pion is spread in a wide region, unlike a free pion which has all its strength accumulated in one point (one energy for a certain value of q). The decay leading to the emission of one pion is drastically reduced in nuclei because of Pauli blocking. However, one extreme of the pion distribution in the nucleus could be saved from Pauli blocking, because we can have a smaller energy for the pion and correspondingly more energy for the nucleon, and thus this part of the nuclear pion spectrum could participate in the Λ decay. Technically we could say that the strength of a free pion, which is accumulated in a δ function, becomes now a Breit Wigner distribution and part of the tail will correspond to a Pauli unblocked situation. Since the width of the Breit Wigner distribution at low pion energies is mostly due to pion absorption through $2p2h$ emission, the new mode would be observed as three particle emission from $\Lambda NN \rightarrow NNN$. This is depicted in Fig. 7.

In order to see this analytically we

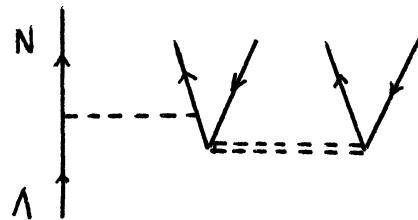


Fig. 7. Schematic representation of the Λ decay coupling to $2p2h$ components through virtual (close to real) pion absorption.

go back to Eq. (9). $\Gamma(k)$ is related to $\text{Im } D(q)$. Assume we have

$$\Pi(q^0, q) = \Pi_{ph} + \Pi_{\Delta h} \quad (29)$$

as done in Ref. 1). Then

$$\text{Im}D(q) = \frac{\text{Im}\Pi_{ph} + \text{Im}\Pi_{\Delta h}}{|q^{0^2} - q^2 - \mu^2 - \Pi|^2}. \quad (30)$$

Around the pion pole, when the denominator in (30) vanishes, $\text{Im } \Pi_{\Delta h}$ is extremely small because there is little phase space for pion quasielastic collisions and the Δ is far off shell. In addition, there $\text{Im } \Pi_{ph} = 0$ because a real pion cannot be absorbed by just one nucleon in nuclear matter. As a consequence we have a δ like distribution which corresponds to a pion in the medium, renormalized by a real pion selfenergy $\text{Re}\Pi \simeq \Pi_{ph} + \Pi_{\Delta h}$. Now, if in addition we consider the $2p2h$ part of the pion selfenergy leading to pion absorption we would have

$$\Pi(q^0, q) = \Pi_{ph} + \Pi_{\Delta h} + \Pi_{2p2h} \quad (31)$$

and now $\text{Im } \Pi_{2p2h} \neq 0$ for (q^0, q) close to on shell pions. As a consequence we will have around the pion pole the following strength of the pion propagator

$$\text{Im}D(q) \simeq \frac{\text{Im}\Pi_{2p2h}}{(q^{0^2} - q^2 - \mu^2 - \Pi_{ph} - \Pi_{\Delta h} - \text{Re}\Pi_{2p2h})^2 + (\text{Im}\Pi_{2p2h})^2}. \quad (32)$$

This is like a Breit-Wigner distribution in q^0 , except for the fact that Π_{2p2h} depends explicitly on the variable q^0 (and \mathbf{q}).

Since now there is overlap between $\text{Im } \Pi_{2p2h}$ and the pion pole one has to be cautious in the separation of the pionic width and the one associated to $2p2h$ emission. In Ref. 26) the calculations were done in infinite nuclear matter at normal nuclear matter density where the mesonic decay channel is forbidden. Hence, all the strength from Eq. (9) with $\text{Im } D(q)$ from Eq. (32) was attributed to the $2p2h$ channel. In finite nuclei, where there is some mesonic decay allowed, Eq. (9) with the distribution of Eq. (32) accounts simultaneously for the mesonic and $2p2h$ excitation channel. The separation of the two channels can be done by calculating the contribution of the pion pole and associating it to pion emission, and then associating to the $2p2h$ excitation channel the difference between the width calculated with Eqs. (9), (32) and the width from the pion pole contribution. The pion pole contribution is calculated by means of Eq. (9) substituting $\text{Im}D(q)$ by $-\pi\delta(q^{0^2} - q^2 - \mu^2 - \text{Re}\Pi(q^0, q))$. This is the way followed in Ref. 27). In addition a more realistic input for Π_{2p2h} is used in Ref. 27) taking care properly of the phase space available for the $2p2h$ excitation.

The results of Ref. 27) indicate that $\Gamma_{2p2h}/\Gamma_{\Lambda} \simeq 0.30$ for different nuclei from ^{12}C up to ^{208}Pb . In Ref. 26) this ratio had a value around 0.60 for values of the g_{Λ}^{\prime} parameter compatible with those used in Ref. 27).

Even with smaller values for $\Gamma_{2p2h}/\Gamma_{\Lambda}$ than those of Ref. 26), the existence of this channel has important repercussions in the number of neutrons and protons emitted in the Λ decay process, a piece of information which is used to determine the ratio of proton to neutron induced Λ decay in the nonmesonic channel. It is clear that in view of the new results one cannot associate all n or p emerging from the experiment to the

primary $\Lambda n \rightarrow nn$ or $\Lambda p \rightarrow np$ reactions and hence a reanalysis of the experimental data is needed. This analysis requires the consideration of the Λ nonmesonic decay channel, which we have not addressed here, hence the reader is addressed to this paper²⁷⁾ for further details.

Up to now the experiments for Λ decay have focused on two channels, the mesonic and the non-mesonic. In view of the former results and the fact that the $2p2h$ channel has a bigger strength than the mesonic one from nuclei like ^{16}O up, it would be very interesting to conduct experimental searches for this channel too.

§ 8. Conclusions

We have made a review of the present situation concerning the mesonic decay of Λ hypernuclei. We have established the formal link between the propagator method, where the huge enhancement of the pionic decay width was first reported, and the finite nuclei approach with wave functions and matrix elements. Shell effects and precise values of the nuclear binding energies are also important in the mesonic width and they are best taken into account in the finite nuclei approach. The intuitive and appealing, but fallacious, link between the nucleon occupation number and the mesonic width has also been discussed, which has served to unveil rough approximations used in other processes to link the pion excess number with contributions of the nuclear meson cloud to some physical observables, like K^+ nucleus scattering. We have also discussed the relevance of the short range ΛN repulsion in the mesonic width of light hypernuclei and showed how the repulsion provided by quark models of the ΛN interaction can naturally account for the present experimental widths. Finally we have discussed the Λ decay induced by pairs of nucleons through the tail of the pion distribution in the nucleus, which “cheats” the Pauli blocking and leads to a three nucleon decay channel, $\Lambda NN \rightarrow NNN$.

With the limited amount of experimental data available on the mesonic channel, the amount of physical information obtained is remarkable. There is support for strong ΛN repulsion at short distances providing indirect support for quark models of the ΛN interaction; the process provides us with the most striking renormalization effect due the pion nucleus interaction. Furthermore, the “cheating” of Pauli blocking by the $2p2h$ induced decay can provide good information on the coupling of the pion to these nuclear components, a very valuable complement to real pion absorption, etc. The sensitivity of the Λ decay to the pion nucleus optical potential can also serve as a tool to choose between different theoretical descriptions of the complex mechanisms of pion nucleus interaction. The decay channel into π^0 can be an excellent instrument to learn about π^0 nucleus interaction, and so on.

It is clear that a systematic experimental search in many nuclei of the mesonic decay channel and its related $2p2h$ induced decay mode will provide us with very valuable information to unravel the intricacies of the pion nucleus interaction or the elementary properties of the ΛN interaction, as well as proper nuclear structure details of the Λ hypernuclei themselves.

Acknowledgements

This work has been partially supported by CICYT contract No. AEN 931205, PB92-0927, PB 92-0761. One of us, J. N. wishes to acknowledge financial support from the European Union.

References

- 1) E. Oset and L. L. Salcedo, Nucl. Phys. **A443** (1985), 704.
- 2) E. Oset and L. L. Salcedo, Nucl. Phys. **A450** (1986), 371c.
- 3) K. Itonaga, T. Motoba and H. Bandō, Z. Phys. **A330** (1988), 209.
- 4) T. Motoba, K. Itonaga and H. Bandō, Nucl. Phys. **A489** (1988), 683.
- 5) T. Motoba, Nucl. Phys. **A527** (1991), 485c; Few Body Systems, Suppl. 5 (1992), 386; Proc. Int. Sym. on Hypernuclear and Strange Particle Physics, Shimoda, 1991 [Nucl. Phys. **A547** (1992), 115c].
- 6) R. Grace et al., Phys. Rev. Lett. **55** (1985), 1055.
- 7) A. Sakaguchi et al., Nuovo Cim. **102A** (1989), 511.
- 8) P. D. Barnes, Nucl. Phys. **A450** (1986), 43c; **A478** (1988), 127c.
- 9) J. J. Szymanski et al., Phys. Rev. **C43** (1991), 849.
- 10) A. Sakaguchi et al., Phys. Rev. **C43** (1991), 73.
- 11) E. Oset, P. Fernández de Córdoba, L. L. Salcedo and R. Brockmann, Phys. Rep. **188** (1990), 79.
- 12) R. J. Glauber, *Lectures in Theor. Phys.* (Interscience, New York, 1959), vol. 1, p. 315.
- 13) J. Nieves and E. Oset, Phys. Rev. **C47** (1993), 1478.
- 14) H. Bandō and H. Takaki, Phys. Lett. **B150** (1985), 409.
- 15) S. Fantoni and V. R. Pandharipande, Nucl. Phys. **A427** (1984), 473.
- 16) P. Fernández de Córdoba and E. Oset, Nucl. Phys. **A528** (1991), 736.
- 17) C. García-Recio, J. Nieves and E. Oset, Phys. Rev. C, to be published.
- 18) S. V. Akulinichev, Phys. Rev. Lett. **68** (1992), 290.
- 19) M. F. Jiang and D. S. Koltun, Phys. Rev. **C46** (1992), 2462.
- 20) J. Nieves, E. Oset and C. García-Recio, Nucl. Phys. **A554** (1993), 509, 554.
- 21) Y. Kurihara, Y. Akaishi and H. Tanaka, Phys. Rev. **C31** (1985), 971.
- 22) E. Oset, L. L. Salcedo and Q. N. Usmani, Nucl. Phys. **A450** (1986), 67c.
- 23) U. Straub, J. Nieves, A. Faessler and E. Oset, Nucl. Phys. **A556** (1993), 531.
- 24) T. Motoba, H. Bandō, T. Fukuda and J. Žofka, Nucl. Phys. **A534** (1991), 597.
- 25) Y. Yamamoto and H. Bandō, Prog. Theor. Phys. **73** (1985), 905; Prog. Theor. Phys. Suppl. No. 81 (1985), ch. II.
- 26) W. M. Alberico, A. de Pace, M. Ericson and A. Molinari, Phys. Lett. **B256** (1991), 134.
- 27) A. Ramos, E. Oset and L. L. Salcedo, Phys. Rev. C, to be published.



ELSEVIER

Nuclear Physics A 611 (1996) 568–586

NUCLEAR
PHYSICS A

Coherent, semicoherent and incoherent pion production in heavy-ion reactions

B. López Alvaredo^a, E. Oset^{a,b}, M.J. Vicente-Vacas^{a,b}, S.W. Huang^a,
P. Fernández de Córdoba^{a,c}, Amand Faessler^a

^a *Institut für Theoretische Physik der Universität Tübingen, Tübingen, Germany*

^b *Departamento de Física Teórica and IFIC, Centro Mixto Universidad de Valencia - CSIC,
46100 Burjassot (Valencia), Spain*

^c *Departamento de Matemática Aplicada, Universidad Politécnica de Valencia, Valencia, Spain*

Received 10 November 1995; revised 1 August 1996

Abstract

Two types of coherent pion production in heavy-ion collisions are studied and calculations are performed for ^{12}C against ^{12}C collisions. The first one, doubly coherent production, produces a pion in one nucleus leaving it in its ground state, while the second nucleus is excited to the 1^+ , $T = 1$ state. The second process, semicoherent production, also leaves in its ground state the nucleus where the pion is produced while the second one is broken. The cross sections for forward pions are compared to the standard incoherent production process. We observe that at energies below 130 MeV/A the semicoherent process dominates the cross section for forward pion angles while at large energies around 800 MeV/A it represents a fraction of around 30% of the incoherent cross section. The doubly coherent process leads to smaller cross sections, still in the measurable range for energies above 200 MeV/A.

PACS: 25.70.-z; 25.40.Qa

1. Introduction

Pion production in heavy-ion reactions has been extensively studied both experimentally [1–7] and theoretically [8–15]. Many of the efforts have been devoted to the interesting phenomenon of subthreshold pion production [2–7]. The fact that pion production is forbidden for a simple NN collision has stimulated a large number of works where either the role of Fermi motion or some cooperative phenomena between the nucleons has been exploited in order to understand the data [16–22]. The different mechanisms, however, rely upon elementary cross sections but possible coherent

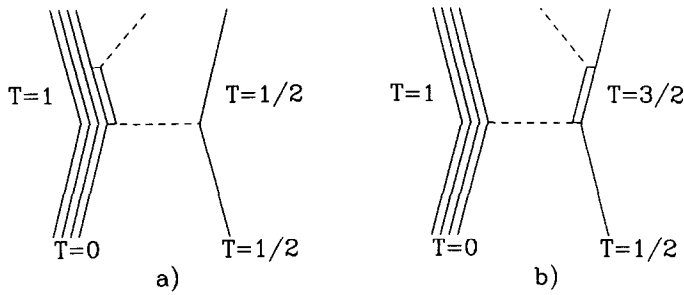


Fig. 1. Two mechanisms for Δ excitation in (α, α') collisions on the proton. (a) Δ excitation in the projectile; (b) Δ excitation in the target (forbidden by isospin).

phenomena, in the quantum mechanical sense, where the individual contribution of the nucleons is summed up in the amplitudes, is ignored. One exception is the work of Ref. [10] where the explicit coherent excitation of the 1^+ , $T = 1$ state in one of the nuclei is studied in detail, while an incoherent sum over the contributions of the nucleons in the other nucleus is done.

The present work continues the line started in Ref. [10] and considers two new mechanisms of coherent production:

- (i) Doubly coherent production, in which one of the nuclei is excited to the 1^+ , $T = 1$ state, while the second one is left in the ground state.
- (ii) Semicoherent production in which one nucleus remains in the ground state and the second one is broken.

The equivalent problem in the proton–nucleus case is coherent pion production induced by protons. This problem, and the related one in the $({}^3\text{He}, t)$ reaction, has attracted much attention lately, with the theoretical observation that a sizable fraction of the pions produced in pA or ${}^3\text{He}A$ collisions corresponds to coherent pion production where the target nucleus is left in its ground state [23–25]. Partial experimental results in the $({}^3\text{He}, t)$ reaction [26] and p –nucleus collisions [27] confirm the theoretical findings. More devoted experiments are now under way [28,29]. Some interesting features are attached to the coherent pion production: (i) the reaction is basically sensitive to the longitudinal part of the spin–isospin interaction in the $NN \rightarrow N\Delta$ transition; (ii) the pions are produced in a narrow cone along the direction of the (p, p') momentum transfer and preferably forward when the p' goes in the forward direction; (iii) the energy distribution has a Δ peak considerably shifted towards lower excitation energies with respect to the free Δ peak in the $NN \rightarrow N\Delta$ reaction. This latter feature is partly responsible for the shift of the Δ peak observed in the $({}^3\text{He}, t)$ reaction on ${}^{12}\text{C}$ [30,31].

The most striking experimental evidence of coherent pion production comes from the (α, α') reaction on proton targets [32]. In this experiment, aimed at looking for the Roper excitation, one finds a much larger Δ peak which correspond to Δ excitation in the projectile. Indeed the Δ excitation in the p target is forbidden by isospin conservation as shown in Fig. 1. Thus the Δ excitation peak in this experiment can be interpreted as coherent pion production on the ${}^4\text{He}$ nucleus, since a pion is produced in the $p{}^4\text{He}$

collision leaving the nucleus of ${}^4\text{He}$ in its ground state.

In Ref. [33], a model for the (α, α') reaction, consistent with the scheme used to evaluate coherent pion production in [25], was used and the experimental data were well reproduced. The same model will be used to describe the doubly coherent and semicoherent pion production processes. The results are compared with the incoherent production mechanisms generated by means of a cascade procedure as done in [34,35].

One of the findings of the calculations is that at high energies the semicoherent process provides a sizable fraction of the forward produced pions and at energies below 130 MeV/A it dominates over the incoherent production mechanisms. The pion energy spectra has also peculiar features which should help identify experimentally this interesting source of subthreshold pion production.

The paper proceeds as follows. In Section 2 we show the scheme to calculate the doubly coherent pion production. In Section 3 we study the semicoherent pion production mechanisms and in Section 4 we outline the method used in Ref. [34] to produce pions incoherently. The results are shown in Section 5 and some concluding remarks are made in Section 6.

2. Doubly coherent pion production

The process we study is

$$A + A \rightarrow A(T = 1) + A(\text{g.s.}) + \pi^0, \quad (1)$$

where A is a spin-isospin saturated nucleus for simplicity. We shall work out the specific case with the nucleus of ${}^{12}\text{C}$. Thus the reaction we study is

$${}^{12}\text{C} + {}^{12}\text{C} \rightarrow {}^{12}\text{C}^*(J^\pi = 1^+, T = 1, 15.11 \text{ MeV}) + {}^{12}\text{C}(\text{g.s.}) + \pi^0 \quad (2)$$

The process is depicted in Fig. 2. The projectile ${}^{12}\text{C}$ emits a virtual pion exciting the ${}^{12}\text{C}^*$. The virtual pion interacts with the ${}^{12}\text{C}$ target and becomes a real pion leaving the target nucleus in the ground state. Note that a $T = 1$ state in the projectile has to be necessarily excited in the mechanisms depicted in Fig. 2.

The analogy with the coherent pion production on ${}^{12}\text{C}$ with the $({}^3\text{He}, t)$ reaction is complete, with some minor differences:

- (i) A π^0 is produced instead of a π^+ in the $({}^3\text{He}, t)$ case. Technically this means a $\sqrt{2}$ isospin factor is now replaced by 1.
- (ii) The $({}^3\text{He}, t)$ transition form factor is now replaced by the $({}^{12}\text{C}, {}^{12}\text{C}^*)$ transition form factor.
- (iii) The kinematics is adjusted to the $({}^{12}\text{C}, {}^{12}\text{C}^*)$ reaction.
- (iv) The distortion of the ${}^3\text{He}$, or t waves through ${}^{12}\text{C}$ is now replaced by the distortion of the ${}^{12}\text{C}$ or ${}^{12}\text{C}^*$ through ${}^{12}\text{C}$.

We can thus use the results from Ref. [25] implementing these minor changes here. We thus save details on the derivation of the formula which can be seen in [25].

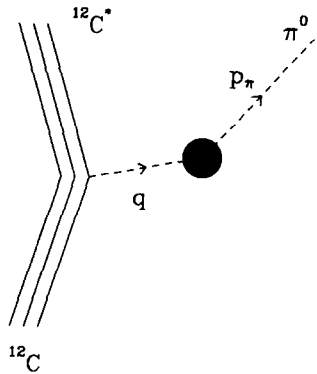


Fig. 2. Mechanism for coherent pion production on the ^{12}C target in ^{12}C scattering against ^{12}C , leading to the $l^+, T = 1$ excited state of ^{12}C in the projectile.

We find then, assuming for the moment that the $^{12}\text{C}^*$ is formed from the beam

$$\frac{d\sigma}{d\Omega^* dE^* d\Omega_\pi} = \frac{1}{(2\pi)^5} \frac{M_C^2 M_{C^*} p_C p_\pi}{\lambda^{1/2}(s, M_C^2, M_C^2)} \sum_M T_M T_M^* \quad (3)$$

where

$$\begin{aligned} -iT_M = & -\frac{f}{\mu} \sqrt{\frac{-q^2}{q^2}} \int d^3x \phi_{C^*}^*(\mathbf{x}) \phi_C(\mathbf{x}) F_{C,C^*}(q) \xi_M^i \left(\frac{q_i F^2(q)}{q^{02} - q^2 - \mu^2} \Pi^{(s)}(\mathbf{x}) \right. \\ & \left. - [V_L' \hat{q}_i \hat{q}_j + V_T'(\delta_{ij} - \hat{q}_i \hat{q}_j)] \bar{\Pi}^{(p)}(\mathbf{x}) i \nabla_j \right) \phi_{\text{out}}^*(\mathbf{p}_\pi, \mathbf{x}), \end{aligned} \quad (4)$$

where $\Pi^{(s)}, \bar{\Pi}^{(p)}$ are the s -wave and p -wave parts of the pion ^{12}C optical potential written as

$$\Pi(\mathbf{r}) = \Pi^{(s)}(\mathbf{r}) + \nabla \bar{\Pi}^{(p)}(\mathbf{r}) \nabla \quad (5)$$

and V_L', V_T' the longitudinal and transverse parts of the spin-isospin interaction

$$V_L'(q) = \frac{q^2}{q^{02} - q^2 - \mu^2} F^2(q) + g', \quad (6)$$

$$V_T'(q) = \frac{q^2}{q^{02} - q^2 - m_\rho^2} F_\rho^2(q) C_\rho + g'. \quad (7)$$

$F(q)$ is the πNN vector form factor and $F_\rho(q)$ the ρNN one. They are taken of the monopole type with $\Lambda_\pi = 1300$ MeV and $\Lambda_\rho = 1400$ MeV and $C_\rho = 3.96$ [36], $g' = 0.6$. $\phi_{\text{out}}^*(\mathbf{p}_\pi, \mathbf{x})$ is the outgoing pion wave function, taken as a solution of the Klein–Gordon equation with the potential of Ref. [37]. ξ_M is the unit vector in the spherical base and $F_{C,C^*}(q)$ the transition C, C^* form factor, which can be obtained from Ref. [10] or from the appendix of Ref. [38]

$$F(q) = \frac{4}{3}\sqrt{2} \left(1 + \frac{q^2}{4\alpha^2}\right) e^{q^2/4\alpha^2}, \quad (8)$$

where the factor q^2 which appears in the usual form factor in the nucleus rest frame (or better the Breit frame) has been substituted by $-q^2$ to allow us using it in any frame of reference. In Eq. (8) $\alpha^2 = 0.37 \text{ fm}^{-2}$ is the ^{12}C oscillator parameter. The factor $\xi_{M \cdot q}$ which appear in the C , C^* form factor induced by the pion has been incorporated in Eq. (4).

Since the process is coherent and we do not want any of the nuclei to break, we must use proper distorted waves and hence we have in an eikonal approximation [25]

$$\phi_{C^*}(\mathbf{x})\phi_C(\mathbf{x}) = \exp(i(\mathbf{p}_C - \mathbf{p}_{C^*})\mathbf{x}) \exp\left[-\frac{1}{2} \int_{-\infty}^{\infty} \sigma(1 - i\eta)\tilde{\rho}(\mathbf{b}, z') dz'\right], \quad (9)$$

where σ is the ^{12}CN total cross section (the elastic part removes flux when the target is broken and the inelastic one when the projectile is broken) and $\eta = 0.275$ is the ratio of the real to imaginary part in the NN interaction, which in practice plays a negligible role here. In Eq. (9) $\tilde{\rho}$ is the convoluted density of ^{12}C – ^{12}C normalized to A and the ^{12}CN total cross section is again calculated with the Glauber formula

$$\sigma_{CN} = 2 \int d^2b \left(1 - \exp\left[-\frac{1}{2} \int_{-\infty}^{\infty} \sigma_{NN}(1 - i\eta)\rho_C(\mathbf{b}, z) dz\right]\right) \quad (10)$$

with $\sigma_{NN} = 40 \text{ mb}$ and ρ_C the ^{12}C density.

In order to care about the Lorentz invariance of the T_M matrix, the factor $\sqrt{-q^2/q^2}$ is implemented in Eq. (4) since the transition form factor is calculated with the σq nonrelativistic vertex, and furthermore \mathbf{q} in V_L^i , V_T^i is evaluated in the frame where $(q + p_N)$ is at rest [25], with p_N an average nucleon momentum in the ^{12}C target nucleus.

In order to make connection and use the same formalism as in the former work of coherent pion production we have assumed the coherent pion production taking place in the target and the $^{12}\text{C}^*$ excitation occurring in the projectile. We can easily get the contribution of the symmetrical case where the coherent pions are produced in the projectile and the excitation of the ^{12}C occurs in the target. The easiest way to implement this is to recall that

$$\sigma = \int \frac{d^3p_\pi}{(2\pi)^3} \frac{1}{2\omega_\pi} F(z), \quad (11)$$

where $F(z)$ is an invariant magnitude under collinear frame transformations, since both σ and $\int d^3p_\pi/\omega_\pi$ are then invariant. Hence in another collinear frame

$$\frac{d\sigma}{d\tilde{\omega}_\pi d\tilde{\Omega}_\pi} = \frac{\tilde{p}_\pi}{p_\pi} \frac{d\sigma}{d\omega_\pi d\Omega_\pi}. \quad (12)$$

In order to get the frame where the pions are produced coherently in the beam we make two steps. From the former frame we pass to the frame where the original ^{12}C

of the beam is at rest. The next step makes a rotation of angle π around the y axis (perpendicular to the z axis and in the scattering plane of the pion) so that the ^{12}C where the pions are produced approaches the target from the left (instead of the right after the boost). In the boosted frame where the original ^{12}C of the beam is now at rest we have

$$\tilde{p}'_{\pi} = \left[\left(\frac{E_A}{M_A} - 1 \right) \frac{\mathbf{p}_A \cdot \mathbf{p}_{\pi}}{p_A^2} - \frac{\omega_{\pi}}{M_A} \right] \mathbf{p}_A + \mathbf{p}_{\pi}, \quad (13)$$

where the subindex A is referring to the ^{12}C of the original beam. If we limit ourselves to the forward direction and after the rotation is made we find

$$\tilde{p}_{\pi} = -\frac{E_A}{M_A} \left(1 - \frac{V_A}{V_{\pi}} \right) p_{\pi}. \quad (14)$$

As we shall see later, at $T_A/A = 100, 200, 500$ MeV and 0° the peak of the pion kinetic energy distribution is around 35, 100, 200 MeV, respectively. Then \tilde{p}_{π} corresponding to these pions is negative and corresponds to backward propagating pions. We thus conclude that the coherent pions produced in the projectile move mostly backwards in the lab frame and contribute little to the forward pion cross section. The main source of forward pions corresponds then to pions produced coherently in the ^{12}C target.

3. Semicoherent pion production

Now we study the process



and we will consider π^0 , π^+ and π^- production. X will account for all excited states of ^{12}C going mostly to nucleon emission. In our approach we shall consider that the ^{12}C as a whole collides with one nucleon of the target, exciting it above the Fermi sea, and will sum the contribution (incoherent since the nucleus breaks) of all nucleons in the target. We also consider the direct contribution of two nucleons in the target, following the approach of Ref. [39] to account for two-nucleon induced Λ decay in nuclei, which has been recently revised in [40].

3.1. One-nucleon mechanism

We assume first that the coherent production of pions occurs in the projectile and the breakup in the target. Later on we shall consider the opposite case. It is then instructive to show explicitly the process of coherent pion production in the projectile. Based on the observation that the pion–nucleus optical potential is dominated by Δ excitation we can write the mechanism for coherent pion production in the projectile with the diagrammatic representation of Fig. 3, which is used to study the (α, α') reaction on the proton in Ref. [33].

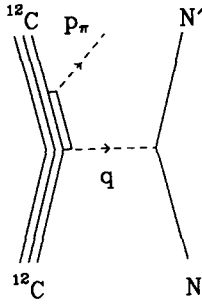


Fig. 3. Model for coherent pion production on the projectile in the scattering of ^{12}C against one nucleon of the ^{12}C target.

The cross section for the process depicted in Fig. 3 for a π^0 production is given by

$$\sigma = \frac{1}{v_{\text{rel}}} \int \frac{d^3 p_{C'}}{(2\pi)^3} \int \frac{d^3 p_{\pi}}{(2\pi)^3} \frac{M_C}{E_C} \frac{M_{C'}}{E_{C'}} \frac{M}{E_N} \frac{M}{E_{N'}} \frac{1}{2\omega_{\pi}} \times F_C(p_{\pi}, q)^2 \overline{\sum} \sum |T|^2 (2\pi) \delta(E_C - E_{C'} + E_N - E_{N'} - \omega_{\pi}). \quad (16)$$

In order to account for the contribution of all nucleons in the target nucleus, considering Pauli blocking and Fermi motion, and taking $M/E_N, M/E'_{N'} = 1$ for the nucleons of the target we write

$$\sum_{i \in F} \pi \delta(z) \equiv 4 \int \frac{d^3 k}{(2\pi)^3} \frac{d^3 r}{(2\pi)^3} n(\mathbf{k}) [1 - n(\mathbf{k} + \mathbf{q})] \pi \delta(q^0 + E_N(\mathbf{k}) - E_N(\mathbf{k} + \mathbf{q})) \equiv - \int d^3 r \text{Im} U(q^0, \mathbf{q}, \rho(\mathbf{r})), \quad (17)$$

where $U(q^0, \mathbf{q})$ is the Lindhard function for ph excitation [41], with the normalization of the appendix of [42] and

$$q^0 = E_C - E_{C'} - \omega_{\pi}, \quad \mathbf{q} = \mathbf{p}_C - \mathbf{p}_{C'} - \mathbf{p}_{\pi}, \quad (18)$$

Hence

$$\frac{d\sigma}{d\omega_{\pi} d\Omega_{\pi}} = \frac{M_C^2 p_{\pi}}{(2\pi)^3 p_C} \int d^3 r \int \frac{d^3 p_{C'}}{(2\pi)^3} \frac{1}{E_{C'}} \times |F_C(p_{\pi}, q)|^2 \overline{\sum} \sum |T|^2 (-) \text{Im} U(q^0, \mathbf{q}, \rho(\mathbf{r})), \quad (19)$$

where $\overline{\sum} \sum |T|^2$ is given in analogy to [33] by

$$\overline{\sum} \sum |T|^2 = 3 \left| 12 \frac{4}{9} \left(\frac{f^*}{\mu} \right)^2 \frac{f}{\mu \sqrt{s_{\Delta}} - M_{\Delta} + i \frac{1}{2} \Gamma(s_{\Delta})} \right|^2 \times \left\{ (V_l'^2 - V_t'^2) \frac{(\mathbf{p}_{\pi} \mathbf{q})^2}{q^2} + V_t'^2 p_{\pi}^2 \right\} \frac{p_{\pi \text{CM}}^2}{p_{\pi}^2}, \quad (20)$$

where V'_l , V'_t are given by Eqs. (6), (7) and $\mathbf{p}_{\pi\text{CM}}$ is the pion CM momentum in the frame where the Δ in Fig. 3 is at rest.

In Eq. (19) we also have the ^{12}C form factor which is given by

$$\begin{aligned} F_C(p_\pi, q) &= F_C(p_C - p_{C'}) \\ &= \int d^3R \exp(i(\mathbf{p}_C - \mathbf{p}_{C'})\mathbf{R}) \int d^3r' \rho(\mathbf{r}') \frac{1}{A} \rho(\mathbf{R} - \mathbf{r}') \\ &\quad \times \exp\left(-\frac{1}{2} \int d^2s \sigma_{NN} T(s) T(\mathbf{b} - \mathbf{s})\right), \end{aligned} \quad (21)$$

where \mathbf{p}_C , $\mathbf{p}_{C'}$ are written in the rest frame of the ^{12}C of the beam, σ_{NN} the NN total cross section, \mathbf{b} is the impact parameter for the variable \mathbf{R} and $T(s)$ is the thickness function. This is the formula of Czȳz and Maximon [43] which takes into account the distortion of the ^{12}C of the beam by the ^{12}C of the target, and explicit formulas for its evaluation in ^{12}C are given in Ref. [10] (Eq. (3.51)). The pion wave should also be distorted. In practice, given the highly peripheral character that the distortion of ^{12}C by ^{12}C gives to this reaction, the distortion of forward pions is small. This is particularly true at low energies when the pions come with small energies for which the distortion is negligible.

Once again we must ask ourselves what is the contribution from coherent pion production in the target. For this purpose we repeat the arguments which led from Eqs. (11) to (14). As we shall see later, now the momenta of the forward pions are very small. For instance at $T_A/A = 100, 200$ MeV the pion energy distribution peaks at around pion kinetic energies of 10, 25 MeV. By means of Eq. (14) one sees now that v_π is smaller than v_A and hence \vec{p}_π has the same sign as p_π and we get a contribution for pions propagating forward. This contribution is, however, small, 20% increase of the cross section at $T_A/A = 100$ and 6% at $T_A/A = 200$ with a tendency to give smaller contributions at higher energies. However, we also get backward-going pions in the frame moving with the projectile. All these correspond to forward pions after the boost and the rotation (Eq. (14)). We will show the corresponding contributions in the results section.

3.2. Two-nucleon mechanism

We have also evaluated the contribution from the excitation of $2p2h$ in the target, by replacing $\text{Im } U$ by the corresponding pion polarization function for the excitation of $2p2h$. The expression of this function in terms of the ordinary Lindhard function is given in Ref. [44] and the normalization is chosen such as to get the experimental strength of the imaginary part of the pion–nucleus optical potential for pionic atoms, following the same steps as in [39,40]. We found negligible results for this contribution and for this reason we omit further details.

4. Incoherent pion production

The incoherent pion production is based on the microscopic transport model of heavy-ion reactions. The first pion production with the transport model was carried out by the cascade model [45]. The cascade model simulates heavy-ion collisions at high bombarding energies on a microscopic level by treating nucleus–nucleus collisions as a superposition of independent two-body BB collisions (B stands for either a nucleon N or a delta resonance Δ).

In the cascade model the Fermi motion cannot be implemented in a consistent way. Later on G.F. Bertsch et al. studied pion production by the BUU equation [46]. In the BUU model the Fermi motion, nuclear selfconsistent mean fields and Pauli blocking are included.

In our calculation of pion production, we employ the QMD model [34] which is widely used by the FOPI collaboration. Instead of the test particle method used in solving the BUU equation, in the QMD model one uses N -particles (N is the total mass number of the projectile and the target) for the simulation for each event. In order to reduce the numerical fluctuations of the mean field, one describes each particle by a Gaussian wave packet. In this model, the Hamiltonian for the system is given by a Skyrme-type NN interaction consisting of two-body and three-body interactions:

$$V^{\text{loc}} = t_1 \delta(\mathbf{r}_1 - \mathbf{r}_2) + t_2 \delta(\mathbf{r}_1 - \mathbf{r}_2) \delta(\mathbf{r}_1 - \mathbf{r}_3). \quad (22)$$

By folding the Gaussian wave packet, one obtains the Hamiltonian for the system as

$$H_N^{\text{QMD}} = \sum_{i=1}^N \frac{\mathbf{p}_{i0}^2}{2m} + \frac{\alpha}{2\rho_0} \sum_i \left[\sum_{j(\neq i)} \frac{1}{(4\pi L)^{3/2}} \exp(-(\mathbf{r}_{i0} - \mathbf{r}_{j0})^2/4L) \right] + \frac{\beta}{\gamma + 1} \frac{1}{\rho_0^\gamma} \sum_i \left[\sum_{j(\neq i)} \frac{1}{(4\pi L)^{3/2}} \exp(-(\mathbf{r}_{i0} - \mathbf{r}_{j0})^2/4L) \right]^\gamma, \quad (23)$$

where the index “0” refers to the center of the Gaussian and ρ_0 is the normal nuclear matter density ($\rho_0 = 0.17 \text{ fm}^{-3}$).

The three-body term in Eq. (22) can be extended using a density-dependent interaction giving an arbitrary γ for the nuclear equation of state (EOS) in nuclear matter [34]. $L = 1.08 \text{ fm}^2$, α , β and γ , the parameters appearing in Eq. (23), are listed in Table 1. The evolution of the particles is governed by the classical Hamilton equations of motion.

In light colliding systems such as the $^{12}\text{C} + ^{12}\text{C}$ collisions considered in this paper, one does not expect to obtain a high-density zone. A series of studies on pion production shows that pion production has a weak dependence on the nuclear EOS [35]. We use the parameter of the soft EOS in our calculations. In our pion production, we emphasize the role of Fermi motion and the role of the delta resonance. The delta resonance can be produced, propagated and annihilated in the simulation of the HI reaction. The pions are produced through the decay of all delta’s at freeze-out, which is defined as the final state where there is no interaction between any two particles [46].

Table 1
The parameters of the Skyrme parametrization for the equation of state and the incompressibilities

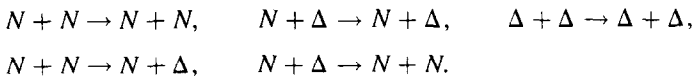
	α (MeV)	β (MeV)	γ	K (MeV)
soft	-356.0	303.0	7/6	200.0
hard	-124.0	70.5	2	380.0

The collision term in QMD is treated in the same way as BUU, i.e. we use the so-called Cugnon parametrization. Two particles may undergo scattering if they approach each other with a minimum distance of less than $\sqrt{\sigma^{\text{tot}}(\sqrt{s})}/\pi$,

$$|\mathbf{r}_{i0} - \mathbf{r}_{j0}| \leq b_{\text{max}} = \sqrt{\frac{\sigma^{\text{tot}}(\sqrt{s})}{\pi}},$$

where σ^{tot} is the total free NN cross section. The Pauli principle is included by Monte Carlo methods.

In the Cugnon parametrizations the Δ resonance is included. So we have the following processes during the time evolution of the nucleus–nucleus collision:



For elastic channels:

$$\text{elastic} : \begin{cases} N + N \rightarrow N + N & \text{(a),} \\ N + \Delta \rightarrow N + \Delta & \text{(b),} \\ \Delta + \Delta \rightarrow \Delta + \Delta & \text{(c),} \end{cases}$$

we use, for the total cross section and the differential cross section:

$$\left\{ \begin{aligned} \sigma_{\text{el}}(\sqrt{s}) &= 55 \text{ [mb]}, & \sqrt{s} &\leq 1.8993 \text{ GeV}, \\ &= 20 + \frac{35}{1 + 100(\sqrt{s} - 1.8993)} \text{ [mb]}, & \sqrt{s} &> 1.8993 \text{ GeV}, \\ \text{angular distribution} &: \frac{d\sigma}{dt} \propto e^{bt}, & t &= -2p^2(1 - \cos \theta), \\ b(\sqrt{s}) &= \frac{6[3.65(\sqrt{s} - 1.866)]^6}{1 + [3.65(\sqrt{s} - 1.866)]^6}. \end{aligned} \right. \quad (24)$$

We have two inelastic channels:

$$\text{inelastic} : \begin{cases} N + N \rightarrow N + \Delta & \text{(d),} \\ N + \Delta \rightarrow N + N & \text{(e).} \end{cases}$$

For the Δ excitation channel (d), we use the total and differential cross sections obtained by the one-boson-exchange model [47], i.e. the total cross section of $NN \rightarrow N\Delta$ is parametrized as

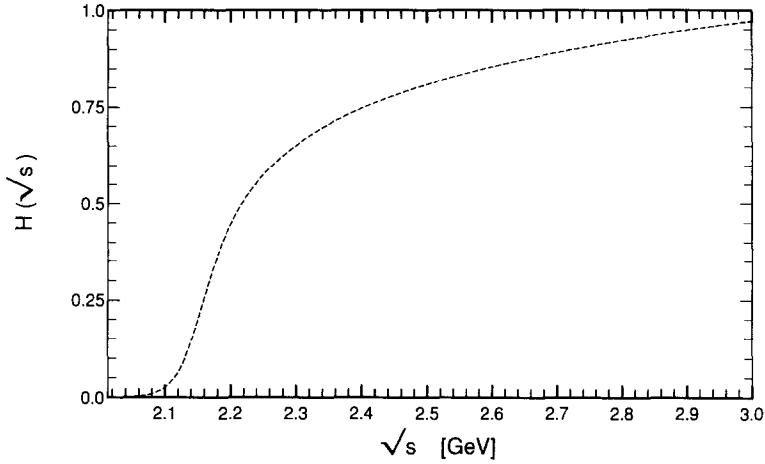


Fig. 4. The factor $H(\sqrt{s})$ of Eq. (29) appearing in the modified detailed balance formula of Eq. (26).

$$\left\{ \begin{array}{ll} \sigma_{NN \rightarrow N\Delta}(\sqrt{s}) = 0, & \sqrt{s} \leq 2.014 \text{ GeV}, \\ = 1341(\sqrt{s} - 2.014)^{2.819} \text{ [mb]}, & 2.014 < \sqrt{s} < 2.20 \text{ GeV}, \\ = 18.51 - 235.2(\sqrt{s} - 2.370)^2 \text{ [mb]}, & 2.20 < \sqrt{s} < 2.45 \text{ GeV}, \\ = 1591(\sqrt{s})^{-4.957} \text{ [mb]}, & 2.45 < \sqrt{s} < 4.50 \text{ GeV} \end{array} \right. \quad (25)$$

and the differential cross section of $NN \rightarrow N\Delta$ is given by

$$\left\{ \begin{array}{ll} \text{angular distribution of } NN \rightarrow N\Delta : & \frac{d\sigma}{d\cos\theta} \propto e^{b|\cos\theta|} \text{ with} \\ b = 19.71(\sqrt{s} - 2.014)^{1.551}, & 2.014 < \sqrt{s} < 2.43 \text{ GeV}, \\ = 33.41 \arctan[0.5404(\sqrt{s} - 2.146)^{0.9784}], & 2.43 < \sqrt{s} < 4.50 \text{ GeV}. \end{array} \right. \quad (26)$$

Since the delta resonance has a width, the cross section for $N\Delta \rightarrow NN$ obtained from detailed balance from the $NN \rightarrow N\Delta$ must take into account that $NN \rightarrow N\Delta$ reaction is restricted to Δ masses with $m_\Delta < \sqrt{s} - m_N$. In our work, we have taken this into account and have improved the Δ absorption by the method of “extended detailed balance”, which has proved to be important in the description of eta and dilepton production [48].

Therefore, the cross section for the Δ absorption, i.e. channel (c), can be obtained from the cross section of $N + N \rightarrow N + \Delta$ with the use of the extended detailed balance principle:

$$\frac{d\sigma_{N\Delta \rightarrow NN}(\sqrt{s})}{d\Omega} = \frac{1}{8} (p_f^2/p_i^2) \frac{d\sigma_{NN \rightarrow N\Delta}(\sqrt{s})}{d\Omega} \frac{1}{\int_{(m_N+m_\pi)^2}^{(\sqrt{s}-m_N)^2} F(M^2) dM^2}, \quad (27)$$

where \sqrt{s} is the invariant mass of two colliding baryons:

$$\sqrt{s} = \sqrt{(E_1 + E_2)^2 - (\mathbf{P}_1 + \mathbf{P}_2)^2}.$$

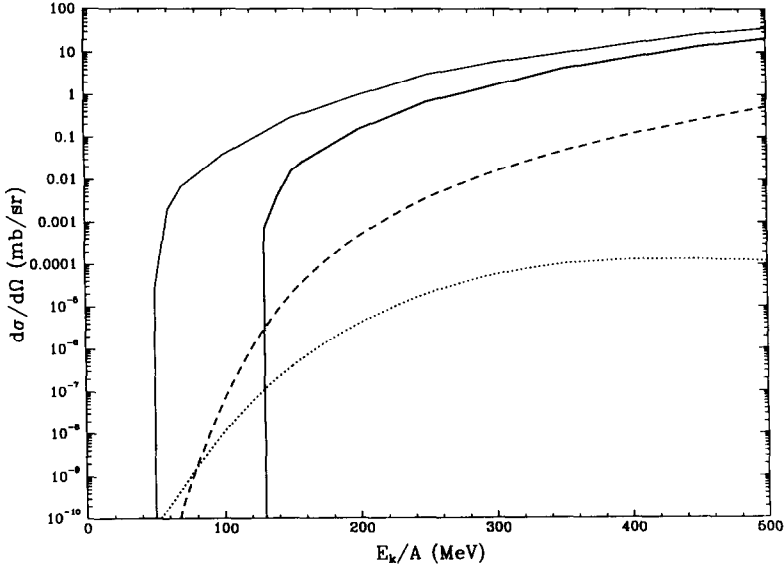


Fig. 5. $d\sigma/d\Omega$ for pion production at $\theta = 0^\circ$ in $^{12}\text{C}-^{12}\text{C}$ collisions as a function of the incoming energy of the projectile. The upper solid curve corresponds to incoherent pion production, omitting the Δ width in the detailed balance of Eq. (27). The lower solid curve corresponds to incoherent pion production including the Δ width in the detailed balance equation. The dashed curve corresponds to semicoherent and the dotted one to doubly coherent pion production.

The mass distribution factor $F(M^2)$ is given by

$$F(M^2) = \frac{1}{\pi} \frac{m_r \Gamma(M)}{(M^2 - m_r^2)^2 + m_r^2 \Gamma^2(M)}, \quad m_r = 1.232 \text{ GeV} \quad (28)$$

with

$$\Gamma(M) = \frac{g_{\pi N \Delta}^2 (E_N + M_N)}{12\pi m_\Delta m_\pi^2} q_N^3, \quad g_{\pi N \Delta} = 2.12,$$

which can be obtained from the interaction Lagrangian

$$\mathcal{L}_{\pi N \Delta} = \frac{g_{\pi N \Delta}}{m_\pi} \left(\bar{\Delta}^\mu T N \cdot \partial_\mu \boldsymbol{\pi} + \text{h.c.} \right) \quad (29)$$

and

$$q_N = \frac{\sqrt{[M^2 - (M_N + M_\pi)^2][M^2 - (M_N - M_\pi)^2]}}{2M}. \quad (30)$$

The factor

$$H(\sqrt{s}) = \int_{(m_N + m_\pi)^2}^{(\sqrt{s} - m_N)^2} F(M^2) dM^2 \quad (31)$$

accounts for the mass distribution of the Δ with finite width, and is plotted in Fig. 4. Due to the energy dependence of the width, the asymptotic value of this factor is slightly less

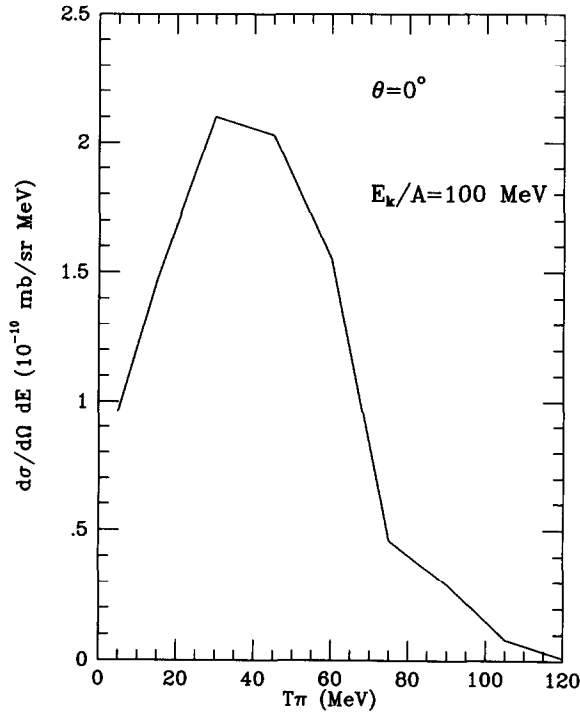


Fig. 6. $d\sigma/dE d\Omega$ at 100 MeV/A and 0° of the pion as a function of the pion kinetic energy for the doubly coherent process of pion production.

than 1. We see that this factor decreases rapidly near the threshold. As a consequence, the Δ 's are more strongly absorbed by the nucleons near the threshold as compared with the conventional detailed balance.

We have proton–neutron symmetry in the $^{12}\text{C} + ^{12}\text{C}$ collisions, therefore the probabilities of π^+ , π^0 and π^- are equal in the present approach.

5. Results and discussion

In Fig. 5 we show the results for the doubly coherent, semicoherent and incoherent cross sections at zero degrees for the pion.

The two solid curves in the figure refer to incoherent pion production. The upper one neglects the Δ width in the detailed balance formula of Eq. (27). The threshold obtained with this prescription, around 50 MeV, is similar to the one obtained in Ref. [46]. The use of the extended detailed balance formula, Eq. (27), moves the threshold at higher energies, around 120 MeV and reduces the cross section at all energies. The incoherent pion production dominates clearly the reaction at energies above 130 MeV/A, which is the lowest energy where we found a nonzero cross section from the simulation. At 120 MeV we found no incoherent events.

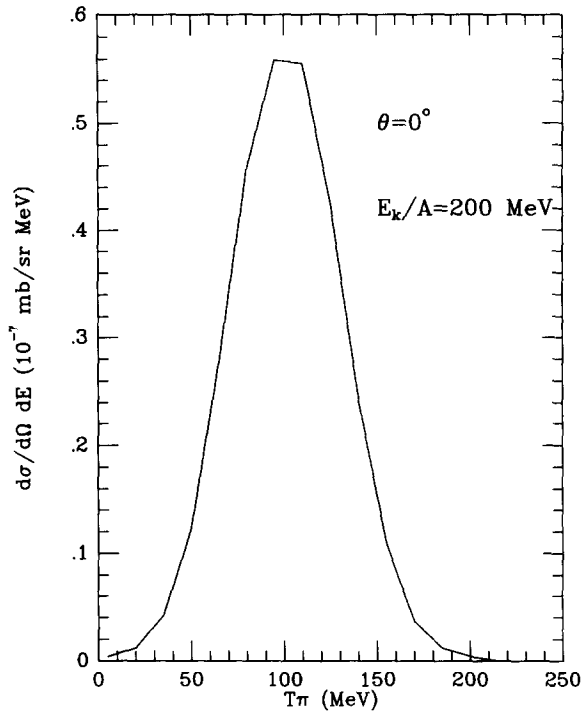


Fig. 7. Same as Fig. 6 for 200 MeV/A.

The trend of the incoherent cross section in Fig. 5, allowing for some statistical uncertainties below 130 MeV/A, indicates that the semicoherent cross section will dominate the pion production cross section at energies around 100 MeV/A, while the doubly coherent process will dominate below 80 MeV/A.

This behaviour in the subthreshold region can be understood in terms of the masses of the particles involved. In the incoherent case the pion production comes from individual collisions. In NN collisions with a nucleon at rest the N threshold energy to produce a pion is $T_N = 289$ MeV in the lab frame. Fermi motion and successive collisions with Δ 's in the intermediate states lower effectively this threshold as one can see from the figure. On the other hand, for the semicoherent process the collision is of a nucleon on the nucleus. In such a case, assuming free kinematics for the nucleon, the threshold for pion production in ^{12}C is $T_N = 152$ MeV. Obviously, Fermi motion lowers effectively this threshold. In the doubly coherent process the threshold for pion production is even lower, since it corresponds to nucleus–nucleus collisions with the nuclei unbroken in the final state. In this case the threshold energy is $T_A/A = 23$ MeV.

The cross section for the coherent and semicoherent channels are weakly dependent on the πNN form factor. We have checked that lowering Λ_π from 1300 to 1000 MeV reduces these cross sections in less than 10%.

At energies around 200 MeV/A and up the cross sections for the semicoherent

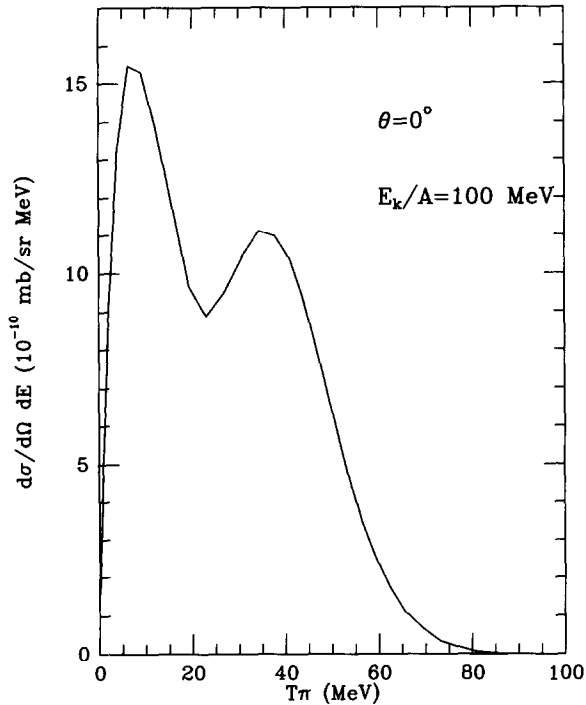


Fig. 8. Same as Fig. 6 for the semicoherent process.

reaction are relatively large and can be measured through techniques like the one used for the (α, α') experiment on the proton [32], although the smaller energy gap for the excitation of ^{12}C with respect to ^4He makes the identification of ^{12}C in its ground state more difficult.

The identification of the doubly coherent process is certainly more difficult. However, techniques to detect the excited $^{12}\text{C}^*$ ($J = 1^+$, $T = 1$, 15.1 MeV) state in $^{12}\text{C} + ^{12}\text{C}$ collisions have already been developed [49].

One of the peculiar features of the doubly coherent and semicoherent reactions are the energy distributions. In Figs. 6, 7 we show the results for $d\sigma/d\omega_\pi d\Omega_\pi$ at 0° for the doubly coherent process as a function of the pion kinetic energy for $E_A/A = 100$ and 200 MeV respectively. At 500 MeV/A the distribution is similar but the peak appears at $T_\pi = 200$ MeV.

On the other hand in Figs. 8, 9 we show the same distributions coming from the semicoherent process. We observe that the pion distributions peak at lower energies in the semicoherent process than in the doubly coherent one.

In Fig. 10 we show the pion energy distribution at 200 MeV/A for the incoherent process. As we can see, the pion distribution peaks at higher energies than in the semicoherent case and resembles more to the one of the doubly coherent scattering.

In the semicoherent process, Figs. 8, 9, we see a double hump in the energy dis-

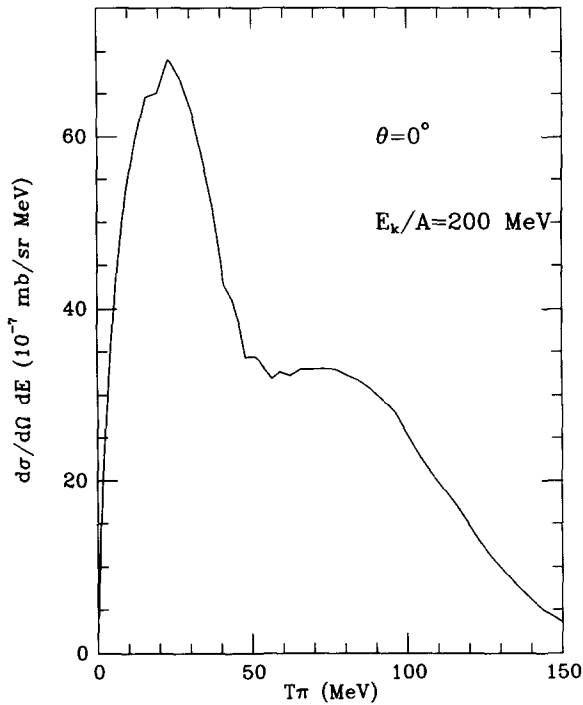


Fig. 9. Same as Fig. 7 for the semicoherent process.

tribution. The peak at lower energies corresponds mostly to pions which are emitted coherently from the projectile, while the peak at higher energies corresponds to pions which are emitted coherently from the target. We can also see that the position of this second peak corresponds approximately to the position of the peak in the doubly coherent process, which, as we discussed, proceeds mostly through pion production in the target.

Coherent pion production takes place preferably in the forward direction. Indeed, in (p, p') reactions, on a nucleus, the coherent pions are produced mostly along the direction of the (p, p') momentum transfer and there is a momentum mismatch between the momentum of the virtual pion produced in the first step and the real pion coming out after the interaction with the nucleus (momenta q and p_π respectively in Fig. 2). This momentum mismatch is taken by the nuclear momentum distribution and the nuclear form factor comes as a reduction factor in the cross section. For a given energy of the pion the momentum mismatch in (p, p') grows as the angle of the p' increases and as consequence the cross section decreases. Hence, the preferred direction for the coherent pions is forward.

The case is different in the incoherent process. At large energies the angle distribution is smooth but still the largest cross section is for forward pions.

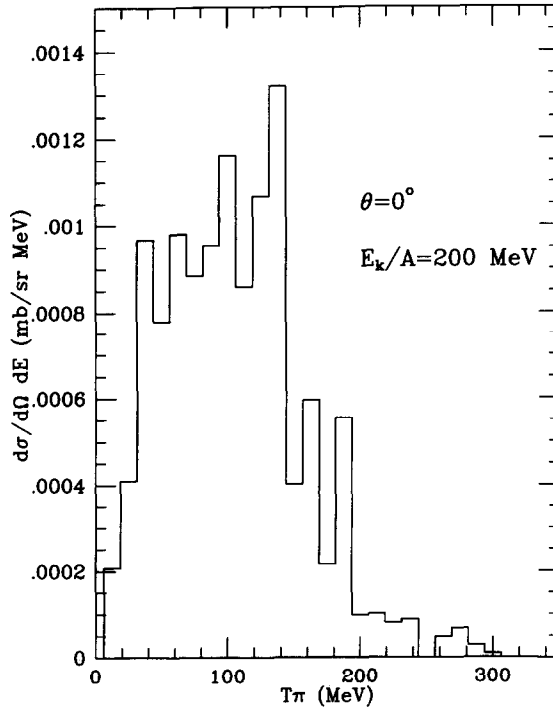


Fig. 10. Same as Fig. 7 for incoherent pion production.

6. Conclusions

We have studied three types of pion production: doubly coherent, semicoherent and incoherent. The traditional approach for pion production in heavy-ion reactions has been cascade calculations, or the use of transport equations, in which some kind of cooperation between nucleons occurs, but the steps are based on two-body cross sections of NN , $N\Delta$ or $\Delta\Delta$. Some coherent effects, in which the contribution of the nucleons to the amplitude is summed, were already considered in [10] in ^{12}C collisions against ^{12}C , where the 1^+ , $T = 1$ state was excited in one nucleus while the other nucleus was broken. Here we have studied two new possibilities of coherent production, both of which involve fully coherent pion production in one of the nuclei, which remains in its ground state, thus all nucleons of the nucleus collaborate coherently to the pion production. In one of the cases the second nucleus was excited to the 1^+ , $T = 1$ state while in the other case the second nucleus was broken. We observe that the doubly coherent scattering leads to smaller cross sections than the semicoherent or the incoherent processes, but for energies of the projectile around or larger than 200 MeV/A leads to cross sections in the measurable range.

These findings should stimulate the search of this new kind of highly cooperative phenomena in heavy-ion reactions, going beyond the gross features of these reactions which are largely dominated by a succession of incoherent processes.

Acknowledgements

This paper has been partially supported by the CICYT contract number AEN 93-1205 and E.O. wishes to acknowledge the support of the Humboldt Foundation and B.L.A., P.F.C and M.J.V.V. the support of the Human Capital and Mobility program of the EU, contract number CHRX-CT93-0323.

References

- [1] I. Tanihata and S. Nagamiya et al., *Phys. Lett. B* 87 (1979) 349.
- [2] S. Nagamiya et al., *Phys. Rev. C* 24 (1981) 971.
- [3] H. Noll et al., *Phys. Rev. Lett.* 52 (1984) 1284.
- [4] T. Johanson et al., *Phys. Rev. Lett.* 48 (1982) 732.
- [5] F. Grosse, *Nucl. Phys. A* 447 (1986) 611c.
- [6] E. Chiavasa et al., *Nucl. Phys. A* 422 (1984) 621.
- [7] B. Jakobsson et al., *Phys. Rev. C* 48 (1982) 732.
- [8] V. Bernard et al., *Nucl. Phys. A* 423 (1984) 511.
- [9] M. Tohyama and U. Mosel, *Nucl. Phys. A* 459 (1986) 711.
- [10] C. Guet, M. Soyeur, J. Bowlin and G.E. Brown, *Nucl. Phys. A* 494 (1989) 558.
- [11] T. Maruyama, S.W. Huang, N. Ohtsuka, G. Li and A. Faessler, *Nucl. Phys. A* 534 (1991) 720.
- [12] G. Li, D.T. Khoa, T. Maruyama, S.W. Huang, N. Ohtsuka, A. Faessler and J. Aichelin, *Nucl. Phys. A* 534 (1991) 697.
- [13] G.Q. Li, T. Maruyama, D.T. Khoa, S.W. Huang, Y. Lotfy, A. Faessler and J. Aichelin, *Z. Phys. A* 340 (1991) 271.
- [14] G.Q. Li, Y. Lotfy, S.W. Huang, T. Maruyama, D.T. Khoa and A. Faessler, *J. Phys. G* 18 (1992) 681.
- [15] S.W. Huang, A. Faessler, G.Q. Li, Dao T. Khoa, E. Lehmann, M.A. Matin, N. Ohtsuka and R.K. Puri, *Prog. Part. Nucl. Phys.* 30 (1993) 105.
- [16] M. Tohyama, R. Kaps, D. Masak and U. Mosel, *Nucl. Phys. A* 437 (1985) 739.
- [17] C. Guet and M. Prakash, *Nucl. Phys. A* 428 (1984) 119c.
- [18] J. Aichelin, *Phys. Lett. B* 146 (1985) 261.
- [19] M. Blann, *Phys. Rev. C* 32 (1985) 1231.
- [20] R. Shyan and J. Kroll, *Nucl. Phys. A* 426 (1984) 606.
- [21] W. Bauer, *Phys. Rev. C* 40 (1989) 715.
- [22] U. Mosel, *Annu. Rev. Nucl. Part. Sci.* 41 (1991) 29.
- [23] P. Oltmanns, F. Osterfeld and T. Udagawa, *Phys. Lett. B* 299 (1993) 194.
- [24] V.F. Dimitriev, *Phys. Rev. C* 48 (1993) 357.
- [25] P. Fernández de Córdoba, J. Nieves, E. Oset and M.J. Vicente-Vacas, *Phys. Lett. B* 319 (1993) 416; P. Fernández de Córdoba, E. Oset and M.J. Vicente-Vacas, *Nucl. Phys. A* 592 (1995) 472.
- [26] T. Hennino et al., *Phys. Lett. B* 303 (1993) 236.
- [27] J. Chiba, in: *Int. Workshop on delta excitation in nuclei*, Tokyo, May 1993, eds. H. Toki, M. Ichimura and M. Ishihara (World Scientific, Singapore, 1994), p. 93.
- [28] S. Rousteau and T. Hennino, private communication.
- [29] R. Gilman, in: *Int. Symposium on spin-isospin responses and weak processes in hadrons and nuclei*, Osaka, March 1994, eds. H. Ejiri, Y. Mizuno and T. Suzuki, *Nucl. Phys. A* 577 (1994).
- [30] V.G. Ableev et al., *Sov. Phys. JETP Lett.* 40 (1984) 763.
- [31] C. Ellegaard et al., *Phys. Rev. Lett.* 50 (1983) 1745.
- [32] P. Morsch et al., *Phys. Rev. Lett.* 69 (1992) 1336.
- [33] P. Fernández de Córdoba, E. Oset, M.J. Vicente Vacas, Yu. Ratis, J. Nieves, B. López Alvarado and F. Gareev, *Nucl. Phys. A* 586 (1995) 586.
- [34] J. Aichelin, *Phys. Rep.* 202 (1991) 233.
- [35] G.Q. Li, A. Faessler and S.W. Huang, *Prog. Part. Nucl. Phys.* 31 (1993) 159, and references therein.
- [36] R. Machleidt, K. Holinde and Ch. Elster, *Phys. Rep.* 149 (1987) 1.
- [37] J. Nieves, E. Oset and C. García-Recio, *Nucl. Phys. A* 554 (1993) 509, 554.

- [38] E. Oset, H. Toki and W. Weise, *Phys. Rep.* 83 (1982) 281.
- [39] W.M. Alberico, A. de Pace, M. Ericson and A. Molinari, *Phys. Lett. B* 256 (1991) 134.
- [40] A. Ramos, E. Oset and L.L. Salcedo, *Phys. Rev. C* 50 (1994) 2314.
- [41] A.L. Fetter and J.D. Walecka, *Quantum Theory of Many Particle Systems* (McGraw Hill, New York, 1971).
- [42] E. Oset, P. Fernández de Córdoba, L.L. Salcedo and R. Brockmann, *Phys. Rep.* 188 (1990) 79.
- [43] W. Czyż and L.C. Maximon, *Ann. Phys.* 52 (1969) 59.
- [44] C. García-Recio, E. Oset and L.L. Salcedo, *Phys. Rev. C* 37 (1988) 194.
- [45] J. Cugnon, D. Kinet and J. Vandermeulen, *Nucl. Phys. A* 379 (1982) 553.
- [46] G.F. Bertsch, H. Kruse and S. Das Gupta, *Phys. Rev. C* 29 (1984) 673;
G.F. Bertsch and S. Das Gupta, *Phys. Rep.* 160 (1988) 189.
- [47] S. Huber, J. Aichelin, *Nucl. Phys. A* 573 (1994) 587.
- [48] Gy. Wolf, W. Cassing and U. Mosel, *Nucl. Phys. A* 552 (1993) 549.
- [49] B. Erasmus et al., *Phys. Rev. C* 44 (1991) 1212.

THE IMAGINARY PART OF THE NUCLEON SELF-ENERGY IN HOT NUCLEAR MATTER

L. Alvarez-Ruso^a, P. Fernández de Córdoba^b
and E. Oset^a

^a*Departamento de Física Teórica and IFIC
Centro Mixto Universidad de Valencia-CSIC
Valencia, Spain*

^b*Departamento de Matemática Aplicada
Universidad Politécnica de Valencia
Valencia, Spain*

Abstract

A semiphenomenological approach to the nucleon self-energy in nuclear matter at finite temperatures is followed. It combines elements of Thermo Field Dynamics for the treatment of finite temperature with a model for the self-energy, which evaluates the second order diagrams taking the needed dynamics of the NN interaction from experiment. The approach proved to be accurate at zero temperature to reproduce $Im\Sigma$ and other properties of nucleons in matter. In the present case we apply it to determine $Im\Sigma$ at finite temperatures. An effective NN cross section is deduced which can be easily used in analyses of heavy ion reactions.

1 Introduction

The imaginary part of the nucleon self-energy Σ has been the subject of intense research in the past [1]. However, these studies have been done at zero temperature, of relevance for physical processes involving nucleon-nucleus scattering. On the other hand, in heavy ion collisions, through multiple collisions of the nucleons, one reaches conditions roughly similar to those of a thermal bath at finite temperature [2]. The imaginary part of the nucleon self-energy in such a bath is an important magnitude which governs processes of nucleon emission, particle production and, in principle, most of the nuclear processes occurring during heavy ion collisions, including the rate of thermalization.

The many body field theoretical treatment at finite temperature becomes, however, technically more involved than at $T = 0$. At the root of it lies the fact that particle annihilation operators do not give a vanishing result when applied to the ground state of the system, which is now a thermal distribution. This does not allow one to use the Wick theorem to generate the Feynman diagrammatic perturbation expansion, as we know for many body systems at $T = 0$, or in ordinary Quantum Field Theory in the absence of a medium. Yet, even if more complicated, the methods to deal with it are available. The traditional approach has been the one of the imaginary time formalism [3, 4], although lately the new method in real time formalism known as Thermo Field Dynamics [5, 6] is proving quite efficient and becomes more and more widely used. A recent review on Thermo Field Dynamics with some applications to nuclear matter looking at collective modes and delta propagation in matter is presented in ref. [7]. A covariant formalism at finite temperature unifying the good features of the two formalisms is presented in ref. [8], with some application to nuclear matter within the relativistic Walecka model [9].

Detailed analyses of nucleon properties along the lines of ref. [1] are available at finite, but small temperatures $T \leq 10 \text{ MeV}$ [10, 11]. Neither of the two approaches mentioned above is followed, but instead the smallness of the temperature justifies some approximations by means of which one finally follows the steps at $T = 0$ substituting the Pauli distribution $n(\vec{k})$ (1 for $|\vec{k}| < k_F$, 0 for $|\vec{k}| > k_F$) by the thermal distribution

$$n(k^0) = [1 + \exp(\frac{k^0 - \mu}{k_B T})]^{-1} \quad (1)$$

with k_B the Boltzmann constant, $k^0 = \varepsilon(\vec{k})$ the nucleon energy and μ the chemical potential. The results of [10] are improved in [11] by considering the correlation diagrams which lead to a large contribution to $Im\Sigma$ at momenta below the Fermi momentum. Similar steps are followed in ref. [12] to deal with the propagation of the Δ at finite temperatures.

The appeal of Thermo Field Dynamics is that one can continue to use Wick's theorem and the Feynman diagrammatic approach as at $T = 0$. The price is the introduction of an auxiliary field by means of which one constructs

a field doublet; the propagators become 2×2 matrices and the Feynman rules are now algebraic operational rules in the space of 2×2 matrices.

In the present work we shall evaluate the imaginary part of the nucleon self-energy at finite temperature. In doing so we shall be following closely the steps of ref. [13], where $Im\Sigma$ was evaluated for nuclear matter at $T = 0$. The approach used in [13] was semiphenomenological, much in line with usual approximations done in the treatment of heavy ion collisions where the results obtained here are bound to be of relevance. The approach of [13] evaluated correctly the second order nucleon self-energy diagrams but bypassed the use of an explicit NN potential. Instead, it used the fact that the sum of ladder diagrams in the low density limit provides the NN scattering t matrix, and its modulus squared, which appears in the evaluation of $Im\Sigma$, is related to the NN cross section. Hence the experimental cross section was used as input and the low density theorem [14, 15] was automatically fulfilled. This theorem states that, as the nuclear density goes to zero, one has

$$Im\Sigma_{\rho \rightarrow 0} = -\frac{1}{2} \sigma_{tot} v \rho \quad (2)$$

where v is the velocity of the nucleon in the rest frame of the Fermi sea and σ_{tot} the total NN cross section. Long range correlations were also considered by means of an RPA sum with a phenomenological particle-hole interaction acting in the spin-isospin transverse channel. The approach proved to be numerically quite successful by comparing the results with those of elaborate and time consuming many body approaches like those of refs. [16, 17]. Spectral functions and occupation numbers were also evaluated in [13] and were very similar to those obtained in other successful many body approaches with special emphasis in selfconsistency [18].

As with respect to the finite temperature treatment, we use the Thermo Field Dynamics approach by following the formalism, normalization and rules of ref. [19], where a comprehensive and practical extract of this method is presented.

2 Finite temperature formalism for the nucleon self-energy

By following ref. [19] we have the thermal doublet for the nucleon field

$$\psi^{(a)}(x) \equiv \left\{ \begin{array}{l} \psi(x) \\ i {}^t \tilde{\psi}^\dagger \end{array} \right\} \quad (3)$$

where $\psi(x)$ is the ordinary nucleon field and $\tilde{\psi}$ a support field for the formalism (t means the transposition with respect to the spinor index and \dagger stands for conjugate). The thermal propagator is now defined as

$$iG^{(a,b)}(x_1, x_2) = \langle 0(\beta) | T[\psi^{(a)}(x_1) \bar{\psi}^{(b)}(x_2)] | 0(\beta) \rangle \quad (4)$$

where $|0(\beta)\rangle$ is the state transformed from the vacuum by a Bogoliubov unitary transformation, and which has the property that the expectation value of an operator in this state is equivalent to its thermal average with the distribution of eq. (1). Hence the component of the Green's function, $G^{(11)}$, is the proper thermal average of the ordinary Green's function.

The thermal free propagator, to be used in perturbation theory in the nonrelativistic approximation which we shall follow here, is given by

$$G^{0(ab)}(p) = G_F^{0(ab)}(p) + G_D^{0(ab)}(p) \quad (5)$$

with

$$G_F^{0(ab)}(p) = \begin{pmatrix} G_F^0(p) & 0 \\ 0 & G_F^{0*}(p) \end{pmatrix}; \quad G_F^0(p) = \frac{1}{p^0 - \varepsilon(\vec{p}) + i\epsilon} \quad (6)$$

$$G_D^{0(ab)}(p) = 2\pi i \delta(p^0 - \varepsilon(\vec{p})) \begin{pmatrix} \sin^2\theta_{p^0} & \frac{1}{2}\sin 2\theta_{p^0} \\ \frac{1}{2}\sin 2\theta_{p^0} & -\sin^2\theta_{p^0} \end{pmatrix} \quad (7)$$

$$\cos\theta_{p^0} = \frac{1}{(1 + e^{-x})^{1/2}}; \quad \sin\theta_{p^0} = \frac{e^{-x/2}}{(1 + e^{-x})^{1/2}}; \quad x = \frac{p^0 - \mu}{k_B T} \quad (8)$$

$$\sin^2\theta_{p^0} = \frac{1}{e^x + 1} = n(p^0) \quad (9)$$

This Green's function is in addition diagonal in spin but we omit the spin indices for simplicity.

An alternative way of writing this propagator which is also suited to write the exact propagator is

$$G^{0(ab)}(p) = \left[U_F(p^0) \begin{pmatrix} G_F^0(p) & 0 \\ 0 & G_F^{0*}(p) \end{pmatrix} U_F^{-1}(p^0) \right]^{(ab)} \quad (10)$$

with

$$U_F(p^0) = \begin{bmatrix} \cos\theta_{p^0} & \sin\theta_{p^0} \\ -\sin\theta_{p^0} & \cos\theta_{p^0} \end{bmatrix} \quad (11)$$

and the exact propagator can be cast as

$$G^{(ab)}(p) = U_F(p^0) \begin{pmatrix} [p^0 - \varepsilon(\vec{p}) - \bar{\Sigma}(p)]^{-1} & 0 \\ 0 & [p^0 - \varepsilon(\vec{p}) - \bar{\Sigma}^*(p)]^{-1} \end{pmatrix} U_F^{-1}(p^0) \quad (12)$$

with $\varepsilon(\vec{p})$ the kinetic energy of the particle and

$$\begin{aligned} \text{Re}\bar{\Sigma}(p) &= \text{Re}\Sigma^{(11)}(p) \\ \text{Im}\bar{\Sigma}(p) &= \text{Im}\Sigma^{(11)}(p)/\cos 2\theta_{p^0} \end{aligned} \quad (13)$$

In particular the $G^{0(11)}(p)$ component has an intuitive form given by

$$G^{0(11)}(p) = \frac{1 - \sin^2\theta_{p^0}}{p^0 - \varepsilon(\vec{p}) - \bar{\Sigma}} + \frac{\sin^2\theta_{p^0}}{p^0 - \varepsilon(\vec{p}) - \bar{\Sigma}^*} \quad (14)$$

which in the limit of $T = 0$ reproduces the standard form of the nucleon propagator in a Fermi sea.

Hence in order to obtain the self-energy $\bar{\Sigma}(p)$ which renormalizes the nucleon propagator, only the thermal component $\Sigma^{(11)}$ needs to be evaluated. In the next section we show the approximation scheme that we follow to evaluate this magnitude.

3 Semiphenomenological model for Σ

This section follows closely ref. [13]. The generic Feynman diagram which we evaluate is the one in fig. 1, where the nucleon propagator in each of the baryonic lines is given by eq. (5). Note that in the limit of $T = 0$, and with the conventional separation of particles and holes, the usual polarization (fig. 2a) and correlation (fig. 2b) graphs which lead to $Im\Sigma$ [14] are automatically generated (together with other two graphs with the interaction lines crossed which do not contribute to $Im\Sigma$).

In fig. 1 the indices a,b,c,d in the vertices are thermal indices. We are interested in $\Sigma^{(11)}$ and hence $a = b = 1$. Assuming for the moment the interaction lines to correspond to meson exchange, and considering also that no such mesons are present in the ground state of our many body fermionic system, the meson propagator would be diagonal in the thermal indices and hence $c = d = 1$.

We thus must evaluate the polarization function $\Pi^{(11)}(q)$

$$\Pi^{(11)}(q) = -4i \int \frac{d^4p}{(2\pi)^4} G^{0(11)}(p) G^{0(11)}(p+q) \quad (15)$$

where the factor 4 takes into account the sum over spin and isospin.

Once again in the limit of $T = 0$, this polarization would account for the two diagrams in fig. 3, which are those accounted for by means of the Lindhard function [4].

By using $G^{0(a,b)}$ from eqs. (6,7) the p^0 integration can be easily performed and one obtains

$$\Pi^{(11)}(q) = 4 \int \frac{d^3p}{(2\pi)^3} \left\{ \frac{\sin^2\theta_{\varepsilon(\vec{p})} \cos^2\theta_{\varepsilon(\vec{p}+\vec{q})}}{q^0 + \varepsilon(\vec{p}) - \varepsilon(\vec{p}+\vec{q}) + i\epsilon} + \frac{\sin^2\theta_{\varepsilon(\vec{p}+\vec{q})} \cos^2\theta_{\varepsilon(\vec{p})}}{-q^0 - \varepsilon(\vec{p}) + \varepsilon(\vec{p}+\vec{q}) + i\epsilon} \right\} \quad (16)$$

Next we evaluate $\Sigma^{(11)}$ corresponding to fig. 1

$$\Sigma^{(11)}(k) = i \int \frac{d^4q}{(2\pi)^4} V^2(q) \Pi^{(11)}(q) G^{0(11)}(k-q) \quad (17)$$

where $V(q)$ would take into account the interaction due to the hypothetical meson exchange.

Here again we follow the steps of ref. [13] and sum the ladder diagrams which would replace $V(q)$ by the scattering t matrix. (Note that medium corrections to t which would appear in the medium G -matrix are taken explicitly into account to second order with the structure of the diagram). We shall continue to use the same t matrix here. The studies of refs. [10, 11, 20] show indeed little dependence of the effective interaction on the temperature.

In order to evaluate $Im\Sigma^{(11)}$ from eq. (17) a Wick rotation was made in ref. [13] which allows one to express $Im\Sigma^{(11)}$ in terms of $Im\Pi^{(11)}$. This is however not possible here because $\Pi^{(11)}$ from eq. (16) has overlapping cuts in the upper and lower half planes of the complex plane (unlike at $T = 0$ where the cuts are confined to the second and fourth quadrant). However, an explicit evaluation of $Im\Sigma^{(11)}$ is possible by first performing the q^0 integral in eq. (17) and then evaluating the imaginary part, with the result

$$Im\Sigma^{(11)}(k) = -4\pi \int \frac{d^3q}{(2\pi)^3} \int \frac{d^3p}{(2\pi)^3} |t|^2 \delta(k^0 + \varepsilon(\vec{p}) - \varepsilon(\vec{k} - \vec{q}) - \varepsilon(\vec{p} + \vec{q})) \cdot \left\{ \cos^2\theta_{\varepsilon(\vec{k}-\vec{q})} \cos^2\theta_{\varepsilon(\vec{p}+\vec{q})} \sin^2\theta_{\varepsilon(\vec{p})} - \sin^2\theta_{\varepsilon(\vec{k}-\vec{q})} \sin^2\theta_{\varepsilon(\vec{p}+\vec{q})} \cos^2\theta_{\varepsilon(\vec{p})} \right\} \quad (18)$$

The spin-isospin averaged value of $|t|^2$ assumed in eq. (18) is then replaced by $4\pi\sigma_{NN}/M^2$, where M is the nucleon mass and σ_{NN} the spin-isospin averaged NN elastic cross section. Since pion production is not explicitly taken into account, this restricts us below the pion production threshold. The final step in ref. [13] is to consider the polarization or RPA corrections to the interaction.

The consideration of the polarization was an important ingredient in ref. [13], which reduced $Im\Sigma$ particularly at small energies, and provided results similar to those found in refs. [16, 17]. We implement it here too. For this purpose we need to evaluate $\Pi^{(11)}(q)$, both the real and imaginary part, which cares about ph excitation, and $\Pi_{\Delta}^{(11)}(q)$, the equivalent term accounting for Δh excitation. At $T = 0$ these quantities are the familiar Lindhard functions $U_N(q), U_{\Delta}(q)$, respectively, used in ref. [13].

The real part of $U_N(q)$, unlike $ImU_N(q)$, is not affected by Pauli blocking [4], hence finite temperature, which modifies occupation numbers, has not much of a consequence in the change of $ReU_N(q)$. On the other hand there is no Pauli blocking in the Δh excitation since we do not have a Fermi sea of Δ 's. For these reasons we keep $Re\Pi^{(11)}$ and $\Pi_{\Delta}^{(11)}$ at finite temperatures equal to $ReU_N(q), U_{\Delta}(q)$ at zero temperature. However, we evaluate $Im\Pi^{(11)}(q)$ from eq. (16) at finite temperature. The reason is that keeping $Im\Pi^{(11)} \neq 0$ is important in order to avoid singularities coming from poles of zero sound (q^0 proportional to $|\vec{q}|$ at small energies) which are strongly damped at finite T .

The expression for $Im\Pi^{(11)}$ obtained from eq. (16) is given by

$$Im\Pi^{(11)}(q^0, q) = -\frac{1}{\pi} \int_{p_{min}}^{\infty} dp \frac{mp}{q} \left\{ \sin^2\theta_{\varepsilon(\vec{p})} + \sin^2\theta_{\varepsilon(\vec{p})+q^0} - 2\sin^2\theta_{\varepsilon(\vec{p})} \sin^2\theta_{\varepsilon(\vec{p})+q^0} \right\} \quad (19)$$

where

$$p_{min} = \frac{m}{p} \left| q^0 - \frac{\vec{q}^2}{2m} \right| \quad (20)$$

The polarization correction replaces the interaction by the induced interaction [21] (see eq. (15) of ref. [13]). Furthermore, we can perform some trivial integrals and eliminate the δ function with the final result

$$\begin{aligned} Im\Sigma^{(11)}(k) = & -\frac{\sigma_{NN}}{M\pi^2} \int_0^\infty qdq \int_{-1}^1 d\cos\theta \int_0^\infty pdp \Theta(1 - A^2) \\ & \cdot \frac{1}{|1 - V_t(q)U(q)|^2} \Big|_{q^0=k^0-\varepsilon(\vec{k}-\vec{q})} \\ & \cdot \left\{ \cos^2\theta_{\varepsilon(\vec{k}-\vec{q})} \cos^2\theta_{\varepsilon(\vec{p}+\vec{q})} \sin^2\theta_{\varepsilon(\vec{p})} - \sin^2\theta_{\varepsilon(\vec{k}-\vec{q})} \sin^2\theta_{\varepsilon(\vec{p}+\vec{q})} \cos^2\theta_{\varepsilon(\vec{p})} \right\} \end{aligned} \quad (21)$$

where $V_t(q)$ is the transverse part of the spin-isospin interaction and $U(q) = \Pi^{(11)}(q) + \Pi_\Delta^{(11)}(q)$. The arguments leading to this modifications and expressions for $V_t(q)$ and $U_N(q)$, $U_\Delta(q)$ can be found in ref. [13] and we do not repeat them here. Furthermore the angle in the integral over $\cos\theta$ in eq. (21) is the angle between \vec{q} and \vec{k} . The magnitude A in the argument of the step function is given by

$$A = \frac{M}{pq} \left\{ k^0 - \frac{k^2}{2M} - \frac{q^2}{M} + \frac{kq\cos\theta}{M} \right\} \quad (22)$$

with k, q the modulus of \vec{k} and \vec{q} respectively.

The value of the chemical potential μ as a function of the density and T is obtained, as usually done, by the normalization condition

$$\rho = 4 \int \frac{d^3k}{(2\pi)^3} \frac{1}{1 + \exp[(\varepsilon(k) - \mu)/k_B T]} \quad (23)$$

Eq. (21) provides $Im\Sigma^{(11)}$ as a function of k^0, \vec{k} . In the next section we show the results which we obtain for this quantity.

4 Results and discussion

In fig. 4 we show the results of $-Im\bar{\Sigma}$ at $T = 0$ for two densities, ρ_0 ($0.17 fm^{-3}$) and $\rho_0/2$, obtained with the present formalism in the limit of $T = 0$. The results agree with those in ref. [13] calculated with the $T = 0$ formalism and also with those of the microscopic approach of ref. [16]. Note that since only kinetic energies are used as input to evaluate $\Sigma^{(11)}$, the value of μ is referred to an origin of energies at $|\vec{k}| = 0$. We are not interested in $Re\Sigma$ and to overcome the arbitrary origin of energies we plot the magnitudes in terms of $\omega - \mu$ ($\omega \equiv k^0$). In fig. 4, $|\vec{k}|$ is taken at the value $\sqrt{2M\omega}$. This justifies small differences with ref. [13] where the value of $|\vec{k}|$ satisfying the dispersion relation between $|\vec{k}|$ and ω was taken. In fig. 4 we observe the

typical features that $Im\bar{\Sigma}$ is proportional to $(\omega - \mu)^2$. In the calculations we find that $Im\Sigma^{(11)}$ changes sign at $\omega = \mu$, with $Im\Sigma^{(11)} < 0$ for $\omega > \mu$. In this case

$$\begin{aligned} \cos 2\theta_{k^0} &= 1 - 2\sin^2\theta_{k^0} \\ &= 1 - 2n(k^0)_{T=0} = \begin{cases} -1 & \omega < \mu \\ 1 & \omega > \mu \end{cases} \end{aligned} \quad (24)$$

and then

$$Im\bar{\Sigma} = \frac{Im\Sigma^{11}}{\cos^2\theta_{k^0}} = -|Im\Sigma^{11}| \quad (25)$$

The Green's function $G^{(11)}$, by using eq. (12), will then be

$$\begin{aligned} &\frac{\Theta(\omega - \mu)}{k^0 - \varepsilon(\vec{k}) - Re\Sigma^{(11)}(k) + i|Im\Sigma^{(11)}|} + \frac{\Theta(\mu - \omega)}{k^0 - \varepsilon(\vec{k}) - Re\Sigma^{(11)}(k) - i|Im\Sigma^{(11)}|} \\ &\equiv \frac{1}{k^0 - \varepsilon(\vec{k}) - \Sigma^{(11)}} \end{aligned} \quad (26)$$

as it should be.

In fig. 5 we plot $Im\Sigma^{(11)}$ at $\rho = \rho_0$ as a function of $\omega - \mu$, with $|\vec{k}| = \sqrt{2M\omega}$ and μ calculated from eq. (23). As can be seen in the figure, $Im\Sigma^{(11)}$ is always zero at $\omega = \mu$. However, $Im\bar{\Sigma}(\mu, k)$ is different from zero at finite temperatures, contrary to the situation at $T = 0$ where it is zero. In order to envisage this we see that the evaluation of $Im\bar{\Sigma}$ from eq. (13) involves a fraction of the type 0/0 which we determine using l'Hôpital rule and find

$$Im\bar{\Sigma}(\mu, k) = \lim_{k^0 \rightarrow \mu} \frac{Im\Sigma^{(11)}(k^0, k)}{1 - 2n(k^0)} = 2k_B T \frac{d}{dk^0} Im\Sigma^{(11)}(k^0, k)|_{k^0=\mu} \quad (27)$$

We can see that $Im\bar{\Sigma}(\mu, k)$ vanishes at $T = 0$, as we already said.

In fig. 6,7,8 we show the results for $-Im\bar{\Sigma}$ as a function of $\omega - \mu$ for different temperatures, calculated for three different densities, $\rho_0/2, \rho_0$ and $2\rho_0$. We can appreciate that as T increases $-Im\bar{\Sigma}$ also increases in all the range of energies calculated there. We should note that in evaluating $Im\bar{\Sigma}$, the factor $\cos 2\theta_{k^0}$ appearing in the denominator of eq. (13) is very important and makes $Im\bar{\Sigma} \neq 0$ at $T \neq 0$ for all the range of energies, while $Im\Sigma^{(11)}$ passed through zero. This is a genuine temperature dependent property which would be lost if a $T = 0$ formalism, changing the Fermi distribution by the thermal distribution of eq. (1), were used.

At this point it is interesting to compare our results for $Im\bar{\Sigma}$ with those which we would obtain using standard formulae of Fermi-liquid theory [22]. The formula used there in our notation for $Im\bar{\Sigma}$, removing the cut off in the integral, would be given by eq. (18) changing the minus sign in the curled

bracket (\cos^2 and \sin^2 terms) by a positive sign. Instead our formula for $Im\bar{\Sigma}$ uses eq. (18) with a minus sign (which provides $Im\Sigma^{(11)}$) and then we divide by $\cos 2\theta_{p_0}$ (as shown in eq. (13)) in order to obtain $Im\bar{\Sigma}$. The same prescription would be taken if one uses instead eq. (21) which incorporates the effects of polarization.

It is easy to see that at $T = 0$ both formulae are identical. Indeed for $\omega > \mu$ only the first term in the curled bracket of eq. (18) (or (21)) (the one with $\cos^2\cos^2\sin^2$) contributes, while for $\omega < \mu$ only the second term in the bracket (the one with $\sin^2\sin^2\cos^2$) contributes. Then when dividing $Im\Sigma^{(11)}$ by $\cos 2\theta_{p_0}$, given by eq. (24), we obtain a formula for $Im\bar{\Sigma}$ given by eq. (18) where the minus sign in the curled bracket is changed to a positive sign, exactly the formula used in Fermi-liquid theory [22].

The identity of the two formulae holds, however, at any temperature. This can be seen analytically using eqs. (8) for $\sin\theta, \cos\theta$ and x , hence

$$\begin{aligned}
& \frac{(\cos^2\theta_{\varepsilon_1}\cos^2\theta_{\varepsilon_2}\sin^2\theta_{\varepsilon_3} - \sin^2\theta_{\varepsilon_1}\sin^2\theta_{\varepsilon_2}\cos^2\theta_{\varepsilon_3})}{\cos 2\theta_{k^0}} \delta(k^0 + \varepsilon_3 - \varepsilon_1 - \varepsilon_2) \\
= & \frac{1}{k_B T} \frac{e^{x_3}[e^{(x_1+x_2-x_3)} - 1]}{(1+e^{x_1})(1+e^{x_2})(1+e^{x_3})} \frac{e^{x_{k^0}} + 1}{e^{x_{k^0}} - 1} \delta(x_{k^0} + x_3 - x_1 - x_2) \\
= & \frac{1}{k_B T} \frac{e^{x_1}e^{x_2} + e^{x_3}}{(1+e^{x_1})(1+e^{x_2})(1+e^{x_3})} \delta(x_{k^0} + x_3 - x_1 - x_2) \\
= & (\cos^2\theta_{\varepsilon_1}\cos^2\theta_{\varepsilon_2}\sin^2\theta_{\varepsilon_3} + \sin^2\theta_{\varepsilon_1}\sin^2\theta_{\varepsilon_2}\cos^2\theta_{\varepsilon_3}) \delta(k^0 + \varepsilon_3 - \varepsilon_1 - \varepsilon_2)
\end{aligned} \tag{28}$$

where the constraints of the δ -function have been used in the second step. This is an interesting finding which stresses the value of the results obtained in Fermi-liquid theory based on the concept of quasiparticles, by comparison to a method in principle more microscopic, like the one used here.

Next we would like to extract a practical magnitude from these results which can be used in calculations of heavy ion collisions. Recall that in the semiclassical approach one has

$$Im\bar{\Sigma} = -\frac{1}{2} \sigma_{NN} v \rho \tag{29}$$

One can then define an effective NN nucleon-nucleon cross section at different T and ρ by means of

$$\sigma_{NN}^{eff} = -2 \frac{Im\bar{\Sigma}}{v\rho} \tag{30}$$

as done in ref. [23], where $\sigma_{NN}^{eff} \rho$ defines a probability of collision per unit length for the nucleon. In order to facilitate the use of this magnitude we have parameterized $v\sigma_{NN}^{eff}$, with $v = |\vec{k}|/M$ for the different densities and temperatures evaluated here. We take the following functional form

$$v\sigma_{NN}^{eff} = \sum_{n=0}^4 a_n(\rho, T) \omega^n \quad (31)$$

where ω is the nucleon kinetic energy, $\vec{k}^2/2M$. The fit is valid for values of $\omega > \mu$ in figures 6,7,8. The coefficients $a_n(\rho, T)$ are given in tables I,II,III. One can obtain $v\sigma_{NN}^{eff}$ for intermediate values of ρ and T interpolating between the values of $v\sigma_{NN}^{eff}$ given by eq. (29).

5 Conclusions

We have used a model to evaluate $Im\bar{\Sigma}$ for a nucleon in nuclear matter at finite temperatures, which combines the formalism of Thermo Field Dynamics with empirical magnitudes of the NN interaction. This model at $T = 0$ coincides with a semiphenomenological approach studied earlier, which proved rather successful in reproducing nucleon properties in nuclear matter obtained with more microscopical approaches.

We have obtained $Im\bar{\Sigma}$ for different values of the nuclear density and several temperatures. One of the interesting findings is that $Im\bar{\Sigma}$ grows steadily with the temperature. The changes produced by the temperature are more striking at energies around the chemical potential where $Im\bar{\Sigma}$ is zero at $T = 0$ and takes finite values at $T \neq 0$.

We found that the genuine effects of the temperature, given naturally in the formalism of Thermo Field Dynamics, were important, and the differences with respect to simple calculations, where $n(\vec{k})$ at $T = 0$ is replaced by the thermal distribution, can be appreciable. In order to facilitate the use of the results obtained here, we have parameterized them by means of easy analytical formulae. The parameterization is given for an effective NN cross section in the medium, such that $\sigma_{NN}^{eff} \rho$ gives the probability of collision per unit length for a nucleon in the nuclear medium. With the given formulae one can easily interpolate the results and obtain this magnitude for different densities and temperatures. These results should be useful in the analysis of heavy ion reactions.

Acknowledgements

We would like to thank Liang-gang Liu and Igor Tkachenko for useful discussions. This work has been partly supported by CICYT contract number AEN 93-1205.

6 Table Captions

Table I Parameters of eq. (28) to evaluate $v\sigma_{NN}^{eff}$ at $\rho = \rho_0/2$. The parameters a_n have dimensions such that, with ω given in MeV , the results for $v\sigma_{NN}^{eff}$ are given in mb .

Table II Same as table I for $\rho = \rho_0$.

Table III Same as table I for $\rho = 2\rho_0$.

7 Figure Captions

Fig. 1. Generic Feynman diagram to evaluate the nucleon self-energy. The indices a, b, c, d are thermal indices. The nucleon propagator corresponding to the baryonic lines is given in eqs. (5-9).

Fig. 2. *a)* polarization, *b)* correlation graphs contributing to $Im\Sigma$ at $T = 0$ and contained in fig. 1. Here the direction of the arrows stands for the conventional hole (down) and particle (up) propagators.

Fig. 3. Polarization graphs appearing at $T = 0$ with the same notation for the lines as in fig. 2.

Fig. 4. $-Im\bar{\Sigma}(\omega, k)$ at $T = 0$ as a function of $\omega - \mu$, with $k = \sqrt{2M\omega}$, evaluated for two densities.

Fig. 5. $Im\Sigma^{(11)}(\omega, k)$ at $\rho = \rho_0$ for several temperatures as a function of $\omega - \mu$ with $k = \sqrt{2M\omega}$. The solid line is for $T = 0$. The other curves correspond to $T = 2 MeV$ (long dashed-dotted line), $T = 4 MeV$ (dashed line), $T = 10 MeV$ (dotted line) and $T = 20 MeV$ (short dashed-dotted line). At values $\omega - \mu < 0$, they appear correlatively with increasing values of $Im\Sigma^{(11)}$ as T increases.

Fig. 6. $-Im\bar{\Sigma}(\omega, k)$ at $\rho = \rho_0/2$ as a function of $\omega - \mu$ for $k = \sqrt{2M\omega}$ for several temperatures $T = 0, 2, 4, 10, 20 MeV$ with the same notation as in fig. 5. $-Im\bar{\Sigma}$ increases with increasing T .

Fig. 7. Same as fig. 6 at $\rho = \rho_0$.

Fig. 8. Same as fig. 6 at $\rho = 2\rho_0$.

References

- [1] C. Mahaux, P. F. Bortignon, R. A. Broglia and C. H. Dasso, Phys. Rep. **120** (1985) 1, and refs. therein.
- [2] R. B. Clare and D. Strottman, Phys. Rep. **141** (1986) 177
- [3] T. Matsubara, Prog. Theor. Phys. **14** (1955) 351.
- [4] A. L. Fetter and J. D. Walecka, Quantum Theory of Many Particle Systems (McGraw-Hill, New York, 1971).
- [5] L. Leplae, H. Umezawa and F. Mancini, Phys. Rep. **10** (1974) 151.
- [6] T. Arimitsu and H. Umezawa, Prog. Theor. Phys. **77** (1987) 32 and 53.
- [7] P. A. Henning, Phys. Rep. **253** (1995) 235.
- [8] R. J. Furnstahl and B. D. Serot, Phys. Rev. **C43** (1991) 105
- [9] B. D. Serot and J. D. Walecka, Adv. Nucl. Phys. **16** (1986) 1.
- [10] A. Lejeune, P. Granje, M. Martzloff and J. Cugnon, Nucl. Phys. **A453** (1986) 189.
- [11] P. Grange, J. Cugnon and A. Lejeune, Nucl. Phys. **A473** (1987) 365.
- [12] J. Helgesson and J. Randrup, Ann. of Phys. (N.Y.) in print
- [13] P. Fernández de Córdoba and E. Oset, Phys. Rev. **C46** (1992) 1697.
- [14] C. B. Dover, J. Hüfner and R. H. Lemmer, Ann. of Phys. (N.Y.) **66** (1971) 248.
- [15] J. Hüfner, Phys. Rep. **21** (1975) 1.
- [16] S. Fantoni, B. L. Friman and V. R. Pandharipande, Nucl. Phys. **A399** (1983) 51.
- [17] S. Fantoni and V. R. Pandharipande, Nucl. Phys. **A427** (1984) 473.
- [18] A. Ramos, A. Polls and W.H. Dickhoff, Nucl. Phys. **A503** (1989) 1.
- [19] K. Saito, T. Maruyana and K. Soutome, Phys. Rev. **C40** (1989) 407.
- [20] J. Cugnon, A. Lejeune, M. Baldo and K. Lombardo, Nucl. Phys. **A492** (1989) 173.
- [21] G. E. Brown, Many Body Problems (North-Holland Amsterdam, 1972)
- [22] G. Baym and C. Pethick, Landau Fermi-Liquid Theory, John Wiley and Sons, 1991, pag. 87.

- [23] G.E. Brown, E. Oset, M.J. Vicente-Vacas and W. Weise, Nucl. Phys. **A505** (1989) 823.

Table I.

T	0 MeV	2 MeV	4 MeV	10 MeV	20 MeV
a_n					
a_0	-2.549	-2.305	-1.425	0.982	5.107
a_1	$9.658 \cdot 10^{-2}$	$9.098 \cdot 10^{-2}$	$7.043 \cdot 10^{-2}$	$3.404 \cdot 10^{-2}$	$-2.170 \cdot 10^{-2}$
a_2	$-9.706 \cdot 10^{-5}$	$-3.996 \cdot 10^{-5}$	$1.569 \cdot 10^{-4}$	$4.367 \cdot 10^{-4}$	$8.413 \cdot 10^{-4}$
a_3	$-4.349 \cdot 10^{-7}$	$-6.674 \cdot 10^{-7}$	$-1.435 \cdot 10^{-6}$	$-2.408 \cdot 10^{-6}$	$-3.857 \cdot 10^{-6}$
a_4	$1.135 \cdot 10^{-9}$	$1.456 \cdot 10^{-9}$	$2.487 \cdot 10^{-9}$	$3.724 \cdot 10^{-9}$	$5.709 \cdot 10^{-9}$

Table II.

T	0 MeV	2 MeV	4 MeV	10 MeV	20 MeV
a_n					
a_0	0.553	0.411	0.793	1.695	3.192
a_1	$-3.541 \cdot 10^{-2}$	$-2.722 \cdot 10^{-2}$	$-3.709 \cdot 10^{-2}$	$-4.496 \cdot 10^{-2}$	$-4.430 \cdot 10^{-2}$
a_2	$7.790 \cdot 10^{-4}$	$6.834 \cdot 10^{-4}$	$7.846 \cdot 10^{-4}$	$8.343 \cdot 10^{-4}$	$7.542 \cdot 10^{-4}$
a_3	$-2.860 \cdot 10^{-6}$	$-2.458 \cdot 10^{-6}$	$-2.861 \cdot 10^{-6}$	$-3.027 \cdot 10^{-6}$	$-2.651 \cdot 10^{-6}$
a_4	$3.521 \cdot 10^{-9}$	$2.963 \cdot 10^{-9}$	$3.501 \cdot 10^{-9}$	$3.719 \cdot 10^{-9}$	$3.215 \cdot 10^{-9}$

Table III.

T	0 MeV	2 MeV	4 MeV	10 MeV	20 MeV
a_n					
a_0	1.493	1.382	1.347	2.205	2.861
a_1	$-5.370 \cdot 10^{-2}$	$-5.017 \cdot 10^{-2}$	$-4.795 \cdot 10^{-2}$	$-6.283 \cdot 10^{-2}$	$-6.065 \cdot 10^{-2}$
a_2	$5.866 \cdot 10^{-4}$	$5.555 \cdot 10^{-4}$	$5.355 \cdot 10^{-4}$	$6.533 \cdot 10^{-4}$	$6.214 \cdot 10^{-4}$
a_3	$-1.659 \cdot 10^{-6}$	$-1.553 \cdot 10^{-6}$	$-1.484 \cdot 10^{-6}$	$-1.874 \cdot 10^{-6}$	$-1.770 \cdot 10^{-6}$
a_4	$1.695 \cdot 10^{-9}$	$1.570 \cdot 10^{-9}$	$1.488 \cdot 10^{-9}$	$1.940 \cdot 10^{-9}$	$1.834 \cdot 10^{-9}$

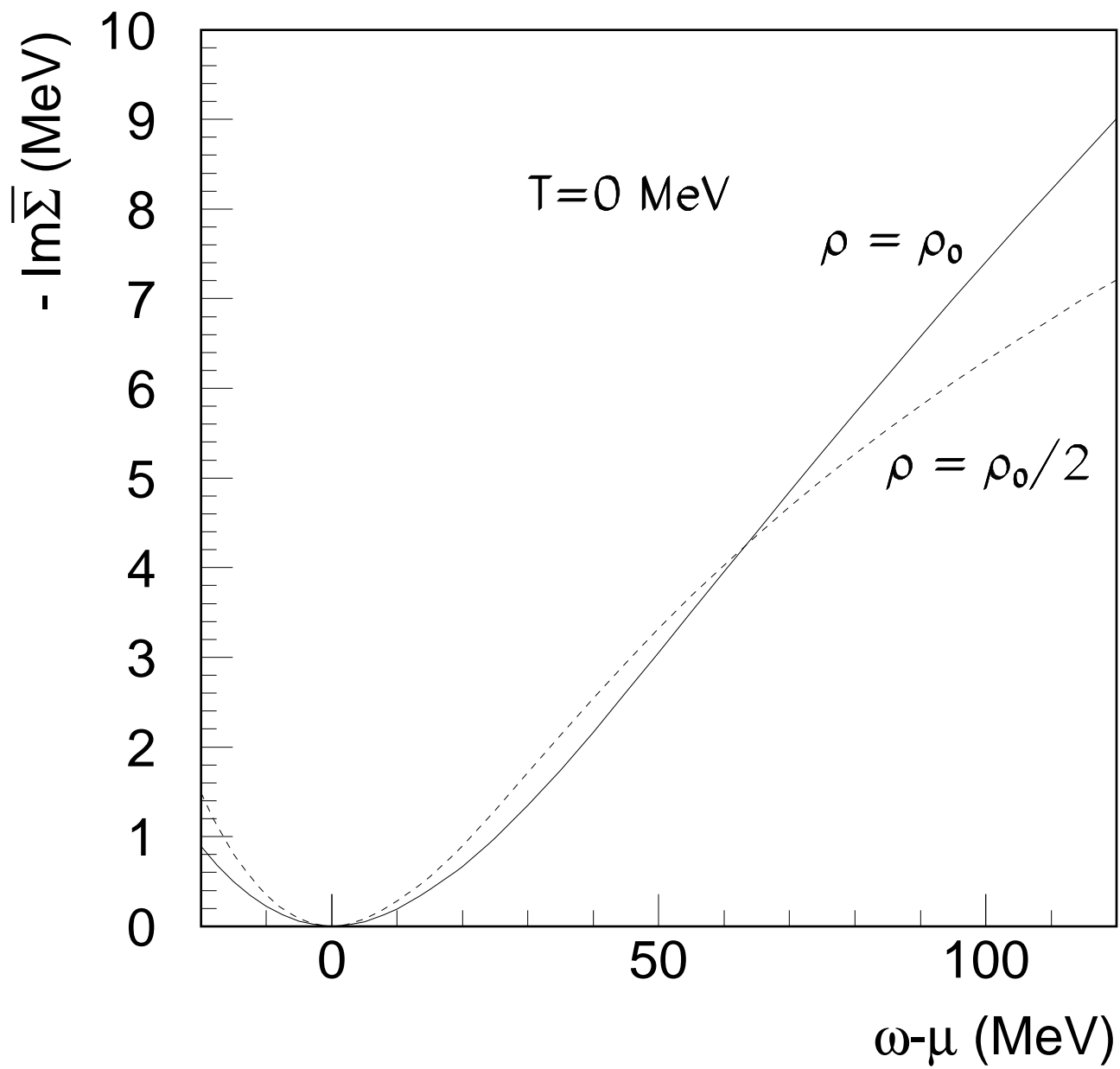


Fig. 4

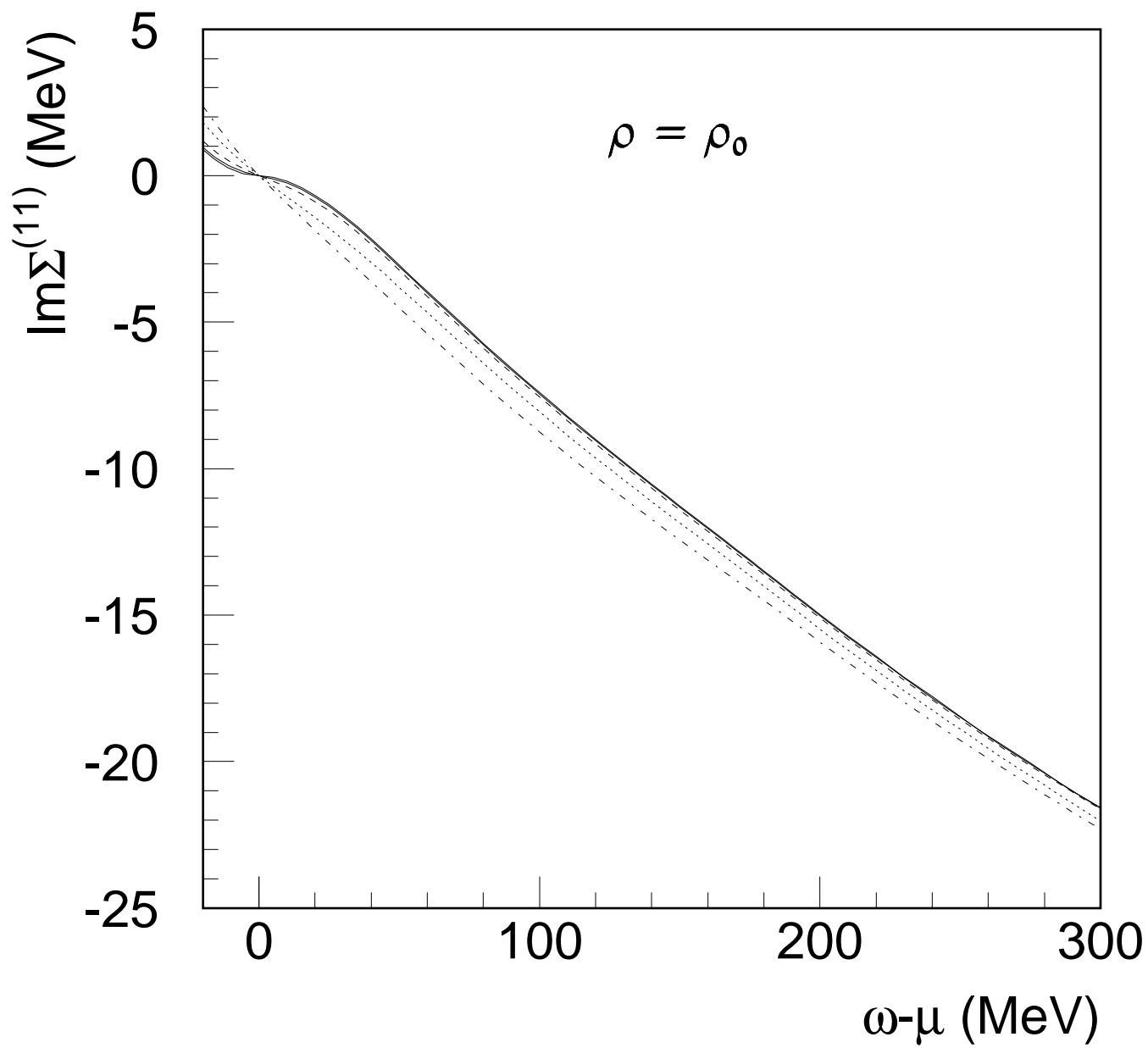


Fig. 5

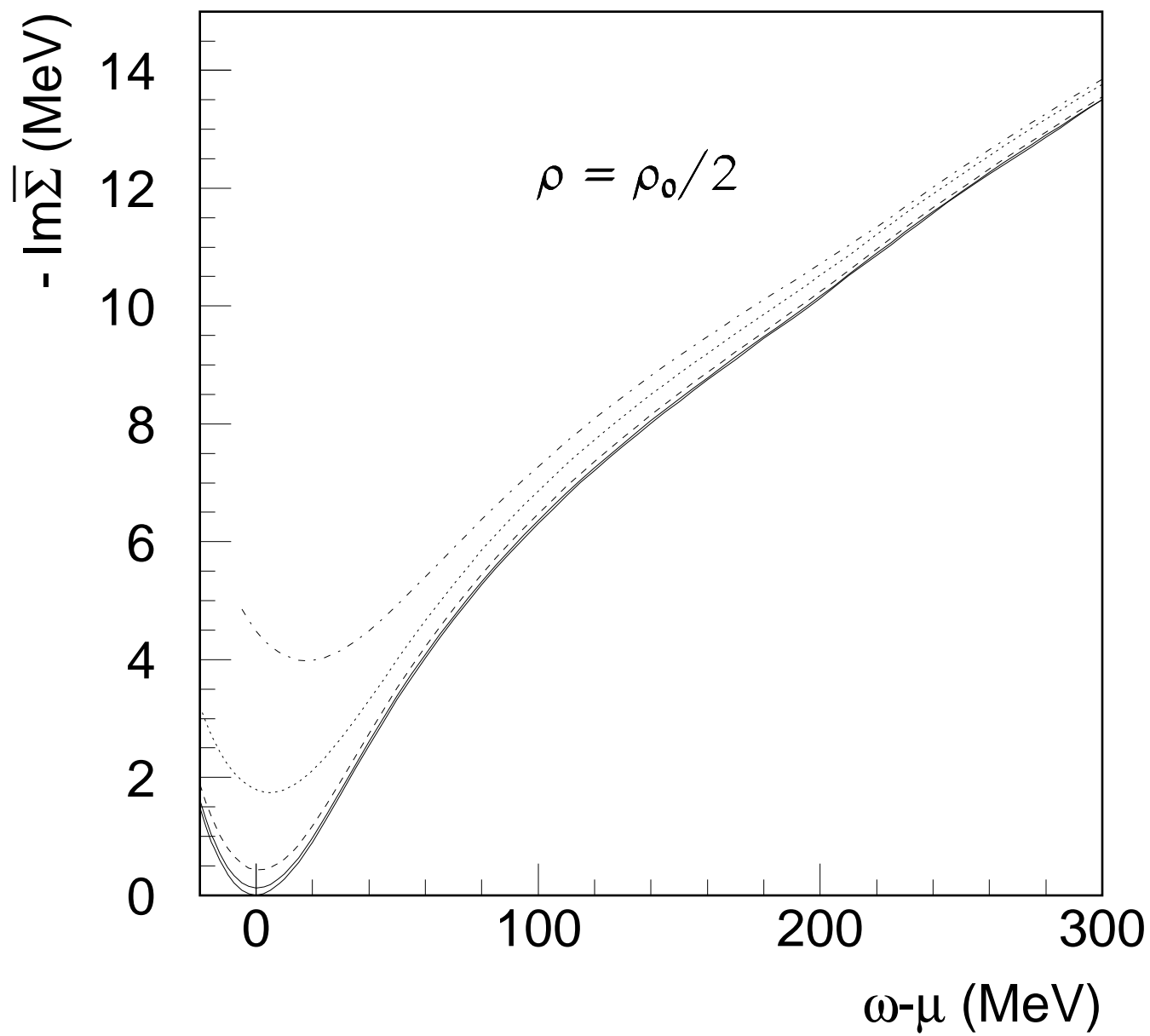


Fig. 6

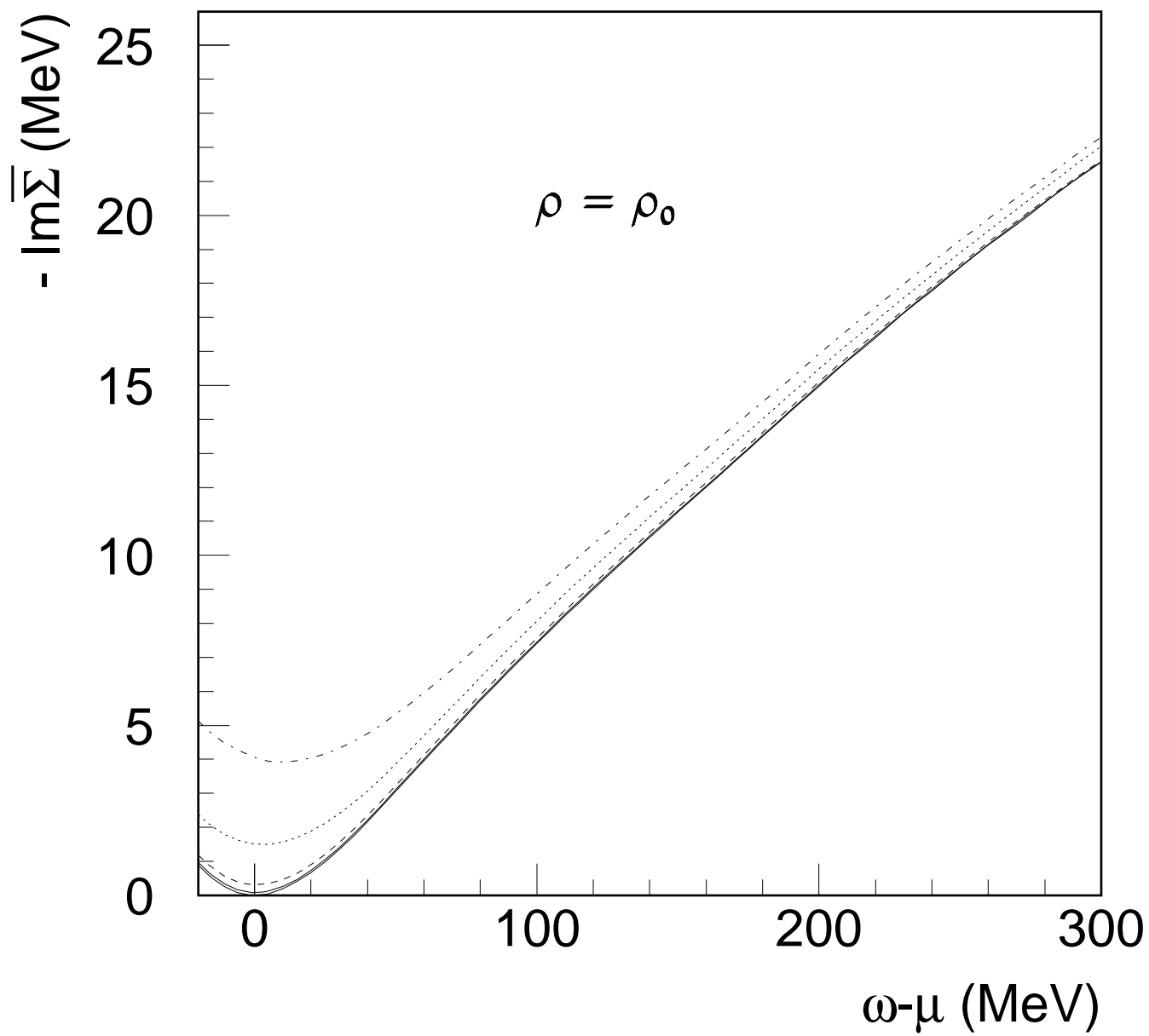


Fig. 7

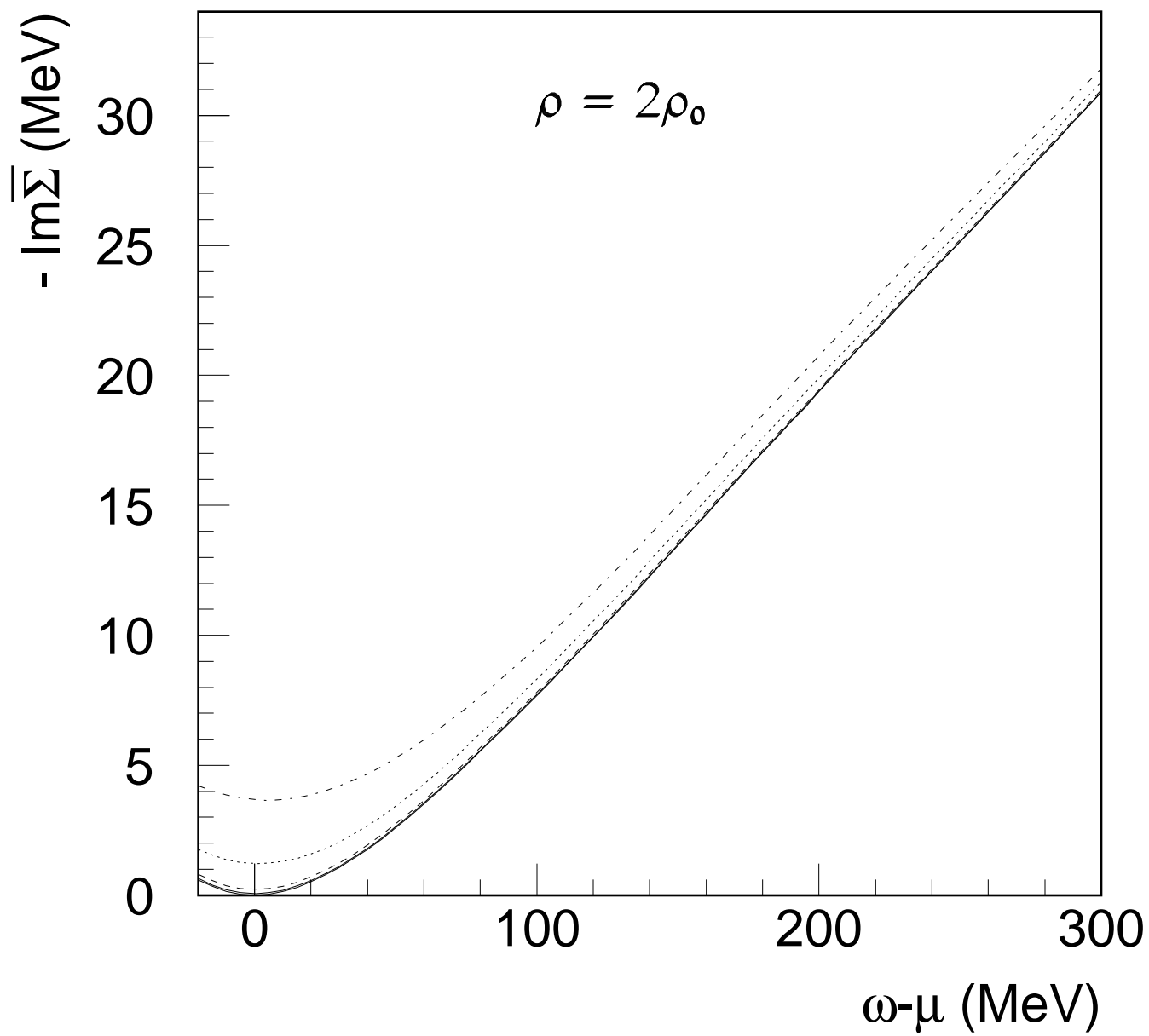


Fig. 8

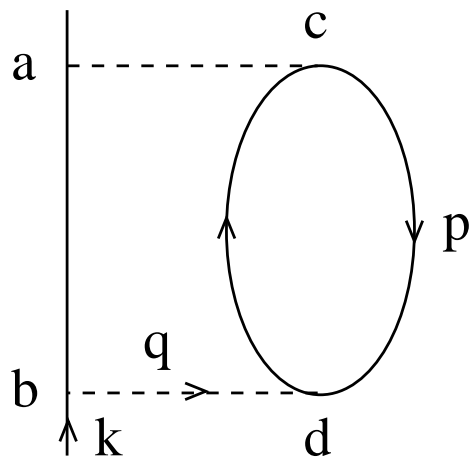


Fig 1

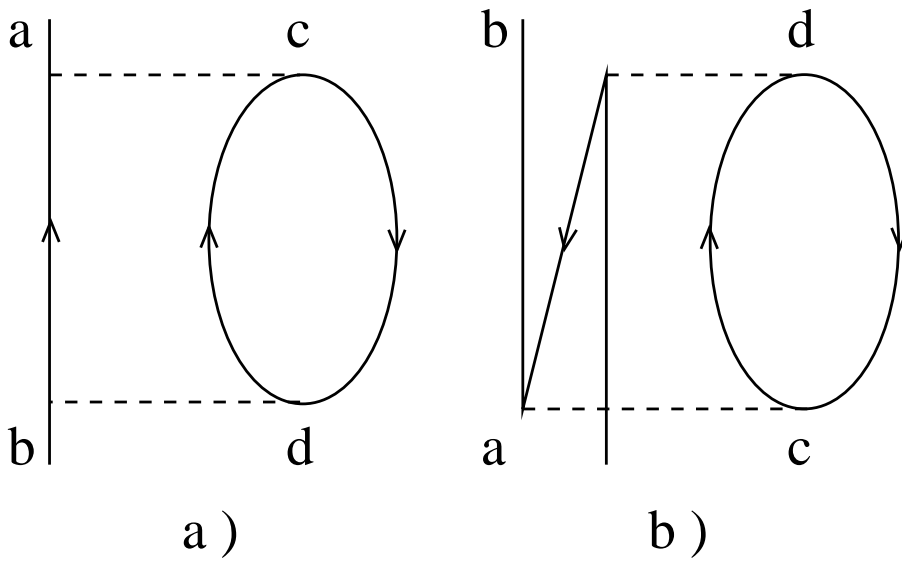


Fig 2

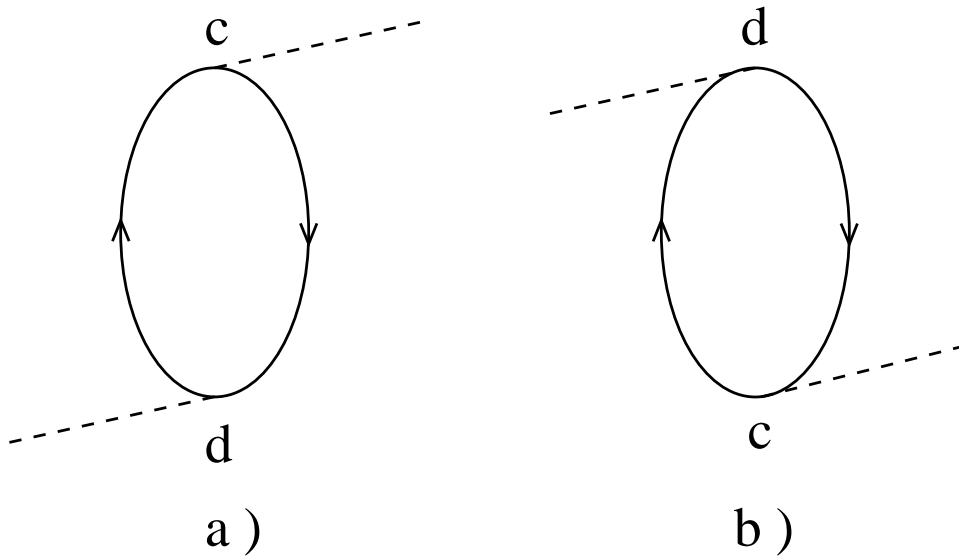


Fig 3

A Parallel Algorithm for the Partial Single-Input Pole Assignment Problem

R. BRU, J. CERDÁN, P. FERNÁNDEZ DE CÓRDOBA AND A. URBANO
Departament de Matemàtica Aplicada, Univ. Politècnica de València
46071 València, Spain

(Received January 1994; accepted February 1994)

Abstract—For a linear control system, we introduce a parallel algorithm to assign a desired subset of eigenvalues to a single-input linear invariant dynamic system. We obtain a sequential algorithm as a particular case. The proposed algorithms are conceptually simple and are based on the computation of left eigenvectors of the state matrix. In addition, the parallel algorithm parallelizes easily as the numerical examples show.

Keywords—Pole eigenvalue assignment, Partial assignment, Single-input, Parallel algorithm.

1. INTRODUCTION

Consider the linear invariant dynamic system $\dot{x}(t) = Ax(t) + bu(t)$, where A is an $n \times n$ real matrix whose spectrum is the set $\{\lambda_1, \dots, \lambda_n\}$, and b is an n real vector. In the partial assignment problem, we search a vector f such that the spectrum $\{\mu_1, \dots, \mu_p, \lambda_{p+1}, \dots, \lambda_n\}$ of the matrix $A - bf^T$ is a conjugated complex set and μ_1, \dots, μ_p are prescribed conjugated complex numbers. This problem is a particular case of the general problem of pole assignment. It is known that this problem has solution if the pair (A, b) is controllable. Moreover, in the single-input case the solution is unique. Notice that any controllable pair (A, b) can be always transformed into the pair (H, c) by orthogonal similarity where H is an unreduced upper Hessenberg matrix and $c = (\alpha, 0, \dots, 0)^T$, with $\alpha \neq 0$ (see [1,2]).

There are different and effective pole placement algorithms in the literature, see [1,3–5]. However, these algorithms have been constructed with the idea to change all possible eigenvalues of the state matrix A of a linear control system. On the other hand, there exist some algorithms which solve directly the partial assignment problem. Saad [6] gave two algorithms. One of them is based on a projection method computing an orthogonal basis of the left-invariant subspace of A associated with the undesirable eigenvalues, and the second one is a sequential algorithm similar to the deflation eigenvalue method. Datta and Saad [7] studied a solution of this problem based on the Arnoldi method. The algorithms given in [6,7] can be considered as sequential.

In this paper, we introduce a parallel algorithm for the partial assignment problem and we obtain a sequential algorithm as a particular case. In the proposed parallel algorithm, the vector f is given as a linear combination of the left eigenvectors of A associated with the undesired eigenvalues with the first component prescribed. That result is based on an algorithm of complete assignment given in [3]. A multi-input version of the algorithm in [3] is given in [8]. Algorithms given by Saad [6] obtain the same result (which was expected since the solution is unique) but in a

Supported by Spanish CICYT Grant Number TIC91-1157-C03-01.

We would sincerely like to thank P. Van Dooren for his valuable comments, which led to improve the quality and reading of the paper.

sequential way. We want to emphasize that the proposed algorithm computes the left eigenvectors solving p triangular systems of size $(n-1) \times (n-1)$ in parallel. Numerical results implemented on a shared memory multiprocessor are given in the last section.

Let A be an $n \times n$ matrix and let λ_j be an eigenvalue of A . We call A_j the matrix obtained from $A - \lambda_j I$, eliminating its first row and its last column, and c_j the vector constituted by the first $(n-1)$ entries of the first row of $A - \lambda_j - I$. We will use this notation in the algorithms.

2. THE PROPOSED ALGORITHM

In this section, we give a parallel algorithm for the partial pole assignment problem in the single-input case, and we obtain a sequential algorithm as a particular case. We obtain the parallel algorithm when we suppose that we change pairwise distinct eigenvalues by pairwise distinct given numbers and the sequential algorithm in the other case. For technical reasons, we suppose that $\sigma(A)$ is a pairwise distinct set and $\{\mu_1, \dots, \mu_p\} \cap \{\lambda_{p+1}, \dots, \lambda_n\} = \emptyset$. Otherwise, some modifications are needed as is explained briefly in Remark 1. In what follows, the spectrum of A and $A - bf^\top$ are conjugated complex numbers sets.

Let (A, b) be a controllable pair in Hessenberg form, where $A \in \mathbb{R}^{n \times n}$ and $b \in \mathbb{R}^{n \times 1}$. If the spectrum of A is $\sigma(A) = \{\lambda_1, \lambda_2, \dots, \lambda_p, \lambda_{p+1}, \dots, \lambda_n\}$, we search a vector f such that $\sigma(A - bf^\top) = \{\mu_1, \dots, \mu_p, \lambda_{p+1}, \dots, \lambda_n\}$ provided that the first p λ 's (and the μ 's) are pairwise distinct sets.

Algorithm II described in [3] obtains a nonsingular matrix $L = [x_1 \ x_2 \ \dots \ x_p \ l_{p+1} \ \dots \ l_n]$ satisfying:

$$\begin{aligned} (A - \mu_j I)x_j &= b, & j &= 1, 2, \dots, p, \\ (A - \lambda_i I)l_i &= 0, & i &= p+1, \dots, n. \end{aligned} \quad (1)$$

According to that algorithm, one computes the vector f by $f^\top L = (\underbrace{1, 1, \dots, 1}_p, \underbrace{0, 0, \dots, 0}_{n-p})$. Let us focus in this equation. We observe

$$f^\top x_j = 1, \quad j = 1, 2, \dots, p, \quad (2)$$

$$f^\top l_i = 0, \quad i = p+1, \dots, n. \quad (3)$$

From the second condition (3), we deduce that f is in span $\{l_{p+1}, l_{p+2}, \dots, l_n\}^\perp$. Then f can be written as

$$f = h_1 + h_2 + \dots + h_p, \quad (4)$$

where h_1, h_2, \dots, h_p are left eigenvectors of A associated with $\lambda_1, \lambda_2, \dots, \lambda_p$, respectively. Then

$$h_j^\top (A - \lambda_j I) = 0, \quad j = 1, 2, \dots, p. \quad (5)$$

From the expressions (2) and (4), we have

$$h_1^\top x_j + h_2^\top x_j + \dots + h_p^\top x_j = 1, \quad j = 1, 2, \dots, p. \quad (6)$$

Fix an index s , $s = 1, 2, \dots, p$. Multiplying the expression (5) by the vector x_s and using (1), we obtain

$$0 = h_j^\top (A - \lambda_j I) x_s = h_j^\top b + (\mu_s - \lambda_j) h_j^\top x_s = h_{1j} + (\mu_s - \lambda_j) h_j^\top x_s,$$

where $h_{1j} = h_j^\top b$ and $j = 1, 2, \dots, p$. Therefore, for a fixed s , we have the following p equations:

$$(\lambda_k - \mu_s) h_k^\top x_s = h_{1k}, \quad k = 1, 2, \dots, p. \quad (7)$$

The addition of the p equations (7) multiplying the k^{th} equation by $\prod_{j=1, j \neq k}^p (\lambda_j - \mu_s)$ gives

$$\prod_{\substack{j=1 \\ j \neq 1}}^p (\lambda_j - \mu_s) h_{11} + \cdots + \prod_{\substack{j=1 \\ j \neq p}}^p (\lambda_j - \mu_s) h_{1p} = \prod_{j=1}^p (\lambda_j - \mu_s),$$

where we used the expression (6). Since the index s varies from 1 to p , we have a system of linear equations whose matrix is a Cauchy matrix for which the solution is known

$$h_{1j} = \frac{\prod_{s=1}^p (\lambda_j - \mu_s)}{\prod_{\substack{s=1 \\ s \neq j}}^p (\lambda_j - \lambda_s)}, \quad j = 1, 2, \dots, p, \quad (8)$$

which is unique because of the conditions on λ 's and μ 's.

The above discussion yields the following result.

THEOREM 1. *Let (A, b) be a controllable pair. Let $\sigma(A) = \{\lambda_1, \lambda_2, \dots, \lambda_p, \lambda_{p+1}, \dots, \lambda_n\}$ be the spectrum of A , with $\lambda_i \neq \lambda_j$, $1 \leq i, j \leq p$, $i \neq j$. Then the vector f , such that $\sigma(A - bf^T) = \{\mu_1, \dots, \mu_p, \lambda_{p+1}, \dots, \lambda_n\}$ (pairwise distinct set), can be written as the sum of p left eigenvectors of A associated with the eigenvalues $\lambda_1, \dots, \lambda_p$, respectively. In addition, the first entries h_{1j} of the left eigenvectors h_i of A , are given by the expression (8).*

Then we can compute in parallel the vectors h_1, h_2, \dots, h_p solving the systems given in (9) whose first components $h_{11}, h_{12}, \dots, h_{1p}$ are given by (8). Since the matrix A is an upper unreduced Hessenberg matrix, each of these systems are reduced to an upper triangular system of size $(n - 1)$.

PARALLEL ALGORITHM. Given the spectrum $\sigma(A) = \{\lambda_1, \dots, \lambda_p, \lambda_{p+1}, \dots, \lambda_n\}$, this algorithm assigns the pairwise distinct spectrum $\{\mu_1, \dots, \mu_p, \lambda_{p+1}, \dots, \lambda_n\}$ to the matrix $A - bf^T$.

1. Compute in parallel h_{1j} by expression (8), for $j = 1, \dots, p$.
2. Solve in parallel the systems $[h_{2j} \ \cdots \ h_{nj}] A_j = -h_{1j} c_j^T$, for $j = 1, \dots, p$.
3. Compute $f = h_1 + h_2 + \cdots + h_p$.

REMARK 1. We supposed $\{\mu_1, \dots, \mu_p\} \cap \{\lambda_{p+1}, \dots, \lambda_n\} = \emptyset$. If $\lambda_{p+1} = \mu_p$, then the systems to solve should be

$$\begin{aligned} (A - \mu_j I) x_j &= b, & j &= 1, \dots, p-1, \\ (A - \mu_p I) x_p &= l_{p+1} + \beta b, \\ (A - \lambda_i I) l_i &= 0, & i &= p+1, \dots, n, \end{aligned}$$

where $\beta \in \mathbb{R}$ makes consistent the equation. In both cases, one obtains the same solution (see [3, Algorithm 3] for details). The technical restriction that $\sigma(A)$ is a pairwise distinct set can be weakened changing the above equations by the corresponding Jordan chain systems.

The restriction of the above algorithm that the set $\{\mu_1, \dots, \mu_p\}$ is a pairwise distinct set disappears if we work in a sequential way. Then, taking $p = 1$ in the above algorithm we obtain the following result.

THEOREM 2. *Let (A, b) be a controllable pair. Let the spectrum of A be $\sigma(A) = \{\lambda_1, \lambda_2, \dots, \lambda_n\}$. Then the vector f , such that the spectrum of the matrix $A - bf^T$ is $\{\mu, \lambda_2, \dots, \lambda_n\}$, is a left eigenvector of A associated with λ_1 whose first entry is $f_1 = \lambda_1 - \mu$.*

Again, we only have to solve a system similar to systems of Step 2, considering the restriction $f_1 = \lambda_1 - \mu$. For assigning p eigenvalues, we can apply this result in a sequential way p times.

SEQUENTIAL ALGORITHM. Let $\sigma(A) = \{\lambda_1, \lambda_2, \dots, \lambda_n\}$ be the spectrum of A . This algorithm assigns the spectrum $\{\mu_1, \dots, \mu_p, \lambda_{p+1}, \dots, \lambda_n\}$ to the matrix $A - bf^\top$.

1. Start with $f = 0$.
2. For $j = 1, \dots, p$.
 - (a) Compute $g_{1j} = \lambda_j - \mu_j$.
 - (b) Solve the system $[g_{2j} \ \dots \ g_{nj}] A_j = -g_{1j}c_j^\top$, considering Step (2.1).
 - (c) Assign $A := A - bg^\top$.
 - (d) Assign $f := f + g$.
3. End.

3. NUMERICAL EXAMPLES

We implemented the algorithm on ALLIANT FX-80 using double precision FORTRAN language and BLAS routines. We computed the eigenvalues of all matrices appearing in the algorithm using LAPACK routine DGEEV. We measured the results computing the eigenvalues of the closed-loop system and measured the error between these computed values and the eigenvalues assigned. In our case, we checked not only the accuracy in the computed assigned eigenvalues $\{\mu_1, \dots, \mu_p\}$ but also the stability of the unmodified spectrum $\{\lambda_{p+1}, \dots, \lambda_n\}$. The algorithm was tested on a different set of unreduced upper Hessenberg matrices: Random and Wilkinson matrices. In order to study the behaviour of the algorithm, we ran our code changing the following parameters: size of the matrix (n), number of eigenvalues to be assigned (p), eigenvalues to be assigned $\{\mu_1, \dots, \mu_p\}$, undesired eigenvalues $\{\lambda_1, \dots, \lambda_p\}$.

The results obtained for the previous matrices are the following:

1. **RANDOM MATRICES.** We ran several examples up to order $n = 513$. We considered unreduced upper Hessenberg matrices with random elements. We assigned the following eigenvalues: $\mu_i = \lambda_s - \alpha \cdot i$, $i = 1, \dots, p$, where λ_s is the smallest eigenvalue of the state matrix A and α is a fixed positive quantity (for these random matrices we take α values running from 10^{-1} to 1).

Our experiments suggest that the *condition number* $\kappa(A_j)$ of the systems in the Step 2 is closely related to the accuracy of the method. We obtained an upper bound of the condition number under which the algorithm is highly successful. This value is around 10^{20} . Therefore, we conclude this method is very stable for random matrices. In Table 1, we present the results obtained with a random matrix of size $n = 513$. As shown in Table 1, E_N stands for the relative error in the new eigenvalues, E_R and E_C stand for the relative errors in the unmodified spectrum (we distinguished between real E_R and complex E_C ones). In the previous example, we generated random numbers from 0.5 to 1.5. We took this range to obtain condition numbers below the upper bound given above. On the other hand, the election of this range produces eigenvalues very close to each other, and then the number of eigenvalues to be assigned must be small.

The proposed algorithm is an efficient parallel algorithm, as can be seen in Table 2. As shown in Table 2, T_0, T_1, T_p mean the times (in seconds) computed for the proposed algorithm compiled with scalar, vectorial and global (with p processors) optimization, respectively. The different values of the speed-up are explicated in the columns S_0 and S_1 .

The efficiency of the proposed algorithm in the previous examples is 0.97 in the $p = 4$ case (executed with 4 processors) and 0.76 in the $p = 8$ case (executed with 8 processors).

2. **WILKINSON MATRICES.** The well-known Wilkinson bidiagonal matrix of size $n \times n$ with very ill-conditioned eigenvalues was used to check our algorithm. The best results were obtained in the case that the undesired eigenvalues were $\lambda_i = n - i + 1$ and the eigenvalues to be assigned were $\mu_i = -i$ with $i = 1, \dots, p$.

Table 1. Relative errors.

	E_N	E_R	E_C
$n = 513, p = 4$	10^{-11}	10^{-10}	10^{-16}
$n = 513, p = 8$	10^{-6}	10^{-9}	10^{-11}

Table 2. Computed times and speed-ups.

	T_0	T_1	T_p	$S_0 = \frac{T_0}{T_p}$	$S_1 = \frac{T_1}{T_p}$
$n = 513, p = 4$	4.327	2.67	0.685	6.316	3.90
$n = 513, p = 8$	8.68	5.29	0.87	9.97	6.08

Table 3. Relative errors in the Wilkinson matrix.

p	1	2	3	4	5	6
E_N	0	10^{-12}	10^{-9}	10^{-6}	10^{-4}	10^{-2}
E_U	0	0	0	0	0	0

Under these conditions, we obtained very accurate results running our code for matrices up to $n = 500$ and $p \leq 6$. We present the results of the proposed algorithm for the Wilkinson matrix of order 256 and different number of new eigenvalues in Table 3. As shown in Table 3, E_N means the same as above, and E_U represents the relative errors in the unmodified spectrum. Because of the structure of the Wilkinson matrix and the eigenvalues selected, the vector solution f has zeroes in the last $(n - p)$ components. Therefore, the eigenvalues placed in the last $(n - p)$ entries of the diagonal are unchanged and then E_U is zero everywhere.

REFERENCES

1. G. Miminis and C.C. Paige, An algorithm for pole assignment of time invariant linear systems, *Int. Journal of Control* **35**, 340–354 (1981).
2. R.V. Patel and P. Misra, Numerical algorithms for eigenvalues assignment by state feedback, *Proc. IEEE* **17**, 1755–1764 (1984).
3. R. Bru, J. Mas and A. Urbano, An algorithm for the single-input pole assignment problem, *SIAM J. on Matrix Anal. and Appl.*, 15–22, 1994 (to appear).
4. B.N. Datta, An algorithm to assign eigenvalues in a Hessenberg Matrix: Single-input case, *IEEE Trans. Automat. Control* **AC-32**, 414–417 (1987).
5. J. Kautsky, N.K. Nichols and P. Van Dooren, Robust pole assignment in linear feedback, *Int. Journal of Control* **41**, 1129–1155 (1985).
6. Y. Saad, A projection method for partial pole assignment in linear state feedback, *IEEE Trans. Automat. Control* **33** (3), 290–297 (1988).
7. B.N. Datta and Y. Saad, Arnoldi methods for large Sylvester-like observer matrix equations, and an associated algorithm for partial spectrum assignment, *Linear Algebra and its Applications*, 154–156, 225–244 (1991).
8. R. Bru, J. Cerdán and A. Urbano, An algorithm for the multi-input pole assignment problem, *Linear Algebra and Applications* (1994) (to appear).

MUON CAPTURE REVISITED

H.C. CHIANG¹, E. OSET and P. FERNÁNDEZ DE CÓRDOBA

*Departamento de Física Teórica and IFIC, Centro mixto Universidad de Valencia-CSIC,
Facultad de Físicas, Burjassot (Valencia), Spain*

Received 21 June 1989

Abstract: The problem of inclusive muon capture in nuclei is studied by calculating the capture rate in asymmetric infinite nuclear matter and using the local density approximation to evaluate the capture rates in nuclei. It is shown that the method is rather reliable and allows one to improve on approximations used in the past. The need for a strong nuclear renormalization is shown, reducing the capture rates by about a factor two in medium and heavy nuclei. By using standard effective interactions in the spin-isospin channel one can account for this renormalization and one finds a remarkable overall agreement with the measured capture rates for a large list of nuclei through the periodic table.

1. Introduction

In this paper we face the problem of total muon capture in nuclei from an unconventional point of view. From the early days of Primakoff¹⁾ the subject has attracted much interest^{2,3)}. The usual approach consists in performing the nonrelativistic approximation in the transition operators, neglecting the nucleon momentum¹⁻⁴⁾, and then doing a closure sum over the final nuclear states. However, the process involves small energy transfers to the nucleus of the order of the typical nuclear excitation energies and the results are very sensitive to the average nuclear excitation energy chosen⁵⁾. To eliminate the uncertainties associated to this energy, or equivalently, to the average neutrino energies, sum rule approaches have been applied⁵⁻⁷⁾ which reduce considerably the dependence on the average energy and hence provide more reliable results. The final results require the evaluation of non-trivial two-body matrix elements in the ground state of the nucleus.

The approximation of an average neutrino energy fixes the momentum transfer, q , and thus, the pseudoscalar term to a determined value. However, the dependence of this term on q is strong because of its approximate proportionality to the pion propagator²⁾. This is particularly relevant since this reaction has been used traditionally to extract information on the value of the pseudoscalar coupling constant²⁻⁸⁾.

Another approximation used to take into account the finite size of the nucleus is the use of the effective charge, Z_{eff} , which introduces a non-negligible source of error in the calculation since the capture rate is proportional to Z_{eff}^4 and certain

¹ On leave of absence from Institute of High Energy Physics, Academia Sinica, Beijing, China.

approximations are involved in its evaluation⁹⁾). In addition there are strong nuclear renormalization effects which are very important and deserve special attention.

Our approach avoids all of these shortcomings and provides a highly accurate method to evaluate the total capture rate in nuclei. Yet the method is much simpler technically than the traditional approaches and the same effort is required to evaluate the rate in light nuclei and in heavy nuclei. Furthermore, it has the virtue of showing that the only relevant nuclear information needed, as normally happens in other inclusive reactions¹⁰⁾, is the neutron and proton densities of the nuclear ground state, which we take from experiment to minimize errors.

The method consists in evaluating the capture rate of a muon in a Fermi sea of neutrons and protons. The calculation can be done exactly in a relativistic framework considering the nucleon momenta and the excitation energies of the Fermi sea, thus going beyond the closure sum or the sum rule approach. With the neutrino energy as a variable of integration, the pion pole structure of the pseudoscalar term is kept in the calculations. The step from infinite matter to finite nuclei is done by means of the local density approximation. The infinite matter calculation provides the muon width as a function of $\rho_{n,p}$ the neutron and proton densities, then we assume $\rho_{n,p} \rightarrow \rho_{n,p}(r)$ and fold this functional with the muon density distribution in the 1s state of the muon atom, from which the capture takes place. The local density approximation is highly accurate in this case, given the very weak q dependence of the matrix elements involved, which makes the transition of very short range. Only the pseudoscalar term depends more strongly on q because of its dependence on the pion propagator, but the moderate contribution of this term ($\sim 15\%$), together with the fairness of the local density prescription in pion nuclear reactions¹¹⁾ involving similar pion momenta, makes the use of the local density prescription a very accurate tool to obtain the total muon capture rate.

Then we avoid using the concept of Z_{eff} . Indeed all we need is to calculate the 1s muon wave function and use it in the folding of the local density prescription. Here we also keep up with our aim of a highly accurate evaluation and use a very precise method to solve the Schrödinger equation¹²⁾, taking into account finite size effects and vacuum polarization corrections.

In addition we include strong nuclear renormalization effects in the operators, and also consider the binding energies of the muons. The calculations are performed for a large list of nuclei over the whole periodic table and the results obtained are very instructive. With the standard coupling constants and form factors for $\mu p \rightarrow \nu_{\mu} n$, we obtain a very good agreement with all nuclei along the periodic table, showing the relevance of the nuclear renormalization in medium and heavy nuclei, which reduces the capture rates in about a factor two from the results without renormalization. The repercussion of such renormalization in other physical processes like pionic atoms or Σ hypernuclei is also stressed.

The paper proceeds as follows. In sect. 2 we evaluate the muon capture rates in infinite nuclear matter. In sect. 3 we discuss the nuclear renormalization and in sect.

4 the local density approximation. Sect. 5 contains the results and discussion and sect. 6 summarizes our results.

2. Muon capture rate in infinite matter

We start from the basic lagrangian for the $\mu^-p \rightarrow n\nu_\mu$ reaction depicted in fig. 1,

$$L(x) = \sqrt{\frac{1}{2}} G J^\mu(x) L_\mu^+(x), \tag{1}$$

with the leptonic and hadronic currents given respectively by

$$L_\mu^+(x) = \bar{\Psi}_\nu \gamma^\mu (1 - \gamma_5) \Psi_\mu, \quad J^\mu(x) = \bar{\Psi}_n B^\mu \Psi_p, \tag{2}$$

with B^μ the hadronic current operator. Their matrix elements between spinors give

$$\begin{aligned} \tilde{L}^{\mu+} &\rightarrow \bar{u}_\nu(p_\nu) \gamma^\mu (1 - \gamma_5) u_\mu(p_\mu), \\ \tilde{J}^\mu &\rightarrow \bar{u}_n(p_n) [g_V \gamma^\mu + i \frac{g_M}{2m_p} \sigma^{\mu\nu} q_\nu + g_A \gamma^\mu \gamma_5 + \frac{g_P}{m_\mu} q^\mu \gamma_5] u_p(p_p), \end{aligned} \tag{3}$$

where we follow Itzykson and Zuber¹³⁾ convention for the γ -matrices, with $q = p_n - p_p$, and g_V, g_M, g_A, g_P the vector, magnetic, axial-vector and pseudoscalar coupling constants respectively, including a form factor dependent on q . The values of the coupling constants and the expressions for the form factors can be seen in appendix A.

Assume for a moment an infinite nuclear medium with a proton density, ρ_p , and the protons at rest. The decay rate of a muon is given by

$$\Gamma = \sigma v_{rel} \rho_p, \tag{4a}$$

with v_{rel} the relative velocity of the muon with respect to the protons, and σ the $\mu p \rightarrow n\nu_\mu$ cross section. We have in Bjorken and Drell convention¹⁴⁾

$$\begin{aligned} \sigma v_{rel} &= \int \frac{d^3 p_\nu}{(2\pi)^3} \frac{2m_\nu}{2E_\nu} \frac{2m_n}{2E_n} \frac{2m_\mu}{2E_\mu} \frac{2m_p}{2E_p} \bar{\Sigma} \Sigma |T|^2 \\ &\times 2\pi \delta(E_\mu + E_p - E_\nu - E_n), \end{aligned} \tag{4b}$$

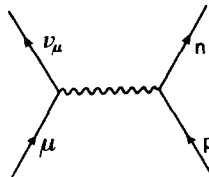


Fig. 1. Diagram for $\mu^-p \rightarrow n\nu_\mu$ process.

where the limit $m_\nu \rightarrow 0$ is to be taken and three momentum conservation is implicitly assumed. The full expression for $\overline{\Sigma} \Sigma |T|^2$ is given in appendix B.

The evaluation of Γ for finite nuclei proceeds in two steps. In the first one we evaluate Γ for a muon in a Fermi sea of protons and neutrons with $N \neq Z$. This is easily accomplished if one realizes that $-\pi\rho_p\delta(E_\mu + E_p - E_\nu - E_n)$ is the static limit of the imaginary part of the Lindhard function $\bar{U}(p_\mu - p_\nu)$ [see ref. ¹⁵] for the ph excitation appearing in fig. 2. This Lindhard function, incorporating the Pauli blocking on the neutrons, is given by

$$\bar{U}(p_\mu - p_\nu) = 2 \int \frac{d^3p}{(2\pi)^3} \frac{n_1(\mathbf{p})[1 - n_2(\mathbf{p} + \mathbf{p}_\mu - \mathbf{p}_\nu)]}{E_\mu - E_\nu + E_p(\mathbf{p}) - E_n(\mathbf{p} + \mathbf{p}_\mu - \mathbf{p}_\nu) + i\epsilon}, \tag{5}$$

where $n_{1,2}(p)$ are the occupation numbers in the Fermi sea of protons and neutrons, respectively. (The Lindhard function contains also the contribution from the backward going ph excitation, which we do not include in eq. (5) because it does not contribute to the imaginary part for $E_\mu - E_\nu > 0$, as we have here.) We observe that the δ function for energy conservation is substituted in $\text{Im } \bar{U}$ by the same δ of conservation but keeping track of the nucleon momenta, integrating over the Fermi sea of the protons and including the Pauli blocking for the neutrons, $[1 - n_2]$ factor.

Hence the actual width of a muon in the infinite matter slab is given by

$$\Gamma = -2 \int \frac{d^3p_\nu}{(2\pi)^3} \frac{2m_\nu}{2E_\nu} \frac{2m_\mu}{2E_\mu} \frac{2m_p}{2E_p} \frac{2m_n}{2E_n} \overline{\Sigma} \Sigma |T|^2 \text{Im } \bar{U}(p_\nu - p_\mu). \tag{6}$$

For E_p, E_n in the explicit factors of eq. (6), the average over the Fermi sea of appendix B is used, although one can take these energies equal to the respective masses with no significant change.

A different derivation for the analogous case of radiative pion capture has been done in ref. ¹⁶) where an explicit analytical formula for $\text{Im } \bar{U}$ is given in the appendix.

Eq. (6) provides the muon capture width as a function of $k_{F,p}$ and $k_{F,n}$, the proton and neutron Fermi momenta or equivalently ρ_p and ρ_n , the proton and neutron densities of the medium ($\rho_{p,n} = k_{F,p,n}^3/3\pi^2$).

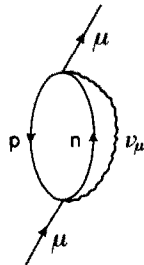


Fig. 2. Many-body Feynman diagram for the muon self-energy related to the $\mu^- p \rightarrow \nu_\mu n$ process.

3. Strong renormalization effects

The dominant contribution, ($\sim 80\%$), to the process comes from the term proportional to g_A^2 in $\bar{\Sigma} \Sigma |T|^2$ of appendix B. The nonrelativistic reduction of the axial-vector term in the nucleon current is of the type $g_A \sigma^i \tau^\lambda$. We know that this external source has the virtue of polarizing the axial charge of the nuclear medium^{17,18} which can produce a sensible renormalization of the capture rate. Microscopically we can depict the situation by saying that the Feynman diagram of fig. 2 is now modified to include the series of diagrams implicit in fig. 3, where the wavy line stands for the spin-isospin ph or Δh interaction¹⁸)

$$V(q) = \frac{f^2}{\mu^2} [V_\ell \hat{q}_i \hat{q}_j + V_t (\delta_{ij} - \hat{q}_i \hat{q}_j)] \sigma_i \sigma_j \tau \tau, \tag{7}$$

for the ph case, or a similar one for the case of ph- Δh or Δh - Δh interaction by substituting $\sigma \rightarrow S$, $\tau \rightarrow T$, the spin and isospin transition operators, and $f \rightarrow f^*$ ($f^2/4\pi = 0.08$, $f^{*2}/4\pi = 0.37$). The term with g_A^2 involves the trace of $g_A^2 \sigma_i \sigma_i \bar{U}$, which equivalently can be written as $g_A^2 \sigma_i \sigma_j \bar{U} [\hat{q}_i \hat{q}_j + (\delta_{ij} - \hat{q}_i \hat{q}_j)]$, explicitly separated into a longitudinal, $(\hat{q}_i \hat{q}_j)$, and a transverse part, $(\delta_{ij} - \hat{q}_i \hat{q}_j)$. The sum implicit in fig. 3 leads to two independent geometric series, in the longitudinal and transverse channels. Hence we have for the case of ph excitation only

$$\begin{aligned} g_A^2 \text{Tr} (\sigma_i \sigma_i \bar{U}) &= 3g_A^2 2\bar{U} \\ &\rightarrow g_A^2 \text{Tr} (\sigma_i \sigma_j) \bar{U} \left\{ \frac{\hat{q}_i \hat{q}_j}{1 - 2\bar{U}V_\ell} + \frac{(\delta_{ij} - \hat{q}_i \hat{q}_j)}{1 - 2\bar{U}V_t} \right\} \\ &= 3g_A^2 2\bar{U} \left\{ \frac{1}{3} \frac{1}{1 - 2\bar{U}V_\ell} + \frac{2}{3} \frac{1}{1 - 2\bar{U}V_t} \right\}, \end{aligned} \tag{8}$$

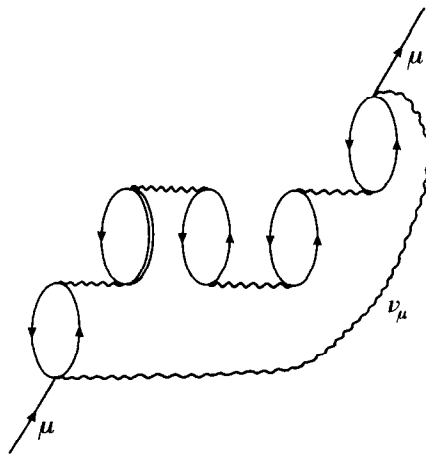


Fig. 3. Many-body Feynman diagrams accounting for the medium polarization in the spin-isospin channel driven by the $\mu^- p \rightarrow \nu_\mu n$ transition.

where the factor 2 in the denominator comes from isospin dependence of eq. (7), since exchange of charged objects is involved in the interaction. Since we had $\text{Im } \bar{U}$ in eq. (6) we have to substitute $3g_A^2 \text{Im } 2\bar{U}$ by the imaginary part of the last expression in eq. (8). Hence the renormalization amounts to substituting,

$$g_A^2 \text{Im } 2\bar{U} \rightarrow g_A^2 \left\{ \frac{1}{3} \frac{\text{Im } 2\bar{U}}{|1-2\bar{U}V_\ell|^2} + \frac{2}{3} \frac{\text{Im } 2\bar{U}}{|1-2\bar{U}V_t|^2} \right\}. \quad (9)$$

Taking account of the Δh excitation and the backward propagating ph excitation (see fig. 3), not accounted for by \bar{U} , is straightforward and can be implemented by substituting $2\bar{U}$ by U , the Lindhard function of refs. ^{15,18}). The different coupling of N and Δ is incorporated in U_Δ ($U = U_N + U_\Delta$) and the same universal interaction V_ℓ, V_t is used for the ph or Δh interaction ^{15,18}).

Thus, ultimately the renormalization can be taken into account by substituting

$$g_A^2 \text{Im } 2\bar{U} \rightarrow g_A^2 \left\{ \frac{1}{3} \frac{\text{Im } 2\bar{U}}{|1-UV_\ell|^2} + \frac{2}{3} \frac{\text{Im } 2\bar{U}}{|1-UV_t|^2} \right\}, \quad (10)$$

where we have used the fact that U_Δ does not have an imaginary part in the kinematical regime where we move. The actual calculations are done by using the expressions of U for symmetrical nuclear matter but the expression for $\text{Im } \bar{U}$, for $\rho_n \neq \rho_p$, in the numerator is kept. This approximation, also done in ref. ¹⁵), is accurate enough for our purposes.

The pieces involving the pseudoscalar term, g_P , behave differently. Indeed the $g_P \sigma \mathbf{q}$ coupling, in the nonrelativistic limit, singles out the longitudinal part of the interaction and the renormalization is then

$$g_P \text{Im } 2\bar{U} \rightarrow g_P \frac{\text{Im } 2\bar{U}}{|1-UV_\ell|^2}, \quad (11)$$

Analogously, the terms involving g_M single out the transverse part of the interaction and we have

$$g_M \text{Im } 2\bar{U} \rightarrow g_M \frac{\text{Im } 2\bar{U}}{|1-UV_t|^2}, \quad (12)$$

The other terms, and the $g_M g_P$ term, which are rather small, are not renormalized.

For the calculations we take the widely used forms

$$\begin{aligned} V_\ell(q) &= \frac{f^2}{\mu^2} \left\{ \frac{\mathbf{q}^2}{q^{02} - \mathbf{q}^2 - \mu^2} \left(\frac{\Lambda^2 - \mu^2}{\Lambda^2 - q^2} \right)^2 + g' \right\}, \\ V_t(q) &= \frac{f^2}{\mu^2} \left(\frac{\mathbf{q}^2}{q^{02} - \mathbf{q}^2 - m_\rho^2} C_\rho \left(\frac{\Lambda_\rho^2 - m_\rho^2}{\Lambda_\rho^2 - q^2} \right)^2 + g' \right), \end{aligned} \quad (13)$$

with $\Lambda \approx 1300$ MeV, $C_\rho = 2$, $\Lambda_\rho = 2500$ MeV and μ, m_ρ the pion and ρ meson masses. The magnitude g' is the Landau-Migdal parameter with accepted values around $g' \approx 0.6-0.8$. We have performed calculations with $g' = 0.7$ which lead to good results compared with experiment.

4. The local density approximation

After performing the renormalization of sect. 2 in eq. (6) we obtain the new muon capture width $\tilde{\Gamma}(\rho_p, \rho_n)$. The local density approximation (LDA) to go to finite nuclei is obtained by replacing $\rho_p \rightarrow \rho_p(\mathbf{r})$, $\rho_n \rightarrow \rho_n(\mathbf{r})$ for the actual nuclei and evaluating

$$\Gamma = \int d^3r |\Phi_{1s}(\mathbf{r})|^2 \tilde{\Gamma}(\rho_p(\mathbf{r}), \rho_n(\mathbf{r})), \quad (14)$$

where $\Phi_{1s}(\mathbf{r})$ is the muon wave function in the 1s state from where the capture takes place. The LDA assumes implicitly a zero range of the interaction, or no dependence on q equivalently. As we can see in appendix A the q -dependence of the form factors is extremely weak and thus the LDA prescription becomes highly accurate. Only the terms with g_p , which contain a pion propagator, have a stronger dependence on q . The LDA prescription would then be less accurate for these terms. However, the fact that these terms contribute about 18% (the $g_p g_A$ term, of sign opposite to the g_A^2 one, is the most important among them) and that the LDA approximation is still fair for pionic processes involving momenta of the range of the pion mass¹¹), make globally the LDA a very accurate tool to evaluate Γ for actual nuclei.

Note, however, that the approach differs substantially from standard ones, which require the evaluation of two-body matrix elements for the ground state of the nucleus. Here we do not evaluate any nuclear matrix element and the only nuclear information needed is the proton and neutron densities. The proton density is taken from the experimental charge distribution¹⁹) and parametrized in terms of two Fermi parameter distribution after correcting for the finite size of the proton¹⁰). For the neutron density we take $\rho_n = (N/Z)\rho_p$. For nuclei smaller than ¹⁸O the harmonic oscillator densities are used.

As pointed out in the introduction some approaches use a closure sum over the nuclear intermediate states¹⁻⁴). Others, more elaborated and accurate⁵⁻⁷), use a sum rule approach which still relies upon an average excitation energy, although the dependence of Γ on this variable is rather smooth, unlike in the closure sum case. Here the Lindhard function has summed the contribution from intermediate nuclear states (the excited states of neutrons on top of the Fermi sea) by keeping track of the energy of such states, which is important when the excitation energy is small like in the present case. However, only the kinetic energy of the nucleons is considered in the Lindhard function. Note, however, that if a local potential $V(\mathbf{r})$ is added to the nucleon energies, it would cancel exactly in the ph propagator of eq. (5). Hence, up to nonlocalities in the nuclear potential the Lindhard function keeps good track of nuclear excitation energies. On the other hand, the nucleon momentum dependence on $\overline{\sum \sum |T|^2}$, which is rather smooth, has also been considered, as shown in appendix B by means of the energy conservation or taking an average of p^2 in the local Fermi sea.

On the other hand, we do not have to rely upon the concept of Z_{eff} . Eq. (14) provides Γ directly from the muon wave function and the function $\tilde{F}(\rho_p(\mathbf{r}), \rho_n(\mathbf{r}))$. In order to evaluate the muon wave function we have considered the Coulomb interaction taking account of the finite size of the nucleus and vacuum polarization, as done for pionic atoms^{20,21}). The numerical calculations have been done by using a very accurate method to solve the Schrödinger equation¹²⁾ which gives us the muon energy and the wave function. For heavy nuclei like ^{208}Pb the binding energy of the muon is about 10 MeV and it is important to take this into account for an accurate determination of the muon capture width.

With all these improvements over previous approaches, it is still remarkable that the present method is quite much simpler technically, as revealed by the basic formulae, eqs. (5), (6) and (14). This has allowed us to perform calculations for a large list of nuclei over the whole periodic table and concentrate on the role on the nuclear renormalization, of much relevance in a variety of nuclear processes, from pionic atoms to Σ or Λ hypernuclei¹⁸⁾.

It is also interesting to recall that we have used here the same model and value of g' that were used in refs.^{22,23)} to account for the observed quenching of g_A in ordinary β -decay. Note, however, that since in β -decay the momentum transfer is negligible, V_e and V_i in eqs. (13) are the same and both repulsive. Also U in the denominator of eq. (10) is rather different to the one here because of the different kinematics, with the Lindhard function in the β -decay due essentially to Δh excitation.

The same model gives good results in these two different kinematical situations and in radiative pion capture¹⁶⁾ where gauge invariance produces a quenching from the transverse part alone. This is a good test of consistency for the nuclear renormalization which, as we shall see, is very important in this case.

6. Results and discussion

Before we proceed to show the results we discuss a few ideas related to the calculations and the results. In the first place, in order to get an approximate idea of the importance of the different terms in appendix B we show the approximate weight of the terms in $|T|^2$, calculated at the peak of the neutrino momentum distribution

$$\begin{aligned} \frac{g_V^2\text{-term}}{1} &= \frac{g_A^2\text{-term}}{3.5} = \frac{g_A g_V\text{-term}}{0.14} = \frac{g_A g_M\text{-term}}{0.5} \\ &= \frac{g_A g_P\text{-term}}{-0.92} = \frac{g_P^2\text{-term}}{0.17}, \end{aligned} \quad (15)$$

with the terms with g_M^2 , $g_M g_P$ and $g_V g_M$ rather small. These ratios change by about 20–30% with respect to those in the standard closure approaches^{1–4)}.

We also mentioned that taking into account the binding of the muon was important in heavy nuclei. Indeed with a binding energy of 11.25 MeV for the 1s state of the muon in ^{208}Pb , taking into account this binding reduces the capture width in 35%.

The neglect of the nucleon momentum in $|T|^2$ also introduces some uncertainties in the calculation. We have made $\mathbf{p} = 0$ in $|T|^2$ in our calculations and have found changes at the level of 10–20% in the individual terms, with a global reduction of 15% with respect to the calculation without neglecting this momentum.

The Pauli blocking effect is very important. In the $\mu^- \text{p} \rightarrow \text{n} \nu_\mu$ reaction the neutron is forbidden to go to any of the neutron occupied states. This is taken into account in our approach by means of the factor $1 - n_2(k)$ in the Lindhard function of eq. (5). Neglecting this factor leads to results for the capture rate about a factor 2.6 times bigger than with the corresponding Pauli blocking for nuclei around ^{16}O and a factor 3.6 for nuclei around ^{208}Pb .

We have also estimated the effects of considering the muon momentum in the calculations (we have set it equal to zero in our results) and have found them to be small, below 5%. We should also note that our calculations of $|T|^2$ have been performed using free relativistic spinors for the nucleons and the muon and neutrino. The nucleons and muon moving in a potential would lead to different spinors. In the case of nucleons in infinite matter, and assuming a scalar potential $V(\mathbf{r})$ given by the Thomas–Fermi approach²⁴⁾, the structure of the spinors would be the same but the mass would be changed to $M + V(\mathbf{r})$. We have performed the calculations with these modifications and found corrections at the level of 2%. The muon spinor in the presence of a point-like Coulomb source is also modified although the modifications are smaller when the finite size of the nucleus is considered²⁵⁾. However, the evaluation of the muon wave function in the nucleus has been done by using the nonrelativistic Schrödinger equation. We have obtained an idea of what the relativistic effects could be by treating the muon as a boson and solving the Klein–Gordon equation instead of the Schrödinger equation, as done for pionic atoms²¹⁾. We found corrections at the level of 2%.

Thus it looks that the approximations that we are still doing are rather under control. However, we have improved on other approximations which were done before in order to make the problem tractable, and which could be easily avoided in our approach.

After this discussion we pass on to present our results. A rather exhaustive list of nuclei has been studied and the results appear in table 1. We show results for nuclei from ^6Li up to ^{209}Bi . The capture rates Γ vary from $0.3 \times 10^4 \text{ s}^{-1}$ to $0.15 \times 10^8 \text{ s}^{-1}$.

We have included in the table the different experimental results which we have extracted from ref.²⁶⁾. The overall agreement between the theoretical results and the experiment is spectacular considering the amount of nuclei studied and the large variation of the rates (four orders of magnitude) from light to heavy nuclei.

One finds larger discrepancies of the order of 30% in some nuclei like ^7Li , ^{44}Ti , ^{59}Co and the isotopes of Ni, but for the large majority of nuclei there is agreement with

experiment or there are differences at the level of 10%. We present a selection of the most stable isotopes as a function of Z in fig. 4 in order to give a visual idea of the quality of the agreement.

As we have mentioned before, the renormalization discussed in sect. 3 has very important effects in this problem. Indeed, in fig. 5 we show the results calculated with and without the renormalization, as a function of Z . We can see that for medium and heavy nuclei the nuclear renormalization reduces the results in about a factor two and it is essential to produce agreement with the experimental numbers. This reduction factor is much bigger than the estimates of ref. ³⁸), where a small quenching due to the axial polarization was suggested. This is a very interesting process, which evidences the strong nuclear renormalization on top of a weak interaction process, which can be brought under control as we have shown here. Although similar effects due to the spin-isospin polarization of the nucleus also appear in many nuclear processes ¹⁸), sometimes it is more difficult to assess their importance since the nuclear interaction itself can be less controllable. However, it is interesting to recall that these medium polarization effects were considered in connection with the problem of Σ decay in nuclei and led to the interesting conclusion that there should be narrow Σ hypernuclear bound states of around $\Gamma \approx 5-7$ MeV [refs. ^{27,28})]. The first of such states has been found recently, ^4_2He , with a width of 4.5 MeV [ref. ²⁹)]. Similarly using the same concept, in connection with the Δ self-energy, it was hinted ³⁰) and shown recently ³¹), that this medium polarization is the key to understanding the problem of the pionic anomalous atoms ^{32,33}). The clean effects of this medium renormalization shown here can only stress and reinforce the interpretation given for these other phenomena.

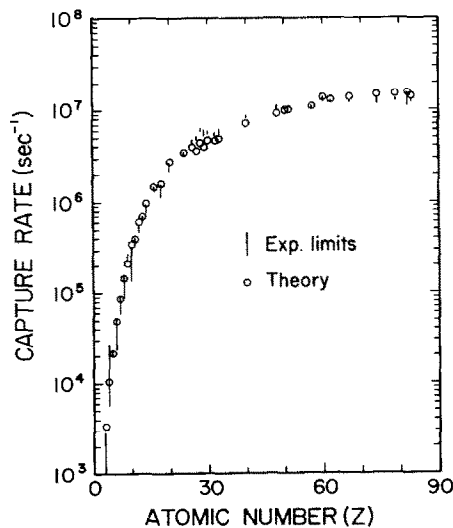


Fig. 4. Total rates for negative muons captured by the most stable isotopes. Circles are our theoretical results. Experimental limits from different groups are shown. Data are from ref. ²⁶).

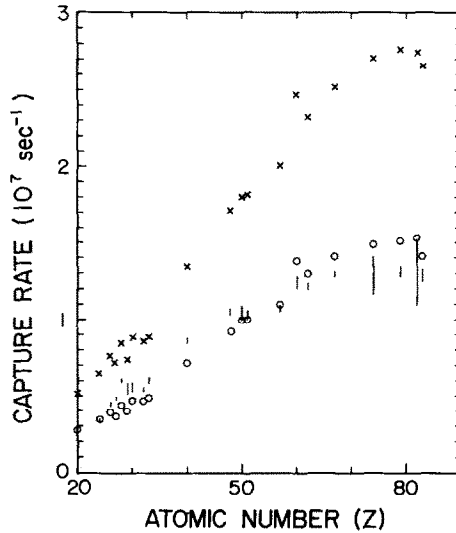


Fig. 5. The nuclear medium renormalization effect in the calculation of total nuclear capture rates of μ^- . Crosses and circles are calculations without and with the renormalization respectively.

Isotopic effects would appear to be tied to the particular shell structure of the nucleus, given the relevance of the Pauli blocking in the problem. It is interesting to show our results for different isotopes. Although the absolute numbers for Γ appear in table 1, we have calculated the ratios for several isotopes and show them in table 2, comparing the theoretical results with those of refs.^{26,34-36}). There are discrepancies of the order of 50% in the Li isotopes. With so few nucleons, shell effects are more important and the concept of a Fermi sea of protons and neutrons with only 3 particles is a bit extreme. The discrepancies are smaller of the order of 10-15% for the C, O and Ca isotopes, and for other nuclei the agreement is very good.

5. Conclusions

We have used a simple, yet reliable method, to evaluate the total muon capture rate in nuclei, which consists in evaluating the muon capture width in infinite nuclear matter with $N \neq Z$ as a function of ρ_p, ρ_n and then adapt the results to finite nuclei via the local density approximation. The method allows for an accurate evaluation of the reaction probability without the need for approximations done in the past, like neglecting the nucleon momentum, using the closure sum or sum rule approaches to sum over nuclear intermediate states, using the concept of an effective Z , neglecting the binding of the muon, taking an average neutrino energy, etc. In addition, we make a highly accurate determination of the muon wave function for the 1s state from where the muon is captured. The method has the virtue of showing that the relevant nuclear magnitudes are the proton and neutron densities and that nuclear

TABLE 1

Theoretical results for total nuclear capture rates of negative muons compared with data. Experiments are taken from ref. ²⁶⁾ and references therein.

A	Z	Calculation (s ⁻¹)	Experiments (10 ³ s ⁻¹)	A	Z	Calculation (s ⁻¹)	Experiments (10 ³ s ⁻¹)
6	3	0.473051 × 10 ⁴	6.100 ± 1.400 4.680 ± 0.120 4.180 ± 0.450	20	10	0.346504 × 10 ⁶	0.204 ± 0.010 0.167 ± 0.030 0.30 ± 0.02 0.235 ± 0.005
7	3	0.338267 × 10 ⁴	1.800 ± 1.100 2.260 ± 0.120 1.810 ± 0.440	23	11	0.398167 × 10 ⁶	0.387 ± 0.015 0.3772 ± 0.0014
9	4	0.106016 × 10 ⁵	18 ± 10 10 ± 2 5.9 ± 0.2 7.4 ± 0.5	24	12	0.611794 × 10 ⁶	0.507 ± 0.020 0.480 ± 0.002 0.52 ± 0.02 0.4841 ± 0.0018
10	5	0.270790 × 10 ⁵	26.5 ± 1.5 27.8 ± 0.7	27	13	0.698167 × 10 ⁶	0.691 ± 0.020 0.662 ± 0.003 0.650 ± 0.015 0.7054 ± 0.0013
11	5	0.215267 × 10 ⁵	21.8 ± 1.6 21.9 ± 0.7	28	14	0.967561 × 10 ⁶	0.777 ± 0.025 0.850 ± 0.003 0.86 ± 0.04 0.8712 ± 0.0018
12	6	0.491425 × 10 ⁵	44 ± 10 36 ± 4 37.3 ± 1.1 36.1 ± 1.0 37 ± 7 39.7 ± 1.3 36.5 ± 2.0 30.3 ± 7.0 37.6 ± 0.4 35.2 ± 2.0 37.7 ± 0.7 38.8 ± 0.5	32	16	0.147345 × 10 ⁷	1.39 ± 0.09 1.31 ± 0.03 1.34 ± 0.01 1.352 ± 0.003
13	6	0.382118 × 10 ⁵	33.8 ± 0.4 37.6 ± 0.7	40	18	0.158576 × 10 ⁷	1.20 ± 0.08 1.41 ± 0.11
14	7	0.876191 × 10 ⁵	86 ± 11 65 ± 4 60.2 ± 0.8 68.4 ± 0.8 69.3 ± 0.8	40	20	0.277102 × 10 ⁷	2.55 ± 0.05 2.444 ± 0.023 2.529 ± 0.008 2.29 ± 0.05 2.557 ± 0.014
16	8	0.146072 × 10 ⁶	0.159 ± 0.014 0.098 ± 0.003 0.098 ± 0.005 0.095 ± 0.008 0.1026 ± 0.0006	44	20	0.212757 × 10 ⁷	1.793 ± 0.040
18	8	0.115035 × 10 ⁶	0.0880 ± 0.0015	44	22	0.364563 × 10 ⁷	2.63 ± 0.06 2.60 ± 0.04 2.590 ± 0.012
19	9	0.212870 × 10 ⁶	0.254 ± 0.022 0.235 ± 0.010 0.231 ± 0.006 0.229 ± 0.001	50	24	0.390693 × 10 ⁷	3.825 ± 0.050
				52	24	0.345514 × 10 ⁷	3.452 ± 0.047
				53	24	0.323095 × 10 ⁷	3.297 ± 0.045
				54	24	0.304124 × 10 ⁷	3.057 ± 0.042
				56	26	0.392927 × 10 ⁷	4.53 ± 0.10 4.38 ± 0.07 4.40 ± 0.05 4.411 ± 0.024

TABLE 1—continued

A	Z	Calculation (s ⁻¹)	Experiments (10 ³ s ⁻¹)	A	Z	Calculation (s ⁻¹)	Experiments (10 ³ s ⁻¹)
59	27	0.365026 × 10 ⁷	4.89 ± 0.09 4.96 ± 0.05 4.940 ± 0.029	119	50	0.999416 × 10 ⁷	10.5 ± 0.4 10.70 ± 0.14 10.44 ± 0.18
58	28	0.439701 × 10 ⁷	6.11 ± 0.10	122	51	0.100345 × 10 ⁸	10.49 ± 0.14 10.21 ± 0.20
60	28	0.398315 × 10 ⁷	5.56 ± 0.10	139	57	0.110223 × 10 ⁸	10.71 ± 0.10
62	28	0.355090 × 10 ⁷	4.72 ± 0.10	144	60	0.138435 × 10 ⁸	12.32 ± 0.14 12.50 ± 0.33
64	29	0.397764 × 10 ⁷	5.79 ± 0.16 5.47 ± 0.20 5.66 ± 0.09 5.67 ± 0.09 5.676 ± 0.037	152	62	0.129497 × 10 ⁸	12.22 ± 0.17
64	30	0.469282 × 10 ⁷	5.76 ± 0.17 5.5 ± 0.1 5.76 ± 0.05 5.834 ± 0.039	165	67	0.141022 × 10 ⁸	12.95 ± 0.13
72	32	0.464783 × 10 ⁷	5.54 ± 0.06 5.569 ± 0.036	184	74	0.149203 × 10 ⁸	11.92 ± 0.30 13.5 ± 0.6 13.07 ± 0.21 12.36 ± 0.24
75	33	0.487336 × 10 ⁷	6.07 ± 0.07 6.06 ± 0.12 6.104 ± 0.043	197	79	0.151167 × 10 ⁸	13.39 ± 0.11 13.07 ± 0.28
90	40	0.719435 × 10 ⁷	8.59 ± 0.07 8.66 ± 0.08	208	82	0.153379 × 10 ⁸	11.70 ± 0.75 14.5 ± 0.75 12.98 ± 0.10 13.27 ± 0.22 13.45 ± 0.18
112	48	0.927524 × 10 ⁷	10.1 ± 0.5 10.63 ± 0.11 10.61 ± 0.18	209	83	0.141154 × 10 ⁸	12.20 ± 0.75 13.26 ± 0.07 13.01 ± 0.18

TABLE 2
Isotope effect in the total nuclear capture rates of negative muons

Isotopes	Calculation	Experiments	Ref.
${}^7\text{Li}/{}^6\text{Li}$	0.71	0.30 ± 0.19	³²⁾
		0.43 ± 0.11	²⁶⁾
${}^{11}\text{B}/{}^{10}\text{B}$	0.79	0.83 ± 0.07	³²⁾
		0.79 ± 0.03	²⁶⁾
${}^{13}\text{C}/{}^{12}\text{C}$	0.78	0.90 ± 0.02	³³⁾
		0.97 ± 0.02	²⁶⁾
${}^{18}\text{O}/{}^{16}\text{O}$	0.79	0.86 ± 0.02	²⁶⁾
${}^{44}\text{Ca}/{}^{40}\text{Ca}$	0.77	0.71 ± 0.02	³⁴⁾
${}^{52}\text{Cr}/{}^{50}\text{Cr}$	0.88	0.90 ± 0.02	³⁴⁾
${}^{53}\text{Cr}/{}^{50}\text{Cr}$	0.83	0.86 ± 0.02	³⁴⁾
${}^{54}\text{Cr}/{}^{50}\text{Cr}$	0.78	0.80 ± 0.02	³⁴⁾
${}^{53}\text{Cr}/{}^{52}\text{Cr}$	0.94	0.96 ± 0.02	³⁴⁾
${}^{54}\text{Cr}/{}^{52}\text{Cr}$	0.88	0.89 ± 0.02	³⁴⁾
${}^{54}\text{Cr}/{}^{53}\text{Cr}$	0.94	0.91 ± 0.02	³⁴⁾
${}^{60}\text{Ni}/{}^{58}\text{Ni}$	0.91	0.91 ± 0.02	³⁴⁾
${}^{62}\text{Ni}/{}^{58}\text{Ni}$	0.81	0.77 ± 0.02	³⁴⁾
${}^{62}\text{Ni}/{}^{60}\text{Ni}$	0.89	0.85 ± 0.02	³⁴⁾

shell effects seem to be relevant only for very light nuclei. With an accurate determination of the process involving the weak interaction we paid special attention to nuclear renormalization effects in the spin-isospin channel which affect the most important terms of the reaction. These effects are very important and we showed that they reduce the capture rates by about a factor two for medium and heavy nuclei.

The overall agreement of our results with experiment is remarkable for the set of 38 nuclei for which we had experimental data. The ratios of rates for different isotopes is also in quite good agreement with experiment except for very light nuclei, where our methods are obviously less reliable.

In summary we can conclude that our present knowledge of the weak processes together with the important nuclear renormalization effects lead to a satisfactory understanding of the process of inclusive muon capture in nuclei. The process has the virtue of showing very clearly the need for the nuclear renormalization. This is of particular importance since a similar renormalization appears in a variety of nuclear processes and leads to particular effects like a substantial reduction of the calculated Σ widths in Σ hypernuclei and is one of the ingredients leading to a solution of the systematic anomalies found in pionic atoms. The results found in this paper give an extra support to the interpretation given to the narrow Σ states and the pionic atom anomalies along the lines of this nuclear type of renormalization.

The continuous discussions with J. Bernabéu along the realization of this work were both enlightening and delighting and we would like to express our gratitude

to him. One of us (H.C.C.) gratefully acknowledges the Ministry of Education of Spain, the Department of Theoretical Physics and the Instituto de Física Corpuscular of Valencia University for their hospitality.

The work is supported by the CICYT.

Appendix A

COUPLING CONSTANTS AND FORM FACTORS

We follow ref. ⁸⁾ for this information actualized with the new information from ref. ³⁷⁾. For the vector and magnetic couplings we have

$$g_V(q^2) = G_{Ep}(q^2) - G_{En}(q^2),$$

$$g_M(q^2) = \frac{1}{1 - q^2/4M_p^2} [G_{Mp}(q^2) - G_{Mn}(q^2) - G_{Ep}(q^2) + G_{En}(q^2)], \quad (\text{A.1})$$

with G_E , G_M the Sachs electromagnetic form factors

$$G_{Ep}(q^2) = \frac{G_{Mp}(q^2)}{1 + \mu_p} = \frac{G_{Mn}(q^2)}{\mu_n} = -\frac{4M_p^2}{q^2} \frac{G_{En}(q^2)}{\mu_n} = G(q), \quad (\text{A.2})$$

with μ_p , μ_n the anomalous magnetic moments of the proton and the neutron respectively, $\mu_p = 1.7928$, $\mu_n = -1.9130$ and $q^2 = q^{02} - q^2$. $G(q^2)$ is given by

$$G(q^2) = \left(\frac{1}{1 - q^2/M_0^2} \right)^2, \quad (\text{A.3})$$

with $M_0^2 = 0.71 \text{ GeV}^2$.

For the axial-vector coupling we have

$$g_A(q^2) = g_A(0) \left(1 + \frac{1}{\pi} \frac{q^2}{4M_p^2} \right), \quad (\text{A.4})$$

with $g_A(0) = -1.259$. The coupling $G = G_0 \cos \theta$ with $G_0 = 1.16637 \times 10^{-5} \text{ GeV}^{-2}$, $\cos \theta = 0.974$.

For g_p we have taken the value extracted in ref. ⁸⁾, $g_p = -10.27$, which was calculated at the kinematics from μ capture from hydrogen. However, we have kept the pion propagator structure of the pseudoscalar term and taken correspondingly

$$g_p(q^2) = \frac{15m_\pi^2}{q^2 - m_\pi^2}, \quad (\text{A.5})$$

which approximately coincides with the numerical value given above for $q^2 = -0.88m_\mu^2$ of the kinematics of the μ capture, and is also very close to the value provided by the Goldberger-Treiman relation ^{2,3)}.

Appendix B

EXPRESSION FOR $\overline{\sum \sum |T|^2}$:

The sum over final polarizations and average over initial ones of $|T|^2$ for the T matrix obtained with the lagrangian of eq. (1) is given by,

$$\begin{aligned}
& 2m_p 2m_n 2m_\nu 2m_\mu \overline{\sum \sum |T|^2} / \frac{1}{2} G^2 \\
&= 16g_V^2 [(p_1 \cdot p_2)(p_3 \cdot p_4) + (p_1 \cdot p_4)(p_2 \cdot p_3) - m_p m_n (p_1 \cdot p_3)] \\
&\quad + 16g_A^2 [(p_1 \cdot p_2)(p_3 \cdot p_4) + (p_1 \cdot p_4)(p_2 \cdot p_3) + m_p m_n (p_1 \cdot p_3)] \\
&\quad + 32g_A g_V [(p_1 \cdot p_4)(p_2 \cdot p_3) - (p_1 \cdot p_2)(p_3 \cdot p_4)] \\
&\quad + 8 \left(\frac{g_M}{2M} \right)^2 [2(p_1 \cdot p_2)(p_3 \cdot q)(p_4 \cdot q) - 2(p_1 \cdot p_2)(p_3 \cdot p_4)q^2 \\
&\quad\quad + 2(p_1 \cdot p_4)(p_2 \cdot q)(p_3 \cdot q) - 2(p_1 \cdot p_4)(p_2 \cdot p_3)q^2 \\
&\quad\quad + (p_1 \cdot p_3)(p_2 \cdot p_4)q^2 - (p_1 \cdot p_3)m_p m_n q^2 \\
&\quad\quad - 2(p_1 \cdot q)(p_3 \cdot q)(p_2 \cdot p_4) - 2(p_1 \cdot q)(p_3 \cdot q)m_n m_p \\
&\quad\quad + 2(p_1 \cdot q)(p_2 \cdot q)(p_3 \cdot p_4) + 2(p_1 \cdot q)(p_4 \cdot q)(p_2 \cdot p_3)] \\
&\quad + 16g_V \frac{g_M}{2M} [-m_p (p_1 \cdot p_3)(p_4 \cdot q) - m_p (p_1 \cdot q)(p_3 \cdot p_4) - m_p (p_3 \cdot q)(p_1 \cdot p_4) \\
&\quad\quad + m_n (p_1 \cdot p_3)(p_2 \cdot q) + m_n (p_1 \cdot q)(p_3 \cdot p_2) + m_n (p_3 \cdot q)(p_1 \cdot p_2)] \\
&\quad + 32g_A \frac{g_M}{2M} [-m_n (p_3 \cdot q)(p_1 \cdot p_2) + m_n (p_2 \cdot p_3)(p_1 \cdot q) \\
&\quad\quad - m_p (p_3 \cdot q)(p_1 \cdot p_4) + m_p (p_3 \cdot p_4)(p_1 \cdot q)] \\
&\quad + 8 \left(\frac{g_P}{\mu} \right)^2 [(2(p_1 \cdot q)(p_3 \cdot q) - q^2(p_1 \cdot p_3))(p_2 \cdot p_4) - m_p m_n] \\
&\quad + 16g_A \frac{g_P}{\mu} [-m_p (p_1 \cdot p_4)(p_3 \cdot q) - m_p (p_1 \cdot q)(p_3 \cdot p_4) + m_p (p_4 \cdot q)(p_1 \cdot p_3) \\
&\quad\quad + m_n (p_1 \cdot p_2)(p_3 \cdot q) + m_n (p_1 \cdot q)(p_2 \cdot p_3) - m_n (p_2 \cdot q)(p_1 \cdot p_3)] \\
&\quad + 16 \frac{g_M}{2M} \frac{g_P}{\mu} [-(p_1 \cdot p_2)(p_3 \cdot q)(p_4 \cdot q) - (p_3 \cdot p_4)(p_1 \cdot q)(p_2 \cdot q) \\
&\quad\quad - q^2(p_1 \cdot p_4)(p_2 \cdot p_3) + (p_1 \cdot p_4)(p_2 \cdot q)(p_3 \cdot q) \\
&\quad\quad + (p_2 \cdot p_3)(p_1 \cdot q)(p_4 \cdot q) + q^2(p_1 \cdot p_2)(p_3 \cdot p_4)] \tag{B.1}
\end{aligned}$$

and we have taken

$$\begin{aligned} p_1 &\equiv p_\mu = (E_\mu, \mathbf{0}), & p_2 &\equiv p_p = (E_p, \mathbf{p}), \\ p_3 &\equiv p_\nu = (p_\nu, \mathbf{p}_\nu), & p_4 &\equiv p_n = (E_n, \mathbf{p} - \mathbf{p}_\nu), \\ q &\equiv p_\mu - p_\nu = (E_\mu - p_\nu, -\mathbf{p}_\nu), \end{aligned} \quad (\text{B.2})$$

with

$$E_p = \sqrt{m_p^2 + \mathbf{p}^2}, \quad E_n = \sqrt{m_n^2 + \mathbf{p}^2 + \mathbf{p}_\nu^2 - 2\mathbf{p} \cdot \mathbf{p}_\nu} \quad (\text{B.3})$$

and $\mathbf{p} \cdot \mathbf{p}_\nu$, from energy conservation, is given by

$$\mathbf{p} \cdot \mathbf{p}_\nu = M \left(p_\nu + \frac{p_\nu^2}{2M} - E_\mu \right), \quad (\text{B.4})$$

with M an average proton and neutron mass. For p^2 in the expressions we take an average over the Fermi sea

$$p^2 \rightarrow \frac{3}{5} \left(3\pi^2 \frac{Z}{A} \rho(\mathbf{r}) \right)^{2/3}. \quad (\text{B.5})$$

References

- 1) H. Primakoff, *Rev. Mod. Phys.* **31** (1959) 802
- 2) R.J. Blin-Stoyle, *Fundamental interactions and the nucleus* (North-Holland, Amsterdam, 1973)
- 3) N.C. Mukhopadhyay, *Phys. Reports* **30** (1977) 1
- 4) J. Bernabéu, Thesis, Valencia, 1970
- 5) J. Bernabéu, *Nucl. Phys.* **A201** (1973) 41
- 6) J. Bernabéu and F. Cannata, *Phys. Lett.* **B45** (1973) 445; *Nucl. Phys.* **A215** (1973) 411
- 7) J. Navarro, J. Bernabéu, J.M.G. Gómez and J. Martorell, *Nucl. Phys.* **A375** (1987) 361
- 8) P. Pascual, *Anales de Fis.* **67** (1971) 197
- 9) R. Pla, Tesina de licenciatura, University of Valencia, 1971;
J. Bernabéu and R. Pla, *Anales de Fis.* **67** (1971) 455
- 10) L.L. Salcedo, E. Oset, M.J. Vicente and C. García-Recio, *Nucl. Phys.* **A484** (1988) 557
- 11) E. Oset, L.L. Salcedo and D. Strottman, *Phys. Lett.* **B165** (1985) 13
- 12) E. Oset and L.L. Salcedo, *Jour. Comp. Phys.* **57** (1985) 155
- 13) C. Itzykson and J.B. Zuber, *Quantum field theory* (McGraw-Hill, New York, 1980)
- 14) J.D. Bjorken and S.D. Drell, *Relativistic quantum fields* (McGraw-Hill, New York, 1965)
- 15) C. García-Recio, E. Oset and L.L. Salcedo, *Phys. Rev.* **C37** (1988) 194
- 16) H.C. Chiang, E. Oset, R. Carrasco, J. Nieves and J. Navarro, *Nucl. Phys.* **A510** (1990) 573
- 17) M. Ericson, *Nucl. Phys.* **A335** (1980) 309;
M. Ericson, A. Figureau and C. Thevenet, *Phys. Lett.* **B45** (1973) 19
- 18) E. Oset, Lectures in the "SERC School of Nuclear Physics" Jaipur, India 1987, ed. B.K. Jain (World Scientific, Singapore, 1987) p. 65
- 19) C.W. de Jager, C. de Vries and H. de Vries, *At. Data Nucl. Data Tables* **14** (1974) 480
- 20) G. Backenstoss, *Ann. Rev. Nucl. Sci.* **20** (1970) 467
- 21) C. García-Recio, Thesis, University of Valladolid, 1986
- 22) I.S. Towner and F.C. Khanna, *Phys. Rev. Lett.* **42** (1979) 51
- 23) E. Oset and M. Rho, *Phys. Rev. Lett.* **42** (1979) 47
- 24) A. Galindo and P. Pascual, *Mecanica Cuantica*, Alhambra, 1978
- 25) J. Bernabéu and R. García-Molina, University of Valencia preprint 1989, *Anales de Física* 1989, in print
- 26) T. Suzuki, D.F. Measday and J.P. Roalsvig, *Phys. Rev.* **C35** (1987) 2212 and references therein

- 27) R. Brockmann and E. Oset, Phys. Lett. **B118** (1982) 33
- 28) E. Oset, L.L. Salcedo and R. Brockmann, Physics Report in print
- 29) R.S. Hayano *et al.*, Phys. Lett. **B231** (1989) 355
- 30) L. Tauscher, C. García-Recio and E. Oset, Nucl. Phys. **A415** (1984) 333
- 31) J. Nieves, E. Oset and C. García-Recio, University of Valencia preprint
- 32) J. Konijn *et al.*, Nucl. Phys. **A326** (1979) 401
- 33) R. Seki, Proc. pion nucleus physics, Los Alamos 1987, eds. R.J. Peterson and D.D. Strottman, AIP Con. Proc. 163, p. 233
- 34) M. Eckhause, T.A. Filippas, R.B. Sutton and R.E. Welsh, Phys. Rev. **132** (1963) 422
- 35) K. Ishida, J.H. Brewer, T. Matsuzaki, Y. Kuno, J. Imazato and K. Nagamine, Phys. Lett. **B167** (1986) 31
- 36) W.A. Cramer, V.L. Telegdi, R. Winston and R.A. Lundy, Nuovo Cim. **24** (1962) 546
- 37) G.P. Yost *et al.*, Rev. Part. properties; Phys. Lett. **B204** (1988) 1
- 38) J. Delorme, M. Ericson, A. Figureau and C. Thevenet, Ann. of Phys. **102** (1976) 273

Coherent pion production in the (${}^3\text{He}, t$) reaction in nuclei

P. Fernández de Córdoba, J. Nieves, E. Oset and M.J. Vicente-Vacas

*Departamento de Física Teórica and IFIC, Centro Mixto Universidad de Valencia-CSIC,
 E-46100 Burjassot, Valencia, Spain*

Received 10 October 1992; revised manuscript received 22 October 1993
 Editor: C. Mahaux

We have evaluated the cross section for coherent pion production in the ${}^3\text{He} + {}^{12}\text{C} \rightarrow t + {}^{12}\text{C} + \pi^+$ reaction. The Δ peak of the energy distribution is considerably shifted with respect to the peak in the $p({}^3\text{He}, t)\Delta^{++}$ reaction. The coherent pions represent a sizable fraction of all pions produced and are a major ingredient in the interpretation of the shift of the Δ peak in the inclusive $({}^3\text{He}, t)$ reaction in nuclei. The coherent production process qualifies as production of virtual pions followed by elastic scattering of the virtual pions with the nucleus and the investigation of this channel will offer information about pion nucleus interaction complementary to the one obtained from scattering of real pions.

The reaction we discuss is



In the coherent production the nucleus is left in its ground state by contrast with the incoherent production where the nucleus is either broken or left in some excited state. Some comments about coherent pion production with strongly interacting particles are done in refs. [1,2] in connection with heavy ion reactions or subthreshold pion production [3,4]. Classical estimates of coherent pion production in p nucleus collision are also done in ref. [5] and a Quantum Mechanical evaluation of coherent π^- production in the (n, p) reaction, leading to deeply bound states, is done in ref. [6]. Very recently the coherent pion production of pions in the continuum with the (p, n) [7] or (He, t) [8] reaction has also been addressed and some experimental data are already available [9]. We are concerned about the production of π^+ in flight with reaction (1) and its relative importance in the inclusive $({}^3\text{He}, t)$ cross section in nuclei. The results of our calculation show that the coherent pion production represents a sizable fraction of all pions produced in this reaction and that it is a key ingredient in the shift of the Δ peak observed in the $({}^3\text{He}, t)$ reaction in nuclei around the Δ -resonance region [10,11].

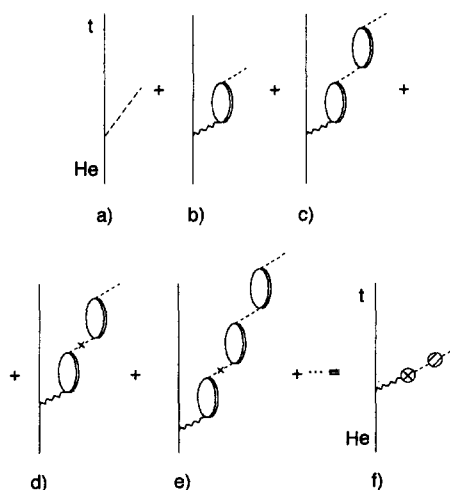


Fig. 1. Diagrammatic representation of coherent pion production. The dashed lines indicate the pion, the wavy lines the spin-isospin interaction and the dotted line with a cross the ingredients in the Δh interaction additional to one pion exchange. The dashed lines with a dashed circle in the middle represent a renormalized pion. The crossed circle indicates the pion selfenergy.

The process of coherent pion production is depicted diagrammatically in fig. 1, where for simplicity in the figure we have assumed that the pion is renormalized exclusively via Δh excitation. The dashed line stands

for a pion line. The crossed dashed line for the ingredients in the Δh interaction apart from one pion exchange (OPE) and the wavy line for the complete ph - Δh interaction. The Δh excitation plus the irreducible diagrams coming from iterated Δh excitation through the additional pieces to OPE are all collected into a pion selfenergy (denoted by a cross bubble in fig. 1f) and the diagrammatic series of fig. 1 is summed up into the diagram of fig. 1f, where the pion line with the dashed circle stands for a renormalized pion (pion wave function in coordinate space). This is a generalized Dyson equation which implies that diagram 1a does not contribute as we shall see. We take a pion selfenergy of the type

$$\Pi(\mathbf{r}) = \Pi^{(s)}(\mathbf{r}) + \nabla \overline{\Pi}^{(p)}(\mathbf{r}) \nabla, \quad (2)$$

which contains an s-wave and a p-wave part. We obtain a cross section for the process of eq. (1),

$$\frac{d\sigma}{d\Omega_t dE_t d\Omega_\pi} = \frac{1}{(2\pi)^5} \frac{M_{\text{He}} M_t M_A p_t p_\pi}{\lambda^{1/2}(s, M_{\text{He}}^2, M_A^2)} |T|^2, \quad (3)$$

where M_{He} , M_t , M_A are the masses of He, t and the target nucleus and p_t , p_π the momenta of the t and pion. By using a pseudovector coupling in the πNN vertex the T matrix for the process is given by

$$\begin{aligned} -iT_i = & -\sqrt{2} \frac{f}{\mu} \sqrt{\frac{-q^2}{q^2}} \int d^3x \varphi_t^*(\mathbf{x}) \varphi_{\text{He}}(\mathbf{x}) F_{\text{He},t}(q) \\ & \times \left(\frac{q_i F^2(q)}{q^{02} - q^2 - \mu^2} \Pi^{(s)}(\mathbf{x}) \right. \\ & \left. - [V'_L \hat{q}_i \hat{q}_j + V'_T (\delta_{ij} - \hat{q}_i \hat{q}_j)] \overline{\Pi}^{(p)}(\mathbf{r}) i \nabla_j \right) \\ & \times \phi_{out}^*(\mathbf{p}_\pi, \mathbf{x}), \end{aligned} \quad (4)$$

where $F_{\text{He},t}(q)$ is the (He, t) transition form factor, given by eq. (6) of ref. [12] and

$$\begin{aligned} V'_L(q) &= \frac{q^2}{q^{02} - q^2 - \mu^2} F^2(q) + g', \\ V'_T(q) &= \frac{q^2}{q^{02} - q^2 - m_\rho^2} F_\rho^2(q) C_\rho + g', \end{aligned} \quad (5)$$

are the longitudinal and transverse parts of the spin-isospin interaction, $F(q)$, $F_\rho(q)$ the πNN and ρNN form factor taken of the monopole type with $A = 1300$ MeV and $A_\rho = 1400$ MeV and $C_\rho = 3.96$ [13].

We take $g' = 0.6$ as used in the study of pionic reactions [14,15]. The pion selfenergy is also taken from [14,15] and the pion wave function is obtained by solving the Klein Gordon equation with this selfenergy.

The square root factor in (4) guarantees that in $|T|^2$ one obtains the correct relativistic factor $(-q^2)$ from the πNN vertex instead of q^2 which one obtains from the implicit use of a σq nonrelativistic vertex after summing over spins.

Since the ${}^3\text{He}$ and t are rather energetic, and we look at the t in the forward direction, their wave functions are given quite accurately in terms of the eikonal approximation

$$\begin{aligned} \varphi_t^*(\mathbf{x}) \varphi_{\text{He}}(\mathbf{x}) &= \exp(i\mathbf{p}_{\text{He}} \mathbf{x}) \\ &\times \exp\left(-\frac{1}{2} \int_{-\infty}^z \sigma(1-i\eta) \rho(\mathbf{b}, z') dz'\right) \\ &\times \exp(-i\mathbf{p}_t \mathbf{x}) \exp\left(-\frac{1}{2} \int_z^{\infty} \sigma(1-i\eta) \rho(\mathbf{b}, z') dz'\right) \\ &\equiv \exp[i(\mathbf{p}_{\text{He}} - \mathbf{p}_t) \mathbf{x}] C(\mathbf{b}), \end{aligned} \quad (6)$$

which defines the distortion factor $C(\mathbf{b})$, with σ the total cross section He (or t) N , η the ratio of real to imaginary part of the He N amplitude, which we take as for nucleons, $\eta = 0.275$, and $\rho(\mathbf{x})$ the nuclear density, with \mathbf{b} the impact parameter. We can see now that the evaluation of diagram 1a requires the integral of the product of the ${}^3\text{He}$, t and pion wave functions. By making use of eq. (6) and carrying out the z integration we obtain $\delta(p_{\text{He}} - p_t - p_{\pi z})$, with $p_{\pi z}$ the pion momentum component along the direction of ${}^3\text{He}$ or t . The argument of the delta function does not vanish for kinematical reasons and the diagram does not contribute as we anticipated

We have evaluated the cross section for (${}^3\text{He}, t$) on ${}^{12}\text{C}$ at $T_{\text{He}} = 2$ GeV and t forward in order to compare with the experimental results. We show our results in fig. 2. Our aim in this letter is to report on the relevance of the coherent channel and all details for its evaluation are contained here. However, in order to place the discussion of this channel in a broader context we also plot in the figure the results obtained for the incoherent channels in ref. [16]. Some details

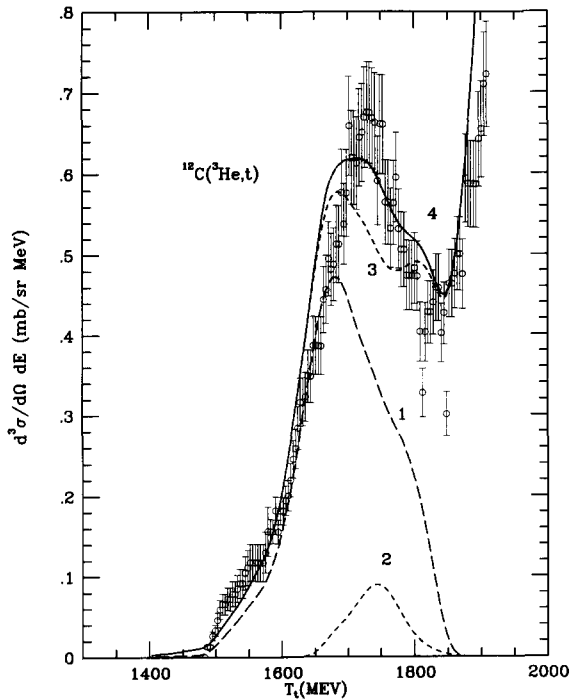


Fig. 2. Different contributions to the cross section for the $(^3\text{He}, t)$ inclusive reaction on ^{12}C . (1) Incoherent pion production. (2) Coherent π^+ production. (3) Sum of incoherent processes (i) to (v). See text. (4) Total: sum of coherent and incoherent processes.

and discussion on these channels are reported in ref. [17]. The channels considered are

- (i) Quasielastic $^3\text{He}N \rightarrow tN$ collisions.
- (ii) Two steps quasielastic collisions $^3\text{He}N \rightarrow ^3\text{He}(t)$ followed by $^3\text{He}(t)N \rightarrow tN$.
- (iii) Two step quasielastic with $^3\text{He}(t)$ break up in the intermediate states.
- (iv) Virtual pion production followed by two (or three body) pion absorption (the virtual pion is in practice substituted by the spin-isospin effective interaction).
- (v) Incoherent inclusive π^+ and π^0 production.

In fig. 2 we show only the incoherent pion production (before final state interaction of the pion is taken into account, which would redistribute this strength in pionic and nucleonic channels), the sum of all the incoherent channels and the coherent pion production.

As seen in fig. 2 the coherent pion production channel accounts for a sizable fraction of the total pion pro-

duction strength at high t energies. The pion energy ranges approximately from the pion mass up to 360 MeV where the coherent distribution dies out rapidly. The peak of the distribution of coherent pions appears at a pion energy of 250 MeV, or accordingly at a t kinetic energy of 1750 MeV. This is precisely the energy where the inclusive $(^3\text{He}, t)$ spectrum has its maximum. It is interesting to note that the peak of the incoherent pion production is not shifted with respect to the position of the peak in the $(^3\text{He}, t)$ reaction on the p or better on the deuteron. This has been confirmed experimentally in ref. [18] where a p and a π^+ are measured in coincidence. The peak of the coherent pion distribution is however considerably shifted.

The shift of the peak in the coherent channel is due to the same reasons as the shift also observed in pion nucleus scattering [19]. They are mainly the effect of the nuclear form factor and the distortion of the pion waves.

It is interesting to see that the sum of the different incoherent channels puts some strength in the region of high energy t but the position of the peak is still not shifted. However, the addition of the coherent channel produces a shift in the peak position and improves the agreement with the data. The coherent channels play then an important role in the production of the shift.

The calculations of refs. [20,21] include the coherent channel and part of the shift found there can be attributed to the contribution of this channel, as it has been made more clear in ref. [8]. All these works, however, do not take into account the quasielastic channels discussed in ref. [17], or the excitation of the Δ in the projectile [12], also accounted for in ref. [17], and which is relevant in the (He, t) reaction on neutrons.

While devoted experiments for coherent pion production are under consideration, the partial results on the coherent channel of ref. [9] are illustrative. They show clearly that the peak position is where we find it theoretically and also that the cross section is rather forward peaked in the direction of the pion along the $(^3\text{He}, t)$ momentum transfer. We have also evaluated the angular distribution for $T_t = 1755$ MeV and show the results in fig. 3. We find a cross section rather forward peaked and in qualitative agreement with ref. [9] (where other angles of t and a sum over different t energies are considered): We also find that the cross section goes roughly as $V_L^2 \cos^2 \theta + V_T^2 \sin^2 \theta$, and is

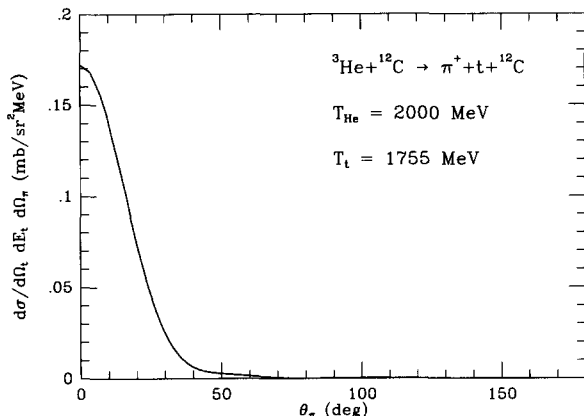


Fig. 3. Differential cross section $d\sigma/d\Omega dE_t d\Omega_\pi$ for $\theta_t = 0$, $T_t = 1755$ MeV.

dominated by the longitudinal channel. The fall down in angle is due to the nuclear form factor (implicitly contained in eq. (4)). Extra confirmation about the peak position of the coherent channel comes from the (p, n) reaction of ref. [22] where the channel where a π^+ alone is seen (meaning no other charged particles) has a very distinct peak, shifted considerably with respect to the position of the peak, in the elementary $p(p, n)$ reaction. As shown in ref. [17] and in the reanalysis of the data [23], a large fraction of the peak is due to coherent π^+ production (there is some background from $pn \rightarrow nn\pi^+$ events) which peaks exactly at the same place as the experimental peak.

We should note here that the interaction used in eqs. (4), (5) differs somewhat from the one used in ref. [12]. There an interaction was used for the $\text{He}N \rightarrow tN$ transition which effectively accounted for distortion effects of the nucleons and pions through He or t . Since here distortion effects are explicitly taken into account we can not use that interaction. Instead, we have reanalyzed the work of ref. [12] with the new interaction, taking into account explicitly the distortion effects, and have found results very similar to those obtained before.

The result obtained here for the coherent pion production are about a factor of two smaller than those obtained in ref. [8]. Until devoted experiments show the strength of the coherent channel, we can get some support for our results from the following discussion: The recent experiment (α, α') on a proton target in the delta region [24] qualifies as coherent pion pro-

duction (with the pionic variables integrated) with the (p, p') or (p, n) reaction on a ${}^4\text{He}$ nucleus. We have carried out the calculations with the same interaction as here and the same method and find a good agreement with experiment, both in energy and angular distributions, at the level of 20% [25].

The infinite matter approaches to coherent pion production [5,26] base the reaction in the change of the pion dispersion relation in the medium and require a minimum strength of the pion selfenergy for it to happen. It is a rough approximation to the finite nucleus and full quantum mechanical approach followed here, which produces always coherent pion production even if the strength of the pion selfenergy is small. Incidentally, in the numerical results of ref. [26] the strength of the pion selfenergy was relatively small and the numerical results shown there only account for the incoherent processes.

We should stress once more that we are facing here a new brand of interesting physics: elastic scattering of virtual pions, with the flexibility of making the initial pion arbitrarily off shell by changing the kinematical conditions or the mass of the projectile. These investigations would give rise to energy and angular distributions for different off shell pions which would constitute very valuable complementary information to the one obtained from the scattering of real pions. This would be welcome in view of the present arbitrariness in the description of pion nucleus interactions in terms of a large variety of very different optical potentials.

The fact that the coherent pions come with a unique energy ($E_{\text{He}} - E_t$, neglecting nucleus recoil) is also an interesting feature. We have observed that at energies around the peak of the coherent pion production the pions are very forward peaked, and with heavier targets than ${}^{12}\text{C}$ they would be even more forward peaked. Hence the coherent pions are a source of highly monochromatic and unidirectional pions. As one of the possible applications we can suggest tagging, as done for photons. In (p, p') reactions π^0 beams would be produced which could be used to study further collisions on the same target, given the short π^0 lifetimes. Further investigation of these practical possibilities is also very interesting.

We would like to acknowledge useful discussions with the Dubna and Saclay teams. P. Fernández de

Córdoba and J. Nieves wish to acknowledge financial support from the CSIC and the Ministerio de Educación y Ciencia. The work is partially supported by CICYT contract number AEN 90-0049. Some of the calculations have been done in the Centro Informático de la Universidad de Valencia.

References

- [1] M. Wakamatsu, *Nuovo Cimento* 56A (1980) 336.
- [2] G.N. Fowler and R.M. Weiner, *Phys. Rev. Lett* 55 (1985) 1373.
- [3] P.A. Deutchman, J.W. Norbury and L.W. Towsend, *Nucl. Phys A* 454 (1986) 733.
- [4] A.H. Blin, C. Guet and B. Hiller, *Nucl. Phys. A* 454 (1986) 746.
- [5] D.B. Ion and W. Stocker, *Phys. Lett B* 273 (1991) 20.
- [6] H. Toki and T. Yamazaki, *Phys. Lett. B* 213 (1988) 129.
- [7] P. Oltmanns, F. Osterfeld and T. Udagawa, *Phys. Lett. B* 299 (1993) 194.
- [8] V.F. Dimitriev, *Phys. Rev. C* 48 (1993) 357.
- [9] T. Hennino et al., *Phys. Lett. B* 303 (1993) 236.
- [10] V.G. Ableev et. al., *Sov. Phys. JETP Lett.* 40 (1984) 763.
- [11] C. Ellegaard et al., *Phys. Rev. Lett.* 50 (1983) 1745.
- [12] E. Oset, E. Shiino and H. Toki, *Phys. Lett. B* 224 (1989) 249.
- [13] R. Machleidt, K. Holinde and Ch. Elster, *Phys. Rep.* 149 (1987) 1.
- [14] C. García-Recio, E. Oset, L.L. Salcedo, D. Strottman and M.J. López, *Nucl. Phys. A* 546 (1991) 685.
- [15] J. Nieves, E. Oset and C. García-Recio, *Nucl. Phys. A* 554 (1993) 509; *A* 554 (1993) 554.
- [16] P. Fernández de Córdoba, PhD Thesis, University of Valencia (1992).
- [17] E. Oset, P. Fernández de Córdoba, J. Nieves and M.J. Vicente- Vacas, *Phys. Scr.* 48 (1993) 101.
- [18] T. Hennino et al., *Phys. Lett. B* 283 (1992) 42.
- [19] T.E.O. Ericson and W. Weise, *Pions and Nuclei* (Clarendon, Oxford, 1988).
- [20] T. Udagawa, S.H. Hong and F. Osterfeld, *Phys. Lett. B* 245 (1990)1; F. Osterfeld, *Rev. Mod. Phys.* 64 (1992) 491.
- [21] J. Delorme and P.A.M. Guichon, *Phys. Lett. B* 263 (1991) 157.
- [22] J. Chiba et al., *Phys. Rev. Lett.* 67 (1991) 1982.
- [23] J. Chiba, Talk in the Intern. Workshop on Delta in Nuclei (Tokyo, May 1993).
- [24] H.P. Morsch et al., *Phys. Rev. Lett.* 69 (1992) 1336.
- [25] P. Fernández de Córdoba, Yu. Ratis, E. Oset, J. Nieves, M.J. Vicente-Vacas, B. López-Alvaredo and F. Gareev, University of Valencia preprint, submitted to *Nucl. Phys.*
- [26] G.E. Brown, E. Oset, M.J. Vicente-Vacas and W. Weise, *Nucl. Phys. A* 505 (1989) 823.
- [27] U. Dittmayer, R. Beck, F. Kalleicher, M. Schmitz, B. Schoch, J.D. Kellie and I. Anthony, MAMI A internal report (1987).

Projectile and target delta excitation in the (^3He , t) and (^3He , ^3He) reactions

P. Fernández de Córdoba and E. Oset

*Departamento de Física Teórica and IFIC, Centro Mixto Universidad de Valencia-CSIC,
46100 Burjassot (Valencia), Spain*

Received 27 January 1992
(Revised 5 March 1992)

Abstract: We study simultaneously the (^3He , t) and (^3He , ^3He) reactions on proton and neutron targets in the region of the delta excitation resonance. We observe that the mechanism of delta excitation in the target dominates the (^3He , t) reaction on the proton, but the mechanism of delta excitation in the projectile is important in the (^3He , t) reaction on the neutron, and largely dominates the (^3He , ^3He) reaction on proton and neutron targets. The two mechanisms give rise to different shapes in the energy distributions of the t or ^3He outgoing particles and the weights and shapes of the mechanism change appreciably with the energy of the projectile. The combined experimental study of both reactions as a function of energy is thus a much richer source of information on the dynamics of these problems than the study of the (^3He , t) reaction alone, where the experimental efforts have so far concentrated.

1. Introduction

The charge exchange reactions of the (p, n) type, either induced by proton beams or light ions, like the (^3He , t) reaction, are receiving increased experimental and theoretical attention¹⁻⁶). The famous shift of the delta peak from the (^3He , t) reaction on the proton to the reaction on nuclei^{7,8}) has been the subject of intense debate [see refs. 1-4) for recent reviews].

In ref. 9), a part of the shift of the peak is attributed to collective effects in the pion channel. In ref. 10), the idea of delta excitation in the projectile was exploited and it was shown to lead to some shift of strength in nuclei. Meanwhile, further experimental research⁴) is showing that the shift is selective and depends on the reaction channel: while no appreciable shift is seen in the πN final-state channel, an appreciable shift is observed in the NN emission channel. This detailed information represents a challenge for theory, which will have to come down to details on the dynamical mechanisms of the reaction. The fact that the shift is seen in the 2N emission channel probably indicates that two-step mechanisms may play some role too. So far, all theoretical approaches rely upon one-step excitation of the delta.

Correspondence to: Prof. E. Oset, Dept. de Física Teórica, Universidad de Valencia, 46100 Burjassot (Valencia), Spain.

Our aim here is to pay attention to the mechanisms of delta excitation in the target and the projectile and to suggest an experimental method to extract relevant information on these mechanisms. It is important to have a good control of these mechanisms. Indeed, the most important finding of ref. ¹⁰⁾ was the fact that the ($^3\text{He}, t$) reaction on the proton and on the neutron had a very different shape. The reason is that the Δ -excitation in the target and the projectile lead to different energy distributions and the weight of these two mechanisms is quite different in the ($^3\text{He}, t$) reaction on the proton or the neutron. As a consequence, the comparison of the ($^3\text{He}, t$) reaction on nuclei with the one on the proton is rather unfair because nuclei are made out of protons and neutrons. This is, however, what is done in most theoretical studies, which also neglect the excitation in the projectile. A fairer approach is to compare with the deuteron. Indeed, the deuteron already shows a displacement of the strength of the energy distribution towards higher energies of the outgoing tritium. This distribution, both in size and shape was well reproduced in the work of ref. ¹⁰⁾.

What we do in the present work is to show that the related ($^3\text{He}, ^3\text{He}$) reaction, which can be performed with minor modifications on the presently running experiments, stresses the mechanism of Δ -excitation in the projectile to the point that it becomes dominant at energies around $T_{\text{He}} = 2 \text{ GeV}$. As a consequence, both the magnitude and shape of the energy distribution are quite different than in the (He, t) reaction. The study of the ($^3\text{He}, ^3\text{He}$) reaction, in connection with the ($^3\text{He}, t$) reaction, is thus a very important tool in order to learn about the dynamical excitation of deltas in nuclei.

2. The model for $\text{NN} \rightarrow \text{NN}\pi$

The basic model for the $\text{NN} \rightarrow \text{NN}\pi$ interaction used in ref. ¹⁰⁾, and which we use here again, is depicted in fig. 1: a pion is produced in the $\text{NN}\pi$ vertex and it rescatters with a second nucleon via an s-wave (1a) or a p-wave (1c) in the $\pi\text{N} \rightarrow \pi\text{N}$ scattering matrix. The p-wave amplitude is given in our model by the Δ -pole. On the other hand, we can have the pion production in the second nucleon and the rescattering in the first one. The corresponding terms with s-wave and p-wave rescattering are depicted in figs. 1b and 1d, respectively. The basic couplings we need in order to construct these amplitudes are the $\text{NN}\pi$ coupling, the $\Delta\text{N}\pi$ coupling and the $\pi\text{N} \rightarrow \pi\text{N}$ s-wave amplitude.

The $\text{NN}\pi$ coupling is given by

$$-i\delta\tilde{H}_{\text{NN}\pi} = \frac{f}{\mu} \boldsymbol{\sigma} \cdot \mathbf{q}\boldsymbol{\tau}^\lambda, \quad (1)$$

where \mathbf{q} is the momentum of an incoming pion in the $\text{NN}\pi$ vertex, and μ the pion mass. The structure of eq. (1) holds exactly from a pseudovector coupling, which we implicitly assume, in a frame with $q^0 = 0$. Since this is not the case here, one

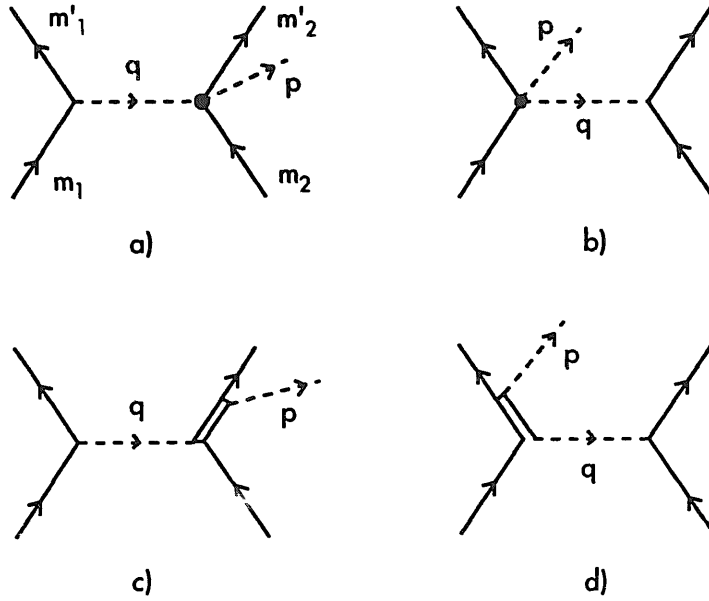


Fig. 1. Feynman diagrams for $NN \rightarrow NN\pi$ with pion production in the target (a), (c) or the projectile (b), (d) induced by the s-wave (a), (b) or p-wave (c), (d) $\pi N \rightarrow \pi N$ interaction.

must replace q^2 coming from the vertices in the final results by $-q^2$, the corresponding invariant magnitude.

We also need the s-wave $\pi N \rightarrow \pi N$ amplitude given by

$$-i\delta\tilde{H}_{\pi\pi NN}^{(s)} = -i4\pi\delta_{m,m'} \left[\frac{2\lambda_1}{\mu} \delta_{m,m'} \delta_{\lambda\lambda'} + i\epsilon_{\alpha\lambda\lambda'} \frac{2\lambda_2}{\mu} \langle m'_1 | \tau^\alpha | m_1 \rangle \right], \quad (2)$$

where m_s, m'_s, m_t, m'_t are the spin and isospin variables of the incoming and outgoing nucleons, and λ_1, λ_2 the isoscalar and isovector couplings.

The $N\Delta\pi$ is given by

$$-i\delta\tilde{H}_{N\Delta\pi} = \frac{f^*}{\mu} \mathbf{S}^+ \cdot \mathbf{q} T^{+\lambda} + \text{h.c.} \quad (3)$$

for an incoming pion with momentum q . Once again, eq. (3) holds in a frame where $q^0 = 0$, and for virtual, space-like pions, one must substitute q^2 by $-q^2$ at the end of the calculations. For real pions where one cannot find the frame with $q^0 = 0$, the invariant vertex is given by the same eq. (3) with q the πN centre-of-mass momentum. We will write q^2 in the formulae for simplicity, with the understanding that the corrections are taken care of at the end.

For the coupling constants we take ¹⁰⁾

$$\frac{f^2}{4\pi} = 0.08, \quad \frac{f^{*2}}{4\pi} = 0.36,$$

$$\lambda_1 = \lambda'_1 + 0.000222[\text{MeV}^{-1}](\sqrt{s} - \mu - M), \quad \lambda'_1 = 0.0075, \quad \lambda_2 = 0.0528, \quad (4)$$

where s is the Mandelstam variable for the πN system and M the nucleon mass.

We also take into account form factors for the πNN and $\pi N\Delta$ vertices of the type

$$F_\pi(q) = \frac{\Lambda^2 - \mu^2}{\Lambda^2 - q^2}, \tag{5}$$

with $\Lambda = 1300$ MeV.

The contribution to the T -matrix from the diagram 1a is given by

$$-iT_r^{(\pi, T)} = -\frac{f}{\mu} \langle m'_1 | \boldsymbol{\sigma} \cdot \mathbf{q} | m_1 \rangle \frac{C(r)i}{q^{02} - q^2 - \mu^2} (-i)4\pi D(r) \delta_{m_i m_f} F_\pi(q), \tag{6}$$

where $D(r)$ is the isospin factor from the $\pi N \rightarrow \pi N$ s-wave vertex

$$D(r) = \begin{cases} \left(\frac{2\lambda_1}{\mu} + \frac{2\lambda_2}{\mu} \right) & \text{for } \begin{cases} \pi^+ p \rightarrow \pi^+ p \\ \pi^- n \rightarrow \pi^- n \end{cases} \\ \left(\frac{2\lambda_1}{\mu} - \frac{2\lambda_2}{\mu} \right) & \text{for } \begin{cases} \pi^+ n \rightarrow \pi^+ n \\ \pi^- p \rightarrow \pi^- p \end{cases} \\ \frac{2\lambda_1}{\mu} & \text{for } \begin{cases} \pi^0 p \rightarrow \pi^0 p \\ \pi^0 n \rightarrow \pi^0 n \end{cases} \\ \sqrt{2} \frac{2\lambda_2}{\mu} & \text{for } \begin{cases} \pi^- p \rightarrow \pi^0 n \\ \pi^0 n \rightarrow \pi^- p \end{cases} \\ -\sqrt{2} \frac{2\lambda_2}{\mu} & \text{for } \begin{cases} \pi^0 p \rightarrow \pi^+ n \\ \pi^+ n \rightarrow \pi^0 p \end{cases} \end{cases}, \tag{7}$$

and $C(r)$ is the isospin factor for the πNN vertex,

$$C = \begin{cases} \sqrt{2} & \text{for charged pions} \\ +1 & \text{for } \pi^0 pp \\ -1 & \text{for } \pi^0 nn \end{cases}. \tag{8}$$

The index T in $T^{(\pi, T)}$ indicates that the π -production has been done in the nucleon target. For the π -production in the projectile, fig. 1b, we shall have:

$$-iT_r^{(\pi, P)} = -i4\pi D(r) \delta_{m_i m_f} \frac{i}{q^{02} - q^2 - \mu^2} \frac{f}{\mu} \langle m'_2 | \boldsymbol{\sigma} \cdot \mathbf{q} | m_2 \rangle C(r) F_\pi(q). \tag{9}$$

Analogously we write for the diagram of fig. 1c

$$\begin{aligned} -iT^{(P, T)} = & -\frac{f}{\mu} \langle m'_1 | \boldsymbol{\sigma} \cdot \mathbf{q} | m_1 \rangle C(r) \frac{i}{q^{02} - q^2 - \mu^2} (-1) \left(\frac{f^*}{\mu} \right)^2 \langle m'_2 | \mathbf{S} \cdot \mathbf{p} \mathbf{S}^* \cdot \mathbf{q} | m_2 \rangle \\ & \times \frac{i}{\sqrt{s_t} - M_\Delta + \frac{1}{2}i\Gamma(s_t)} E(r) F_\pi(q)^2, \end{aligned} \tag{10}$$

where M_Δ is the Δ -mass and we must replace

$$\mathbf{S}_i \mathbf{S}_j^* = \frac{2}{3} \delta_{ij} - i \frac{1}{3} \epsilon_{ijk} \sigma_k. \tag{11}$$

$E(r)$ is the isospin coefficient for the Δ -term

$$E(r) = (-1)^{N_\pi} C(1\frac{1}{2}\frac{3}{2}; t_\pi, t_N, t_\Delta) C(1\frac{1}{2}\frac{3}{2}; t'_\pi, t'_N, t_\Delta) \tag{12}$$

with N_{π} the number of π coming in or going out in the direction of the Fermionic line. The factor $(-1)^{N_{\pi}}$ appears because of our isospin convention¹²⁾ where the $|\pi^{\pm}\rangle = -|1, 1\rangle$ (state of isospin).

For the sake of completeness we write here the coefficients

$$E(r) = \begin{cases} 1 & \text{for } \begin{cases} \pi^+ p \rightarrow \pi^+ p \\ \pi^- n \rightarrow \pi^- n \end{cases} \\ 1 & \text{for } \begin{cases} \pi^+ n \rightarrow \pi^+ n \\ \pi^- p \rightarrow \pi^- p \end{cases} \\ 2 & \text{for } \begin{cases} \pi^0 p \rightarrow \pi^0 p \\ \pi^0 n \rightarrow \pi^0 n \end{cases} \\ \frac{1}{\sqrt{2}} & \text{for } \begin{cases} \pi^- p \rightarrow \pi^0 n \\ \pi^0 n \rightarrow \pi^- p \end{cases} \\ -\frac{1}{\sqrt{2}} & \text{for } \begin{cases} \pi^0 p \rightarrow \pi^+ n \\ \pi^+ n \rightarrow \pi^0 p \end{cases} \end{cases} \quad (13)$$

For the excitation of the Δ in the projectile corresponding to fig. 1d we have

$$-iT_r^{(p,p)} = -\left(\frac{f^*}{\mu}\right)^2 \langle m_1' | \mathbf{S} \cdot \rho \mathbf{S}' \cdot \mathbf{q} | m_1 \rangle E(r) \frac{i}{\sqrt{s_p} - M_{\Delta} + \frac{1}{2}i\Gamma(s_p)} \\ \times \frac{f}{\mu} \langle m_2' | \boldsymbol{\sigma} \cdot \mathbf{q} | m_2 \rangle C(j) F_{\pm}(q)^2 \frac{i}{q^{02} - q^2 - \mu^2}, \quad (14)$$

where s_t, s_p corresponds to the Mandelstam variable in either mechanism, target and projectile.

In addition, in the case when we have the Δ -excitation, we have p-wave couplings in both vertices. In such case, ρ -exchange also plays some role, and the nuclear correlations eliminate the short-range part of both π - and ρ -exchange (δ -like interaction in the absence of form factors). We then substitute the π exchange by the effective spin-isospin interaction. Hence we change

$$q, q, D_0(q) F_{\pm}(q)^2 \rightarrow V_L' \hat{q}_i \hat{q}_i + V_T' (\delta_{ij} - \hat{q}_i \hat{q}_j),$$

with

$$V_L' = q^2 D_0(q) F_{\pm}^2(q) + g', \\ V_T' = q^2 D_{\rho}(q) F_{\rho}^2(q) C_{\rho} + g', \\ C_{\rho} = 3.95, \quad g' = 0.61, \quad (15)$$

where V_L', V_T' are the longitudinal and transverse part of the interaction and $F_{\rho}(q)$ is the ρ form factor, of the monopole type as eq. (5) with $A_{\rho} = 1400$ MeV [ref. ¹¹⁾]. The q^2 factor in eq. (15) comes from the vertices (1) and (3) and must be replaced by $-q^2$ as we indicated.

With the detailed table of isospin coefficients (8) and (13) we can write the global isospin factor $E(j)C(j)$ entering the calculation of the Δ -excitation part for different charge configurations.

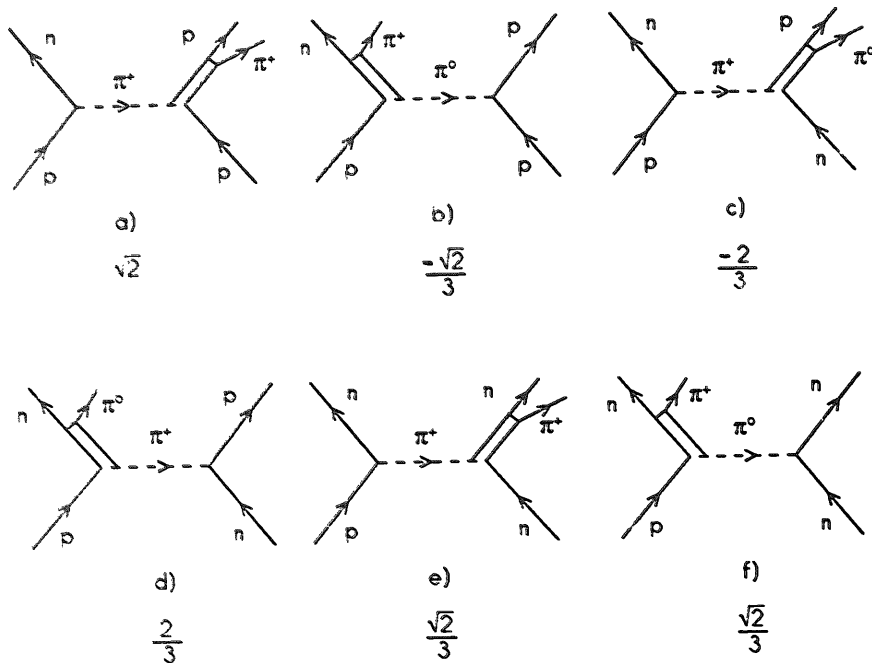


Fig. 2. Feynman diagrams for pion production in the (p, n) reaction, on proton or neutron targets, with Δ -excitation on the target and the projectile.

We plot in fig. 2 the set of diagrams which enter the (p, n) reaction on proton and neutron targets, together with the isospin coefficients corresponding to each diagram. If we square these coefficients we observe that, in terms of cross sections, the Δ -excitation in the target with a proton target (fig. 2a) is nine times bigger than the Δ -excitation in the projectile (fig. 2b). On the other hand, the target Δ -excitation with a neutron target (figs. 1c and 1e) has the same strength as the projectile excitation (figs. 1d and 1f). Another feature worth noting is that the target Δ -excitation mechanism on the proton target has a strength a factor of three larger than the corresponding mechanism on the neutron target.

All these features will show up when we study the $({}^3\text{He}, t)$ and $({}^3\text{He}, {}^3\text{He})$ reactions.

3. The $({}^3\text{He}, t)$ and $({}^3\text{He}, {}^3\text{He})$ reactions

We will need to evaluate expectation values of σ , τ and $\sigma'\tau^A$ operators within wave functions of ${}^3\text{He}$ and t , or ${}^3\text{He}$ and ${}^3\text{He}$. For this purpose we take for ${}^3\text{He}$ or t a wave function in complete analogy to the quark model for the p and n , with the difference that the wave function in spin-isospin will now be antisymmetric rather than symmetric as we have in the quark model¹³). The $SU(2) \times SU(2)$ antisymmetric wave function is given by

$$\psi = \frac{\sqrt{3}}{2}(\phi_{MS}\chi_{MA} - \phi_{MA}\chi_{MS}), \quad (16)$$

with ϕ_{MS} , ϕ_{MA} the mixed symmetric and antisymmetric isospin wave functions and

χ_{MS} , χ_{MA} the corresponding ones for spin, in the nomenclature of ref.¹³). In particular the wave function for ${}^3\text{He}$ with spin $\frac{1}{2}$ is

$$\begin{aligned} \psi({}^3\text{He } \uparrow) &= \sqrt{\frac{1}{6}}(-\text{pnp}\downarrow\uparrow\uparrow + \text{npp}\uparrow\downarrow\uparrow - \text{ppn}\uparrow\downarrow\uparrow + \text{ppn}\downarrow\uparrow\uparrow + \text{pnp}\uparrow\uparrow\downarrow - \text{npp}\uparrow\uparrow\downarrow), \\ \psi(\text{t } \uparrow) &= \sqrt{\frac{1}{6}}(-\text{pnn}\uparrow\downarrow\uparrow + \text{pnn}\uparrow\uparrow\downarrow + \text{npn}\downarrow\uparrow\uparrow - \text{npn}\uparrow\uparrow\downarrow + \text{nnp}\uparrow\downarrow\uparrow - \text{nnp}\downarrow\uparrow\uparrow). \end{aligned} \quad (17)$$

Then we can show that

$$\begin{aligned} \langle \psi({}^3\text{He } \uparrow) | \sum_i \sigma_z^i | \psi({}^3\text{He } \uparrow) \rangle &= 1, \\ \langle \psi({}^3\text{He } \uparrow) | \sum_i \tau_z^i | \psi({}^3\text{He } \uparrow) \rangle &= 1, \\ \langle \psi({}^3\text{He } \uparrow) | \sum_i \sigma_z^i \tau_z^i | \psi({}^3\text{He } \uparrow) \rangle &= -1, \end{aligned} \quad (18)$$

where the sum runs over the nucleons.

In general we can write these matrix elements in the base of states of total spin $\frac{1}{2}$ and isospin $\frac{1}{2}$ for ${}^3\text{He}$ and t. Indicating by \tilde{N} the states of either ${}^3\text{He}$ or t, we have

$$\langle \tilde{N}' | \sum_i \sigma_\lambda^i | \tilde{N} \rangle = \langle T = \frac{1}{2}, M'_i; S = \frac{1}{2}, M'_i | \sigma_\lambda | T = \frac{1}{2}, M_i; S = \frac{1}{2}, M_i \rangle, \quad (18a)$$

$$\langle \tilde{N}' | \sum_i \tau_\lambda^i | \tilde{N} \rangle = \langle T = \frac{1}{2}, M'_i; S = \frac{1}{2}, M'_i | \tau_\lambda | T = \frac{1}{2}, M_i; S = \frac{1}{2}, M_i \rangle, \quad (18b)$$

$$\langle \tilde{N}' | \sum_i \sigma_\lambda^i \tau_\rho^i | \tilde{N} \rangle = -\langle T = \frac{1}{2}, M'_i; S = \frac{1}{2}, M'_i | \sigma_\lambda \tau_\rho | T = \frac{1}{2}, M_i; S = \frac{1}{2}, M_i \rangle. \quad (18c)$$

With the help of these results or simply with direct calculation, as in eq. (18), we can evaluate the Δ -propagator operators between states of ${}^3\text{He}$ and t,

$$\begin{aligned} \langle \pi^\Lambda \tilde{N}' | \sum_i P_{\Delta,i} | \tilde{N} \pi^\Lambda \rangle &= \langle \pi^\Lambda \tilde{N}' | \sum_i (S_i S_i^+ T^\Lambda T^{\Lambda+}) | \tilde{N} \pi^\Lambda \rangle \\ &= \langle \pi^\Lambda \tilde{N}' | \sum_i (\frac{2}{3} \delta_{ij} - \frac{1}{3} i \epsilon_{ijk} \sigma_k) | \tilde{N} \pi^\Lambda \rangle. \end{aligned} \quad (19)$$

Thus we find the following results, which we need later

$$\begin{aligned} \langle \pi^+ \text{t} | \sum_i P_{\Delta,i} | {}^3\text{He } \pi^0 \rangle &= -\frac{1}{3} \sqrt{2} \langle M'_i | (\frac{2}{3} \delta_{ij} + \frac{1}{3} i \epsilon_{ijk} \sigma_k) | M_i \rangle, \\ \langle \pi^0 \text{t} | \sum_i P_{\Delta,i} | {}^3\text{He } \pi^- \rangle &= \frac{1}{3} \sqrt{2} \langle M'_i | (\frac{2}{3} \delta_{ij} + \frac{1}{3} i \epsilon_{ijk} \sigma_k) | M_i \rangle, \\ \langle \pi^+ {}^3\text{He} | \sum_i P_{\Delta,i} | \pi^+ {}^3\text{He} \rangle &= \langle M'_i | (\frac{7}{3} \delta_{ij} - \frac{11}{33} i \epsilon_{ijk} \sigma_k) | M_i \rangle, \\ \langle \pi^0 {}^3\text{He} | \sum_i P_{\Delta,i} | \pi^0 {}^3\text{He} \rangle &= \langle M'_i | (\frac{2}{3} \delta_{ij} - \frac{1}{3} i \epsilon_{ijk} \sigma_k) | M_i \rangle, \\ \langle \pi^- {}^3\text{He} | \sum_i P_{\Delta,i} | \pi^- {}^3\text{He} \rangle &= \langle M'_i | (\frac{2}{3} \delta_{ij} - \frac{1}{3} i \epsilon_{ijk} \sigma_k) | M_i \rangle. \end{aligned} \quad (20)$$

Note that in the case of the (${}^3\text{He}$, t) transition, the matrix element is as in the (p, n) case except that the spin-flip term has opposite sign. One can also see this in a different way by recalling that the τ -operator is implicit in the transition (it comes from $T^\Lambda T^{\Lambda+} = \frac{2}{3} \delta_{\lambda\lambda'} - \frac{1}{3} i \epsilon_{\lambda'\lambda\mu} \tau_\mu$) and hence the spin-independent term corresponds

in fact to eq. (18b) and the spin-flip terms corresponds to eq. (18c). For practical purposes, since when summing over polarization there is no interference between the spin-flip and the spin-non-flip terms, we can treat the ($^3\text{He}, t$) transition as if we were dealing with the (p, n) one. This is, however, not the case in the ($^3\text{He}, ^3\text{He}$) transition. As we can see, the coherent sum over the nucleons enhances the spin-independent part of the amplitudes, which are then quite different to the corresponding ones in the (p, p) transitions.

In the ($^3\text{He}, t$) reaction we would have now the same diagrams as in fig. 2, replacing the p and n to the left of the diagrams by ^3He and t, respectively. The p-wave T -matrix for the different terms is still given by eqs. (10) and (14) for Δ -excitation in the target and the projectile with the following changes:

(i) Δ -excitation in the target, eq. (10): $\sigma_i \rightarrow -\sigma_i$.

(ii) Δ -excitation in the projectile, eq. (14): $S_i^+ S_j \rightarrow \frac{2}{3}\delta_{ij} + \frac{1}{3}i\epsilon_{ijk}\sigma_k$. (Note change of sign in the σ_k term.)

With respect to the ε -wave terms, we would get the same diagrams as in fig. 2 replacing the Δ -pole by the $\pi N \rightarrow \pi N$ s-wave scattering matrix. The contribution of the diagrams is given by eqs. (6) and (9) with the changes:

(i) $\pi N \rightarrow \pi N$ s-wave excitation in the target, eq. (6): $\sigma_i \rightarrow -\sigma_i$.

(ii) $\pi N \rightarrow \pi N$ s-wave excitation in the projectile, eq. (9): No changes.

This last property follows immediately from eq. (18b).

The different terms for the ($^3\text{He}, ^3\text{He}$) are depicted in fig. 3. The p-wave amplitudes corresponding to these diagrams are given again by eqs. (10) and (14) for target and projectile excitation respectively, with the following changes:

(i) Δ -excitation in the target, eq. (10): $\sigma_i \rightarrow -\sigma_i$.

(ii) Δ -excitation in the projectile, eq. (14): $S_i S_j^+ E(r) \rightarrow$ m.e. of eq. (20).

In fig. 3 we have written below each diagram the weight of the global isospin coefficient in front of the spin-independent term, in analogy to the coefficients in fig. 2. By analogy, for each of the diagrams in fig. 3 we have the corresponding one with the $\pi N \rightarrow \pi N$ s-wave amplitude replacing the Δ -pole. These terms are calculated using again the formulas of eqs. (6) and (9) with the changes:

(i) $\pi N \rightarrow \pi N$ s-wave excitation in the target, eq. (6): $\sigma_i \rightarrow -\sigma_i$.

(ii) $\pi N \rightarrow \pi N$ s-wave excitation in the projectile, eq. (9): replace $\lambda_1 \rightarrow 3\lambda_1$ in all coefficients $D(r)$ with ^3He playing the role of p and t the role of n in eq. (7). (The λ_2 coefficient is not changed in virtue of eq. (18b).)

In addition to these changes we must now implement the nuclear transition form factor taken from ref. ¹⁴) slightly modified in ref. ¹⁰)

$$F(q) = \exp(\alpha q^2)(1 + \varepsilon q^4), \quad \alpha = 16 \text{ GeV}^{-2}, \quad \varepsilon = 20 \text{ GeV}^{-4}, \quad (21)$$

with $q^2 = q'^2 - q^2$ [$q = p'_{\text{He}} - p_t$ in the ($^3\text{He}, t$) transition, or $q = p'_{\text{He}} - p_{\text{He}}$ in the ($^3\text{He}, ^3\text{He}$) transition]. The factor $F(q)$ multiplies the amplitudes discussed above in all terms.

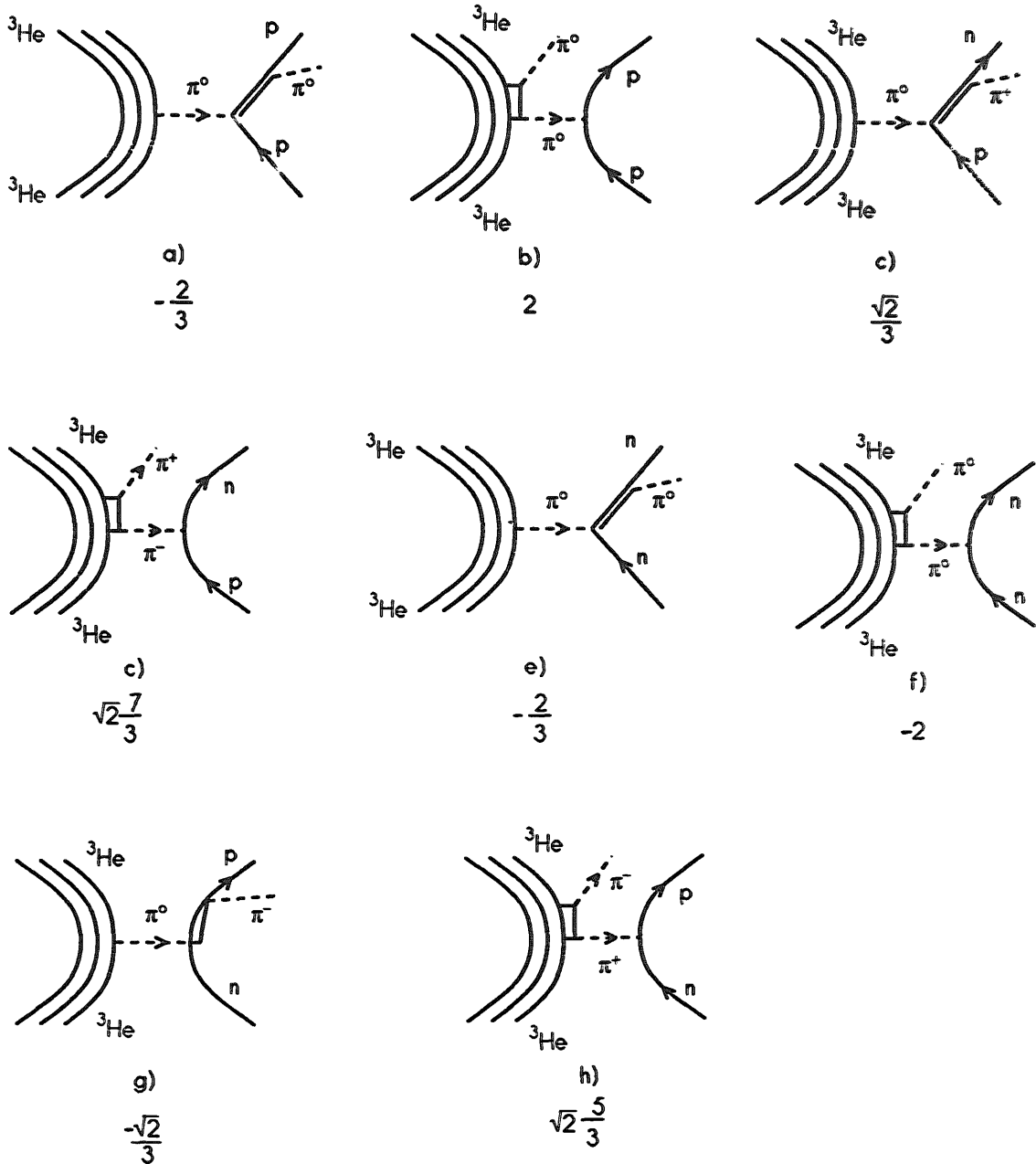


Fig. 3. Feynman diagrams for pion production in the (^3He , ^3He) reaction, on proton and neutron targets, with Δ -excitation on the target and the projectile.

It is now instructive to look at the weight of the diagrams with Δ -excitation in the target or the projectile. As we saw before, the weight for target to projectile excitation in (^3He , t) on the proton is 9. By looking at the coefficients in fig. 3 for the (^3He , ^3He) (neglecting the fact that the spin-flip amplitudes are different, because they are small compared to the spin-independent part) we obtain a factor $\frac{3}{67}$ for the same ratio.

Conversely the weight of the mechanism of Δ -excitation in the projectile has passed from being $\frac{1}{9}$ of the target excitation mechanism in (^3He , t) on the p to being a factor about 22 in the (^3He , ^3He) reaction on the proton.

With respect to the excitation on the neutron, the ratio of the projectile/target mechanisms passes from being 1 in the (^3He , t) reaction to $\frac{43}{3}$ in the (^3He , ^3He) reaction. We thus see that in both p and n cases the (^3He , ^3He) reaction is dominated by the Δ -excitation in the projectile and, hence, both should have the same shape, and correspondingly also the (^3He , ^3He) excitation on the deuteron.

The other point worth noting is that due to the large weight of the projectile excitation mechanisms we expect a much larger cross sections in the (^3He , ^3He) than in the (^3He , t) reaction.

In addition to the diagrams which we have discussed we should consider the antisymmetric partners, but they are very small when using nuclear projectiles¹⁴⁾ since they involve exchange between bound and free particles and, hence, extra form factors. This is obviously not the case in the (p, n) reaction with free particles for what some of the results obtained here in the (^3He , t) reaction are not necessarily similar in the (p, n) reactions.

The cross section for the (^3He , t) reaction is given by¹⁰⁾

$$\frac{d^2\sigma}{d\Omega_t dE_t} = \frac{p_t}{(2\pi)^5} \frac{M_{\text{He}} M_t M^2}{\lambda^{1/2}(s, M_{\text{He}}^2, M^2)} \times \int d^3p_\pi \frac{1}{E(p')\omega(p_\pi)} \bar{\Sigma} \Sigma |T|^2 \delta(E_{\text{He}} + E(p) - E_t - E(p') - \omega(p_\pi)), \quad (22)$$

where momentum conservation is assumed, $p_{\text{He}} + p = p_t + p' + p_\pi$, with p, p' the momenta of the incoming and outgoing nucleon, and relativistic kinematics is used, with $E(p)$ and $\omega(p_\pi)$ the total energy of nucleons and pions, respectively, the function $\lambda(\dots)$ is the Källén function.

For the (^3He , ^3He) reaction we replace in eq. (22) the tritium variables by those of the outgoing ^3He and the matrix element as indicated before.

The width of the Δ is taken as¹⁵⁾:

$$\Gamma(s) = \frac{1}{6} \left(\frac{f^*}{\mu} \right)^2 \frac{M}{\sqrt{s}} \frac{2M_\Delta}{\sqrt{s} + M_\Delta} q_N^3, \quad (23)$$

with q_N the c.m. nucleon momentum for the decay of the Δ with invariant mass \sqrt{s} into a pion and a nucleon.

In the magnitude $d^2\sigma/d\Omega dE$ in the lab system the Δ -excitation in the target and in the projectile (DEP) give rise to different distributions. Indeed we have for the Δ -excitation in the target (DET)

$$\begin{aligned} q_{\text{tg}} &= p_{\text{He}} - p_t, \\ s_{\text{tg}} &= (\bar{p} + q_{\text{tg}})^2, \end{aligned} \quad (24)$$

while for the Δ -excitation in the projectile we have

$$q_{pr} = p_{He} - p_t - p_\pi, \\ \sqrt{s_{pr}} = [(p_t + p_\pi)^2]^{1/2} - 2M. \quad (25)$$

The difference is apparent, in the DET mechanism for a fixed angle and energy of the t, both q_{tg} and s_{tg} are fixed. The invariant mass of the delta is then fixed for this mechanism. The p_π integration can be carried out and leads to the Δ -width allowing to cast the DET mechanism in a different way which is widely used in the literature where $d^2\sigma/d\Omega dE$ is proportional to Γ

$$\left. \frac{d^2\sigma}{d\Omega dE} \right|_{DET} \propto \frac{\Gamma(s_{tg})}{(\sqrt{s_{tg}} - M_\Delta)^2 + (\frac{1}{2}\Gamma(s_{tg}))^2} \propto -\text{Im} \frac{1}{\sqrt{s_{tg}} - M_\Delta + \frac{1}{2}i\Gamma(s_{tg})}. \quad (26)$$

However, the DEP mechanism does not allow this simplification because both q_{pr} and s_{pr} depend now explicitly on the variable of integration p_π . As a consequence there is a range of values of the delta invariant mass $\sqrt{s_{pr}}$ which are covered in the DEP mechanism and this gives rise to a shape quite distinct to the one in the DET mechanism. In ref. ¹⁰⁾ it was found that at $T_{He} = 2$ GeV the DEP mechanism peaks at much larger values of E_t than the corresponding DET mechanism. The other noticeable difference is that, in the DET mechanism, the shape does not depend on the absolute value of E_{He} but only on the difference $p_{He} - p_t$, while in the DEP mechanism it depends on the absolute value of E_t and we obtain different shapes at different energies.

We carry out the calculation of the cross section by means of eq. (22) for all the mechanisms and take into account the interference, although small, of the DEP and DET mechanisms and the s-wave pieces, which are also rather small by themselves.

4. Results and discussion

In fig. 4 we show the results for the ($^3\text{He}, t$) reaction on the proton and the neutron, as a function of T_t for $\theta = 0^\circ$. We observe that on proton targets the contribution of the DEP mechanism is rather small but modifies the cross section at higher t-energies and leads to a better agreement with the data ¹⁶⁾. The effect of the DEP mechanism is more apparent in the ($^3\text{He}, t$) reaction on the n-target and leads to a substantial strength in the region of high T_t . The shapes of the reaction on the proton and on the neutron are rather different, as one can see in the figure. Neglecting screening effects and two step processes in the deuterium nucleus, which should be small for the inclusive process ($^3\text{He}, t$) on the d-target, we can obtain this cross section by adding the cross sections on the n and the p. The results are shown in fig. 5 and compared with the experiment ¹⁷⁾. The agreement is rather good but our peak is too sharp. By adding the p- and n-excitations we are shifting some strength toward higher T_t energies and this is also apparent in the experiment.

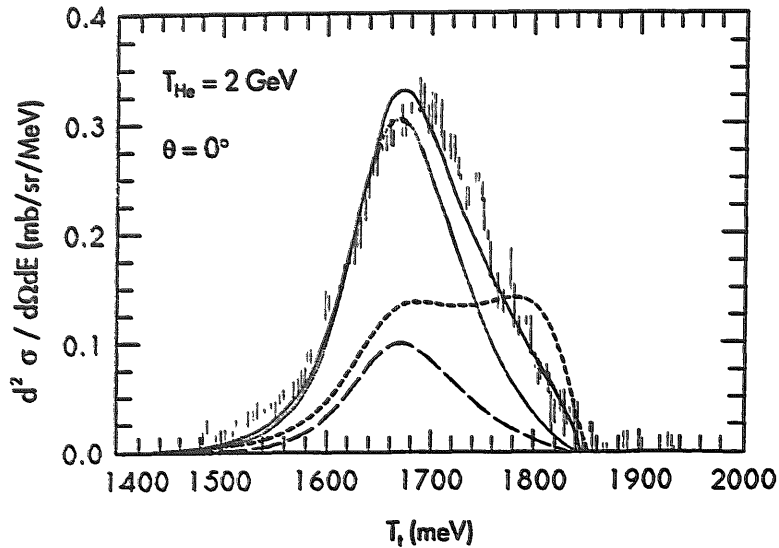


Fig. 4. Double-differential cross section for (${}^3\text{He}, t$) on proton and neutron targets at fixed angle ($\theta = 0^\circ$) as a function of the t kinetic energy. Dotted line: DET on a proton target. Continuous line: DET+DEP+s-wave on a proton target. Experimental points for (${}^3\text{He}, t$) on a proton target from ref. ¹⁶). Long-dashed line: DET on a neutron target. Short-dashed line: DET+DEP+s-wave on a neutron target.

We should also mention that, as noted in ref. ¹⁰), the sum of our two distributions shifts the strength but not the peak. In the experiment the peak is shifted a bit and has not the sharp features of our results, indicating that further corrections are needed. The basic features are however reproduced by the simple sum of the neutron and proton distributions. These corrections and other many body corrections will have to be accounted for when looking at the more apparent shift in heavy nuclei. Note that the fact that the peak is not moved in our approach, which considers the πN emission channel is in agreement with present findings in ref. ⁴), where it is shown that the peak in the explicit πN channel in different nuclei appears at the same place as for proton targets. The peak for $2N$ emission is however largely displaced at higher t -energies when using nuclear targets and is mostly responsible for the shift of the peak ⁴). The shift of strength apparent in the deuteron is nicely interpreted here in terms of the contribution of the DEP mechanism for the neutron distribution and is one element to consider in the study of (${}^3\text{He}, t$) reactions in nuclei.

The study done here is meant to give further support to the DEP mechanism: by selecting the analogous reaction to the (${}^3\text{He}, t$), which however stresses the role of this mechanism. This reaction is the (${}^3\text{He}, {}^3\text{He}$) reaction, as we discussed in sect. 3.

In fig. 6 we show the results for the (${}^3\text{He}, {}^3\text{He}$) reaction on the proton at $T_{\text{He}} = 2.0$ GeV as a function of the outgoing He kinetic energy and for $\theta = 0^\circ$. Two features appear worth noting. In the first place the strength of the cross section is much bigger than for the corresponding (${}^3\text{He}, t$) reaction. One can see there that the reaction is dominated by the DEP mechanism, as we saw in the former section, and

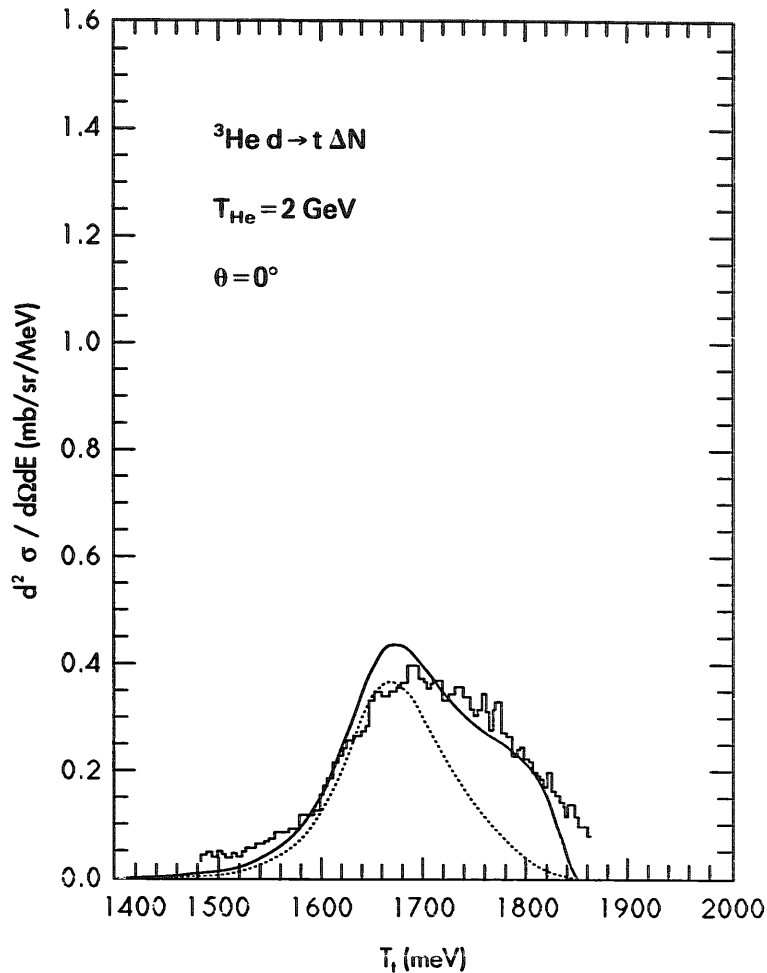


Fig. 5. Double-differential cross section for ($^3\text{He}, t$) on deuteron target at fixed angle as a function of the t kinetic energy. Dotted curve: DET mechanism done. Solid curve: DET+DEP+s-wave. Histogram: experimental results from ref. ¹⁷).

that the cross section with the DET mechanism alone is a negligible fraction of the total. On the other hand, the other apparent feature is that the peak of the distribution is displaced at higher outgoing He kinetic energies than the corresponding t -energies in the ($^3\text{He}, t$) reaction.

As we mentioned, the strength and shape of the DEP mechanism depends on the absolute value of the incoming He energy. Thus we have calculated the results at $T_{\text{He}} = 10.0$ GeV. In fig. 7 we show the results for the ($^3\text{He}, t$) reaction at $T_{\text{He}} = 10$ GeV. The strength has increased as a consequence of the fact that $q^2 \approx 0$ here and the nuclear form factor close to unity, but the shape and widths of the distribution is much like in fig. 4. We can also see in the figure that the role of the DEP mechanism is now negligible. On the other hand, in fig. 8 we plot the results for the ($^3\text{He}, ^3\text{He}$) reaction at $T_{\text{He}} = 10$ GeV and we see that the shape is still different to the one in the ($^3\text{He}, t$) reaction. On the other hand, while the strength of the ($^3\text{He}, t$) reaction

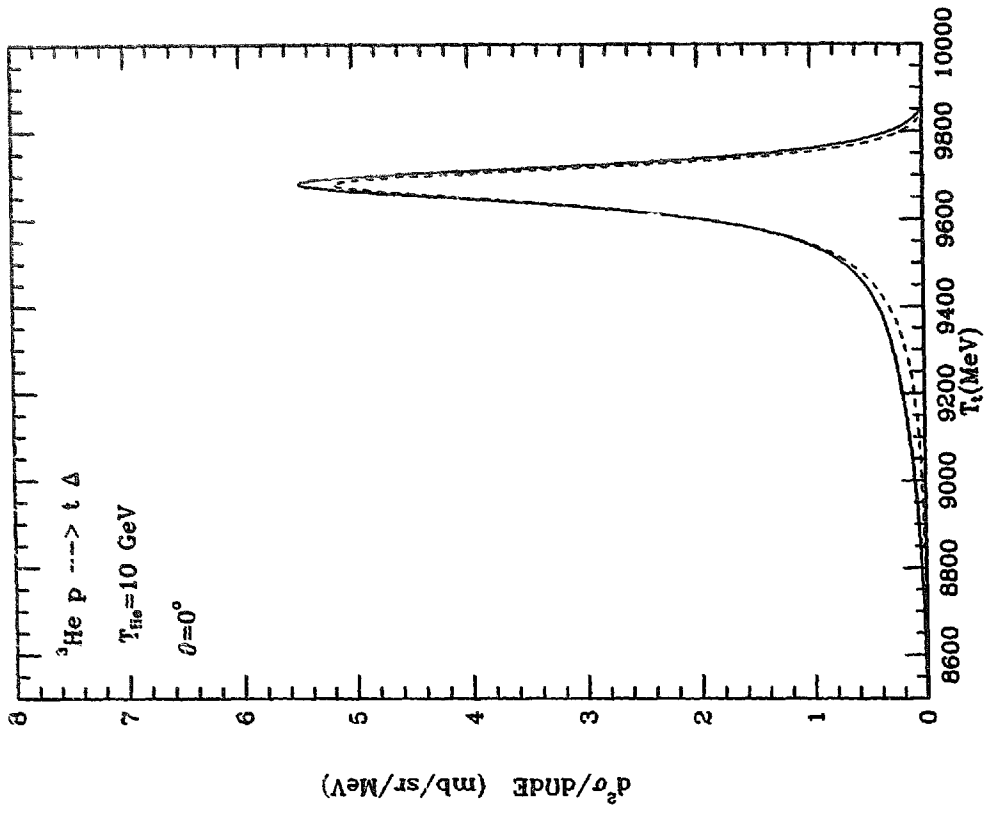


Fig. 7. Double-differential cross section for ($^3\text{He}, t$) on a proton target at $T_{\text{He}} = 10$ GeV. Dashed line: DET mechanism. Full line: DET + DEP + s-wave.

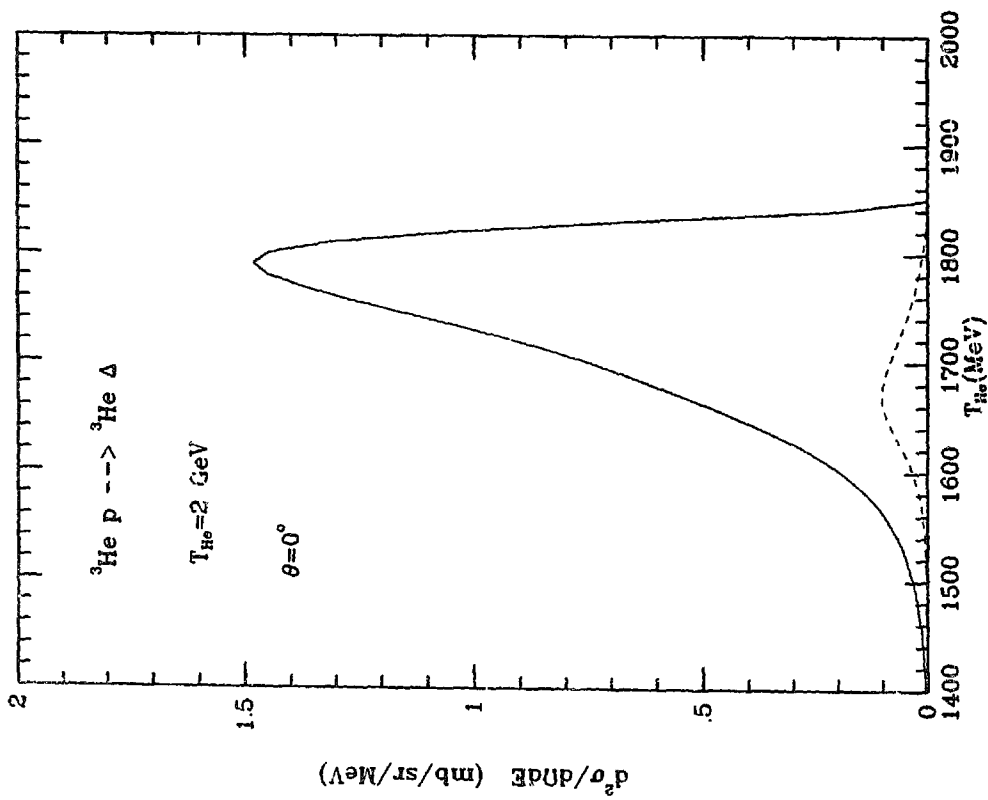


Fig. 6. Double-differential cross section for ($^3\text{He}, ^3\text{He}$) on a proton target at fixed angle as a function of the outgoing ^3He kinetic energy. Dashed line: DET mechanism. Full line: DET + DEP + s-wave.

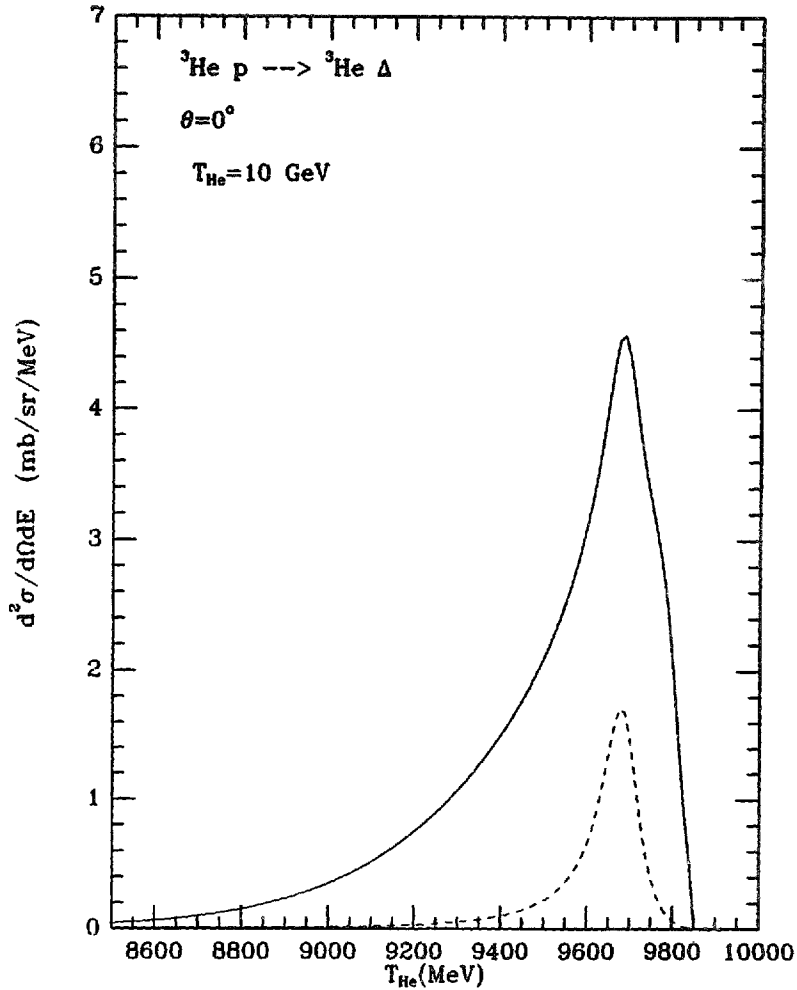


Fig. 8. As in fig. 7 but for the ($^3\text{He}, ^3\text{He}$) reaction.

cross section has increased, the one for the ($^3\text{He}, ^3\text{He}$) reaction has decreased with respect to the values at $T_{\text{He}} = 2$ GeV. The decrease of the ($^3\text{He}, ^3\text{He}$) cross section is a consequence of the fact that the DEP mechanism plays now a smaller role, because the phase space does not favour placing the Δ on-shell in the DEP mechanism. The DET mechanism plays now a more important role than at 2 GeV, but the DEP mechanism is still important and leads to a different shape than the one in the ($^3\text{He}, t$) reaction.

Finally, in figs. 9–11 we show the results for the excitation on the neutron: In fig. 9 for the ($^3\text{He}, ^3\text{He}$) reaction at 2 GeV, in fig. 10 for the ($^3\text{He}, t$) at 10 GeV and in fig. 11 for the ($^3\text{He}, ^3\text{He}$) reaction at 10 GeV.

Our absolute values for 10 GeV should in principle be less accurate, since one is extrapolating the effective interaction of eq. (15) to a much higher energy regime than the one where this interaction is tested. The qualitative features about the relative strength of the different mechanisms should, however, be quite firm.

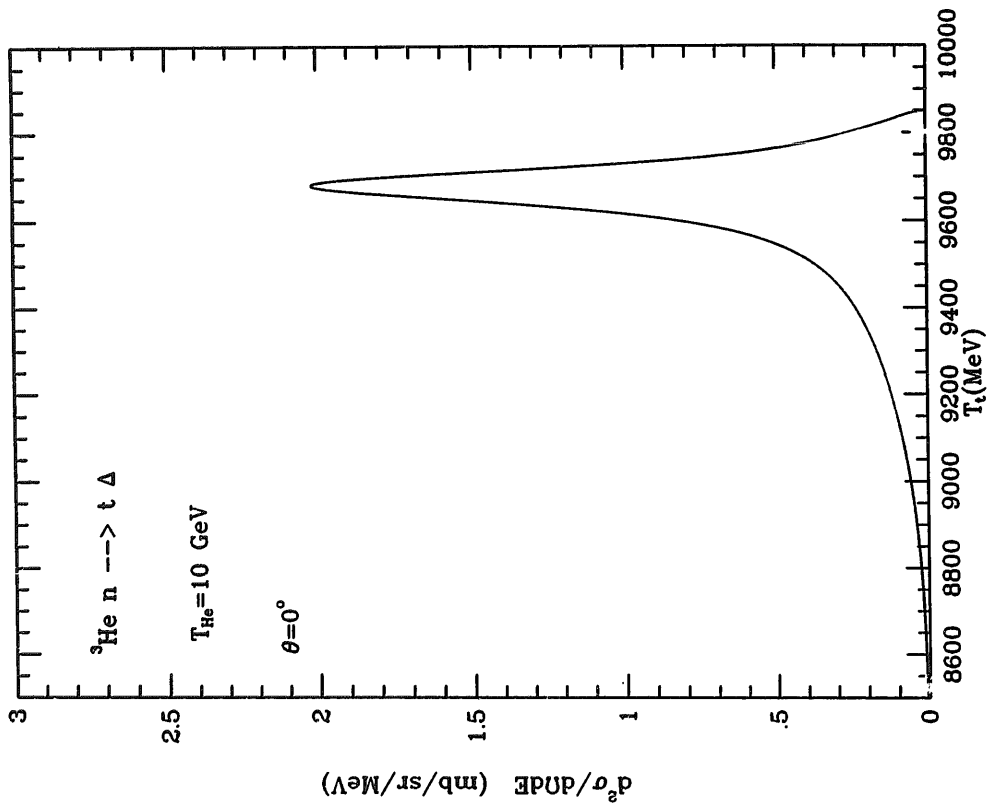


Fig. 10. Results for the (${}^3\text{He}, t$) reaction on the neutron target at 10 GeV.

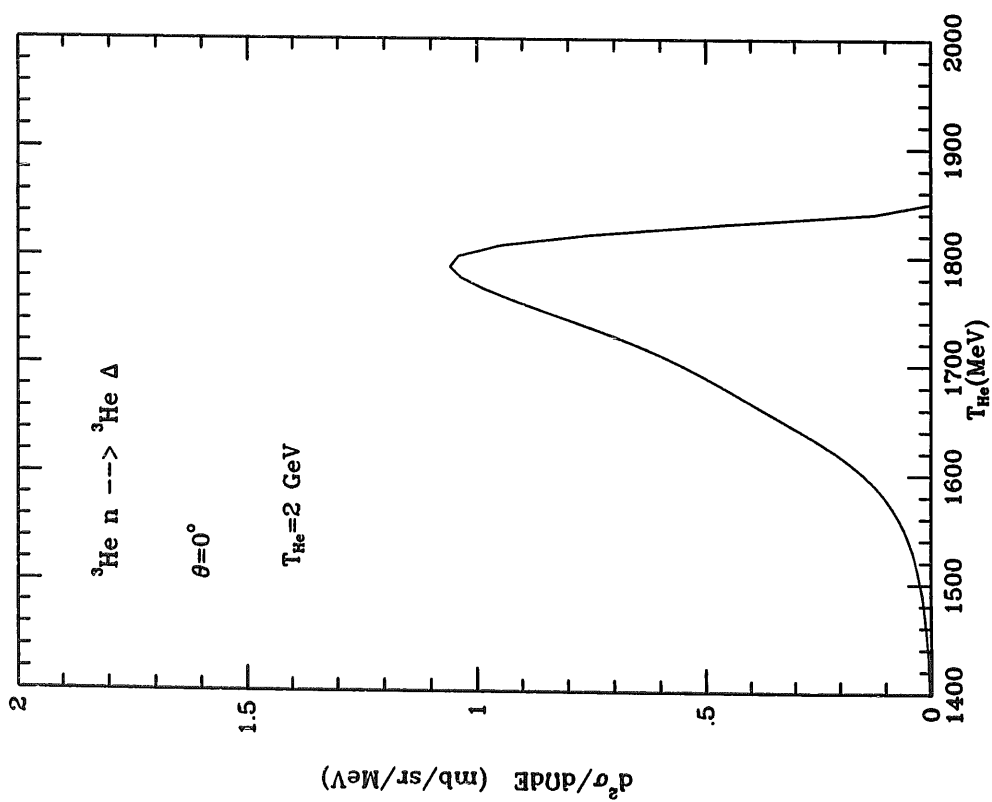


Fig. 9. Results for the (${}^3\text{He}, {}^3\text{He}$) reaction on a neutron target at 2 GeV.

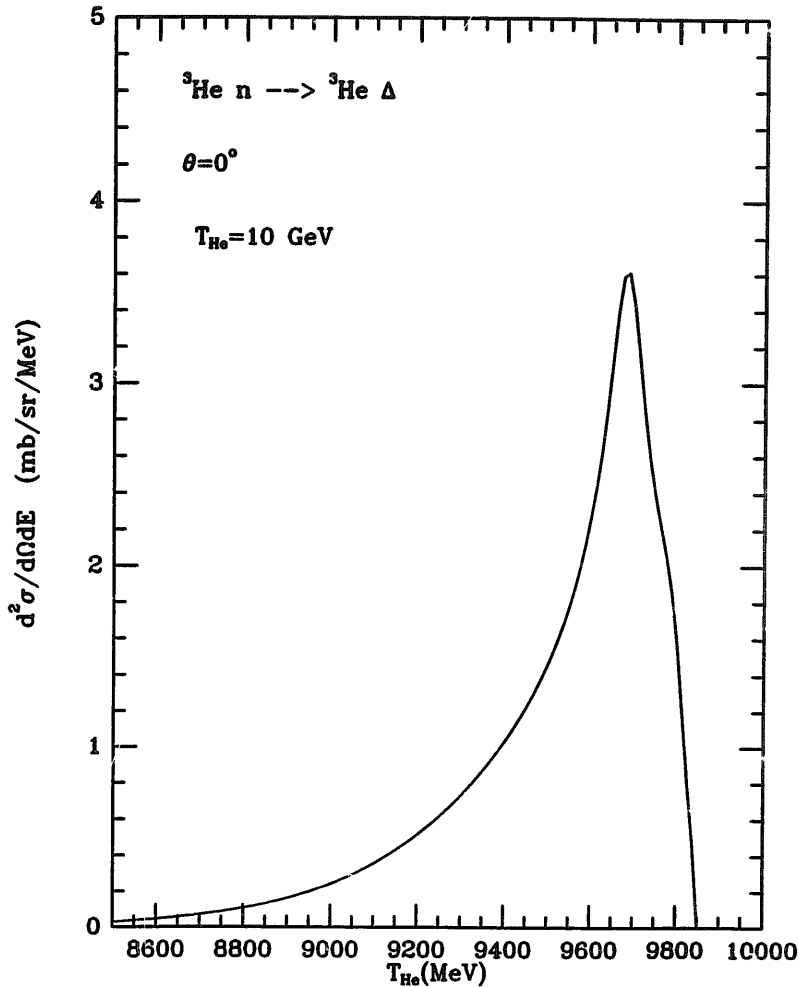


Fig. 11. Results for the (${}^3\text{He}, {}^3\text{He}$) reaction on a neutron target at 10 GeV.

5. Conclusions

We have studied the (${}^3\text{He}, t$) and (${}^3\text{He}, {}^3\text{He}$) reaction on the proton and the neutron at $T_{He} = 2$ and 10 GeV. We have made emphasis in the mechanisms of Δ -excitation on the target and the projectile and have found that while the DEP is rather small for the (${}^3\text{He}, t$) reaction on the proton, it is quite important for the reaction on the neutron. This leads to a shift of strength towards higher t -energies of the differential cross section on the deuteron with respect to the one on the proton target.

However, the most spectacular effects of the DEP mechanism are found in the (${}^3\text{He}, {}^3\text{He}$) reaction, where we find that the DEP mechanism is mostly responsible for the reaction at $T_{He} = 2$ GeV, giving rise to a cross section quite different in shape and magnitude to the (${}^3\text{He}, t$) one.

At high energies, $T_{\text{He}} = 10$ GeV, the DEP mechanism becomes less important and is negligible in the ($^3\text{He}, t$) reaction, but it still has some appreciable strength in the ($^3\text{He}, ^3\text{He}$) reaction.

It is clear that the simultaneous study of the ($^3\text{He}, t$) and ($^3\text{He}, ^3\text{He}$) reactions offers an interesting insight in the reaction mechanisms of the nucleon excitation in the delta region and the charge exchange reactions. While the ($^3\text{He}, t$) reaction has received much experimental attention, the ($^3\text{He}, ^3\text{He}$) reaction has not yet been studied experimentally. The present work indicates that a simultaneous study of the two reactions is a much richer source of information on the reaction mechanisms than the ($^3\text{He}, t$) reaction alone, and we urge the experimentalist to carry out this reaction.

This work is partially supported by CICYT project no. AEN 90-0049. P. Fernández de Córdoba wishes to acknowledge the fellowship from the Consejo Superior de Investigaciones Científicas. The computations are done in part in the Centro Informático de la Universidad de Valencia.

References

- 1) C. Gaarde, Nucl. Phys. **A478** (1988) 475c
- 2) F.A. Gareev, Yu.L. Ratis, E.A. Strokovsky, O. Melkinova and J.S. Vaagen, talk at Hirschegg Meeting (Austria) January 1991
- 3) F.A. Gareev, Yu.L. Ratis, E.A. Strokovsky and J.S. Vaagen, talk at Varenna Meeting (Italy), June 1991
- 4) G. Gaarde, talk at the Int. Workshop on pions in nuclei, ed. E. Oset, M.J. Vicente-Vacas and C. García-Recio, Peñíscola, June 1991 (World Scientific, Singapore) p. 375
- 5) B.K. Jain, *ibid*, p. 406
- 6) E.A. Strokovsky, F.A. Gareev and Yu L. Ratis, *ibid*, p. 395
- 7) V.G. Ableev *et al.*, Sov. Phys. JETP Lett. **40** (1984) 763; Phys. Lett. **B264** (1991) 264
- 8) C. Ellegaard *et al.*, Phys. Rev. Lett. **50** (1983) 1745
- 9) J. Delorme and P.A.M. Guichon, Phys. Lett. **B263** (1991) 157
- 10) E. Oset, E. Shiino and H. Toki, Phys. Lett. **B224** (1989) 249
- 11) R. Machleidt, K. Holinde and Ch. Elster, Phys. Reports **149** (1981) 1
- 12) J.D. Bjorken and S.D. Drell, Relativistic quantum fields (McGraw-Hill, New York, 1965)
- 13) F.E. Close, An introduction to quarks and partons (Academic Press, New York, 1979)
- 14) V. Dimitriev, O. Suchkov and C. Gaarde, Nucl. Phys. **A459** (1986) 503
- 15) E. Oset and W. Weise, Nucl. Phys. **A319** (1979) 477
- 16) C. Ellegaard *et al.*, Phys. Lett. **B154** (1985) 110
- 17) C. Gaarde, Nucl. Phys. **A478** (1988) 475c

BB

CERN LIBRARIES, GENEVA



SCAN-9410304

84 9444

COHERENT PION PRODUCTION INDUCED BY PROTONS AND LIGHT IONS

P. Fernández de Córdoba, E. Oset and M.J. Vicente-Vacas.

*Departamento de Física Teórica and IFIC
Centro Mixto Universidad de Valencia - CSIC
46100 Burjassot (Valencia), Spain.*

Abstract

We study coherent pion production by means of the (p, n) and (He, t) reactions on different nuclei and at different energies of the projectile. Energy and angular distributions are calculated. The angular distributions are rather narrow along the direction of the momentum transfer, particularly in heavy nuclei. The reaction provides valuable information on the longitudinal part of the elementary $NN \rightarrow N\Delta$ interaction. It is also a good tool to obtain information on the pion nuclear interaction, complementary to that offered by reactions with real pions.

1 Introduction.

Coherent pion production in (p, n) or $({}^3\text{He}, t)$ collisions in nuclei, where the target nucleus is left in its ground state, has emerged as a byproduct of the study of the shift of the Δ peak in charge exchange reactions in nuclei [1, 2]. Although many reaction channels are responsible for the shift of strength in these reactions [3] it was found theoretically that the peak of the coherent channel is shifted by about 60 MeV towards lower excitation energies with respect to the peak in the elementary reaction, (p, n) or $({}^3\text{He}, t)$ on proton targets [4, 5, 6]. Experimental work on the issue has just begun. There is some preliminary work on the $({}^3\text{He}, t)$ reaction on ${}^{12}\text{C}$ target [7] confirming the peak position and the angular dependence found in [6] and some estimates of the coherent channel in the (p, n) reaction on ${}^{12}\text{C}$ in [8]. Work is in progress in two more experiments [9, 10]. Actually, even if the pion was not detected, the first clear evidence of coherent pion production was shown in ref. [11]. This experiment was aimed at exciting the Roper resonance with an isoscalar probe in the (α, α') reaction on protons. A signal for the Roper excitation was found but a larger peak for ' Δ excitation in the projectile' (the α particle) was found in the reaction. The Δ decays producing pions and the α particle remains in its ground state (emerging α'). This reaction viewed in the frame of reference where the α particle is at rest qualifies as coherent pion production on ${}^4\text{He}$ with the (p, n) and (p, p') reactions, and a large strength for these channels was found in this reaction. A recent theoretical work on the (α, α') reaction is done in [12] establishing the connection between the mechanism of Δ excitation in the projectile and coherent pion production. The data are well reproduced.

So far experiments looking for coherent pions have only been done in ${}^{12}\text{C}$ and at very specific energies. Also the calculations have all been done in ${}^{12}\text{C}$ and the extension of the calculations to heavier nuclei is technically difficult with the approaches of refs. [4, 5] which require the specific treatment of large spaces of Δh states. The work of ref. [6] uses instead a different approach to the Δh model of [13] which was tested with success in pion nucleus scattering around resonance for different nuclei from ${}^{16}\text{O}$ to ${}^{208}\text{Pb}$ [14] and at low energies, going beyond the Δh approach, in ref. [15] with equally good results. The method consists in the evaluation of a microscopical optical potential with a local term and a non-local one. However some other non localities implicit in the detailed Δh approach [13] are proved to be unessential and are taken into account by means of appropriate local functions. Thus the evaluation of the scattering amplitudes or the pion waves is done in an easy way by means of a numerical solution of the Klein-Gordon equation with the optical potential written in terms of the nuclear density, for which the experimental information is used. The problem becomes then as easy in heavy as in light nuclei and allows us to make predictions of coherent pion production over the periodic table.

In this paper we present the first results for coherent pion production in

nuclei other than ${}^{12}\text{C}$. It is important that both experiments and calculations are done in different nuclei in order to gain control on this reaction from where much information concerning the transition amplitude $NN \rightarrow N\Delta$ and the interaction of off shell pions with nuclei is expected to come [4, 5, 6, 16].

Additional information should come from the study of the dependence of the cross section on the energy of the incoming beams. Both these aspects, mass dependence and dependence on the beam energy are dealt with in the present work.

Another interesting aspect discussed here is the angular dependence of the pions, which come out in a narrow cone along the direction of the (p, n) momentum transfer. The angular cone becomes narrower in heavy nuclei and the process leads to highly monochromatic and unidirectional pions with analogies to the photons produced in the tagging technique. However, there are substantial dynamical differences with the ordinary Bremsstrahlung and the process of coherent pion production does not qualify for this name, as we shall see.

2 Formalism for coherent pion production.

We study the (p, n) reaction in nuclei producing a π^+ and leaving the nucleus in the ground state

$$p + A(g.s.) \rightarrow n + A(g.s.) + \pi^+ \quad (1)$$

In the first place it is useful to establish from the beginning the difference between this process and a similar one, coherent Bremsstrahlung in e^- nucleus scattering. This latter process is given by

$$e + A(g.s.) \rightarrow e + A(g.s.) + \gamma \quad (2)$$

and is a standard problem in QED [17]. The process proceeds via the mechanisms depicted in fig. 1. The electron interacts with the Coulomb potential of the nucleus and the photon goes out as a free wave. It is thus the fact that the e^- dispersion relation is changed by the interaction with the nucleus what makes it possible for a free photon to emerge. The long range character of the Coulomb interaction ($1/\vec{q}^2$ dependence of the amplitude) and the zero mass of the photon, which places the e^- propagator near its mass shell, collaborate to make the mechanism of fig. 1 extremely efficient in producing photons in the direction of the electron momentum transfer.

In the case of the pions the situation is different because of the finite mass of the pion and the strong interaction of the nucleons. We can see that the analogous mechanism of fig. 1 does not work in the case of pions, at least for the case of forward propagating neutrons, which makes the production of pions most efficient by means of other mechanisms. Indeed, because of the strong interaction of the nucleons with the nucleus we can no longer use perturbation

theory as in fig. 1, but must replace the p and n free waves by their corresponding wave functions in the nucleus. This is depicted in fig. 2 where the pion is still kept as a free wave in analogy to the mechanism of photon emission. For forward propagation of the nucleons, and relatively large energies of the nucleons, as needed to produce pions, we can rely upon Glauber theory. Thus the matrix element for the transition $p \rightarrow n\pi$ in fig. 2 would be proportional to

$$A = \int d^3x \phi_n^*(\vec{x}) \epsilon^{-i\vec{p}_\pi \cdot \vec{x}} \phi_p(\vec{x}) \delta(E_p - E_n - E_\pi) \quad (3)$$

with

$$\begin{aligned} \phi_p(\vec{x}) &= \epsilon^{i\vec{p}_p \cdot \vec{x}} \epsilon x p \left(-\frac{1}{2} \int_{-\infty}^z \sigma(1-i\eta) \rho(\vec{b}, z') dz' \right) \\ \phi_n^*(\vec{x}) &= \epsilon^{-i\vec{p}_n \cdot \vec{x}} \epsilon x p \left(-\frac{1}{2} \int_z^{\infty} \sigma(1-i\eta) \rho(\vec{b}, z') dz' \right) \end{aligned} \quad (4)$$

where σ is the spin-isospin averaged NN cross section, η the ratio of real to imaginary part in the forward NN amplitude (we take $\eta = 0.275$ in our calculations), \vec{b} the impact parameter and $\rho(\vec{r})$ the nuclear density. The two exponentials in eq. (4), accounting for the distortion of the nucleon waves, combine to provide a function which depends on \vec{b} but not on z . Hence the matrix element of eq. (3) becomes

$$A = \int d^3x \epsilon^{i(\vec{p}_p - \vec{p}_n - \vec{p}_\pi) \cdot \vec{x}} C(\vec{b}) \delta(E_p - E_n - E_\pi)$$

with

$$C(\vec{b}) = \epsilon x p \left(-\frac{1}{2} \int_{-\infty}^{\infty} \sigma(1-i\eta) \rho(\vec{b}, z') dz' \right) \quad (5)$$

and thus

$$A = 2\pi \delta(p_{pz} - p_{nz} - p_{\pi z}) \int d^2b \epsilon^{i(\vec{p}_p - \vec{p}_n - \vec{p}_\pi) \cdot \vec{b}} C(\vec{b}) \delta(E_p - E_n - E_\pi) \quad (6)$$

The large mass of the nucleon and finite mass of the pion do not allow the two arguments of the δ functions to be simultaneously zero, and the mismatch in energy and longitudinal momentum is quite large for momenta of the nucleons and pions of the order of their respective masses. Only in the limit of forward propagation of the particles and ultrarelativistic nucleons and pions the two arguments can approach zero simultaneously. We are concerned here about the production of intermediate energy pions, around the Δ region and below and there the energy and momentum mismatch in eq. (6) is very large and the Bremsstrahlung-like mechanism of fig. 2 does not proceed.

In order to have coherent pion production we must then look at the interaction of the pion with the nucleus. This is depicted diagrammatically in fig. 3 for the particular case when the pion interaction with the nucleus proceeds via Δh excitation.

The diagrammatic expansion is selfexplanatory. The pion selfenergy contains Δh excitation plus the iteration of Δh excitations with the ingredients of the Δh interaction additional to one pion exchange. After the diagrams which are included in the pion selfenergy we find either one pion alone or a pion line followed by Δh excitations and their iteration by the whole spin isospin interaction. The whole sum of the free pion line and the iterative excitation of Δh states is nothing but a renormalized pion in the medium. This is depicted diagrammatically in the second member of the equation in fig. 3, which already accounts for the fact that the first term (fig. 3a) does not contribute, as we have seen. According to refs. [14, 15] the pion selfenergy can be written as

$$\Pi(\vec{r}) = \Pi^{(s)}(\vec{r}) + \vec{\nabla} \Pi^{(p)}(\vec{r}) \vec{\nabla} \quad (7)$$

where the first term is associated to the s-wave πN interaction and the second one to the p-wave one, but the potential contains the lowest order in density and higher order corrections.

The cross section for the reaction of eq. 1 is given in the lab system by

$$\frac{d\sigma}{d\Omega_n dE_n d\Omega_\pi} = \frac{1}{(2\pi)^5} \frac{M_p M_n p_n p_\pi}{2p_p} |\vec{T}|^2 \quad (8)$$

where the matrix element \vec{T} is given by [6]

$$-iT_i = -\sqrt{2} \frac{f}{\mu} \sqrt{\frac{-q^2}{\vec{q}^2}} \int d^3x \phi_n^*(\vec{x}) \phi_p(\vec{x})$$

$$\left(\frac{q_i F^2(q)}{q^{02} - \vec{q}^2 - \mu^2} \Pi^{(s)}(\vec{x}) - [V_L' \hat{q}_i \hat{q}_j + V_T' (\delta_{ij} - \hat{q}_i \hat{q}_j)] \Pi^{(p)}(\vec{r}) i \nabla_j \right) \phi_{\text{int}}^*(\vec{p}_\pi, \vec{x}) \quad (9)$$

Where the longitudinal and transverse parts of the spin-isospin interaction are given by

$$\begin{aligned} V_L'(q) &= \frac{\vec{q}^2}{q^{02} - \vec{q}^2 - \mu^2} F^2(q) + g' \\ V_T'(q) &= \frac{\vec{q}^2}{q^{02} - \vec{q}^2 - m_\rho^2} C_\rho F_\rho^2(q) + g' \end{aligned} \quad (10)$$

The factor $(-q^2/\vec{q}^2)^{1/2}$ in eq. (9) is included to make invariant the πNN coupling, $\frac{f}{\mu} \vec{\sigma} \vec{q}$, assumed implicitly in eqs. (9,10). $F(q)$, $F_\rho(q)$ are the π , ρ form factors taken of the monopole type with $\Lambda = 1.3 \text{ GeV}$ and $\Lambda_\rho = 1.4 \text{ GeV}$ and $C_\rho = 3.96$ [18] and \vec{q} in eqs. (10) is evaluated in the Δ rest frame. We take $g' = 0.6$ as used in the study of pionic reactions [14, 15]. The pion

wave function $\phi_{out}^*(\vec{p}_r, \vec{r})$ is obtained by solving numerically the Klein Gordon equation with the potential of eq. (7) and imposing to it the proper boundary conditions. This is done in the following way: first we use the property [19]

$$\phi_{out}^*(\vec{p}_r, \vec{r}) = \phi_{in}(-\vec{p}_r, \vec{r}) \quad (11)$$

and

$$\phi_{in}(\vec{q}, \vec{r}) = 4\pi \sum_l i^l \sum_l Y_{lm}^*(\hat{q}) Y_{lm}(\hat{r}) \tilde{j}_l(q; r) \quad (12)$$

with $\tilde{j}_l(q; r)$ solutions of the radial differential equation with the asymptotic properties

$$j_l(q; r)|_{r \rightarrow \infty} \simeq e^{i\delta_l} \frac{1}{qr} \sin(qr - l\frac{\pi}{2} + \delta_l) \text{ for } \pi^0$$

$$j_l(q; r)|_{r \rightarrow \infty} \simeq e^{i(\delta_l + \sigma_l)} \frac{1}{qr} \sin(qr - l\frac{\pi}{2} + \sigma_l + \delta_l - \eta \ln 2qr) \text{ for } \pi^\pm \quad (13)$$

with η and σ_l defined in [19] and δ_l the complex phase shifts obtained from the numerical solution of the Klein Gordon equation.

The results obtained can be immediately generalized to the (${}^3He, t$) or ($t, {}^3He$) reactions. For instance the cross section for the (${}^3He, t$) reaction would be obtained by changing the p variables to those of the 3He and the n variables to those of the t and one must multiply the matrix element of eq. (9) by the (He, t) transition form factor [20].

$$F_{He,t}(q) = e^{-\alpha^2(1+\epsilon q^4)}; \alpha = 16 \text{ GeV}^{-2}; \epsilon = 20 \text{ GeV}^{-4} \quad (14)$$

Furthermore σ in eq. (4) becomes now the cross section 3HeN or tN averaged over spin-isospin, which are about the same, and the ${}^{12}C$ density is changed to the convoluted density with the finite size of the 3He .

Similarly we can also use the formulas of eqs. (8), (9) to evaluate coherent π^0 production with the (p, p') reaction. This is simple: one removes the factor $\sqrt{2}$ in eq. (9) and substitutes the outgoing n by the p' . Also the optical pion potential becomes now the one of a π^0 . For spin-isospin saturated nucleus, and neglecting the small effect of the Coulomb interaction on the pion wave function, the cross section is the same as for (p, n) divided by two.

3 Results and discussion.

We look first at the energy distribution of pions. We choose a particular energy of the incoming nucleon, $T_p = 800 \text{ MeV}$, and integrate eq. (8) over the pion angles. Thus we obtain $d\sigma/d\Omega_n dE_n$ as a function of the outgoing n kinetic energy T_n . In fig. 4 we show this energy distribution for ${}^{12}C$, ${}^{40}Ca$ and ${}^{208}Pb$

for neutrons in the forward direction. The cross sections have similar strength in the different nuclei and show a peak around the Δ excitation region. We should also note that the peak of the distribution appears at $T_n \simeq 525 \text{ MeV}$, or equivalently $T_\pi = 135 \text{ MeV}$, while in the πN system with the nucleon at rest the Δ peak appears at $T_\pi = 190 \text{ MeV}$. Thus there is a shift of the peak by about 55 MeV toward lower excitation energies. This shift appears in all sort of phenomena where the pion is produced coherently in the delta region. Two examples are coherent π^0 photoproduction [21, 22] and coherent π^0 electroproduction [23], also shows up clearly in the simplest coherent process: pion nucleus elastic scattering [24]. Although one can justify this shift technically in different languages, there are intuitive physical arguments which can be used to explain the shift: the nuclear form factor and the distortion of the pion wave. The nuclear form factor acts like a reducing factor as the energy increases, because for the same angle the momentum transfer increases with the energy and the form factor is reduced (in the region of the first maximum from where the angular integrated cross section gets most of its strength). On the other hand, as we approach the Δ resonance energy in the process of elastic pion nucleus scattering there is an increasing loss of pion flux because of quasielastic collisions or pion absorption whose strength increases as we approach the Δ peak. Thus, the nuclear process involves a combination of the $\pi N \rightarrow \pi N$ strength mediated by the Δ , which has its strength at the free Δ peak, the distortion factor which has a minimum at that energy and the form factor effect which is a decreasing function of the energy. The consequence of all these effects is a shift of the Δ peak at lower excitation energies.

The coherent pion production process, as shown in fig. 3, qualifies as virtual pion production followed by elastic scattering of the pion. The qualification is appropriate even if in the production step we have the whole spin-isospin interaction V_L^+, V_T^+ of eqs. (10) and not only pion exchange, because this is also the case in intermediate steps of multiple scattering in pion nucleus collisions. Furthermore, as we shall see, the longitudinal part of the interaction in the case of the p-wave part, and the one pion exchange in the case of the s-wave part (see eq. (9)) dominate the cross section. The longitudinal part V_L^+ is also dominated by one pion exchange in this process, particularly as the energy of the nucleons and the pion increases.

In figures 5, 6, 7 we show differential cross sections in different nuclei for the (p, n) reaction. The cross sections are rather forward peaked and show a diffraction structure like in pion scattering. The cross section for the case of ${}^{208}Pb$ is rather narrow peaked. One can envisage the (p, n) or (p, p') reaction in heavy nuclei as a source of highly monochromatic and unidirectional pions, in analogy with the production of photons with these properties with the tagging technique in (e, e') scattering on nuclei.

In fig. 5 we have also separated the contributions from the transverse part by omitting V_L^+ and the s-wave part in eq. (9). As we can see the contribution is rather small and does not contribute at zero angle. This is because the combination of the transverse part projected into the longitudinal channel

of the final pion state induces a factor $\sin^4\theta$ like in pion photoproduction [21, 22]. Thus, coherent pion production in the forward direction around the resonance region is giving us information on the longitudinal part of the $NN \rightarrow N\Delta$ transition. Combined studies of coherent pion production, inclusive pion production, where V_L', V_T' appear with different weights, and the elementary reaction [25, 26], should put more constraints on the different models which exist for this amplitude [4, 5, 6, 27].

Next we discuss the dependence of the cross section as a function of the energy beam. This is shown in fig. 8. We observe that the cross section increases as the energy increases and the peak of the pion energy distribution is shifted towards higher pion energies.

Obviously, at low p energies, the phase space factor p_n/p_p of eq. (8) reduces drastically the cross section, as we can see for $E_p = 400\text{MeV}$. Also the nuclear form factor (implicitly contained in the pion nucleus optical potential, acts as a reduction factor, particularly at low p energies. At higher energies when the p_n/p_p is of the order of unity the changes must be found elsewhere. One of the reasons for this behaviour must be seen in the fact that as we go to higher energies the virtual pion produced in the (p, n) vertex becomes progressively more real. To envisage this let us assume the nucleons and the pions relativistic, such that their momenta are bigger than the mass. If we stick to the forward direction for nucleons and the pion we have

$$p_\pi = p_p - p_n \equiv q$$

$$\begin{aligned} E_p - E_n &= \sqrt{p_p^2 + M^2} - \sqrt{p_n^2 + M^2} \simeq p_p - p_n + \frac{M^2}{2p_p} - \frac{M^2}{2p_n} \\ &= (p_p - p_n)\left(1 - \frac{M^2}{2p_p p_n}\right) \\ \omega_\pi &= \sqrt{(p_p - p_n)^2 + m_\pi^2} \simeq (p_p - p_n)\left(1 - \frac{m_\pi^2}{2(p_p - p_n)^2}\right) \end{aligned} \quad (15)$$

The one pion exchange part of V_L' in eq. (10) becomes

$$V_\pi(q) \simeq \frac{q^2}{\frac{M^2 q^2}{p_p p_n} - \mu^2}; \quad (q \equiv |\vec{q}|) \quad (16)$$

Assuming q fixed $|V_\pi|$ increases when p_p increases. Assuming $M^2/p_p p_n \ll 1$ and fixed, $|V_\pi(q)|$ increases with q . These are the features which show up in fig. 8 and which tell us that by looking at the reaction at different beam energies one is placing different weight into the components of V_L' and one can investigate the structure of this interaction.

As discussed in section 2. the formalism serves equally to study coherent π^0 production with the (p, p') reaction, and the cross sections are approximately one half of those of the (p, n) reaction. Coherent π^0 production through the

(p, p') reaction would provide the first opportunity to study elastic scattering of π^0 with nuclei for near on shell π^0 . Comparison with coherent π^+ production in the same nucleus through the (p, n) reaction (dividing by two this cross section) would provide the ratio of elastic scattering for the two pions. Eventually, with sufficient intensities of the p beam, the secondary beam of real π^0 's, whose energy and direction is known, would have enough intensity to induce other collisions in other elements of the target, in spite of its short lifetime, and allow us to have direct measurements of π^0 scattering with protons for instance.

At the present moment there are no experimental data on the coherent π production with the (p, n) reaction. The closest experiment which can serve as a test of our results is the one of [28] channels where several exclusive were measured in the (p, n) reaction on ^{12}C . One of the channels measured in [28] is one where a π^+ alone is detected in the final state. This is not all coherent pion production since events where no other charged particles are emitted are also included. Hence incoherent π^+n emission is also included. But all the coherent channel is contained there. The authors of [28] mention that some of the events correspond to cases where the π^+ carries the maximum possible energy (i.e., coherent π^+ since no energy is used to excite nucleons). The other interesting feature is that the peak for ' π^+ alone' is shifted considerably towards lower excitation energies with respect to the elementary peak of the Δ excitation, as it corresponds to the findings for the coherent channel.

In fig. 9 we compare our results with the channel ' π^+ alone' of [28] adopting the same experimental cuts and folding with their resolution. We obtain a cross section (note that now we plot $d\sigma/d\Omega dp$) with a peak at around $p_n = 1175\text{MeV}/c$, or equivalently a π^+ with $T_p = 125\text{MeV}$. The strength of the cross section at the peak is about 0.02mb/srMeV , which is about 1/3 of the strength of the experimental peak. The rest we would expect to come from the inclusive process $pn \rightarrow nn\pi^+$, which as we know from [20] collects its strength in roughly equal parts from Δ excitation in the target and in the projectile.

We would like to compare our results with those of ref. [29]. The features for the coherent cross section are similar, however by comparison of fig. 19 of ref. [29] with the present result we observe that the peak in [29] appears at $T_\pi \simeq 85\text{MeV}$ while here it appears at about $T_\pi \simeq 125\text{MeV}$ and the strength in [29] is about twice as big as here. The authors of [29] also evaluate the incoherent cross section coming from $pn \rightarrow nn\pi^+$, but only Δ excitation in the target is included while from ref. [20] one knows that this channel contains a large fraction of strength coming from Δ excitation in the projectile.

It is clear that devoted experiments are needed to help unravel the details of the $NN \rightarrow N\Delta$ interaction as well as those of virtual pion interaction in nuclei, the two basic elements coming into the theoretical interpretation of these reactions.

4 Coherent π^+ production with the (${}^3\text{He}, t$) reaction.

This channel was studied explicitly in [6]. The cross section is increased with respect to the (p, n) one because of the factor $M_{He}M_t$, instead of M_pM_n , in the numerator of the cross section in eq. (8). On the other hand the transition (He, t) form factor and the distortion in ${}^{12}\text{C}$ by the ${}^3\text{He}$ or t instead of the p or n , decrease the cross section. As a result we find cross sections of similar strength as in (p, n), still bigger in the (${}^3\text{He}, t$) reaction. However, we find a faster decrease of the cross section as the mass number increases.

In the present calculations there is a small correction with respect to ref. [20]. $V_L(q)$ and $V_T(q)$ are calculated with q in the rest frame of the Δ instead of the rest frame of the nucleus, as was done in ref. [20]. This is consistent with the fact that the $\Delta N\pi$ coupling $\vec{S}\vec{q}$ is taken in the Δ rest frame. The elementary $NN \rightarrow N\Delta$ interaction was well reproduced with this interaction [12].

At the same time we have taken advantage to take into account the finite range of the ${}^3\text{He}$, by using convoluted densities of the target nucleus with the size of ${}^3\text{He}$. The combined affect of these corrections results in a reduction of the cross sections of [20] by about 20%. With this in mind one can obtain cross sections on ${}^{12}\text{C}$ from the results of [20] and we do not duplicate the information here.

We have also performed calculations of the (${}^3\text{He}, t$) cross sections for other nuclei. At $T_{He} = 6\text{GeV}$ we find at $T_t = 1.755\text{GeV}$, close to the peak, the following cross sections : 0.062, 0.036, 0.018 mb/srMeV for ${}^{12}\text{C}$, ${}^{40}\text{Ca}$ and ${}^{208}\text{Pb}$ respectively. The cross section in ${}^{208}\text{Pb}$ has fallen down by a factor 3.7 with respect to ${}^{12}\text{C}$, while in the (p, n) case it only falls by a factor 1.5. This is due to the effect of the increased distortion in the (${}^3\text{He}, t$) case.

At present there is very little experimental information available. In ref. [7] there are some data for the (${}^3\text{He}, t$) reaction. The data are extracted from the inclusive data since the experiment was not aimed at searching for the coherent channel. Devoted experiments at SATURNE with the same reaction are under way [9].

As noted in [6] the qualitative features of our results agree with those of [7]. The peak position is at the same place, the angular distribution is also about the same and the total strength is also consistent with the estimations of [7]. However it will be very interesting to do detailed comparisons with the data when the experiments are completed.

Our theoretical results have some features in common with the results of ref. [5], like the peak position of the energy distribution. However, the strength at the peak is in our case about a factor 2.5 smaller than in the case of [5]. As in the case of the (p, n) reaction the experimental results are much needed to help us gain control on details of the $NN \rightarrow \Delta N$ transition and the propagation of virtual pions in the nuclear medium.

5 Conclusions.

We have studied coherent pion production induced by protons or light ions. We have carried out calculations in different nuclei in order to study the mass dependence of the cross section and have also studied the dependence on the energy of the beam.

The process qualifies as virtual pion production followed by elastic scattering of the virtual pion with the nucleus till it becomes real, hence it allows to investigate properties of π^0 elastic scattering on nuclei, providing a quite novel information. It also allows one to study elastic scattering of pions, charged or neutral, for off shell situations of the pion, which can be varied at will. This would provide extra constraints on theories and should help us increase our microscopic understanding of the pion nucleus interaction.

The energy dependence of this reaction and its comparison with incoherent and elementary processes should also provide information on the elementary $NN \rightarrow N\Delta$ transition.

We observed that the process was mostly sensitive to the longitudinal part of the $NN \rightarrow N\Delta$ amplitude and that by changing the energy of the beam the weight of the different components of V_L^i changed. Hence a systematic study of this process as a function of the energy, together with information from the elementary $NN \rightarrow N\Delta$ reaction and inclusive pion production experiments should ultimately give us precise answers for the elementary $NN \rightarrow N\Delta$ amplitude which at present seems to be reproduced by a large variety of different models.

Another feature worth mentioning is the analogy of the process with the production of monochromatic and unidirectional photons with the tagging technique. The possibility of making some practical applications of the similar properties in the coherent pions is worth receiving some thoughts.

Comparison with the first experimental analysis supports the basic features which we have stressed about the reaction. However, devoted experiments in different nuclei and a broad range of energies are necessary to push forward this novel and interesting field.

Acknowledgments: this work is partially supported by CICYT contract number AEN 93 - 1205.

Figure captions:

fig. 1: Diagrams for coherent Bremsstrahlung in (e, e') reactions on nuclei.

fig. 2: Bremsstrahlung like mechanism for coherent π^+ production on nuclei with the (p, n) reaction. The crossed circle indicates the p or n distorted wave in the nucleus.

fig. 3: Diagrammatic representation of coherent pion production. The dashed lines indicate the pion, the wavy lines the spin-isospin interaction and the dotted line with a cross the ingredients in the Δh interaction additional to one pion exchange. The dashed lines with a dashed circle in the middle represent a renormalized pion. The crossed circle indicates the pion selfenergy.

fig. 4: Double differential cross section for coherent π^+ production with the (p, n) reaction on ^{12}C , ^{40}Ca and ^{208}Pb at $T_p = 0.8 GeV$ and $\Theta_n = 0^\circ$, as a function of the n kinetic energy.

fig. 5: Angular distribution of the pion for π^+ coherent production on ^{12}C at $T_p = 800 MeV$, $T_n = 525 MeV$ and $\Theta_n = 0^\circ$. The dashed line represents the contribution of the transverse part of the $NN \rightarrow N\Delta$ interaction.

fig. 6: Same as fig. 5 for ^{40}Ca .

fig. 7: Same as fig. 5 for ^{208}Pb .

fig. 8: Coherent π^+ production cross sections for the (p, n) reaction on ^{12}C at several energies of the incoming proton, as a function of the pion kinetic energy for $\Theta_n = 0^\circ$.

fig. 9: Experimental results for the " π^+ alone" channel in the (p, n) reaction on ^{12}C from ref. [28] which accounts for coherent π^+ production plus the incoherent $pn \rightarrow nn\pi^+$ channel. The dots on the continuous line indicate our results for coherent π^+ production with the same cuts as done in the experiment ($12^\circ \leq \Theta_n \leq 141^\circ$, and Θ_n measured between 0° and 6°).

References

- [1] T. Hemino et al., Phys. Lett. B 303 (1993) 236.
- [2] V.G. Ableev et. al., Sov. Phys. JETP Lett. 40 (1984) 763.
- [3] E. Oset, P. Fernández de Córdoba, J. Nieves and M.J. Vicente-Vacas, Phys. Scr. 48 (1993) 101; P. Fernández de Córdoba, E. Oset and M.J. Vicente-Vacas, University of Valencia preprint.
- [4] P. Oltmanns, F. Osterfeld and T. Udagawa, Phys. Lett. B 299 (1993) 194.
- [5] V.F. Dimitriev, Phys. Rev. C 48 (1993) 357.
- [6] P. Fernández de Córdoba, J. Nieves, E. Oset and M.J. Vicente-Vacas, Phys. Lett. B 319 (1993) 416.
- [7] T. Hemino et al., Phys. Lett. B 303 (1993) 236.
- [8] J. Chiba, Talk in the Intern. Workshop on Delta excitation in Nuclei (Tokyo, May 1993).
- [9] S. Roustean and T. Hemino, private communication.
- [10] R. Gilman, talk at International Symposium on spin-isospin responses and weak processes in hadrons and nuclei, Osaka, March 1994, Nucl. Phys. in print
- [11] H.P. Morsch et al., Phys. Rev. Lett. 69 (1992) 1336.
- [12] P. Fernández de Córdoba, E. Oset, J. Nieves, M.J. Vicente-Vacas, Yu. Ratis, J. Nieves, B. López-Alvaredo and F. Gareev, submitted to Nucl. Phys.
- [13] E. Oset and W. Weise, Nucl. Phys. A 319 (1979) 477.
- [14] C. García-Recio, E. Oset, L.L. Salcedo, D. Strottman and M.J. López, Nucl. Phys. A526 (1991) 685.
- [15] J. Nieves, E. Oset and C. García-Recio, Nucl. Phys. A554 (1993) 554.
- [16] T.E.O. Ericson, talk at PANIC 93, Peruggia; *ibid.*, talk at the International Symposium on spin-isospin responses and weak processes in hadrons and nuclei, Osaka, March 1994, Nucl. Phys. in print.
- [17] F. Mandl and G. Shaw, Quantum Field Theory, John Wiley 1988.
- [18] R. Machleidt, K. Holinde and Ch. Elster, Phys. Rep. 149 (1987) 1.
- [19] A. Galindo and P. Pascual, Quantum Mechanics (Springer, New York, 1991).

- [20] E. Oset, E. Shiino and H. Toki, Phys. Lett. B 224 (1989) 249.
- [21] I. Laktineh, W.M. Alberico, J. Delorme, M. Ericson, Nucl. Phys. A555 (1993)237
- [22] R.C. Carrasco, J. Nieves and E. Oset, Nucl. Phys. A565 (1993) 797.
- [23] S. Hirenzaki, J. Nieves, E. Oset and M.J. Vicente-Vacas, Phys Lett B304 (1993)198.
- [24] T.E.O. Ericson and W. Weise, Pions and Nuclei, Clarendon Press, Oxford, 1988.
- [25] A. B. Wicklung et al. Phys. Rev. D 35 (1987) 2670.
- [26] F. Shimizu et al., Nucl. Phys. A386 (1982) 571.
- [27] B.K. Jain and A.B. Santra, Phys. Lett. B244 (1990) 5; *ibid.*, Nucl. Phys. A519 (1990) 697.
- [28] J. Chiba et al., Phys. Rev. Lett. 65 (1991) 1982
- [29] T. Udagawa, P. Oltmanns, F. Osterfeld and S.W. Hong, Phys. Rev. C49(1994)3162

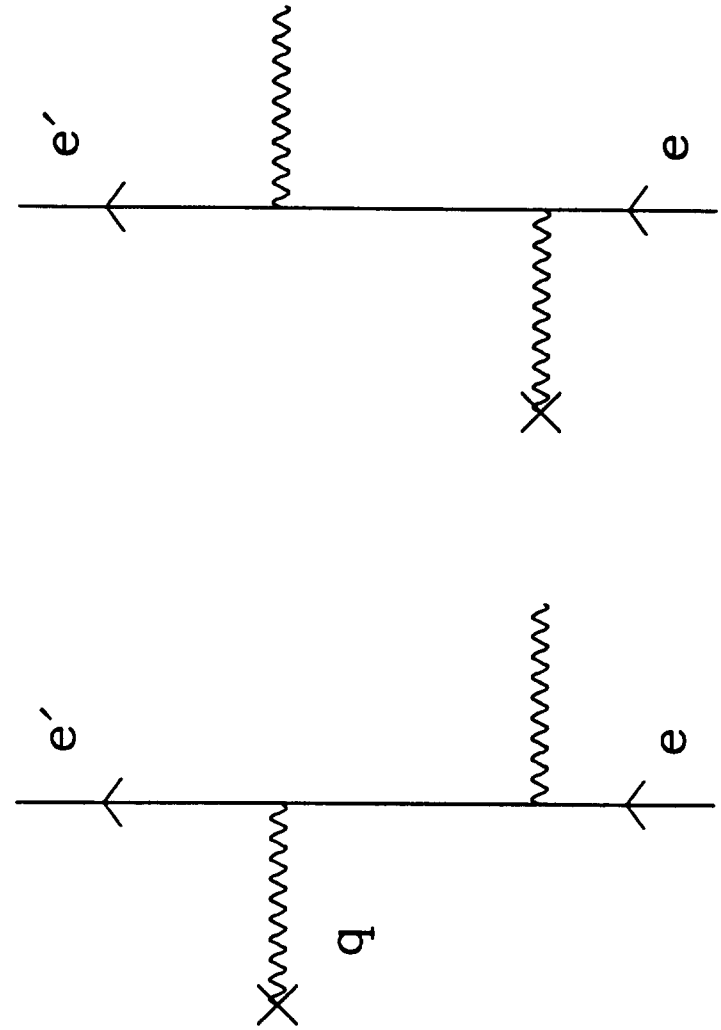


fig. 1

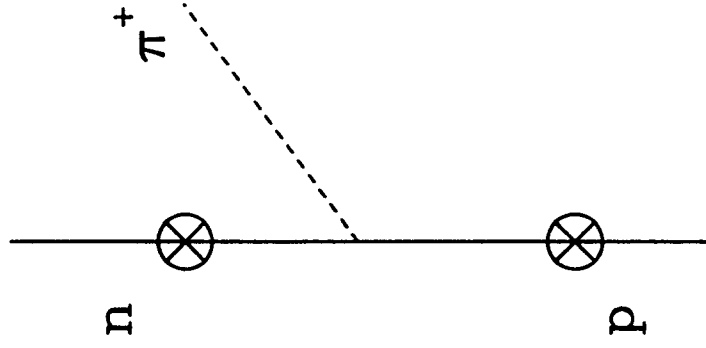


fig. 2

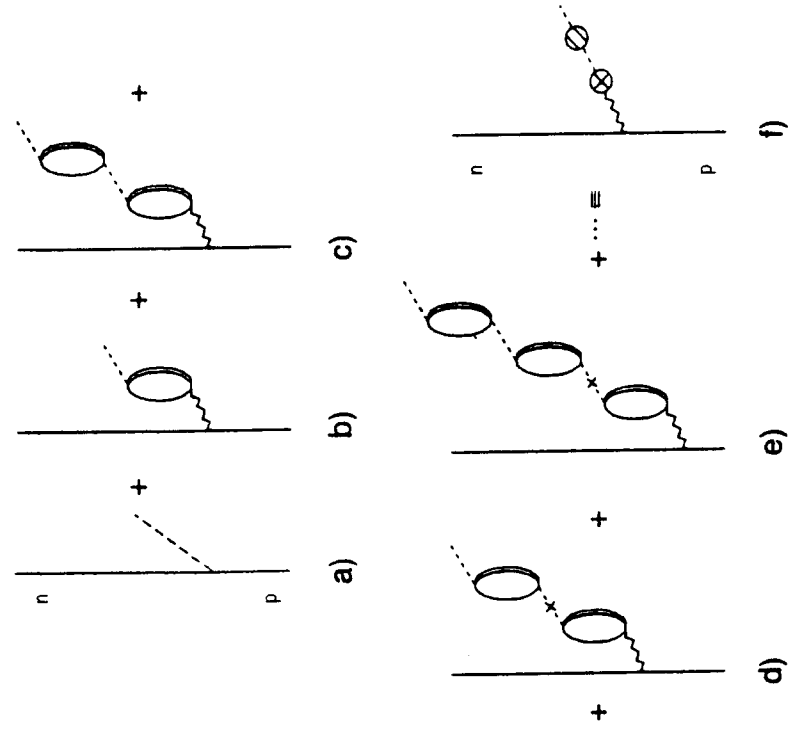


Fig. 3

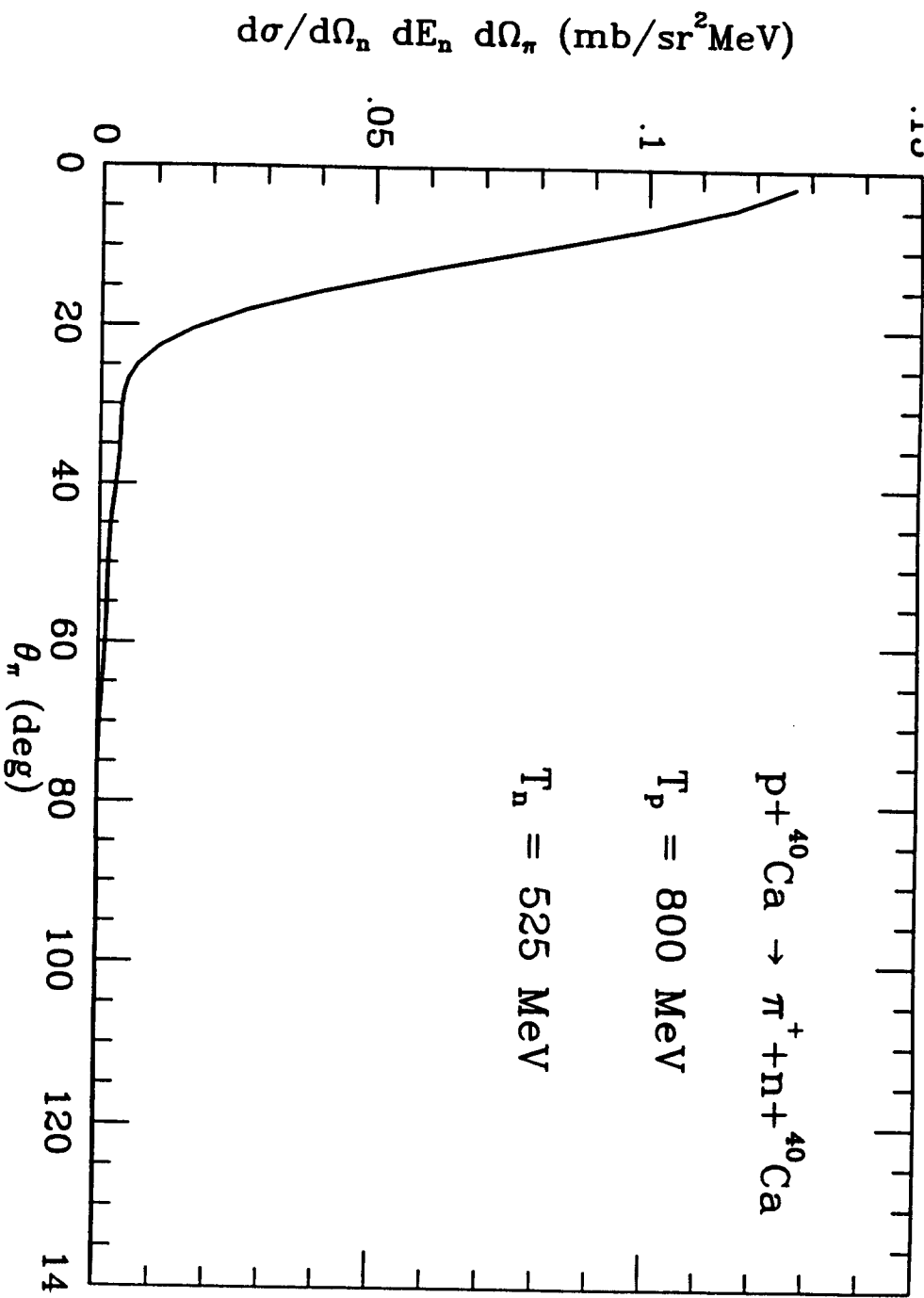
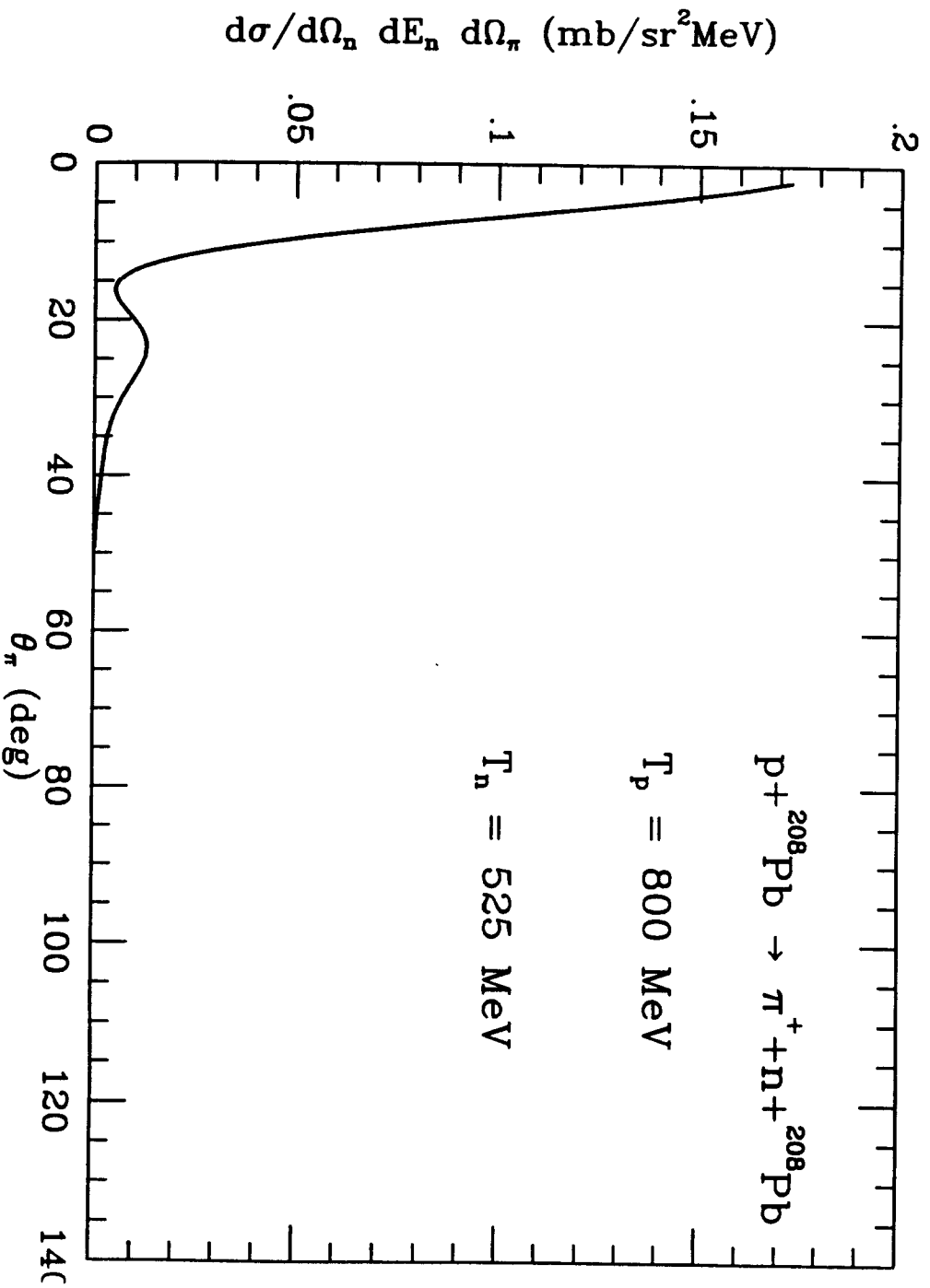


Fig. 6



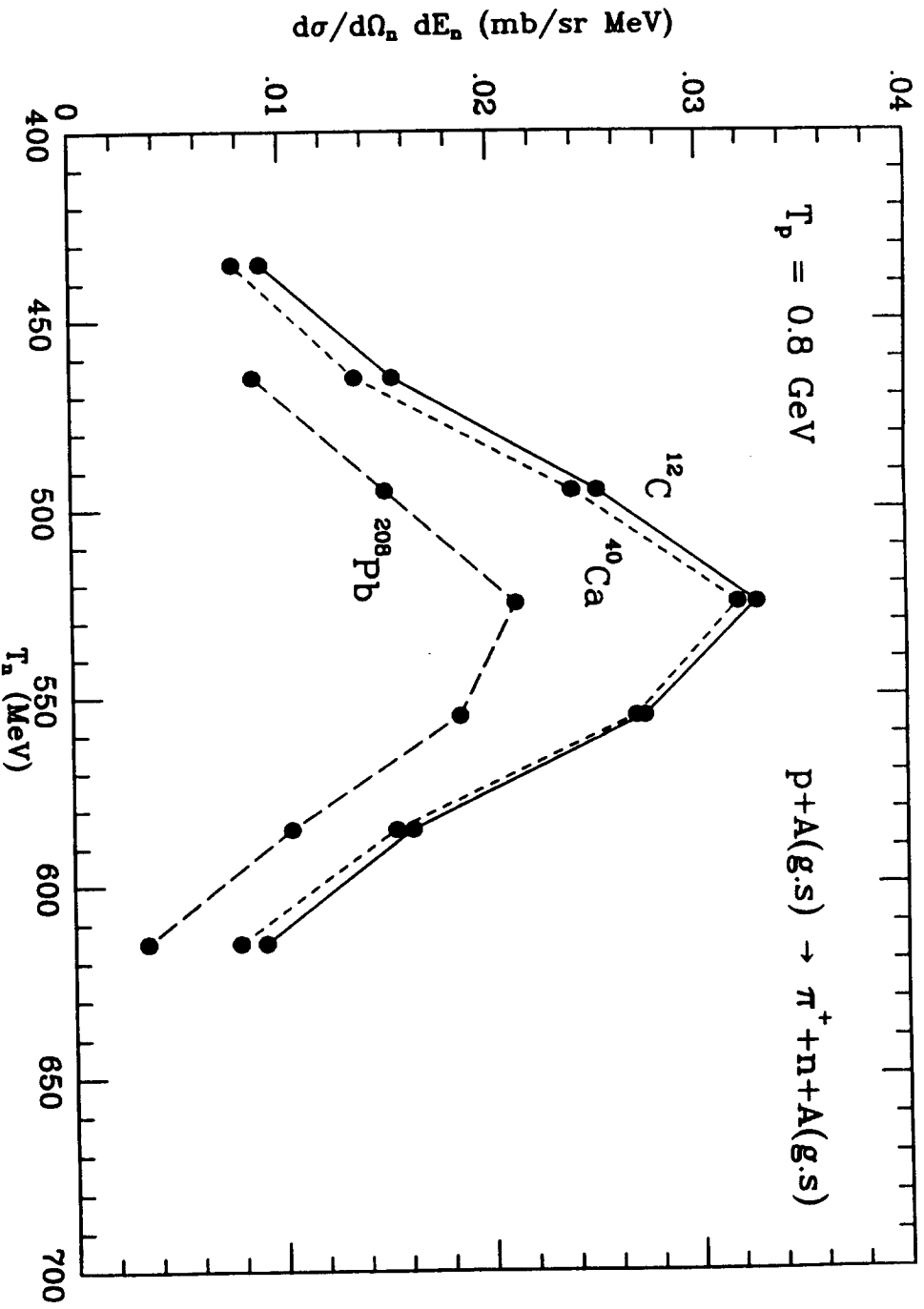
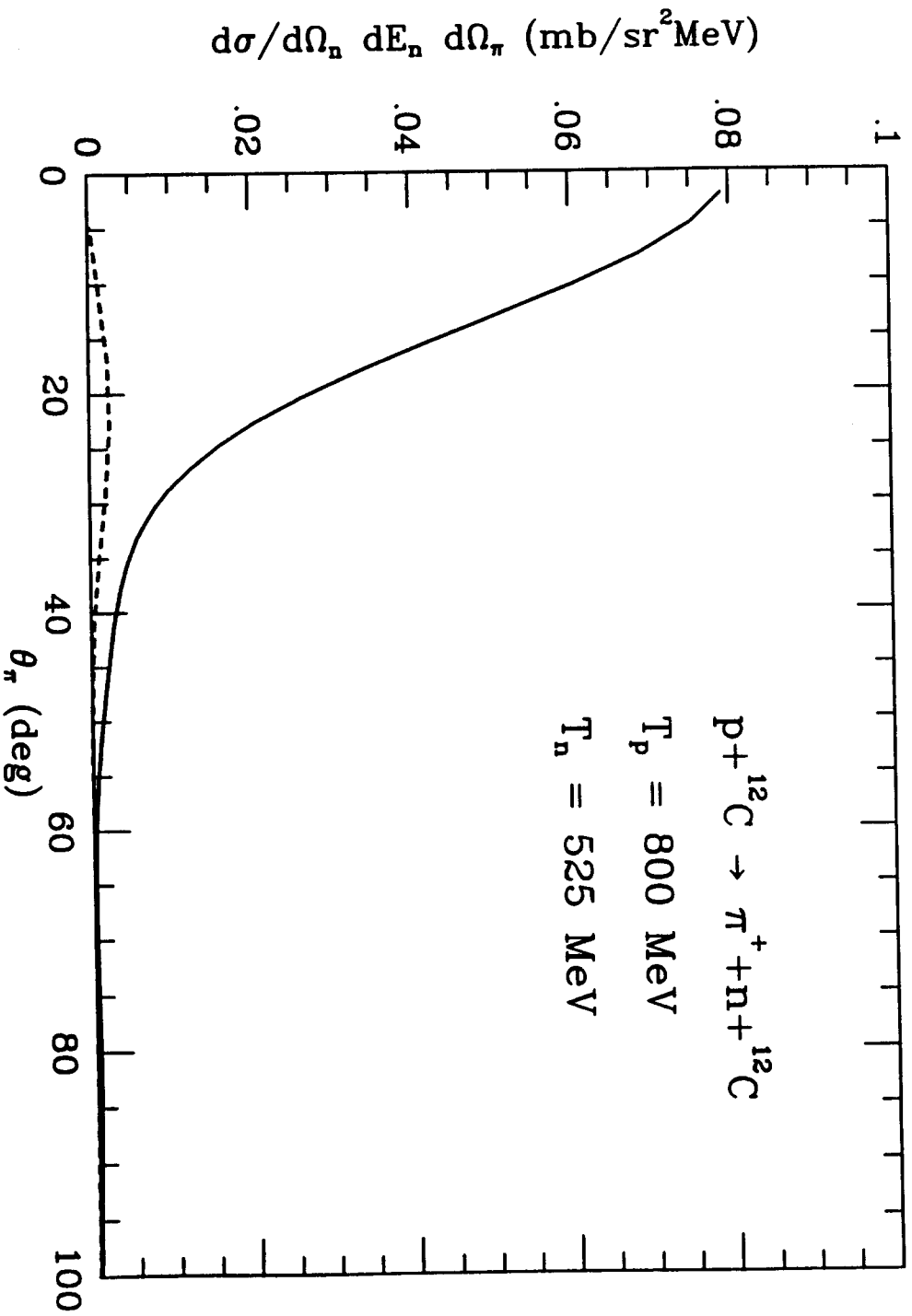


Fig. 4



MUON CAPTURE REVISITED

H.C. CHIANG¹, E. OSET and P. FERNÁNDEZ DE CÓRDOBA

*Departamento de Física Teórica and IFIC, Centro mixto Universidad de Valencia-CSIC,
Facultad de Físicas, Burjassot (Valencia), Spain*

Received 21 June 1989

Abstract: The problem of inclusive muon capture in nuclei is studied by calculating the capture rate in asymmetric infinite nuclear matter and using the local density approximation to evaluate the capture rates in nuclei. It is shown that the method is rather reliable and allows one to improve on approximations used in the past. The need for a strong nuclear renormalization is shown, reducing the capture rates by about a factor two in medium and heavy nuclei. By using standard effective interactions in the spin-isospin channel one can account for this renormalization and one finds a remarkable overall agreement with the measured capture rates for a large list of nuclei through the periodic table.

1. Introduction

In this paper we face the problem of total muon capture in nuclei from an unconventional point of view. From the early days of Primakoff ¹) the subject has attracted much interest ^{2,3}). The usual approach consists in performing the nonrelativistic approximation in the transition operators, neglecting the nucleon momentum ¹⁻⁴), and then doing a closure sum over the final nuclear states. However, the process involves small energy transfers to the nucleus of the order of the typical nuclear excitation energies and the results are very sensitive to the average nuclear excitation energy chosen ⁵). To eliminate the uncertainties associated to this energy, or equivalently, to the average neutrino energies, sum rule approaches have been applied ⁵⁻⁷) which reduce considerably the dependence on the average energy and hence provide more reliable results. The final results require the evaluation of non-trivial two-body matrix elements in the ground state of the nucleus.

The approximation of an average neutrino energy fixes the momentum transfer, q , and thus, the pseudoscalar term to a determined value. However, the dependence of this term on q is strong because of its approximate proportionality to the pion propagator ²). This is particularly relevant since this reaction has been used traditionally to extract information on the value of the pseudoscalar coupling constant ²⁻⁸).

Another approximation used to take into account the finite size of the nucleus is the use of the effective charge, Z_{eff} , which introduces a non-negligible source of error in the calculation since the capture rate is proportional to Z_{eff}^4 and certain

¹ On leave of absence from Institute of High Energy Physics, Academia Sinica, Beijing, China.

approximations are involved in its evaluation⁹⁾). In addition there are strong nuclear renormalization effects which are very important and deserve special attention.

Our approach avoids all of these shortcomings and provides a highly accurate method to evaluate the total capture rate in nuclei. Yet the method is much simpler technically than the traditional approaches and the same effort is required to evaluate the rate in light nuclei and in heavy nuclei. Furthermore, it has the virtue of showing that the only relevant nuclear information needed, as normally happens in other inclusive reactions¹⁰⁾, is the neutron and proton densities of the nuclear ground state, which we take from experiment to minimize errors.

The method consists in evaluating the capture rate of a muon in a Fermi sea of neutrons and protons. The calculation can be done exactly in a relativistic framework considering the nucleon momenta and the excitation energies of the Fermi sea, thus going beyond the closure sum or the sum rule approach. With the neutrino energy as a variable of integration, the pion pole structure of the pseudoscalar term is kept in the calculations. The step from infinite matter to finite nuclei is done by means of the local density approximation. The infinite matter calculation provides the muon width as a function of $\rho_{n,p}$ the neutron and proton densities, then we assume $\rho_{n,p} \rightarrow \rho_{n,p}(r)$ and fold this functional with the muon density distribution in the 1s state of the muon atom, from which the capture takes place. The local density approximation is highly accurate in this case, given the very weak q dependence of the matrix elements involved, which makes the transition of very short range. Only the pseudoscalar term depends more strongly on q because of its dependence on the pion propagator, but the moderate contribution of this term ($\sim 15\%$), together with the fairness of the local density prescription in pion nuclear reactions¹¹⁾ involving similar pion momenta, makes the use of the local density prescription a very accurate tool to obtain the total muon capture rate.

Then we avoid using the concept of Z_{eff} . Indeed all we need is to calculate the 1s muon wave function and use it in the folding of the local density prescription. Here we also keep up with our aim of a highly accurate evaluation and use a very precise method to solve the Schrödinger equation¹²⁾, taking into account finite size effects and vacuum polarization corrections.

In addition we include strong nuclear renormalization effects in the operators, and also consider the binding energies of the muons. The calculations are performed for a large list of nuclei over the whole periodic table and the results obtained are very instructive. With the standard coupling constants and form factors for $\mu p \rightarrow \nu_{\mu} n$, we obtain a very good agreement with all nuclei along the periodic table, showing the relevance of the nuclear renormalization in medium and heavy nuclei, which reduces the capture rates in about a factor two from the results without renormalization. The repercussion of such renormalization in other physical processes like pionic atoms or Σ hypernuclei is also stressed.

The paper proceeds as follows. In sect. 2 we evaluate the muon capture rates in infinite nuclear matter. In sect. 3 we discuss the nuclear renormalization and in sect.

4 the local density approximation. Sect. 5 contains the results and discussion and sect. 6 summarizes our results.

2. Muon capture rate in infinite matter

We start from the basic lagrangian for the $\mu^-p \rightarrow n\nu_\mu$ reaction depicted in fig. 1,

$$L(x) = \sqrt{\frac{1}{2}} G J^\mu(x) L_\mu^+(x), \tag{1}$$

with the leptonic and hadronic currents given respectively by

$$L_\mu^+(x) = \bar{\Psi}_\nu \gamma^\mu (1 - \gamma_5) \Psi_\mu, \quad J^\mu(x) = \bar{\Psi}_n B^\mu \Psi_p, \tag{2}$$

with B^μ the hadronic current operator. Their matrix elements between spinors give

$$\begin{aligned} \tilde{L}^{\mu+} &\rightarrow \bar{u}_\nu(p_\nu) \gamma^\mu (1 - \gamma_5) u_\mu(p_\mu), \\ \tilde{J}^\mu &\rightarrow \bar{u}_n(p_n) [g_V \gamma^\mu + i \frac{g_M}{2m_p} \sigma^{\mu\nu} q_\nu + g_A \gamma^\mu \gamma_5 + \frac{g_P}{m_\mu} q^\mu \gamma_5] u_p(p_p), \end{aligned} \tag{3}$$

where we follow Itzykson and Zuber¹³⁾ convention for the γ -matrices, with $q = p_n - p_p$, and g_V, g_M, g_A, g_P the vector, magnetic, axial-vector and pseudoscalar coupling constants respectively, including a form factor dependent on q . The values of the coupling constants and the expressions for the form factors can be seen in appendix A.

Assume for a moment an infinite nuclear medium with a proton density, ρ_p , and the protons at rest. The decay rate of a muon is given by

$$\Gamma = \sigma v_{rel} \rho_p, \tag{4a}$$

with v_{rel} the relative velocity of the muon with respect to the protons, and σ the $\mu p \rightarrow n\nu_\mu$ cross section. We have in Bjorken and Drell convention¹⁴⁾

$$\begin{aligned} \sigma v_{rel} &= \int \frac{d^3 p_\nu}{(2\pi)^3} \frac{2m_\nu}{2E_\nu} \frac{2m_n}{2E_n} \frac{2m_\mu}{2E_\mu} \frac{2m_p}{2E_p} \bar{\Sigma} \Sigma |T|^2 \\ &\times 2\pi \delta(E_\mu + E_p - E_\nu - E_n), \end{aligned} \tag{4b}$$

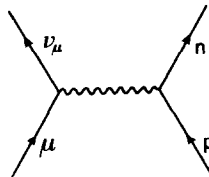


Fig. 1. Diagram for $\mu^-p \rightarrow n\nu_\mu$ process.

where the limit $m_\nu \rightarrow 0$ is to be taken and three momentum conservation is implicitly assumed. The full expression for $\bar{\Sigma} \sum |T|^2$ is given in appendix B.

The evaluation of Γ for finite nuclei proceeds in two steps. In the first one we evaluate Γ for a muon in a Fermi sea of protons and neutrons with $N \neq Z$. This is easily accomplished if one realizes that $-\pi\rho_p\delta(E_\mu + E_p - E_\nu - E_n)$ is the static limit of the imaginary part of the Lindhard function $\bar{U}(p_\mu - p_\nu)$ [see ref. ¹⁵] for the ph excitation appearing in fig. 2. This Lindhard function, incorporating the Pauli blocking on the neutrons, is given by

$$\bar{U}(p_\mu - p_\nu) = 2 \int \frac{d^3p}{(2\pi)^3} \frac{n_1(\mathbf{p})[1 - n_2(\mathbf{p} + \mathbf{p}_\mu - \mathbf{p}_\nu)]}{E_\mu - E_\nu + E_p(\mathbf{p}) - E_n(\mathbf{p} + \mathbf{p}_\mu - \mathbf{p}_\nu) + i\epsilon}, \tag{5}$$

where $n_{1,2}(p)$ are the occupation numbers in the Fermi sea of protons and neutrons, respectively. (The Lindhard function contains also the contribution from the backward going ph excitation, which we do not include in eq. (5) because it does not contribute to the imaginary part for $E_\mu - E_\nu > 0$, as we have here.) We observe that the δ function for energy conservation is substituted in $\text{Im } \bar{U}$ by the same δ of conservation but keeping track of the nucleon momenta, integrating over the Fermi sea of the protons and including the Pauli blocking for the neutrons, $[1 - n_2]$ factor.

Hence the actual width of a muon in the infinite matter slab is given by

$$\Gamma = -2 \int \frac{d^3p_\nu}{(2\pi)^3} \frac{2m_\nu}{2E_\nu} \frac{2m_\mu}{2E_\mu} \frac{2m_p}{2E_p} \frac{2m_n}{2E_n} \bar{\Sigma} \sum |T|^2 \text{Im } \bar{U}(p_\nu - p_\mu). \tag{6}$$

For E_p, E_n in the explicit factors of eq. (6), the average over the Fermi sea of appendix B is used, although one can take these energies equal to the respective masses with no significant change.

A different derivation for the analogous case of radiative pion capture has been done in ref. ¹⁶) where an explicit analytical formula for $\text{Im } \bar{U}$ is given in the appendix.

Eq. (6) provides the muon capture width as a function of $k_{F,p}$ and $k_{F,n}$, the proton and neutron Fermi momenta or equivalently ρ_p and ρ_n , the proton and neutron densities of the medium ($\rho_{p,n} = k_{F,p,n}^3/3\pi^2$).

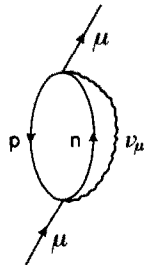


Fig. 2. Many-body Feynman diagram for the muon self-energy related to the $\mu^- p \rightarrow \nu_\mu n$ process.

3. Strong renormalization effects

The dominant contribution, ($\sim 80\%$), to the process comes from the term proportional to g_A^2 in $\bar{\Sigma} \Sigma |T|^2$ of appendix B. The nonrelativistic reduction of the axial-vector term in the nucleon current is of the type $g_A \sigma^i \tau^\lambda$. We know that this external source has the virtue of polarizing the axial charge of the nuclear medium^{17,18} which can produce a sensible renormalization of the capture rate. Microscopically we can depict the situation by saying that the Feynman diagram of fig. 2 is now modified to include the series of diagrams implicit in fig. 3, where the wavy line stands for the spin-isospin ph or Δh interaction¹⁸)

$$V(q) = \frac{f^2}{\mu^2} [V_\ell \hat{q}_i \hat{q}_j + V_t (\delta_{ij} - \hat{q}_i \hat{q}_j)] \sigma_i \sigma_j \tau \tau, \tag{7}$$

for the ph case, or a similar one for the case of ph- Δh or Δh - Δh interaction by substituting $\sigma \rightarrow S$, $\tau \rightarrow T$, the spin and isospin transition operators, and $f \rightarrow f^*$ ($f^2/4\pi = 0.08$, $f^{*2}/4\pi = 0.37$). The term with g_A^2 involves the trace of $g_A^2 \sigma_i \sigma_i \bar{U}$, which equivalently can be written as $g_A^2 \sigma_i \sigma_j \bar{U} [\hat{q}_i \hat{q}_j + (\delta_{ij} - \hat{q}_i \hat{q}_j)]$, explicitly separated into a longitudinal, $(\hat{q}_i \hat{q}_j)$, and a transverse part, $(\delta_{ij} - \hat{q}_i \hat{q}_j)$. The sum implicit in fig. 3 leads to two independent geometric series, in the longitudinal and transverse channels. Hence we have for the case of ph excitation only

$$\begin{aligned} g_A^2 \text{Tr} (\sigma_i \sigma_i \bar{U}) &= 3g_A^2 2\bar{U} \\ &\rightarrow g_A^2 \text{Tr} (\sigma_i \sigma_j) \bar{U} \left\{ \frac{\hat{q}_i \hat{q}_j}{1 - 2\bar{U}V_\ell} + \frac{(\delta_{ij} - \hat{q}_i \hat{q}_j)}{1 - 2\bar{U}V_t} \right\} \\ &= 3g_A^2 2\bar{U} \left\{ \frac{1}{3} \frac{1}{1 - 2\bar{U}V_\ell} + \frac{2}{3} \frac{1}{1 - 2\bar{U}V_t} \right\}, \end{aligned} \tag{8}$$

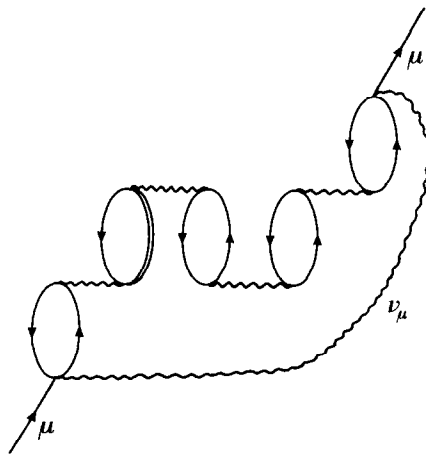


Fig. 3. Many-body Feynman diagrams accounting for the medium polarization in the spin-isospin channel driven by the $\mu^- p \rightarrow \nu_\mu n$ transition.

where the factor 2 in the denominator comes from isospin dependence of eq. (7), since exchange of charged objects is involved in the interaction. Since we had $\text{Im } \bar{U}$ in eq. (6) we have to substitute $3g_A^2 \text{Im } 2\bar{U}$ by the imaginary part of the last expression in eq. (8). Hence the renormalization amounts to substituting,

$$g_A^2 \text{Im } 2\bar{U} \rightarrow g_A^2 \left\{ \frac{1}{3} \frac{\text{Im } 2\bar{U}}{|1-2\bar{U}V_\ell|^2} + \frac{2}{3} \frac{\text{Im } 2\bar{U}}{|1-2\bar{U}V_t|^2} \right\}. \quad (9)$$

Taking account of the Δh excitation and the backward propagating ph excitation (see fig. 3), not accounted for by \bar{U} , is straightforward and can be implemented by substituting $2\bar{U}$ by U , the Lindhard function of refs. ^{15,18}). The different coupling of N and Δ is incorporated in U_Δ ($U = U_N + U_\Delta$) and the same universal interaction V_ℓ, V_t is used for the ph or Δh interaction ^{15,18}).

Thus, ultimately the renormalization can be taken into account by substituting

$$g_A^2 \text{Im } 2\bar{U} \rightarrow g_A^2 \left\{ \frac{1}{3} \frac{\text{Im } 2\bar{U}}{|1-UV_\ell|^2} + \frac{2}{3} \frac{\text{Im } 2\bar{U}}{|1-UV_t|^2} \right\}, \quad (10)$$

where we have used the fact that U_Δ does not have an imaginary part in the kinematical regime where we move. The actual calculations are done by using the expressions of U for symmetrical nuclear matter but the expression for $\text{Im } \bar{U}$, for $\rho_n \neq \rho_p$, in the numerator is kept. This approximation, also done in ref. ¹⁵), is accurate enough for our purposes.

The pieces involving the pseudoscalar term, g_P , behave differently. Indeed the $g_P \sigma \mathbf{q}$ coupling, in the nonrelativistic limit, singles out the longitudinal part of the interaction and the renormalization is then

$$g_P \text{Im } 2\bar{U} \rightarrow g_P \frac{\text{Im } 2\bar{U}}{|1-UV_\ell|^2}, \quad (11)$$

Analogously, the terms involving g_M single out the transverse part of the interaction and we have

$$g_M \text{Im } 2\bar{U} \rightarrow g_M \frac{\text{Im } 2\bar{U}}{|1-UV_t|^2}, \quad (12)$$

The other terms, and the $g_M g_P$ term, which are rather small, are not renormalized.

For the calculations we take the widely used forms

$$\begin{aligned} V_\ell(q) &= \frac{f^2}{\mu^2} \left\{ \frac{\mathbf{q}^2}{q^{02} - \mathbf{q}^2 - \mu^2} \left(\frac{\Lambda^2 - \mu^2}{\Lambda^2 - q^2} \right)^2 + g' \right\}, \\ V_t(q) &= \frac{f^2}{\mu^2} \left(\frac{\mathbf{q}^2}{q^{02} - \mathbf{q}^2 - m_\rho^2} C_\rho \left(\frac{\Lambda_\rho^2 - m_\rho^2}{\Lambda_\rho^2 - q^2} \right)^2 + g' \right), \end{aligned} \quad (13)$$

with $\Lambda \approx 1300$ MeV, $C_\rho = 2$, $\Lambda_\rho = 2500$ MeV and μ, m_ρ the pion and ρ meson masses. The magnitude g' is the Landau-Migdal parameter with accepted values around $g' \approx 0.6-0.8$. We have performed calculations with $g' = 0.7$ which lead to good results compared with experiment.

4. The local density approximation

After performing the renormalization of sect. 2 in eq. (6) we obtain the new muon capture width $\tilde{\Gamma}(\rho_p, \rho_n)$. The local density approximation (LDA) to go to finite nuclei is obtained by replacing $\rho_p \rightarrow \rho_p(\mathbf{r})$, $\rho_n \rightarrow \rho_n(\mathbf{r})$ for the actual nuclei and evaluating

$$\Gamma = \int d^3r |\Phi_{1s}(\mathbf{r})|^2 \tilde{\Gamma}(\rho_p(\mathbf{r}), \rho_n(\mathbf{r})), \quad (14)$$

where $\Phi_{1s}(\mathbf{r})$ is the muon wave function in the 1s state from where the capture takes place. The LDA assumes implicitly a zero range of the interaction, or no dependence on q equivalently. As we can see in appendix A the q -dependence of the form factors is extremely weak and thus the LDA prescription becomes highly accurate. Only the terms with g_p , which contain a pion propagator, have a stronger dependence on q . The LDA prescription would then be less accurate for these terms. However, the fact that these terms contribute about 18% (the $g_p g_A$ term, of sign opposite to the g_A^2 one, is the most important among them) and that the LDA approximation is still fair for pionic processes involving momenta of the range of the pion mass¹¹), make globally the LDA a very accurate tool to evaluate Γ for actual nuclei.

Note, however, that the approach differs substantially from standard ones, which require the evaluation of two-body matrix elements for the ground state of the nucleus. Here we do not evaluate any nuclear matrix element and the only nuclear information needed is the proton and neutron densities. The proton density is taken from the experimental charge distribution¹⁹) and parametrized in terms of two Fermi parameter distribution after correcting for the finite size of the proton¹⁰). For the neutron density we take $\rho_n = (N/Z)\rho_p$. For nuclei smaller than ¹⁸O the harmonic oscillator densities are used.

As pointed out in the introduction some approaches use a closure sum over the nuclear intermediate states¹⁻⁴). Others, more elaborated and accurate⁵⁻⁷), use a sum rule approach which still relies upon an average excitation energy, although the dependence of Γ on this variable is rather smooth, unlike in the closure sum case. Here the Lindhard function has summed the contribution from intermediate nuclear states (the excited states of neutrons on top of the Fermi sea) by keeping track of the energy of such states, which is important when the excitation energy is small like in the present case. However, only the kinetic energy of the nucleons is considered in the Lindhard function. Note, however, that if a local potential $V(\mathbf{r})$ is added to the nucleon energies, it would cancel exactly in the ph propagator of eq. (5). Hence, up to nonlocalities in the nuclear potential the Lindhard function keeps good track of nuclear excitation energies. On the other hand, the nucleon momentum dependence on $\overline{\sum \sum |T|^2}$, which is rather smooth, has also been considered, as shown in appendix B by means of the energy conservation or taking an average of p^2 in the local Fermi sea.

On the other hand, we do not have to rely upon the concept of Z_{eff} . Eq. (14) provides Γ directly from the muon wave function and the function $\tilde{F}(\rho_p(\mathbf{r}), \rho_n(\mathbf{r}))$. In order to evaluate the muon wave function we have considered the Coulomb interaction taking account of the finite size of the nucleus and vacuum polarization, as done for pionic atoms^{20,21}). The numerical calculations have been done by using a very accurate method to solve the Schrödinger equation¹²⁾ which gives us the muon energy and the wave function. For heavy nuclei like ²⁰⁸Pb the binding energy of the muon is about 10 MeV and it is important to take this into account for an accurate determination of the muon capture width.

With all these improvements over previous approaches, it is still remarkable that the present method is quite much simpler technically, as revealed by the basic formulae, eqs. (5), (6) and (14). This has allowed us to perform calculations for a large list of nuclei over the whole periodic table and concentrate on the role on the nuclear renormalization, of much relevance in a variety of nuclear processes, from pionic atoms to Σ or Λ hypernuclei¹⁸⁾.

It is also interesting to recall that we have used here the same model and value of g' that were used in refs.^{22,23)} to account for the observed quenching of g_A in ordinary β -decay. Note, however, that since in β -decay the momentum transfer is negligible, V_e and V_i in eqs. (13) are the same and both repulsive. Also U in the denominator of eq. (10) is rather different to the one here because of the different kinematics, with the Lindhard function in the β -decay due essentially to Δh excitation.

The same model gives good results in these two different kinematical situations and in radiative pion capture¹⁶⁾ where gauge invariance produces a quenching from the transverse part alone. This is a good test of consistency for the nuclear renormalization which, as we shall see, is very important in this case.

6. Results and discussion

Before we proceed to show the results we discuss a few ideas related to the calculations and the results. In the first place, in order to get an approximate idea of the importance of the different terms in appendix B we show the approximate weight of the terms in $|T|^2$, calculated at the peak of the neutrino momentum distribution

$$\begin{aligned} \frac{g_V^2\text{-term}}{1} &= \frac{g_A^2\text{-term}}{3.5} = \frac{g_A g_V\text{-term}}{0.14} = \frac{g_A g_M\text{-term}}{0.5} \\ &= \frac{g_A g_P\text{-term}}{-0.92} = \frac{g_P^2\text{-term}}{0.17}, \end{aligned} \quad (15)$$

with the terms with g_M^2 , $g_M g_P$ and $g_V g_M$ rather small. These ratios change by about 20–30% with respect to those in the standard closure approaches^{1–4)}.

We also mentioned that taking into account the binding of the muon was important in heavy nuclei. Indeed with a binding energy of 11.25 MeV for the 1s state of the muon in ^{208}Pb , taking into account this binding reduces the capture width in 35%.

The neglect of the nucleon momentum in $|T|^2$ also introduces some uncertainties in the calculation. We have made $\mathbf{p} = 0$ in $|T|^2$ in our calculations and have found changes at the level of 10–20% in the individual terms, with a global reduction of 15% with respect to the calculation without neglecting this momentum.

The Pauli blocking effect is very important. In the $\mu^- \text{p} \rightarrow \text{n} \nu_\mu$ reaction the neutron is forbidden to go to any of the neutron occupied states. This is taken into account in our approach by means of the factor $1 - n_2(k)$ in the Lindhard function of eq. (5). Neglecting this factor leads to results for the capture rate about a factor 2.6 times bigger than with the corresponding Pauli blocking for nuclei around ^{16}O and a factor 3.6 for nuclei around ^{208}Pb .

We have also estimated the effects of considering the muon momentum in the calculations (we have set it equal to zero in our results) and have found them to be small, below 5%. We should also note that our calculations of $|T|^2$ have been performed using free relativistic spinors for the nucleons and the muon and neutrino. The nucleons and muon moving in a potential would lead to different spinors. In the case of nucleons in infinite matter, and assuming a scalar potential $V(\mathbf{r})$ given by the Thomas–Fermi approach²⁴⁾, the structure of the spinors would be the same but the mass would be changed to $M + V(\mathbf{r})$. We have performed the calculations with these modifications and found corrections at the level of 2%. The muon spinor in the presence of a point-like Coulomb source is also modified although the modifications are smaller when the finite size of the nucleus is considered²⁵⁾. However, the evaluation of the muon wave function in the nucleus has been done by using the nonrelativistic Schrödinger equation. We have obtained an idea of what the relativistic effects could be by treating the muon as a boson and solving the Klein–Gordon equation instead of the Schrödinger equation, as done for pionic atoms²¹⁾. We found corrections at the level of 2%.

Thus it looks that the approximations that we are still doing are rather under control. However, we have improved on other approximations which were done before in order to make the problem tractable, and which could be easily avoided in our approach.

After this discussion we pass on to present our results. A rather exhaustive list of nuclei has been studied and the results appear in table 1. We show results for nuclei from ^6Li up to ^{209}Bi . The capture rates Γ vary from $0.3 \times 10^4 \text{ s}^{-1}$ to $0.15 \times 10^8 \text{ s}^{-1}$.

We have included in the table the different experimental results which we have extracted from ref.²⁶⁾. The overall agreement between the theoretical results and the experiment is spectacular considering the amount of nuclei studied and the large variation of the rates (four orders of magnitude) from light to heavy nuclei.

One finds larger discrepancies of the order of 30% in some nuclei like ^7Li , ^{44}Ti , ^{59}Co and the isotopes of Ni, but for the large majority of nuclei there is agreement with

experiment or there are differences at the level of 10%. We present a selection of the most stable isotopes as a function of Z in fig. 4 in order to give a visual idea of the quality of the agreement.

As we have mentioned before, the renormalization discussed in sect. 3 has very important effects in this problem. Indeed, in fig. 5 we show the results calculated with and without the renormalization, as a function of Z . We can see that for medium and heavy nuclei the nuclear renormalization reduces the results in about a factor two and it is essential to produce agreement with the experimental numbers. This reduction factor is much bigger than the estimates of ref. ³⁸), where a small quenching due to the axial polarization was suggested. This is a very interesting process, which evidences the strong nuclear renormalization on top of a weak interaction process, which can be brought under control as we have shown here. Although similar effects due to the spin-isospin polarization of the nucleus also appear in many nuclear processes ¹⁸), sometimes it is more difficult to assess their importance since the nuclear interaction itself can be less controllable. However, it is interesting to recall that these medium polarization effects were considered in connection with the problem of Σ decay in nuclei and led to the interesting conclusion that there should be narrow Σ hypernuclear bound states of around $\Gamma \approx 5\text{--}7$ MeV [refs. ^{27,28})]. The first of such states has been found recently, ${}^4_2\text{He}$, with a width of 4.5 MeV [ref. ²⁹)]. Similarly using the same concept, in connection with the Δ self-energy, it was hinted ³⁰) and shown recently ³¹), that this medium polarization is the key to understanding the problem of the pionic anomalous atoms ^{32,33}). The clean effects of this medium renormalization shown here can only stress and reinforce the interpretation given for these other phenomena.

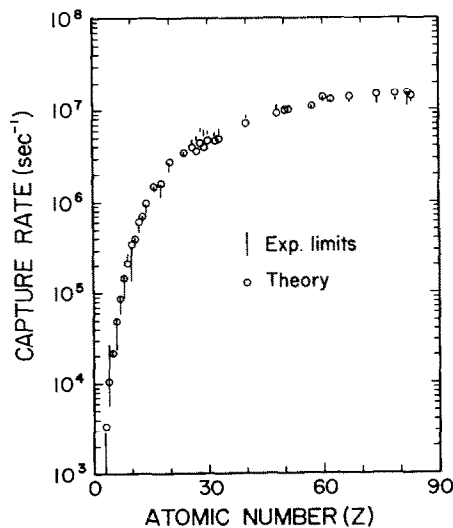


Fig. 4. Total rates for negative muons captured by the most stable isotopes. Circles are our theoretical results. Experimental limits from different groups are shown. Data are from ref. ²⁶).

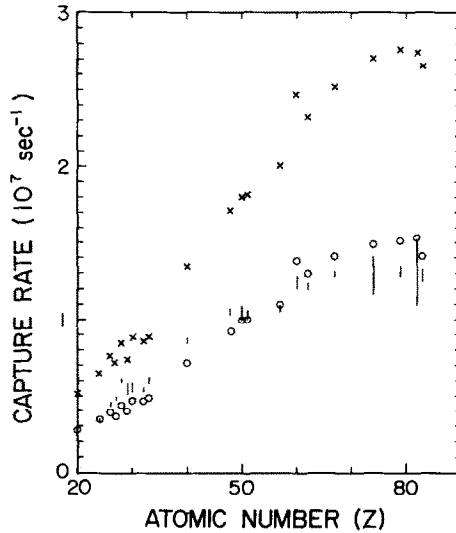


Fig. 5. The nuclear medium renormalization effect in the calculation of total nuclear capture rates of μ^- . Crosses and circles are calculations without and with the renormalization respectively.

Isotopic effects would appear to be tied to the particular shell structure of the nucleus, given the relevance of the Pauli blocking in the problem. It is interesting to show our results for different isotopes. Although the absolute numbers for Γ appear in table 1, we have calculated the ratios for several isotopes and show them in table 2, comparing the theoretical results with those of refs.^{26,34-36}). There are discrepancies of the order of 50% in the Li isotopes. With so few nucleons, shell effects are more important and the concept of a Fermi sea of protons and neutrons with only 3 particles is a bit extreme. The discrepancies are smaller of the order of 10-15% for the C, O and Ca isotopes, and for other nuclei the agreement is very good.

5. Conclusions

We have used a simple, yet reliable method, to evaluate the total muon capture rate in nuclei, which consists in evaluating the muon capture width in infinite nuclear matter with $N \neq Z$ as a function of ρ_p, ρ_n and then adapt the results to finite nuclei via the local density approximation. The method allows for an accurate evaluation of the reaction probability without the need for approximations done in the past, like neglecting the nucleon momentum, using the closure sum or sum rule approaches to sum over nuclear intermediate states, using the concept of an effective Z , neglecting the binding of the muon, taking an average neutrino energy, etc. In addition, we make a highly accurate determination of the muon wave function for the 1s state from where the muon is captured. The method has the virtue of showing that the relevant nuclear magnitudes are the proton and neutron densities and that nuclear

TABLE 1

Theoretical results for total nuclear capture rates of negative muons compared with data. Experiments are taken from ref. ²⁶⁾ and references therein.

A	Z	Calculation (s ⁻¹)	Experiments (10 ³ s ⁻¹)	A	Z	Calculation (s ⁻¹)	Experiments (10 ³ s ⁻¹)
6	3	0.473051 × 10 ⁴	6.100 ± 1.400 4.680 ± 0.120 4.180 ± 0.450	20	10	0.346504 × 10 ⁶	0.204 ± 0.010 0.167 ± 0.030 0.30 ± 0.02 0.235 ± 0.005
7	3	0.338267 × 10 ⁴	1.800 ± 1.100 2.260 ± 0.120 1.810 ± 0.440	23	11	0.398167 × 10 ⁶	0.387 ± 0.015 0.3772 ± 0.0014
9	4	0.106016 × 10 ⁵	18 ± 10 10 ± 2 5.9 ± 0.2 7.4 ± 0.5	24	12	0.611794 × 10 ⁶	0.507 ± 0.020 0.480 ± 0.002 0.52 ± 0.02 0.4841 ± 0.0018
10	5	0.270790 × 10 ⁵	26.5 ± 1.5 27.8 ± 0.7	27	13	0.698167 × 10 ⁶	0.691 ± 0.020 0.662 ± 0.003 0.650 ± 0.015 0.7054 ± 0.0013
11	5	0.215267 × 10 ⁵	21.8 ± 1.6 21.9 ± 0.7	28	14	0.967561 × 10 ⁶	0.777 ± 0.025 0.850 ± 0.003 0.86 ± 0.04 0.8712 ± 0.0018
12	6	0.491425 × 10 ⁵	44 ± 10 36 ± 4 37.3 ± 1.1 36.1 ± 1.0 37 ± 7 39.7 ± 1.3 36.5 ± 2.0 30.3 ± 7.0 37.6 ± 0.4 35.2 ± 2.0 37.7 ± 0.7 38.8 ± 0.5	32	16	0.147345 × 10 ⁷	1.39 ± 0.09 1.31 ± 0.03 1.34 ± 0.01 1.352 ± 0.003
13	6	0.382118 × 10 ⁵	33.8 ± 0.4 37.6 ± 0.7	40	18	0.158576 × 10 ⁷	1.20 ± 0.08 1.41 ± 0.11
14	7	0.876191 × 10 ⁵	86 ± 11 65 ± 4 60.2 ± 0.8 68.4 ± 0.8 69.3 ± 0.8	40	20	0.277102 × 10 ⁷	2.55 ± 0.05 2.444 ± 0.023 2.529 ± 0.008 2.29 ± 0.05 2.557 ± 0.014
16	8	0.146072 × 10 ⁶	0.159 ± 0.014 0.098 ± 0.003 0.098 ± 0.005 0.095 ± 0.008 0.1026 ± 0.0006	44	20	0.212757 × 10 ⁷	1.793 ± 0.040
18	8	0.115035 × 10 ⁶	0.0880 ± 0.0015	44	22	0.364563 × 10 ⁷	2.63 ± 0.06 2.60 ± 0.04 2.590 ± 0.012
19	9	0.212870 × 10 ⁶	0.254 ± 0.022 0.235 ± 0.010 0.231 ± 0.006 0.229 ± 0.001	50	24	0.390693 × 10 ⁷	3.825 ± 0.050
				52	24	0.345514 × 10 ⁷	3.452 ± 0.047
				53	24	0.323095 × 10 ⁷	3.297 ± 0.045
				54	24	0.304124 × 10 ⁷	3.057 ± 0.042
				56	26	0.392927 × 10 ⁷	4.53 ± 0.10 4.38 ± 0.07 4.40 ± 0.05 4.411 ± 0.024

TABLE 1—continued

A	Z	Calculation (s ⁻¹)	Experiments (10 ³ s ⁻¹)	A	Z	Calculation (s ⁻¹)	Experiments (10 ³ s ⁻¹)
59	27	0.365026 × 10 ⁷	4.89 ± 0.09 4.96 ± 0.05 4.940 ± 0.029	119	50	0.999416 × 10 ⁷	10.5 ± 0.4 10.70 ± 0.14 10.44 ± 0.18
58	28	0.439701 × 10 ⁷	6.11 ± 0.10	122	51	0.100345 × 10 ⁸	10.49 ± 0.14 10.21 ± 0.20
60	28	0.398315 × 10 ⁷	5.56 ± 0.10	139	57	0.110223 × 10 ⁸	10.71 ± 0.10
62	28	0.355090 × 10 ⁷	4.72 ± 0.10	144	60	0.138435 × 10 ⁸	12.32 ± 0.14 12.50 ± 0.33
64	29	0.397764 × 10 ⁷	5.79 ± 0.16 5.47 ± 0.20 5.66 ± 0.09 5.67 ± 0.09 5.676 ± 0.037	152	62	0.129497 × 10 ⁸	12.22 ± 0.17
64	30	0.469282 × 10 ⁷	5.76 ± 0.17 5.5 ± 0.1 5.76 ± 0.05 5.834 ± 0.039	165	67	0.141022 × 10 ⁸	12.95 ± 0.13
72	32	0.464783 × 10 ⁷	5.54 ± 0.06 5.569 ± 0.036	184	74	0.149203 × 10 ⁸	11.92 ± 0.30 13.5 ± 0.6 13.07 ± 0.21 12.36 ± 0.24
75	33	0.487336 × 10 ⁷	6.07 ± 0.07 6.06 ± 0.12 6.104 ± 0.043	197	79	0.151167 × 10 ⁸	13.39 ± 0.11 13.07 ± 0.28
90	40	0.719435 × 10 ⁷	8.59 ± 0.07 8.66 ± 0.08	208	82	0.153379 × 10 ⁸	11.70 ± 0.75 14.5 ± 0.75 12.98 ± 0.10 13.27 ± 0.22 13.45 ± 0.18
112	48	0.927524 × 10 ⁷	10.1 ± 0.5 10.63 ± 0.11 10.61 ± 0.18	209	83	0.141154 × 10 ⁸	12.20 ± 0.75 13.26 ± 0.07 13.01 ± 0.18

TABLE 2
Isotope effect in the total nuclear capture rates of negative muons

Isotopes	Calculation	Experiments	Ref.
${}^7\text{Li}/{}^6\text{Li}$	0.71	0.30 ± 0.19	³²⁾
		0.43 ± 0.11	²⁶⁾
${}^{11}\text{B}/{}^{10}\text{B}$	0.79	0.83 ± 0.07	³²⁾
		0.79 ± 0.03	²⁶⁾
${}^{13}\text{C}/{}^{12}\text{C}$	0.78	0.90 ± 0.02	³³⁾
		0.97 ± 0.02	²⁶⁾
${}^{18}\text{O}/{}^{16}\text{O}$	0.79	0.86 ± 0.02	²⁶⁾
${}^{44}\text{Ca}/{}^{40}\text{Ca}$	0.77	0.71 ± 0.02	³⁴⁾
${}^{52}\text{Cr}/{}^{50}\text{Cr}$	0.88	0.90 ± 0.02	³⁴⁾
${}^{53}\text{Cr}/{}^{50}\text{Cr}$	0.83	0.86 ± 0.02	³⁴⁾
${}^{54}\text{Cr}/{}^{50}\text{Cr}$	0.78	0.80 ± 0.02	³⁴⁾
${}^{53}\text{Cr}/{}^{52}\text{Cr}$	0.94	0.96 ± 0.02	³⁴⁾
${}^{54}\text{Cr}/{}^{52}\text{Cr}$	0.88	0.89 ± 0.02	³⁴⁾
${}^{54}\text{Cr}/{}^{53}\text{Cr}$	0.94	0.91 ± 0.02	³⁴⁾
${}^{60}\text{Ni}/{}^{58}\text{Ni}$	0.91	0.91 ± 0.02	³⁴⁾
${}^{62}\text{Ni}/{}^{58}\text{Ni}$	0.81	0.77 ± 0.02	³⁴⁾
${}^{62}\text{Ni}/{}^{60}\text{Ni}$	0.89	0.85 ± 0.02	³⁴⁾

shell effects seem to be relevant only for very light nuclei. With an accurate determination of the process involving the weak interaction we paid special attention to nuclear renormalization effects in the spin-isospin channel which affect the most important terms of the reaction. These effects are very important and we showed that they reduce the capture rates by about a factor two for medium and heavy nuclei.

The overall agreement of our results with experiment is remarkable for the set of 38 nuclei for which we had experimental data. The ratios of rates for different isotopes is also in quite good agreement with experiment except for very light nuclei, where our methods are obviously less reliable.

In summary we can conclude that our present knowledge of the weak processes together with the important nuclear renormalization effects lead to a satisfactory understanding of the process of inclusive muon capture in nuclei. The process has the virtue of showing very clearly the need for the nuclear renormalization. This is of particular importance since a similar renormalization appears in a variety of nuclear processes and leads to particular effects like a substantial reduction of the calculated Σ widths in Σ hypernuclei and is one of the ingredients leading to a solution of the systematic anomalies found in pionic atoms. The results found in this paper give an extra support to the interpretation given to the narrow Σ states and the pionic atom anomalies along the lines of this nuclear type of renormalization.

The continuous discussions with J. Bernabéu along the realization of this work were both enlightening and delighting and we would like to express our gratitude

to him. One of us (H.C.C.) gratefully acknowledges the Ministry of Education of Spain, the Department of Theoretical Physics and the Instituto de Física Corpuscular of Valencia University for their hospitality.

The work is supported by the CICYT.

Appendix A

COUPLING CONSTANTS AND FORM FACTORS

We follow ref. ⁸⁾ for this information actualized with the new information from ref. ³⁷⁾. For the vector and magnetic couplings we have

$$g_V(q^2) = G_{Ep}(q^2) - G_{En}(q^2),$$

$$g_M(q^2) = \frac{1}{1 - q^2/4M_p^2} [G_{Mp}(q^2) - G_{Mn}(q^2) - G_{Ep}(q^2) + G_{En}(q^2)], \quad (\text{A.1})$$

with G_E , G_M the Sachs electromagnetic form factors

$$G_{Ep}(q^2) = \frac{G_{Mp}(q^2)}{1 + \mu_p} = \frac{G_{Mn}(q^2)}{\mu_n} = -\frac{4M_p^2}{q^2} \frac{G_{En}(q^2)}{\mu_n} = G(q), \quad (\text{A.2})$$

with μ_p , μ_n the anomalous magnetic moments of the proton and the neutron respectively, $\mu_p = 1.7928$, $\mu_n = -1.9130$ and $q^2 = q^{02} - q^2$. $G(q^2)$ is given by

$$G(q^2) = \left(\frac{1}{1 - q^2/M_0^2} \right)^2, \quad (\text{A.3})$$

with $M_0^2 = 0.71 \text{ GeV}^2$.

For the axial-vector coupling we have

$$g_A(q^2) = g_A(0) \left(1 + \frac{1}{\pi} \frac{q^2}{4M_p^2} \right), \quad (\text{A.4})$$

with $g_A(0) = -1.259$. The coupling $G = G_0 \cos \theta$ with $G_0 = 1.16637 \times 10^{-5} \text{ GeV}^{-2}$, $\cos \theta = 0.974$.

For g_p we have taken the value extracted in ref. ⁸⁾, $g_p = -10.27$, which was calculated at the kinematics from μ capture from hydrogen. However, we have kept the pion propagator structure of the pseudoscalar term and taken correspondingly

$$g_p(q^2) = \frac{15m_\pi^2}{q^2 - m_\pi^2}, \quad (\text{A.5})$$

which approximately coincides with the numerical value given above for $q^2 = -0.88m_\mu^2$ of the kinematics of the μ capture, and is also very close to the value provided by the Goldberger-Treiman relation ^{2,3)}.

Appendix B

EXPRESSION FOR $\bar{\Sigma} \Sigma |T|^2$:

The sum over final polarizations and average over initial ones of $|T|^2$ for the T matrix obtained with the lagrangian of eq. (1) is given by,

$$\begin{aligned}
& 2m_p 2m_n 2m_\nu 2m_\mu \bar{\Sigma} \Sigma |T|^2 / \frac{1}{2} G^2 \\
&= 16g_V^2 [(p_1 \cdot p_2)(p_3 \cdot p_4) + (p_1 \cdot p_4)(p_2 \cdot p_3) - m_p m_n (p_1 \cdot p_3)] \\
&\quad + 16g_A^2 [(p_1 \cdot p_2)(p_3 \cdot p_4) + (p_1 \cdot p_4)(p_2 \cdot p_3) + m_p m_n (p_1 \cdot p_3)] \\
&\quad + 32g_A g_V [(p_1 \cdot p_4)(p_2 \cdot p_3) - (p_1 \cdot p_2)(p_3 \cdot p_4)] \\
&\quad + 8 \left(\frac{g_M}{2M} \right)^2 [2(p_1 \cdot p_2)(p_3 \cdot q)(p_4 \cdot q) - 2(p_1 \cdot p_2)(p_3 \cdot p_4)q^2 \\
&\quad\quad + 2(p_1 \cdot p_4)(p_2 \cdot q)(p_3 \cdot q) - 2(p_1 \cdot p_4)(p_2 \cdot p_3)q^2 \\
&\quad\quad + (p_1 \cdot p_3)(p_2 \cdot p_4)q^2 - (p_1 \cdot p_3)m_p m_n q^2 \\
&\quad\quad - 2(p_1 \cdot q)(p_3 \cdot q)(p_2 \cdot p_4) - 2(p_1 \cdot q)(p_3 \cdot q)m_n m_p \\
&\quad\quad + 2(p_1 \cdot q)(p_2 \cdot q)(p_3 \cdot p_4) + 2(p_1 \cdot q)(p_4 \cdot q)(p_2 \cdot p_3)] \\
&\quad + 16g_V \frac{g_M}{2M} [-m_p (p_1 \cdot p_3)(p_4 \cdot q) - m_p (p_1 \cdot q)(p_3 \cdot p_4) - m_p (p_3 \cdot q)(p_1 \cdot p_4) \\
&\quad\quad + m_n (p_1 \cdot p_3)(p_2 \cdot q) + m_n (p_1 \cdot q)(p_3 \cdot p_2) + m_n (p_3 \cdot q)(p_1 \cdot p_2)] \\
&\quad + 32g_A \frac{g_M}{2M} [-m_n (p_3 \cdot q)(p_1 \cdot p_2) + m_n (p_2 \cdot p_3)(p_1 \cdot q) \\
&\quad\quad - m_p (p_3 \cdot q)(p_1 \cdot p_4) + m_p (p_3 \cdot p_4)(p_1 \cdot q)] \\
&\quad + 8 \left(\frac{g_P}{\mu} \right)^2 [(2(p_1 \cdot q)(p_3 \cdot q) - q^2(p_1 \cdot p_3))(p_2 \cdot p_4) - m_p m_n] \\
&\quad + 16g_A \frac{g_P}{\mu} [-m_p (p_1 \cdot p_4)(p_3 \cdot q) - m_p (p_1 \cdot q)(p_3 \cdot p_4) + m_p (p_4 \cdot q)(p_1 \cdot p_3) \\
&\quad\quad + m_n (p_1 \cdot p_2)(p_3 \cdot q) + m_n (p_1 \cdot q)(p_2 \cdot p_3) - m_n (p_2 \cdot q)(p_1 \cdot p_3)] \\
&\quad + 16 \frac{g_M}{2M} \frac{g_P}{\mu} [-(p_1 \cdot p_2)(p_3 \cdot q)(p_4 \cdot q) - (p_3 \cdot p_4)(p_1 \cdot q)(p_2 \cdot q) \\
&\quad\quad - q^2(p_1 \cdot p_4)(p_2 \cdot p_3) + (p_1 \cdot p_4)(p_2 \cdot q)(p_3 \cdot q) \\
&\quad\quad + (p_2 \cdot p_3)(p_1 \cdot q)(p_4 \cdot q) + q^2(p_1 \cdot p_2)(p_3 \cdot p_4)] \tag{B.1}
\end{aligned}$$

and we have taken

$$\begin{aligned} p_1 &\equiv p_\mu = (E_\mu, \mathbf{0}), & p_2 &\equiv p_p = (E_p, \mathbf{p}), \\ p_3 &\equiv p_\nu = (p_\nu, \mathbf{p}_\nu), & p_4 &\equiv p_n = (E_n, \mathbf{p} - \mathbf{p}_\nu), \\ q &\equiv p_\mu - p_\nu = (E_\mu - p_\nu, -\mathbf{p}_\nu), \end{aligned} \quad (\text{B.2})$$

with

$$E_p = \sqrt{m_p^2 + \mathbf{p}^2}, \quad E_n = \sqrt{m_n^2 + \mathbf{p}^2 + \mathbf{p}_\nu^2 - 2\mathbf{p} \cdot \mathbf{p}_\nu} \quad (\text{B.3})$$

and $\mathbf{p} \cdot \mathbf{p}_\nu$, from energy conservation, is given by

$$\mathbf{p} \cdot \mathbf{p}_\nu = M \left(p_\nu + \frac{p_\nu^2}{2M} - E_\mu \right), \quad (\text{B.4})$$

with M an average proton and neutron mass. For p^2 in the expressions we take an average over the Fermi sea

$$p^2 \rightarrow \frac{3}{5} \left(3\pi^2 \frac{Z}{A} \rho(\mathbf{r}) \right)^{2/3}. \quad (\text{B.5})$$

References

- 1) H. Primakoff, *Rev. Mod. Phys.* **31** (1959) 802
- 2) R.J. Blin-Stoyle, *Fundamental interactions and the nucleus* (North-Holland, Amsterdam, 1973)
- 3) N.C. Mukhopadhyay, *Phys. Reports* **30** (1977) 1
- 4) J. Bernabéu, Thesis, Valencia, 1970
- 5) J. Bernabéu, *Nucl. Phys.* **A201** (1973) 41
- 6) J. Bernabéu and F. Cannata, *Phys. Lett.* **B45** (1973) 445; *Nucl. Phys.* **A215** (1973) 411
- 7) J. Navarro, J. Bernabéu, J.M.G. Gómez and J. Martorell, *Nucl. Phys.* **A375** (1987) 361
- 8) P. Pascual, *Anales de Fis.* **67** (1971) 197
- 9) R. Pla, Tesina de licenciatura, University of Valencia, 1971;
J. Bernabéu and R. Pla, *Anales de Fis.* **67** (1971) 455
- 10) L.L. Salcedo, E. Oset, M.J. Vicente and C. García-Recio, *Nucl. Phys.* **A484** (1988) 557
- 11) E. Oset, L.L. Salcedo and D. Strottman, *Phys. Lett.* **B165** (1985) 13
- 12) E. Oset and L.L. Salcedo, *Jour. Comp. Phys.* **57** (1985) 155
- 13) C. Itzykson and J.B. Zuber, *Quantum field theory* (McGraw-Hill, New York, 1980)
- 14) J.D. Bjorken and S.D. Drell, *Relativistic quantum fields* (McGraw-Hill, New York, 1965)
- 15) C. García-Recio, E. Oset and L.L. Salcedo, *Phys. Rev.* **C37** (1988) 194
- 16) H.C. Chiang, E. Oset, R. Carrasco, J. Nieves and J. Navarro, *Nucl. Phys.* **A510** (1990) 573
- 17) M. Ericson, *Nucl. Phys.* **A335** (1980) 309;
M. Ericson, A. Figureau and C. Thevenet, *Phys. Lett.* **B45** (1973) 19
- 18) E. Oset, Lectures in the "SERC School of Nuclear Physics" Jaipur, India 1987, ed. B.K. Jain (World Scientific, Singapore, 1987) p. 65
- 19) C.W. de Jager, C. de Vries and H. de Vries, *At. Data Nucl. Data Tables* **14** (1974) 480
- 20) G. Backenstoss, *Ann. Rev. Nucl. Sci.* **20** (1970) 467
- 21) C. García-Recio, Thesis, University of Valladolid, 1986
- 22) I.S. Towner and F.C. Khanna, *Phys. Rev. Lett.* **42** (1979) 51
- 23) E. Oset and M. Rho, *Phys. Rev. Lett.* **42** (1979) 47
- 24) A. Galindo and P. Pascual, *Mecanica Cuantica*, Alhambra, 1978
- 25) J. Bernabéu and R. García-Molina, University of Valencia preprint 1989, *Anales de Física* 1989, in print
- 26) T. Suzuki, D.F. Measday and J.P. Roalsvig, *Phys. Rev.* **C35** (1987) 2212 and references therein

- 27) R. Brockmann and E. Oset, Phys. Lett. **B118** (1982) 33
- 28) E. Oset, L.L. Salcedo and R. Brockmann, Physics Report in print
- 29) R.S. Hayano *et al.*, Phys. Lett. **B231** (1989) 355
- 30) L. Tauscher, C. García-Recio and E. Oset, Nucl. Phys. **A415** (1984) 333
- 31) J. Nieves, E. Oset and C. García-Recio, University of Valencia preprint
- 32) J. Konijn *et al.*, Nucl. Phys. **A326** (1979) 401
- 33) R. Seki, Proc. pion nucleus physics, Los Alamos 1987, eds. R.J. Peterson and D.D. Strottman, AIP Con. Proc. 163, p. 233
- 34) M. Eckhause, T.A. Filippas, R.B. Sutton and R.E. Welsh, Phys. Rev. **132** (1963) 422
- 35) K. Ishida, J.H. Brewer, T. Matsuzaki, Y. Kuno, J. Imazato and K. Nagamine, Phys. Lett. **B167** (1986) 31
- 36) W.A. Cramer, V.L. Telegdi, R. Winston and R.A. Lundy, Nuovo Cim. **24** (1962) 546
- 37) G.P. Yost *et al.*, Rev. Part. properties; Phys. Lett. **B204** (1988) 1
- 38) J. Delorme, M. Ericson, A. Figureau and C. Thevenet, Ann. of Phys. **102** (1976) 273

DEEP INELASTIC LEPTON SCATTERING IN NUCLEI AT $x > 1$ AND THE NUCLEON SPECTRAL FUNCTION

P. Fernández de Córdoba, E. Marco, H. Müther, E. Oset and Amand Faessler

Institut für Theoretische Physik, Universität Tübingen, 72076 Tübingen, Germany.

Abstract

The nuclear structure function $F_{2A}(x)$ has been studied in the Bjorken limit for (l, l') scattering on nuclei in the region of $x > 1$ and was found to be very sensitive to the information contained in the nucleon spectral function in nuclei, particularly the correlations between momenta and energies in the region of large momenta. Calculations were done in a local density approximation using two different spectral functions for nuclear matter. Results are compared to those obtained for a spectral function which has been evaluated directly for the finite nucleus, ^{16}O , under consideration. For values of x around 1.5 and larger the quasi-particle contribution is negligible, thus stressing the sensitivity of the present reaction to the dynamical properties of nuclei beyond the shell model approach. Several approximations which are usually employed in studies of the EMC effect have been analyzed and their inaccuracy in this region is demonstrated. The results stress the fact that the nuclear structure function contains important information on nuclear dynamical correlations. Therefore further measurements of $F_{2A}(x)$ in that region and for many nuclei would be most welcome.

1 Introduction

Deep inelastic scattering of leptons on nuclei in the region of asymptotic freedom and the ratio $R(x)$ of the nuclear structure function compared to the corresponding one for the deuteron (EMC effect [1]) has been one of the topics in the interface of nuclear and particle physics intensively studied in the recent past [2–5]. After multiple discussions, pionic effects [4, 6–8], binding effects [9–11] and Fermi motion [3, 6, 12] have turned out to be important ingredients to describe the main characteristics of the ratio $R(x)$: the small enhancement beyond unity around $x \simeq 0.1$, the small depletion around $x \simeq 0.6$ and the steady increase around $x \simeq 0.8$ and above, respectively.

The increase of $R(x)$ at x close to one was soon identified to be a consequence of Fermi motion [3, 6, 12] and this is one of the points where there seems to be consensus among scientists. Probably the lack of controversy on this issue prevented a systematic exploration of the region of $x > 1$, in spite of the fact that in nuclei only the variable $x_A = -q^2/2M_Aq^0$ is limited between 0 and 1, while $x = -q^2/2Mq^0$ varies from 0 to M_A/M . Since $F_{2N}(x)$, the structure function of a free nucleon, is zero for $x > 1$, the fact that $F_{2A}(x)$ is different from zero for $x > 1$ must necessarily be attributed to modifications of the nucleon properties inside nuclei, i.e. to genuine many body effects. The region of $x > 1$ is hence a source of very interesting information on nuclear properties, as we shall see.

The fact that Fermi motion was so important at $x \simeq 1$ induced people to investigate the region of $x > 1$ with the same idea [11–14]. These works essentially employed phenomenological nuclear matter momentum distributions, with the main conclusion that a nonvanishing value of $F_{2A}(x)$ for $x > 1 + k_F/M$ (with k_F the Fermi momentum) would require a tail in the momentum distribution $n(\vec{k})$ for $k > k_F$. The occupation number $n(\vec{k})$ is different from zero for $k > k_F$ as soon as the effects of a residual NN interaction are considered leading to a correlated many-body system of Fermions.

However, it is quite dangerous to reduce the effects of correlations to a discussion of a momentum distribution only, because in a system of interacting Fermions the energy and momentum distributions are correlated by means of the spectral function, and the simultaneous consideration of both distributions is necessary in principle, and also in the practice of the present case, as we shall see. Disregarding the energy and momentum correlations leads sometimes to quite erroneous results, like in the study of the Λ mesonic decay in nuclei where the results for the width based exclusively on the nucleon momentum distribution in nuclei are three orders of magnitude bigger than the results obtained with a spectral function, or the experimental results [13]. The same warning, in the present context, was raised in ref. [16] where $F_{2A}(x)$ was evaluated for ${}^3\text{He}$. Further work in this direction was done in refs. [17–19].

In the present work we have evaluated $F_{2A}(x)$ for several nuclei by using spectral functions of infinite nuclear matter and the local density approximation. This approximation is good when dealing with volume processes like the

present one. In order to quantify uncertainties from the many body approach used, we have performed the calculations using two spectral functions evaluated with rather different methods. On the other hand, since large momentum components are necessarily involved in the process, relativistic corrections are bound to be relevant [20,21] and we have worked within a relativistic approach.

We evaluate $F_{2A}(x)$ for values of $1 \leq x \leq 1.5$. At $x = 1.5$ the value of the structure function decreases by about three orders of magnitude with respect to $x = 1$, but is still well within measurable range. We also show results using the momentum distributions alone, within several approximations, and find appreciable differences (of two or more orders of magnitude) with respect to the accurate results using the spectral functions. These results show that the study of nuclear structure functions at values of $x > 1$ is a very interesting tool to learn about nuclear dynamical correlations beyond the nuclear properties described in a shell model approach.

In this paper we not only discuss results obtained within the local density approximation but also consider a spectral function calculated directly for the nucleus ^{16}O . After this introduction we discuss in section 2 the calculation of the nuclear structure function and its relation to the spectral function. The various approaches for the spectral functions are presented in section 3. The results of our studies are presented and discussed in section 4. The last section summarizes the main conclusions.

2 The nuclear structure function

Deep inelastic electron (or muon) scattering on an unpolarized nucleon can be described in terms of two structure functions, $W_1(x, Q^2)$, $W_2(x, Q^2)$, where the Bjorken variable x is given by

$$x = \frac{-q^2}{2pq} = \frac{Q^2}{2pq} \quad (1)$$

with q the momentum of the virtual photon and p the momentum of the nucleon. In the Bjorken limit, $q^0 \rightarrow \infty$, $Q^2 \rightarrow \infty$ and x fixed, it is common to define the structure functions F_1 and F_2 which depend only on the variable x , up to some smooth logarithmic dependence on Q^2 from QCD corrections. In this limit one has

$$\begin{aligned} \frac{p \cdot q}{M} W_2(x, Q^2) &\equiv F_2(x) \\ MW_1(x, Q^2) &\equiv F_1(x) \end{aligned} \quad (2)$$

and $F_2(x)$, $F_1(x)$ are related by the Callan-Gross relation

$$2xF_1(x) = F_2(x) \quad (3)$$

Using these structure functions W_1 and W_2 the hadronic tensor for the absorption of the virtual photon can be written:

$$\begin{aligned}
W'^{\mu\nu} &= (-g^{\mu\nu} + \frac{q^\mu q^\nu}{q^2})W_1 + p'^\mu p'^\nu \frac{W_2}{M^2} \\
p'^\mu &= p^\mu - \frac{p \cdot q}{q^2} q^\mu
\end{aligned} \tag{4}$$

It is practical to work in a frame where \vec{q} is parallel to the z direction. Adopting this frame and inspecting the transversal W'^{xx} component in the Bjorken limit, one finds that the term proportional to W_2 in eq. (4) vanishes and W'^{xx} is related to W_1 for nucleons in nuclei with the same coefficient in front as for one nucleon in the vacuum, independent on its momentum or energy. This allows one to write the structure function F_{1A} derived from lepton scattering from a nucleus with baryon number A in a nonrelativistic formalism using eq. (2).

$$\frac{F_{1A}(x_A)}{M_A} = \int \frac{d^3p}{(2\pi)^3} \int_{-\infty}^{\mu} d\omega \mathcal{S}_h(\omega, p) \frac{F_{1N}(x_N)}{M} \theta(x_N) \theta(1 - x_N) \tag{5}$$

where $\mathcal{S}_h(\omega, p)$ denotes the hole spectral function, i.e. the probability of finding a nucleon with energy ω and momentum p in the nucleus, the integration limit μ the chemical potential or Fermi energy and

$$x_A = \frac{-q^2}{2p_A q} = \frac{-q^2}{2M_A q^0}; \quad x_N = \frac{-q^2}{2pq}; \quad p \equiv (\omega, \vec{p}) \tag{6}$$

Instead of x_A one normally uses the variable x ,

$$x = \frac{-q^2}{2Mq^0} = \frac{M_A}{M} x_A \tag{7}$$

so we will write F_{1A} and F_{2A} as functions of x from now on.

By means of eq. (3) for nuclear targets we can calculate F_{2A} which is the structure function used in studies of the *EMC* effect. We then write

$$F_{2A}(x) = \int \frac{d^3p}{(2\pi)^3} \int_{-\infty}^{\mu} \mathcal{S}_h(\omega, p) \frac{x}{x_N} F_{2N}(x_N) \theta(x_N) \theta(1 - x_N) \tag{8}$$

Instead of using the spectral function \mathcal{S}_h calculated directly for the nucleus under consideration, it is common practice to employ a local density approximation and represent this spectral function in terms of a spectral function $S_h(\omega, p; \rho)$ evaluated for infinite nuclear matter at various densities ρ which is normalized by

$$4 \int \frac{d^3p}{(2\pi)^3} \int_{-\infty}^{\mu} d\omega S_h(\omega, p; \rho) = \rho, \tag{9}$$

with a factor 4 on the left side of this equation to account for the spin-isospin degeneracy of symmetric nuclear matter. Assuming a density profile $\rho(r)$ for the finite nucleus to be studied, one can determine the local density approximation for the spectral function of this nucleus by

$$\mathcal{S}_h(\omega, p) = 4 \int d^3r S_h(\omega, p; \rho(r)) \quad (10)$$

which ensures that

$$4 \int d^3r \int \frac{d^3p}{(2\pi)^3} \int_{-\infty}^{\mu} d\omega S_h(\omega, p; \rho(r)) = \int \frac{d^3p}{(2\pi)^3} \int_{-\infty}^{\mu} d\omega \mathcal{S}_h(\omega, p) = A. \quad (11)$$

For nuclear matter the spectral function can be evaluated in terms of the nucleon selfenergy $\Sigma(\omega, p)$ by

$$S_h(\omega, p) = \frac{1}{\pi} \frac{Im\Sigma(\omega, p)}{[\omega - \varepsilon(\vec{p}) - Re\Sigma(\omega, p)]^2 + [Im\Sigma(\omega, p)]^2} \quad (12)$$

where we have dropped the variable ρ identifying the density dependence of the self-energy and spectral function. In eq. (12), $\varepsilon(\vec{p})$ is used to represent the nucleon kinetic energy.

Relativistic corrections accounting for the kinematics of the nucleon have been included in deep inelastic scattering. Prescriptions based on the normalization of the relativistic current operator lead to corrections of the static, or shell model, structure function of the nucleus [22]. Further corrections have been considered in [20, 21] at $x \simeq 1$. In ref. [23] a different relativistic treatment is developed which allows to write all quantities in terms of the nucleon propagators. Only the region $0 < x < 1$, which was measured by the *EMC* collaboration, is studied there. As in ref. [4, 6, 7], pionic corrections are shown to be relevant in the region of $x < 0.6$, but they play no role in the region $x > 1$ which we study here.

Employing the treatment described in ref. [23], which uses a relativistic spectral function from the beginning, one can avoid introducing any flux factors as in ref. [22] to account for relativistic corrections in non-relativistic nuclear wave functions.

Since the relativistic corrections are important here we take advantage to discuss briefly and complement the details of ref. [23].

In fig. 1a we show the Feynman diagram that symbolizes the deep inelastic process on a nucleon. The final hadronic state X will contain at least one baryon and will have baryonic number one. In a nucleus the nucleon N will have a certain momentum and energy distribution given by the spectral function. The most practical way to take this into account and have a covariant formulation of the nuclear problem is to fold the amplitude in fig. 1a and convert it into a many body diagram for the selfenergy of an electron in the nuclear medium, fig. 1b. Here the nucleon N in fig. 1a gets converted into a hole line and with the baryon existing in X it completes a fermionic loop. In section 3 of ref. [23] one evaluates this selfenergy in infinite nuclear matter and, by means of the local density approximation, the (e, e') cross section, is related to the imaginary part of the electron selfenergy. The imaginary part of the e

selfenergy is evaluated using Cutkosky rules and this means that the intermediate states e' and X are placed on shell in the integrations over the momenta of these states. The formalism is originally covariant in the sense that everything is written in terms of propagators of the particles and we can write the nucleon propagator in a covariant relativistic way. However, Cutkosky rules select the imaginary part of the propagator of nucleon N for the occupied states and when doing that the apparent covariant structure might not show up clearly.

In our formalism we start from a free nucleon propagator which we split into its positive and negative energy parts [24]

$$\frac{\not{p} + M}{p^2 - M^2 + i\epsilon} \equiv \frac{M}{E(\vec{p})} \left\{ \frac{\sum_r u_r(\vec{p})\bar{u}_r(\vec{p})}{p^0 - E(\vec{p}) + i\epsilon} + \frac{\sum_r v_r(-\vec{p})\bar{v}_r(-\vec{p})}{p^0 + E(\vec{p}) - i\epsilon} \right\} \quad (13)$$

where $M, E(\vec{p})$ are the nucleon mass and the relativistic nucleon energy $(\vec{p}^2 + M^2)^{1/2}$ and $u_r(\vec{p}), v_r(\vec{p})$ are the ordinary spinors which we take normalized as $\bar{u}_r(\vec{p})u_r(\vec{p}) = 1$. We recall that $u_r(\vec{r})$ are functions of three momentum and they are the only spinors which appear in our framework.

In order to account for binding and momentum distribution of the occupied nucleons we need the nucleon propagator in the nucleon medium.

Note that even if a nucleon is off shell, $p^0 \neq E(\vec{p})$, in the propagator of eq. (13) and we have $\not{p} + M \rightarrow p^0\gamma^0 - \vec{p}\vec{\gamma} + M$, the positive energy part has the Dirac structure $2M \sum_r u_r(\vec{p})\bar{u}_r(\vec{p}) = E(\vec{p})\gamma^0 - \vec{p}\vec{\gamma} + M$, corresponding to on shell nucleons of momentum \vec{p} .

Following a standard relativistic notation [25] the nucleon propagator in a spin saturated system would be

$$G(p^0, p) = \frac{1}{\not{p} - M - \Sigma^s - \Sigma^v\gamma^0} \quad (14)$$

which includes a scalar and vector terms in the nucleon selfenergy (the inclusion of a term of the type $\vec{\gamma}\vec{p}$ does not change the arguments and conclusions which follow). The extraction of hole and particle spectral functions requires the evaluation of $Re\Sigma^{s,v}$ and particularly $Im\Sigma^{s,v}$, which is a non trivial task.

We respect the structure of eq. (14) but follow a different path in order to single out the imaginary part of the positive energy piece of the nucleon propagator. We start from the realization that for this latter purpose, in a perturbative expansion of the propagator of eq. (14) in terms of the free propagator of eq. (13), the terms of positive energy will be singular and dominate over those of negative energy. This allows us to write the desired part of the propagator as

$$\begin{aligned} \tilde{G}(p^0, p) &= \frac{M}{E(\vec{p})} \sum_r u_r(\vec{p})\bar{u}_r(\vec{p}) \frac{1}{p^0 - E(\vec{p})} + \\ &\frac{M}{E(\vec{p})} \sum_r \frac{u_r(\vec{p})\bar{u}_r(\vec{p})}{p^0 - E(\vec{p})} \Sigma(p^0, p) \frac{M}{E(\vec{p})} \sum_s \frac{u_s(\vec{p})\bar{u}_s(\vec{p})}{p^0 - E(\vec{p})} + \dots \end{aligned}$$

$$= \frac{M}{E(\vec{p})} \sum_r \frac{u_r(\vec{p})\bar{u}_r(\vec{p})}{p^0 - E(\vec{p}) - \bar{u}_r(\vec{p})\Sigma(p^0, p)u_r(\vec{p})\frac{M}{E(\vec{p})}} \quad (15)$$

This expansion is rather useful because both Σ^s and $\Sigma^v\gamma^0$ (and $\vec{\gamma}\vec{p}$) are diagonal in the base of the $u_r(\vec{p})$ spinors, which converts eq. (15) in an ordinary geometric series, not a matricial series, which can be summed trivially as shown in the last step of eq. (15).

It might look surprising that one obtains a Dirac structure $u_r(\vec{p})\bar{u}(\vec{p})$ in $\tilde{G}(p^0, p)$ as for free nucleons, even when the renormalized nucleons will be off shell. This is less striking if one recalls that also in eq. (13) the positive energy part (corresponding to \tilde{G}) has the same structure $u_r(\vec{p})\bar{u}_r(\vec{p})$ even if the nucleon is off shell. In any case the structure might not match the one coming from eq. (14) and one has lost the covariance shown by eq. (14). The reason for this loss of covariance is that one loses terms with admixture of the positive and negative parts of the nucleon propagator of eq. (13) in the perturbative expansion. This is, in the sum of eq. (15) one is summing terms of the type of fig. 2a,b,c,d, where in the intermediate fermion lines one only has the part of positive energy of the propagator. One is missing terms of the type of fig. 2e (where the line pointing down stands for the negative energy part of the free nucleon propagator), which would naturally appear in a covariant expansion of eq. (14).

On the other hand while all the terms of fig. 2c,d etc. are summed up automatically in eq. (15) in terms of a selfenergy given exclusively by the term in fig. 2b, the second order terms of fig. 2e is not accounted for. We argued that this latter term (which has an intermediate propagator of order $1/2M$, and is of ρ^2 type) should be small with respect to the diagrams contained in figs. 2b, c, d, ... But in any case it can be included as a nucleon selfenergy part in the sum of eq. (15) and then diagrams e,f, etc. would be automatically included. This means that even if the covariance is lost in eq. (15) one can still regain all the terms in the series by including these mixed terms in the selfenergy Σ appearing in eq. (15). Of course, this selfenergy is now different to the one appearing in eq. (14). These mixed terms are also diagonal in $u_r(\vec{p})$ and do not change the structure of eq. (15). This is the philosophy which we follow, only that the diagrams of fig. 2e, 2f are not evaluated, although they are implicitly accounted for as we pass to discuss. The reason is that these diagrams only contribute to the real part of Σ , not to the imaginary part, and in our scheme, which evaluates accurately $Im\Sigma$, there are pieces missing in the real part of Σ which are added phenomenologically in order to ensure the exact experimental binding energy of each nucleus [23]. The particular structure of eq. (15) allows one to write

$$\tilde{G}(p^0, p) = \frac{M}{E(\vec{p})} \sum_r u_r(\vec{p})\bar{u}_r(\vec{p}) \left[\int_{-\infty}^{\mu} d\omega \frac{S_h(\omega, p)}{p^0 - \omega - i\eta} \right]$$

$$+ \int_{\mu}^{\infty} d\omega \frac{S_p(\omega, p)}{p^0 - \omega + i\eta}] \quad (16)$$

with the relationships

$$S_h(p^0, p) = \frac{1}{\pi} \frac{\frac{M}{E(\vec{p})} \text{Im}\Sigma(p^0, p)}{[p^0 - E(\vec{p}) - \frac{M}{E(\vec{p})} \text{Re}\Sigma(p^0, p)]^2 + [\frac{M}{E(\vec{p})} \text{Im}\Sigma(p^0, p)]^2} \quad \text{for } p^0 \leq \mu$$

$$S_h(p^0, p) = -\frac{1}{\pi} \frac{\frac{M}{E(\vec{p})} \text{Im}\Sigma(p^0, p)}{[p^0 - E(\vec{p}) - \frac{M}{E(\vec{p})} \text{Re}\Sigma(p^0, p)]^2 + [\frac{M}{E(\vec{p})} \text{Im}\Sigma(p^0, p)]^2} \quad \text{for } p^0 > \mu \quad (17)$$

$$k_{F,p}(\vec{p}) = [3\pi^2 \rho_p(\vec{p})]^{1/3} \quad k_{F,n}(\vec{r}) = [3\pi^2 \rho_n(\vec{r})]^{1/3} \quad (18)$$

where for simplicity Σ is now $\bar{u}\Sigma u$ which is independent of spin.

By means of this new nucleon propagator the modifications introduced by our relativistic formalism, described in detail in ref. [23], are rather intuitive, easy to employ and can be summarized as:

- i) The normalization of the spectral function which ensures the proper normalizations of the charge (or baryonic charge) of a nucleus is exactly the same as in eq.(9). However, the spectral function of eq.(12) is now replaced by eq. (17)
- ii) On the other hand the structure function $F_{2A}(x)$ of eq.(8) is replaced by

$$F_{2A}(x) = 4 \int d^3r \int \frac{d^3p}{(2\pi)^3} \frac{M}{E(\vec{p})} \int_{-\infty}^{\mu} d\omega S_h(\omega, p) \frac{x}{x_N} F_{2N}(x_N) \theta(x_N) \theta(1-x_N) \quad (19)$$

where the relativistic factor $\frac{M}{E(\vec{p})}$ plays the role of a Lorentz contraction factor, appearing in the probability per unit time of electron collision with the nucleon, and which remains in the formula of the nuclear cross section because one divides the sum of all probabilities by a unique electron flux, the one of the electron with respect to the CM of the nucleus.

The questions of normalization and conservation of baryonic number, which have been the subject of much attention [2], are discussed in detail in [23].

There are other terms which would be included in a covariant formalism of the (e, e') reaction and do not appear in our formalism. These are terms

which have a negative energy state coupled to the hadronization vertex, as shown in fig. 3. Once again such terms are reduced by the large energy denominator of the negative energy state. Only in cases when one uses an operator which magnifies the $N\bar{N}$ coupling with respect to the NN , as in the case of the axial charge, such terms can be relevant [26], although more accurate nonperturbative calculations find smaller results [27]. With the use of scalar potentials Σ^s smaller than the typical ones in the Walecka model when one imposes constraints from information in the negative energy sector, as done in [28], terms like in fig. 3 would be of the order of 10-15 % if one has an operator like in the axial charge, $\gamma^0\gamma_5$, but much smaller than this if electromagnetic current operators are used [27].

Furthermore, in as much as one assumes that the structure functions for the positive or negative energy states are the same and one uses a nucleon spectral function which conserves the baryonic number, one would be including the strength of these pieces into the scheme which we follow, up to small differences coming from different medium corrections to the positive and negative energy states. Estimates based on the findings of [27] would put the difference between this covariant scheme and ours at the level of 1-2% in the EMC region and probably a few percent in the $x > 1$ region that we explore.

In practical terms our scheme respects special relativity in the positive energy sector and amounts to using free $u_r(\vec{p})$ spinor in the evaluation of the matrix elements of the $\gamma^*N \rightarrow X$ process while keeping the proper energy and momentum balance in the δ function of conservation of fourmomentum, with the ω, p distribution of the occupied nucleon given by the spectral function and the energy and momentum of the final states in X being those of their asymptotic states. This is in fact the most standard method in the study of many nuclear processes involving scattering or decay. The approximations which we have done here, sacrificing covariance in a controlled way, lead us to this calculational scheme where everything is defined. Covariant formalisms like those used in [29, 30] generate some off shell dependence in the hadronic tensor, which are accounted for in terms of new structure functions for which there is no empirical information, so several different assumptions are made in [29, 30] which produce moderate changes in the EMC results.

Our relativistic corrections thus stem from the consideration of special relativity in the positive energy sector, although, as we discussed, it accounts in an approximate way for the contributions involving negative energy states, which are small anyway.

We will show results both with the relativistic and non-relativistic formalism. The relativistic corrections are found to be relevant in the region of $x > 1$, particularly at large values of x .

It is easy to see qualitatively why eq.(8) or eq.(19) lead to a non-vanishing structure function for $x > 1$. The nucleon structure function appears with argument x_N in this equation and in the Bjorken limit one has

$$x_N = \frac{x_N}{x} x = \frac{M}{\omega - p_z} x \quad (20)$$

For certain combinations of ω and p_z one can obtain values of $x_N < 1$ even if $x > 1$. Since both ω and p_z appear in eq.(20) it is very important to take into account the correlations between ω and p provided by the spectral function $S_h(\omega, p)$, and one sees that approximations which neglect these correlations are bound to provide unrealistic results.

3 The nucleon spectral function in nuclear matter and finite nuclei

We have used three different approaches to evaluate the spectral function. The first one is a semiphenomenological one relating the spectral function of nuclear matter to the experimental cross section for NN scattering. The second approach is microscopic in the sense that the spectral function for nuclear matter is derived from a many-body calculation employing a realistic One-Boson-Exchange model for the NN interaction. In the third model we avoid the local density approximation and evaluate the spectral function \mathcal{S}_h directly for finite nuclei. We briefly describe these models below.

3.1 Semiphenomenological approach

This model is described in detail in ref. [31]. It evaluates $Im\Sigma(\omega, p)$ from a second order diagram and uses the fact that ladder diagrams evaluated from the NN potential lead to the NN t matrix. Pauli blocking corrections are taken into account in the explicit diagram evaluated and $|t|^2$, which appears in the evaluation of $Im\Sigma$, is written in terms of the experimental NN cross section. Polarization effects from the RPA iteration of ph and Δh excitations are also taken into account. The real part of the selfenergy is obtained via a dispersion relation and the Fock term from pion exchange is also included. Hartree terms, which require the explicit knowledge of a potential, are missing in the approach but these are terms independent of energy and momentum. The nucleon properties evaluated in [31] as a function of $\omega - \mu$ compare favourably with those of more microscopic evaluations [32, 33]. In order to complete the model and obtain absolute values for $Re\Sigma$, another phenomenological piece is added here. This Hartree contribution is assumed to be proportional to ρ and its value is adjusted, in order to fit the empirical value of the binding energy per nucleon in each particular nucleus. For this purpose we recall the sum rule for the binding energy per nucleon [34]

$$|\varepsilon_A| = -\frac{1}{2} \left(\langle E - M \rangle + \frac{A-1}{A-2} \langle T \rangle \right) \quad (21)$$

and we evaluate $\langle T \rangle$ and $\langle E \rangle$ as

$$\begin{aligned}
\langle T \rangle &= \frac{4}{A} \int d^3r \int \frac{d^3p}{(2\pi)^3} (E(\vec{p}) - M) \int_{-\infty}^{\mu} S_h(\omega, p) d\omega \\
\langle E \rangle &= \frac{4}{A} \int d^3r \int \frac{d^3p}{(2\pi)^3} \int_{-\infty}^{\mu} S_h(\omega, p) \omega d\omega
\end{aligned} \tag{22}$$

By means of this, one takes also into account empirically contributions from terms like in fig. 2e, which are in principle small, and even if they are of ρ^2 type would not differ appreciably from a $\rho \rho_{eff}$ form, with ρ_{eff} an effective average nuclear density.

The evaluation of $Im\Sigma(\omega, p)$ was done nonrelativistically in [31]. For consistency with the relativistic formalism used here we should have kept the factors $\frac{M}{E}$ in the nucleon propagators evaluating $Im\Sigma(\omega, p)$ in ref. [31]. However, the range of momenta in the loop integrals in $Im\Sigma(\omega, p)$ is quite limited and they would modify the values of $Im\Sigma(\omega, p)$ by less than 10%. By means of the explicit calculations carried out here we have observed that an increase of 10 % in $Im\Sigma(\omega, k)$ leads to increases of $F_{2A}(x)$ of the order 2 % at $0 < x < 0.6$ and always below the 10 % level for large x , hence we have continued to use the same $Im\Sigma(\omega, p)$ as obtained in ref. [31].

3.2 Microscopic approach in nuclear matter

The spectral function of nuclear matter which has been used in this second approach has been evaluated using the techniques described in ref. [35]. The starting point of this many-body calculation is a Brueckner-Hartree-Fock (BHF) calculation of nuclear matter considering the realistic One-Boson-Exchange (OBE) potential B as defined in [36] for the NN interaction. The G -matrix resulting from this BHF calculation as well as the BHF single-particle spectrum $\epsilon_{BHF}(p)$ are used to define the nucleon self-energy including all terms up to second order in G . The single-particle Green's function $g(p, \omega)$ is derived from a solution of the Dyson equation

$$g(p, \omega) = g^{(BHF)}(p, \omega) + g^{(BHF)}(p, \omega) [\Sigma^{(2)}(p, \omega)] g(p, \omega) \tag{23}$$

Here $\Sigma^{(2)}$ is the contributions to the self-energy in second order. The single-particle Green's function in the BHF approximation is given by

$$g^{(BHF)}(p, \omega) = \frac{\Theta(k_F - p)}{\omega - \epsilon_p - i\eta} + \frac{\Theta(p - k_F)}{\omega - \epsilon_p + i\eta}, \tag{24}$$

where k_F denotes the Fermi momentum of nuclear matter at the density under consideration. The term with $\Sigma^{(2)}$ in eq. (23) contains a contribution with intermediate particle-particle states, which is taken into account already in the BHF approximation. This doublecounting is removed as described in [35]. The spectral function $S_h(\omega, p)$ can then be calculated from the imaginary part of the single-particle Green's function by

$$S_h(\omega, p) = \frac{1}{\pi} \text{Im} g(p, \omega) \quad (25)$$

This calculation yields a Fermi energy μ depending on the density of nuclear matter. The energy variable ω is defined with respect to this Fermi energy. In the local density approximation for the spectral function discussed above, the empirical Fermi energy of the finite nucleus has been chosen to be the reference point for the energy variable ω .

3.3 Microscopic approach for finite nuclei

The spectral function can be calculated directly for finite nuclei using the procedure described and applied to ^{16}O in ref. [37]. For nuclei with spherical symmetry the self-energy is evaluated in a partial wave basis, $\Sigma_{lj}(p, p')$, assuming that orbital angular momentum l and total angular momentum j are conserved quantum numbers. As discussed above, the total self-energy is decomposed in a BHF part and terms of second order in the Brueckner G-matrix. The corresponding single-particle Green's function can be evaluated by solving a Dyson equation of the form

$$g_{l,j}(p, p'; \omega) = g_{l,j}^{(BHF)}(p, p'; \omega) + \int dk_1 \int dk_2 g_{l,j}^{(BHF)}(p, k_1; \omega) \times \left[\Sigma_{l,j}^{(2)}(k_1, k_2; \omega) \right] g_{l,j}(k_2, p'; \omega) \quad (26)$$

The spectral function for the various partial waves is then obtained from the imaginary part of the Green's function $g_{l,j}(p, p; \omega)$ applying eq.(25). A problem of this partial wave expansion for the momentum distribution is related to the fact that non-negligible contributions are obtained at large momenta and energies in high partial waves. Therefore we prefer to apply an approach which has been introduced and discussed in ref. [33]. In this approximation one splits the spectral function, for nuclear matter as well as for finite nuclei, into a quasiparticle contribution describing the contribution to the spectral function around the quasiparticle pole and a background contribution which contains the information about the spectral function at energies away from the respective quasiparticle pole. For finite nuclei a quasiparticle pole contribution is only observed for those partial waves, which are occupied in the HF or independent particle model. Therefore the sum on partial waves in

$$S^{QP}(\omega, p) = \sum_{l,j} 2(2j+1)n_{l,j} \delta(\omega - \epsilon_{l,j}^{QP}) |\Phi_{l,j}(p)|^2 \quad (27)$$

is restricted to $l=0$ and 1 in our example of ^{16}O . In this equation $\epsilon_{l,j}^{QP}$ stands for the energy of the quasiparticle pole, $\Phi_{l,j}(p)$ for the corresponding single-particle wave function in momentum space and $n_{l,j}$ for the occupation probability for this pole. This quasiparticle pole contribution is supplemented by

the background contribution calculated in a local density approximation from the background contribution in nuclear matter

$$S_{h,A}(\omega, p) = S^{QP}(\omega, p) + 4 \int d^3r S_h^B(\omega, p; \rho(r)) \quad (28)$$

where S_h^B stands for the background contribution of the spectral function calculated in nuclear matter at the local density $\rho(r)$. Care is taken that the whole spectral function is normalized such that

$$\int \frac{d^3p}{(2\pi)^3} \int_{-\infty}^{\mu} d\omega S_{h,A}(\omega, p) = A \quad (29)$$

with A the total number of nucleons.

3.4 Approximations to be avoided

If no reliable model for the spectral function for nucleons in nuclear matter is available, one may be tempted to use certain approximations. One of such approximations, which has frequently been used [12–14] is to ignore the special correlations between momentum and energies of nucleons provided by the spectral function and simply use the energy-integrated spectral function, which is the momentum distribution. We are going to discuss three different approximations and try to explore their reliability by comparing with the results obtained in the more sophisticated models for the spectral function discussed above. Although discussions around different approximations to the nuclear wave functions, and other different approximations, have been common in the past [2, 4, 7, 38], the comparison of different approximations to the results obtained using spectral functions has not been exploited, particularly in the region of $x > 1$ which we study here.

a) The uncorrelated Fermi sea distribution.

This is the simplest approximation, which is usually very accurate, except of course in processes which test the momentum distribution at momenta which are large compared to the Fermi momentum, as is the case in the present problem. In this approximation the spectral function within the local density approximation is assumed to have the form

$$S_h^{UFS}(\omega, p; \rho) = n_{FS}(\vec{p}) \delta(\omega - E(\vec{p}) - \Sigma) \quad (30)$$

with an occupation probability of

$$n_{FS}(\vec{p}) = \begin{cases} 1 & \text{if } |\vec{p}| < p_F(r) \\ 0 & \text{if } |\vec{p}| > p_F(r) \end{cases} \quad (31)$$

with a local Fermi momentum $p_F(r)$ which is related to the local density $\rho(r)$ by

$$p_F(r) \equiv \left(\frac{3\pi^2 \rho(r)}{2} \right)^{1/3} \quad (32)$$

and an expression for the local single-particle potential

$$\Sigma \equiv \Sigma(r) = V_{TF}(r) + D\rho(r) \quad (33)$$

where $V_{TF}(r)$ is the Thomas Fermi potential, $-p_F^2(r)/2M$ and D a phenomenological constant fitted to reproduce the binding energy per nucleon in the nucleus, as done in section 3.1.

b) Use of the momentum distribution of the correlated Fermi sea.

Since large momentum components are needed to generate $F_{2A}(x)$ at $x > 1$, one is tempted to use the realistic momentum distribution of the nucleus as a way to improve on this approximation. This means that we assume an expression for the spectral function S_h^{MD} like in eq.(30) but replace the momentum distribution of the free Fermi gas n_{FS} by the momentum distribution of the interacting Fermi gas

$$n_I(\vec{p}) = \int_{-\infty}^{\mu} S_h(\omega, p) d\omega \quad (34)$$

where we have used the spectral function of nuclear matter discussed above to calculate n_I . Note, however, that the energy-momentum relation is still determined by the δ -function in (30), with Σ defined with the same prescription as in the subsection above, eq. (33).

c) Use of the correlated momentum distribution and the corresponding mean value for the energy.

Finally we want to consider an approximation in which we assume again a definite relation between momentum and energy of a nucleon in the hole spectral function

$$S_h^{MED}(\omega, p; \rho) = n_I(\vec{p}) \delta(\omega - \langle \omega(\vec{p}) \rangle) \quad (35)$$

but determine the momentum distribution n_I (see eq.(34)) as well as the mean value of the energy for a given momentum

$$\langle \omega(\vec{p}) \rangle = \frac{\int_{-\infty}^{\mu} S_h(\omega, p) \omega d\omega}{\int_{-\infty}^{\mu} S_h(\omega, p) d\omega} \quad (36)$$

from the complete spectral function for nuclear matter discussed above.

4 Results and discussion

In a first step we want to compare the two approaches to determine the spectral function for nuclear matter, which we describe in sections 3.1 and 3.2 and which

we are going to employ for the calculation of the structure function. For that purpose we present in Fig. 4 the momentum distribution $n_I(p)$ (see eq.(34)) calculated at the empirical saturation density, $\rho = \rho_0$, of nuclear matter.

The momentum distributions obtained by these two very different methods are very similar. At small values of p the microscopic approach of [33] provides an occupation number of the order of 3 % bigger than the semiphenomenological one [31]. For momenta above the Fermi momentum the distributions are also similar although for momenta around two times the Fermi momentum ($\sim 550 \text{ MeV}/c$) the differences become more appreciable. The semiphenomenological approach provides a little less strength below the Fermi momentum, which is then redistributed to larger momenta where $n_I(\vec{p})$ is larger than in the microscopic approach. The precise values of $n_I(\vec{p})$ calculated in a microscopic many-body theory, depend on the model of the NN interaction which is considered and the method which is used to determine the effects of correlations. For instance in the self-consistent Green's function approach of ref. [33], using the Reid soft-core potential, the occupation number for momenta below k_F is around 0.85, smaller than in both the approaches considered here. This demonstrates that the semiphenomenological approach provides a result which is in agreement with the microscopic calculations within the uncertainties of the microscopic approach caused by the approximation in the many-body theory as well as NN interaction. The differences found in $n_I(\vec{p})$ in the two approaches discussed have little repercussion in the values of $F_{2A}(x)$, which come very close to each other in the two approaches, as we shall see below.

As a second quantity characterizing the bulk properties of the spectral functions calculated by these two methods, we show in Fig. 5 the mean value for the energy as a function of \vec{p} calculated according to eq.(36) at the nuclear density ρ_0 . Fig. 5 shows in a qualitative way that there is an important correlation between the momenta and the mean value of the energy for the bound nucleons. The absolute value of this mean energy $|\langle \omega(\vec{p}) - M \rangle|$ decreases as a function of momentum with increasing momenta for momenta below the Fermi momentum. This momentum dependence is mainly due to the momentum of the quasiparticle peak, which is approaching the Fermi energy for $p \rightarrow p_F$. There is no quasiparticle contribution to the hole-spectral function S_h for momenta larger than the Fermi momentum p_F . Therefore at these momenta, the mean value is determined only from the background contribution. The coupling to 2 hole-1 particle and more complicated configurations with total momenta p , described by these background terms yields a mean value of $\langle \omega - M \rangle$, which decreases with increasing momentum. From this figure it is evident, however, that the energy-momentum relation obtained from a realistic spectral function is quite different from the simple relation used in eqs. (30), (33), which provides a dispersion relation which is always an increasing function with increasing momentum.

The values obtained for $|\langle \omega(\vec{p}) \rangle|$ in the two approaches discussed in sections 3.1, 3.2 are very similar, with differences of the order of 10 % at most.

This is another indication that the basic features of the spectral function are not very sensitive to the method used in the evaluation and that also the semiphenomenological approach yields quite a reliable result.

In Fig. 6 we show the results for $F_{2A}(x)$ calculated with the three different spectral functions introduced in sections 3.1 to 3.3, for the case of ^{16}O . The density distributions $\rho(r)$ for ^{16}O and the other nuclei, which are required to apply the local density approximation, are taken from refs. [39, 40]. Since the microscopic nuclear matter and finite nuclei approaches are nonrelativistic, we have also taken the nonrelativistic version of the semiphenomenological approach, for comparison, omitting all the $\frac{M}{E(p)}$ factors in eqs. (17), (19). The experimental values for $F_{2N}(x_N)$ are taken from ref. [41]. The results obtained with the two spectral functions of nuclear matter (solid line and dashed line) are rather similar. At $x \simeq 1$ the microscopic spectral function provides results about 20 % higher than the semiphenomenological one. At values of $x \simeq 1.22$ the two approaches coincide and for $x \simeq 1.5$, where the structure function has decreased three orders of magnitude with respect to the value at $x = 1$, the semiphenomenological approach provides values of F_{2A} about 40 % larger than the microscopic one. This reflects the fact that the former model provides a larger probability for the momentum distribution at high momenta than the latter one, as seen in Fig. 4.

The results for the structure function obtained with the spectral function of eq.(28) evaluated directly for the finite nucleus are represented by the dot-dashed line in Fig. 6. They should be compared with those displayed by the solid line since the background contribution to eq.(28) is obtained from the same nuclear matter result. These two results can hardly be separated on the logarithmic scale of the figure. We observe that at $x \simeq 1$ the results with the spectral function of the finite nucleus are about 8 % bigger than with the nuclear matter approach. The differences become smaller as x increases and for values of $x \simeq 1.5$ the two approaches give the same results. This latter fact is telling us that at large values of x one is getting practically all contributions from the background part of the spectral function and none from the quasiparticle part. The comparison of these two curves also tells us that the use of the nuclear matter spectral functions, together with the local density approximation, is an excellent tool to evaluate $F_{2A}(x)$. If one compares the results at values of x studied in the *EMC* effect, $0 < x < 0.6$, the differences among the three calculations are of the order of 3 %.

In Fig. 7 we show results obtained with the semiphenomenological approach using the relativistic and nonrelativistic formalisms. The trend of the results is similar, however, the relativistic corrections induce a reduction of 25 % around $x = 1$ and roughly reduce the structure function F_{2A} to one half of the non relativistic results at $x \simeq 1.5$. The relativistic effects are significant in the sense that they are bigger than the differences found between various nonrelativistic approaches, which reflect the uncertainties in the treatment of correlations.

Results obtained for $F_{2A}(x)$ using the different approximations discussed in section 3.4 are displayed in Fig. 8. The first one, which originates from the assumption of an uncorrelated Fermi sea, eq. (30), is represented by the dot-dashed line. We can see that at $x \simeq 1$ it already provides a structure function of around a factor two smaller than the one obtained with the proper spectral function (short dashed-line). However, as one moves to higher x , the discrepancies get bigger and at values of $x \simeq 1.2$ the uncorrelated Fermi sea gives already values for the structure function which are about two orders of magnitude smaller than the correct ones. It is clear that one is exploring the region of large momenta, above the Fermi momentum, which are not accounted for by the uncorrelated Fermi sea.

Another approximation corresponds to using the realistic momentum distribution $n_I(\vec{p})$ of eq. (34) and associating an energy to each \vec{p} given by its kinetic energy plus a potential, eq. (33). The results (solid line) are outrageously wrong. This demonstrates that the naive use of a momentum distribution, although calculated in a realistic way, may lead to results which are worse than those obtained for an uncorrelated system, if one does not treat the energy-momentum correlation properly. As we have discussed already in Fig. 5, the mean value of the energy $\langle \omega(\vec{p}) \rangle$ decreases above the Fermi momentum with increasing momenta. On the other hand, the energy associated to \vec{p} in eq. (30) grows like the kinetic energy as $|\vec{p}|$ increases. The discrepancies with the correct results are about a factor three at $x \simeq 1$ and three orders of magnitude at $x \simeq 1.5$, providing a gross overestimate of the results for $F_{2A}(x)$. The same gross overestimate found here for this approximation was also found in ref. [15] in connection with the mesonic Lambda decay in nuclei.

In view of the deficiencies of the previous approximations and the reasons for it, one might think that the results should be improved by replacing the kinetic plus potential energy, eq. (30), by the mean value of $\langle \omega(\vec{p}) \rangle$ calculated from the spectral function (see eq.(36)). This is indeed the case (see curve with long dashes in Fig. 8), although the discrepancies with the exact results are still large enough to discourage this approximation too. We can see in Fig. 8 that at values of $x \simeq 1$ (and also in the EMC region below) the approximation turns out to be quite good. However, for values of $x \simeq 1.3$ and above the discrepancies with the correct results are already as big as one order of magnitude or more.

The results discussed here stress the importance of using the spectral function to evaluate $F_{2A}(x)$ since all the information contained in it, correlating energies and momenta, is very important, particularly at large x . We showed that some schemes which use only a partial information from the spectral function lead to rather inaccurate results and should thus be avoided.

Finally in Fig. 9 we show results obtained for different nuclei. They are calculated at $Q^2 = 5 \text{ GeV}^2$. We can see that $F_{2A}(x)/A$ is very similar for the different nuclei. We have taken nuclei with $N = Z$ or close by, to be able to use a unique Fermi sea for protons and neutrons as done in symmetric nuclear matter. For heavier nuclei with $N \neq Z$ the results obtained here could

be easily extended by dealing with two different Fermi seas, but this would require the extension of the work of ref. [31] to non symmetric nuclear matter. We do not expect, however, any special effects apart from those exposed here.

When evaluating absolute values of nuclear structure function, not ratios to the nucleon or the deuteron, it is very important to take into account the Q^2 dependence of the structure function. This is particularly true for values of $Q^2 \simeq 1 - 10 \text{ GeV}^2$, but even at $Q^2 \simeq 100 \text{ GeV}^2$ and above, where there is approximate Bjorken scaling, the Q^2 dependence is weak but one still has to consider it if one wants to make accurate predictions.

For the Q^2 dependence of the nucleon structure function we have taken the parametrizations given in ref. [42].

It is interesting to compare our results with the scarce experimental data available. Our results refer exclusively to the deep inelastic contribution to electron nucleus scattering. The quasielastic contribution (where only one nucleon is knocked out in the first step $eN \rightarrow e'N$) is not taken into account in our formalism. At low values of Q^2 and $x \geq 1$, the quasielastic contribution is dominant [19] and one has to go to values of $Q^2 > 20 \text{ GeV}^2$ to have a dominance of the deep inelastic contribution [17]. For this reason we compare our results with measurements done at $Q^2 = 61, 85$ and 150 GeV^2 in ref. [43], which improve the preliminary results reported in ref. [44] where much larger values were obtained.

The results can be seen in fig. 10. The three theoretical curves correspond to each one of the values of Q^2 and the results decrease as a function of increasing Q^2 . The agreement with the data is qualitative. The slope as a function of x seems well reproduce but the theoretical results are in average 40 % higher than experiment up to $x = 1.05$. At $x = 1.15$ and 1.3 there are only upper bounds which are compatible with our predictions.

Experimental results at $Q^2 < 5 \text{ GeV}^2$ have however, a large contamination of quasielastic contribution [17-19]. This is reflected by the large dispersion of the results as a function of Q^2 [45] and in the approximate y scaling of these results, which is characteristic of the quasielastic collisions. Nevertheless, we have also evaluated the deep inelastic contribution corresponding to the results in [45] with largest values of Q^2 . We evaluate the structure function corresponding to the lowest curve in fig. 1 of ref. [45]. This corresponds to different values of Q^2 for each value of x since the data correspond to electron scattering with fixed initial electron energy ($E_e = 3.595 \text{ GeV}$), fixed scattering angle, $\theta = 39^\circ$ and variable final electron energy. We show the results in fig. 11. The values of Q^2 increase with increasing x . At $x = 1$, $Q^2 = 3.11 \text{ GeV}^2$ and at $x = 1.25$, $Q^2 = 3.42$. We can see that our results lie below the experimental data, particularly at large values of x . However, one can observe a tendency to be in agreement with the data at values of $x < 0.8$ if one extrapolates the data smoothly. In fact in fig. 1 of ref. [45] we see a confluence of the data for different values of Q^2 in the region of $x = 0.4 - 0.6$ with values which agree with our results of fig. 11. This would be in agreement with the conclusions reached in [45] where the large dispersion of the results as a function of Q^2

for large values of x indicates the dominance of the quasielastic contribution, while the tendency to stabilize the results at values of $x < 0.8$ indicate that this region of x is dominated by the deep inelastic contribution. In such case our results should be comparable to the data and this is indeed the case.

5 Conclusions

We have evaluated the nuclear structure function $F_{2A}(x)$ at values of x bigger than unity, especially in the range $1 < x < 1.5$ where the values obtained are well within measurable range. For this purpose we have used sophisticated nuclear spectral functions which account for nuclear correlations and relativistic effects. The structure function decreases three orders of magnitude from $x = 1$ to $x = 1.5$.

The strength of $F_{2A}(x)$ in that range of x is tied to the components of the nuclear wave function with nucleons of large momenta. These components are due to the two-nucleon correlations originating from realistic NN interactions. The momentum distribution of nucleons in the nuclear many-body system, however, is strongly correlated with the energy distribution of these nucleons. These are dynamical effects which go beyond the shell model picture of the nucleus and which are taken into account in terms of the nucleon spectral functions. The results for $F_{2A}(x)$ are very sensitive to the correlations between ω and p , to the extreme that usual approximations made in calculations of the *EMC* effect fail badly in the region of $x > 1$. In particular, at $x \simeq 1.5$ the quasiparticle bound states (the occupied states of the shell model), which are only partly occupied in an interacting nucleus, give a negligible contribution to $F_{2A}(x)$ and all the strength comes from the background part of the spectral function.

We have discussed in detail the results obtained with several approximations which use only rough spectral functions or partial information from realistic ones, and which are often used. We showed that in this region of x none of them can be taken as a substitute of the calculation using the whole information of the spectral function.

In order to quantify the intrinsic theoretical uncertainties of the results we used two different models for the spectral function evaluated in infinite nuclear matter and $F_{2A}(x)$ for nuclei was calculated using the local density approximation. A version of the spectral function for finite nuclei was used also for ^{16}O . The differences between the models were small, of the order of 10-30 % depending on the region of x . We also found that the use of the local density approximation was an excellent tool, providing results very close to those obtained by direct evaluation for the finite nucleus.

Relativistic effects were checked and found to be important. They reduce the results for $F_{2A}(x)$ obtained with the nonrelativistic approximation by amounts ranging from 25 % at $x \simeq 1$ to nearly a factor two at $x \simeq 1.5$.

On the other hand we have evaluated $F_{2A}(x)$ for different nuclei and find

that $F_{2A}(x)/A$ becomes very similar for $N = Z$ nuclei from ^{40}Ca on.

The experimental results at $x > 1$ are scarce, particularly at large values of Q^2 . We compared our results with available data at $Q^2 = 61, 85, 150 \text{ GeV}^2$ and found our results about 40% higher than experiment, although the fall down with x was well reproduced. At values of Q^2 significantly smaller, $Q^2 < 4 \text{ GeV}^2$, we found that our results for $x > 1$ were much smaller than the experimental data, which was in agreement with theoretical and experimental findings that this region is dominated by quasielastic scattering. At lower values of x , around $x = 0.4 - 0.6$ our results matched the experimental data, in agreement with the theoretical and experimental findings that this region is dominated by the deep inelastic contribution.

The present investigation and the importance of the nucleon spectral function for the precise determination of $F_{2A}(x)$ is telling us that measurements of this quantity for different values of x and a wide range of nuclei would provide important information on the components of the nuclear wave function at large momenta and energies and the strong correlations between momenta and energy. This information would be very important as a test of the many body theories which are employed for the determination of the spectral function and would unveil interesting details on nuclear correlations, which complement our knowledge of nuclear structure beyond the basic information contained in the shell model wave functions.

Acknowledgments:

We would like to thank discussions with D.B. Day, J. S. McCarthy and R. Minehart concerning their experiment [45] and with G.I. Smirnov concerning the experiment of ref. [43]. Discussions with F. Gross and S. Liuti on theoretical issues are equally appreciated.

One of us, E.O. wants to thank the Humbold Foundation who supported his stay at Tübingen. P.F. and E.M. wish to thank the financial support of the Human Capital and Mobility program of the EU, contract no. CHRX-CT 93-0323. The work is partly supported by CICYT contract no. AEN 93-1205.

Figure Captions:

Fig. 1: a) Feynman diagram for deep inelastic electron-nucleon scattering and, b) electron selfenergy diagram associated to it.

Fig. 2: a,b,c,d) Feynman diagrams of the Dyson series in the evaluation of the nucleon propagator including only intermediate positive energy states. e) Feynman diagram of the Dyson series with a negative energy intermediate state. f) Higher order terms in the Dyson series originated from the selfenergy

term of diagram and its iteration through positive energy intermediate states.

Fig. 3. Feynman diagram for deep inelastic electron scattering with an interacting nucleon, through the coupling of the photon to the negative energy components.

Fig. 4: Momentum distributions at $\rho = \rho_0$. Solid line: microscopic model of [33]; dashed line: semiphenomenological model [31].

Fig. 5: Mean value of the energy of nucleons as a function of \vec{p} , from eq. (36), at $\rho = \rho_0$. Solid line: microscopic model [33]; dashed line: semiphenomenological model [31].

Fig. 6: Results obtained for the structure function of ^{16}O . Solid line: microscopic nuclear matter model [33]; dot-dashed line: microscopic finite nuclei model eq.(23); dashed line: nonrelativistic semiphenomenological model [31].

Fig. 7: Results obtained for the structure function of ^{16}O using the semiphenomenological model [31]. Solid line: nonrelativistic formalism; dashed line: relativistic formalism.

Fig. 8: Results obtained for the structure function of ^{16}O using different approximations. Dot-dashed line: uncorrelated Fermi sea, eq. (25); solid line: momentum distribution of the correlated Fermi sea, eq. (29); long dashed line: momentum distribution of the correlated Fermi sea and average energy $\langle \omega(\vec{p}) \rangle$, eq. (30); short dashed line: spectral function, eq. (13). $Q^2 = 5 \text{ GeV}^2$.

Fig. 9: Results obtained for the structure function per nucleon for different nuclei. Solid line: ^{40}Ca ; short dashed line: ^{56}Fe ; dot-long dashed line: ^{12}C ; dot-short dashed line: ^{16}O ; long dashed line: 6Li . All results are obtained using the relativistic version of the spectral function, eq. (13). $Q^2 = 5 \text{ GeV}^2$.

Fig. 10: Results for the structure function of ^{12}C at $Q^2 = 61, 85$ and 150 GeV^2 (solid, short-dashed and long dashed lines respectively). The data are from ref. [43] crosses for 61 GeV^2 , squares for 85 GeV^2 and triangles for 150 GeV^2 . The data for the two largest values of x are upper bounds.

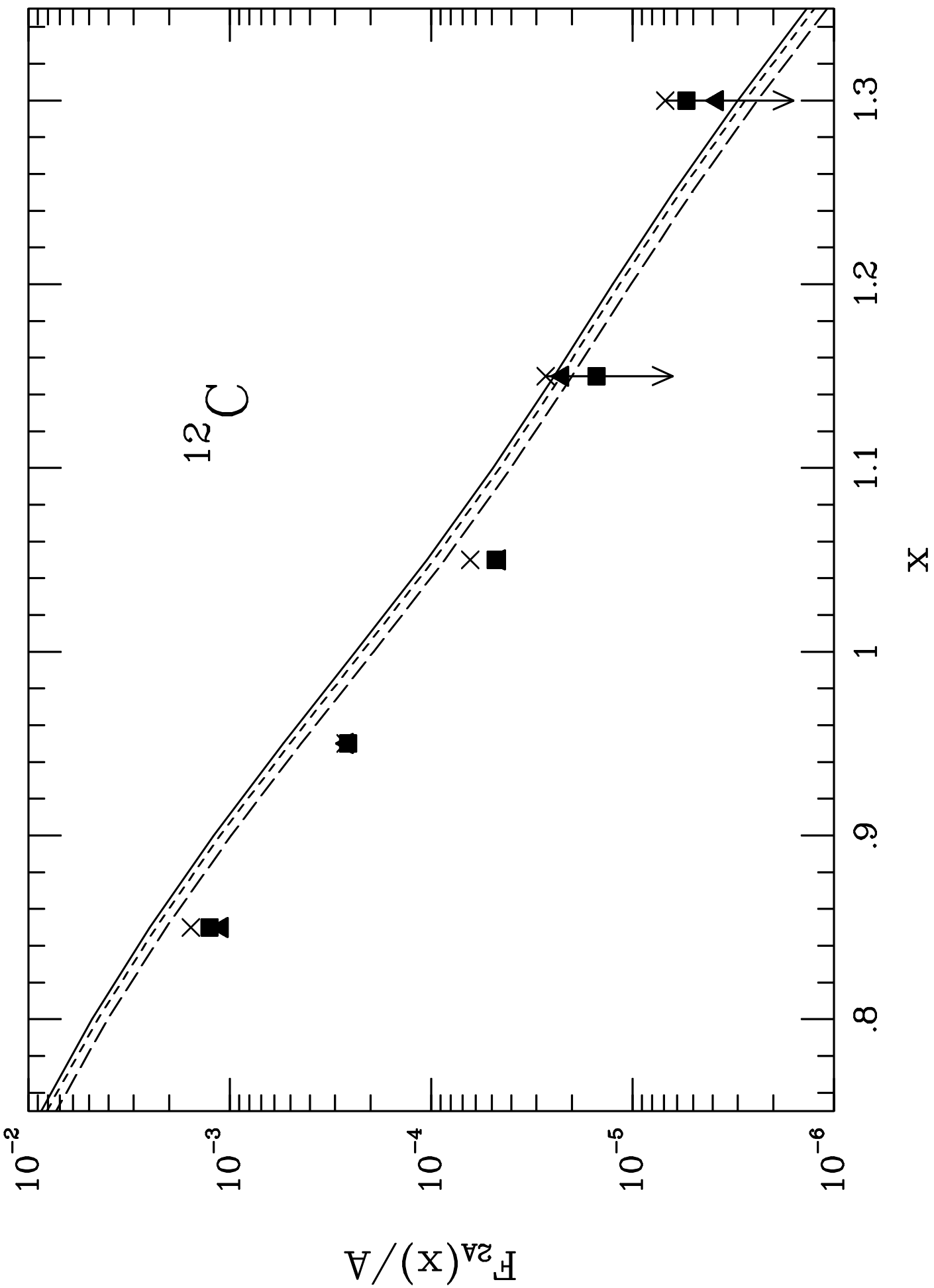
Fig. 11: Results for the deep inelastic structure function of ^{56}Fe at different values of Q^2 around 3 GeV^2 , see text, compared with experimental inclusive data results of [45]. The experimental data for values of $x > 1$ are dominated by the quasielastic contribution while for values of $x < 0.8$ the deep inelastic contribution dominates the reaction.

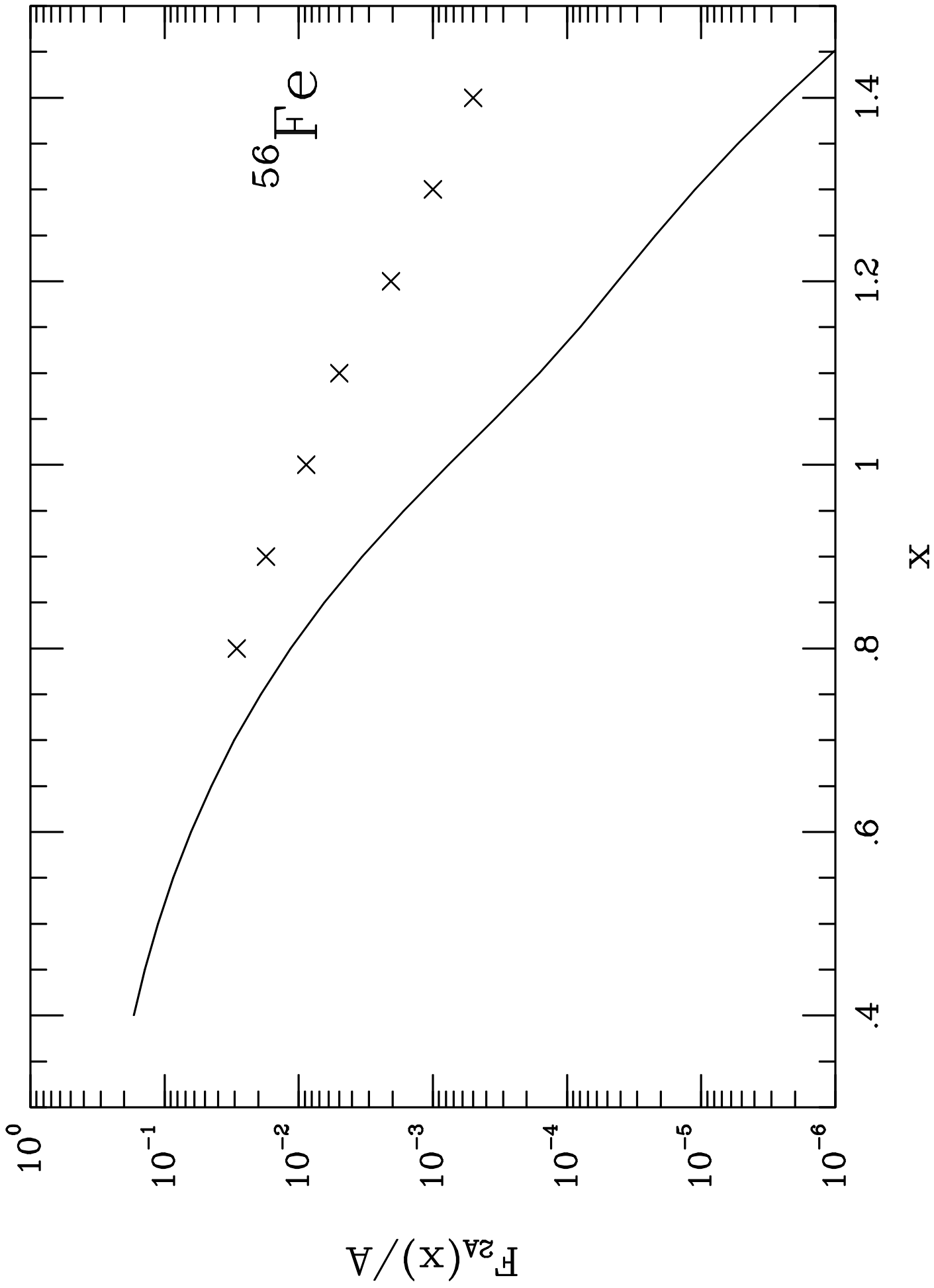
References

- [1] E.M. Collaboration, J.J. Aubert al., Phys. Lett. B123 (1983) 275.
- [2] L.L. Frankfurt and M.I. Strikman, Phys. Rep. 160 (1988) 236.

- [3] R.P. Bickerstaff and A.W. Thomas, *J. Phys.* G15 (1989) 1523.
- [4] A. B. Migdal, E.E. Saperstein, M.A. Troitskii and D.N. Voskresenskii, *Phys. Rep.* 192 (1990) 179.
- [5] M. Arneodo, *Phys. Rep.* 240 (1994) 301.
- [6] C.H. Llewellyn Smith, *Phys. Lett.* B128 (1983) 107.
- [7] M. Ericson and A.W. Thomas, *Phys. Lett.* B128 (1983) 112.
- [8] V. Sanjosé, V. Vento and S. Noguera, *Nucl. Phys.* A470 (1987) 509. P. González and V. Vento, *Mod. Phys. Lett.* A8 (1993) 1563.
- [9] S.V. Akulinichev, S. A. Kulagin and G.M. Vagradov, *Pis'ma Zh. Eksp. Teor. Fiz.* 42 (1985) 105; *JETP Lett.* 42 (1985) 127; *Phys. Lett.* 158B (1985) 485.
- [10] G. V. Dunne and A.W. Thomas, *Phys. Rev.* D33 (1986) 2061.
- [11] S. V. Akulinichev and S. Shlomo, *Phys. Rev.* C33 (1986) 1551.
- [12] A. Bodek and J.L. Ritchie, *Phys. Rev.* D23 (1981) 1070.
- [13] H. Araseki and T. Fujita, *Nucl. Phys.* A439 (1985)681.
- [14] K. Saito and T. Uchiyama, *Z. Phys.* A322 (1985) 299.
- [15] P. Fernández de Córdoba and E. Oset, *Nucl. Phys.* A528 (1991) 736.
- [16] C. Ciofi degli Atti and S. Liuti, *Phys. Rev.* C41 (1990) 1100.
- [17] S. Liuti, *Phys. Rev.* C47 (1993) R1854.
- [18] S. Simula, *Few Body Systems Suppl.* 8 (1995) 423.
- [19] O. Benhar, A. Fabrocini, S. Fantoni and I. Sick, *Phys. Lett.* B343 (1995) 47.
- [20] F. Gross and S. Liuti, *Phys. Rev.* C45 (1992) 1374.
- [21] S. Liuti and F. Gross, *Phys. Lett.* B356 (1995) 157.
- [22] L.L. Frankfurt and M.I. Strikman, *Phys. Lett.* B183 (1987) 254.
- [23] E. Marco, P. Fernández de Córdoba and E. Oset, University of Valencia, preprint, [nucl-th/9510060](https://arxiv.org/abs/nucl-th/9510060).
- [24] C. Itzykson and J.B. Zuber, *Quantum Field Theory* (McGraw Hill, NY, 1980).
- [25] B. D. Serot and J.D. Walecka, *Adv. Nucl. Phys.* 16 (1986) 1.

- [26] M. Kirchbach, D.O. Riska and K. Tsushima, Nucl. Phys. A542 (1992) 616.
- [27] A. Gil, M. Kleinmann, H. Müther and E. Oset, Nucl. Phys. A584 (1995) 621.
- [28] J. A. Tjon and S.J. Wallace, Phys. Rev. C32 (1985) 267; C35 (1987) 280; C36 (1987) 1085.
- [29] W. Melnitchouk, A.W. Schreiber and A.W. Thomas, Phys. Rev. D49 (1994) 1183.
- [30] S. A. Kulagin, G. Piller and W. Weise Phys. Rev. C50 (1994) 1154.
- [31] P. Fernández de Córdoba and E. Oset, Phys. Rev. C46 (1992) 1697.
- [32] S. Fantoni, B.L. Friman and V.R. Pandharipande, Nucl. Phys. A 399 (1983) 51; S. Fantoni and V. R. Pandharipande, Nucl. Phys. A427 (1984) 473.
- [33] A. Ramos, A. Polls and W.H. Dickhoff, Nucl. Phys. A 503 (1989) 1.
- [34] D.S. Koltun, Phys. Rev. C9 (1974) 484.
- [35] H. Müther, G. Knehr and A. Polls, Phys. Rev. C., C52 (1995) 2955.
- [36] R. Machleidt, Adv. Nucl. Phys. 19 (1989) 189.
- [37] H. Müther, A. Polls and W. H. Dickhoff, Phys. Rev. C51 (1995) 3040.
- [38] G. B. West, Phys. Lett. B37 (1971) 509.
- [39] H. de Vries, C. W. de Jager and C. De Vries, At. Data and Nucl. Data Tables, 36 (1987) 495.
- [40] G. C. Li, I. Sick, R. R. Whitney and M. R. Yearian, Nucl. Phys. A162 (1971) 583.
- [41] J. J. Aubert et al., Phys. Lett. B114 (1982) 291.
- [42] D.W. Duke and J.F. Owens, Phys. Rev. D30 (1984) 49.
- [43] A. C. Benvenuti et al., Z. Phys. C63 (1994) 29.
- [44] A. M. Baldin, Nucl. Phys. A434 (1985) 695c.
- [45] B. W. Filippone et al., Phys. Rev. C45 (1992) 1582.





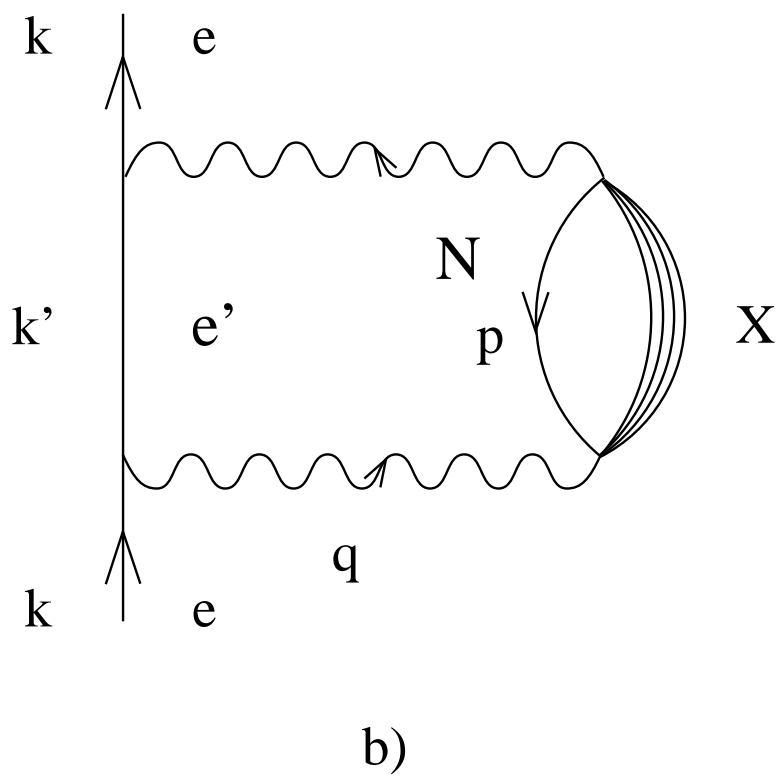
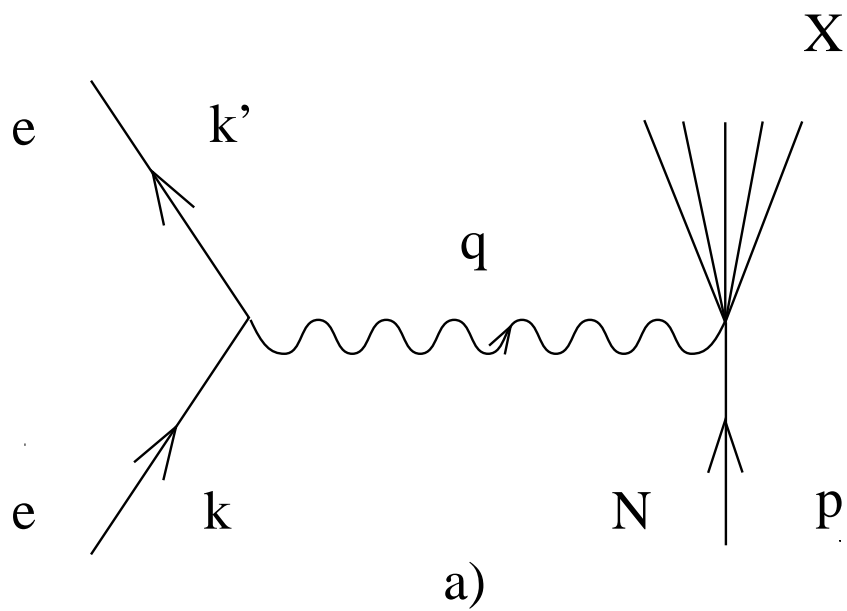


Fig. 1

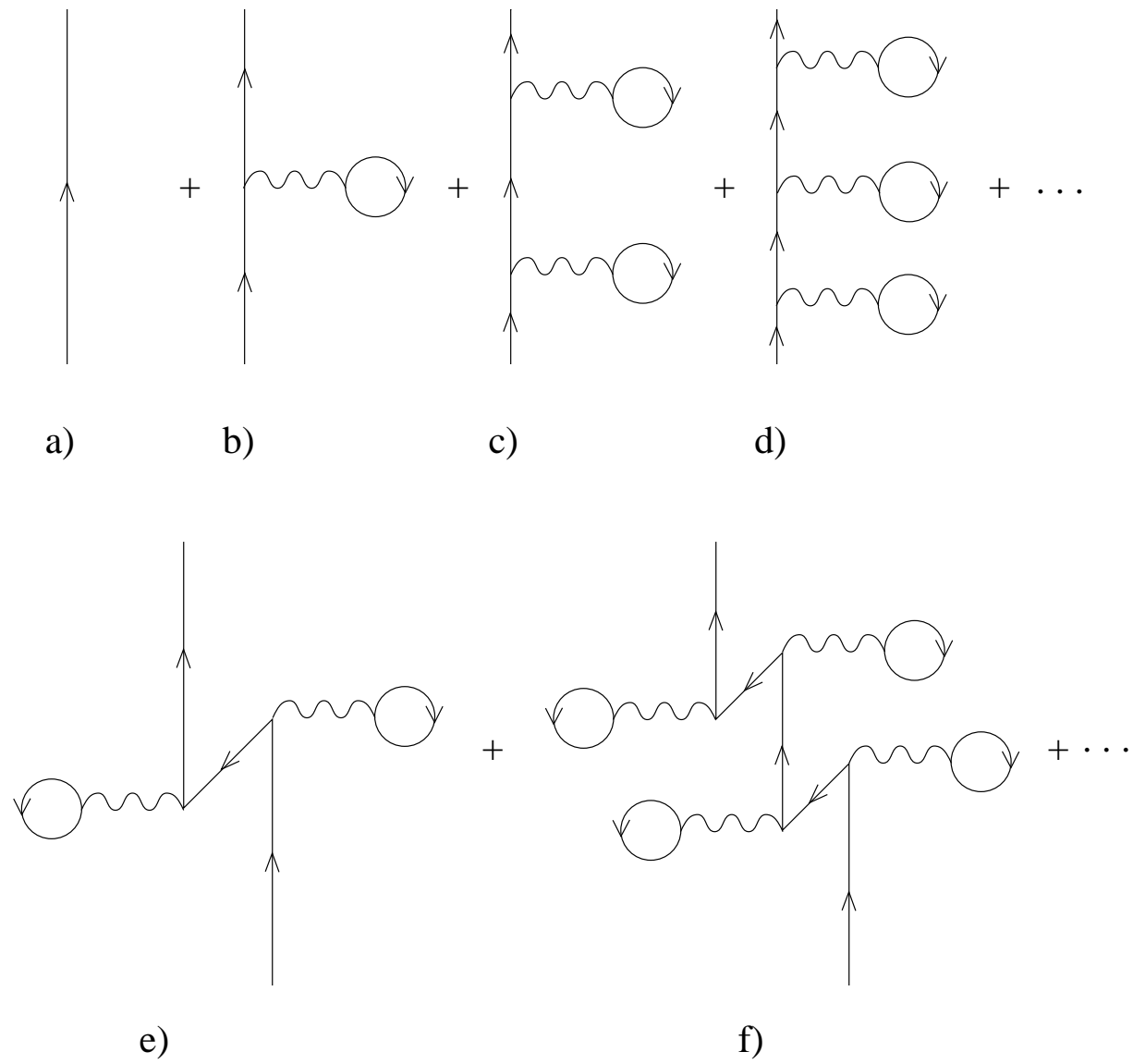


Fig. 2

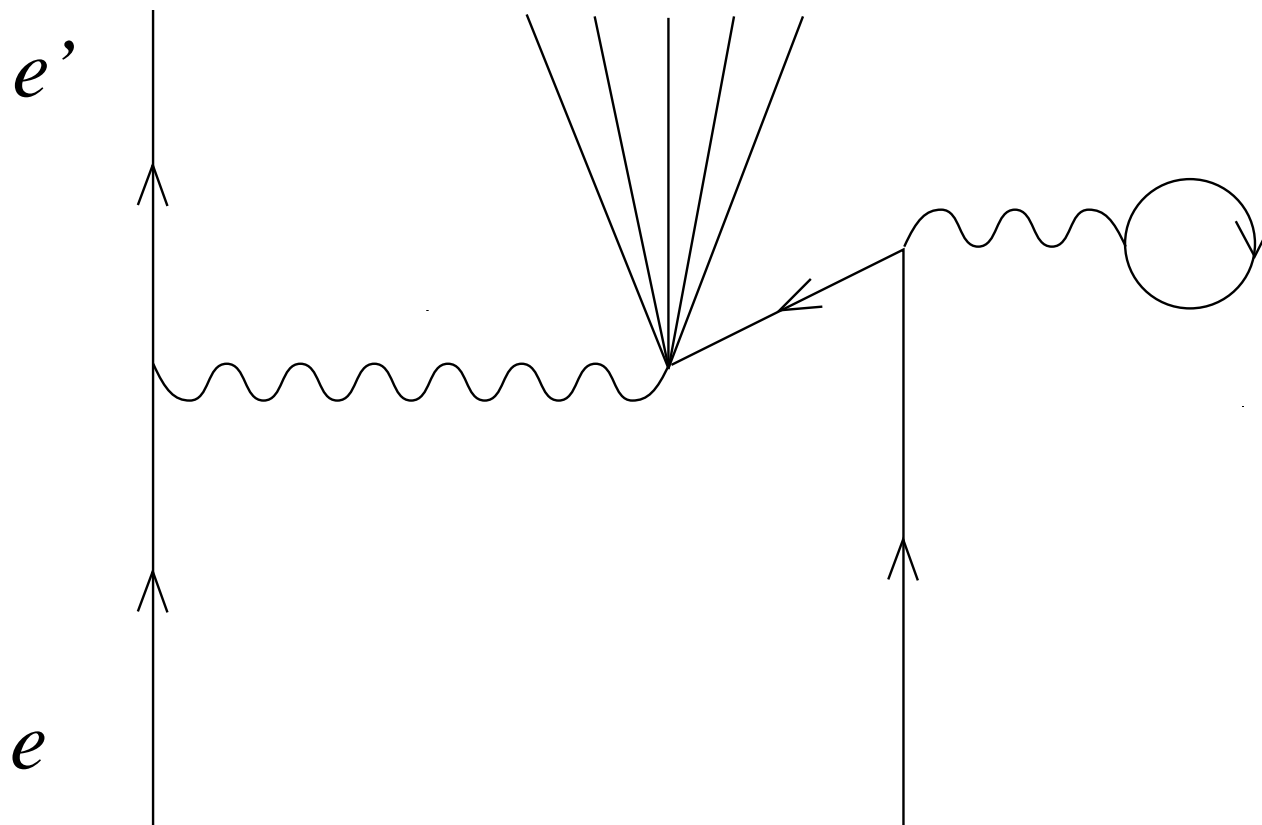
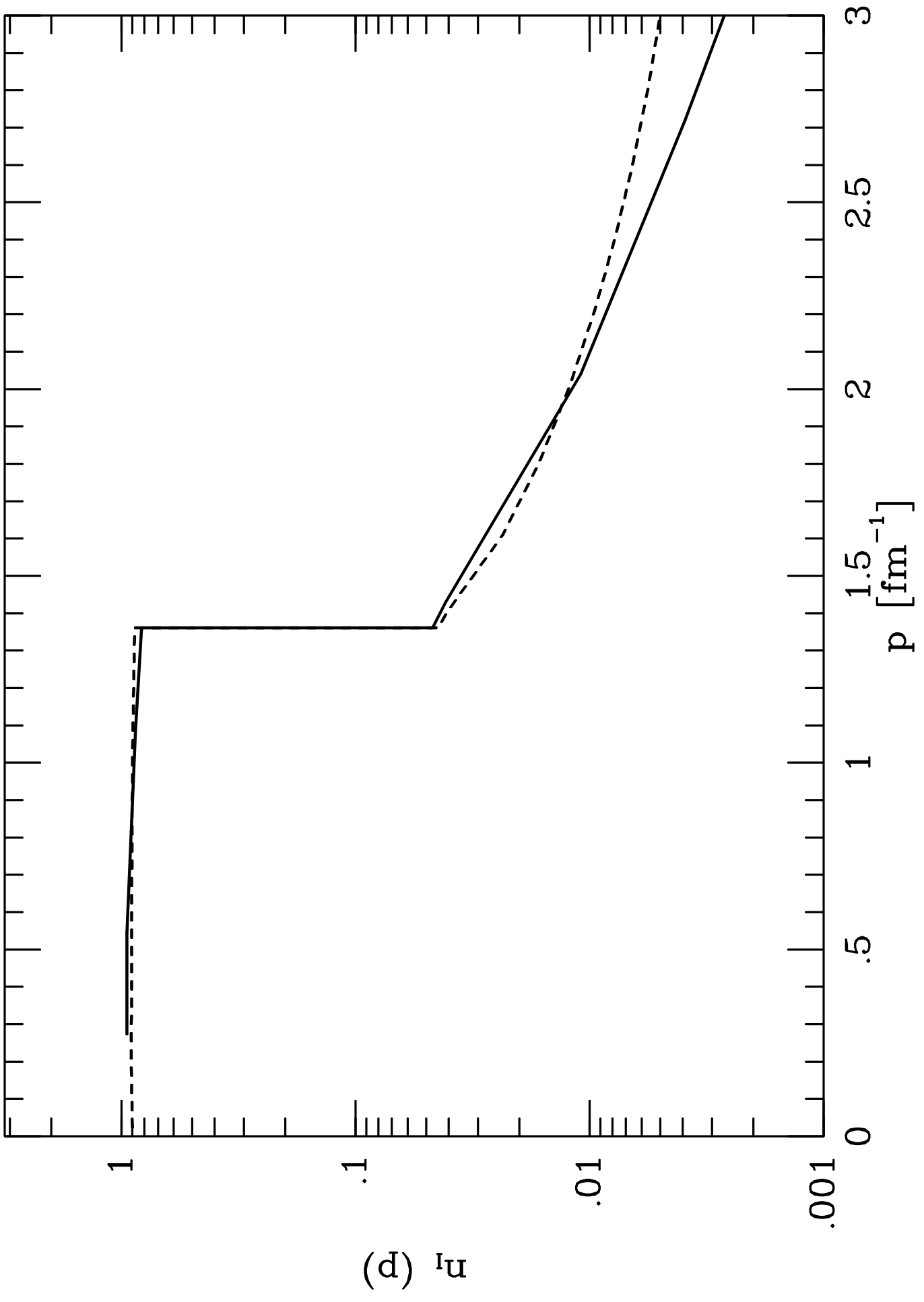
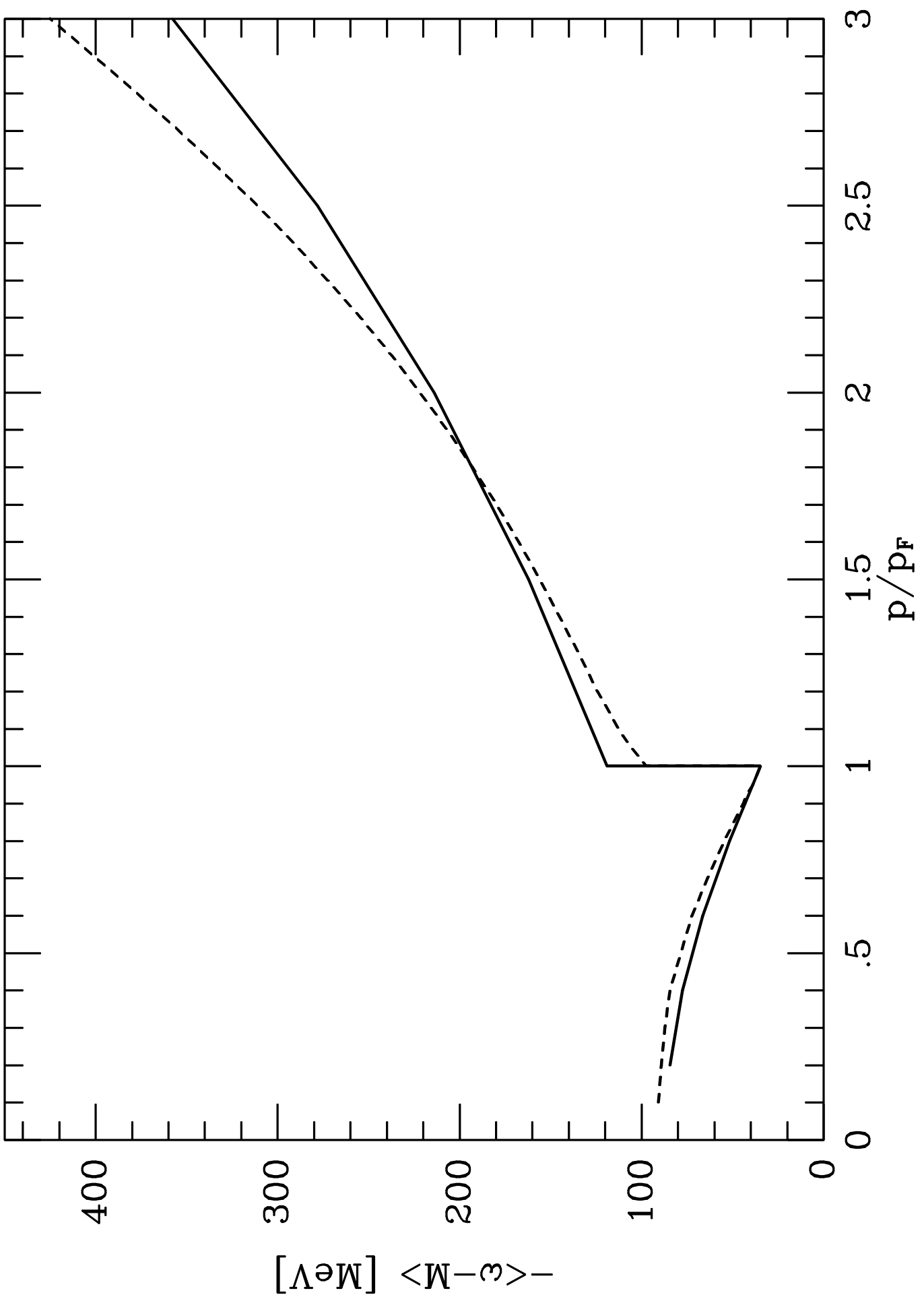
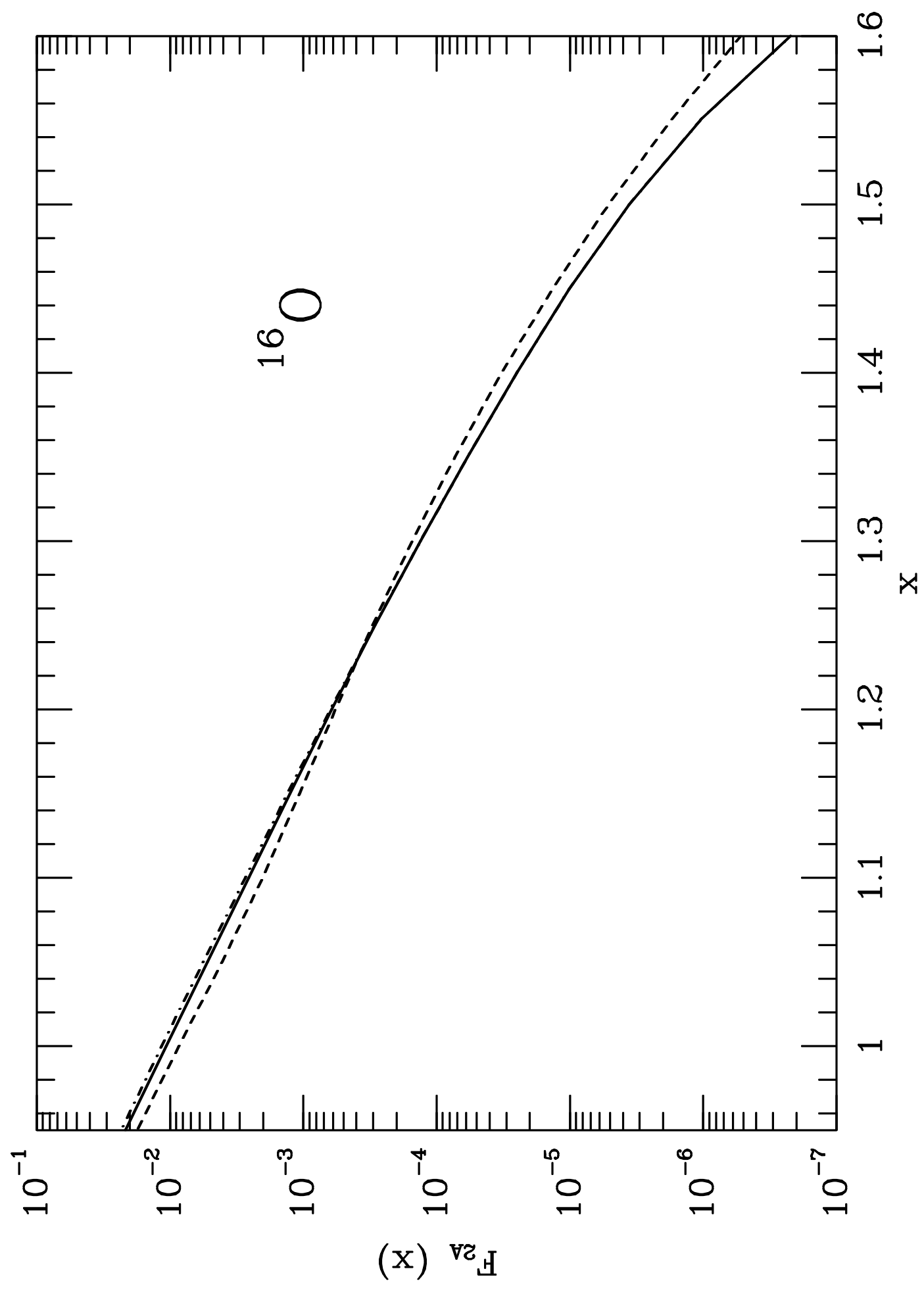
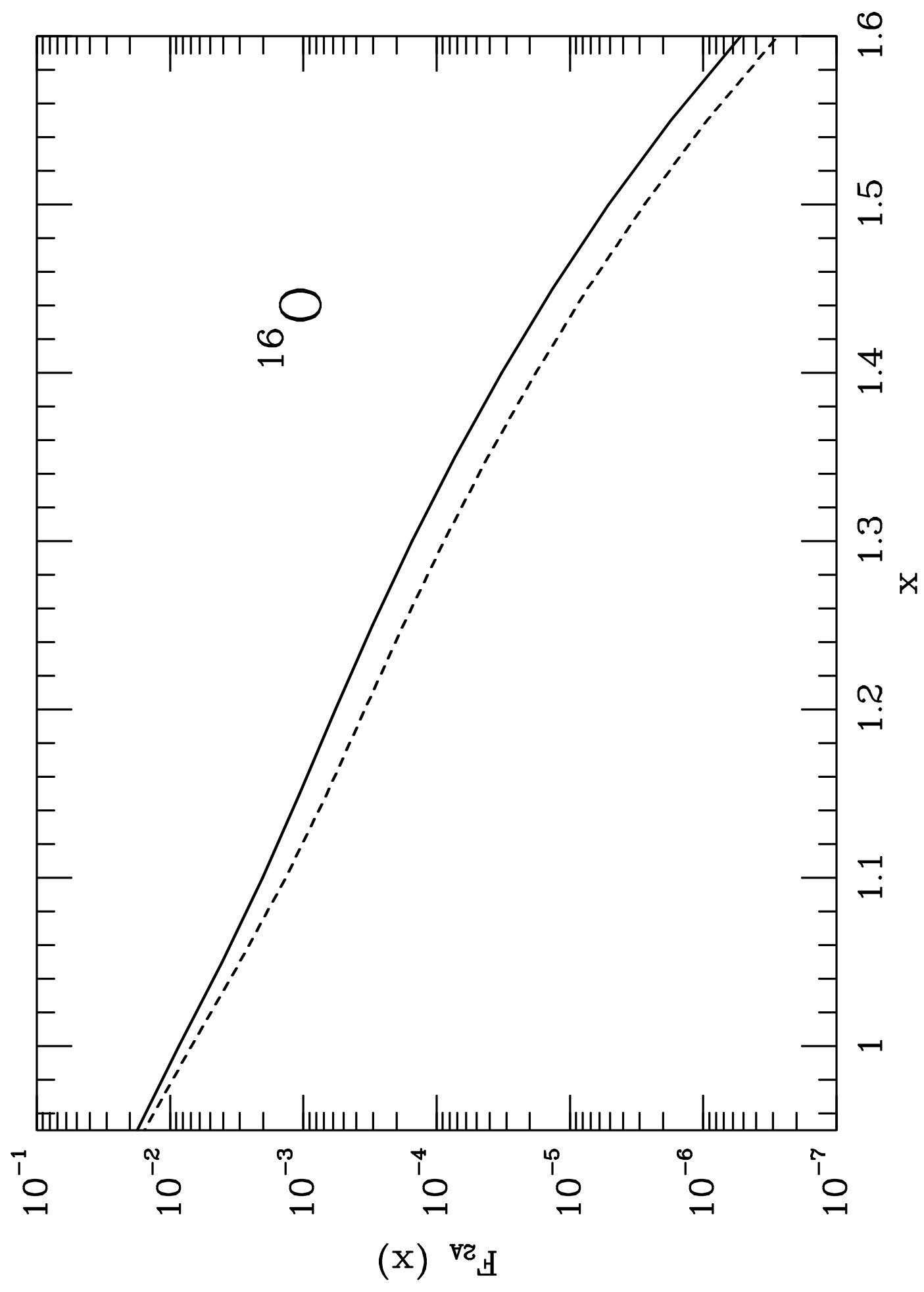


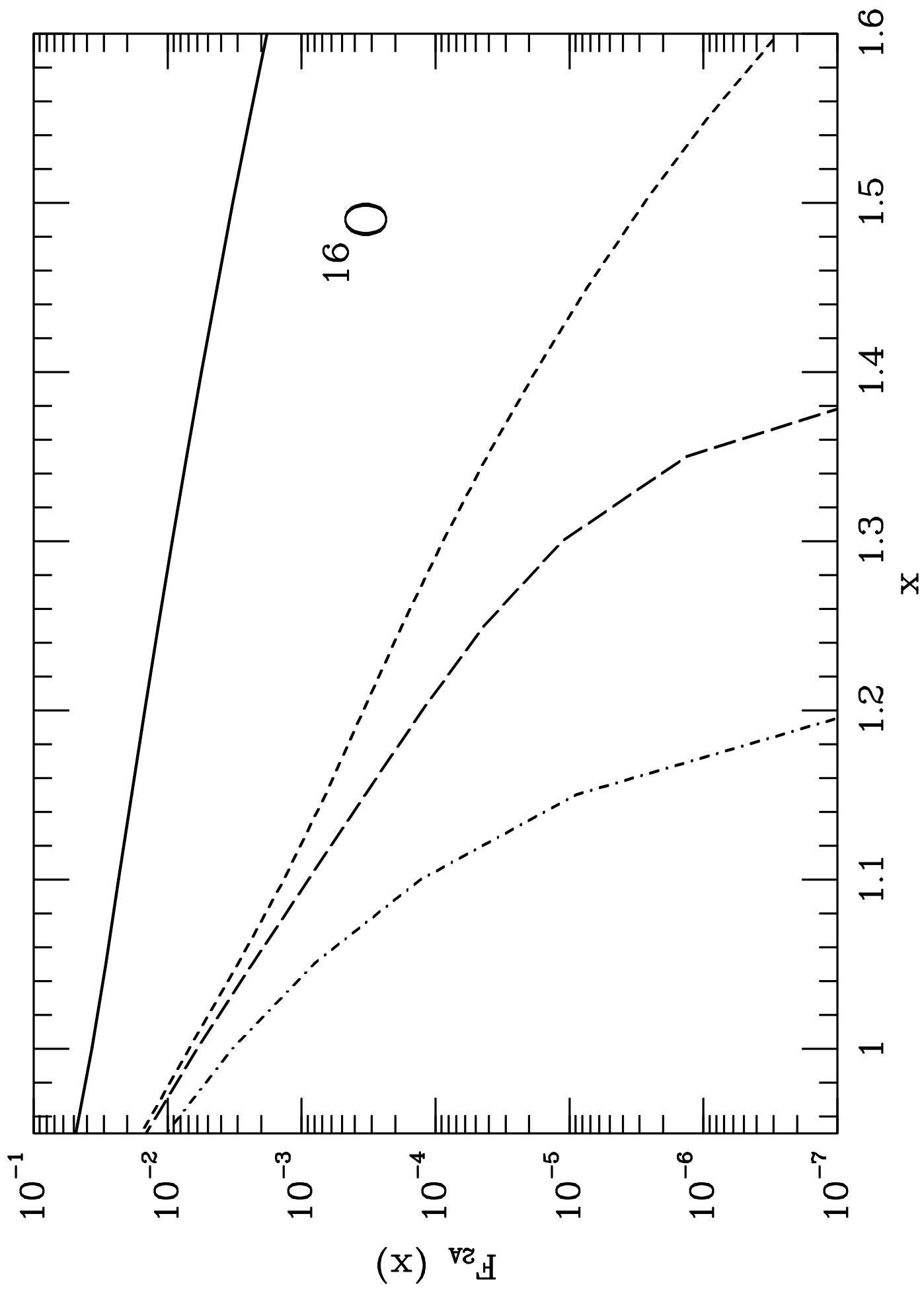
Fig. 3

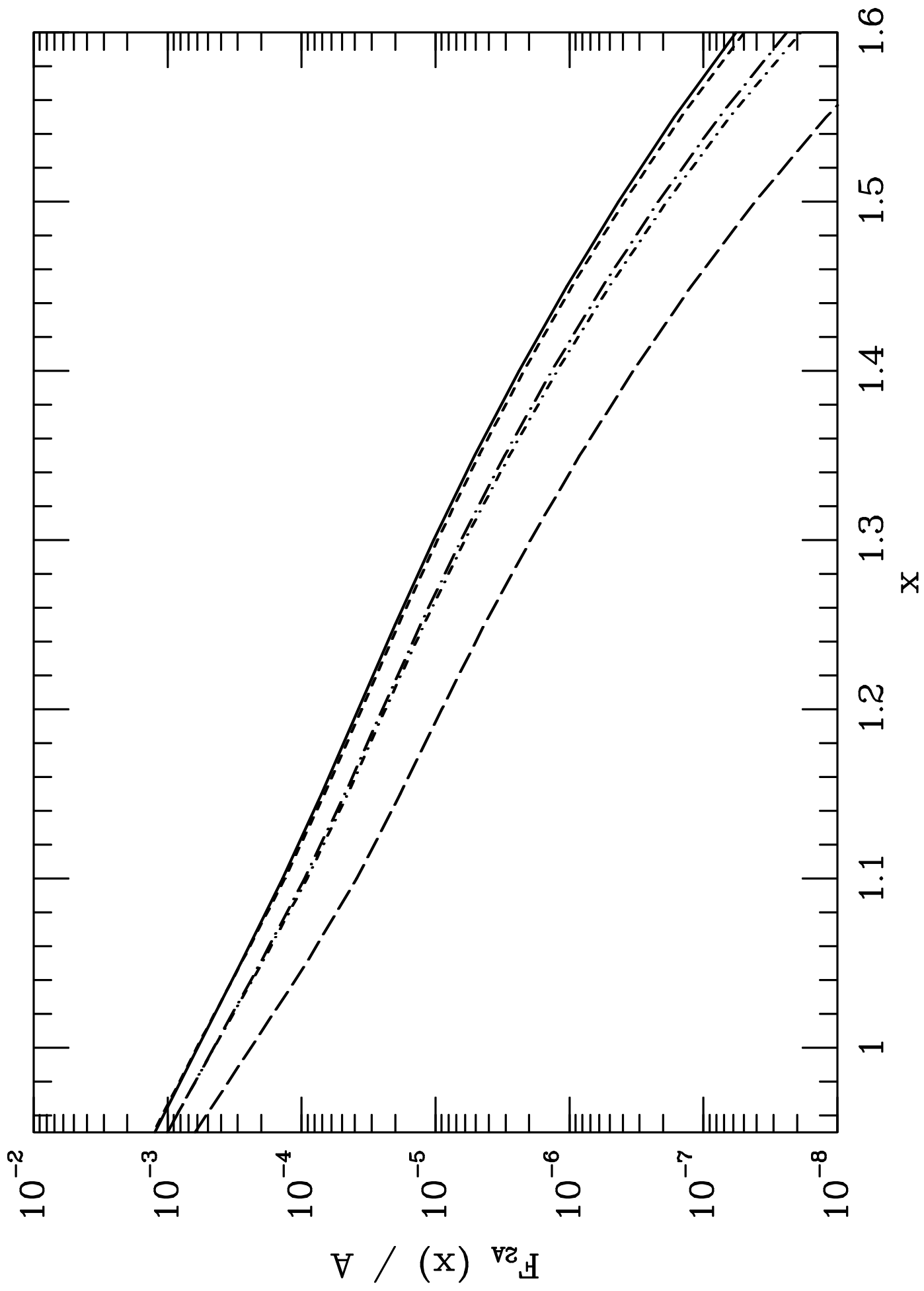












A MESONIC DECAY IN NUCLEI AND THE OCCUPATION NUMBER

P. FERNÁNDEZ DE CÓRDOBA and E. OSET

*Departamento de Física Teórica and IFIC, Centro Mixto Universidad de Valencia-CSIC,
46100 Burjassot, Valencia, Spain*

Received 6 November 1990

Abstract: The Pauli exclusion principle forbids mesonic Λ decay in nuclear matter at normal density and leads to very small values of the mesonic width in heavy nuclei. The intuitive idea is that, because the Fermi sea is only partly occupied, the mesonic width should be of the order of $1 - n(k) \approx 0.15$ times the free width. The problem is analyzed in detail in terms of the Lehmann representation for the nucleon propagator and the intuitive idea is found to be only a beautiful fallacy.

1. Introduction

Assume a Λ particle at rest in a slab of infinite nuclear matter at normal density. In the mesonic decay, $\Lambda \rightarrow N\pi$, the nucleon carries about 100 MeV/ c momentum while the Fermi momentum is $k_F = 269$ MeV/ c . Hence this decay is forbidden by the Pauli exclusion principle. In finite nuclei the Λ momentum distribution, together with the fact that k_F is smaller in the surface, lead to non-zero values of the Λ mesonic width, Γ_m . Actual evaluations of Γ_m with a finite nucleus treatment of the Pauli blocking¹⁾, or infinite nuclear matter treatment complemented with the local density approximation²⁾, are in good common agreement and lead to widths in heavy nuclei around 10^{-4} times the free Λ width. Experimentally the existence of the mesonic decay channel, as well as a fast decrease of Γ_m with the mass number, are well established³⁻⁵⁾. One of the interesting findings^{2,6)} in the Λ mesonic decay is that renormalization of the pion properties in matter leads to a substantial increase of Γ_m with respect to the unrenormalized results. The reason is that for a given momentum of the pion the attraction of the medium lowers the pion energy, thus giving more energy to the nucleon and increasing the chances that it overcomes the Fermi energy. A different formulation of this effect, leading to the same conclusion, can be seen in refs.^{7,8)}. There the pion wave carries a certain energy but, inside the nucleus, picks up larger momentum components than those corresponding to the pion on-shell and this makes the population of the unoccupied states easier.

A different effect seems intuitively to lead to very drastic changes in Γ_m . As noted before, the reason for the small values in Γ_m for heavy nuclei is Pauli blocking, but the results are based on an uncorrelated Fermi sea²⁾ or exact shell-model nuclear wave functions¹⁾. However, we know that when nuclear correlations are considered,

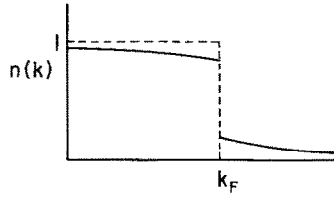


Fig. 1. Schematic representation of the nucleon occupation number for an interacting Fermi sea.

the Fermi sea is only partly occupied and some strength is moved to states above the Fermi sea ⁹⁾. This is depicted qualitatively in fig. 1. The occupation number for states of momentum k below the Fermi momentum is $n(k) \approx 0.85$ or equivalently the level of unoccupancy around 15%. We could expect that these states are occupied by the nucleons from the $A \rightarrow N\pi$ decay and hence Γ_m would saturate at values around $0.15 \Gamma_{free}$, up to small corrections for the absorption of the final pions (low-energy pions). At first sight, this argument appears correct and in fact it has already been exploited in the literature. Indeed, in ref. ¹⁰⁾ the level of occupancy was assumed to be 90% and using the above arguments it was concluded there that the mesonic width for nuclei with $A \approx 100$ was substantially increased with respect to a calculation assuming full occupancy of the states. In what follows we make a detailed derivation of the mesonic width and show that, although intuitive and appealing, the idea is not correct.

2. Formal derivation of the Λ width

We follow the derivation of the mesonic Λ width as given in refs. ^{2,11)}. We start from a basic lagrangian coupling the Λ to the $N\pi$ system given by

$$L_{\pi\Lambda N} = Gm_\pi^2 \bar{\Psi}_N (A - B\gamma_5) \boldsymbol{\tau} \boldsymbol{\Phi} \Psi_\Lambda + \text{h.c.}, \tag{1}$$

with G the weak coupling constant and A, B the terms with parity violation and parity conservation, respectively. We have $(Gm_\pi^2)^2/8\pi = 1.945 \times 10^{-15}$, m_π the pion mass, $A = 1.06$, $B = 7.10$. We assume the Λ to behave as the state $|\frac{1}{2} - \frac{1}{2}\rangle$ of an isospin doublet and then eq. (1) implements automatically the $\Delta T = \frac{1}{2}$ rule ¹²⁾.

In order to obtain the Λ decay width, we evaluate the Λ self-energy, Σ^* , corresponding to the diagram in fig. 2 and then use $\Gamma = -2 \text{Im} \Sigma^*$. After a non-

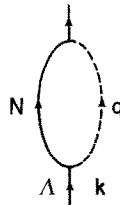


Fig. 2. Feynman diagram for the Λ self-energy.

relativistic reduction ¹¹), we obtain

$$\Sigma^*(k) = 3i(Gm_\pi^2)^2 \int \frac{d^4q}{(2\pi)^4} \left[A^2 + \left(\frac{B}{2M} \right)^2 q^2 \right] G(k-q) D_0(q), \tag{2}$$

with M the nucleon mass, $D_0(q)$ the free pion propagator and $G(p)$ the nucleon propagator. For a Fermi sea of nucleons the non-interacting nucleon propagator is

$$G(k-q) = \frac{1 - n_0(\mathbf{k}-\mathbf{q})}{k^0 - q^0 - \mathcal{E}(\mathbf{k}-\mathbf{q}) + i\varepsilon} + \frac{n_0(\mathbf{k}-\mathbf{q})}{k^0 - q^0 - \mathcal{E}(\mathbf{k}-\mathbf{q}) - i\varepsilon}, \tag{3}$$

with $n_0(\mathbf{p}) = 1$ for $|\mathbf{p}| \leq k_F$ and $n_0(\mathbf{p}) = 0$ for $|\mathbf{p}| > k_F$, (k_F is the Fermi momentum).

Hence, for the variable q^0 we get the pole structure shown in fig. 3 for the integrand of eq. (2). This suggests that we perform the Wick rotation indicated in the figure.

We use Cauchy's theorem

$$\begin{aligned} & \int_{-\infty}^{\infty} dq^0 + \int_{i\infty}^{-i\infty} dq^0 + \int_C dq^0 \\ &= 2\pi i \theta(k^0 - \mathcal{E}(\mathbf{k}-\mathbf{q})) \text{Res}(q^0 = k^0 - \mathcal{E}(\mathbf{k}-\mathbf{q}), 1 - n_0 \text{ term}) \\ & \quad - 2\pi i \theta(\mathcal{E}(\mathbf{k}-\mathbf{q}) - k^0) \text{Res}(q^0 = k^0 - \mathcal{E}(\mathbf{k}-\mathbf{q}), n_0 \text{ term}) \end{aligned} \tag{4}$$

and the fact that the integral along the circles vanishes at infinity, plus the fact that the integral along the imaginary axis gives rise to a real part in Σ^* , and then we obtain

$$\begin{aligned} \text{Im } \Sigma^*(k) &= 3(Gm_\pi^2)^2 \text{Im} \int \frac{d^3q}{(2\pi)^3} \left[A^2 + \left(\frac{B}{2M} \right)^2 q^2 \right] \\ & \times \frac{1}{k^0 - \mathcal{E}(\mathbf{k}-\mathbf{q}) - \omega(\mathbf{q}) + i\varepsilon} \frac{1}{k^0 - \mathcal{E}(\mathbf{k}-\mathbf{q}) + \omega(\mathbf{q}) - i\varepsilon} \\ & \times \{ \theta(k^0 - \mathcal{E}(\mathbf{k}-\mathbf{q}))(1 - n_0(\mathbf{k}-\mathbf{q})) - \theta(\mathcal{E}(\mathbf{k}-\mathbf{q}) - k^0)n_0(\mathbf{k}-\mathbf{q}) \}. \end{aligned} \tag{5}$$

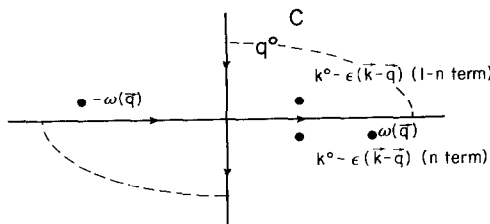


Fig. 3. Analytical structure of the integrand of eq. (2) in the complex variable q^0 .

The second term in the curly brackets does not contribute since $k^0 = M_\Lambda - M - B_\Lambda \approx 160$ MeV (B_Λ is the binding energy of the Λ) and the maximum value of $\mathcal{E}(\mathbf{k} - \mathbf{q}) = (\mathbf{k} - \mathbf{q})^2/2M$, with $\mathbf{k} - \mathbf{q}$ below the Fermi surface, is $k_F^2/2M = 39$ MeV at $\rho = \rho_0$. This value becomes zero when the potential energy of the nucleons is included, as we do below.

Hence

$$\Gamma(k) = 3(Gm_\pi^2)^2 \int \frac{d^3q}{(2\pi)^3} \left[A^2 + \left(\frac{B}{2M} \right)^2 q^2 \right] \times \theta(k^0 - \mathcal{E}(\mathbf{k} - \mathbf{q}))(1 - n_0(\mathbf{k} - \mathbf{q})) \frac{1}{2\omega(\mathbf{q})} 2\pi\delta(k^0 - \mathcal{E}(\mathbf{k} - \mathbf{q}) - \omega(\mathbf{q})) \quad (6)$$

with $\omega(\mathbf{q}) = (q^2 + m_\pi^2)^{1/2}$, which exhibits explicitly the Pauli blocking factor in the Λ decay. The θ -function can be omitted in the presence of the δ -function.

Eq. (6) gives the Λ width in nuclear matter. In order to obtain the width in finite nuclei we make use of the local density approximation and take the average over the momentum of the Λ in the nucleus, as was done in ref. ²⁾. Hence

$$\Gamma = \int d^3r |\varphi_\Lambda(\mathbf{r})|^2 \int d^3k |\tilde{\varphi}_\Lambda(\mathbf{k})|^2 \Gamma(k, \rho(\mathbf{r})). \quad (7)$$

We take a Fermi distribution ¹³⁾ for the density of the nuclei and for the Λ wave function we take the $1s_{1/2}$ wave function of a harmonic oscillator with parameter $\hbar\omega = [45A^{-1/3} - 25A^{-2/3}]$ MeV (where A is the mass number). The binding of the Λ is taken as the lowest eigenvalue of a Woods-Saxon potential with depth 32 MeV and the shape of the nuclear density. The magnitude $\mathcal{E}(\mathbf{k} - \mathbf{q})$ is the nucleon energy

$$\mathcal{E}(\mathbf{p}) = \frac{\mathbf{p}^2}{2M} + V_N(\mathbf{r}) \quad (8)$$

and $V_N(\mathbf{r})$ is taken from the Thomas-Fermi model

$$V_N(\mathbf{r}) = -\frac{1}{2M} (3\pi^2\rho(\mathbf{r})/2)^{2/3}. \quad (9)$$

We show the results for several nuclei in table 1. As we can see, for heavy nuclei Γ_m/Γ_{free} is of the order of 10^{-4} .

TABLE 1
 Γ_m/Γ_{free}

	¹⁶ O	⁴⁰ Ca	²⁰⁸ Pb
Fermi sea propagator	8.63×10^{-2}	1.84×10^{-2}	1.95×10^{-4}
Spectral function representation	9.20×10^{-2}	2.06×10^{-2}	3.06×10^{-4}

It might look at first sight as though an improved result could be obtained by replacing $n_0(\mathbf{p})$ in eq. (3) by the occupation number found in realistic calculations of an interacting Fermi sea⁹⁾, $n(\mathbf{k})$. Then, since $n(\mathbf{k}) \approx 0.85$ for nucleons with momentum smaller than k_F and the δ -function in eq. (6) allows only such momenta (for small values of k), we should expect a width in nuclear matter of about $1 - n(k) \approx 0.15$ times the free width. However, we show below that such a procedure is highly incorrect.

Indeed, the proper way to include the effects of the nuclear interaction is to replace the non-interacting nucleon propagator of eq. (3) by the exact interacting nucleon propagator in the nucleus. This propagator can be written by means of the Lehmann representation in terms of the spectral functions for particles and holes $S_p(\omega, \mathbf{k})$, $S_h(\omega, \mathbf{k})$ as¹⁴⁾

$$G(k^0, \mathbf{k}) = \int_{-\infty}^{\mu} \frac{S_h(\omega, \mathbf{k})}{k^0 - \omega - i\epsilon} d\omega + \int_{\mu}^{\infty} \frac{S_p(\omega, \mathbf{k})}{k^0 - \omega + i\epsilon} d\omega, \quad (10)$$

with μ the chemical potential.

By substituting the new nucleon propagator, eq. (10), in eq. (2) and performing the Wick rotation again we obtain

$$\begin{aligned} \text{Im } \Sigma^*(k) = & 3(Gm_{\pi}^2)^2 \text{Im} \int \frac{d^3q}{(2\pi)^3} \left[A^2 + \left(\frac{B}{2M} \right)^2 q^2 \right] \\ & \times \left(- \int_{-\infty}^{\mu} d\omega S_h(\omega, \mathbf{k} - \mathbf{q}) \theta(\omega - k^0) \frac{1}{k^0 - \omega - \omega(\mathbf{q}) + i\epsilon} \right. \\ & \times \frac{1}{k^0 - \omega + \omega(\mathbf{q}) - i\epsilon} + \int_{\mu}^{\infty} d\omega S_p(\omega, \mathbf{k} - \mathbf{q}) \theta(k^0 - \omega) \\ & \left. \times \frac{1}{k^0 - \omega - \omega(\mathbf{q}) + i\epsilon} \frac{1}{k^0 - \omega + \omega(\mathbf{q}) - i\epsilon} \right). \quad (11) \end{aligned}$$

Once again the hole part (S_h term) does not contribute because ω is restricted to below $\mu \approx k_F^2/2M$ and cannot be bigger than k^0 . The same holds when the potential energy of the nucleons is included. This is exactly the same argument as in the non-interacting case. Hence we finally obtain

$$\begin{aligned} \Gamma(k) = & 3(Gm_{\pi}^2)^2 \int \frac{d^3q}{(2\pi)^3} (A^2 + (B/2M)^2 q^2) \frac{1}{2\omega(\mathbf{q})} \\ & \times \int_{\mu}^{\infty} d\omega S_p(\omega, \mathbf{k} - \mathbf{q}) 2\pi \delta(k^0 - \omega - \omega(\mathbf{q})), \quad (12) \end{aligned}$$

where we have omitted the θ -function because it becomes inoperative in the presence of the δ -function.

We recover eq. (6) by noting that in the non-interacting case we have

$$S_p(\omega, \mathbf{k} - \mathbf{q}) = \theta(|\mathbf{k} - \mathbf{q}| - k_F) \delta\left(\omega - \frac{(\mathbf{k} - \mathbf{q})^2}{2M}\right),$$

$$\mu = k_F^2/2M. \tag{13}$$

In practice for $|\mathbf{k}| > k_F$, $S_p(\omega, \mathbf{k})$ peaks around $\mathcal{E}(\mathbf{k})$ (see fig. 4a) ($\mathcal{E}(\mathbf{k})$ is the physical energy for a particle of momentum \mathbf{k} in the medium, $k^2/2M + \text{Re } \Sigma_N$). We make arguments using the kinetic energy for simplicity. The extension to include the potential energy is straightforward. Hence the contributions from eqs. (6) and (12) for values of $|\mathbf{k} - \mathbf{q}| > k_F$ are very similar. For $\mathbf{k} = 0$ this contribution is however zero in nuclear matter at $\rho = \rho_0$ because the δ -function forces $|\mathbf{q}| < k_F$ in eq. (6). This is also the case with eq. (12), since with $k^0 - \omega < k^0 - \mu$ no values of $|\mathbf{q}|$ above k_F are allowed at $\rho = \rho_0$ and for a wide range of densities below ρ_0 only values of $|\mathbf{q}|$ below k_F are allowed. However, eq. (12) has now the virtue of allowing the contribution of components with $|\mathbf{k} - \mathbf{q}| < k_F$. This is so because $S_p(\omega, \mathbf{k})$ for $|\mathbf{k}| < k_F$ does not vanish, but it has a shape like the one shown in fig. 4b, instead of the peak of fig. 4a for $|\mathbf{k}| > k_F$.

Next, imagine for a moment that we can replace ω in the argument of the δ -function in eq. (12) by an average value $\omega \approx (\mathbf{k} - \mathbf{q})^2/2M$ and then use the property¹⁵⁾

$$\int_{\mu}^{\infty} d\omega S_p(\omega, \mathbf{k}) = 1 - n(\mathbf{k}), \tag{14}$$

where $n(\mathbf{k})$ is the occupation number, $\langle 0|a^+(\mathbf{k})a(\mathbf{k})|0\rangle$.

We obtain again eq. (6), however, with $n_0(\mathbf{k} - \mathbf{q})$ replaced by $n(\mathbf{k} - \mathbf{q})$. Once again, with values of $n(\mathbf{k} - \mathbf{q}) \approx 0.85$ for $|\mathbf{k} - \mathbf{q}| < k_F$ we would expect $\Gamma \approx 0.15 \Gamma_{\text{free}}$. However there are several fallacies in this argumentation. First is that we cannot replace ω by $|\mathbf{k} - \mathbf{q}|^2/2M$ if this momentum is going to be below the Fermi surface, because ω is strictly forced to be larger than μ . This means that with $\omega > \mu$ in eq. (12), the range of \mathbf{q} momenta allowed by the δ -function is much more restricted than in the integral for the free width (eq. (6) omitting $n_0(\mathbf{k} - \mathbf{q})$). On the other hand eq. (14) requires the integration over ω in the whole range allowed, but if we have the combination $S_p\delta$ of eq. (12) it is clear that there are severe restrictions in the ω

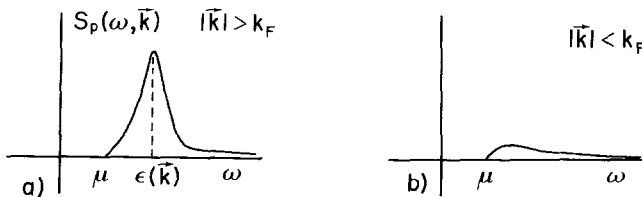


Fig. 4. Schematic representation of the spectral function, $S_p(\omega, |\mathbf{k}|)$, as a function of ω for two cases, (a) $|\mathbf{k}| > k_F$; (b) $|\mathbf{k}| < k_F$. $\mathcal{E}(\mathbf{k})$ is the physical energy associated to the particle with momentum \mathbf{k} .

integration. This is clearly visualized if we take $\mathbf{k} = \mathbf{0}$ and use the \mathbf{q} integration to eliminate the δ -function. Eq. (6) gives us a result proportional to $1 - n_0(\mathbf{q})$ while eq. (12) would give us something proportional to

$$\int_{\mu}^{k^0 - m_{\pi}} d\omega S_p(\omega, \mathbf{q}) \Big|_{q = [(k^0 - \omega)^2 - m_{\pi}^2]^{1/2}}. \quad (15)$$

As we can see we have two problems if we wish to extract $1 - n(\mathbf{q})$ from eq. (15). The first one is that \mathbf{q} is not fixed but is a function of ω in the integrand. The second one is that the integration variable now runs from μ to $k^0 - m_{\pi}$ instead of from μ to ∞ , which restricts the integration domain very much.

The above discussions have illustrated clearly that substituting $1 - n_0(\mathbf{k} - \mathbf{q})$ in eq. (6) by $1 - n(\mathbf{k} - \mathbf{q})$ is highly fallacious and overcounts the contribution to Γ .

It would however, be, interesting to compute Γ of eq. (12) with a realistic spectral function. $S_p(\omega, k)$ is given in terms of the nucleon self-energy by ¹⁶⁾

$$S_p(\omega, k) = -\frac{1}{\pi} \frac{\text{Im } \Sigma(\omega, k)}{(\omega - k^2/2M - \text{Re } \Sigma(\omega, k))^2 + (\text{Im } \Sigma(\omega, k))^2} \quad \text{for } \omega > \mu. \quad (16)$$

So all that is needed is to evaluate the nucleon self-energy in the whole range of energy and momentum.

For such a purpose we have followed a rather phenomenological line and taken a model ¹⁸⁾ that relies upon the elementary NN cross sections, satisfies the low-density theorem ¹⁷⁾, has the right analytical properties and introduces a quenching mechanism to reproduce the results of ref. ⁹⁾ at high densities. We do not elaborate further on the model but the results that it produces are rather similar to those of ref. ¹⁶⁾, which is sufficiently realistic for the purposes of this paper.

Once $\Gamma(k)$ is calculated as a function of ρ with eq. (12), we take the averages of eq. (7) and evaluate Γ for different nuclei. The results can be seen in the second row of table 1. Once again the results range from 10^{-1} in ^{16}O to 10^{-4} in ^{208}Pb . The remarkable thing to note is that the results are very similar to those obtained with the non-interacting Fermi sea with variations of the order of 6% in light nuclei and 45% in heavy nuclei. However, there is nothing close to the change in three orders of magnitude as naively we could expect.

The renormalization of the pion wave has, however, drastic consequences as noted in refs. ^{2,7,8)}. On the one hand the real part of the pion-nucleus optical potential, attractive for the pions from the Λ mesonic decay, reduces the pion energy for a certain value of the momentum and the nucleons carry more energy thus reducing the effect of Pauli blocking. On the other hand the imaginary part of the potential takes into account the loss of pion flux. However, one should note that a distortion of the pion by the full optical potential removes from the pion channel all events that go into quasielastic collisions or into π absorption ^{7,8)}. Since the pions that undergo quasielastic collisions do not disappear, one should not remove them in the calculations. This means that the only pions that should be removed are those

which undergo pion absorption. We have done this here using the same procedure as in ref. ¹⁹⁾ and we observe reductions of 13% in ¹⁶O and 30% in ²⁰⁸Pb with respect to those in table 1.

3. Conclusions

We have analyzed in detail the appealing idea that because Pauli blocking is responsible for a large reduction of the *A* mesonic width in nuclei, the fact that the Fermi sea is only partly occupied would have a large effect on this mesonic width, giving rise to values of the order of 10% of the free width. A thorough study of the mesonic decay was done by using the spectral representation of the nucleon propagator in the medium, which allowed us to see the fallacies that go into that appealing idea. The fact that energy has to be conserved in the reaction puts severe constraints that did not allow the *A* mesonic width in the medium to be represented in terms of the occupation number of an interacting Fermi sea. The actual results by using a realistic spectral function representation lead to mesonic widths which differ only at the level of 6% in light nuclei to 45% in heavy nuclei with respect to those obtained from a non-interacting Fermi sea. With the effects on the nucleon renormalization being so small, the effects on the pion renormalization studied before ^{2,6-8)} stand as the major factor in enhancing the *A* mesonic decay with respect to the calculations based on free nucleons and pions but taking into account the Pauli blocking.

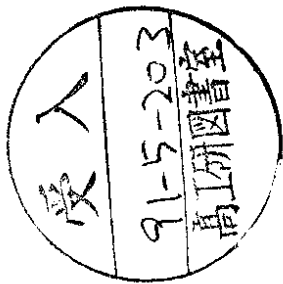
The ideas discussed here are also of particular value in order to put into the proper context some approximations made in the literature where the nucleon propagator is approximated by the non-interacting one, eq. (3), substituting $n_0(\mathbf{k})$ by $n(\mathbf{k})$. As shown clearly here, such substitution can be highly unrealistic in many problems similar to the present one where energy conservation is at stake.

This paper is partially supported by CICYT. One of us, P. Fernández de Córdoba, wishes to acknowledge a fellowship from the Consejo Superior de Investigaciones Científicas. Discussions with V.R. Pandharipande and A. Polls are appreciated.

References

- 1) H. Bandō and H. Takaki, Prog. Theor. Phys. **72** (1984) 106
- 2) E. Oset and L.L. Salcedo, Nucl. Phys. **A443** (1985) 704
- 3) A. Montwill *et al.*, Nucl. Phys. **A234** (1974) 413
- 4) C.B. Dover and G.E. Walker, Phys. Reports **89** (1982) 1
- 5) R. Grace *et al.*, Phys. Rev. Lett. **55** (1985) 1055
- 6) E. Oset and L.L. Salcedo, Nucl. Phys. **A450** (1986) 371c
- 7) K. Itonaga, T. Motoba and H. Bandō, Z. Phys. **A330** (1988) 209
- 8) T. Motoba, K. Itonaga and H. Bandō, Nucl. Phys. **A489** (1988) 683
- 9) S. Fantoni and V.R. Pandharipande, Nucl. Phys. **A427** (1984) 473
- 10) H. Bandō and H. Takaki, Phys. Lett. **B150** (1985) 409
- 11) E. Oset, P. Fernández de Córdoba, L.L. Salcedo and R. Brockmann, Phys. Reports **188** (1990) 79
- 12) B.H.J. McKellar and B.F. Gibson, Phys. Rev. **C30** (1984) 322

- 13) H. De Vries, C.W. de Jager and C. de Vries, *Atomic Data Nucl. Data Tables* **36** (1987) 495
- 14) A.L. Fetter and J.D. Walecka, *Quantum theory of many particle systems* (McGraw-Hill, New York, 1971)
- 15) R.D. Mattuck, *A guide to Feynman diagrams in the many body problem* (McGraw-Hill, New York, 1976)
- 16) A. Ramos, A. Polls and W.H. Dickhoff, *Nucl. Phys.* **A503** (1989) 1
- 17) C.B. Dover, J. Hüfner and R.H. Lemmer, *Ann. of Phys.* **66** (1971) 248
- 18) P. Fernández de Córdoba, *Tesina de Licenciatura, Universidad de Valencia* (1990)
- 19) E. Oset and M.J. Vicente-Vacas, *Nucl. Phys.* **A454** (1986) 637



IFIC/91-7
FTUV/91-7

SEMIPHENOMENOLOGICAL APPROACH TO NUCLEON
PROPERTIES IN NUCLEAR MATTER

P. Fernández de Córdoba and E. Oset

*Departamento de Física Teórica and IFIC,
Centro Mixto Universidad de Valencia CSIC,
46100 Burjassot (Valencia) Spain.*

Abstract

We have evaluated the nucleon selfenergy in a model that has proper analytical properties, satisfies the low density theorem and provides values of $\text{Im}\Sigma$ for high densities comparable to those of realistic microscopic approaches. The model, however, relies only upon the NN experimental cross sections and the empirical spin-isospin interaction, which induces an important polarization of the medium. The results obtained for the spectral functions, occupation numbers and effective masses are quite reasonable. However, the sharp peak of the ω and effective masses found in approaches relying in central potential models is not found here. We discuss this point and show the importance of performing realistic microscopical calculations incorporating tensor forces, satisfying the low density theorem and considering the polarization of the medium. The model does not give the absolute value of the nucleon selfenergy but only differences with respect to the Fermi energy. On the other hand it provides an easy and efficient way of evaluating many of the nucleon properties in the nuclear medium.

1.- INTRODUCTION

The nucleon properties in nuclear matter have been thoroughly studied microscopically with several levels of approximation (see ref. ¹⁾ for a review). Most calculations rely upon the second order Brueckner Hartree Fock expansion¹⁾, although some steps leading to selfconsistent schemes have been given^{2,3)}. Non perturbative schemes as the hypernetted chain have also brought their share of progress to the field⁴⁾. With this wealth of microscopic work one can wonder what new information can bring along a semiphenomenological analysis. The answer can come from several viewpoints. On the one hand it is interesting to trace back the origin of several nucleon properties to measurable magnitudes of the nucleon-nucleon interaction, such as the scattering cross section, rather than to the nucleon-nucleon interaction itself through the black box of involved many body calculations. On the other hand one can make use of the low density theorems for the nucleon selfenergy and implement them automatically in the semiphenomenological scheme. This guaranties that the low density regime is accurately given, which is by no means true in many microscopical calculations. Finally in many applications in Nuclear Physics one needs only partial information about the nucleon properties which can be easily provided by this semiphenomenological model without the need to recur to sophisticated and elaborate calculations.

With the model we will be able to calculate nucleon properties in nuclear matter as effective masses, imaginary part of the nucleon selfenergy, spectral functions, occupation numbers etc. However we renounce from the beginning to obtain the absolute value of the real part of the nucleon selfenergy, and the nuclear binding as a consequence. This piece of information is more deeply tied to details of the nucleon-nucleon interaction and escapes our simplified analysis. In the study of many nuclear processes this information is however unnecessary since the nucleon selfenergy enters only through differences of selfenergies for two nucleon lines and such information can still be provided by the

semiphenomenological model.

2.- THE LOW DENSITY THEOREM FOR THE NUCLEON SELFENERGY.

At low nuclear densities, ρ , we can make use of an important property which relates the nucleon selfenergy with the NN elementary scattering amplitude. The theorem states that the nucleon selfenergy in nuclear matter is given by^{5,6)}

$$\Sigma(k^0, \vec{k}) = t(k^0, \vec{k})\rho \quad (1)$$

$\rho \rightarrow 0$

where t is the average over the Fermi sea and spin of the forward scattering matrix for the collision of the nucleon with momentum (k^0, \vec{k}) and a nucleon of the Fermi sea.

The normalization of the invariant t matrix is such that the NN cross section is given by

$$\frac{d\sigma}{d\Omega} = \frac{1}{4\pi^2} \frac{M^4}{s} \sum \sum |t|^2 \quad (2)$$

with M the nucleon mass, and $s = (p_1 + p_2)^2$ (p_1, p_2 momenta of the initial nucleons). We obtain an interesting consequence of eq. (1) by taking its imaginary part

$$\begin{aligned} \text{Im} \Sigma(k^0, \vec{k}) &= \text{Im} t(k^0, \vec{k})\rho \\ &= -\frac{2k_{\text{CM}}\sqrt{s}}{2M} \sigma_{\text{tot}} \rho = -\frac{k}{2M} \sigma_{\text{tot}} \rho = -\frac{1}{2} \sigma_{\text{tot}} v \rho \end{aligned} \quad (3)$$

with v the velocity of the particle and σ_{tot} the total NN cross section. In eq. (3) we have used the optical theorem and the fact that $k_{\text{CM}} = kM/\sqrt{s}$, assuming the nucleons of the Fermi sea at rest.

Eq. (3) puts an important constraint on Σ providing a model independent limit which is easy to check. Most models used in the literature violate this theorem, at some point, because of the approximate NN potentials used or because of the approximations used in the solution of the many body problem. The work of refs. 2, 3) is one example of it. Indeed, relying upon the central part of the NN interaction and neglecting tensor forces, as one increases the nucleon energy the NN cross section is progressively underestimated⁷⁾.

The test of eq. (3) is very useful since it allows us to have an idea of the accuracy expected from a theory or the kinematical regions where the results are unreliable.

There is another point worth mentioning. As we see, in eq. (3) we have the total NN cross section. At nucleon momenta beyond 1 GeV/c the pion production inelastic channels open up and the NN cross section contains a fair amount of inelastic cross section. Pion production can also proceed with only one nucleon, provided we have off shell nucleon energies, above the pion mass. While this channel is considered in evaluations of the Δ selfenergy θ , it is usually neglected in evaluations of the nucleon selfenergy which rely upon static NN potentials. Eq. (3) certainly requires the inclusion of this channel as soon as the energy allows it. However one must be aware that for some practical applications the inclusion of this channel might be relatively irrelevant. Indeed, for pion scattering the region of energies where pion production is allowed is dominated by the Δ resonance and the nucleon pole terms are very small. One might think that in electronuclear processes, where one can single out the longitudinal response function and exclude the Δ channel, the π production channel will be important. While this is certainly true, the question is that pion excitation by virtual photons not only proceeds through $N \rightarrow N\pi$ or $NN \rightarrow NN\pi$ steps, but there are direct $\gamma N \rightarrow \pi N$ terms, like the pion pole and Kroll Ruderman terms, which are dominant at low pion energies and which can not be cast in terms of the nucleon selfenergy. This is visualized in fig. 1.

Instead of including pion production in the nucleon selfenergy it is more practical to look globally at the pion electroproduction process by means of the diagram of fig. 1d where the dashed circle stands for all terms contributing to $\gamma N \rightarrow \pi N$. This example shows us that the input in the nucleon selfenergy has to be looked at in the context of the physical process that one wants to study. With this in mind we shall also exclude the pion production channels from our model and remember that we have to deal explicitly with this degree of freedom in whichever process we wish to apply the model.

3.- MODEL FOR THE NUCLEON SELFENERGY.

The diagrammatic meaning of eq. (1) is given in fig. 2, where the Lippmann Schwinger series leading to the NN t matrix is shown explicitly. Diagram a) does not contribute to the imaginary part of Σ , while all the others do. In order to evaluate it we concentrate in diagram 2b. The selfenergy for this diagram is given by

$$-i\Sigma(\vec{k}) = \int \frac{d^4q}{(2\pi)^4} i \left\{ \frac{t - n(\vec{k} - \vec{q})}{k^0 - q^0 - \varepsilon(\vec{k} - \vec{q}) + i\epsilon} + \frac{n(\vec{k} - \vec{q})}{k^0 - q^0 - \varepsilon(\vec{k} - \vec{q}) - i\epsilon} \right\} \quad (4)$$

$$(-i)V(q) \{-i\}V(q) i U_N(q)$$

where the curled bracket accounts for the nucleon propagator, $G(\vec{k} - \vec{q})$, with $\varepsilon(\vec{k})$ the nucleon kinetic energy, and we assume that the NN interaction, $V(q)$, depends only on the momentum transfer for simplicity. $U_N(q)$ is the Lindhard function for p-h excitation with the normalization given in the appendix of ref. 9). In order to obtain the imaginary part we first perform the q^0 integration by means of a Wick rotation as shown in fig. 3, which shows the pole structure of the integrand of eq. (4). The crosses correspond to the poles of the Lindhard function and even if $V(q)$ was assumed non static (q^0 dependence) it would have the structure of a propagator and the poles

would be like those of $U_N(q)$.

The integral over the circuit of fig. 3 leads to

$$\int_{-\infty}^{\infty} dq_0 + \int_{-i\infty}^{-i0} dq_0 = 2\pi i R(k^0 - \varepsilon(\vec{k} - \vec{q})) \Theta(k^0 - \varepsilon(\vec{k} - \vec{q})) (1 - n(\vec{k} - \vec{q})) (1 - n(\vec{k} - \vec{q})) \text{ term} \\ - 2\pi i R(k^0 - \varepsilon(\vec{k} - \vec{q})) \Theta(\varepsilon(\vec{k} - \vec{q}) - k^0) (n(\vec{k} - \vec{q})) \text{ term} \quad (5)$$

The integral over the imaginary axis gives a real contribution to $\Sigma(k)$ since there are cancellations of the imaginary parts of the integral for the positive and negative values of the axis. Thus we obtain:

$$\text{Im } \Sigma(k) = \text{Im} \int \frac{d^3 q}{(2\pi)^3} \left\{ (1 - n(\vec{k} - \vec{q})) \Theta(\vec{k}^0 - \varepsilon(\vec{k} - \vec{q})) - n(\vec{k} - \vec{q}) \Theta(\varepsilon(\vec{k} - \vec{q}) - k^0) \right\} \\ \cdot V(q)^2 U_N(q) \Big|_{q^0 = k^0 - \varepsilon(\vec{k} - \vec{q})} \quad (6)$$

$$= \int \frac{d^3 q}{(2\pi)^3} \left\{ (1 - n(\vec{k} - \vec{q})) \Theta(k^0 - \varepsilon(\vec{k} - \vec{q})) - n(\vec{k} - \vec{q}) \Theta(\varepsilon(\vec{k} - \vec{q}) - k^0) \right\} \\ \cdot V(q)^2 \text{Im } U_N(q) \Big|_{q^0 = k^0 - \varepsilon(\vec{k} - \vec{q})}$$

where, since we renounce to include the pionic channels, the only source of imaginary part comes from $U(q)$. As we can see we obtain an imaginary part with the factor $1 - n(\vec{k} - \vec{q})$ when $k^0 > \varepsilon_F$ and another one with the factor $n(\vec{k} - \vec{q})$ when $k^0 < \varepsilon_F$. The reason why the two contributions come together in our scheme is because $U_N(q)$ accounts for forward and backward ph excitation as shown in fig. 4. As a consequence the two conventional diagrams¹⁾, polarization, fig. 5a, and correlations, fig. 5b, are automatically accounted for in our scheme.

Next we calculate the imaginary part of the selfenergy associated

to diagrams c), d) etc. Note that by means of the Wick rotation we have placed on shell the intermediate nucleon line, through the pole of the nucleon propagator, (eq. (5)), and the ph excitation, through $\text{Im } U_N(q)$ in eq. (6). This is the manifestation of Cutkosky rules which tell us that the imaginary part of the selfenergy is obtained when the particles cut by a horizontal line are placed on shell (see fig. 6). The series of cuts shown in fig. 6 can be reordered in the way shown in fig. 7. We then observe that by summing the diagrams in arrows we generate the t matrix in the upper part of the cut, while summing over columns we generate the t matrix in the lower part of the cut. Hence, the sum of all these diagrams is easily taken into account by simply replacing $V(q)$ in eq. (6) by the t matrix. Analytically this is obtained by means of the relationship

$$\text{Im}(V + VGV + VGVGV + \dots) = \\ (V + VGV + VGVGV + \dots) \text{Im } G (V + VGV + VGVGV + \dots) \quad (7)$$

where G is the only source of imaginary part, which in our case corresponds to the Lindhard function. The only novelty with respect to the conclusion from the diagrammatic expansion is that one of the T matrices appears complex conjugate. This is indeed one of the prescription of the Cutkosky rules which have its heart in the optical theorem¹⁰⁾.

Hence we obtain for the imaginary part of the nucleon selfenergy the result

$$\text{Im } \Sigma(k) = \\ = \int \frac{d^3 q}{(2\pi)^3} \left\{ (1 - n(\vec{k} - \vec{q})) \Theta(k^0 - \varepsilon(\vec{k} - \vec{q})) - n(\vec{k} - \vec{q}) \Theta(\varepsilon(\vec{k} - \vec{q}) - k^0) \right\} \\ \text{Im } U_N(q) \sum_{|q^0 = k^0 - \varepsilon(\vec{k} - \vec{q})} |t|^2 \quad (8)$$

where we have also included the sum and average of $|t|^2$ over final and initial polarizations. One of the initial nucleon states is the hole state of the Lindhard function and we should sum, not average over its spin. The factor two of spin is included in U_N and hence we average $|t|^2$.

So far the derivation is rigorous. The t matrix corresponds to the diagrammatic series implicit in fig. 2, with the nucleon propagators containing both particle and hole parts, as the curled bracket of eq. (4). This leads to a t matrix different than the free one, which is the Galitskii t matrix t_0 . In most studies in the Literature only the particle part of the propagator is taken and one obtains then the Bethe-Goldstone G -matrix. However, the approach of refs. 2,3) relies upon the Galitskii equation. One of our approximations is to take t of eq. (8) as the free NN t matrix. Another one is to substitute $|t|^2$ by its average over angles relating it to the NN cross section by means of the relationship, based on eq. (2)

$$\bar{\Sigma} \sum |t|^2 \rightarrow \frac{\pi s}{M^4} \sigma_{elas} \simeq \frac{4\pi}{M^2} \sigma_{elas} \quad (9)$$

where σ_{elas} is the elastic NN cross section averaged over isospin, since $U_N(q)$ also contains a factor 2 for isospin. The last step in eq. (9) is made for consistency with other nonrelativistic approximations made in the Lindhard function, etc. At the heart of the replacement of the Galitskii t matrix by the free t matrix is the fact that as $\rho \rightarrow 0$ they coincide and that by including the contribution of holes the Galitskii equation does not restrict the phase space so much as the Bethe-Goldstone equation and leads to closer results to the free t matrix than the Bethe-Goldstone G -matrix. The density modifications to this formula will come in our approach from the medium polarization, which at low energies plays a very important role.

We have taken the results for σ_{elas} from the particle data tables and we take it dependent on the Mandelstam variable s . When $s < 4M^2$,

where evidently there is no scattering, but $|t|^2 \neq 0$, we have taken the value of σ_{elas} for $s = 4M^2$.

At this point we would like to raise a word of caution not to use eq. (4), for the second order diagram, to evaluate the real part of the nucleon selfenergy by replacing $V(q)$ by the t matrix, as we have done to calculate $\text{Im} \Sigma$. This would lead to doublecounting since two interaction lines on the upper part of the diagram and one in the lower will be counted twice when we consider also one interaction line in the upper part and two in the lower. There was not doublecounting in the imaginary part because the cut giving rise to $\text{Im} \Sigma$ could be placed between any two interaction lines (see figs. 6 and 7).

It is instructive to see that our approximation satisfies exactly the low density theorem. Indeed, as $\rho \rightarrow 0$ we can take $n(\vec{n}-\vec{q}) = 0$ in eq. (8) and by means of the useful approximation

$$\Theta(q_0) \text{Im} U_N(q) \underset{\rho \rightarrow 0}{\simeq} -\pi \rho \delta(q_0 - \vec{q}^2/2M) \quad (10)$$

and the change of variable $\vec{q} = \vec{q}' + \vec{k}/2$ we perform immediately the integral in eq. (8) with the result given in eq. (3) for on shell nucleons ($k_0 = \vec{k}^2/2M$). The only difference is that we obtain σ_{elas} instead of σ_{tot} , because, as discussed above, we renounce to incorporate the pion production channels in our approach.

Eq. (8) gives us $\text{Im} \Sigma(k)$ also for the case where the original nucleon is off shell ($k_0 \neq \vec{k}^2/2M$). We have to give a prescription on how to evaluate t when the initial nucleon is off shell. This requires the knowledge of the dynamics of the NN interaction. If we think in terms of meson exchange models for the interaction we would have a form factor $F(q)$ in each of the four vertices in the diagram of fig. 2b. In an off shell situation q^2 would change with respect to the on shell value q_{on}^2 and by multiplying σ by $(F(q)/F(q_{on}))^4$ we would account for the off shell effects due to the

vertices. The propagators would also change. However, it is easy to prove that if we assume the hole line in the Lindhard function to have as an average a momentum $p_2 = (m, \vec{0})$, we can also make an average for the longitudinal component of \vec{q} along the \vec{k} direction which provides $q_L = k/2$. Then we find the average value of $\vec{q}^2 = Mk^0$ and $q^0 = \vec{q}^2/2M$ irrespective of whether (k^0, \vec{k}) is on shell or off shell. Then our prescription is very clear: for any off shell situation, (k^0, \vec{k}) , we take the cross section σ corresponding to the on shell situation, $(k^0, k = \sqrt{2Mk^0})$.

The scheme which we have developed has as a main virtue to satisfy the low density theorem, but it automatically provides an analytical extrapolation of these results to finite densities, incorporating Pauli blocking effects through the Lindhard function and the two terms of eq. (8). It also provides an off shell extrapolation, through the explicit dependence of eq. (8) on k^0 and \vec{k} . It has also the appropriate analytical properties, $\text{Im } \Sigma(k)$ vanishes at $k^0 = \varepsilon_F = k_F^2/2M$ and is negative for $k^0 > \varepsilon_F$ and positive for $k^0 < \varepsilon_F$, as demanded by general theorems¹⁴⁾. However, as shown in ref. ⁹⁾, for densities $\rho = \rho_0$, $\rho_0/2$ (ρ_0 normal nuclear matter density) and $k^0 = \varepsilon_F + 85$ MeV the present scheme provides $\text{Im } \Sigma \approx -10.4$ MeV, -7.2 MeV, versus the value -6.5 MeV both for ρ_0 and $\rho_0/2$ provided by the microscopic calculations of ref. ⁴⁾. This reflects the fact that at higher densities there are quenching mechanisms beyond Pauli blocking which further reduce the results from the scheme exposed above.

It is interesting to recall the basic ingredients incorporated in the hypernetted chain approach of ref. ⁴⁾. From the diagrammatic point of view it incorporates ladder sums, which we have already summed in the t matrix, and polarization sums obtained by allowing the interaction to excite ph components in an iterative way. This is shown diagrammatically in fig. 8. We wish to include these effects in our scheme and we do this in the next section.

4.- POLARIZATION EFFECTS.

In order to include the polarization effects of fig. 8 we must perform the geometric series implicit in the figure and there we need the ph interaction. Here again we adopt a phenomenological approach. At energies of the nucleon $k^0 > \varepsilon_F + 50$ MeV the value of q exceeds 200 MeV/ c . This momenta are already bigger than the pion mass and make the tensor force of the NN interaction appreciable. Our position here is that at these energies the ph interaction is dominated by the spin-isospin effective interaction and we shall use this one for the iteration of the ph excitation in fig. 8. This interaction is given by

$$V_{s-1}(q) = \left\{ V_1(q) \hat{q}_1 \hat{q}_1 + V_t(q) (\delta_{ij} - \hat{q}_1 \hat{q}_1) \right\} \sigma_1 \sigma_j \vec{\tau} \vec{\tau} \quad (11)$$

with

$$V_1(q) = \frac{f^2}{m_\pi^2} \left[\frac{\vec{q}^2}{q^0{}^2 - \vec{q}^2 - m_\pi^2} F_\pi^2(q) + g' \right] \quad (12)$$

$$V_t(q) = \frac{f^2}{m_\pi^2} \left[\frac{\vec{q}^2}{q^0{}^2 - \vec{q}^2 - m_\pi^2} F_\rho^2(q) C_\rho + g' \right]$$

where $F_1(q)$ is the meson-NN form factor which we take of the monopole type $F_1(q) = (\Lambda_1^2 - m_\pi^2)/(\Lambda_1^2 - q^2)$ with $\Lambda_\pi = 1300$ MeV, $\Lambda_\rho = 1400$ MeV¹⁵⁾. C_ρ is the ratio of squares of ρ NN and π NN coupling constants, for which we take $C_\rho = 3.94$ from ref. ¹⁵⁾ and $f^2/4\pi = 0.08$. Finally g' is the Landau-Migdal parameter for which we take $g' = 0.7$ in our calculations. Accounting for the geometrical series is trivial and we obtain two independent series, one for the longitudinal part, V_l , and another one for the transverse part, V_t . However, due to the smallness of the ρ -meson contribution in V_t , this term is approximately equal to g' , while in the longitudinal part, due to the smallness of the pion mass there are cancellations between the pion exchange contribution and g' and then V_l is small compared to V_t . We

hence assume for simplicity that the ρ h excitation is driven by the transverse part alone and then the whole series leading to the induced interaction (6) of fig. 8 is accounted for by replacing in the formulas

$$U_N(q) \longrightarrow \frac{U_N(q)}{1 - V_t(q) U_N(q)} \quad (13)$$

However since in $\text{Im} \Sigma(k)$ what we needed is $\text{Im} U_N(q)$, the replacement to be made in eq. (8) is

$$\text{Im} U_N(q) \longrightarrow \text{Im} \frac{U_N(q)}{1 - V_t(q) U_N(q)} = \frac{\text{Im} U_N(q)}{|1 - V_t(q) U_N(q)|^2} \quad (14)$$

The last step in this process is that with the spin-isospin interaction one can also excite Δ h components. We can easily account for that by replacing $U_N(q)$ by $U(q) = U_N(q) + U_\Delta(q)$, with $U_\Delta(q)$ incorporating ratios of coupling constants and spin-isospin factors and normalized as in ref. 9). However, since the source of $\text{Im} U_\Delta(q)$ is the decay $\Delta \rightarrow \pi N$ and we neglect this channel here (we also neglect other sources of $\text{Im} U_\Delta(q)$ studied in ref. 8) and which would lead to $3p2h$ excitation in the nucleon selfenergy) the final prescription is to substitute

$$\text{Im} U_N(q) \longrightarrow \frac{\text{Im} U_N(q)}{|1 - V_t(q) U(q)|^2} \quad (15)$$

Hence Δ h excitation does not contribute directly to $\text{Im} \Sigma$ because we omit the pion creation channel, but the virtual Δ h excitation plays an indirect role through the medium polarization.

The consideration of the polarization brings our results for $\text{Im} \Sigma$ in close agreement with the results of ref. 4) as we shall see in the results section.

5.- THE REAL PART OF THE NUCLEON SELFENERGY.

We can of course take eq. (1) and rely upon the free NN

elementary amplitude in order to obtain the low density limit. The high density limit would require the use of the Galitskii t matrix, although higher orders and a self-consistent treatment also have some influence in the results²⁾. This is one of the magnitudes where the details of the interaction matter most. Indeed the strong repulsion at short distances would make this magnitude even change sign at sufficiently high densities. We renounce to have all the information on $\text{Re} \Sigma$, but as we shall see we can obtain the relevant information to evaluate a great deal of nuclear properties relying again on the same phenomenological input used so far.

Since our results for $\text{Im} \Sigma$, fulfilling the low density theorem and in agreement with the results of ref. 4) for high densities, are sufficiently realistic, we can use a dispersion relation to obtain the real part from the imaginary part. Considering the analytical structure of our selfenergy we obtain^{1,2)}

$$\begin{aligned} \text{Re} \Sigma(\omega, k) = & -\frac{1}{\pi} \mathcal{P} \int_{\epsilon_F}^{\infty} d\omega' \frac{\text{Im} \Sigma(\omega', k)}{\omega - \omega'} + \\ & + \frac{1}{\pi} \mathcal{P} \int_{-\infty}^{\epsilon_F} d\omega' \frac{\text{Im} \Sigma(\omega', k)}{\omega - \omega'} \end{aligned} \quad (16)$$

With this expression of course we only evaluate the real part associated to the diagrams of figs. 2b, c, d, which provide the source of $\text{Im} \Sigma$. The Hartree term, fig. 2a and the Fock term, not shown but understood in the series are not taken into account by means of eq. (16) and have to be added explicitly (note that the antisymmetry in the NN amplitude is incorporated phenomenologically in σ for the other terms of the series).

We are interested only in the pieces of $\text{Re} \Sigma$ which depend on k^0 and k in order to obtain effective masses, strength at the pole etc. This means that we do not need to evaluate the Hartree piece, but the Fock piece gives rise to an important k dependence and we must consider it.

The Fock term is shown diagrammatically in fig. 9. The contribution of a static pion exchange ($q^0 = 0$) is easily evaluated and we obtain

$$\begin{aligned} \Sigma^{(F)}(k) &= -3 \int \frac{d^3q}{(2\pi)^3} n(\vec{k}-\vec{q}) \frac{f^2}{m_\pi^2} \frac{\vec{q}^2}{-\vec{q}^2 - m_\pi^2} F^2(q) \\ \{k-q = q'\} &= -3 \int \frac{d^3q'}{(2\pi)^3} n(\vec{q}') \frac{f^2}{m_\pi^2} \frac{(\vec{k}-\vec{q}')^2}{-(\vec{k}-\vec{q}')^2 - m_\pi^2} F(k-q')^2 \end{aligned} \quad (17)$$

We see that the Fock term with a static potential depends on k but not on k^0 , it is static. It is also real. This is by contrast to the piece in eq. (16) which depends on both $k^0 = \omega$ and k and is tied to pieces which have an imaginary part. The other observation is that the k dependence comes because of the πNN vertex, $\sigma(\vec{k}-\vec{q}')$, leading to the factor $(\vec{k}-\vec{q}')^2$ in the numerator of eq. (17) and because of the pion propagator. If instead of a pion we exchange an ω meson we do not have the derivative coupling (or at least is rather small) and $(\vec{k}-\vec{q}')^2$ in the ω propagator would be weighed against m_ω^2 , which is much larger than m_π^2 . Hence the dependence on \vec{k}^2 of the corresponding Fock piece would be weak. These ideas were discussed in ref. 17) where the sources of k^0 and k dependence of the nucleon selfenergy, were traced back to the series of terms of figs. 8 and 9 with the spin-isospin part of the nucleon interaction. Hence in order to complete the real part given by eq. (16) we must add the Fock term with the interaction of eq. (11). The result for this piece is

$$\Sigma^{(F)}(k) = -3 \int \frac{d^3q}{(2\pi)^3} n(\vec{k}-\vec{q}) [V_1(q) + 2V_t(q)] \quad (18)$$

Thus, eq. (8) implementing eqs. (9) and (15) for $\text{Im}\Sigma$, together with eqs. (16) and (18) for $\text{Re}\Sigma$ give us the nucleon selfenergy, up to a smoothly k^0, k dependent part, which we disregard.

6.- APPLICATIONS.

a) - Spectral functions.

With the amount of information which we have we can calculate the spectral functions. The Lehmann representation for the nucleon propagator is given by

$$G(\omega, k) = \int_{\mu}^{\infty} d\omega' \frac{S_p(\omega', k)}{\omega - \omega' + i\eta} + \int_{-\infty}^{\mu} \frac{S_h(\omega', k)}{\omega - \omega' - i\eta} \quad (19)$$

where μ is the chemical potential and S_p, S_h the particle and hole spectral functions.

By comparing it to the Dyson representation

$$G(\omega, k) = \frac{1}{\omega - (\vec{k}^2/2M) - \Sigma(\omega, k)} \quad (20)$$

one has the relationships

$$\omega > \mu, \quad S_p(\omega, k) = -\frac{1}{\pi} \text{Im} G(\omega, k) = -\frac{1}{\pi} \frac{\text{Im} \Sigma(\omega, k)}{A + B}$$

$$A = (\omega - (\vec{k}^2/2M) - \text{Re} \Sigma(\omega, k))^2$$

$$B = (\text{Im} \Sigma(\omega, k))^2$$

$$\omega < \mu, \quad S_h(\omega, k) = +\frac{1}{\pi} \text{Im} G(\omega, k) = +\frac{1}{\pi} \frac{\text{Im} \Sigma(\omega, k)}{A + B} \quad (21)$$

The chemical potential in our scheme is given by

$$\mu = \frac{k_F^2}{2M} + \text{Re} \Sigma \left(\frac{k_F^2}{2M}, k_F \right) \quad (22)$$

However the calculations of the selfenergy have been performed assuming only kinetic energies for the nucleon lines. Thus, when the energy

is $k_F^2/2M$, then $\text{Im } \Sigma(k_F^2/2M, k_F)$ is zero. The results are invariant if we add a constant real piece to the nucleon energy, because one is always dealing with differences of energies. Hence we can refer the selfenergies to the value at the Fermi surface and define

$$\tilde{\Sigma}(\omega, k) = \Sigma(\omega, k) - \text{Re } \Sigma\left(\frac{k_F^2}{2M}, k_F\right) \quad (23)$$

and as a consequence

$$\tilde{\Sigma}\left(\frac{k_F^2}{2M}, k_F\right) = 0, \quad \mu = \frac{k_F^2}{2M}$$

and $\Sigma(\omega, k)$ is calculated using the kinetic energy in the internal nucleon lines as we have done so far.

We can then represent the spectral functions for fixed k as a function of ω , but ω has to be understood as the difference between the actual energy and the exact value of $\text{Re } \Sigma(\omega_F, k_F)$. By means of that we eliminate the unknown missing pieces in our approach.

As long as $\Sigma(\omega, k) - \text{Re } \Sigma(k_F^2/2M, k_F)$ is small compared to the kinetic energies, ω is approximately the kinetic energy of the particle, and at the Fermi surface ω means exactly the Fermi kinetic energy. In eqs. (20), (21) we would then replace $\Sigma(\omega, k)$ by $\tilde{\Sigma}(\omega, k)$.

b.- Occupation number.

One can easily prove (14) that

$$\begin{aligned} \langle \psi_0 | a+(\vec{k}) | \psi_0 \rangle &= \int_{-\infty}^{\mu} d\omega' S_H(\omega', \vec{k}) \\ \langle \psi_0 | a(\vec{k}) a+(\vec{k}) | \psi_0 \rangle &= \int_{\mu}^{\infty} d\omega' S_P(\omega', \vec{k}) \end{aligned} \quad (24)$$

or equivalently

$$n(\vec{k}) = \int_{-\infty}^{\mu} d\omega' S_H(\omega', \vec{k}) \quad (25)$$

$$1-n(\vec{k}) = \int_{\mu}^{\infty} d\omega' S_P(\omega', \vec{k})$$

which leads to the sum rule

$$\int_{-\infty}^{\mu} d\omega' S_H(\omega', \vec{k}) + \int_{\mu}^{\infty} d\omega' S_P(\omega', \vec{k}) = 1 \quad (26)$$

c.- Effective masses and other quasiparticle properties.

We can also evaluate the usual, k , ω and effective masses.

$$\frac{M_\omega}{M} = 1 - \frac{\partial \text{Re } \tilde{\Sigma}(\omega, \vec{k})}{\partial \omega} \Big|_{\omega = \omega(\vec{k})} \quad (27)$$

$$\frac{Mk}{M} = \left(1 + \frac{M}{k} \frac{\partial \text{Re } \tilde{\Sigma}(\omega, \vec{k})}{\partial k} \right)^{-1} \Big|_{\omega = \omega(\vec{k})}$$

$$\frac{M^*}{M} = \frac{M_\omega}{M} \cdot \frac{Mk}{M}$$

where $\omega(\vec{k})$ is the quasiparticle energy associated to the momentum \vec{k} given by the solution to the equation

$$\omega - \frac{\vec{k}^2}{2M} - \text{Re } \tilde{\Sigma}(\omega, \vec{k}) = 0 \quad (28)$$

The inverse of M_ω/M is the quasiparticle strength

$$Z(k) = \left[1 - \frac{\partial \operatorname{Re} \tilde{\Sigma}(\omega, k)}{\partial \omega} \right]_{\omega = \omega(k)}^{-1} \quad (29)$$

7.- RESULTS AND DISCUSSION.

In fig. 10 we show the results for $\operatorname{Im} \Sigma(\omega, k)$ for $k = k(\omega)$, given by the eq. (28), as a function of $\omega - \mu$. We represent the results for two densities, $\rho = \rho_0$ and $\rho = \rho_0/2$. We see that below $\omega - \mu = 60$ MeV $\operatorname{Im} \Sigma(\omega, k)$ for $\rho = \rho_0/2$ is bigger than for $\rho = \rho_0$ and above that energy the opposite occurs. This shows the drastic effects of the polarization, together with Pauli blocking, which are more apparent at low energies. The results have been obtained with a value $g' = 0.7$ for the Landau - Migdal parameter. The results in fig. 10 agree remarkably well in magnitude with those of ref. 4) for both densities and the range of energies in the figure. This gives us confidence about the accuracy of the numerical results of the present approach.

In fig. 11 we show the results for M_ω/M as a function of k at $\rho = \rho_0$. While the results are numerically similar to other approaches¹⁾, one feature immediately calls our attention. The peak present in most calculations around the Fermi momentum, $k_F \simeq 1.36 \text{ fm}^{-1}$, is absent in our approach. A trace of it remains at much lower momenta. The peak around the Fermi surface appears in approaches based in second order perturbation calculations, as reported in ref. 1), or even selfconsistent schemes, but which neglect the polarization of the medium, and rely essentially on central potentials. We have checked that neglecting the polarization changes the results but does not change appreciably the shape of the effective mass. On the other hand we have used an interaction like the one of the model reported in eq. (3. 7. 23) of ref. 1) and performed the calculation. We have replaced in eq. (9)

$$\frac{4\pi}{M^2} \sigma_{\text{elas}} \rightarrow 3 \left(\frac{1}{q^2 + m_\pi^2} \right)^2 \quad (30)$$

which is equivalent to accepting a Yukawa potential as interaction (the factor 3 is introduced to have similar strengths in the two terms). We reproduce the peak in M^*/M as reported in ref. 1). We tend to conclude that the fact that the central potentials, neglecting tensor forces, provide small NN cross sections at large energies is the main factor responsible for the sharp peak in the effective mass, and that this peak should not be present if realistic calculations, fulfilling the low density theorem at all energies, are used.

In fig. 12 we show the results for M_k/M at $\rho = \rho_0$. The results are similar in shape and size to those of other approaches^{1, 2)}. The smoothness of the curve is the most distinctive feature of this magnitude. Finally in fig. 13 we show the results for M^*/M at $\rho = \rho_0$, which show a flat character around k_F and a fall down at low energies. The effective mass is practically constant and equal to about 0.95 M in a large stretch around k_F . This is compatible with experimental results based on the spacing of levels around the Fermi surface^{1, 18)}. The values of M^* at low energies are also compatible with the level structure of deeply bound states¹⁾. However, the values of M^* at energies above the Fermi energy would seem to contradict the experimental evidence about the energy dependence of the strength of the potential. This one seems to support $M^* = 0.7 M$ at energies $\omega - \mu > 20 \text{ MeV}$ ¹⁾. However, we would like to call the attention at the way that this is obtained. Following ref. 1) we recall that a potential with a Woods Saxon shape is assumed, with a radius slightly larger than the nuclear radius. The strength depends on the energy but the shape is assumed independent of it. We should note that the shape proportional to ρ with a certain finite range is not supported by the present or other calculations which provide a different density functional, also rather energy dependent. Second, the range implemented in the Woods Saxon potential should also be energy

reduction of a factor 2 in the integrand and the integral converges slowly.

It is interesting to recall that the input in our model was the elementary NN cross section and the spin-isospin effective interaction. Any potential model which gave rise to the same NN cross section would lead to the same results in our approach. We find occupation numbers very similar to those obtained in other approaches. The link between the occupation number and short range correlations which has been invoked some times²⁾ appears unclear in view of the results of the present model which does not require any specific potential.

The approach followed here has the virtue of showing that many of the dynamical properties of nucleon propagation in nuclear matter can be traced to simple dynamical features of the NN interaction reflected in observable magnitudes as cross sections, etc.

8.- CONCLUSIONS.

The approach followed here is semiphenomenological. It starts from a formal derivation of the nucleon selfenergy but at some point relates the input needed of the NN interaction to the NN cross section which is taken from experiment. By means of that we obtain an imaginary part of the nucleon selfenergy which satisfies the low density theorem. Another important ingredient in the approach is the polarization of the medium which produces an appreciable quenching of $\text{Im } \Sigma$ at low energies and high densities. The results obtained with these ingredients for $\text{Im } \Sigma$ are in good agreement with those of the hypernetted chain approach. With these realistic results for $\text{Im } \Sigma$ one evaluates $\text{Re } \Sigma$ by means of dispersion relations. This quantity is a dynamical one in the sense that it depends on ω and k as independent variables. To this piece we add a Fock term which is static, and hence depends only on k . This completes the model for the selfenergy which misses some pieces of Hartree type, which depend upon ρ but not on ω or k . Hence the model allows one to obtain all sort of quasiparticle properties which depend upon derivatives of Σ , or other

dependent, since, as we increase the energy, p -waves or higher partial waves will become relevant and they give rise to different range corrections in the potential^{9, 19, 20}.

The spectral functions show the characteristic features of these functions. In fig. 14 we show $S_p(\omega, k)$ as a function of $\omega - \mu$ for $k > k_F$. We can see that the spectral function resembles very much a δ function like peak since it corresponds to a Lorentzian distribution with a very narrow width (see eq. (21)). However, in fig. 15 we show $S_p(\omega, k)$ for $k < k_F$. The shape is completely different since S_p is very small and has a long range. The reason for this behaviour is that with $k < k_F$ and $\omega > \mu$ one is far away from the peak of the Lorentzian distribution of eq. (21). (Note different scales in figs. 14 and 15).

The situation is reversed for $S_n(\omega, k)$ which has a pronounced peak for $k < k_F$ (see fig. 16) and is very small and stretches for a long span when $k > k_F$ (see fig. 17).

With the values of the spectral functions we can obtain occupation numbers. In table I we show the occupation number $n(\vec{k})$ and $1 - n(\vec{k})$ obtained using eqs. (25), together with the check of the sum rule, which is fulfilled with an average error of three per thousand. We obtain occupation numbers around 0.9 below the Fermi sea and values going down fast from around 0.1 above the Fermi sea. Our results also show the discontinuity of $n(\vec{k})$ around the Fermi surface. For values of $k \approx 1000$ MeV our results become less trustworthy because of the nonrelativistic treatment, neglect of pion production channels and other approximations done. We can see that in the fact that the integral

$$\frac{3}{k_F} \int_0^\infty dk k^2 n(k) \quad (31)$$

which should be unity give values around 1.2 at $k_F = 1.4 \text{ fm}^{-1}$, coming from the large weight given to large values of k where $n(\vec{k})$ is more unreliable. Note that between $k = 1.45 \text{ fm}^{-1}$ and $k = 3 \text{ fm}^{-1}$ there has been only a

properties but referred to the variable $\omega-\mu$, since we are unable to evaluate the absolute value of μ .

We have evaluated spectral functions for particles and holes and then occupation numbers with quite acceptable results.

We have also evaluated effective masses. The k -mass has a similar behaviour to most approaches but the ω -mass and, as a consequence, the effective mass, have a different behaviour to most approaches and does not have a sharp peak around the Fermi surface but a rather flat behaviour. The peak seems to be tied to the use of central potentials in standard approaches, which leads to small NN cross sections at high energies. Our approach, relying upon experimental cross sections, incorporates implicitly the effect of tensor forces, which are important at high energies.

The approach can provide many nucleon properties using a minimum amount of experimental information. In this sense it provides some clarification to the problem since in many elaborate many body calculations it is difficult to trace back the results to some basic properties of the interaction. In the other sense it provides a calculational scheme sufficiently realistic and far simpler than other realistic calculations, which can be used in the study of physical processes where the nucleon selfenergy is needed. Finally, the relative flatness of the effective mass around the Fermi energy challenges the results of many calculations. It would be very interesting to perform microscopic calculations incorporating tensor forces, satisfying the low density theorem, and taking care of the polarization of the medium, in order to see whether they support the results obtained here or they are consequence of some of the approximations done.

P. Fernández de Córdoba wishes to acknowledge a fellowship from Ministerio de Educación y Ciencia. This work is partially supported by CICYT.

REFERENCES

- 1.- C. Mahaux, P. F. Bortignon, R. A. Broglia and C. H. Dasso, *Phys. Reports* 120 (1985) 1.
- 2.- A. Ramos, A. Polls and W. H. Dickhoff, *Nucl. Phys.* A503 (1989) 1.
- 3.- W. H. Dickhoff, P. P. Dmitrovich, K. Allaart, M. G. E. Brand, F. Muller, G. Rijnsdijk, A. Polls and A. Ramos, *Proc. Topical Workshop on two nucleon emission reactions*, Elba 1989, in print.
- 4.- S. Fantoni and V. R. Pandharipande, *Nucl. Phys.* A427 (1984) 473.
- 5.- C. B. Dover, J. Hüfner and R. H. Lemmer, *Ann. Phys.* 66 (1971) 248.
- 6.- J. Hüfner, *Phys. Reports* 21 (1975) 1.
- 7.- A. Polls, private communication.
- 8.- E. Oset and L. L. Salcedo, *Nucl. Phys.* A468 (1987) 631.
- 9.- E. Oset, P. Fernández de Córdoba, L. L. Salcedo and R. Brockmann, *Phys. Reports* 188 (1990) 79.
- 10.- C. Itzykson and B. Zuber, *Quantum Field Theory*, McGraw Hill, 1980.
- 11.- V. M. Galitskii, *Sov. Phys. JETP*, 7 (1958) 104.
- 12.- A. L. Fetter and J. D. Walecka, *Quantum Theory of many particle systems*, McGraw Hill, 1971.
- 13.- C. Garcia-Recio and E. Oset, *Phys. Rev.* C37 (1988) 194.
- 14.- R. D. Mattuck, *A guide to Feynman diagrams in the many body problem*, McGraw Hill, 1976.
- 15.- R. Machleidt, K. Holinde and Ch. Elster, *Phys. Reports* 149 (1987) 1.

- 16.- G. E. Brown, *Many Body Problems*, North Holland, 1972.
- 17.- E. Oset and A. Palanques, *Nucl. Phys.* **A359** (1981) 289.
- 18.- G. E. Brown, J. H. Gunn and P. Gould, *Nucl. Phys.* **46** (1963) 598.
- 19.- A. M. Green and S. Wycech, *Nucl. Phys.* **A377** (1982) 441.
- 20.- T. Suzuki and H. Narumi, *Phys. Lett.* **B125** (1983) 251; *Nucl. Phys.* **A426** (1984) 413.

FIGURE CAPTIONS.

- Fig. 1.*- Diagrams entering electron scattering with nuclei leading to pion production. a) $\gamma N \rightarrow \pi N$ nucleon pole term; b) Kroll Ruderman term; c) pion pole term; d) symbolic representation of all these terms involving the $\gamma N \rightarrow \pi N$ scattering matrix represented by the dashed circle.
- Fig. 2.*- Ladder sum for the nucleon selfenergy. The dashed lines indicate a NN potential.
- Fig. 3.*- Path followed in the Wick rotation used to evaluate eq. (6). The crosses indicate the poles (or rather the analytical cut) of $U_N(q)$.
- Fig. 4.*- The two diagrams, direct (a) and crossed (b), accounted for by the Lindhard function.
- Fig. 5.*- Two diagrams leading to $\text{Im } \Sigma$. a) polarization diagram; b) correlation diagram.
- Fig. 6.*- The series of fig. 2 showing the sources of $\text{Im } \Sigma$ when the particles cut by the dotted lines are placed on shell in the integrations.
- Fig. 7.*- Reordering of the series of fig. 6 leading to the last diagram of the figure, where the serrated line indicates the medium t -matrix.
- Fig. 8.*- Selfenergy diagram including the effects of the medium polarization.
- Fig. 9.*- The Fock piece of the nucleon selfenergy.
- Fig. 10.*- $\text{Im } \Sigma(\omega, k(\omega))$ as a function of $\omega - \mu$ for two nuclear densities.
- Fig. 11.*- The ω -mass as a function of k .
- Fig. 12.*- The k -mass as a function of k .
- Fig. 13.*- The effective mass as a function of k .

Fig. 14.- $S_p(\omega, k)$ for $k > k_F$ as a function of $\omega - \mu$.

Fig. 15.- $S_p(\omega, k)$ for $k < k_F$ as a function of $\omega - \mu$.

Fig. 16.- $S_h(\omega, k)$ for $k < k_F$ as a function of $\omega - \mu$.

Fig. 17.- $S_h(\omega, k)$ for $k > k_F$ as a function of $\omega - \mu$.

TABLE I

k (fm ⁻¹)	$K_F = 1.40$ fm ⁻¹		Sum
	$n(k) = \int_{-\infty}^{\mu} d\omega S_h(\omega, k)$	$1 - n(k) = \int_{\mu}^{\infty} d\omega S_p(\omega, k)$	
0.1	0.9123	0.0841	0.9964
0.2	0.9152	0.0842	0.9994
0.3	0.9141	0.0847	0.9988
0.5	0.9014	0.0872	0.9886
0.7	0.9097	0.0912	1.000
0.8	0.9073	0.0937	1.001
0.9	0.9041	0.0968	1.000
1.0	0.8978	0.1007	0.9985
1.1	0.8948	0.1056	1.000
1.2	0.8869	0.1117	0.9986
1.30	0.8757	0.1205	0.9962
1.35	0.8522	0.1267	0.9789
1.45	0.1076	0.8599	0.9675
1.5	0.096	0.8925	0.988
1.6	0.079	0.9205	0.999
1.7	0.067	0.9301	0.997
1.8	0.057	0.9374	0.994
1.9	0.054	0.9494	1.003
2.0	0.044	0.9546	0.9986
2.25	0.032	0.9656	0.9976
2.5	0.025	0.9712	0.9962
2.75	0.021	0.9754	0.9964
3.0	0.016	0.9825	0.9985
5.0	0.000		

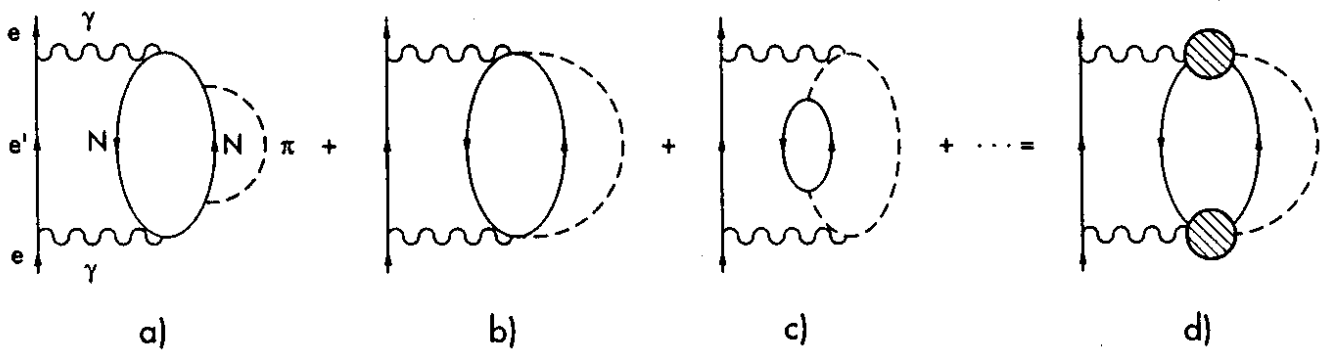


fig. 1

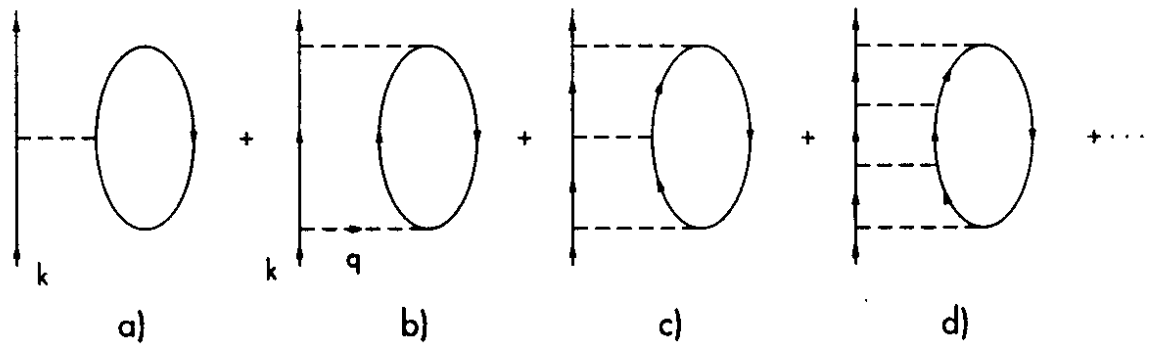


fig. 2

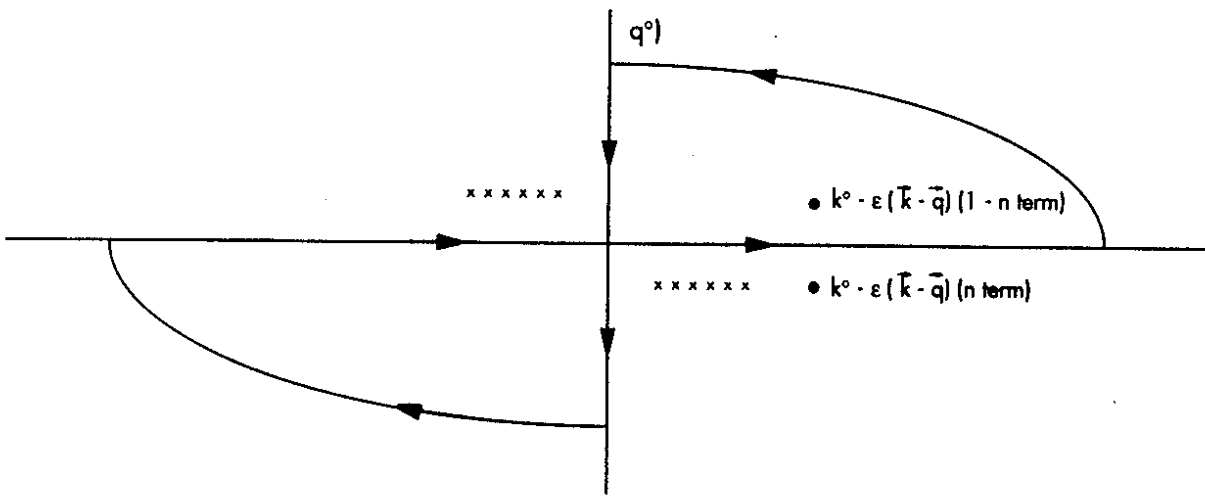


fig. 3

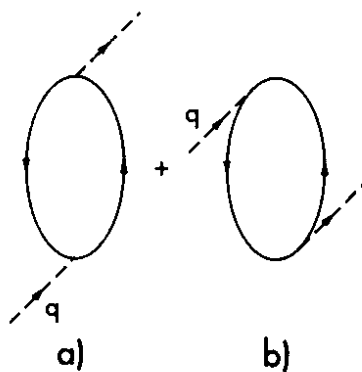


fig. 4

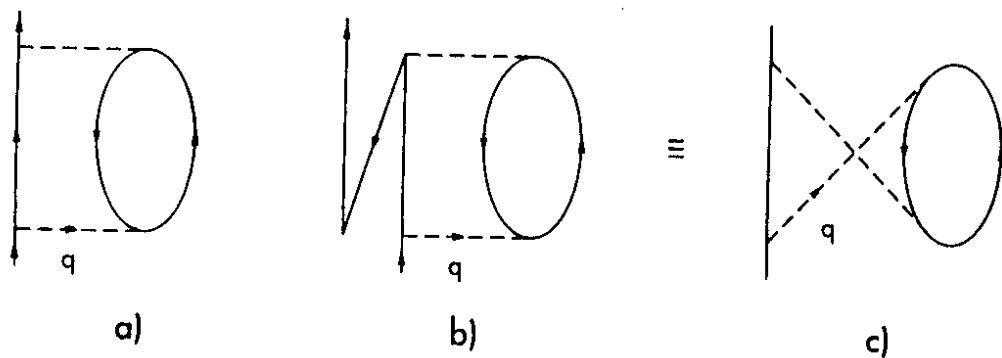


fig. 5

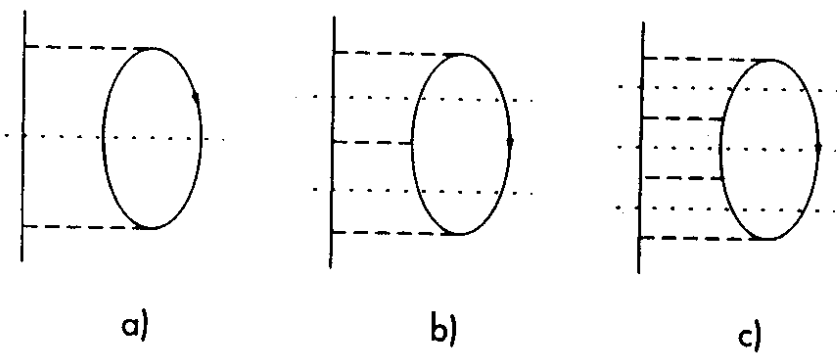
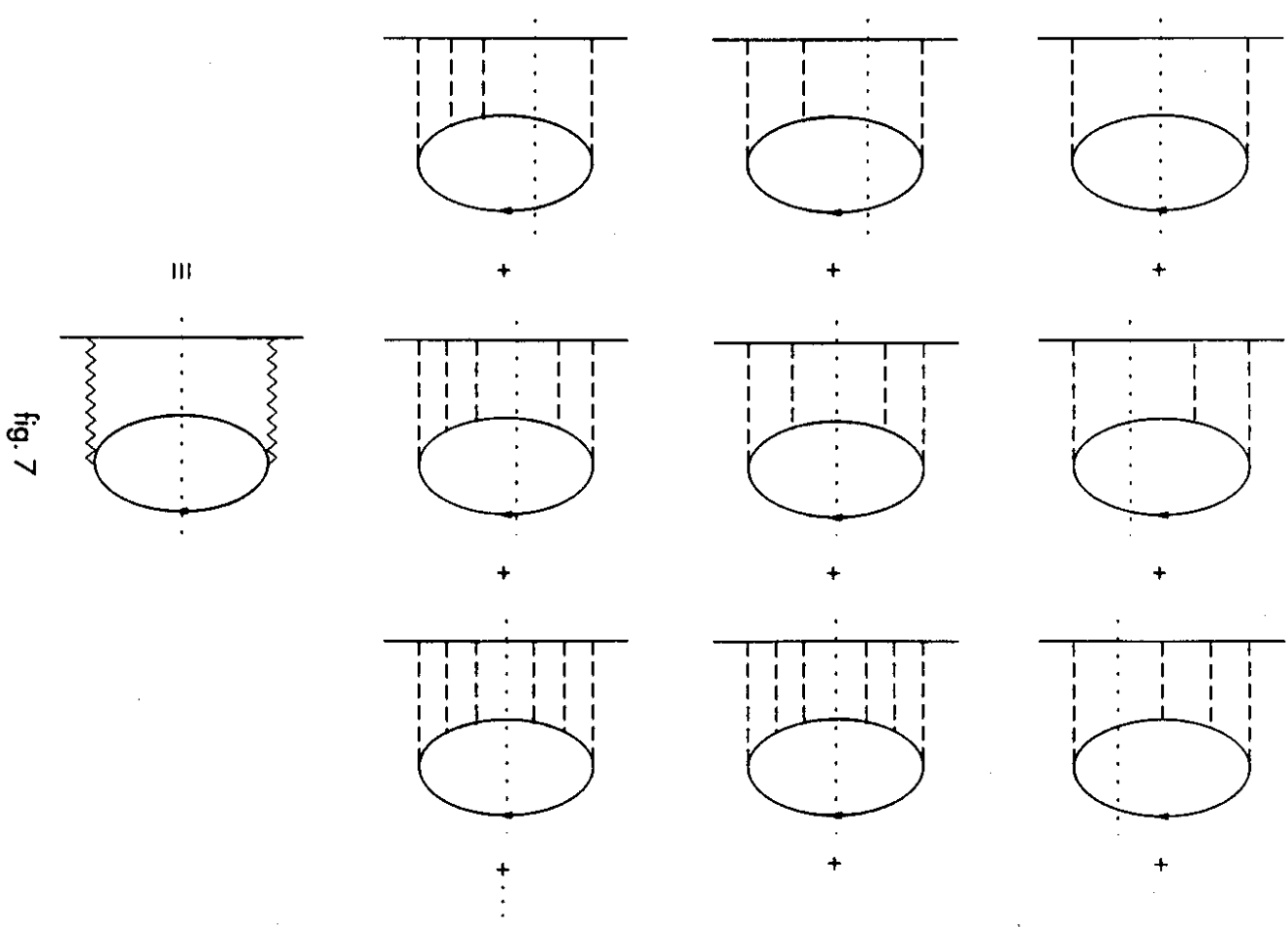


fig. 6



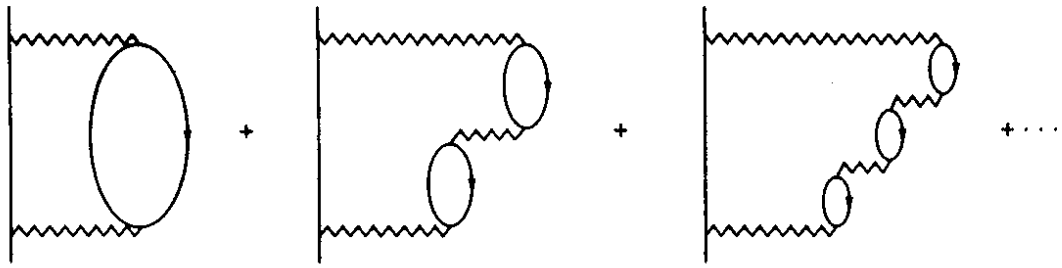


fig. 8

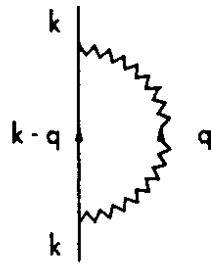


fig. 9

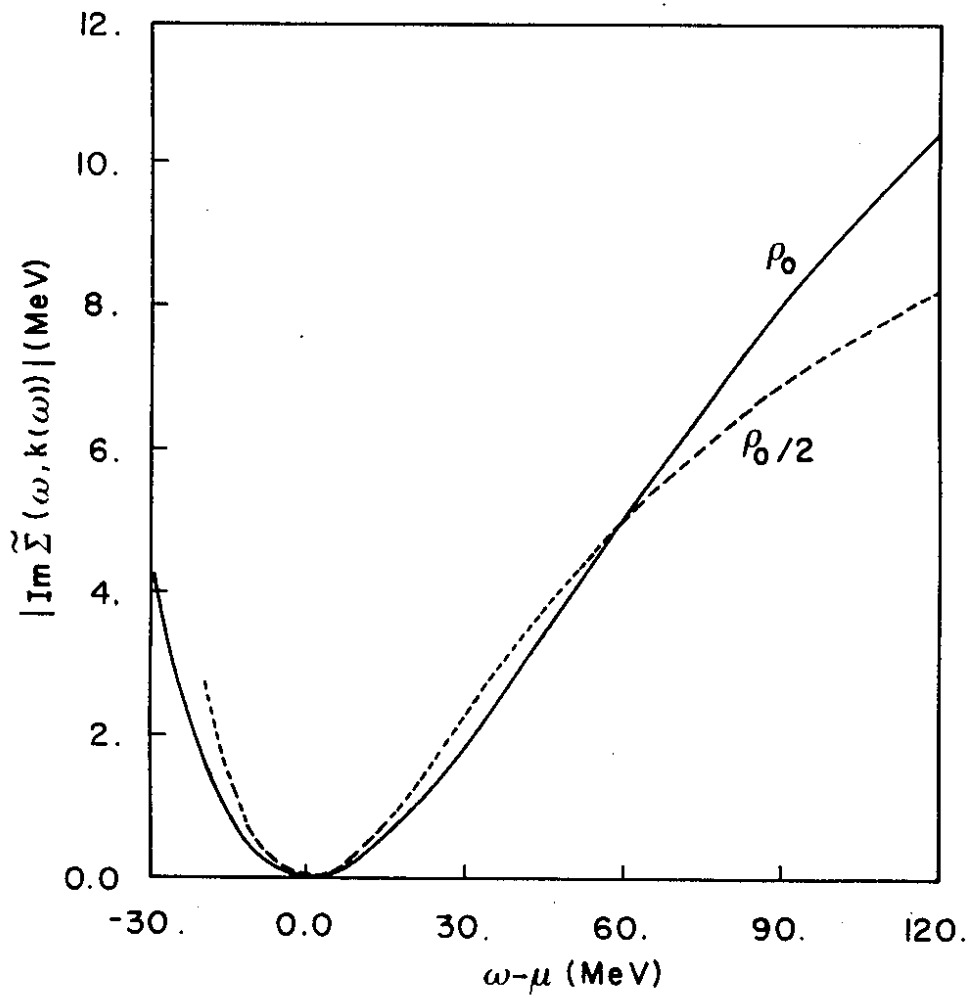


fig. 10

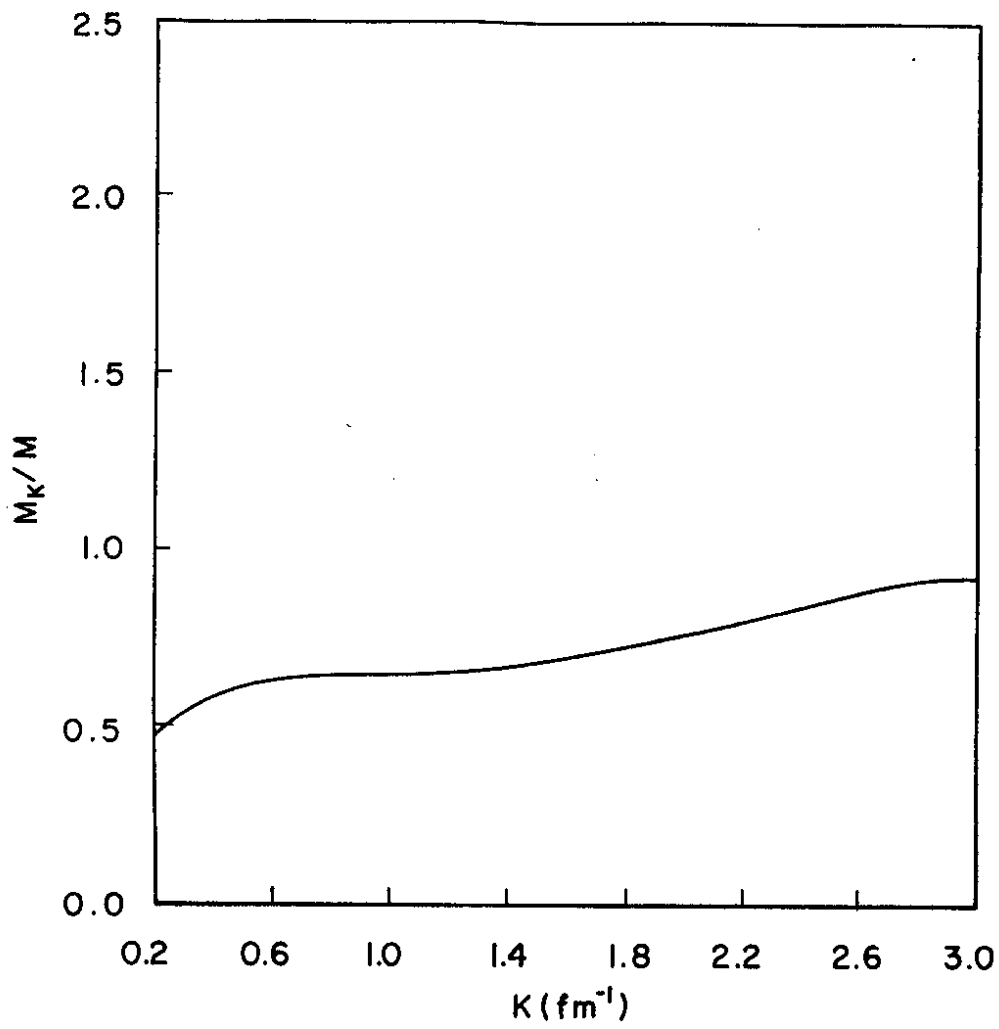


fig. 12

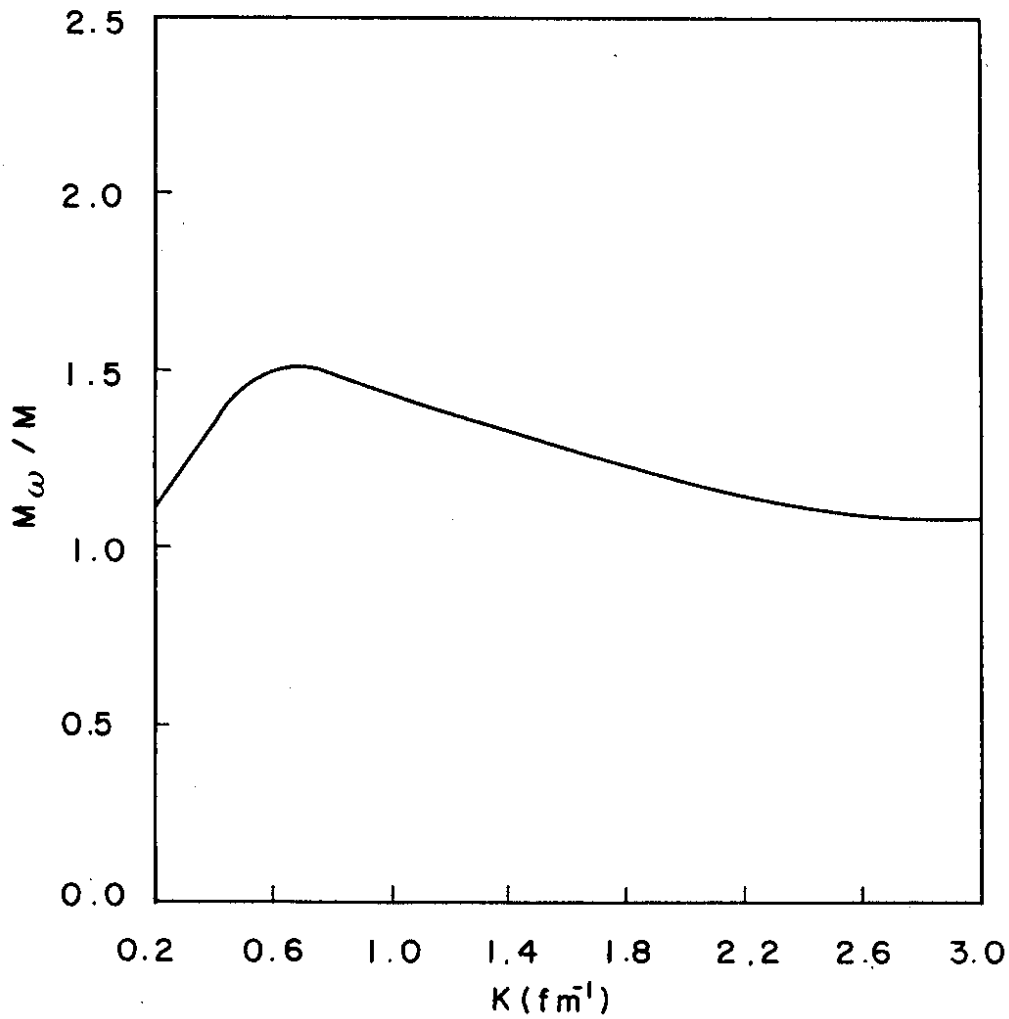


fig. 11

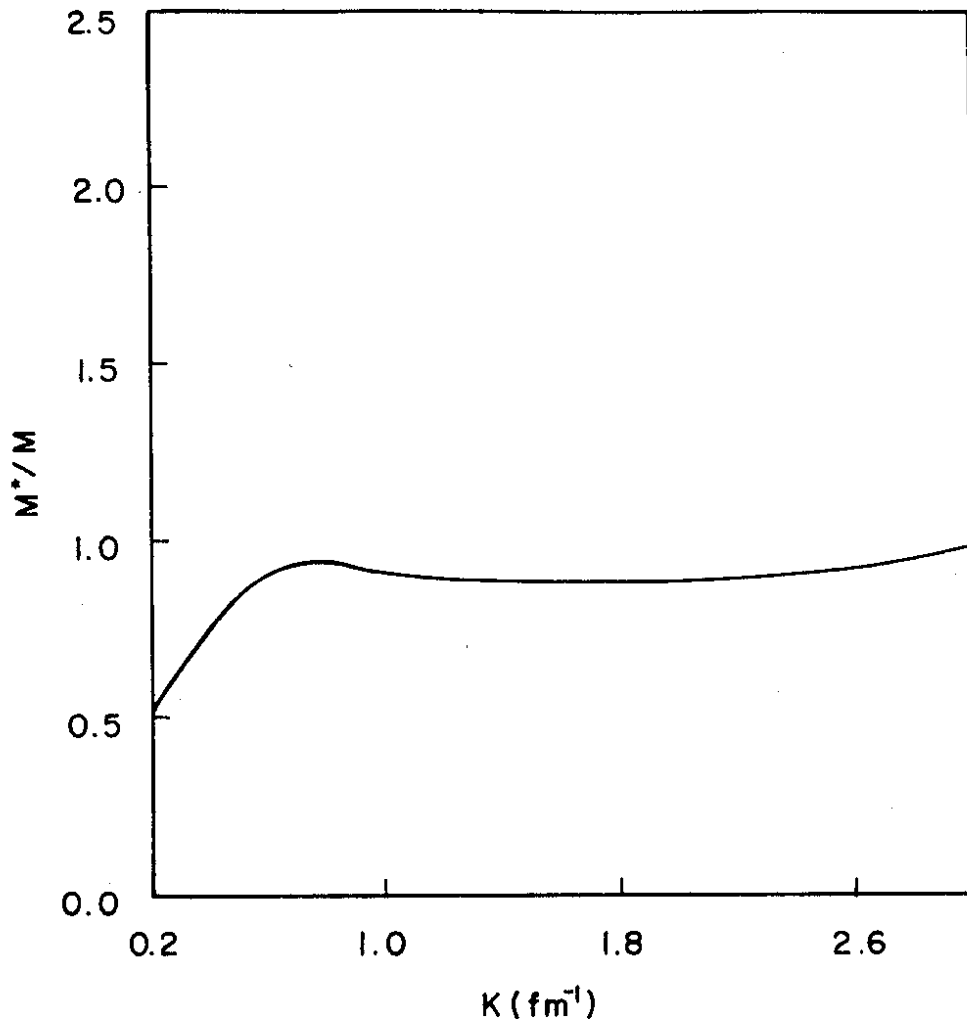


fig. 13

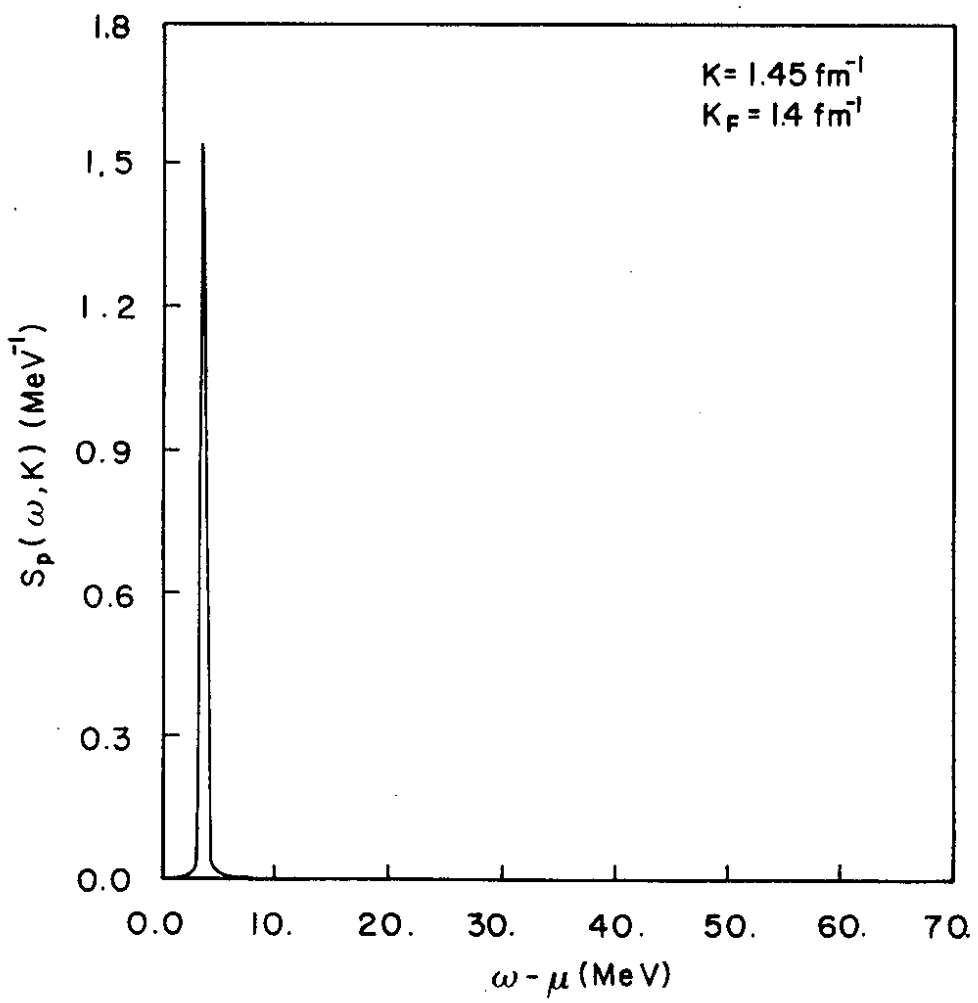


fig 14

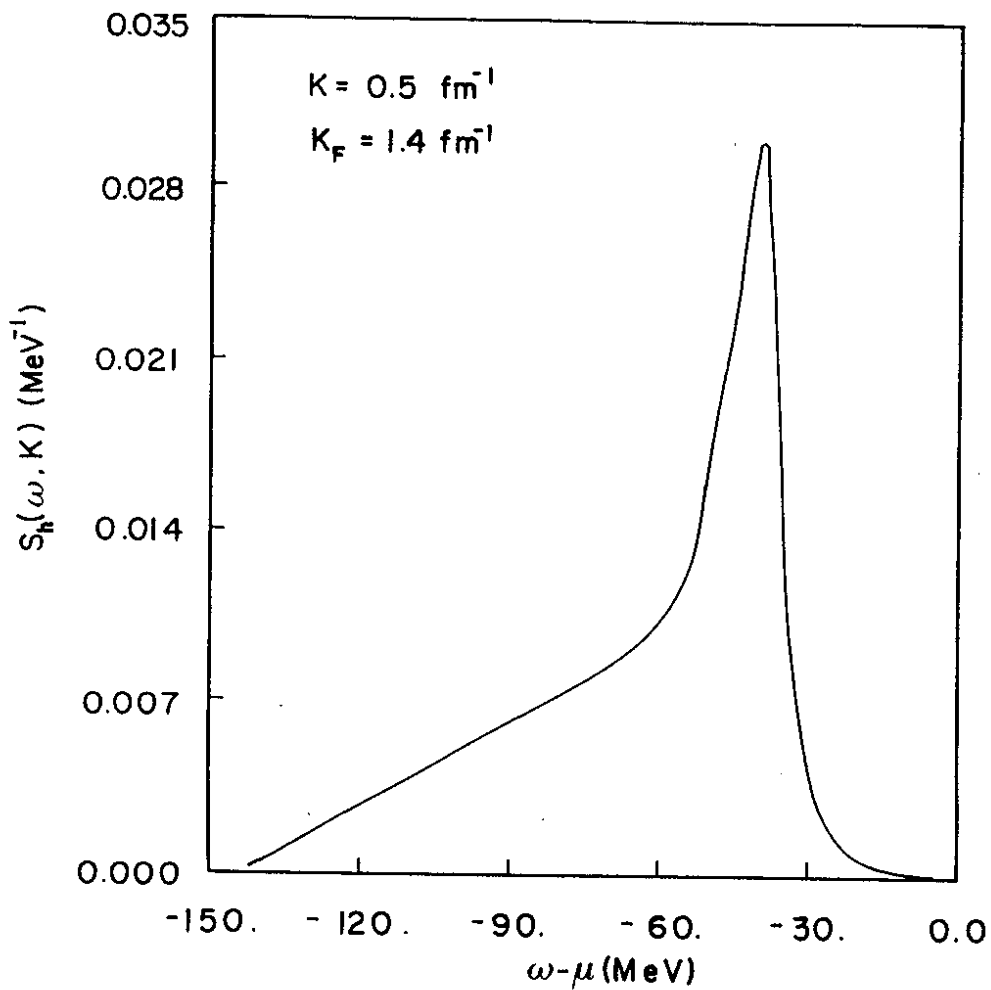


fig. 16

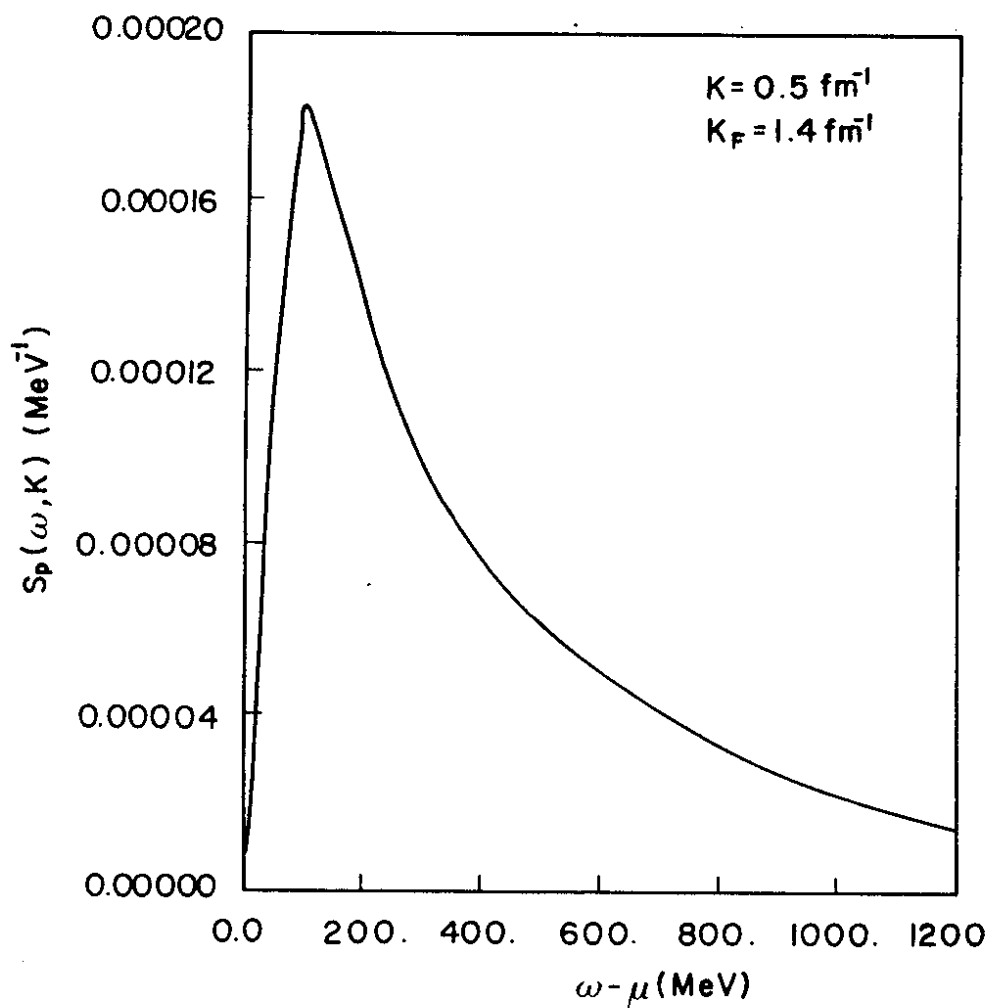


fig. 15

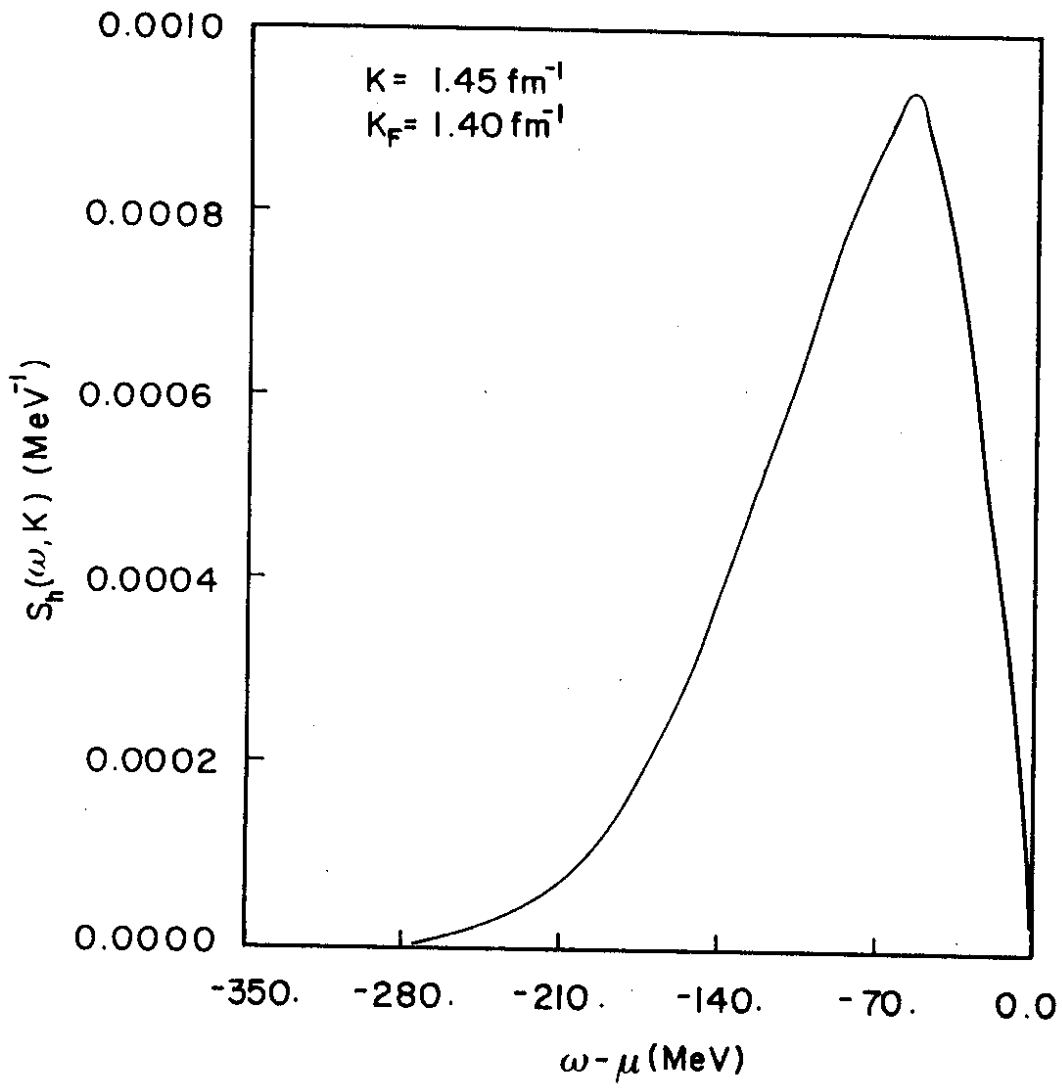


fig. 17



ELSEVIER

Nuclear Physics A 587 (1995) 787–801

NUCLEAR
PHYSICS A

$(^3\text{He},t)$ reactions on unstable nuclei at intermediate energies

S. Hirenzaki ^{a,1}, P. Fernández de Córdoba ^b, N. Fukunishi ^a, D. Hirata ^{a,c},
H. Kitagawa ^a, M.J. Vicente-Vacas ^d

^a *Institute of Physical and Chemical Research (RIKEN), 2-1 Hirosawa, Wako, Saitama 351-01, Japan*

^b *Departamento de Matemática Aplicada, Universidad Politécnica de Valencia 46022 Valencia, Spain*

^c *Instituto de Estudos Avancados – CTA, São José dos Campos, Brazil*

^d *Departamento de Física Teórica and IFIC, Centro Mixto Universidad, de Valencia-CSIC,
46100 Burjassot, Valencia, Spain*

Received 3 May 1994; revised 26 October 1994

Abstract

We study the charge-exchange ($^3\text{He},t$) reactions on unstable nuclei theoretically. Since this charge-exchange reaction takes place on the nuclear surface, this reaction is very sensitive to the neutron skin, and we show that the calculated cross sections are affected strongly by the existence of the neutron skin. This reaction can be observed using the inverse-kinematics method. We think the ($^3\text{He},t$) reaction is very useful to observe the neutron skins and also to get new information on isospin dependence of the Δ excitation mechanism in nuclei.

1. Introduction

The properties of nuclei far from stability have been one of the most interesting subjects in nuclear physics since we got a new tool, “beams of unstable nuclei” [1,2]. Many experimentalists have studied the properties of unstable nuclei extensively in the laboratories where secondary beams of unstable nuclei are available. Many theorists, on their side, have also studied them using the models which were established for stable nuclei [3]. One of the most exciting findings in this field was

¹ Present address: Departamento de Física Teórica, Universidad de Valencia, 46100 Burjassot, Valencia, Spain.

the neutron halo around the ^9Li core in ^{11}Li [1], and the properties of ^{11}Li have been studied extensively [3]. Recently the existence of a thick neutron skin, which has a much larger neutron density than the neutron halo of ^{11}Li , was strongly suggested both theoretically and experimentally [4,5] as a general feature of neutron-rich nuclei. The existence of a proton halo was also suggested [6]. So we are very interested in the surface of unstable nuclei which are expected to have the thick neutron skin or proton skin. And we think that we need to study the neutron skin and proton skin for various nuclei systematically using a proper method.

We consider that the charge-exchange ($^3\text{He},t$) reactions at intermediate energies are suitable to study the nuclear surface since (1) the reaction takes place in the nuclear surface due to the large distortion effects of ^3He and t , (2) the charge-exchange reaction depends strongly on the numbers of neutrons and/or protons which participate in the reaction, (3) the reaction mechanism is relatively simple at intermediate energies and (4) we can perform the experiments using the

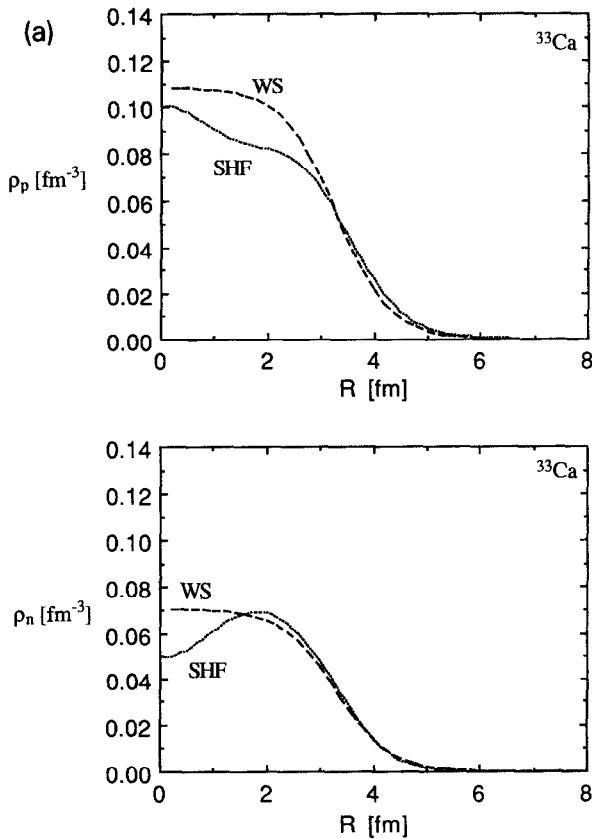


Fig. 1a. The calculated density distributions for ^{33}Ca , which is the proton-drip nucleus in SHF. The dotted lines indicate densities by SHF and the dashed lines indicate densities by the empirical WS density.

The elementary cross sections of $p(^3\text{He},t)$ and $n(^3\text{He},t)$ are very different since (1) positively-charged particles like π^+ must be produced in $p(^3\text{He},t)$ because of the charge conservation, while $n(^3\text{He},t)$ can occur in the $Q \sim 0$ region without any particle production, (2) the Δ -excitation spectra are different for $p(^3\text{He},t)$ and $n(^3\text{He},t)$ [10]. To see this clearly we show the experimental results of $(^3\text{He},t)$ for proton-target and deuteron-target cases in Fig. 2. Roughly speaking the cross section from a neutron target can be obtained by subtracting the spectrum with a proton target from that with a deuteron target. These very different shapes of the cross sections make it possible to know if the neutron and/or proton skin exist or not.

In Fig. 3 we show the calculated N_p and N_n for O, Ca and Zr isotopes as a function of the neutron numbers of the nucleus and compare the results calculated with two different kinds of densities, WS and RMF, which were explained in Section 2. We can see that the RMF densities predicate the rapid change of effective numbers with neutron numbers for all three isotopes. This is a natural result from the density distribution of RMF, which provides the neutron skin for neutron-rich nuclei, and thus N_n can be larger and N_p can be smaller than those calculated with the empirical WS densities for neutron-rich nuclei. We find that the N_n with the RMF densities could even be twice the N_n with the WS densities. From the qualitative study using effective numbers we can expect that the cross sections of the $(^3\text{He},t)$ reactions are very sensitive to the existence of neutron and proton skins.

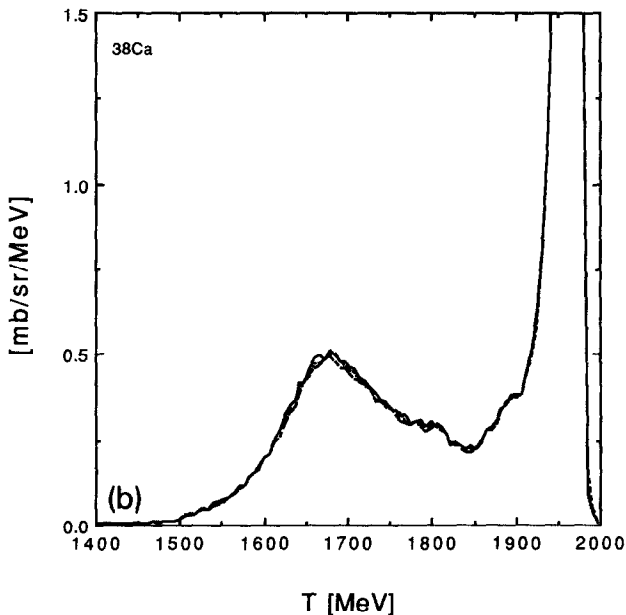


Fig. 5b. As Fig. 5a, using the cascade model for ^{38}Ca , which is the proton-drip nucleus in RMF. The solid line indicates the spectrum with RMF density. The density distributions are shown in Fig. 1b.

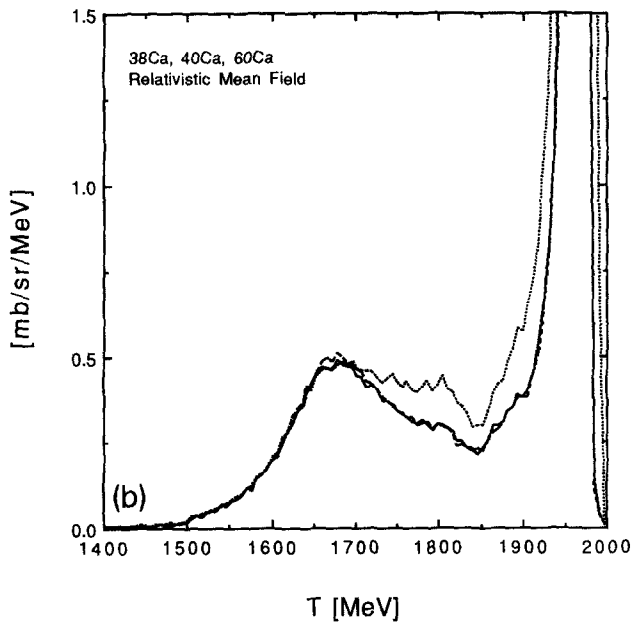


Fig. 4b. As Fig. 4a, using the cascade model with RMF nuclear densities. Here the dashed line is for ^{38}Ca and the dotted line for ^{60}Ca .

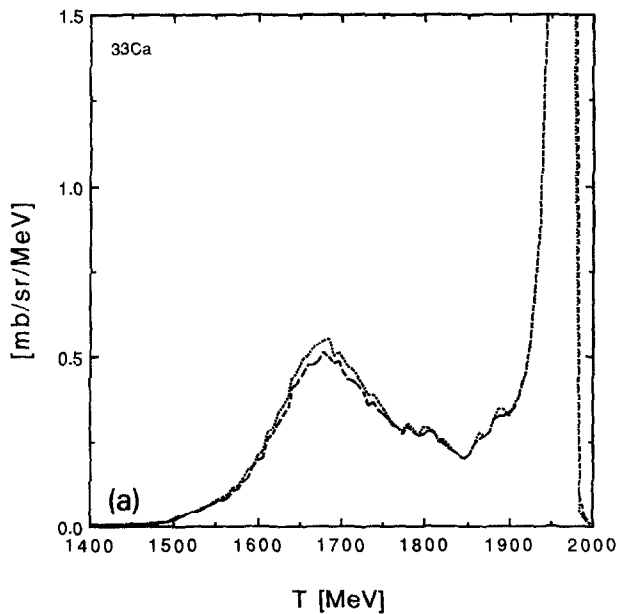


Fig. 5a. Calculated energy spectra of the $(^3\text{He}, t)$ reaction at 2 GeV using the cascade model for ^{33}Ca , which is the proton-drip nucleus in SHF. The cross sections are integrated for the angular range $\theta_{\text{Lab}} = 0-3.2$ (degree). The dotted line indicates the spectrum calculated with SHF density and the dashed line indicates the spectrum with the empirical WS density. The density distributions are shown in Fig. 1a.

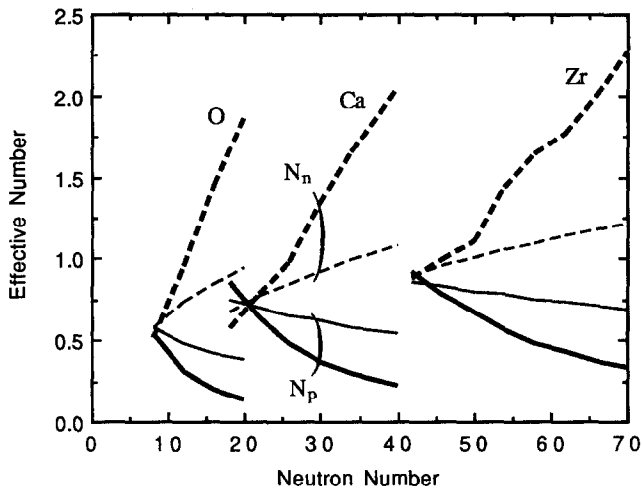


Fig. 3. Proton and neutron effective numbers as a function of the neutron number of the nucleus. The solid lines are the proton effective numbers (N_p) and the dashed lines are the neutron effective numbers (N_n). The thick lines are the results with densities of the relativistic mean-field model (RMF) and the thin lines are the results with the empirical Woods-Saxon densities (WS).

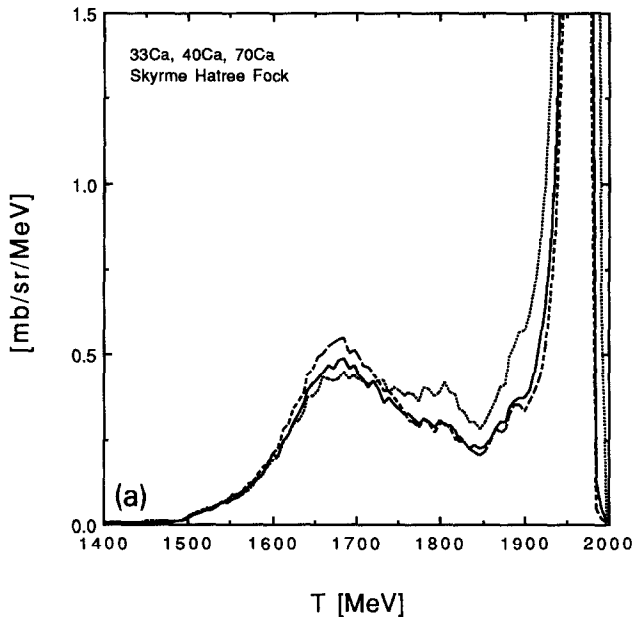


Fig. 4a. Calculated energy spectra of the ($^3\text{He},t$) reaction at 2 GeV using the cascade model with SHF nuclear densities. The cross sections are integrated for the angular range $\theta_{\text{Lab}} = 0-3.2$ (degree). The solid line is the spectrum for ^{40}Ca , the dashed line for ^{33}Ca , and the dotted line for ^{70}Ca .

reactions to the nuclear surface qualitatively, we calculate the effective number of protons and neutrons which participate in the reaction [15]. This method is a good approximation when the incident energy is high enough for the impulse approximation. The effective number of protons and neutrons in the inclusive ${}^A Z({}^3\text{He}, t)X$ reactions can be written as follows:

$$N_i = \int d^3r \rho_i(\mathbf{r}) \exp\left(-\bar{\sigma} \int_{-\infty}^{\infty} dz' \rho(\mathbf{b}, z')\right), \quad (1)$$

where the index i indicates the p(roton) and/or n(eutron) and $\bar{\sigma} = (\sigma_{tN} + \sigma_{hN})/2$. The triton–nucleon and ${}^3\text{He}$ –nucleon total cross sections are written as σ_{tN} and σ_{hN} , respectively. Here $\rho(\mathbf{r}) = \rho_p(\mathbf{r}) + \rho_n(\mathbf{r})$ is the density distribution of the nucleus and $\rho(\mathbf{b}, z)$ indicates the nuclear density at an impact parameter \mathbf{b} and beam-direction coordinate z . Using the N_p and N_n we can write the cross section approximately as

$$\left(\frac{d\sigma}{d\Omega dE}\right)_{AZ({}^3\text{He}, t)X} = N_p \left(\frac{d\sigma}{d\Omega dE}\right)_{p({}^3\text{He}, t)X} + N_n \left(\frac{d\sigma}{d\Omega dE}\right)_{n({}^3\text{He}, t)X}, \quad (2)$$

with the elementary cross sections of a proton and neutron target. In this expression the many nucleon contributions and Fermi motion are neglected.

$$\frac{d^2\sigma}{dEd\Omega} \left[\frac{\text{mb}}{\text{sr}\cdot\text{MeV}} \right]$$

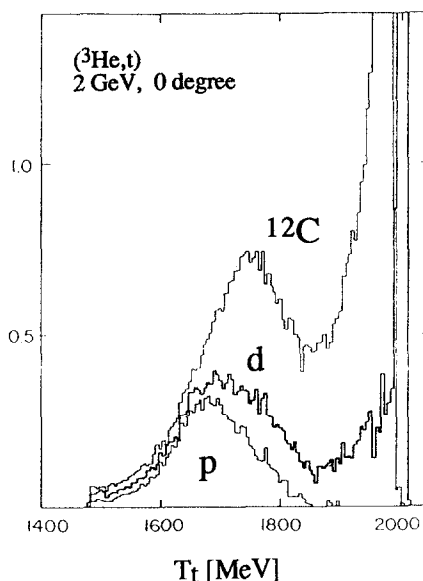


Fig. 2. Double differential cross section for the $({}^3\text{He}, t)$ reaction in the laboratory system for the targets p, d and ${}^{12}\text{C}$. Experimental results are taken from Ref. [7].

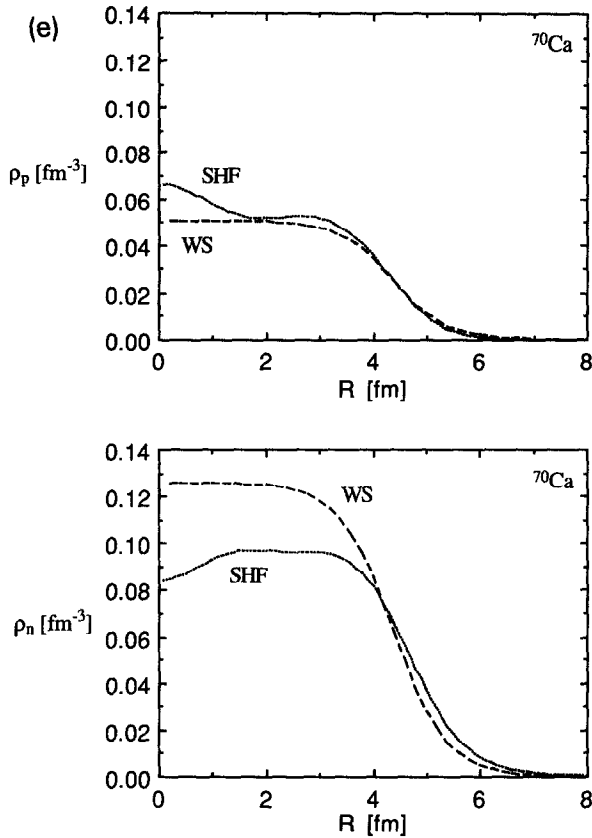


Fig. 1e. The calculated density distributions for ^{70}Ca , which is the neutron-drip nucleus in SHF. Lines as in Fig. 1b

These three kinds of density distributions for Ca isotopes are shown in Fig. 1. We show the densities for ^{33}Ca which is the proton-drip nucleus in SHF in Fig. 1a, for ^{38}Ca which is the proton-drip nucleus in RMF in Fig. 1b, for ^{40}Ca which is the typical stable nucleus in Fig. 1c, for ^{60}Ca which is the neutron-drip nucleus in RMF in Fig. 1d, and for ^{70}Ca which is the neutron-drip nucleus in SHF in Fig. 1e. We can see from Fig. 1c that all three models provide almost the same distributions on the surface of the stable nucleus. However, the three models provide different surface distributions for unstable nuclei. For example, for the neutron-rich nucleus ^{60}Ca , different tail shapes of neutron distributions are given by the three models. This means that the theoretical models for the nuclear-surface distribution have certain ambiguities and further studies are necessary.

3. Effective number approach

The data of $(^3\text{He},t)$ reactions go like $A^{1/3}$ which indicates that the reaction takes place in the nuclear surface [7]. In order to show the sensitivity of the $(^3\text{He},t)$

2. Nuclear-density distributions

In this section we summarize the density distributions of the target nucleus which we use in this paper to get the ($^3\text{He},t$) reaction cross sections.

- (1) The Woods–Saxon (WS) density distribution with the radius parameter $R = 1.18A^{1/3} - 0.48$ (fm) and the diffuseness $a = 0.5$ (fm). This distribution was established by the study of the stable nuclei and does not provide the neutron skin.
- (2) The calculated density distribution by the relativistic mean-field model (RMF) [12]. All the details of the RMF are described in Ref. [4] including the definitions of parameter sets used in the model. Here we used the parameter set NL1. It provides the thick neutron skin of neutron-rich nuclei.
- (3) The calculated density distributions by Hatree–Fock theory with the standard SIII Skyrme interaction (SHF) [13]. All details of the calculation are given in Ref. [14]. This model also provides the thick neutron skin.

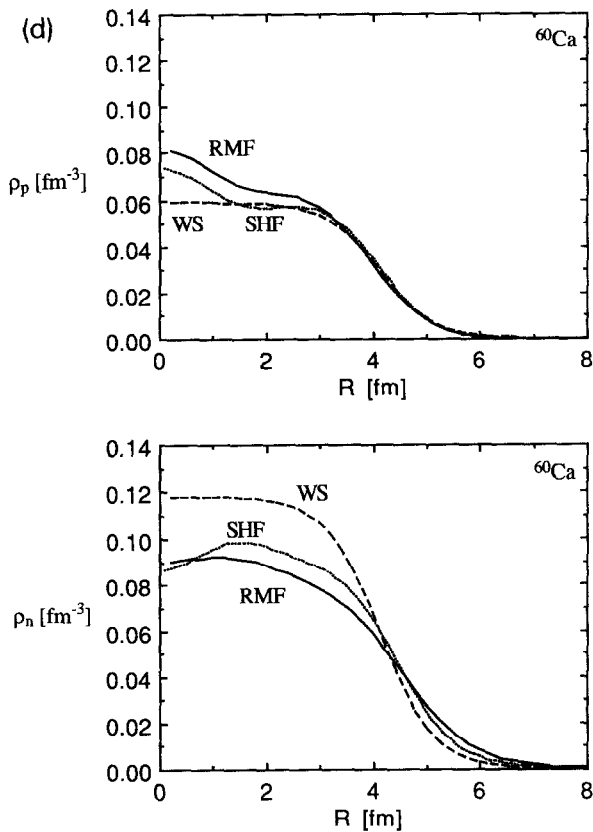


Fig. 1d. The calculated density distributions for ^{60}Ca , which is the neutron-drip nucleus in RMF. Lines as in Fig. 1b.

inverse kinematics with unstable-nuclei beams. These conditions are also satisfied for other charge-exchange reactions such as (p,n), (^{14}N , ^{14}C), and so on. They are, roughly to say, the same as the (^3He ,t) reactions except for a few differences; those are: (1) the (p,n) reaction is not so sensitive to the nuclear surface because of a smaller distortion than (^3He ,t), and (2) the charge-exchange reactions with heavier projectiles are restricted to a smaller Q -value region because of their form factors. We consider here the (^3He ,t) reactions since the reaction has been studied extensively for stable nuclei [7], and we can calculate the reaction cross section reliably using the model of Ref. [8].

In addition to the possible sensitivity to the nuclear surface of the unstable nuclei, the Δ -excitation by the (^3He ,t) reactions is an interesting subject since the Δ -peak shifts were found in stable nuclei. The Δ -peak position in nuclei was found to be shifted from the position of the Δ -excitation in the proton, and this shift was

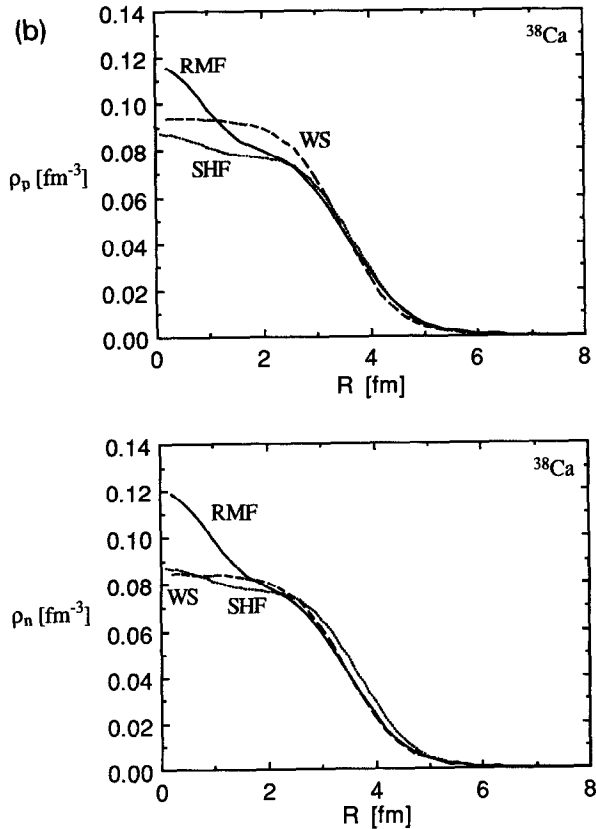


Fig. 1b. The calculated density distributions for ^{38}Ca , which is the proton-drip nucleus in RMF. The dotted lines indicate densities by SHF and the dashed lines indicate densities by the empirical WS density. The solid lines indicate densities by RMF.

found to be independent of the target mass [9] for stable nuclei. We think that to observe the Δ -resonances in unstable nuclei is a method to see the nucleon isospin dependence of the reaction mechanism since the unstable nuclei are expected to have a thick neutron/proton skin. In other words we can observe the Δ -excitation on a neutron target by $({}^3\text{He},t)$ reactions on neutron-rich nuclei because of the neutron skin. In the models [8,10,11] the isospin dependence is essential to understand the peak shift. Therefore, we can expect to obtain new information on the Δ -excitation mechanisms by $({}^3\text{He},t)$ reactions on unstable nuclei.

In Section 2 we summarize the proton and neutron densities which we use in this paper. We apply the effective number approach to the $({}^3\text{He},t)$ reaction and show qualitatively the sensitivity of the neutron and proton skin to the reaction cross section in Section 3. We calculate the quantitative cross sections in Section 4. Section 5 is devoted to the summary.

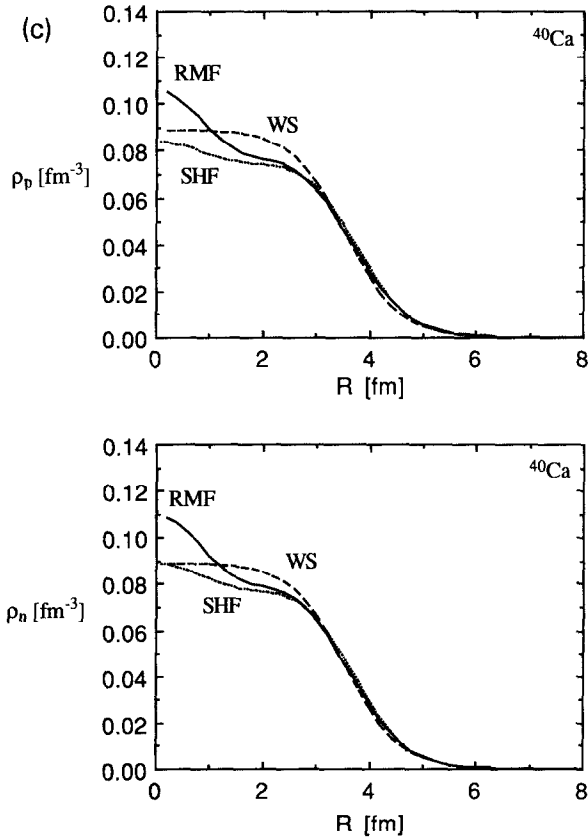


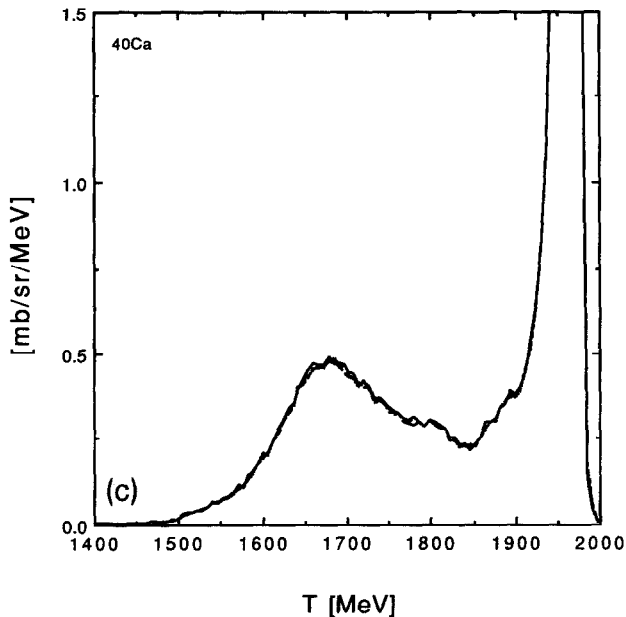
Fig. 1c. The calculated density distributions for ${}^{40}\text{Ca}$, which is the typical stable nucleus. Lines as in Fig. 1b.

4. Cross sections of ($^3\text{He},t$) reactions

In this section we show the calculated cross sections of the ($^3\text{He},t$) reactions. To get realistic results, we used the cascade program which was developed to study the inclusive ($^3\text{He},t$) reaction on nuclei in Ref. [8].

In Figs. 4a and b we show the isospin dependence of the calculated ($^3\text{He},t$) spectra in SHF and RMF. We can see the isospin dependence well in both models. For proton-rich nuclei the peak of the Δ -excitation can be seen clearly, while for neutron-rich nuclei the spectra have a flat shape in the region of $T = 1650\text{--}1800$ MeV. This feature reflects directly the fact that the ($^3\text{He},t$) spectrum from a neutron target does not have a clear peak [10]. With these results we can expect to get new information on the Δ -excitation mechanism by the ($^3\text{He},t$) experiments on unstable nuclei. Especially we can expect to have the spectrum from the neutron target using the neutron skin. We can also see that the quasi-elastic region ($T \sim 1950$ MeV) depends strongly on nuclear isospin. Because of the charge conservation, the proton target can not contribute to the quasi-elastic region. So the quasi-elastic cross section is larger for neutron-richer nuclei.

We would like to check next if we can distinguish the model of nuclear structure by the ($^3\text{He},t$) reactions. For this purpose, we compare the spectra that are calculated using the three nuclear-structure models in Fig. 5. The models of nuclear structure are described in Section 2. We see from Fig. 5c that all models



ig. 5c. As Fig. 5b, using the cascade model for ^{40}Ca , which is the typical stable nucleus. The density distributions are shown in Fig. 1c.

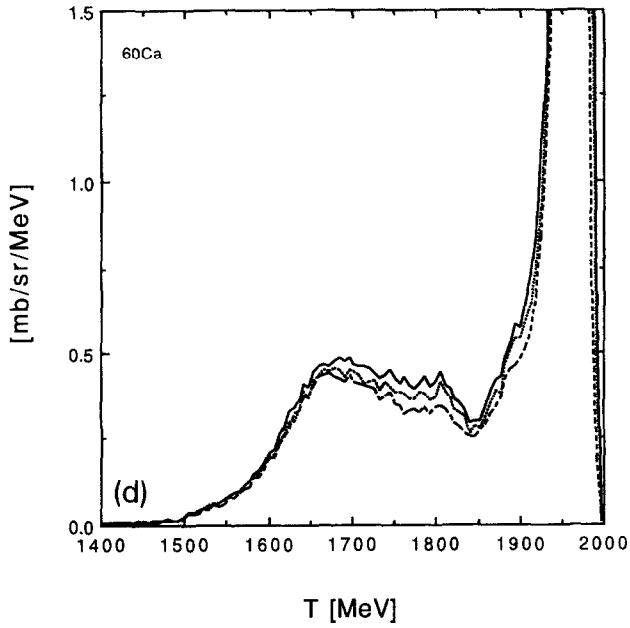


Fig. 5d. As Fig. 5b, using the cascade model for ^{60}Ca , which is the neutron-drip nucleus in RMF. The density distributions are shown in Fig. 1d.

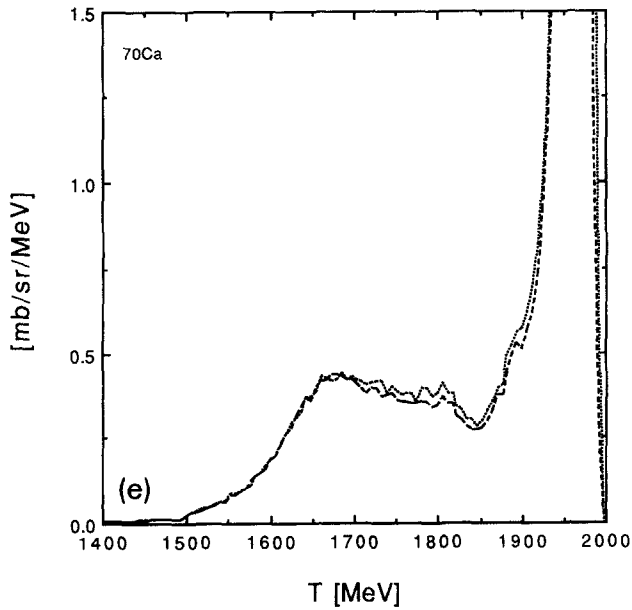


Fig. 5e. As Fig. 5b, using the cascade model for ^{70}Ca , which is the neutron-drip nucleus in SHF. The density distributions are shown in Fig. 1e.

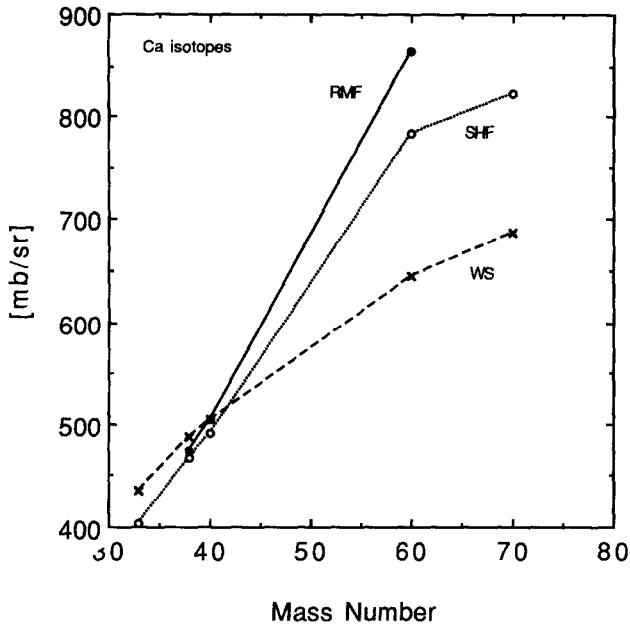


Fig. 6. Energy-integrated cross section at $\theta_{\text{Lab}} = 0-0.5$ (degree) for Ca isotopes. The dotted line indicates the cross section calculated with the SHF density, the dashed line indicates the cross section with the empirical WS density, and the solid line indicates the cross section with the RMF density.

provide almost the same spectrum of ^{40}Ca . This is natural since all models have been checked in the stable nuclei. The discrepancies are small for proton-rich nuclei, ^{33}Ca and ^{38}Ca . For the neutron-rich nucleus ^{60}Ca we can see a certain gap between each spectrum. The gap is, however, still small and we must have both excellent data and theory of the reaction to distinguish the models of nuclear structure. We show the energy-integrated differential cross sections at forward angles in Fig. 6. The cross sections of ^{40}Ca are almost the same for the three densities again. We can see from the figure that the cross section strongly depends on the neutron number and the model of nuclear structure. This is mainly due to the isospin dependence of the quasi-elastic contribution. The energy-integrated cross section will be a good observable to distinguish the nuclear structure models. Our results for the Woods–Saxon case have a similar dependence on the neutron and proton number as the one found in Ref. [16].

5. Summary

In summary, we have studied the charge-exchange $^AZ(^3\text{He},t)$ reactions on unstable nuclei. Since the reaction takes place in the surface region and is a charge-exchange reaction, it is sensitive to the structure of the nuclear surface,

especially to the neutron and proton skin. And we think that this feature makes it possible to study the nuclear surface and/or the isospin dependence of the reaction mechanism.

We applied the effective number approach to the reaction and showed that the existence of the neutron skin changes the cross section of ${}^A Z({}^3\text{He}, t)$ considerably. Then we studied the reaction using a realistic cascade model with three kinds of calculated density distributions. The results show that (1) the isospin dependence of the reaction mechanism, especially in the Δ -excitation region, will be seen in the shape of the energy spectrum of the reaction, and (2) the energy-integrated cross section will be a good observable to check the model of the nuclear structure. For the study of the reaction mechanism, the present work is complementary to the work of Ref. [11].

Experiments of this (${}^3\text{He}, t$) reaction can be performed for unstable nuclei using the inverse-kinematics method in which the target ${}^3\text{He}$ is bombarded by a secondary unstable nuclear beam. The reaction, therefore, can be a powerful tool for a systematic study of the neutron skin of unstable nuclei. Finally we mention that heavier projectiles are more sensitive to the nuclear surface than ${}^3\text{He}$ and t because of larger distortion effects. Hence, it is also interesting to use heavier particles in experiments. In these cases, however, the Δ -resonance peak may not be seen well because of the projectile–ejectile form-factor effect.

Acknowledgements


We would like to express our appreciation to Profs. H. Toki and E. Oset for fruitful discussions. We are also most grateful to Profs. I. Tanihata and T. Kobayashi for their many suggestions. We acknowledge useful discussions with Dr. K. Sumiyoshi on neutron-rich nuclei. This work is supported by the Special Researcher's Basic Science Program of RIKEN and CICYT, under contract AEN 93-1205.

References

- [1] I. Tanihata, H. Hamagaki, O. Hashimoto, Y. Shiba, N. Yoshikawa, K. Sugimoto, O. Yamakawa, T. Kobayashi and N. Takahashi, *Phys. Rev. Lett.* 55 (1985) 2676.
- [2] I. Tanihata, *Treatise on heavy-ion science*, Vol. 8, ed. D.A. Bromley (Plenum Press, New York, 1989) p. 443.
- [3] K. Ikeda and Y. Suzuki, Eds., *Proc. Int. Symp. on Structure and reactions of unstable nuclei* (World Scientific, Singapore, 1991).
- [4] D. Hirata, H. Toki, T. Watabe, I. Tanihata and B.V. Carlson, *Phys. Rev. C* 44 (1991) 1467.
- [5] I. Tanihata, D. Hirata, T. Kobayashi, S. Shimoura, K. Sugimoto and H. Toki, *Phys. Lett. B* 289 (1992) 261.
- [6] T. Minamisono, T. Ohtsubo, I. Minami, S. Fukuda, A. Kitagawa, M. Fukuda, K. Matsuta, Y. Nojiri, S. Takeda, H. Sagawa and H. Kitagawa, *Phys. Rev. Lett.* 69 (1992) 2058.
- [7] C. Gaarde, *Nucl. Phys. A* 478 (1988) 475c.
- [8] P. Fernández de Córdoba, PhD thesis, University of Valencia (1992);

- P. Fernández de Córdoba, E. Oset and M.J. Vicente-Vacas, *Nucl. Phys. A*, submitted;
E. Oset, P. Fernández de Córdoba, J. Nieves and M.J. Vicente-Vacas, *Phys. Scripta* 48 (1993) 101.
- [9] D. Contardo, M. Bedjidian, J.Y. Grossiord, A. Guichard, R. Haroutunian, J.R. Pizzi, C. Ellegaard, C. Gaarde, J.S. Larsen, C. Goodman, I. Bergqvist, A. Brockstedt, L. Carlen, P. Ekstrom, D. Bachelier, J.L. Boyard, T. Hennino, J.C. Jourdain, M. Roy-Stephan, M. Boivin and P. Radvanyi, *Phys. Lett. B* 168 (1986) 331.
- [10] E. Oset, E. Shiino and H. Toki, *Phys. Lett. B* 224 (1989) 249.
- [11] P. Fernández de Córdoba and E. Oset, *Nucl. Phys. A* 544 (1992) 793.
- [12] B.D. Serot and J.R. Walecka, *Adv. Nucl. Phys.* 16 (1986) 1.
- [13] M. Beiner, H. Flocard, N. Van Giai and P. Quentin, *Nucl. Phys. A* 238 (1975) 29.
- [14] N. Fukunishi, T. Otsuka and I. Tanihata, *Phys. Rev. C* 48 (1993) 1648.
- [15] G.F. Bertsch and O. Scholten, *Phys. Rev. C* 25 (1982) 804.
- [16] C. Gaarde, *Ann. Rev. Nucl. Part. Sci.* 41 (1991) 187.

Isoscalar Roper Excitation in $p(\alpha, \alpha')$ Reactions in the 10 – 15 GeV Region

S. Hirenzaki^a, , E. Oset^a, P. Fernández de Córdoba^b

^a Departamento de Física Teórica and IFIC, Centro Mixto Universidad de Valencia - CSIC, 46100 Burjassot (Valencia) Spain.

^b Departamento de Matemática Aplicada, Universidad Politécnica de Valencia, 46022 Valencia, Spain.

Abstract

Recent experiments at Saturne at 4 GeV showed that the (α, α') reaction on the proton shows two distinctive peaks, which were associated to Δ projectile excitation and Roper target excitation. A subsequent theoretical analysis has shown that this picture is qualitatively correct but there are important interference effects between the two mechanisms. Furthermore, at this energy the ratio of strengths for the Roper and Δ peak is about 1/4. In the present paper we show that by going to the 10 – 15 GeV region the interference effects become negligible, the signal for the Roper excitation is increased by more than an order of magnitude and the ratio of cross sections at the peaks for Roper and Δ excitation becomes of the order of unity, thus making this range of energies ideal for studies of isoscalar Roper excitation.

¹ JSPS research fellow

The (α, α') reaction on proton targets at kinetic energy $T_\alpha = 4.2 \text{ GeV}$ was studied at SATURNE [1] and two distinctive peaks were identified (see Fig. 1), which were associated to Δ excitation in the α projectile and Roper excitation in the proton target (see Fig. 2). In a recent theoretical analysis we showed that the two mechanisms of Fig. 2 were dominant in the reaction and that other possible mechanisms, like Roper excitation on the projectile or two Δ excitation, were negligible [2]. However, it was found that the interference between the two mechanisms in Fig. 2 was appreciable and it was important to consider for a proper analysis of the data and the excitation of the isoscalar $NN \rightarrow NN^*$ transition amplitude.

In Fig. 1 one can see the results for the projectile Δ excitation, Roper target excitation and interference. One observes there that the interference term is large and that the strength of the Roper is about 1/4 of the strength of the Δ excitation at their peaks.

It would be interesting to have other experiments which magnified the strength of Roper excitation, both in absolute terms and relative to the Δ and if possible diminished the interference term, which makes a theoretical model necessary in order to separate the Roper contribution. All these things are accomplished by performing the (α, α') reaction at higher energies, as we explain here.

We take the same model which was used in [2] to analyse the (α, α') reaction at 4 GeV . The cross section for the processes

$$\alpha + p \rightarrow \alpha + p + \pi^0$$

$$\alpha + p \rightarrow \alpha + n + \pi^+ \quad (1)$$

is given by

$$\begin{aligned} \frac{d^2\sigma}{dE_{\alpha'}d\Omega_{\alpha'}} &= \frac{p_{\alpha'}}{(2\pi)^5} \frac{M_{\alpha'}^2 M^2}{\lambda^{1/2}(s, M^2, M_{\alpha'}^2)} \int d^3p_{\pi} \frac{1}{E_{N'}\omega_{\pi}} \\ &\times \bar{\Sigma}\Sigma|T|^2\delta(E_{\alpha} + E_N - E_{\alpha'} - E_{N'} - \omega_{\pi}), \end{aligned} \quad (2)$$

where $\lambda(\dots)$ is the Källén function and s the Mandelstam variable for the initial $p - \alpha$ system.

By means of eq. (2) we can take into account the mechanisms of Δ excitation in the projectile, Fig. 2a, and the Roper excitation in the target, Fig. 2b, with the Roper decaying into a nucleon and a pion (which accounts for about 65% of the N^* free width). The contribution of the Roper decay into $\pi\pi N$ is also accounted for in [2] and is included in the final results here but it does not interfere with the amplitude of Δ excitation in the projectile, since the final states are different.

The T matrix for the diagram 2a is evaluated taking into account $\pi + \rho$ exchange together with the Landau Migdal induced correction. For the diagram of Fig. 2b, which enforces the exchange of an isoscalar object, we take an effective " σ " exchange, which incorporates the possible exchange of an ω meson and the effect of nuclear correlations. The strength of this isoscalar exchange piece is determined by making a fit to the experiment of ref. [4]. The expressions for the Δ and Roper terms and the interference can be seen in eq. (4) of ref. [3] and eqs. (4), (20) of ref. [2]. Their reproduction here is not necessary to understand the results.

We have evaluated the cross section for the (α, α') reaction on the proton, using the same model, for kinetic energies 10 *GeV* and 15 *GeV* of the α particle. We show in Fig. 3 the results obtained for 15 *GeV*. Those at 10 *GeV* are qualitatively similar but the Roper and Δ peaks have a strength of about 4 [*mb/(sr·MeV)*]. In Fig. 3 we show the results of the Roper excitation (with decay of the Roper into πN), those of the Δ projectile excitation, their interference and the sum, which includes also the contribution of the $N^* \rightarrow \pi\pi N$ decay (with the distortion of the two pions by the ${}^4\text{He}$ nucleus which must remain unbroken). Comparison of Fig. 3 with Fig. 1 shows the welcome feature of the 15 *GeV* reaction:

- i) The cross section for the Roper excitation is increased by more than an order of magnitude with regard to the one at 4 *GeV*.
- ii) The strength of the Roper and Δ peaks is similar, while at 4 *GeV* the former had a strength of about 1/4 of the latter.
- iii) The interference term is practically negligible compared to the Roper contribution. This is in contrast with the 4 *GeV* case where the strength of these two terms was similar.

A situation like the one in Fig. 3 makes experimentally much easier the extraction of information on the properties of Roper excitation by an isoscalar source. Such experiments can be easily implemented in the Synchrophasotron of Dubna which accelerates nuclei up to $T_{kin} \simeq 4 \text{ GeV}/A$ and in the new superconductive synchrotron, the Nuclotron, which accelerates nuclei up to $T_{kin} \simeq 6 \text{ GeV}/A$ [4]. In fact in a related experiment carried out at Dubna

on the $C(d, d')X$ reaction [3] at $8.9 \text{ GeV}/c$, a reanalysis of the data in terms of M_X calculated for the $p(d, d')$ kinematics shows a clear peak around the Roper mass [6].

It is relatively easy to understand the features observed in the results at 15 GeV . In the first place the small interference. It is easy to see that as the energy of the beam increases it becomes progressively more difficult to have the same kinematic configuration of α, N, π in the final state for the two mechanisms of Fig. 2. Indeed, in the lab. system the pion coming from the decay of the Roper in the mechanism of Fig. 2b will be distributed in a wide range of angles (it would be isotropic for the N^* decay at rest, but the effective σ brings some momentum along). However, the pion coming from the Δ decay in the mechanism of Fig. 2a will be directed in a very narrow cone along the direction of motion of the α particle in the frame where the initial proton is at rest. The cone becomes narrower as the α particle energy increases and, hence, the overlap of the final state configurations in the two mechanisms of Fig. 2 (and the interference term) becomes smaller as T_α increases.

In order to understand the change of strength of the Roper and Δ excitations and their relative weight we must look at another factor. The reason in this case lies in the nucleus form factor which one has in this reaction.

Indeed, in both the mechanisms of Fig. 2 the amplitude contains the nuclear form factor [3]

$$F_{He}(\vec{k}) = \int d^3r \rho_{He}(\vec{r}) \exp \left[-\frac{1}{2} \int_{-\infty}^{\infty} \sigma_{NN} \rho_{He}(\vec{b}, z') dz' \right] e^{i\vec{k}\cdot\vec{r}}$$

$$\times \exp \left[-\frac{i}{2} \int_0^\infty \frac{1}{p_\pi} \Pi(p_\pi, \rho_{He}(\vec{r}')) d\ell \right], \quad (3)$$

where

$$\begin{aligned} \vec{r}' &= \vec{r} + \frac{\vec{p}_\pi}{|\vec{p}_\pi|} \ell, \\ \vec{k} &= \vec{p}_\alpha - \vec{p}_{\alpha'}. \end{aligned} \quad (4)$$

The momenta $\vec{p}_\alpha, \vec{p}_{\alpha'}, \vec{p}_\pi$ appearing in eqs. (3), (4) are evaluated in the frame where the initial α particle is at rest. In eq. (3) $\rho_{He}(\vec{r})$ is the Harmonic - Oscillator density distribution of the α particle, σ_{NN} the nucleon-nucleon total cross section and $\Pi(p_\pi, \rho)/2\omega_\pi$ is the pion nuclear optical potential, taken from ref. [7] up to $T_\pi \simeq 250 MeV$ and extrapolated at high energies when needed using the lowest order optical potential [2].

The form factor of eq. (3) is the 4He nuclear form factor incorporating the distortion of the proton and pion waves, both in the eikonal approximation. Now when T_α increases, for a same energy transfer the momentum transfer is smaller. Indeed in the forward direction of the α' we have

$$\begin{aligned} p_\alpha - p_{\alpha'} &= \sqrt{E_\alpha^2 - M_\alpha^2} - \sqrt{E_{\alpha'}^2 - M_\alpha^2} \\ &\simeq E_\alpha - E_{\alpha'} - \frac{M_\alpha^2}{2E_\alpha} + \frac{M_\alpha^2}{2E_{\alpha'}} = (E_\alpha - E_{\alpha'}) \left(1 + \frac{M_\alpha^2}{2E_\alpha E_{\alpha'}} \right). \end{aligned} \quad (5)$$

Hence, the invariant four momentum transfer squared will be

$$-q^2 \simeq (E_\alpha - E_{\alpha'})^2 \left(\left[1 + \frac{M_\alpha^2}{2E_\alpha E_{\alpha'}} \right]^2 - 1 \right) \quad (6)$$

which decreases as E_α increases. The magnitude $-q^2$ is equivalent to \vec{k}^2 in the Breit frame of the nucleus and is essentially also \vec{k}^2 of eqs. (3), (4) for the ${}^4\text{He}$ at rest. Hence, we should expect an increase of the value of the nucleus form factor, $F_{He}(\vec{k})$ as E_α increases. Furthermore the relative increase in the form factor (think in terms of the undistorted $\exp[-\vec{k}^2/4\alpha^2]$ form factor of ${}^4\text{He}$ with $\alpha^2 = 0.76\text{fm}^{-2}$) will be bigger if the excitation energy $E_\alpha - E_{\alpha'}$ is bigger. This is actually what we see in Fig. 4, where we plot the ratio of $|F_{He}(\vec{k})|^2$ at two different T_α energies, 10 GeV and 4.2 GeV, and 15 GeV and 4.2 GeV.

We observe in Fig. 4 that at $\omega = E_\alpha - E_{\alpha'}$ around 200 MeV, where the Δ peak appears, the increase of the form factor is moderate. However, at $\omega = 550$ MeV, where the Roper peak appears, the ratio of form factors squared has a value of the order of four to five. This factor is the one responsible for the relative increase of strength of the Roper excitation versus the Δ excitation at $T_\alpha = 15$ GeV with respect to the experiment of [1] at 4.2 GeV.

The absolute increase in strength both for the Roper and Δ excitation can be traced back both to the form factor effect and the phase space factor $p_{\alpha'}$ in the numerator of the cross section formula of eq. (2).

One might think that performing more exclusive experiments, *i.e.*, detecting a pion and a nucleon in coincidence and making a plot in terms of the πN invariant mass, one would magnify the Roper peak with respect to a background. We have checked theoretically, within our model, that this is

not the case and the invariant mass distribution which one obtains resemble very much the ω distributions of Fig. 1 and 3.

In our theoretical model we have neglected any dependence of the interaction on the energy, since we have no elements to think that this might be the case. Obviously a certain energy dependence cannot be ruled out, an information which would be provided by the same experiment and which would be much useful to help construct microscopic models for the interaction.

The results obtained here should encourage the implementation of the experiments. After decades of studies around the Δ region the time has come to study in detail the properties of the next nucleon excitation. Quark models have difficulties to explain the properties of the Roper [8]; the authors of ref. [9] suggested that the Roper could be interpreted as a monopole excitation of the nucleon (breathing mode); the decay of the Roper into two pions in S-wave plays an important role in the $\pi N \rightarrow \pi\pi N$ reaction close to threshold [9, 10], which must be brought under control in order to make predictions about the $\pi\pi$ scattering length, *etc.*

The proposed experiments exciting the Roper with an isoscalar source will bring new information about this resonance, its decay and its coupling to different hadronic components and will pose new challenge to models of this resonance.

We would like to acknowledge useful discussions with E. Strokovsky. One of us (S. H.) acknowledges the hospitality of Departamento de Física Teórica,

Univ. de Valencia where this work has been done. This work has been partly supported by CICYT contract no. AEN 93-1205.

References

- [1] H. P. Morsch *et.al.*, Phys. Rev. Lett. 69 (1992) 1336.
- [2] S. Hirenzaki, P. Fernández de Córdoba, E. Oset, Phys. Rev. C in print.
- [3] P. Fernández de Córdoba, E. Oset, M. J. Vicente-Vacas, Yu. Ratis, J. Nieves, B. López-Alvaredo, and F. Gareev, Nucl. Phys. A586 (1995) 586.
- [4] E. A. Strokovsky, talk in the European Few Body 95 Conf., Peniscola (Spain), June 1995, Ed. R. Guardiola, Few Body Systems Suppl. (1995) to be published.
- [5] V. G. Ableev *et.al.*, Yad. Fiz 37 (1983) 348, Sov. J. Nucl. Phys. 37 (1983) 209; E. A. Strokovsky and F. A. Gareev, Phys. At. Nucl. 58 (1995) 1.
- [6] E. A. Strokovsky, private communication.
- [7] J. Nieves, E. Oset, C. Garcia-Recio, Nucl. Phys. A554 (1993) 509.
- [8] B. Silvestre-Brac, C. Gignoux, Phys. Rev. D32 (1985) 743.
- [9] E. Oset, M. J. Vicente-Vacas, Nucl. Phys. A446 (1985) 584.
- [10] V. Bernard, N. Kaiser and U. G. Meißner, preprint, [hep-ph/9507418](https://arxiv.org/abs/hep-ph/9507418).
- [11] H. P. Morsch, private communication.

Figure Caption

Fig. 1 Calculated cross sections of the target Roper process [2] and the projectile Δ process [3] at $E_\alpha = 4.2 \text{ GeV}$ and $\theta_{Lab} = 0.8^\circ$. The variable ω is the energy transfer defined as $\omega = E_\alpha - E_{\alpha'}$. The thick line indicates the sum of all contributions. Experimental data are taken from ref. [11]. Here we used $g_{\sigma NN^*}^2/4\pi = 1.33$, $M^* = 1430 \text{ MeV}$, $\Gamma^*(s = M^{*2}) = 300 \text{ MeV}$.

Fig. 2 Diagrams for the (α, α') reaction which we consider in this paper. They are (a) Δ excitation in the projectile [3], (b) Roper excitation in the target [2]. The σ exchange must be interpreted as an effective interaction in the $T = 0$ exchange channel [2].

Fig. 3 Same as Fig. 1. Here $E_\alpha = 15 \text{ GeV}$ and $\theta_{Lab} = 0^\circ$.

Fig. 4 The squared ratio of the α form factor is plotted as a function of the energy transfer $\omega = E_\alpha - E_{\alpha'}$. The line (1) indicates the squared ratio of the form factor of $E_\alpha = 10 \text{ GeV}, \theta_{Lab} = 0^\circ$ case to $E_\alpha = 4.2 \text{ GeV}, \theta_{Lab} = 0.8^\circ$ case, and the line (2) the squared ratio of $E_\alpha = 15 \text{ GeV}, \theta_{Lab} = 0^\circ$ to $E_\alpha = 4.2 \text{ GeV}, \theta_{Lab} = 0.8^\circ$. The form factor F is defined by eq. (3) in text.

This figure "fig1-1.png" is available in "png" format from:

<http://arxiv.org/ps/nucl-th/9512035v1>

This figure "fig2-1.png" is available in "png" format from:

<http://arxiv.org/ps/nucl-th/9512035v1>


This figure "fig1-2.png" is available in "png" format from:

<http://arxiv.org/ps/nucl-th/9512035v1>

This figure "fig2-2.png" is available in "png" format from:

<http://arxiv.org/ps/nucl-th/9512035v1>

Roper Excitation in Alpha-Proton Scattering

S. Hirenzaki^a, , P. Fernández de Córdoba^b, E. Oset^a

^a Departamento de Física Teórica and IFIC, Centro Mixto

Universidad de Valencia - CSIC, 46100 Burjassot (Valencia) Spain.

^b Departamento de Matemática Aplicada, Universidad Politécnica de Valencia,
46022 Valencia, Spain.

Abstract

We study the Roper excitation in the (α, α') reaction. We consider all processes which may be relevant in the Roper excitation region, namely, Roper excitation in the target, Roper excitation in the projectile, and double Δ excitation processes. The theoretical investigation shows that the Roper excitation in the proton target mediated by an isoscalar exchange is the dominant mechanism in the process. We determine an effective isoscalar interaction by means of which the experimental cross section is well reproduced. This should be useful to make predictions in related reactions and is a first step to construct eventually a microscopic $NN \rightarrow NN^*$ transition potential, for which the present reaction does not offer enough information.

¹ JSPS research fellow

1 Introduction

We investigate theoretically the (α, α') reaction on a proton target at intermediate energies in order to obtain new information on the reaction mechanism and the properties of hadron resonances, especially the Roper resonance. The fact that the α particle has isospin $T=0$ is particularly useful, since, due to isospin conservation, it reduces the number of reaction mechanisms which contribute to the reaction and allows an easier interpretation of the results.

The experimental study of the (α, α') reaction on the proton target was done in ref. [1]. Two clear peaks were observed there; a large one, which was associated in ref. [1] with Δ excitation in the projectile (DEP), and a small one, at higher excitation energies, which was attributed in ref. [1] to the Roper excitation in the target. This latter assumption requires the Roper to be excited by the mediation of an isoscalar interaction which stimulated the author of ref. [1] to interpret the Roper resonance as a monopole excitation of the nucleon.

The idea of the DEP mechanism was suggested theoretically in ref. [2] in connection with the $({}^3He, t)$ reaction on nucleons and nuclei. It was found there that this mechanism produced small changes in the $({}^3He, t)$ reaction on proton targets with respect to the dominant mechanism of Δ excitation in the target (DET), but the changes were important in the reaction on neutron targets. Thanks to this mechanism, the excitation function of the $({}^3He, t)$ reaction on deuteron targets [3] was well reproduced [4]. However, the clearest proof of the DEP mechanism was found in the experiment of ref. [1] since, for reason of isospin conservation, the DET mechanism is forbidden and all the strength for Δ excitation comes from the DEP mechanism. A theoretical study was done in ref. [5] along these lines and the large peak corresponding to Δ excitation was nicely reproduced.

Another interesting aspect of the work of ref. [5] is that it provides an accurate tool to evaluate the "background" of the (α, α') reaction which is necessary in order to obtain the strength for the Roper excitation. Given the fact that this background is much larger than the Roper signal, the precise determination of the background is important in order to assess the magnitude of the Roper excitation. In ref. [1] some approximations and assumptions were done to determine the shape of the Δ projectile contribution, and the strength was

fitted to reproduce the peak. In ref. [5] a more elaborate microscopic evaluation was done and both the shape and magnitude of the cross section were determined. As a consequence there are some differences (not too large) in the Δ background evaluated in refs. [1] and [5], and the strength of the Roper at its peak is about 20% larger if the background of [5] is subtracted instead of the one in [1].

In the present paper we study the different mechanisms that can lead to the Roper excitation in the (α, α') reaction on the proton. However, instead of extracting the Roper signal by subtracting the Δ background from the experimental cross section, we use the theoretical model of ref. [5], which provides the Δ excitation, and add to it the new mechanisms that excite the Roper. This includes also the interference term between the target Roper and the projectile Δ excitation, which are found to be the dominant mechanisms. With this global model we obtain cross sections which are compared to the data in order to extract new information on the Roper resonance. We find that the reaction provides the strength of an effective isoscalar exchange for the $NN \rightarrow NN^*$ transition.

In section 2 we calculate all processes which may be relevant in the energy region of ref. [1], namely: Roper excitation in the target, Roper excitation in the projectile, and double Δ excitation process. We compare the calculated results with experimental data in section 3. We summarize this paper in section 4.

2 Model for the (α, α') reaction

In this section we consider a theoretical model of the (α, α') reaction on the proton target in the Δ and Roper energy region. The reaction mechanisms which we consider here are summarized in Fig. 1. We include all processes which may be important in this energy region. In Fig. 1 (a), we show the Δ excitation in the projectile. Since the Δ can not be excited in the target [5], this is the only process to excite the single Δ in the reaction. We can find the detailed description of the calculation and the results for this channel in ref. [5]. All the other channels are new and they are discussed below.

We consider the diagrams for the Roper resonance excitation depicted in Figs. 1 (b-d).

In Fig. (b) the Roper is excited in the target by the exchange of some isoscalar objects between the α and the proton. Because of isospin conservation of the α , the isovector mesons (π and ρ) do not contribute in this process. The cross section for this process is given by

$$\frac{d^2\sigma}{dE_{\alpha'}d\Omega_{\alpha'}} = \frac{p_{\alpha'}}{(2\pi)^3} \frac{2M_\alpha^2 M}{\lambda^{1/2}(s, M^2, M_\alpha^2)} \bar{\Sigma}\Sigma |T|^2 |G^*(s^*)|^2 \Gamma^*(s^*), \quad (1)$$

where $\lambda(\dots)$ is the Kallen function and $G^*(s)$ is the propagator of the Roper resonance defined as

$$G^*(s) = \frac{1}{\sqrt{s} - M^* + \frac{i}{2}\Gamma^*(s)}, \quad (2)$$

where M^* is the mass of the N^* , $M^* = 1440 MeV$ and $\Gamma^*(s)$ is the energy dependent Roper width [6],

$$\Gamma^*(s) = \Gamma^*(s = M^{*2}) \frac{q_{cm}^3(s)}{q_{cm}^3(M^{*2})}, \quad (3)$$

with $\Gamma^*(s = M^{*2}) = 350 MeV$ and $q_{cm}(s)$ the π momentum in the center of mass frame of πN system with the energy \sqrt{s} . Eq. (3) assumes for the s dependence that the dominant decay channel is $N^* \rightarrow \pi N$. We will modify the width in the next section as described in the Appendix in order to be more consistent with the experimental data. In what follows, for simplicity, we construct a model assuming σ exchange alone as responsible for the isoscalar part of the $NN \rightarrow NN^*$ transition. Further on we shall reinterpret the meaning of this phenomenologically derived " σ " exchange. The spin sum and average of $|T|^2$ can be written as

$$\bar{\Sigma}\Sigma |T|^2 = 16F_\alpha^2 g_{\sigma NN^*}^2 g_{\sigma NN}^2 |D_\sigma(q) F_\sigma^2(q)|^2, \quad (4)$$

where we are assuming couplings of the σ to the N and N^* of the type $g_{\sigma NN} \bar{\psi}\psi\phi$ and $g_{\sigma NN^*} \bar{\psi}_{N^*}\psi\phi + h.c.$. In eq. (4) $D_\sigma(q)$ is the propagator of the σ -meson defined as

$$D_\sigma(q) = \frac{1}{q^0{}^2 - \vec{q}^2 - m_\sigma^2}, \quad (5)$$

with $m_\sigma = 550$ MeV , $F_\sigma(q)$ is the σ form factor [7],

$$F_\sigma(q) = \frac{\Lambda_\sigma^2 - m_\sigma^2}{\Lambda_\sigma^2 - q^2} \quad (6)$$

with $\Lambda_\sigma = 1700$ MeV. In Eq. (4) F_α is the $\alpha - \alpha'$ transition form factor which includes the distortion effects and depends on the momentum transfer between α and α' . The form factor is the same as that explained in ref. [5] and accounts for the distortion of the nucleon wave plus the distortion of a pion wave from the point of production of the pion. It thus implicitly assumes that the resonance will decay into the πN system. The pion distortion is slightly changed here. We use the same eikonal form as in ref. [5] but take $Im\Pi = -p_\pi\sigma\rho$ with σ the πN experimental cross section and ρ the nuclear density. This is appropriate at the higher energies met in the present problem where the model of ref. [5] is not meant to be applied. The σNN coupling constant is taken from the Bonn potential [7], $g_{\sigma NN}^2/4\pi = 5.69$, and the σNN^* coupling constant, $g_{\sigma NN^*}$, is an unknown parameter which we shall determine from the experimental data. We should however bare in mind that we are constructing an effective isoscalar interaction and those couplings have not to be taken literally as the meson baryon couplings of a microscopic model like in [7]. Yet it is useful to take $g_{\sigma NN}$ as in the Bonn model since it already provides the appropriate scale of the interaction strength.

In order to get eq. (1) we have replaced the energy conservation δ -function in terms of the Roper propagator and width as follows;

$$\delta(E_\alpha + E_N - E_{\alpha'} - E^*) \rightarrow \frac{\Gamma^*(s^*)}{2\pi} \frac{E^*}{M^*} |G^*(s^*)|^2, \quad (7)$$

so as to include all decay channels of the Roper resonance.

In the process shown in Fig. 1 (c), the Roper is excited in the projectile, α particle, and decays into πN . The Roper is excited by π and ρ exchange between the target and the projectile. We include both π^+ and π^0 for the final state. We can write the cross section as:

$$\frac{d^2\sigma}{dE_{\alpha'}d\Omega_{\alpha'}} = \frac{p_{\alpha'}}{(2\pi)^5} \frac{M_\alpha^2 M^2}{\lambda^{1/2}(s, M^2, M_\alpha^2)} \int d^3p_\pi \frac{1}{E_{N'}\omega_\pi} \bar{\Sigma}\Sigma |T|^2 \delta(E_\alpha + E_N - E_{\alpha'} - E_{N'} - \omega_\pi). \quad (8)$$

The spin sum and average of $|T|^2$ for this process is ;

$$\begin{aligned} \bar{\Sigma}\Sigma|T|^2 &= 48F_\alpha^2 \left(\frac{f}{\mu}\right)^2 \left(\frac{f'}{\mu}\right)^4 |G^*(s^*)|^2 \\ &\times [(V_l'^2(q) - V_t'^2(q))(\vec{p}_{\pi CM} \cdot \hat{q})^2 + V_t'^2(q)\vec{p}_{\pi CM}^2] \left(\frac{-q^2}{\vec{q}^2}\right), \end{aligned} \quad (9)$$

where $q = p_N - p_{N'}$, $\vec{p}_{\pi CM}$ is the pion momentum in the Roper rest frame and $f^2/4\pi = 0.08$, $f' = 0.472$ [6]. The factor $(-q^2/\vec{q}^2)$ arises from the relativistic invariant πNN vertex [5]. V_l' , V_t' stand for the longitudinal and transverse part of the $NN \rightarrow NN^*$ interaction. We have taken,

$$V_l'(q) = \left(\frac{\vec{q}^2}{q^{02} - \vec{q}^2 - \mu^2} F_\pi^2(q) + g' \right) \quad (10)$$

$$V_t'(q) = \left(\frac{\vec{q}^2}{q^{02} - \vec{q}^2 - m_\rho^2} F_\rho^2(q) C_\rho + g' \right), \quad (11)$$

where $F_\pi(q)$ and $F_\rho(q)$ are the pion and ρ -meson form factor in the form of eq. (6) with $\Lambda_\pi = 1300 MeV$ and $\Lambda_\rho = 1400 MeV$, $C_\rho = 3.96$ [7], and g' , the Landau-Migdal parameter, is taken to be 0.60. The momentum q in eqs. (10), (11) are taken in the Roper rest frame [5]. The invariant mass $\sqrt{s^*}$ of the Roper is approximated to be

$$s^* = (q^0 + M)^2 - \left(\frac{\vec{q} + \vec{p}_\pi}{2} \right)^2 \quad (12)$$

using the momentum variables in the α rest frame [5]. In this approximation the momentum transfer is shared equally by the initial and final nucleon in the α .

Now we consider the process of Fig. 1 (d), the projectile Roper excitation which decays into the nucleon and the two pions in the $T = 0$, S -wave channel, which carries a certain fraction of the Roper width [8]. We have again only the isoscalar exchange contribution because of isospin conservation, which is accounted for by means of the effective σ exchange used for diagram (b). The cross section can be expressed as,

$$\frac{d^2\sigma}{dE_{\alpha'} d\Omega_{\alpha'}} = \frac{p_{\alpha'}}{2(2\pi)^8} \frac{M_\alpha^2 M^2}{\lambda^{1/2}(s, M^2, M_\alpha^2)} \int d^3 p_{\pi_2} \frac{1}{\omega_{\pi_2}} \int d^3 p_{\pi_1} \frac{1}{E_{N'} \omega_{\pi_1}}$$

$$\times \bar{\Sigma}\Sigma|T|^2\delta(E_\alpha + E_N - E_{\alpha'} - E_{N'} - \omega_{\pi_1} - \omega_{\pi_2}). \quad (13)$$

The spin sum and average of $|T|^2$ is now,

$$\bar{\Sigma}\Sigma|T|^2 = \frac{3}{2}64F_\alpha^2C^2g_{\sigma NN}^2g_{\sigma NN^*}^2|G^*(s^*)|^2|D_\sigma(q)F_\sigma^2(q)|^2, \quad (14)$$

where C is the coupling constant of the $N^* \rightarrow N + 2\pi$ decay and $C = -2.66\mu^{-1}$ [6]. The variable s^* is obtained in a similar way as in eq. (12),

$$s^* = (q^0 + M)^2 - \left(\frac{\vec{q} + \vec{p}_{\pi_1} + \vec{p}_{\pi_2}}{2}\right)^2 \quad (15)$$

with the momenta in the α rest frame.

We omit details of the effective Lagrangians and couplings used for the different vertices. All of them are compiled in appendices A and B of ref. [6] and we follow them strictly. The factor $\frac{3}{2}$ in front of eq. (14) is an isospin factor which sums the contribution of the $\pi^+\pi^-$ decay channel and the $\pi^0\pi^0$ decay channel (which has the factor $\frac{1}{2}$ of symmetry).

In addition to this decay channel we could add the $N^* \rightarrow \pi\Delta$ channel which carries a fraction of 20 – 30% of the N^* decay width. However, as we shall see, the projectile Roper excitation mechanism with the dominant N^* decay channel, $N^* \rightarrow \pi N$ (Fig. 1(c)), which we have studied before, gives a negligible contribution, basically because of the small πNN^* coupling. Since in this case one has again the exchange of π and ρ mesons as in Fig. 1(c), and the fraction of the $N^* \rightarrow \pi\Delta$ decay is smaller than that of $N^* \rightarrow \pi N$, this mechanism should give even a smaller contribution and we do not evaluate it here.

Finally we consider the double Δ excitation process as shown in Fig. 1 (e). We have π and ρ meson exchange in this process and we have two Δ resonances, one is in the target and the other one in the projectile. The cross section is,

$$\frac{d^2\sigma}{dE_{\alpha'}d\Omega_{\alpha'}} = \frac{p_{\alpha'}}{(2\pi)^6} \frac{M_\alpha^2 M}{\lambda^{1/2}(s, M^2, M_\alpha^2)} \int \frac{d^3p_\pi}{\omega_\pi} \bar{\Sigma}\Sigma|T|^2 |G_{\Delta_T}(s_{\Delta_T})|^2 \Gamma_{\Delta_T}(s_{\Delta_T}) \quad (16)$$

where the propagator and the width of the Δ are defined as,

$$G_{\Delta}(s) = \frac{1}{\sqrt{s} - M_{\Delta} + \frac{i}{2}\Gamma_{\Delta}(s)}, \quad (17)$$

and

$$\Gamma_{\Delta}(s) = \frac{2}{3} \frac{1}{4\pi} \left(\frac{f^*}{\mu} \right)^2 \frac{M}{\sqrt{s}} q_{cm}^3 \quad (18)$$

with $M_{\Delta} = 1232 MeV$, $f^{*2}/4\pi = 0.36$ and q_{cm} the π momentum for Δ decay at rest with mass \sqrt{s} in the πN system. The index Δ_T indicates the Δ resonance in the target. Here we replaced the energy conservation δ -function in terms of the Δ propagator and the width in the target in the same way as eq. (7). The sum and average over spin of $|T|^2$ is given as,

$$\bar{\Sigma}\Sigma|T|^2 = \left(\frac{16}{9} \right)^2 \frac{4}{3} F_{\alpha}^2 \left(\frac{f^*}{\mu} \right)^6 |G_{\Delta_P}(s_{\Delta_P})|^2 [(V_l'^2(q) - V_t'^2(q))(\vec{p}_{\pi CM} \cdot \hat{q})^2 + V_t'^2(q)\vec{p}_{\pi CM}^2], \quad (19)$$

where V_l', V_t' are defined in eqs. (10) and (11). The index Δ_P indicates the Δ resonance in the projectile. The magnitude of s_{Δ_P} is defined as eq. (12). Eq. (19) already accounts for the possibility of π^0, π^+, π^- decay of the projectile Δ and all isospin channels of the target Δ .

As we shall see later on, the diagrams of Figs. 1 (c), (d), (e) are negligible and the two important mechanisms are given by the diagrams of Figs. 1 (a), (b). When we compare our calculated results with the data [1], we include the interference of the two processes. Obviously we must select only the $N^* \rightarrow \pi N$ decay channel in Fig. 1 (b) and evaluate the amplitude for this process explicitly in order to have the same final state as in Fig. 1 (a) and thus have some interference. The interference contribution is given by eq. (8) replacing $\bar{\Sigma}\Sigma|T|^2$ by

$$\begin{aligned} & \bar{\Sigma}\Sigma(T_{N^*}^* T_{\Delta} + T_{\Delta}^* T_{N^*}) \\ &= 2Re \left[\frac{64}{3} F_{\alpha}^2 \left(g_{\sigma NN} F_{\sigma} D_{\sigma} g_{\sigma NN^*} F_{\sigma} G^* \frac{f'}{\mu} \right)^* \right] \end{aligned}$$

$$\times \left(\frac{f^*}{\mu} G_{\Delta} \frac{f^*}{\mu} [(V_l' - V_t')(\vec{p}_{\pi\Delta} \cdot \hat{q})(\vec{p}_{\pi^*} \cdot \hat{q}) + V_t'(\vec{p}_{\pi\Delta} \cdot \vec{p}_{\pi^*})] \frac{f}{\mu} \sqrt{\frac{-q^2}{\bar{q}^2}} \right) \quad (20)$$

where T_{N^*} is the T matrix of the target Roper process followed by πN decay, T_{Δ} is that of the projectile Δ process, and $\vec{p}_{\pi\Delta}$ is the pion momentum in the Δ rest frame and \vec{p}_{π^*} is in the N^* rest frame. This last expression sums the contribution from the production of a π^0 and a π^+ .

We should note that the interference between the $T = 1/2$ and $T = 3/2$ excitations (with the simultaneous different spin excitation) has appeared because they occur on different nucleons, one in the target and the other one in the projectile. Should these excitations had occurred both on the target nucleon there would have been no interference. In our case the Δ excitation in the target is forbidden but it would have appeared if we had a 3He projectile instead of 4He , and there would be no interference between Δ excitation and Roper excitation on the target.

3 Numerical Results

We should mention first the gross features of the data. As can be seen in ref. [1], the observed cross section has a peak around $\omega = 550 MeV$ after subtracting the contribution of the projectile Δ excitation (Fig. 1 (a)) of ref. [1], which indicates the Roper excitation [1]. The data of the energy integrated cross section of this N^* peak are also available at several angles [1]. The data of ref. [1] has been reanalysed with a more precise background subtraction [9]. With these corrections the height at the Δ peak is about 15% lower than in ref. [1]. In Fig. 2 we show the new spectrum [9] with the appropriate normalization deduced from the scales in the energy integrated cross section of ref. [1] and the correction in ref. [9]. By subtracting the Δ background evaluated in ref. [5] we can see that the strength of the Roper excitation at its peak is of the order of 0.25 [mb/sr/MeV].

We evaluate the cross section with the mechanisms discussed in the former section and show the results in Fig. 3. As we said, in the diagrams Fig. 1(c) and Fig. 1(e) all the couplings are known. Hence, we can calculate the cross section from these diagrams, which

we show in the figure. As we can see there, their strength is very small and by no means can they account for the strength in the Roper region. This leaves diagrams Fig. 1(b) and 1(d) to do the job. The cross sections for these two processes are both proportional to $g_{\sigma NN^*}^2$. Even without knowing anything about this coupling, we can determine the ratio of the cross sections for these two mechanisms. We found that the target Roper process is much more important than the projectile Roper process followed by $\pi\pi N$ decay by about a factor 100. The cross section of the projectile process is suppressed because of the final state phase space which involves two pions.

Hence, diagram Fig. 1(b) for Roper excitation in the target stands as the only likely mechanism to explain the data. Thus we fix for the moment the strength of $g_{\sigma NN^*}$, the only unknown in the theory, in order to reproduce a strength of the peak of about 0.25 [mb/sr/MeV]. The value of the coupling constant that we get is $g_{\sigma NN^*}^2/4\pi = 1.79$. With this coupling we can now evaluate the diagram Fig. 1(d) and we find, as shown in the figure, a very small contribution.

We can explain the reasons why those terms are so small here. The cross section of the projectile Roper excitation can be compared with that of the projectile Δ excitation (Fig. 1(a)) in ref. [5] directly. They have the same phase space and the same T matrix except for some factors. We found that the cross section is so small simply because of the small coupling constants. The cross section of the projectile Roper excitation can be evaluated from that of projectile Δ excitation using a ratio of the coupling constants, $(f'/f^*)^4 = 2.4 \times 10^{-3}$.

For the double Δ process the reasons are the following: first, the peak position of the target Δ excitation is different from that of the projectile Δ excitation because of the kinematics [2,4]. Hence, the cross section is the result of a small overlap of two different resonance peaks. Second, the resonant strength associated to Δ excitation in the projectile, which peaks at small excitation energies, is now considerably reduced because the phase space available is very restricted when one forces another Δ to be excited simultaneously in the target. To confirm our results we try to evaluate the result of the double Δ process using the available ones, from that of the projectile Δ process. The T matrix is the same in both processes except for some factors. The phase space is now different due to the

different final states. To simulate the double Δ process we increase the final nucleon mass of the projectile Δ process. We found that the projectile Δ process with 940+250 [MeV] final nucleon mass has a peak at the same position of that of the double Δ process, and its height is around 1/100 of the original projectile Δ process because of the phase space differences. In addition the peak height of the double Δ process must be even lower than this peak because of the Δ width in the target. Hence, we can reconfirm qualitatively the small contribution of the double Δ process.

All these things considered, the Roper excitation in the target of Fig. 1 (b) is the only mechanism which is left to explain the data. All other processes (Fig.1 (c-e)) provide typically two orders of magnitude smaller cross section than the experimental data. As we can see in the figure, we need only the target Roper excitation and we neglect all the other processes hereafter, except for the projectile Δ excitation which is large and has already been evaluated [5].

We show the target Roper contribution together with the projectile Δ contribution [5] and their interference in Fig. 2 and compare them to the data. Here we take the $g_{\sigma NN^*}^2/4\pi = 2.35$. We found that the Roper excitation produces a wide peak around $\omega = 520MeV$. The interference has a negative contribution to the cross section and peaks around $\omega = 350MeV$. The calculated cross section provides a fair account of the cross section but the dip region between N^* and Δ excitation is poorly reproduced. We have chosen a particular sign for $g_{\sigma NN^*}$, the same as $g_{\sigma NN}$, which leads to destructive interference. If the opposite sign is chosen, the constructive interference leads to a cross section in large disagreement with the data.

In order to obtain a better agreement with the data we change the expression of the width of the Roper resonance in eq. (3). Experiments tell us that the Roper resonance decays not only into $\pi + N$ (65%) but also into $\pi + \pi + N$ (35%) [8]. We describe in the Appendix how we take into account the $2\pi + N$ decay. The Roper width Γ^* in eqs. (1) and (2) is replaced by this new form and the distortion effects of final 2π are also considered in F_α . Then we take the freedom to change the Roper mass and width in the range of their uncertainties [8] and try to obtain a best fit to the data by changing $M^*, \Gamma^*(s = M^{*2})$, and $g_{\sigma NN^*}$. The calculated results depend generally on these parameters in the following

way: the peak moves to a lower ω value for larger width and smaller mass, the peak is higher for smaller width and larger $g_{\sigma NN^*}$, the peak is steeper for smaller width, and the interference is relatively more important for smaller $g_{\sigma NN^*}$. The result for our best fit is shown in Fig. 4, where we see that the data are well reproduced. The best fit parameters have been : $M^* = 1430 MeV$, $\Gamma^*(s = M^{*2}) = 300 MeV$, and $g_{\sigma NN^}^2/4\pi = 1.33$.

We show the calculated angular distribution of the Roper excitation in Fig. 5. The interference contribution is not included in this distribution. The data are from ref. [1] and they should be corrected by the new background subtraction [9]. We should also notice that the fact that the interference term between the projectile Δ and target Roper mechanism is not small does not allow a clean experimental separation of these mechanisms. With this caveat, the comparison of our results with the experimental data should only be taken as qualitative. The main point we want to stress here is that the monotonous fall down of the cross section is reproduced and, in our theoretical analysis, it is mostly a consequence of the (α, α') transition form factor and not a property tied to the Roper itself. We found that our results reproduce the trend of the data well.

Finally we want to comment on the πN scattering amplitude of P_{11} channel. In this channel the observed amplitude [11, 12] has a different form than the standard Breit-Wigner form of the Roper resonance due to the coupling to the nucleon. In the energy region which we consider in this paper, the differences are as follows; first the real part of the observed amplitude has the opposite sign to the Breit-Wigner form at $\sqrt{s} \leq 1.2 GeV$ and second the shape of the real part of the observed scattering amplitude is steeper than the Breit-Wigner form at $1.2 \leq \sqrt{s} \leq 1.3 GeV$ because of the off-shell nucleon effect . In order to see the effect of these differences we calculated the α spectrum with a modified Roper propagator which has a steeper real part at $1.2 \leq \sqrt{s} \leq 1.3 GeV$ according to the data of the scattering amplitude. We have checked that including these modifications in the "Roper" excitation changes only a bit the results of Fig. 4 in the region of the dip, reducing moderately the cross section there. Theoretically the inclusion of the nucleon pole term in addition to the Roper pole would help producing the shape in the P_{11} channel.

Now we would like to comment on the meaning of the " σ " exchange interaction obtained. In a more microscopic description of the $NN \rightarrow NN^*$ transition along the lines of

the boson exchange model, in the isoscalar channel which we have investigated we would also have a contribution from ω exchange and from uncorrelated 2π exchange. It is easy to see that assuming a similar scaling here for ω exchange and the uncorrelated 2π exchange, with respect to σ exchange, as one has in the NN potential [7], the effect of ω and uncorrelated 2π exchange are very important and one finds large cancellation between σ and ω exchange. In addition one should use this as input for a transition potential and initial and final state interactions of the NN or NN^* systems (correlations) should also be taken into account. For all these reasons the " σ " exchange potential which we have obtained should not be interpreted as a σ exchange for the $NN \rightarrow NN^*$ transition along the lines of a one boson exchange model. It is simply an effective interaction which accounts for all the ingredients in the $T = 0$ exchange channel, (σ , ω and correlations). One may wonder why using there the explicit σ mass in the exchange. There is certainly no justification for it, except that a posteriori one finds that the mass of the object exchanged is irrelevant in the description of the cross section and it can be equally reproduced using any other mass. Hence the " σ " exchange obtained stands only as a useful and intuitive parameterization of the effective interaction in the $T = 0$ channel. With this easy interaction one can make predictions for analogous reactions using other nuclei, one can evaluate cross sections at other energies of the beam, etc.

Obviously, although the limited information of the present reaction does not allow one to extract enough information to construct a one boson exchange model for the $NN \rightarrow NN^*$ transition, the job done here, separating the Δ projectile excitation from the Roper excitation, provides some partial, but useful information, on the $NN \rightarrow NN^*$ transition to be used in the future in attempts to construct a microscopical model for this interaction. Some steps in this direction, by looking at the role of uncorrelated 2π exchange, have been given in ref. [13].

4 Summary

We have studied the Roper excitation in the (α, α') reaction on the proton target. All processes which may be relevant in this energy region were investigated. We found that the experimental α' spectrum can be reproduced by two processes, the projectile

Δ excitation and the target Roper process. The target Roper process is mediated by an isoscalar exchange between the α and the proton and we have determined from the experiment the effective isoscalar $NN \rightarrow NN^*$ transition t matrix.

We could find a good reproduction of the data with values of M^* and Γ^* close to the average values quoted in the particle data table [8]. We found a good agreement with the data with $M^* = 1430MeV$, $\Gamma^*(s = m^{*2}) = 300MeV$ and a certain choice of the parameters of the effective interaction.

The experimental dependence of the cross section on the α' angle was qualitatively reproduced and found to be tied to the α form factor, not to the properties of the Roper.

The present work also lays the ground for extension of studies of N^* excitation in nuclei in order to study the modification of the N^* properties in a nuclear medium. The excitation of the N^* with the (α, α') reaction, because of the large strength and clean signature, would be probably one of the ideal tools for such studies.

Acknowledgements

We would like to thank useful discussions with E. Hernández, M. J. Vicente-Vacas and H. P. Morsch. We would also like to thank the latter for providing us with the results of the reanalysis of the experiment. One of us S. Hirenzaki would like to acknowledge the hospitality of the University of Valencia where this work was done. This work is supported partially by CICYT contract number AEN-93-1205.

Appendix Decay Width of the Roper resonance

In this appendix we will explain our model of the widths of the Roper resonance. We include the $N^* \rightarrow \pi + N$ and $N^* \rightarrow \pi + \pi + N$ decay channels. Writing the decay width of each channel by Γ_π^* and $\Gamma_{\pi\pi}^*$, we define the total decay width as,

$$\Gamma^*(s) = \Gamma_\pi^*(s) + \Gamma_{\pi\pi}^*(s). \quad (21)$$

The width of the $\pi + N$ decay channel has the same form as that of ref. [6],

$$\Gamma_\pi^*(s) = \Gamma_\pi^*(s = M^{*2}) \frac{q_{cm}^3(s)}{q_{cm}^3(M^{*2})}, \quad (22)$$

where $\Gamma_\pi^*(s = M^{*2}) = P_\pi \Gamma^*(s = M^{*2})$, with $\Gamma^*(s = M^{*2})$ the experimental Roper width and P_π the πN decay branching ratio. The magnitude $q_{cm}(s)$ is the π momentum in the center of mass frame of the πN system with energy \sqrt{s} .

For the width of the $\pi + \pi + N$ decay channel, we assume the $N^* \rightarrow \pi + \Delta$ as an intermediate state in this paper and express the width as follows,

$$\Gamma_{\pi\pi}^*(s) = \int \frac{d^3 p_\pi}{(2\pi)^3} \frac{d^3 p_\Delta}{(2\pi)^3} \frac{M_\Delta}{E_\Delta} \frac{1}{2\omega_\pi} \bar{\Sigma} \Sigma |T|^2 (2\pi)^4 \delta^4(p^* - p_\pi - p_\Delta), \quad (23)$$

where $p^{*\mu}$ is the four momenta of the Roper resonance and is $(\sqrt{s}, \vec{0})$ in the Roper rest frame. The $\pi\Delta N^*$ coupling is taken to be of the same form that of $\pi N\Delta$ with the coupling strength $f_{\pi\Delta N^*}$ [6]. After replacing the energy conservation δ -function into the Δ propagator and width as in eq. (7) in the text, we find the $\Gamma_{\pi\pi}^*$ is described as,

$$\Gamma_{\pi\pi}^*(s) = \frac{1}{3\pi^2} \left(\frac{f_{\pi\Delta N^*}}{\mu} \right)^2 \int dp_\pi \frac{p_\pi^4}{\omega_\pi} |G_\Delta(s_\Delta)|^2 \Gamma_\Delta(s_\Delta), \quad (24)$$

which has included all the isospin channels, where G_Δ and Γ_Δ are defined in eqs. (17) and (18), respectively. The coupling constant, $f_{\pi\Delta N^*}$, is determined by the normalization condition, $\Gamma_{\pi\pi}^*(s = M^{*2}) = P_{\pi\pi} \Gamma^*(s = M^{*2})$ with $\Gamma^*(s = M^{*2})$ the experimental Roper width and $P_{\pi\pi}$ the $\pi\pi N$ decay branching ratio. We obtain $f_{\pi\Delta N^*} = 2.47$ for $M^* = 1440 MeV$, $\Gamma^*(s = M^{*2}) = 350 MeV$ and $P_{\pi\pi} = 0.35$ [8].

References

- [1] H. P. Morsch *et al.*, Phys. Rev. Lett. **69** (1992) 1336.
- [2] E. Oset, E. Shiino, and H. Toki, Phys. Lett. **B224** (1989) 249.
- [3] C. Gaarde, Nucl. Phys. **A478** (1988) 475c.
- [4] P. Fernández de Córdoba and E. Oset, Nucl. Phys. **A544** (1992) 793.
- [5] P. Fernández de Córdoba, E. Oset, M. J. Vicente-Vacas, Yu. Ratis, J. Nieves, B. López-Alvaredo, and F. Gareev, Nucl. Phys. **A586** (1995) 586.
- [6] J. A. Gómez Tejedor and E. Oset, Nucl. Phys. **A571** (1994) 667.
- [7] R. Machleidt, K. Holinde, and Ch. Elster, Phys. Rep. **149** (1987) 1.
- [8] Review of Particle Properties, Phys. Rev. **D50** (1994) 1173.
- [9] H. P. Morsch, private communication.
- [10] K. Holinde, private communication.
- [11] R. A. Arndt, J. M. Ford, L. D. Roper, Phys. Rev. **D32** (1985) 1085.
- [12] R. E. Cutkosky and S. Wang, Phys. Rev. **D42** (1990) 235.
- [13] B. Desplanques, Z. Phys. **A330** (1988) 331.

Figure Caption

Fig. 1 Diagrams for the (α, α') reaction which we consider in this paper. They are (a) Δ excitation in the projectile calculated in ref. [5], (b) Roper excitation in the target, (c) Roper excitation in the projectile with decay into πN , (d) Roper excitation in the projectile with decay into $\pi\pi N$, and (e) double Δ excitation. The σ exchange must be interpreted as an effective interaction in the $T = 0$ exchange channel (see text).

Fig. 2 Calculated cross sections of the target Roper process and the projectile Δ process [5] at $E_\alpha = 4.2$ GeV and $\theta = 0.8$ deg. The variable ω is the energy transfer defined as $\omega = E_\alpha - E_{\alpha'}$. The thick line indicates the sum of all contributions. Experimental data are taken from ref. [11]. Here we used $g_{\sigma NN^*}^2/4\pi = 2.35$.

Fig. 3 Calculated cross sections $d\sigma/d\Omega dE$ for (α, α') on the proton at $E_\alpha = 4.2$ GeV and $\theta = 0.8$ deg. The variable ω is the energy transfer defined as $\omega = E_\alpha - E_{\alpha'}$. Each line indicates the contribution from the process shown in Fig. 1. Here we used $g_{\sigma NN^*}^2/4\pi = 1.79$.

Fig. 4 Same as in Fig. 2. Here we used $g_{\sigma NN^*}^2/4\pi = 1.33$, $M^* = 1430$ MeV, $\Gamma^*(s = M^{*2}) = 300$ MeV and the Roper width discussed in the appendix.

Fig. 5 Calculated differential cross sections, $d\sigma/d\Omega$, of the target Roper process as a function of the scattering angle in the laboratory frame. The parameters are the same as in Fig. 4. The experimental data are taken from ref. [1]. See warnings in the text about the interpretation of the results.

This figure "fig1-1.png" is available in "png" format from:

<http://arxiv.org/ps/nucl-th/9511036v1>

This figure "fig2-1.png" is available in "png" format from:

<http://arxiv.org/ps/nucl-th/9511036v1>

This figure "fig1-2.png" is available in "png" format from:

<http://arxiv.org/ps/nucl-th/9511036v1>

This figure "fig2-2.png" is available in "png" format from:

<http://arxiv.org/ps/nucl-th/9511036v1>

This figure "fig1-3.png" is available in "png" format from:

<http://arxiv.org/ps/nucl-th/9511036v1>

COHERENT PION PRODUCTION IN NEUTRINO NUCLEUS COLLISION IN THE 1 GEV REGION

N. G. Kelkar^(1,2), E. Oset⁽¹⁾ and P. Fernández de Córdoba⁽³⁾

¹ *Departamento de Física Teórica and IFIC, Centro Mixto Universidad de Valencia-CSIC, 46100 Burjassot (Valencia), Spain.*

² *Laboratori Nazionali di Frascati, INFN, Italy*

³ *Departamento de Matemática Aplicada, Universidad Politécnica de Valencia*

Keywords: Coherent pion production, neutrino nucleus scattering, Δh excitation with neutrinos.

PACs numbers: 25.30-c, 25.30. pt

Abstract

We calculate cross sections for coherent pion production in nuclei induced by neutrinos and antineutrinos of the electron and muon type. The analogies and differences between this process and the related ones of coherent pion production induced by photons, or the (p, n) and $({}^3\text{He}, t)$ reactions are discussed. The process is one of the several ones occurring for intermediate energy neutrinos, to be considered when detecting atmospheric neutrinos. For this purpose the results shown here can be easily extrapolated to other energies and other nuclei.

1 Introduction

Electron and muon neutrinos and antineutrinos at intermediate energies are produced in cosmic ray interactions with the earth's atmosphere and they are classified as "atmospheric neutrinos". From basic counting from pion and muon decays one expects twice as many muon neutrinos and antineutrinos as the corresponding electron ones, which seems to be in contradiction with measurements at IMB [1] and Kamiokande [2], where the ratio obtained by studying charged current neutrino nucleus reactions in large underground water detectors is about one. One of the attractive hypothesis is the existence of neutrino oscillations. However, firm conclusions on the reasons of the puzzle can only come if we have a good control on the neutrino nucleus reactions occurring in the detectors, as well as the detector characteristics.

The neutrino nuclear reactions at intermediate energies can be rather complicated if one compares with analogous reactions induced by photons [3]. Most of the studies of neutrino nucleus collisions only consider the ph excitation channel [4, 5, 6]. Others include Δh excitation as a source of renormalization of the ph excitation channel but not as an excitation channel by itself [7, 8]. All these approaches are fine in order to evaluate the nucleon emission channel, and at energies below 300-400 MeV they can also provide accurate results for the total neutrino cross section. Indeed, most of the neutrino energy is transferred to the lepton (in charged currents reactions) and only a fraction of it is used to excite the nucleus. Hence, one has to go to relatively large neutrino energies in order to excite Δ 's and other resonances in the nucleus. Yet, whenever this happens the cross sections for Δh excitation are large and comparable in size with those of ph excitation. A recent evaluation of these cross sections is done in ref. [9] and the astrophysical consequences of the consideration of these channels are discussed in ref. [10].

One of the interesting channels discussed in ref. [10] is the coherent pion production following Δ excitation in the nucleus. The reaction is

$$\nu_l + A \rightarrow l^- + A + \pi^+ \quad (1)$$

where the final nucleus is the same as the original one and it is left in its ground state. The cross section for the reaction is evaluated in [10] using the impulse approximation (IA), neglecting the Δ renormalization in the medium and using plane waves for the pion. The authors, however, make a call for accurate calculations which would take those elements into account. Fortunately, such elements have been thoroughly tested in pion nuclear reactions and are readily available. The Δ selfenergy in a nuclear medium has been evaluated theoretically [11] and tested in all sorts of pion nuclear reactions: elastic [12] absorption, inclusive quasielastic, charge exchange and double charge exchange [13], as well as in pion production processes like coherent π^0 photoproduction [14] or coherent pion production in (p, p') and related reactions [15].

Coherent pion production in (p, n) or $({}^3He, t)$ reactions resembles much

the present process and the findings of those reactions can serve as a guideline for the study of the present one. Coherent pion production in the $({}^3\text{He}, t)$ reaction has received most of the attention [16, 17, 18] since it is one of the channels contributing to the inclusive $({}^3\text{He}, t)$ reaction in nuclei, where an apparent shift of the Δ peak with respect to the peak of the elementary reaction on proton targets was observed [19, 20]. In fact the coherent pion production channel shows the peak of the Δ shifted towards lower excitation energies in all the calculations [16, 17, 18], something already observed in pion elastic scattering as a consequence of the pion multiple scattering [21].

Coherent pion production in neutrino reactions can offer additional information over the $(p, p'), ({}^3\text{He}, t)$ and (p, n) reactions on Δ properties and pion propagation in the medium. The reason is that in neutrino reactions the range of energy and momentum transferred to the nucleus is different than the one in the hadron induced reactions. On the other hand in the hadronic reactions one has to fight the distortion of the nucleons, or ${}^3\text{He}, t$ in their passage through the nucleus, which makes the pion production reaction quite peripheral. Instead, in the neutrino induced reaction neither the neutrino nor the lepton is distorted by the nucleus and one can test the Δ and the pions in the interior of the nucleus. One may argue that the same occurs in coherent π^0 photoproduction. However, in this latter case the combination of the spin transverse photons and the spin longitudinal pions leads to a factor $\sin\theta$ in the amplitude which eliminates the contribution of small angles to the cross section. As a consequence the cross section picks up its strength from finite angles where the momentum transfer is larger and hence the nuclear form factor smaller. This reduction due to the form factor becomes more apparent as the energy increases, for a given angle, and as a result of this the Δ peak is shifted to much smaller energies than in coherent pion production induced by $(p, p'), ({}^3\text{He}, t)$, etc. The contribution of bigger densities is partly to be blamed for the shift, but to a much smaller extent than the reasons discussed above.

In the neutrino induced coherent pion production reaction we do not have the circumstances explained in the photon case and, as we shall see, the largest contribution to the cross section comes from small angles. Then the situation is rather different and we can obtain new information with respect to both the photonuclear and strong interaction induced processes of coherent pion production.

In this sense the neutrino induced coherent pion production reaction is a nice complement to other existing reactions which can enrich our understanding of the nuclear excitation mechanisms at intermediate energies providing new tests for the present theoretical models.

We shall follow the steps and the formalism developed in refs. [15, 17]. Although accurate experimental data on coherent pion production from the (p, p') or $({}^3\text{He}, t)$ reactions do not exist, the results of ref. [17] and the preliminary data of ref. [22] for the $({}^3\text{He}, t)$ induced reaction are in relatively good agreement, which gives us a certain confidence to extend the method to the neutrino induced reaction.

2 Coherent pion production amplitude

The experiments on (${}^3\text{He}, t$) induced pion production [19, 20, 22] show that the process is dominated by Δh excitation, even at energies of the beam of 10 GeV. The excitation of other resonances is suppressed with respect to the Δ . Only in experiments where the Δ excitation on the target is forbidden, as in the (α, α') reaction on a proton target, has the Roper some chances to show up [23], and even then, the Roper signal is small compared to a large background of Δ excitation in the projectile [23, 24, 25]. The coherent production process still restricts more the excitation of higher resonances since this requires larger momentum transfers which make the nuclear form factor smaller.

The mechanism for coherent pion production in the (ν, l^-) induced reaction proceeds as shown in fig. 1. The W^+ emitted from the (ν, l^-) vertex excites a Δ in the nucleus, which decays to $N\pi$ later on, the nucleon remaining in the same original state in order to ensure the coherence.

In order to construct the amplitude for the process we recall the $\nu n \rightarrow lp$ weak interaction Lagrangian

$$L = \frac{G}{\sqrt{2}} \cos \theta_c l^\mu J_\mu \quad (2)$$

with

$$\begin{aligned} l^\mu &= \bar{u}(k') \gamma^\mu (1 - \gamma_5) u(k) \\ J_\mu &= \bar{u}(p') [F_1^{(v)}(q^2) \gamma_\mu + \frac{i}{2M} F_2^{(v)}(q^2) \sigma_{\mu\nu} q^\nu \\ &\quad + F_A^{(v)}(q^2) \gamma_\mu \gamma_5 + F_P^{(v)}(q^2) q_\mu \gamma_5] u(p) \end{aligned} \quad (3)$$

where G is the Fermi weak coupling constant, M is the nucleon mass and θ_c is the Cabbibo angle. We follow the nomenclature and use the same form factors as in ref. [7]. The momenta involved in eqs. (3) are depicted in fig. 2.

In order to construct the $\nu N \rightarrow l^- \Delta$ transition we make the nonrelativistic reduction of the terms in eqs. (3), neglecting only terms of order $O(\frac{p}{2M})^2$. Linear terms in $\frac{\vec{p}}{2M}, \frac{\vec{p}'}{2M}, \frac{\vec{q}}{2M}$ are kept, but those terms linear in \vec{p} , the momentum of the occupied nucleons, also give rise to $O(\frac{p}{2M})^2$ corrections when integrating over the momenta. Hence these terms are dropped, which is equivalent to taking $\vec{p} = 0, \vec{p}' = \vec{q}$. For the $\nu N \rightarrow l^- \Delta$ transition we take the terms involving spin operators in the $\nu N \rightarrow l^- N$ transition and make the substitution

$$\frac{f}{\mu} \sigma^i \tau^\lambda \rightarrow \frac{f^*}{\mu} S^{\dagger i} T^{\dagger \lambda} \quad (4)$$

where S^i, T^λ are the spin, isospin transition operators from 1/2 to 3/2, normalized as

$$\langle 3/2 \ M_s | S_\mu^\dagger | 1/2 \ m_s \rangle = C(1/2 \ 1 \ 3/2; m_s, \mu, M_s) \quad (5)$$

and the same for $T^{\dagger\lambda}$. The couplings f, f^* correspond to the $NN\pi$ and $N\Delta\pi$ vertices, $f^2/4\pi = 0.08$, $f^{*2}/4\pi = 0.36$ and μ in eq. (4) is the pion mass. The current J_μ of eq. (3) contains implicitly a factor $\sqrt{2}$ of the operator τ_+ responsible for the $n \rightarrow p$ transition.

Hence we must substitute

$$\sigma^i \rightarrow \frac{f^*}{f} \frac{1}{\sqrt{2}} S^{\dagger i} T_+^{\dagger} \quad (6)$$

and from the Δ decay into πN we take $f^*/f = 2.12$, a value in between the factor 2.2 taken in ref. [26] and the factor 2 considered in ref. [9]

We find

$$\begin{aligned} J_\mu^\Delta = & \frac{1}{\sqrt{2}} \frac{f^*}{f} \{ i[F_1^{(v)}(q^2) + F_2^{(v)}(q^2)] \frac{1}{2M} (\vec{S}^\dagger \times \vec{q})^i \delta_{\mu i} \\ & + [F_A^{(v)}(q)^2 - q^0 F_P^{(v)}(q^2)] \frac{\vec{S}^\dagger \vec{q}}{2M} \delta_{\mu 0} - F_p^{(v)}(q^2) \frac{\vec{S}^\dagger \vec{q}}{2M} q^i \delta_{\mu i} \\ & + F_A^{(v)} S^{\dagger i} \delta_{\mu i} \} T_+^{\dagger} \end{aligned} \quad (7)$$

For the Δ coupling to a nucleon and a real pion in fig. 1 we use the standard vertex

$$-i\delta\tilde{H} = -\frac{f^*}{\mu} \vec{S} \cdot \vec{p}_\pi T^\lambda \quad (8)$$

where \vec{p}_π is assumed in the Δ CM frame. The amplitude corresponding to fig. 1 is readily evaluated for a spin saturated nucleus using the property

$$\sum_{M_s} S_i S_j^\dagger = \frac{2}{3} \delta_{ij} - \frac{i}{3} \epsilon_{ijl} \sigma_l \quad (9)$$

One of the findings in coherent pion production induced by the (${}^3\text{He}, t$) reaction was the negligible contribution from the transverse part of the $NN \rightarrow N\Delta$ transition amplitude. This occurred because the emitted pion couples longitudinally to the Δ and the transverse part of the interaction contributes to the cross section with the factor $\sin^2\theta$, as we indicated for the case of coherent pion photoproduction. This forces the contribution at finite angles where the nuclear form factor reduces the cross section. This is also the case here, where in addition the transverse terms are further reduced by a factor $q/2M$. Hence we neglect the transverse parts from the beginning.

With all these considerations, the coherent pion production cross section corresponding to the process of fig. 1, on summing over all occupied nucleons in the amplitude, is given by

$$\frac{d\sigma}{d\Omega_e dE_e d\Omega_\pi} = \frac{1}{8} \frac{|\vec{k}'| |\vec{p}_\pi|}{|\vec{k}|} \frac{1}{(2\pi)^5} \Pi_f 2m_f \bar{\Sigma} \Sigma |t|^2 \quad (10)$$

where the product of the fermion masses, $2m_f$, appears because of our normalization of the spinors as $\bar{u}u = 1$. The T matrix squared, summed and averaged over spins, is given by

$$\Pi_f 2m_f \bar{\Sigma} \Sigma |t|^2 = L_{00} |V^0|^2 + L_{33} |V^3|^2 + 2L_{03} \text{Re}\{V^0 V^{3*}\} \quad (11)$$

where $L_{\mu\nu}$ is the leptonic tensor

$$L_{\mu\nu} = 4[k_\mu k'_\nu + k'_\mu k_\nu - k \cdot k' g_{\mu\nu}] \quad (12)$$

and

$$V^\mu \equiv \begin{Bmatrix} V^0 \\ 0 \\ 0 \\ V^3 \end{Bmatrix}$$

$$V^0 = B[F_A^{(v)}(q^2) - q^0 F_P^{(v)}(q^2)] \quad (13)$$

$$V^3 = B[F_A^{(v)}(q^2) \frac{2Mq}{q^2} - F_P^{(v)}(q^2)q]$$

with

$$B = -\frac{f^*}{f} \frac{f^*}{\mu} \frac{G}{6} \cos \theta_c G_\Delta(p_\Delta) F(\vec{q} - \vec{p}_\pi) \frac{1}{\sqrt{s_\Delta}} \quad (14)$$

In the factor B , $G_\Delta(p_\Delta)$ is the Δ propagator and $F(\vec{q} - \vec{p}_\pi)$ is the nuclear form factor modulated by the isospin factors. We have

$$G_\Delta(p_\Delta) = \frac{1}{\sqrt{s_\Delta} - M_\Delta + i\frac{\tilde{\Gamma}}{2} - \Sigma_\Delta} \quad (15)$$

where $s_\Delta = p_\Delta^2 - \vec{p}_\Delta^2$, and $\tilde{\Gamma}$, Σ_Δ are the Pauli blocked Δ width and the rest of the Δ selfenergy which contains pieces related to quasielastic scattering, $2N$ and $3N$ pion absorption. The evaluations are done in ref. [11] and we take the analytic expressions derived there. We also include in the selfenergy the term $\frac{4}{9}(\frac{f^*}{\mu})^2 g' \rho$ to account for irreducible pieces of Δh propagation mediated by the Landau-Migdal effective interaction [12].

On the other hand the nuclear form factor is given by

$$F(\vec{q} - \vec{p}_\pi) = \int d^3r [\rho_p(\vec{r}) + \frac{1}{3}\rho_n(\vec{r})] e^{i\vec{q}\cdot\vec{r}} \vec{p}_\pi \cdot \vec{q} e^{-i\vec{p}_\pi\cdot\vec{r}} \quad (16)$$

where for convenience we have included the factor $\vec{p}_\pi \cdot \vec{q}$.

In the derivation of eq. (11) we have taken \vec{q} in the z direction for simplicity and furthermore we have also kept only the longitudinal part of \vec{p}_π along the q axis for consistency with the neglect of the transverse parts. The structure of eq. (11) is also the same as the one found in ref. [10].

It is interesting to note that when \vec{k}' is parallel to \vec{k} , which leads to the largest cross sections, the contribution of F_P cancels. Hence, the axial term $F_A^{(v)}(q^2)$ is the relevant term in the process.

So far the formalism has used the bound wave functions of the nucleus, which appear in the nuclear form factor via the proton and neutron densities,

eq. (16), but has considered only a plane wave for the pion. The renormalization of the pion is a very important thing in this process. Hence, in the next step we replace

$$\vec{p}_\pi \cdot \vec{q} e^{-i\vec{p}_\pi \cdot \vec{r}} \rightarrow i\vec{q} \cdot \vec{\nabla} \phi_{out}^*(\vec{p}_\pi, \vec{r}) \quad (17)$$

where $\phi_{out}^*(\vec{p}_\pi, \vec{r})$ is an outgoing solution of the Klein Gordon equation for the pion, which we solve along the lines of ref. [27] and with the pion nucleus optical potential developed there, which gives rise to good pion elastic, absorption and quasielastic cross sections [27].

3 Results and discussion

In fig. 3 we plot $d\sigma/d\Omega_e dE_e d\Omega_\pi$, for $\theta_e = 0^\circ$ with respect to the neutrino direction, for coherent pion production in $\nu_e + {}^{16}\text{O} \rightarrow e^- + {}^{16}\text{O} + \pi^+$ as a function of the pion angle measured with respect to \vec{q} . We choose a neutrino energy of 800 MeV and an electron energy of 545 MeV which lead to a value of q suited to excite the Δ resonance. The dashed line corresponds to the impulse approximation, meaning free Δ width and no Δ selfenergy in the Δ propagator and no pion distortion. The solid line is the accurate calculation, which accounts for both effects. We can see that there is a net reduction of about a factor three from both renormalizations, bigger than what appears in coherent pion production induced by the $({}^3\text{He}, t)$ reaction, which is more peripheral.

The cross section is forward peaked, as was also the case in the $({}^3\text{He}, t)$ or (p, n) reactions. However the fall down with angle is not so drastic here as in the hadronic reactions because in the latter ones, for the same energy of the pion, the momentum transferred to the nucleus is bigger than in the neutrino case, as a consequence of the large mass of the nucleons, and the nuclear form factor reduces more the cross section. The cross sections are of the order of $10^{-15} \text{ fm}^2/\text{MeVsr}^2$.

In fig. 4 we show the cross section for the same reaction integrated over the pion angles. Here we plot it as a function of q^0 , the total pion energy (we neglect the nucleus recoil energy). We observe again the sizeable renormalization factor from dressing the Δ and the pion in the nuclear medium. It is also worth looking at the shift to lower energies of the peak of the excitation function, with respect to the one of the impulse approximation. This is mostly due to the distortion of the pion, as we already indicated in the introduction. The argument goes as follows: since the πN cross section and pion absorption are largest at resonance, there is a depletion of the pion wave when the pion goes through the nucleus, and much of the pion flux is lost into quasielastic channels or pion absorption. On the other hand the pion production step is resonance peaked. The combination of these two factors has as a consequence a shift of the peak to lower excitation energies where the pion depletion is not so strong. Note, however, that the free Δ position would appear at $q^0 = 338 \text{ MeV}$ in the

plot. Hence, we see a shift of the peak already in the IA due to the nuclear form factor, as indicated in the introduction, and a further shift due to the pion distortion.

The nuclear form factor acts as follows: from energy conservation we have $\omega_\pi = q^0$, $p_\pi = (q^{02} - \mu^2)^{1/2}$. Hence, the momentum transfer to the nucleus, $\vec{q} - \vec{p}_\pi$, is always finite since $q > q^0$ and it increases as q^0 increases. As a consequence, the nuclear form factor decreases with increasing q^0 and this has the same effect as the distortion when one approaches the Δ energy, leading to a shift of the Δ peak to lower excitation energies.

The Δ peak in fig. 4 appears around $q^0 = 255 \text{ MeV}$, which is lower than the value 275 MeV found in coherent π^+ production with the (p, n) reaction. Once again the peripheral character of the (p, n) reaction should be blamed for it. However, it is interesting to note that, in spite of the fact that here we are exploring the whole volume of the nucleus, like in coherent π^0 photoproduction, the peak appears at higher values of q^0 in the neutrino case than in the (γ, π^0) [14, 28] case. In the latter case the Δ peak was shifted to energies around $190 - 220 \text{ MeV}$ depending on the nucleus. The reason, already discussed in the introduction, is the factor $\sin^2\theta$ of coherent π^0 photoproduction which forces finite angles in the cross section where the momentum transfer is larger and the nuclear form factor smaller.

As we can see, the combination of results of coherent pion production induced by photons, neutrinos or hadronic reactions presents complementary aspects related to the nuclear properties and the propagation of the Δ and the pion in the nuclear medium.

In fig. 5 we show the results for the cross section of the same reaction integrated now over the electron angles. We observe similar features as in fig. 4. The magnitude of the cross section has now decreased more with respect to the case where we integrate over the pion angles (see figs. 3 and 4), indicating that the cross section as a function of the electron angle is more forward peaked than with the pion angle. This is intuitive since the electron momentum is bigger than the pion momentum and a change in angle generates larger momentum transfers in the case of the electron, which would lead to a larger reduction of the nuclear form factor.

In fig. 6 we show the results for $d\sigma/dE_e$ as a function of q^0 for different neutrino energies. We can see that the cross section increases with the neutrino energy, but at energies above 1GeV the increase is more moderate. This is also reminiscent of the findings of ref. [15] in the (p, n) reaction.

In fig. 7 we show the results of $d\sigma/dE_e$ as a function of q^0 , for neutrinos of 1 GeV scattering from three different nuclei, ^{16}O , ^{37}Cl and ^{71}Ga used as neutrino detectors in several experiments. We observe that the cross section grows with A . This is quite different from the results found for the (p, n) reaction where the cross section decreased from ^{12}C to ^{40}Ca and ^{208}Pb . The reason for the decrease in the hadronic reaction was the distortion of the p and n waves, which does not occur now, since the neutrino and the electron are not distorted by the nucleus. Finally in fig. 8 we show the results for the

reaction

$$\nu_\mu + A \rightarrow \mu^- + A + \pi^+ \quad (18)$$

corresponding to fig. 7 with electrons.

The evaluation of the cross section in the ν_μ case is simple since both the leptonic tensor and the vector V^μ have the same expressions. The only change is in the kinematics in the (ν_μ, μ) vertex because of the finite mass of the muon. The cross sections for the ν_μ case are decreased by about 20% with respect to those of ν_e in all nuclei. The reason for the decrease is that for a given value of q^0 the corresponding value of q is larger in the μ case and hence it leads to larger momentum transfers to the nucleus and smaller nuclear form factors.

Since the Laboratory energetic neutrinos are muon neutrinos, the reaction studied here could be implemented with muon neutrinos in present Laboratories.

As for the evaluation of cross sections with antineutrinos, the changes to be done to obtain them from the ones evaluated in this work are minimal, once the transverse parts are neglected as done here. One should change

$$\rho_p + \frac{1}{3}\rho_n \rightarrow \rho_n + \frac{1}{3}\rho_p \quad (19)$$

which in practice amounts to multiplying the neutrino cross sections by the factor $(3N + Z)/(3Z + N)$, which is unity for isospin symmetric nuclei, as noted in ref. [10].

4 Conclusions

We have calculated cross sections for coherent pion production in neutrino (antineutrino) nucleus collisions, of both electron and muon type. The calculations have been done accurately taking into account the renormalization of the Δ and pion properties in the nuclear medium. We observed that the cross section was quite sensitive to these properties, and their inclusion in the calculation decreased the cross section by about a factor three with respect to the impulse approximation, and shifted the peak position to lower excitation energies.

Some of the features, like the shift of the Δ peak, were reminiscent of similar findings in coherent pion production in $({}^3He, t)$ or (p, n) reactions, but the fact that the latter are rather peripheral because of the distortion of the hadronic beam, by contrast to the neutrino reaction which occur throughout the nuclear volume, confers the neutrino reaction some peculiar features. These features are also different to those found in coherent π^0 photoproduction, also testing the whole nuclear volume, because in the latter case there is a factor $\sin^2\theta$ in the cross section which reduces the contribution of forward angles from where the neutrino cross sections get most of their contribution.

All these analogies and differences tell us that the coherent pion production induced by neutrinos is an important complement of the hadronic and photonuclear processes of pion production in order to give information on pion and Δ renormalization in a nuclear medium.

On the other hand it is clear that in order to obtain proper information about atmospheric neutrinos one has to have a control on the different ν -nuclear reactions occurring at intermediate energies of the neutrinos, to interpret properly the results of the neutrino detectors. The present reaction is one of them.

In order to test the validity of the model used to obtain the present results, which can be easily extrapolated to other nuclei and other energies, it would be interesting to perform some experiment. The cross sections, although small, are in the same range as in many experiments performed at present facilities [29] and hence are experimentally accessible.

Acknowledgements:

We would like to acknowledge partial support from CICYT contract no. AEN 96- 1719. One of us, N. G. K. wishes to acknowledge the hospitality of the Valencia University where this work has been done.

References

- [1] R. Becker-Szendy et al., Phys. Rev. D **46**, 3720 (1992).
- [2] K. S. Hirata et al., Phys. Lett. **280B**, 146 (1992); E. W. Beier et al., Phys. Lett. **283B**, 446 (1992).
- [3] R. C. Carrasco and E. Oset, Nucl. Phys. **A536**, 445 (1992).
- [4] W.C. Haxton, Phys. Rev. D **36**, 2283 (1987).
- [5] K. Kubodera and S. Nozawa, Int. J. Mod. Phys. **E3**, 101 (1994).
- [6] J. Engel, S. Pittel and P. Vogel, Phys. Rev. Lett. **67**, 426 (1991); Phys. Rev. C **50**, 1702 (1994).
- [7] S. K. Singh and E. Oset, Nucl. Phys. **A542**, 587 (1992); Phys. Rev. C **48**, 1246 (1993).
- [8] T. S. Kosmas and E. Oset, Phys. Rev. C **53**, 1409 (1996).
- [9] H. Kim, S. Schramm and C. J. Horowitz, Phys. Rev. C **53**, 2468 (1996).
- [10] H. Kim, S. Schramm and C. J. Horowitz, Indiana preprint IU/NTC 96-02.
- [11] E. Oset and L.L. Salcedo, Nucl. Phys. **A468**, 631 (1987).
- [12] C. García-Recio, E. Oset, L.L. Salcedo, D. Strottman and M.J. López, Nucl. Phys. **A526**, 685 (1991).
- [13] L.L. Salcedo, E. Oset, M.J. Vicente Vacas and C. García Recio, Nucl. Phys. **A484**, 557 (1988).
- [14] R.C. Carrasco, J. Nieves and E. Oset, Nucl. Phys. **A565**, 797 (1993).
- [15] P. Fernández de Córdoba, E. Oset and M.J. Vicente-Vacas, Nucl. Phys. **A592**, 472 (1995).
- [16] P. Oltmanns, F. Osterfeld and T. Udagawa, Phys. Lett. **299B**, 194 (1993).
- [17] P. Fernández de Córdoba, J. Nieves, E. Oset and M.J. Vicente-Vacas, Phys. Lett **319B**, 416 (1993).
- [18] V. F. Dmitriev, Phys. Rev. C **48**, 357 (1993).
- [19] C. Ellegaard et al., Phys. Rev. Lett. **50**, 1795 (1983).
- [20] V. G. Ableev et al., Sov. Phys. JEPT Lett. **40**, 763 (1984).
- [21] T.E.O. Ericson and W. Weise, Pions and Nuclei, Clarendon, Oxford, 1988.
- [22] T. Hennino et al., Phys. Lett. **303B**, 236 (1993).

- [23] H.P. Morsch et al., Phys. Rev. Lett. **69**, 1336 (1992).
- [24] P. Fernández de Córdoba, E. Oset, M.J. Vicente-Vacas, Yu. Ratis, J. Nieves, B. López-Alvaredo and F. Gareev, Nucl. Phys. **A586**, 586 (1995).
- [25] S. Hirenzaki, P. Fernández de Córdoba and E. Oset, Phys. Rev. C **53**, 277 (1996).
- [26] M.J. Dekker, P.J. Brussard and J.A. Tjon, Phys. Rev. C **49**, 2650 (1994).
- [27] J. Nieves, E. Oset and C. García-Recio, Nucl. Phys. **A554**, 554 (1993).
- [28] I. Laktineh, W.M. Alberico, J. Delorme and M. Ericson, Nucl. Phys. **A555**, 237 (1993).
- [29] B. Zeitnitz, Prog. Part. Nucl. Phys. **32**, 351 (1994).

Figure Captions

1. Diagrammatic representation of the coherent pion production process $\nu_e + A(g.s) \rightarrow e^- + A(g.s.) + \pi^+$.
2. Kinematics of the $\nu n \rightarrow e^- p$ process.
3. Angular distribution of the pions from coherent π^+ production on ^{16}O with neutrino beam of energy 800 MeV, $T_e = 545$ MeV and $\theta_e = 0^0$. The solid curve corresponds to the full calculation which includes renormalization of the Δ and pion in the nuclear medium. The dashed curve is the impulse approximation calculation.
4. Energy spectrum of the coherent pions produced on ^{16}O with neutrinos of beam energy 1 GeV, and $\theta_e = 0^0$. The solid curve corresponds to the full calculation with renormalized pions and deltas and dashed line is the impulse approximation calculation.
5. Same as fig.4, but integrated over the electron solid angle.
6. Energy spectra of the coherent pions produced on ^{16}O , at three different neutrino energies, with the Δ and pion renormalizations included in the calculations.
7. Energy spectra of the coherent pions scattered from three different nuclei by neutrinos of 1 GeV energy.
8. Energy spectra of the coherent pions scattered from three different nuclei by muon type neutrinos of 1 GeV energy.

MESONIC AND BINDING CONTRIBUTIONS TO THE EMC EFFECT IN A RELATIVISTIC MANY BODY APPROACH

E. Marco¹, E. Oset¹ and P. Fernández de Córdoba²

¹ *Departamento de Física Teórica and IFIC, Centro Mixto Universidad de Valencia-CSIC, 46100 Burjassot (Valencia), Spain*

² *Departamento de Matemática Aplicada, Universidad Politécnica de Valencia*

Abstract

We revise the conventional nuclear effects of Fermi motion, binding and pionic effects in deep inelastic lepton scattering using a relativistic formalism for an interacting Fermi sea and the local density approximation to translate results from nuclear matter to finite nuclei. In addition we also consider effects from ρ -meson renormalization in the nucleus. The use of nucleon Green's functions in terms of their spectral functions offers a precise way to account for Fermi motion and binding. On the other hand the use of many body Feynman diagrams in a relativistic framework allows one to avoid using prescriptions given in the past to introduce relativistic corrections in a non relativistic formalism.

We show that with realistic nucleon spectral functions and meson nucleus selfenergies one can get a reasonable description of the EMC effect for $x > 0.15$, outside the shadowing region.

1 Introduction

The EMC effect [1] is probably one of the topics in the interplay of nuclear and particle physics which has attracted more attention. Pioneering work on Fermi motion and pionic effects [2, 3, 4] was followed by many different ideas like binding of the nucleons in the nucleus, multi-quark cluster effects or Q^2 rescaling (see refs. [5, 6, 7] for reviews on the topic). Here we shall pay attention only to conventional nuclear degrees of freedom, mesons (π and ρ) and nucleons. One of the interesting ideas along these lines was the effect of the nuclear binding [8, 9, 10], which, with ups and downs, has come to be accepted as, largely or at least partly, responsible for the depletion of $R(x) = 2F_{2A}(x)/AF_{2D}(x)$ in the region of the minimum.

Criticism on this latter work was raised in [11], where it was shown that the introduction of relativistic corrections in the usual nuclear nonrelativistic treatment of the binding effects resulted in a flux factor which reduced the conventional binding effects [11, 12]. This flux factor led to a different normalization of the spectral function which preserved the baryonic number calculated relativistically [11]. The argument of the normalization of the baryonic number is an important one and the idea has met with followers [12, 13, 14]. However, it is a prescription on how to convert the nonrelativistic nuclear wave function into a relativistic spectral function [15] and the prescription is not shared by others [6]. Furthermore, these are not the only relativistic corrections as shown in [16, 17].

This issue justifies a work like the present one, where we construct from the beginning a relativistic nucleon spectral function and define everything within a field theoretical formalism which uses the nucleon propagators written in terms of this spectral function. The relativistic formalism is taken from the beginning and the baryonic number is naturally well normalized. Since all the nuclear information needed is contained in the nucleon spectral function, one does not need to use ordinary nuclear wave functions, which are anyway static (no spreading in the energy distribution, which is just concentrated in the single particle energies of the shell model) and hence one does not need any step to introduce relativistic effects into the nonrelativistic wave functions, as done in [11]. Furthermore, the use of non static spectral functions is important. This was already seen in refs. [13, 13] which showed that the use of more realistic spectral functions accounting for nuclear correlations resulted in an enhancement of the binding effects. The reason is that, for a given average binding energy, the approach with a realistic spectral function leads to a larger kinetic and potential energy in absolute value than the shell model approach.

The other issue that we have revisited here is the pionic contribution. Large effects from the pionic cloud associated with the pion excess number in the nucleus were found in [2, 3, 7]. We have taken up the idea and recalculated these effects within the many body field theoretical approach using input which has been checked in a variety of nuclear reactions testing real and virtual pions: pionic reactions [18], muon capture [19], inclusive neutrino scattering [20] and

photonuclear reactions [21]. In addition we have also included corrections from the modification of ρ -meson cloud in the nucleus, in complete analogy with the pionic contribution.

Altogether we find that the use of the spectral function for the nucleons together with the mesonic effects can approximately account for the measured EMC effect.

The calculations are done using the spectral function for nucleons in nuclear matter, followed by the local density approximation. This was shown to be an excellent tool to deal with photonuclear reactions in the absence of shadowing effects [21]. Hence, a natural limit of our results is the region of shadowing, $x \leq 0.15$, where indeed there are discrepancies with the data, and other ingredients should be considered that we do not want to tackle [22, 23].

2 Relativistic nucleon propagator in nuclear matter

2.1 Nonrelativistic nucleon propagator and spectral functions

Let us recall first the nonrelativistic nucleon propagator for a noninteracting Fermi sea, which is given in momentum space by

$$G(p^0, p) = \frac{1 - n(\vec{p})}{p^0 - \varepsilon(\vec{p}) + i\epsilon} + \frac{n(\vec{p})}{p^0 - \varepsilon(\vec{p}) - i\epsilon} \quad (1)$$

where $n(\vec{p})$ is the Fermi occupation number $n(\vec{p}) = 1$ for $|\vec{p}| \leq k_F$, $n(\vec{p}) = 0$ for $|\vec{p}| > k_F$ and $\varepsilon(\vec{p})$ is the nonrelativistic nucleon energy. Eq. (1) can be recast as

$$G(p^0, p) = \frac{1}{p^0 - \varepsilon(\vec{p}) + i\epsilon} + 2\pi i n(\vec{p}) \delta(p^0 - \varepsilon(\vec{p})) \quad (2)$$

which separates the propagator into the free propagator and the medium correction.

For an interacting Fermi sea the nucleon propagator can be written in terms of its nonstatic selfenergy $\Sigma(p^0, p)$

$$G(p^0, p) = \frac{1}{p^0 - \varepsilon(\vec{p}) - \Sigma(p^0, p)} \quad (3)$$

which can be rewritten in terms of the spectral functions for holes and particles as [24]

$$G(p^0, p) = \int_{-\infty}^{\mu} \frac{S_h(\omega, p)}{p^0 - \omega - i\epsilon} d\omega + \int_{\mu}^{\infty} \frac{S_p(\omega, p)}{p^0 - \omega + i\epsilon} d\omega \quad (4)$$

with the following relationships

$$\begin{aligned}
S_h(p^0, p) &= \frac{1}{\pi} \frac{\text{Im}\Sigma(p^0, p)}{[p^0 - \varepsilon(\vec{p}) - \text{Re}\Sigma(p^0, p)]^2 + [\text{Im}\Sigma(p^0, p)]^2} \\
&\quad \text{for } p^0 \leq \mu \\
S_p(p^0, p) &= -\frac{1}{\pi} \frac{\text{Im}\Sigma(p^0, p)}{[p^0 - \varepsilon(\vec{p}) - \text{Re}\Sigma(p^0, p)]^2 + [\text{Im}\Sigma(p^0, p)]^2} \\
&\quad \text{for } p^0 > \mu
\end{aligned} \tag{5}$$

let us also recall that the momentum distribution of the nucleon in this interacting Fermi sea is given by

$$\begin{aligned}
n_I(\vec{p}) &= \int_{-\infty}^{\mu} S_h(\omega, p) d\omega \\
1 - n_I(\vec{p}) &= \int_{\mu}^{\infty} S_p(\omega, p) d\omega
\end{aligned} \tag{6}$$

with the automatic sum rule

$$\int_{-\infty}^{\mu} S_h(\omega, p) d\omega + \int_{\mu}^{\infty} S_p(\omega, p) d\omega = 1 \tag{7}$$

In passing we also note that in physical reactions $n_I(\vec{p})$ does not factorize out in the physical cross sections because other factors dependent on ω and \vec{p} appear simultaneously in the formulae, and restrictions due to energy and momentum conservation do not allow the infinite ranges in the ω integration required in eq. (6). Failure to realize that, and the naive substitution of $n(\vec{p})$ in eq. (1) by $n_I(\vec{p})$ of eq. (6), as sometimes done, leads to erroneous results which can be off by three orders of magnitude in some cases [25]. This gives us a warning that we should express all our magnitudes in terms of the spectral functions, not the momentum distributions.

2.2 Relativistic nucleon propagator and spectral functions.

The free relativistic nucleon propagator is given by

$$\frac{\not{p} + M}{p^2 - M^2 + i\epsilon} \equiv \frac{M}{E(\vec{p})} \left\{ \frac{\sum_r u_r(\vec{p}) \bar{u}_r(\vec{p})}{p^0 - E(\vec{p}) + i\epsilon} + \frac{\sum_r v_r(-\vec{p}) \bar{v}_r(-\vec{p})}{p^0 + E(\vec{p}) - i\epsilon} \right\} \tag{8}$$

where we have separated in the second member the contribution from positive and negative energy states [26]. $M, E(\vec{p})$ in eq. (8) are the nucleon mass and the relativistic nucleon energy $(\vec{p}^2 + M^2)^{1/2}$, and $u_r(\vec{p}), v_r(\vec{p})$ are the ordinary spinors which we take normalized as $\bar{u}_r(\vec{p}) u_r(\vec{p}) = 1$. We recall that $u_r(\vec{p})$ are functions of three momentum and they will be the only spinors which will appear in our framework.

The relativistic nucleon propagator for a noninteracting Fermi sea is easily derived and, by analogy to eq. (2), can be written as

$$G(p^0, p) = \frac{\not{p} + M}{p^2 - M^2 + i\epsilon} + 2\pi i n(\vec{p})(\not{p} + M) \theta(p^0) \delta(p^2 - M^2) \quad (9)$$

which by means of the identity of eq. (8) can be recast as

$$G(p^0, p) = \frac{M}{E(\vec{p})} \left\{ \sum_r u_r(\vec{p}) \bar{u}_r(\vec{p}) \left[\frac{1 - n(\vec{p})}{p^0 - E(\vec{p}) + i\epsilon} + \frac{n(\vec{p})}{p^0 - E(\vec{p}) - i\epsilon} \right] + \frac{\sum_r v_r(-\vec{p}) \bar{v}_r(-\vec{p})}{p^0 + E(\vec{p}) - i\epsilon} \right\} \quad (10)$$

Apart from the negative energy contribution, which will play no role in our problem, the only difference between eq. (10) and the nonrelativistic propagator of eq. (1) is the presence of the factor $M/E(\vec{p})$ and the projector over the space of positive energies $\sum_r u_r(\vec{p}) \bar{u}_r(\vec{p})$, which are both unity in the nonrelativistic approximation.

Now we proceed to construct the relativistic propagator in the interacting Fermi sea. We wish to sum the Dyson series for the diagrams shown in fig. 1, where although not shown, one would also have other sources of nucleon self-energies. We will write them in terms of the operator $\Sigma(p^0, p)$. It will become clear later on that we only need the imaginary part of the nucleon propagator for the positive energy states, in which case we neglect from the beginning the negative energy states (their weight becomes negligible compared to the singular part of the positive energy propagator). Hence, for the purpose of the present problem, the nucleon propagator needed will be

$$\begin{aligned} G(p^0, p) &= \frac{M}{E(\vec{p})} \sum_r u_r(\vec{p}) \bar{u}_r(\vec{p}) \frac{1}{p^0 - E(\vec{p})} + \\ &\frac{M}{E(\vec{p})} \sum_r \frac{u_r(\vec{p}) \bar{u}_r(\vec{p})}{p^0 - E(\vec{p})} \Sigma(p^0, p) \frac{M}{E(\vec{p})} \sum_s \frac{u_s(\vec{p}) \bar{u}_s(\vec{p})}{p^0 - E(\vec{p})} + \dots \\ &= \frac{M}{E(\vec{p})} \sum_r \frac{u_r(\vec{p}) \bar{u}_r(\vec{p})}{p^0 - E(\vec{p}) - \bar{u}_r(\vec{p}) \Sigma(p^0, p) u_r(\vec{p}) \frac{M}{E(\vec{p})}} \end{aligned} \quad (11)$$

where we have used the fact that Σ should be diagonal in spin for spin saturated matter which we only consider.

Comparison of eqs. (11) and (3) shows again the differences between the relativistic and nonrelativistic propagators.

The structure of eq. (11) allows one to define a spectral representation of the nucleon propagator by means of $S_h(\omega, p)$ and $S_p(\omega, p)$ as

$$G(p^0, p) = \frac{M}{E(\vec{p})} \sum_r u_r(\vec{p}) \bar{u}_r(\vec{p}) \left[\int_{-\infty}^{\mu} d\omega \frac{S_h(\omega, p)}{p^0 - \omega - i\eta} \right]$$

$$+ \int_{\mu}^{\infty} d\omega \frac{S_p(\omega, p)}{p^0 - \omega + i\eta} \quad (12)$$

with the relationships

$$S_h(p^0, p) = \frac{1}{\pi} \frac{\frac{M}{E(\vec{p})} \text{Im}\Sigma(p^0, p)}{\left[p^0 - E(\vec{p}) - \frac{M}{E(\vec{p})} \text{Re}\Sigma(p^0, p) \right]^2 + \left[\frac{M}{E(\vec{p})} \text{Im}\Sigma(p^0, p) \right]^2} \quad \text{for } p^0 \leq \mu$$

$$S_p(p^0, p) = -\frac{1}{\pi} \frac{\frac{M}{E(\vec{p})} \text{Im}\Sigma(p^0, p)}{\left[p^0 - E(\vec{p}) - \frac{M}{E(\vec{p})} \text{Re}\Sigma(p^0, p) \right]^2 + \left[\frac{M}{E(\vec{p})} \text{Im}\Sigma(p^0, p) \right]^2} \quad (13)$$

$$\text{for } p^0 > \mu$$

where for simplicity Σ is now $\bar{u}\Sigma u$ which is independent of the spin. Eqs. (13) are now the generalizations of eqs. (5) using relativistic kinematics. Note that S_p and S_h defined in eq. (12) are not the nonrelativistic spectral functions normally used. Hence one should not expect the same normalization as in [11, 12, 14]. The normalization of S_h , which we will need, is easily obtained by imposing baryon number conservation, as done in [11]. For this purpose we evaluate the electromagnetic form factor at $q = 0$. For the case of the nucleon (fig. 2a)) we have (assume all baryons have charge unity for normalization purposes),

$$\langle N | B^\mu | N \rangle \equiv \bar{u}(\vec{p}) \gamma^\mu u(\vec{p}) = B \frac{p^\mu}{M}; \quad B = 1, \quad p^\mu \equiv (E(\vec{p}), \vec{p}) \quad (14)$$

For the case of nucleons in the medium we must evaluate the many body diagram of fig. 2b).

$$\langle A | B^\mu | A \rangle = (-) \int \frac{d^4 p}{(2\pi)^4} V \text{iTr} [G(p^0, p) \gamma^\mu] e^{ip^0 \eta} \quad (15)$$

where $\exp(ip^0 \eta)$, with $\eta \rightarrow 0^+$, is the convergence factor for loops appearing at the same time [24] and V the volume of our normalization box.

By means of eq. (12) we can see that the convergence factor limits the contribution to the hole spectral function and we get

$$\langle A | B^\mu | A \rangle = V \int \frac{d^3 p}{(2\pi)^3} \frac{M}{E(\vec{p})} \text{Tr} \left[\sum_r u_r(\vec{p}) \bar{u}_r(\vec{p}) \gamma^\mu \right]$$

$$\cdot \int_{-\infty}^{\mu} S_h(\omega, p) d\omega$$

$$\begin{aligned}
&= V \int \frac{d^3p}{(2\pi)^3} \frac{M}{E(\vec{p})} \text{Tr} \left[\frac{(\not{p} + M)_{on\ shell}}{2M} \gamma^u \right] \int_{-\infty}^{\mu} S_h(\omega, p) d\omega \\
&= 2V \int \frac{d^3p}{(2\pi)^3} \frac{M}{E(\vec{p})} \frac{p_{on\ shell}^\mu}{M} \int_{-\infty}^{\mu} S_h(\omega, p) d\omega \equiv B \frac{P_A^\mu}{M_A} \quad (16)
\end{aligned}$$

where in the last step we have imposed that this matrix element gives the right current with B baryons, in analogy to eq. (14), and P_A^μ is the momentum of the nucleus. Note that $p_{on\ shell}^\mu$ appears in eq. (16) because the operator $(\not{p} + M)_{on\ shell}$ comes from $u_r(\vec{p})\bar{u}_r(\vec{p})$ which depends only on \vec{p} (it corresponds to free particles with $p^\mu \equiv (E(\vec{p}), \vec{p})$). Obviously eq. (16) must be evaluated in the rest frame of our Fermi sea where all magnitudes are defined. Only $\mu = 0$ is then relevant and we obtain the desired normalization

$$2V \int \frac{d^3p}{(2\pi)^3} \int_{-\infty}^{\mu} S_h(\omega, p) d\omega = B \quad (17)$$

(Note that the factors $\frac{M}{E(\vec{p})}$, $\frac{p_{on\ shell}^\mu}{M}$ have cancelled in eq. (16)). The factor 2 is a spin factor. By a simple inspection of eq. (17) we can see that with the definition of the spectral functions in eq. (12) one can use eq. (6) to determine momentum distributions in both the nonrelativistic and relativistic cases.

In our formalism we do not have a box of constant density, but elements of volume d^3r with local density $\rho_p(\vec{r}), \rho_n(\vec{r})$, the nuclear proton and neutron densities at the point \vec{r} . Hence our spectral functions for protons and neutrons are functions of the local Fermi momentum

$$k_{F,p}(\vec{r}) = [3\pi^2\rho_p(\vec{r})]^{1/3}; \quad k_{F,n}(\vec{r}) = [3\pi^2\rho_n(\vec{r})]^{1/3} \quad (18)$$

and then the equivalent normalization to eq. (17) is

$$2 \int \frac{d^3p}{(2\pi)^3} \int_{-\infty}^{\mu} S_h(\omega, p, k_{F,p,n}(\vec{r})) d\omega = \rho_{p,n}(\vec{r}) \quad (19)$$

In practice we shall work with symmetric nuclear matter of density $\rho(\vec{r})$. Hence we have a unique Fermi momentum defined as $k_F(\vec{r}) = [3\pi^2\rho(\vec{r})/2]^{1/3}$ and then one has

$$4 \int \frac{d^3p}{(2\pi)^3} \int_{-\infty}^{\mu} S_h(\omega, p, k_F(\vec{r})) d\omega = \rho(\vec{r}) \quad (20)$$

or equivalently

$$\int d^3r \quad 4 \int \frac{d^3p}{(2\pi)^3} \int_{-\infty}^{\mu} S_h(\omega, p, k_F(\vec{r})) d\omega = A \quad (21)$$

with A the mass number of each nucleus. The density $\rho(\vec{r})$ of each nucleus is taken from experiment in our case, and expressed in terms of a two Fermi parameter distribution for medium and heavy nuclei [27] and mod harmonic

oscillator for light nuclei [27, 28]. Eq. (21) is fulfilled at the level of 2 - 3 % in our case, in spite of the non trivial structure of the spectral function and the integrals involved. The small numerical deviation from the right normalization is taken care by dividing by the integral of eq. (21) instead of by A in the evaluation of $R(x)$, since a similar integration weighed by the structure functions appears in the numerator, as we shall see. Although one could separate the contribution of protons and neutrons in the calculation, we have only applied the results to nuclei with $N = Z$, or very close, like ^{56}Fe and hence, we work with the symmetric nuclear matter version.

3 Deep inelastic electron scattering from nuclei

Let us recall the basic ideas in deep inelastic scattering. Consider the (e, e') process on a nucleon of fig. 3a). The invariant T matrix for the process is

$$-iT = ie\bar{u}_e(\vec{k}')\gamma^\mu u_e(\vec{k}) \frac{-ig_{\mu\nu}}{q^2}(-ie) \langle X|J^\nu|N \rangle \quad (22)$$

where $\langle X|J^\nu|N \rangle$ is the invariant matrix element of the hadronic current. The cross section for the process $eN \rightarrow e'X$ is given in Mandl and Shaw normalization [29] by

$$\begin{aligned} \sigma &= \frac{1}{v_{rel}} \frac{2m}{2E_e(\vec{k})} \frac{2M}{2E(\vec{p})} \int \frac{d^3k'}{(2\pi)^3} \frac{2m}{2E_e(\vec{k}')} \\ &\Pi_{i=1}^N \int \frac{d^3p'_i}{(2\pi)^3} \Pi_{l\epsilon f} \left(\frac{2M'_l}{2E'_l} \right) \Pi_{j\epsilon b} \left(\frac{1}{2\omega'_j} \right) \bar{\Sigma}\Sigma|T|^2(2\pi)^4 \\ &\delta^4(p + k - k' - \Sigma_{i=1}^N p'_i) \end{aligned} \quad (23)$$

where m is the electron mass, f stands for fermions and b for bosons in the final state X . The factor $\frac{2M}{2E(\vec{p})}$ becomes $\frac{1}{2\omega(\vec{p})}$ if we study the cross section on a pion. The index i is split in l, j for fermions and bosons respectively.

In the nucleon rest frame one can then write the differential cross section, with Ω', E' referring to the outgoing electron, as

$$\frac{d^2\sigma}{d\Omega' dE'} = \frac{\alpha^2}{q^4} \frac{k'}{k} L'_{\mu\nu} W'^{\mu\nu} \quad (24)$$

with $\alpha = e^2/4\pi$ and $L'_{\mu\nu}$ the leptonic tensor

$$L'_{\mu\nu} = 2k_\mu k'_\nu + 2k'_\mu k_\nu + q^2 g_{\mu\nu} \quad (25)$$

and $W'^{\mu\nu}$ the hadronic tensor defined as

$$W'^{\mu\nu} = \frac{1}{2\pi} W^{\mu\nu} \quad (26)$$

with

$$W^{\mu\nu} = \bar{\Sigma}_{s_p} \Sigma_X \Sigma_{s_i} \prod_{i=1}^N \int \frac{d^3 p'_i}{(2\pi)^3} \Pi_{l\epsilon f} \left(\frac{2M'_l}{2E'_l} \right) \Pi_{j\epsilon b} \left(\frac{1}{2\omega'_j} \right) \\ < X | J^\mu | H >^* < X | J^\nu | H > (2\pi)^4 \delta^4(p + q - \Sigma_{i=1}^N p'_i) \quad (27)$$

where q is the momentum of the virtual photon, s_p the spin of the nucleon and s_i the spin of the fermions in X .

Lorentz covariance and gauge invariance allow one to write $W'^{\mu\nu}$ as [\[30\]](#)

$$W'^{\mu\nu} = \left(\frac{q^\mu q^\nu}{q^2} - g^{\mu\nu} \right) W_1 + \left(p^\mu - \frac{p \cdot q}{q^2} q^\mu \right) \left(p^\nu - \frac{p \cdot q}{q^2} q^\nu \right) \frac{W_2}{M^2} \quad (28)$$

where W_1, W_2 are the two structure functions of the nucleon and are functions of $q^2, p \cdot q$.

Now we evaluate the cross section for (e, e') on the nucleus. In order not to miss flux factors and be able to write everything in terms of propagators, we evaluate the electron selfenergy corresponding to the diagram in fig. 3 b). We obtain

$$-i\Sigma(k) = \int \frac{d^4 q}{(2\pi)^4} \bar{u}_e(\vec{k}) i e \gamma^\mu i \frac{\not{k}' + m}{k'^2 - m^2 + i\epsilon} i e \gamma^\nu u_e(\vec{k}) \\ \frac{-i g_{\mu\rho}}{q^2} (-i) \Pi^{\rho\sigma}(q) \frac{-i g_{\sigma\nu}}{q^2} \quad (29)$$

which for unpolarized electrons can be written as

$$\Sigma(k) = i e^2 \int \frac{d^4 q}{(2\pi)^4} \frac{1}{q^4} \frac{1}{2m} L'_{\mu\nu} \frac{1}{k'^2 - m^2 + i\epsilon} \Pi^{\mu\nu}(q) \quad (30)$$

with $\Pi^{\mu\nu}(q)$ the photon selfenergy.

In order to evaluate the cross section we need only $Im\Sigma(k)$ which can be easily evaluated by means of Cutkosky rules [\[26\]](#).

$$\begin{aligned} \Sigma(k) &\rightarrow 2i Im\Sigma(k) \\ D(k') &\rightarrow 2i\theta(k'^0) ImD(k') \text{ (boson propagator)} \\ \Pi^{\mu\nu}(q) &\rightarrow 2i\theta(q^0) Im\Pi^{\mu\nu}(q) \\ G(p) &\rightarrow 2i\theta(p^0) ImG(p) \text{ (fermion propagator)} \end{aligned} \quad (31)$$

with the result

$$Im\Sigma(k) = e^2 \int \frac{d^3 q}{(2\pi)^3} \frac{1}{2E_e(\vec{k} - \vec{q})} \theta(q^0) Im\Pi^{\mu\nu}(q) \frac{1}{q^4} \frac{1}{2m} L'_{\mu\nu} \quad (32)$$

with $q^0 = k^0 - E_e(\vec{k} - \vec{q})$.

The cross section is readily evaluated from there. Inspection of eq. (11) for the relativistic fermion propagator tells us that the electron width is given by

$$\Gamma(k) = -\frac{2m}{E_e(\vec{k})} \text{Im}\Sigma(k) \quad (33)$$

by means of which the contribution to the cross section from an element of volume d^3r in the rest frame of the nucleus is

$$\begin{aligned} d\sigma &= \Gamma dt dS = \Gamma \frac{dt}{dl} dl dS = \frac{\Gamma}{v} d^3r = \\ &= \Gamma \frac{E_e(\vec{k})}{k} d^3r = -\frac{2m}{k} \text{Im} \Sigma d^3r \end{aligned} \quad (34)$$

Hence we immediately write the (e, e') cross section in the nucleus as

$$\frac{d^2\sigma}{d\Omega' dE'} = -\frac{\alpha}{q^4} \frac{k'}{k} \frac{1}{(2\pi)^2} L'_{\mu\nu} \int d^3r \text{Im} \Pi^{\mu\nu}(q) \quad (35)$$

with $q^0 = k^0 - E_e(\vec{k} - \vec{q}) = k^0 - k'^0$, which is always positive in this experiment, so we drop the $\theta(q^0)$ function. Comparison of eq. (35) with eq. (24) used for nuclear targets tells as that

$$W'_A{}^{\mu\nu}(q) = -\frac{1}{e^2} \frac{1}{\pi} \int d^3r \text{Im} \Pi^{\mu\nu}(q) \quad (36)$$

Next we evaluate $\Pi^{\mu\nu}(q)$ corresponding to the right hand side of the diagram of fig. 3b) using again the Feynman rules in terms of propagators. We have

$$-i\Pi^{\mu\nu}(q) = (-) \int \frac{d^4p}{(2\pi)^4} iG(p) \Sigma_X \Sigma_{s_p, s_i} \Pi_{i=1}^N \int \frac{d^4p'_i}{(2\pi)^4}$$

$$\Pi_l iG_l(p'_l) \Pi_j iD_j(p'_j) (-i)^2 e^2 \langle X | J^\mu | H \rangle \langle X | J^\nu | H \rangle^* (2\pi)^4 \delta^4(q + p - \Sigma_{i=1}^N p'_i) \quad (37)$$

which by means of Cutkosky rules (31) and the use of free propagators, eq. (8), for the final states and the medium propagator, eq. (12), for $G(p)$, plus eq. (36), leads immediately to

$$\begin{aligned} W'_A{}^{\mu\nu} &= \Sigma_{n,p} \int d^3r \int \frac{d^3p}{(2\pi)^3} \frac{M}{E(\vec{p})} \int_{-\infty}^{\mu} S_h(p^0, p) dp^0 \\ &\frac{1}{2\pi} \Sigma_X \Sigma_{s_p} \Sigma_{s_i} \Pi_{i=1}^N \int \frac{d^3p'_i}{(2\pi)^3} \Pi_{lcf} \left(\frac{2M'_l}{2E'_l} \right) \Pi_{jeb} \left(\frac{1}{2\omega'_j} \right) \\ &\langle X | J^\mu | H \rangle \langle X | J^\nu | H \rangle^* (2\pi)^4 \delta^4(q + p - \Sigma_{i=1}^N p'_i) \end{aligned} \quad (38)$$

which by means of eq. (27) can be rewritten for an isospin symmetric nucleus as

$$W'_A{}^{\mu\nu} = 4 \int d^3r \int \frac{d^3p}{(2\pi)^3} \frac{M}{E(\vec{p})} \int_{-\infty}^{\mu} dp^0 S_h(p^0, p) \\ W'_N{}^{\mu\nu}(p, q)$$

with

$$p \equiv (p^0, \vec{p}); W'_N{}^{\mu\nu} = \frac{1}{2}(W'_p{}^{\mu\nu} + W'_n{}^{\mu\nu}) \quad (39)$$

Note that $W'_N{}^{\mu\nu}(p, q)$ appears with the off shell arguments of p , the bound nucleon.

In the steps from eq.(37) to (38) the spinors $u(\vec{p})$ are included in the matrix elements of the currents and we have considered that there is necessarily a fermion loop (hence the first minus sign in eq. (37)) with a free particle in the final state and the nucleon in the medium in the initial state. The corresponding energy integration in the loop (if we had used a Wick rotation explicitly instead of Cutkosky rules) necessarily picks up the hole part of the propagator of eq. (12), and at the same time relaxes the condition $\theta(p^0)$ of Cutkosky rules which does not appear for the hole part.

In eq. (39) there is an apparent lack of normalization, since assuming $W'^{\mu\nu}$ constant (which actually cannot be in practice) we would expect $W'_A{}^{\mu\nu} = AW'^{\mu\nu}$. However given the normalization of the spectral function in eq. (21), this is not the case. In eq. (39) we get the extra factor $\frac{M}{E(\vec{p})}$ which does not appear in eq. (21). It is interesting to see the meaning of this factor in eq. (39). If we look at the formula of the eN cross section in eq. (23), and by means of eqs. (25) and (27) we find

$$\sigma = \frac{\alpha^2 M}{v_{rel} E_e(\vec{k}) E(\vec{p})} \int \frac{d^3k'}{E_e(\vec{k}')} \frac{1}{q^4} L'_{\mu\nu} W'_N{}^{\mu\nu} \quad (40)$$

where $L'_{\mu\nu} W'^{\mu\nu}$ is a Lorentz invariant and the content of the integral in eq. (40) also. For collinear frames of reference we also have

$$v_{rel} E_e(\vec{k}) E(\vec{p}) = Mk \quad (41)$$

where k is the electron momentum in the frame where the nucleon is at rest and hence

$$\sigma = \frac{\alpha^2}{k} \int \frac{d^3k'}{E_e(\vec{k}')} \frac{1}{q^4} L'_{\mu\nu} W'_N{}^{\mu\nu} \quad (42)$$

Now if we have a system of moving nucleons the cross section for scattering of the electron with the nucleus can not be obtained as a sum of individual cross sections, because the relative eN flux is different for each nucleon. Instead, one has to sum the probabilities of collision per unit time for each nucleon and

divide by a unique flux, the one relative to the CM of the nucleus. By taking for v_{rel} in eq. (40) the velocity of the electron with respect to the CM of the nucleus and suming over all the nucleons in eq. (40) we will be calculating the electron nucleus cross section. Hence we obtain in the rest frame of the nucleus

$$\begin{aligned}\sigma_A &= \frac{\alpha^2}{k} \int \frac{d^3k'}{E_e(\vec{k}')} \frac{1}{q^4} L'_{\mu\nu} \sum_{\vec{p}} \frac{M}{E(\vec{p})} W_N'^{\mu\nu}(p, q) \\ &= \frac{\alpha^2}{k} \int \frac{d^3k'}{E_e(\vec{k}')} \frac{1}{q^4} L'_{\mu\nu} 4 \int d^3r \int \frac{d^3p}{(2\pi)^3} \frac{M}{E(\vec{p})} \int_{-\infty}^{\mu} dp^0 S_h(p^0, p) W_N'^{\mu\nu}(p, q)\end{aligned}\tag{43}$$

where k is the electron momentum in the nucleus rest frame. Since our nuclear cross section is given in terms of $W_A'^{\mu\nu}$ by (see eqs. (35), (36))

$$\sigma_A = \frac{\alpha^2}{k} \int \frac{d^3k'}{E_e(\vec{k}')} L'_{\mu\nu} W_A'^{\mu\nu}\tag{44}$$

then eq. (39) follows immediately.

The previous discussion has shown that the factor $\frac{M}{E(\vec{p})}$ is a factor appearing in the probability of reaction per unit time for each nucleon, and remains in the integral when we divide by a unique flux in order to obtain the nuclear cross section. It is thus a Lorentz contraction factor.

In the limit of small densities, when $M/E(\vec{p}) = 1$, eq. (39) with the consideration of eq. (21) would give $W_A'^{\mu\nu} = AW_N'^{\mu\nu}$ as it should be. Eq. (39) accounts for Fermi motion and binding and includes the relativistic Lorentz contraction factor $M/E(\vec{p})$ and the change of the arguments in $W'^{\mu\nu}(p, q)$. Note in passing that the relativistic factor $m/E_e(\vec{k})$ of eq. (33), which we extracted from the relativistic propagator of eq. (11), has been essential to provide the right normalization.

4 Contribution from the pion cloud

Let us first see the free pion structure function. The same formula eq. (24) is used for pions and this defines $W_\pi'^{\mu\nu}$. Given the normalization of the fields which we follow [29], the cross section of eq. (23) contains the factor $1/2\omega(\vec{p})$ instead of $2M/2E(\vec{p})$. Hence, this means that the definition $W_\pi'^{\mu\nu}$ is given by eq. (27) dividing the right hand side of the equation by $2m_\pi$ (and obviously the average over the spin of the nucleon does not appear now for the pion case).

In order to derive the contribution from the virtual pions in the medium we evaluate again the electron selfenergy related to the diagram of fig. 4. We can save all the steps given before simply by noting the differences in the two cases:

i) The bound nucleon propagator is substituted by a pion propagator. From the use of Cutkosky rules we must change

$$-2\pi \frac{M}{E(\vec{p})} \int_{-\infty}^{\mu} d\omega S_h(\omega, p) \delta(p^0 - \omega)$$

by

$$2\theta(p^0) \text{Im} D(p) \quad (45)$$

with $D(p)$ the pion propagator (in the medium).

ii) One must take into account that $W_{\pi}^{\prime\mu\nu}$ is given by eq. (27) divided by $2m_{\pi}$.

iii) The sum over spins of the bound nucleon in eq. (37) does not appear now for the case of the pion.

iv) There are three charged states of pions.

With only these four rules we can already write

$$W_{A,\pi}^{\prime\mu\nu} = 3 \int d^3r \int \frac{d^4p}{(2\pi)^4} \theta(p^0) (-2) \text{Im} D(p) 2m_{\pi} W_{\pi}^{\prime\mu\nu}(p, q) \quad (46)$$

Now there are two obvious subtractions to eq. (46). First one should subtract the contribution from a free pion, which has nothing to do with medium effects. However, this is zero because one electron can not decay into another electron, one pion and X. Then assuming the pion is dressed in the medium by exciting ph and Δh as we shall do, one is left with the contributions shown in fig. 5.

Now there is no problem to get a contribution since $\text{Im} D(p)$ gets strength from ph excitation. The physical channel would correspond to $e \rightarrow e' + X + ph$, or equivalently $eN \rightarrow e'N'X$, which is now allowed. The physical channels are easily visualized by cutting the intermediate states in the diagrams with a horizontal line and placing on shell the particles cut by the line. This is actually the essence of Cutkosky rules to obtain the imaginary part of the selfenergy of a diagram.

The former discussion also tells us that part of what we are calculating is already contained in the nucleon structure function. This is because we are also calculating the contribution from the pions contained in a free nucleon. This has to be subtracted. This is easily done by substituting in eq. (46)

$$\text{Im} D(p) \rightarrow \delta \text{Im} D(p) \equiv \text{Im} D(p) - \rho \left. \frac{\partial \text{Im} D(p)}{\partial \rho} \right|_{\rho=0} \quad (47)$$

since we subtract A times the contribution from the pion cloud to the structure function of the free nucleon. In technical words, we can say that we are only considering terms with at least two ph or $1ph1\Delta h$ (the most important terms) etc. in fig. 5 (up to Pauli blocking corrections in the ph Lindhard function, which are automatically included by the procedure of eq. (47)).

Hence the genuine pionic contribution is given by

$$W_{A,\pi}'^{\mu\nu} = 3 \int d^3r \int \frac{d^4p}{(2\pi)^4} \theta(p^0) (-2)\delta ImD(p) 2m_\pi W_\pi'^{\mu\nu}(p, q) \quad (48)$$

Eqn. (39) and (48) are the basic equations which provide the nucleonic and pionic contributions.

In passing we can mention that the distribution of the excess number of pions, per unit volume in the nucleus, $\delta N_\pi(p)$, which contains the averages of $\langle a_p^+ a_p \rangle$, $\langle a_p^+ a_{-p}^+ \rangle$ and $\langle a_p a_{-p} \rangle$, is given by [31]

$$\frac{\delta N_\pi(\vec{p})}{2\omega(\vec{p})} = -3 \int_0^\infty \frac{dp^0}{2\pi} \delta ImD(p) \quad (49)$$

such that in the case of a structure function $W_\pi'^{\mu\nu}(p, q)$ independent of p^0 , eq. (48) could be considered as a weighed integral of the pion structure function over the pion excess distribution in the nucleus. However, the strong dependence of $W_\pi'^{\mu\nu}(p, q)$ on p^0 (imposed by energy and momentum conservation) does not allow that factorization, and hence a relationship of the pion excess number with the pionic contribution to the structure function cannot be established. The apparent extra factor 2 which we obtain in this counting (apart from the Lorentz contraction factor, $m_\pi/\omega(\vec{p})$) is obtained because one is automatically accounting for the imaginary part of the Compton $\gamma\pi$ amplitude which is crossing symmetric and contains the two diagrams of fig. 6, while the pion structure function for on shell pions contains only the imaginary part of the diagram 6a). (see refs. [31] and [32] for an elaborate discussion of these issues in the problem of the pion cloud contribution to K^+ nucleus scattering). It is worth noting that there is no overlap between the Feynman diagrams accounted for in the pionic contribution, fig 5, and those of the nucleonic contribution with Fermi motion and binding, which come from selfenergy insertions in the nucleon line of fig. 3b). Hence, these contributions to the nuclear structure function are independent.

5 The Bjorken limit

We have evaluated the contribution of nucleons and pions to the hadron structure function of the nucleus. We now proceed to write these expressions in terms of the Bjorken structure functions [33].

For nucleons (and similarly for pions or the nucleus) one introduces the Bjorken variables

$$x = \frac{-q^2}{2pq} ; \nu = \frac{p \cdot q}{M} ; Q^2 = -q^2 \quad (50)$$

and for large values of q^0 and Q^2 simultaneously and fixed x one has the Bjorken scaling

$$\nu W_2(x, Q^2) \equiv F_2(x)$$

$$MW_1(x, Q^2) \equiv F_1(x) \quad (51)$$

and the Callan-Gross relation

$$2xF_1(x) = F_2(x) \quad (52)$$

up to some, *QCD* corrections in $\ln Q^2$. Since the same Q^2 will be chosen for the nucleus and the nucleon and we perform ratios of structure functions we shall not worry about this dependence here.

In view of the relations (51), (52) the most practical way to proceed is to work with transverse components of $W'^{\mu\nu}$. For this purpose assume \vec{q} along the z direction, as usually done in the study of the e, e' reaction, and evaluate W'^{xx} . We find from eq. (28)

$$\begin{aligned} W'^{xx} &= W_1 + \frac{(p_x)^2}{M^2} W_2 \equiv \frac{F_1(x)}{M} + \frac{(p_x)^2}{M^2} \frac{F_2(x)}{\nu} \\ &= \frac{F_1(x)}{M} \quad \text{in the Bjorken limit} \end{aligned} \quad (53)$$

this component has the virtue that the coefficient of W_1 is independent of p and hence is the same for on shell or off shell nucleons, or pions, or the nucleus. Hence we can write

$$\begin{aligned} \frac{F_{1A,N}(x_A)}{M_A} &= 4 \int d^3r \int \frac{d^3p}{(2\pi)^3} \frac{M}{E(\vec{p})} \int_{-\infty}^{\infty} dp^0 S_h(p^0, p) \frac{F_{1N}(x_N)}{M} \\ \frac{F_{1A,\pi}(x_A)}{M_A} &= 3 \int d^3r \int \frac{d^4p}{(2\pi)^4} \theta(p^0) (-2) \delta \text{Im} D(p) 2m_\pi \frac{F_{1\pi}(x_\pi)}{m_\pi} \\ x_A &= -q^2/2M_A q^0 \equiv \frac{x}{A} \quad , \quad \text{with } x = -q^2/2Mq^0 \\ x_N &= -q^2/2pq \quad ; \quad x_\pi = -q^2/-2pq \end{aligned} \quad (54)$$

where the extra minus sign in x_π is because of the direction of p in fig. 4.

Here $F_{1N}(x) = (F_{1p}(x) + F_{1n}(x))/2$ as implicit in eq. (39).

We still have to exert some caution since $0 < x_N < 1$. On the other hand $x_\pi < 1$ but $x_\pi > x$ because in our scheme the emerging particle from the coupling of the pion to a nucleon of the nucleus is on shell when we excite $ph, \Delta h$ with the pion and take the imaginary part of $D(p)$ [3].

Since usually one compares ratios of the F_2 structure functions, this is easily accomplished by making use of the Callan-Gross relation (52) and we find

$$F_{2A,N}(x_A) = 4 \int d^3r \int \frac{d^3p}{(2\pi)^3} \frac{M}{E(\vec{p})} \int_{-\infty}^{\mu} dp^0 S_h(p^0, p) \frac{x}{x_N} F_{2N}(x_N) \theta(x_N) \theta(1-x_N) \quad (55)$$

$$F_{2A,\pi}(x_A) = -6 \int d^3r \int \frac{d^4p}{(2\pi)^4} \theta(p^0) \delta Im D(p) \frac{x}{x_\pi} 2M F_{2\pi}(x_\pi) \theta(x_\pi - x) \theta(1-x_\pi) \quad (56)$$

where we have again $F_{2N} = (F_{2p} + F_{2n})/2$ as implicit in eq. (39).

In the Bjorken limit the evaluation of eq. (55) does not require the knowledge of the variable q since

$$\frac{x}{x_N} \rightarrow \frac{p^0 - p^3}{M} \quad ; \quad \frac{x}{x_\pi} = \frac{-p^0 + p^3}{M} \quad (57)$$

but it is implicit in the structure functions which are taken at a certain Q^2 .

When reaching this point it is worth considering also the contribution of the ρ meson cloud. Both the pion and the ρ meson couple to nucleons and delta with derivative couplings, which give rise to relatively large meson self-energies in the range of momenta which contributes to the structure functions. Furthermore, as found already in ref. [31], the pion cloud contribution comes mostly from the combined ph and Δh excitation, with the ph on shell (in $\delta Im D(p)$), and one finds a negligible contribution of two ph excitations. Only π and ρ can excite the Δh components and this makes these two mesons special when looking at the mesonic contribution to the nuclear structure function. In addition there is an interplay between π and ρ exchange. Indeed, the ρ meson, through nuclear correlations, contributes both to the longitudinal and transverse parts of the spin-isospin ph and Δh interaction and it is an important element contributing to the Landau-Migdal g' parameter in a microscopic derivation of this interaction [34]. The value of this parameter governs to some extent the pionic (and ρ -meson) contribution to the structure function [3].

The contribution of the ρ -meson cloud to the structure function is given, by analogy to eq. (56) by

$$F_{2A,\rho}(x_A) = -12 \int d^3r \int \frac{d^4p}{(2\pi)^4} \theta(p^0) \delta Im D_\rho(p) \frac{x}{x_\rho} 2M F_{2\rho}(x_\rho) \theta(x_\rho - x) \theta(1 - x_\rho) \quad (58)$$

where $D_\rho(p)$ is now the ρ -meson propagator and $F_{2\rho}(x_\rho)$ is the ρ -meson structure function, which we take equal to the one of the pion following refs. [35, 36]. In addition x_ρ is also given, in analogy to eq. (57), by

$$\frac{x}{x_\rho} = \frac{-p^0 + p^3}{M} \quad (59)$$

Eq. (58) contains an extra factor of two compared to the pionic contribution of eq. (56). This is because of the two transverse polarizations of the ρ -meson and the fact that the coupling of the ρ to nucleons and deltas which we consider, following ref. [34] is only of transverse nature ($(\vec{\sigma} \times \vec{p})\vec{\epsilon}$ for nucleons and $(\vec{S}^+ \times \vec{p})\vec{\epsilon}$ for deltas, with $\vec{\epsilon}$ the polarization vector of the ρ meson and \vec{S}^+ the spin transition operator from spin 1/2 to 3/2).

The expression of $F_{1A,N}(x_A)$ in eq. (54) shows the same lack of normalization discussed in connection with eq. (39), since assuming $F_{1N}(x_N)$ constant (which is not the case) $F_{1A,N}$ is not A times F_{1N} , due to the Lorentz contraction factor $\frac{M}{E(\vec{p})}$. The same can be said about eq. (55) in general. However, eq. (55), shows a particular normalization property. Indeed, if we take an ensemble of nucleons on shell ($p^0 = E(\vec{p})$) and $x = 0$ (and hence $x_N = 0$, by virtue of eq. (57)), then the Lorentz contraction factor $\frac{M}{E(\vec{p})}$ cancels in average the dynamical factor $\frac{x}{x_N}$ and we get $F_{2A,N}(0) = AF_{2N}(0)$ for on shell nucleons. This cancellation, however, will not show up when the nucleons are off shell since in our formalism we still obtain the factor $\frac{M}{E(\vec{p})}$ but the dynamical factor $\frac{x}{x_N}$ will now be different.

In this discussion we are implicitly assuming that eqs. (54) and (55) stand as they are for the case of off shell nucleons simply by taking for x_N the expression of eq. (57) using the nucleon off shell variables. This is certainly the easiest form of the analytical continuation in the off shell regime, although there have been other prescriptions in the Literature [37, 38, 39].

We would like to justify our assumption. Indeed, in our framework we use nucleon propagators which are based on the free spinors (eq. (12)). Hence in eq. (38) the matrix elements would be defined in terms of free spinors, the final particles are free particles and the off shell dependence appears only in the $\delta(\)$ function. Obviously one can not look in detail at all channels implicit in eq. (38). However, one can use the same philosophy in the parton model which is used to find out the scaling of the structure functions. We follow here the steps of ref. [33] and assume that partons carry a fraction x_q of the nucleon momentum p and its mass M , that the electron parton amplitude is given by the on shell expression and that the outgoing parton is a free one, but the $\delta(\)$ function appears with the off shell variables.

One finds then

$$\begin{aligned} W_1 = W'^{xx} &= \sum_i \int dx_q f_i(x_q) e_i^2 \frac{1}{2} (-q^2) \frac{1}{x_q M} \delta(q^2 + 2pqx_q) \\ &= \sum_i e_i^2 f_i(x_N) \frac{1}{2M} = \frac{F_1(x_N)}{M}; x_N = \frac{-q^2}{2pq} \end{aligned} \quad (60)$$

where F_1 appears with argument x_N which is defined in terms of the off shell variables. Similarly one obtains

$$\frac{pq}{M} W_2 = \sum_i e_i^2 f_i(x_N) x_N = F_2(x_N) \quad (61)$$

whith p, q , and x_N defined in terms of the off shell variables.

We would like to note here that our finding $F_{2A}(0) \neq AF_{2N}(0)$, or equivalently $R(0) \neq 1$, where $R(x) = F_{2A}(x)/AF_{2N}(x)$, is not so unconventional. Indeed, in ref. [16] the authors also find this property and they literally quote “Note that a feature of the results is that $R(0) \neq 1$... It does not reflect any violation of baryon conservation, which is ensured by the normalization condition”, in our case eq. (21).

The issue of the normalization still stirs much controversy. We have devoted many thoughts to it throughout this paper looking at it from some points of view not discussed before. We see that for an ensemble of uncorrelated nucleons $F_{2A,N}(0) = AF_{2N}(0)$ but as soon as interactions are accounted for this normalization is lost. A similar thing would happen should we evaluate the structure function F_{3A} , which appears in neutrino scattering. This structure function when integrated over x is normalized to 3 for the nucleon if one assumes models with only three valence quarks, or to $3A$ for the nucleus. Once again this normalization would be lost if QCD interaction corrections are accounted for [40] and equivalently if NN interactions are included in the nuclear case, and experimentally this is the case [40]. Also, experimentally $F_{2A,N}(0) \neq AF_{2N}(0)$. Clear as the question looks to us, we are aware that this point of view is not universally accepted. Further thoughts and discussions on the issue should be welcome which would help settle the question in a way acceptable to all.

Eqs. (55, 56, 58) are the final equations which we use in the analysis.

For the nucleon and pion structure functions $F_{2N}(x), F_{2\pi}(x)$ we take the experimental values of refs. [41, 42].

6 The meson propagators

The pion propagator in the medium is given by

$$D(p) = [p^{02} - \vec{p}^2 - m_\pi^2 - \Pi_\pi(p^0, p)]^{-1} \quad (62)$$

with Π_π the pion selfenergy. We consider the contribution of the ph and Δh excitations to the pion selfenergy in connection with the Landau-Migdal correction in the pionic channel, as well as off shell pion nucleon form factors.

Since for δImD we need $D - D_0$, it is practical to write

$$D(p) - D_0(p) = D_0^2(p) \frac{\frac{f^2}{m_\pi^2} F^2(p) \vec{p}^2 \Pi^*(p)}{1 - \frac{f^2}{m_\pi^2} V'_L(p) \Pi^*(p)} \quad (63)$$

where $F(p)$ is the πNN form factor, which we take of the monopole type

$$F(p) = \frac{\Lambda^2 - m_\pi^2}{\Lambda^2 - p^2} \quad (64)$$

with $\Lambda = 1300 \text{ MeV}$ [43] and $f^2/4\pi = 0.08$. $V'_L(p)$ is the longitudinal part of the spin-isospin interaction and $\Pi^*(p)$ is the irreducible pion selfenergy, which contains all selfenergy diagrams which are not connected by $V'_L(p)$.

For the ρ -meson we can write

$$D_\rho(p) - D_{0\rho}(p) = D_{0\rho}^2(p) \frac{\frac{f^2}{m_\pi^2} C_\rho F_\rho^2(p) \vec{p}^2 \Pi^*(p)}{1 - \frac{f^2}{m_\pi^2} V'_T(p) \Pi^*(p)} \quad (65)$$

with $V'_T(p)$ the transverse part of the spin-isospin interaction, $C_\rho = 3.94$ [43] and $F_\rho(p)$ the ρNN form factor given by

$$F_\rho(p) = \frac{\Lambda_\rho^2 - m_\rho^2}{\Lambda_\rho^2 - p^2} \quad (66)$$

and $\Lambda_\rho = 1400 \text{ MeV}$ [43].

For $V'_L(p), V'_T(p)$ we take the expressions which are derived from a model with π and ρ exchange in the presence of short range nuclear correlations [44], which are given by

$$\begin{aligned} V'_L(p) &= \vec{p}^2 D_0(p) F^2(p) - \vec{p}^2 \tilde{D}_0(p) \tilde{F}^2(p) \\ &\quad - \frac{1}{3} q_c^2 \tilde{D}_0(p) \tilde{F}^2(p) - \frac{2}{3} q_c^2 \tilde{D}_{0\rho}(p) \tilde{F}_\rho^2(p) C_\rho \end{aligned} \quad (67)$$

$$\begin{aligned} V'_T(p) &= \vec{p}^2 D_{0\rho}(p) F_\rho^2(p) C_\rho - \frac{1}{3} q_c^2 \tilde{D}_0(p) \tilde{F}^2(p) \\ &\quad - (\vec{p}^2 + \frac{2}{3} q_c^2) \tilde{D}_{0\rho}(p) \tilde{F}_\rho^2(p) C_\rho \end{aligned} \quad (68)$$

Here $q_c \simeq 780 \text{ MeV}$ is the inverse of a typical correlation distance and $\tilde{D}(p), \tilde{F}(p), \tilde{D}_\rho(p), \tilde{F}_\rho(p)$ are the corresponding propagators and form factors substituting \vec{p}^2 by $\vec{p}^2 + q_c^2$. The irreducible selfenergy $\Pi^*(p)$ is in our case the sum of the Lindhard functions $U_N(p), U_\Delta(p)$ for ph and Δh excitation with the normalization and analytical expressions of the appendix of ref. [45]. It is interesting to note that for the values of p^0, p which contribute most to the structure function, both $V'_L(p)$ and $V'_T(p)$ are negative and this leads to positive values of $F_{2A,\pi}$ and $F_{2A,\rho}$.

It was also found in [31] that in order to evaluate the contribution of the pion cloud by using the pion propagator, as done here, it is important that it satisfies the sum rule

$$- \int_0^\infty \frac{dp^0}{\pi} 2p^0 \text{Im} D(p^0, p) = 1 \quad (69)$$

which expresses the equal time commutation relation of the pion fields. Our model satisfies this equation at the level of one per thousand.

7 The nucleon spectral function

Section 2.2 has established the framework for the relativistic nucleon propagator which we need here. The only input needed is the nucleon selfenergy. We take it from the work of ref. [46]. This is a semiphenomenological, quite successful approach, which uses as input the NN cross section and the spin-isospin effective interaction. This allows one to evaluate $Im\Sigma$, which is remarkably close to $Im\Sigma$ of the elaborate many body calculations of ref. [47, 48]. The real part is evaluated by means of a dispersion relation, and the Fock term from the pionic contribution is also included. Only pieces of the Hartree type, which should be independent of the momentum, are missing for which one needs more information. Hence, up to an unknown momentum independent piece in the selfenergy the rest of the nucleon properties in the medium can be calculated, like effective masses, spectral functions, etc, which are also in good agreement with sophisticated many body calculations [49, 50]. Actually, what might appear a drawback is now a welcome feature because since the proper binding energy is an important ingredient in the EMC effect, we also include phenomenologically a function $C(\rho)$ in the nucleon selfenergy and demand that the binding energy per nucleon be the experimental one for each nucleus. Then the model is complete, realistic and technically much simpler to handle than the sophisticated many body calculations [47, 49, 50].

With this improvement, momentum distributions and average binding energies are also in good agreement with other infinite nuclear matter [51] and finite nuclei calculations [52].

A small inconvenience appears because the selfenergy of ref. [46] is evaluated non relativistically. However we have checked that a proper calculation including relativistic factors of the type $M/E(\vec{p})$ in the nucleon propagators in the integrals over the loops which appear in the evaluation of $Im\Sigma$ in [46], would only introduce corrections in $Im\Sigma$ below the level of 10%. Second, we have changed $Im\Sigma$ by 10% and found that the ratio $R(x)$ changes only at the level of 1%. Thus we take the values for Σ from ref. [46] and use them in the relativistic propagators of section 2.2. For the average kinetic and total nucleon energy we have

$$\begin{aligned} \langle T \rangle &= \frac{4}{A} \int d^3r \int \frac{d^3p}{(2\pi)^3} (E(\vec{p}) - M) \int_{-\infty}^{\mu} S_h(p^0, p) dp^0 \\ \langle E \rangle &= \frac{4}{A} \int d^3r \int \frac{d^3p}{(2\pi)^3} \int_{-\infty}^{\mu} S_h(p^0, p) p^0 dp^0 \end{aligned} \quad (70)$$

and the binding energy per nucleon is then given by the sum rule [53]

$$|E_A| = -\frac{1}{2} \left(\langle E - M \rangle + \frac{A-1}{A-2} \langle T \rangle \right) \quad (71)$$

which is also used in [54, 53] in connection with the study of the EMC effect. We take experimental numbers for each nucleus for $|E_A|$ and adjust the func-

tion $C(\rho)$ to fit $|E_A|$. We take $C(\rho)$ linear in the density, $C\rho(r)$. This quantity provides around $30MeV$ repulsion at $\rho = \rho_0$ in most of the nuclei. Detailed values for $\langle T \rangle$, $\langle E \rangle$ and E_A can be seen in Table I.

As noted in refs. [13, 54, 55], the use of nucleon propagators in terms of non static spectral functions leads to bigger values of the average kinetic energy and $|\langle E - M \rangle|$ than the shell model of the nucleus and as a consequence to reduced values of $R(x)$ (for $x < 0.7$). We can see this here also by taking the uncorrelated Fermi sea and adding a function $D\rho(r)$ to the ordinary Thomas-Fermi potential $V_{TF}(r) = -k_F(r)^2/2M$ such as to get the same binding energy via eq. (71). We can make use of the same formalism by simply considering that

$$S_h^{UFS}(p^0, p) = n(\vec{p}) \delta(p^0 - E(\vec{p}) - \Sigma)$$

$$\Sigma(r) = V_{TF}(r) + D\rho(r) \tag{72}$$

Eq. (72) associates one energy to a given momentum, (the essence of the shell model in infinite nuclear matter) while the spectral function has a peak around the quasiparticle energy and then spreads out at larger values of \vec{p} for a given energy. This results in a larger value of the average kinetic energy.

In Table I we show the results for different nuclei and compare them with those of ref. [54]. As one can see, the results that we obtain with the uncorrelated Fermi sea and the spectral functions are remarkably close respectively to those of the Hartree Fock and spectral function used in [54].

We shall evaluate $R(x)$ using both the spectral function approach and the uncorrelated Fermi sea. We have integrated over the momentum up to four times the Fermi momentum for each energy. This gives the normalization of A at the level of 2 – 3% which is sufficient for our purposes, but can lead to higher uncertainties in the kinetic energy, which weighs the integral with a higher power of \vec{p} . Even a conservative error of 20% in the kinetic energy has repercussions in the *EMC* effect only at the level of 2%.

8 Results and discussion

8.1 Nucleonic contribution

In fig. 7 we show the results for $R(x)$ from the nucleonic contribution calculated as

$$R_N(x) = \frac{F_{2A,N}(x_A)}{AF_{2N}(x)} \tag{73}$$

We do not divide by $F_{2D}(x)$ as experimentally done. One reason for it is that the techniques used here with the local density approximation cannot be used for deuterium and hence we cannot calculate the nuclei and deuterium

with the same model. However the price we pay is small. We rely upon the results for $F_{2D}(x)$ calculated for deuterium in [13]. We can see there that for $0 < x < 0.7$ $F_{2D}(x)/F_{2N}(x)$ ranges between $0.98 - 1$. Hence, our results should be increased by $1 - 2\%$ and we will not worry about this amount. More serious is the region for $x > 0.7$, where due to Fermi motion the former ratio increases rapidly. Hence, in that region we should expect to overcount the experiment as it is indeed the case.

In fig. 7 we plot the results obtained for ^{56}Fe . This nucleus has $N \neq Z$ but by a little amount. Furthermore, the experimental results are corrected by the isoscalarity factor to convert them into an equivalent isoscalar nucleus [13, 56], hence our calculations done for symmetric nuclear matter are appropriate. We see a minimum around $x = 0.6$ as in the experiment and a steep rise at $x > 0.75$ as it corresponds to Fermi motion [57, 4, 6]. The region around $x = 0.6$ agrees well with experiment. However at $x \simeq 0.15 - 0.2$ we are below the data by about $10 - 15\%$. This region will be filled up latter by the mesonic contribution.

In the same figure we show the results obtained with the uncorrelated Fermi sea (local step function distribution) of eq. (72). We observe that $R_N(x)$ takes values closer to unity than the results with the spectral function for $x < 0.6$. The reduction of $R_N(x)$ with the use of the spectral function with respect to a static picture of the nucleus, like Hartree Fock or the equivalent uncorrelated Fermi sea in our case, was already shown and explained in ref. [54]. The results here are qualitatively similar to those in [54] and the explanation lies in the increased binding provided by the spectral functions. Both the factor x/x_N of eq. (57), as well as the restrictions of phase space $\theta(x_N)\theta(1 - x_N)$, are responsible for the decrease of $R_N(x)$ in this region.

On the other hand there is a novelty in these results with respect to those in [54]. $R_N(x)$ does not go to 1 at $x = 0$ as in [54] and are systematically lower in all the range of x . The reduction at $x = 0$ is easy to see from the formulae. In eq. (55) $F_{2N}(x_N = 0)$ will take a constant value, and with respect to the normalization integral of eq. (21) the novelties in eq. (55) are the extra factors $M/E(\vec{p})$ and x/x_N which both go into reducing the contribution of the integrand for off shell nucleons.

The overshooting of the results in the region of $x \simeq 0.8$ was already announced as a result of dividing F_{2A} by F_{2N} and not $F_{2D}/2$. But the qualitative features due to Fermi motion are reproduced. A very detailed discussion of these effects is given in ref. [6], but qualitatively we can see that

$$x_N \rightarrow \frac{x_N}{x} = \frac{M}{p^0 - p^3}$$

$$(x \rightarrow 1) \tag{74}$$

and one can pick up values of p^3 in the integrations such that $x_N < 1$. Hence $F_{2A,N}$ will be different from zero while $F_{2N}(x = 1) = 0$, and $R_N(x)$ from eq. (73) necessarily goes to ∞ .

It is interesting to call on the attention to the crossing of the two lines in fig. 7. The binding effects reduce $R_N(x)$. On the other hand Fermi motion increases $R_N(x)$ close to 1, as we noted. Fermi motion is more important in the interacting Fermi sea because now one has larger momentum components. On the other hand the interacting Fermi sea has also more binding. As a consequence we see that at $x < 0.6$, where the binding effects dominate over the Fermi motion, $R_N(x)$ for the interacting Fermi sea is smaller than with the non interacting Fermi sea, while for $x > 0.7$, where the Fermi motion effect dominates, the situation is just opposite.

8.2 Mesonic contributions

In figs. 8, 9, 10, 11 we show the mesonic contribution to $R(x)$, together with the nucleonic one discussed above, for different nuclei, ${}^6\text{Li}$, ${}^{12}\text{C}$, ${}^{40}\text{Ca}$ and ${}^{56}\text{Fe}$. The general features are the same in all nuclei, but, of course, the mesonic contribution is smaller in lighter nuclei. The mesonic contribution is calculated with the structure function of ref. [42]. We have also calculated it with the older structure functions of ref. [58, 59]. We find that around $x = 0.2$, the results for $R(x)$ decrease in about 3% if one uses the pion structure function of ref. [58] and increase in about 5% if one uses the one of ref. [59]. This should give us an idea of the uncertainties of this contribution. In fig. 11, for ${}^{56}\text{Fe}$, we split the mesonic contribution into the pion and ρ -meson ones. We observe, that although the pionic contribution is bigger, the one from the ρ -meson cloud is also important, and both of them are positive in all the range of x . Similarly, as obtained in other calculations [2, 3, 7] the mesonic contribution vanishes around $x = 0.6$ and increases as x decreases. We can see that thanks to the mesonic contribution the agreement with the data becomes much better. The slope of $R(x)$ from $x = 0.15$ to $x = 0.6$ is not reproduced by the contribution of the nucleons alone, a feature which is shared by the results of ref. [54]. The mesonic contribution comes to produce the right slope.

As we said, the qualitative features of the pionic contribution are similar to those in [2, 3, 7]. There are also some differences. In ref. [2] the pionic contribution is evaluated assuming different amounts of pion excess in the nucleus, but no evaluation of this excess is made. Furthermore one should recall our warnings in section 4 not to use the excess number in the evaluation. In ref. [3] an actual evaluation is done of the pionic contribution. Even if the formalisms here and there might look quite different, they are actually quite similar and one can see that $\text{Im}D(q) \equiv |D(q)|^2 \text{Im}\Pi_\pi$ of eq. (48) appears in ref. [3] as $\text{Im}\Pi_\pi |D_0(q)|^2$, with $|D(q)|^2$ changed to $|D_0(q)|^2$, which is not very problematic when the pions are off shell. Furthermore, the Δh contribution is obtained from an extrapolation of the pionic atom data, which is more problematic when one goes to the off shell situations which one finds here. Furthermore, this Δh is taken real in [3], while here the Δh Lindhard function is explicitly evaluated as a function of q^0, q by keeping the Δ width. An accurate evaluation of the imaginary parts of the diagrams is necessary

in order to fulfill the sum rule of eq. (69). On the other hand what one evaluates in ref. [3] is the fractional increase of $R(x)$ with respect to the one in the Sullivan process (deep inelastic scattering with the pion cloud of a free nucleon) [50, 51] and not the absolute value of the contribution of the pionic cloud.

In ref. [7] the absolute contribution of the pion cloud is obtained by subtracting the “free” parts contained in the response function of a free nucleon, as done here. The formalism is similar to ours but some approximations are done which are improved here. For instance the Δh contribution is again taken real and other approximations are done to relate some magnitudes to the pion excess number (recall our warnings about this).

The input which we have used for the meson nucleus interaction, $V_L(p)$, $V_T(p)$, etc, is the one of section 6. It has the virtue of having been tested in a large variety of reactions and we have not changed it here. This gives us much confidence about the strength of the mesonic contribution obtained here. The fact that it fills up the part of $R(x)$ missed by the nucleonic contribution is certainly a welcome feature which reinforces our confidence on this mesonic model.

The agreement of the results that we obtain with the experimental data can be considered rather good by comparison with results obtained with other theoretical approaches. The trend of the data is well reproduced and the remaining discrepancies are not incompatible with the intrinsic theoretical uncertainties of our model, particularly of the mesonic contribution and more specially of the ρ -meson cloud which is somewhat tied to the form factors and the nuclear correlation function, the fact that we divide by $F_{2N}(x)$ instead of $F_{2D}(x)/2$, etc.

Our results for $R(x)$ in ^{40}Ca and ^{56}Fe look already very similar and we have checked that $R(x)$ does not change much for heavier nuclei. Obviously one should take into account that for heavier nuclei $N \neq Z$ and our approach with symmetric nuclear matter should be less accurate. Actual calculations keeping different neutron and proton densities lead to a slight decrease of the minimum of $R(x)$ as Z increases [53].

9 Conclusions

We have evaluated the nucleonic and mesonic contributions to the ratio $R(x)$ of the *EMC* effect, with particular emphasis on an accurate treatment of effects shown in the past to be relevant, like binding effects, Fermi motion and a dynamical (non static) treatment of the nucleons and the mesons in the medium.

In order to avoid having to take some prescription on how to include relativistic effects in the approach, which has led to many discussions in the past, we started with a relativistic approach from the beginning and have made a covariant treatment which allows us to write all magnitudes in terms of nucleon

and meson propagators in the medium. The approach was made practical by evaluating the relevant magnitudes in an infinite medium and calculating the structure functions in finite nuclei by means of the local density approximation. This procedure is fine for $x > 0.1$ but certainly breaks down for $x < 0.1$ where there is nuclear shadowing.

We could see that the use of the spectral functions to construct the nucleon selfenergy was relevant in reducing somewhat the ratio $R(x)$ with respect to a static picture of the nucleus, like a shell model, or in our case an uncorrelated Fermi sea. This reconfirmed qualitatively earlier findings in the same direction.

Although our results for the nucleonic contribution differ somewhat from other results in the literature, we share their conclusions that the nucleonic contribution alone does not explain the data, particularly the slope from $x = 0$ to $x = 0.6$.

On the other hand, we evaluated the contribution from the pion and ρ -meson clouds rather accurately. Recent work done before on the contribution of the pion cloud to the K^+ nucleus selfenergy had taught us some important lessons, particularly the importance of using an input which satisfies a sum rule, not trivial to satisfy unless the analytical properties of the pion selfenergy are strictly fulfilled, and the need to avoid any relationship to the “pion excess number”. In addition, experience gained in dealing with reactions which involve real and virtual pions allowed us to use information on the pion nucleus selfenergy which is realistic enough and has been tested in many such reactions. Hence, we consider the present calculation of the pionic effects as an improvement over work done in the past and we think these results are rather reliable. However, there are still small uncertainties in the pionic contribution stemming from different results for the pion structure function obtained in different analyses of the Drell-Yan process.

The strength of the pionic effects is moderate. So is the one from the ρ -meson cloud, but, when they are added to the nucleonic contribution one obtains a good description of the data in the region of $0.1 < x < 0.7$.

In summary we could conclude that the main features of the *EMC* effect can be described in terms of conventional degrees of freedom, nucleons and mesons. It does not exclude explanations in terms of more elementary degrees of freedom like quarks and gluons. It is simply a question of which degrees of freedom are more economical and transparent, as stressed by Jaffe in ref. [15]. The fact that we could deal with these degrees of freedom with a certain accuracy, and establish the relationship of the effects found to familiar concepts in conventional nuclear physics, makes these degrees of freedom rather appropriate to look at the *EMC* and related effects.

Acknowledgements

We would like to acknowledge useful discussions with F. Gross, S. Liuti, C. García-Recio, A. Polls and V. Vento.

This work has been partially supported by CICYT contract number AEN 93-1205. One of us E. M. wishes to acknowledge a fellowship from the Ministerio de Educación y Ciencia.

References

- [1] E. M. Collab., J. J. Aubert et al., Phys. Lett. B 123 (1983) 275
- [2] C. H. Llewellyn Smith, Phys. Lett. 128 B (1983) 107
- [3] M. Ericson and A. W. Thomas, Phys. Lett. 128 B (1983) 112
- [4] V. Sanjosé, V. Vento and S. Noguera, Nucl. Phys. A470 (1987) 509; P. González and V. Vento, Mod. Phys. Lett. A8 (1993) 1563
- [5] L. L. Frankfurt and M. I. Strikman, Phys. Rep. 160 (1988) 236
- [6] R. P. Bickerstaff and A. W. Thomas, J. Phys. G15 (1989) 1523
- [7] A. B. Migdal, E. E. Saperstein, M. A. Troitskii and D. N. Voskresenskii, Phys. Rep. 192 (1990) 179
- [8] S. V. Akulinichev, S. A. Kulagin and G. M. Vagradov, Pis' ma Zh. Eksp. Teor. Fiz 42 (1985) 105; JETP Lett. 42 (1985) 127; Phys. Lett. 158 B (1985) 485
- [9] G. V. Dunne and A. W. Thomas, Phys. Rev. D 33 (1986) 2061
- [10] S. V. Akulinichev and S. Shlomo, Phys. Rev. C 33 (1986) 1551
- [11] L. L. Frankfurt and M. I. Strikman, Phys. Lett. B 183 (1987) 254
- [12] G. L. Li, K. F. Liu and G. E. Brown, Phys. Lett. B 213 (1988) 531
- [13] C. Ciofi degli Atti and S. Liuti, Phys. Rev. C 41 (1990) 1100
- [14] B. L. Birbrair, E. M. Levin and A. G. Shuvaev, Nucl. Phys. A 491 (1989) 618
- [15] R. L. Jaffe, Nucl. Phys. A 478 (1988) 3c
- [16] F. Gross and S. Liuti, Phys. Rev. C 45 (1992) 1374
- [17] S. Liuti and F. Gross, Phys. Lett. B 356 (1995) 157

- [18] J. Nieves, E. Oset and C. Garcia-Recio, Nucl. Phys. A 554 (1993) 509; ibid, pag. 554
- [19] H. C. Chiang, E. Oset and P. Fernández de Córdoba, Nucl. Phys. A 510 (1990) 591
- [20] S. K. Singh and E. Oset, Nucl. Phys. A 542 (1992) 587
- [21] R. C. Carrasco and E. Oset, Nucl. Phys. A 536 (1992) 445; R. C. Carrasco, E. Oset and L. L. Salcedo, Nucl. Phys. A 541 (1992) 585
- [22] S. A. Kulagin, G. Piller and W. Weise, Phys. Rev. C 50 (1994) 1154
- [23] N. N. Nikolaev and B. G. Zakharov, Phys. Lett. B 327 (1994) 157
- [24] A. L. Fetter and J. D. Walecka, Quantum Field Theory of Many Particle Systems, (McGraw Hill, NY, 1971)
- [25] P. Fernández de Córdoba and E. Oset, Nucl. Phys. A 528 (1991) 736
- [26] C. Itzykson and J. B. Zuber, Quantum Field Theory (McGraw Hill, NY, 1980)
- [27] H. de Vries, C. W. de Jager and C. de Vries, At. Dat. Nucl. Dat. Tables 36 (1987) 495
- [28] G. C. Li, I. Sick, R. R. Whitney and M. R. Yearian, Nucl. Phys. A 162 (1971) 583
- [29] F. Mandl and G. Shaw, Quantum Field Theory, John Wiley, 1984
- [30] E. Amaldi, S. Fubini and G. Furlan, Pion Electroproduction, Springer tracts in modern physics, Vol 83 (Springer, Berlin, 1979)
- [31] C. Garcia-Recio, J. Nieves and E. Oset, Phys. Rev. C 51 (1995) 237
- [32] M. F. Jiang and D. S. Koltun, Phys. Rev. C 46 (1992) 2462
- [33] I. J. R. Aitchison and A. J. G. Hey, Gauge theories in particle physics, Edit Adam Hilger
- [34] G. Baym and G. E. Brown, Nucl. Phys. A 247 (1975) 395
- [35] W. Y. P. Hwang, J. Speth and G. E. Brown, Z. Phys. A 339 (1991) 383
- [36] A. Szczurek and J. Speth, Nucl. Phys. A 555 (1993) 249
- [37] L. Heller and A. W. Thomas, Phys. Rev. C 41 (1990) 2756
- [38] U. Oelfke, P. U. Sauer and F. Coester, Nucl. Phys A 518 (1990) 593

- [39] W. Melnitchouk, A. W. Schreiber and A. W. Thomas, Phys. Rev. D 49 (1994) 1183
- [40] P. Berge et al. Z. Phys. C49 (1991) 187
- [41] EMC, J. J. Aubert et al., Phys. Lett B 114 (1982) 291
- [42] M. Glück, E. Reya and A. Vogt, Z. Phys. C 53 (1992) 651
- [43] R. Machleidt, K. Holinde and Ch. Elster, Phys. Reports 149 (1987) 1
- [44] E. Oset and W. Weise, Nucl. Phys. A 319 (1979) 477
- [45] E. Oset, P. Fernández de Córdoba, L. L. Salcedo and R. Brockmann, Phys. Reports 188 (1990) 79
- [46] P. Fernández de Córdoba and E. Oset, Phys. Rev. C 46 (1992) 1697
- [47] S. Fantoni, B. L. Friman and V. R. Pandharipande, Nucl. Phys. A 399 (1983) 51
- [48] S. Fantoni and V. R. Pandharipande, Nucl. Phys. A 427 (1984) 473
- [49] C. Mahaux, P. F. Bortignon, R. A. Broglia and C. H. Dasso, Phys. Rep. 120 (1985) 1
- [50] A. Ramos, A. Polls and W. H. Dickhoff, Nucl. Phys. A 503 (1989) 1
- [51] H. Müther, G. Knehr and A. Polls, Phys. Rev. C 52 (1995) 2955
- [52] H. Müther, A. Polls and W. H. Dickhoff, Phys. Rev. C 51 (1995) 3040
- [53] D. S. Koltun, Phys. Rev. C 9 (1974) 484
- [54] C. Ciofi degli Atti and S. Liuti, Phys. Lett. B 225 (1989) 215
- [55] C. Ciofi degli Atti and S. Liuti, Phys. Rev. C 44 (1991) R 1269
- [56] R. G. Arnold et al., Phys. Rev. Lett. 52 (1984) 727
- [57] A. Bodek and J. L. Ritchie, Phys. Rev. D 23 (1981) 1070
- [58] J. Badier et al., Z. Phys. C 18 (1983) 281
- [59] P. Castorina and A. Donnachie, Z. Phys. C 45 (1990) 497
- [60] J. D. Sullivan, Phys. Rev. D 5 (1972) 1732
- [61] Ch. H. Chung and W. Y. P. Hwang, Phys. Rev. D 49 (1994) 2221
- [62] J. Gómez et al., Phys. Rev. D 49 (1994) 4348
- [63] A. C. Benvenuti et al., Phys. Lett. B 189 (1987) 483

[64] NMC Collaboration, M. Arneodo et al., Nucl. Phys. B 441 (1995) 12

[65] NMC Collaboration, P. Amaudruz et al., Nucl. Phys. B 441 (1995) 3

Figures captions.

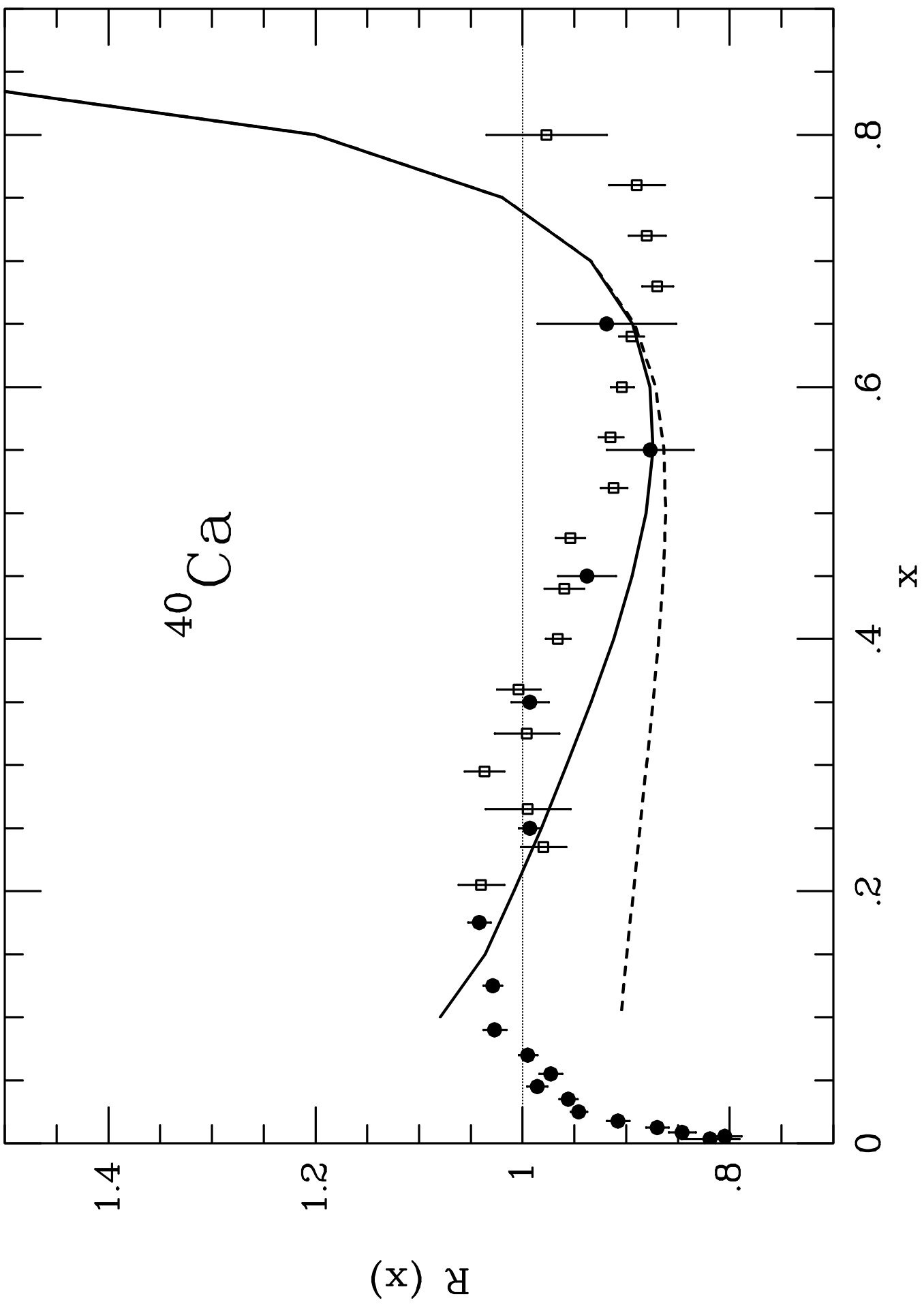
- Figure 1: Selfenergy diagrams of the nucleon.
- Figure 2: Electromagnetic form factors for the cases a) free nucleon, b) Fermi sea with B baryons.
- Figure 3: (a) Feynman diagram for deep inelastic electron-nucleon scattering and (b), electron selfenergy diagram associated.
- Figure 4: Electron selfenergy diagram accounting for electron-pion deep inelastic scattering.
- Figure 5: Diagrams of the electron selfenergy including $1ph$, $1\Delta h$, $1ph1\Delta h$, etc..
- Figure 6: Two diagrams (a) direct and (b) crossed, which contribute to Compton $\gamma\pi$ scattering.
- Figure 7: Results of $R_N(x)$ for ^{56}Fe . Solid line: using the spectral function; dashed line: using the uncorrelated Fermi sea. Experimental points from ref. [62] (solid dots), ref. [63] (open squares).
- Figure 8: Results of $R(x)$ for 6Li . Solid lines: whole calculation including the nucleons and the mesons; dashed line: contribution of the nucleons. Experimental points from ref. [64] (solid dots). Density for 6Li from ref. [28].
- Figure 9: Same as fig. 8 for ^{12}C . Experimental points from ref. [64] (solid dots), ref. [62] (open squares).
- Figure 10: Same as fig. 8 for ^{40}Ca . Experimental points from ref. [65] (solid dots), ref. [62] (open squares).
- Figure 11: Results for $R(x)$ for ^{56}Fe . Solid line: whole calculation including the nucleons and the mesons; dashed line: contribution of the nucleons; dot-dashed line: contribution of nucleons plus pions. Experimental points from ref. [62] (solid dots), ref. [63] (open squares).

Table I

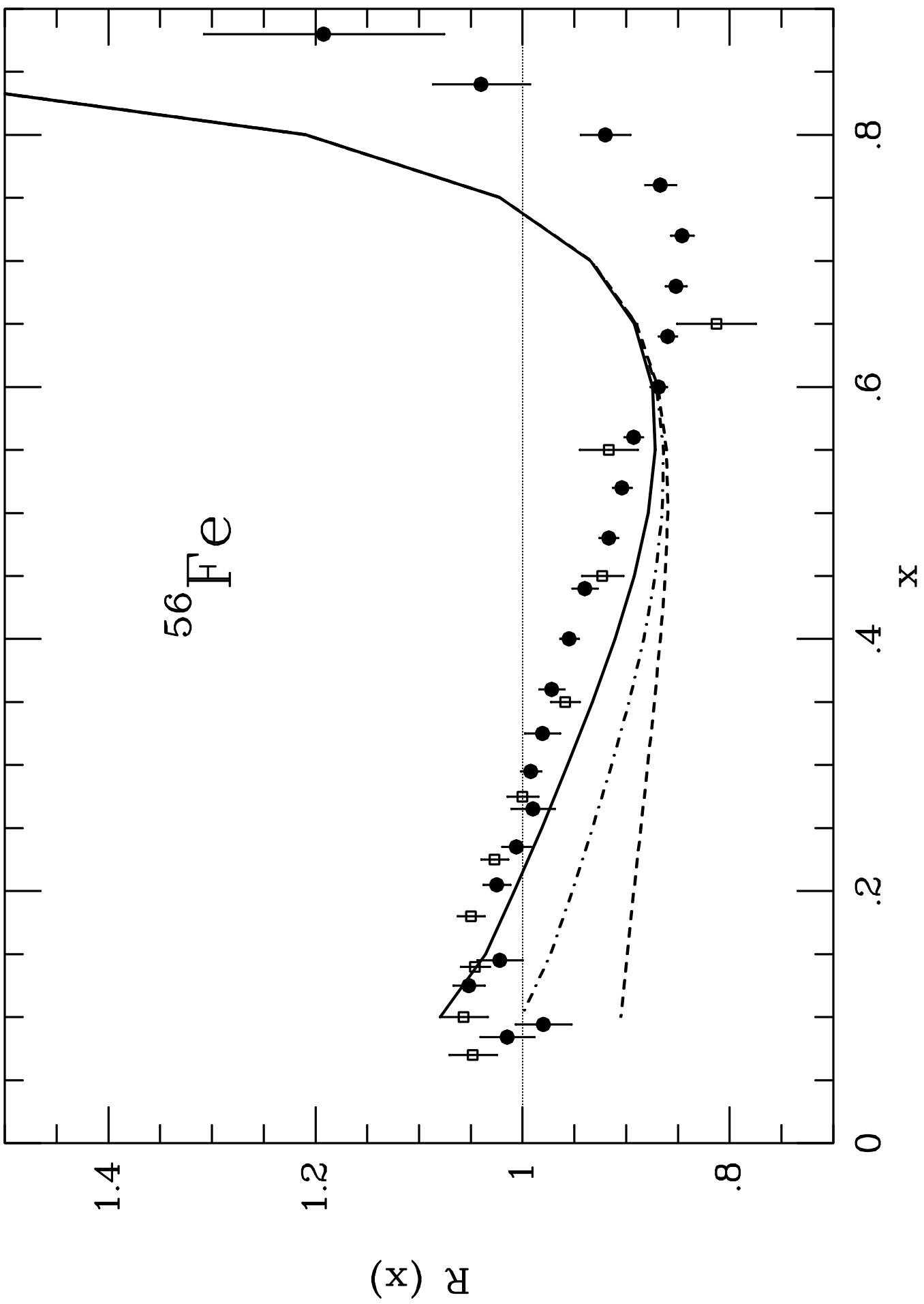
		$\langle T \rangle$ [MeV]	$\langle E - M \rangle$ [MeV]	$ \varepsilon_A $ [MeV]
6Li	UFS	9.3	22.1	5.2
	SF	18.8	33.8	5.2
${}^{12}C$	UFS	13.7 (17.0)	31.0 (23.0)	8.0
	SF	31.7 (37.0)	50.4 (49.0)	7.8
${}^{40}Ca$	UFS	16.0 (16.5)	33.5 (26.6)	8.5
	SF	40.4 (36.0)	58.6 (52.1)	8.6
${}^{56}Fe$	UFS	16.1 (17.0)	34.1 (25.0)	8.9
	SF	40.4 (33.0)	58.6 (49.8)	8.7

UFS: uncorrelated Fermi sea. SF: spectral function. The numbers in brackets correspond to those obtained in ref. [54] respectively for the Hartree-Fock and spectral functions (the latter called there SRC, from short range correlations).

^{40}Ca



^{56}Fe



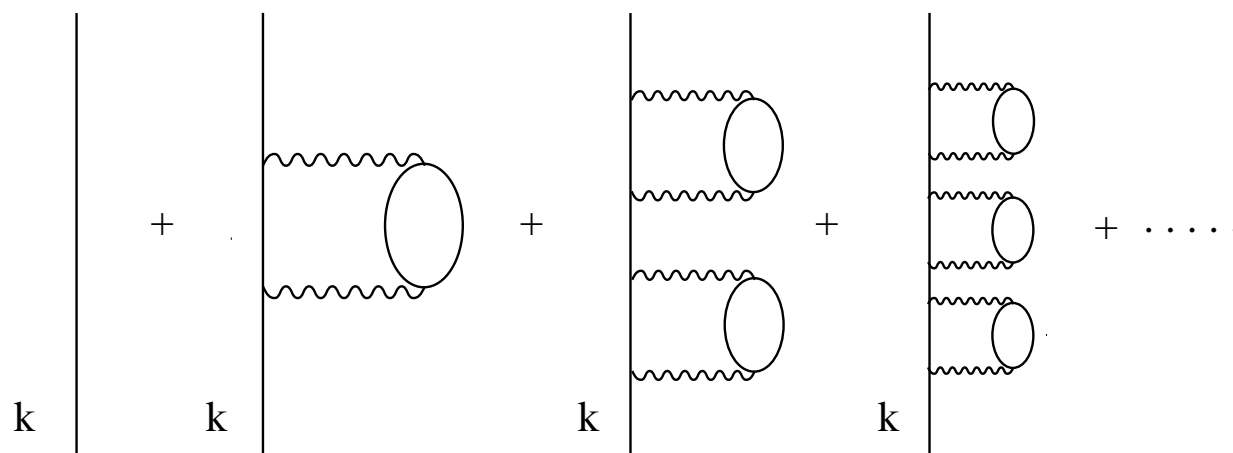
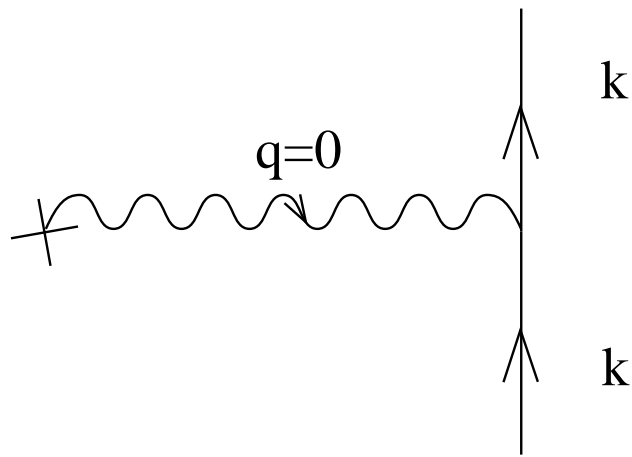
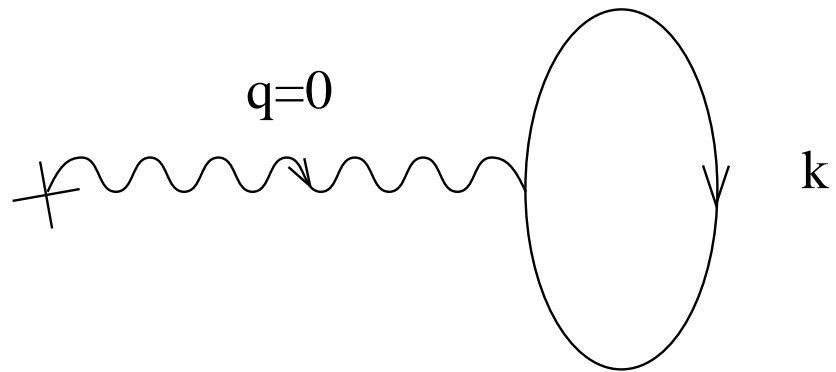


fig. 1



a)



b)

Fig. 2

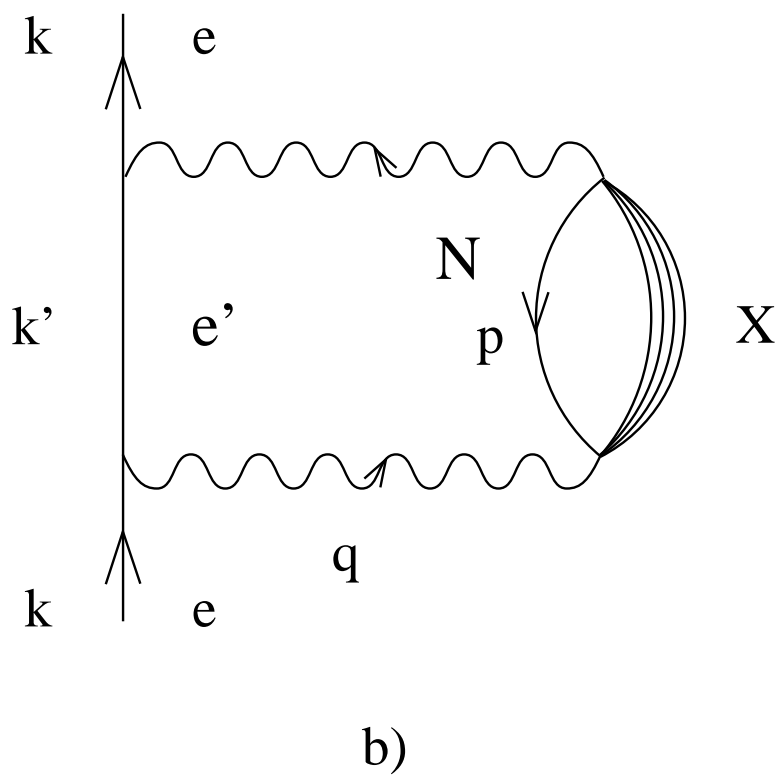
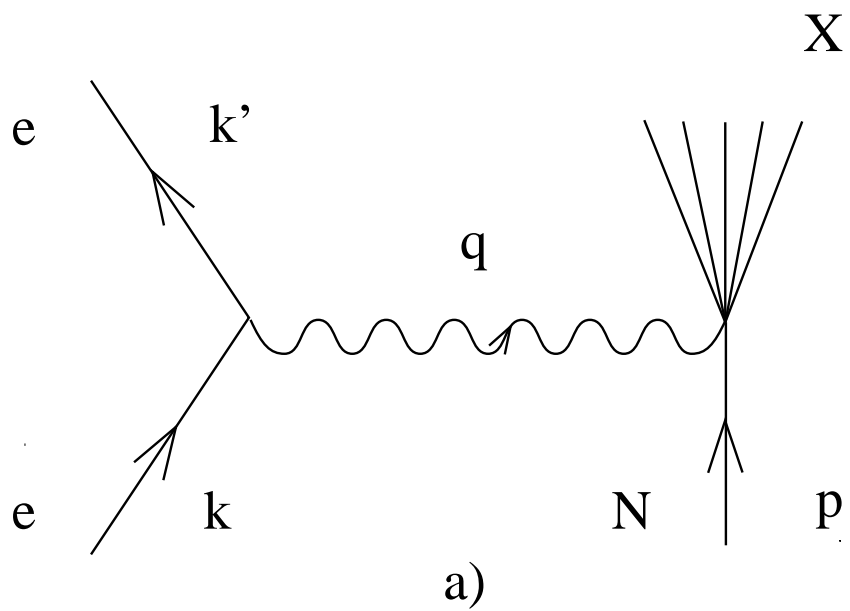


Fig. 3

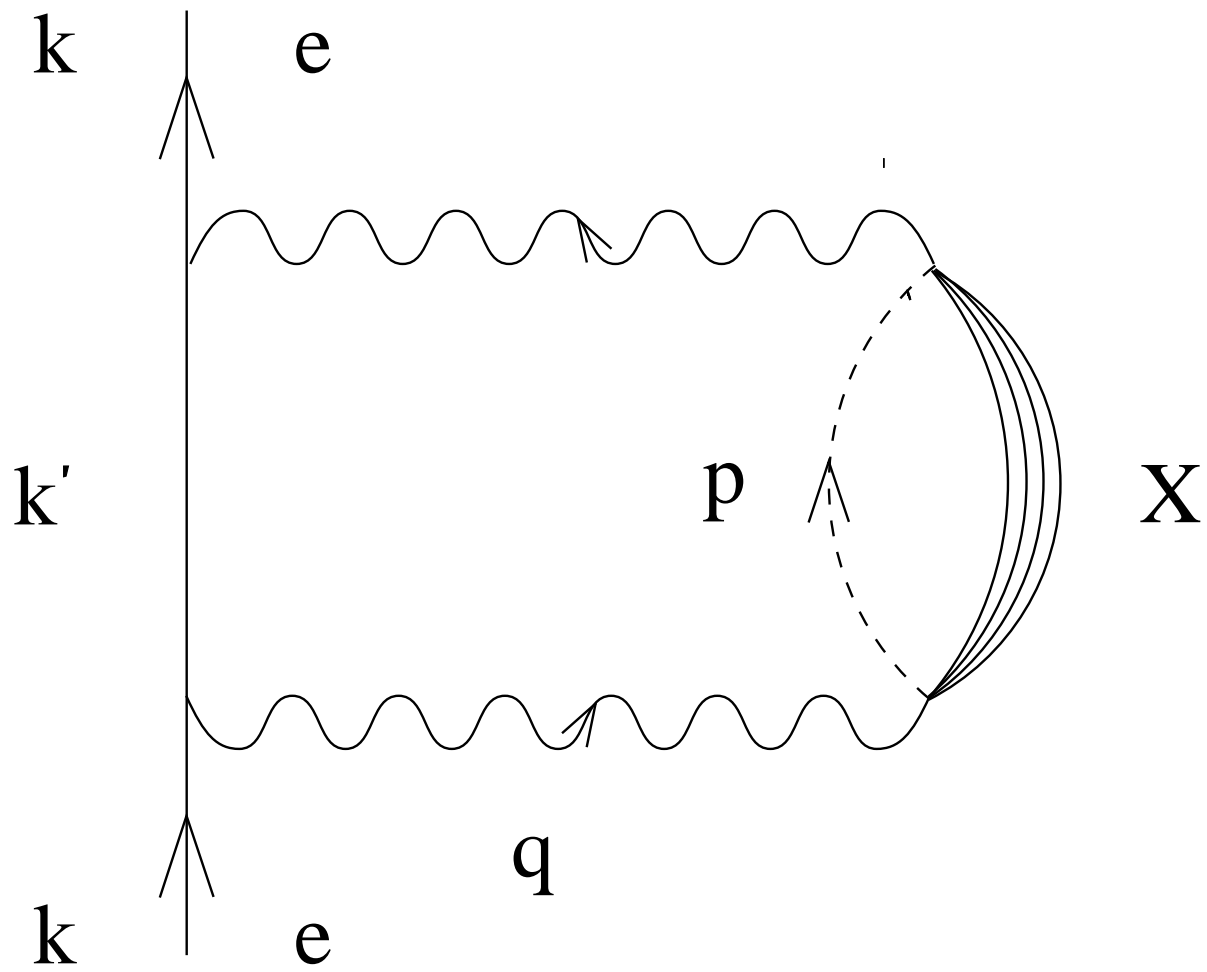


Fig. 4

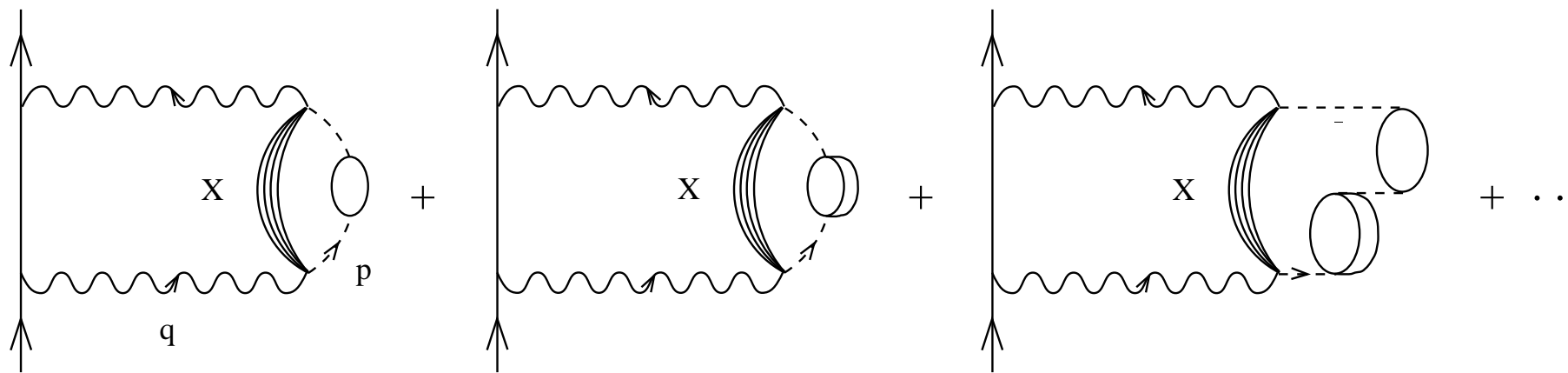


Fig. 5

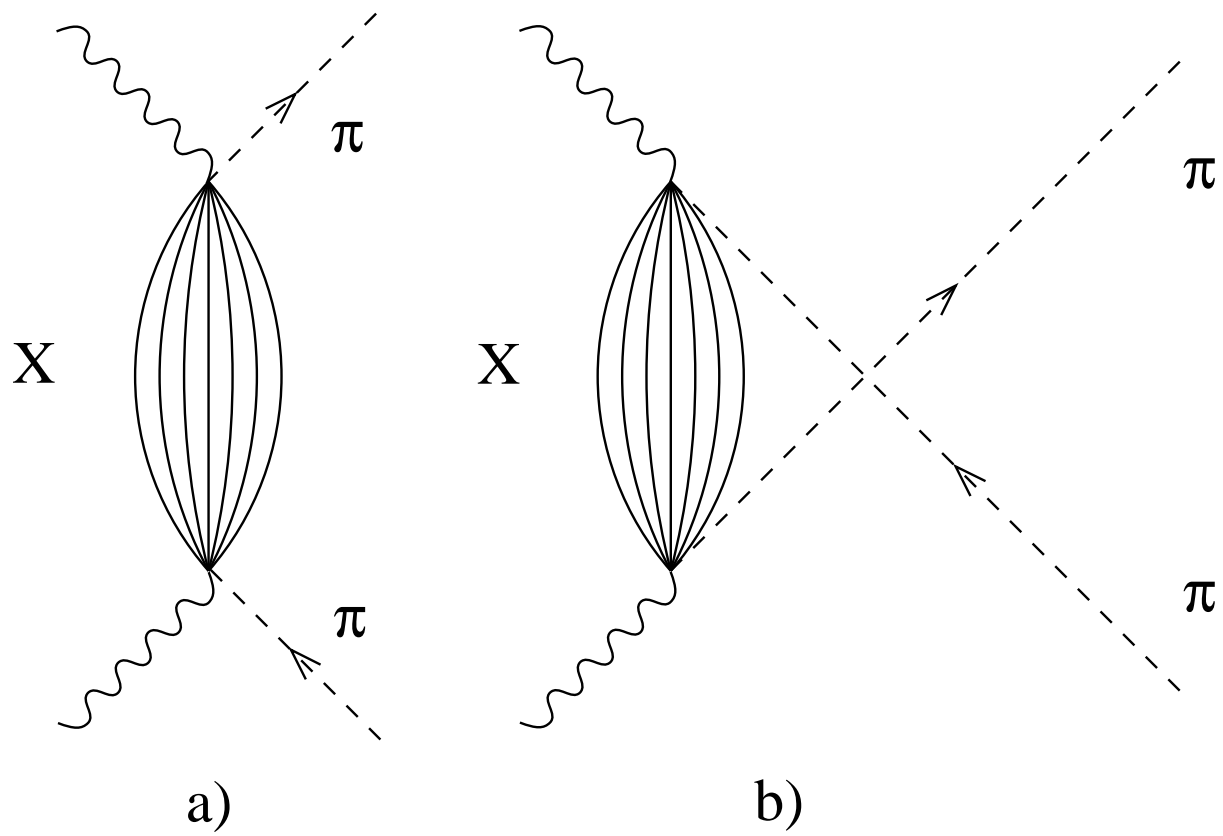
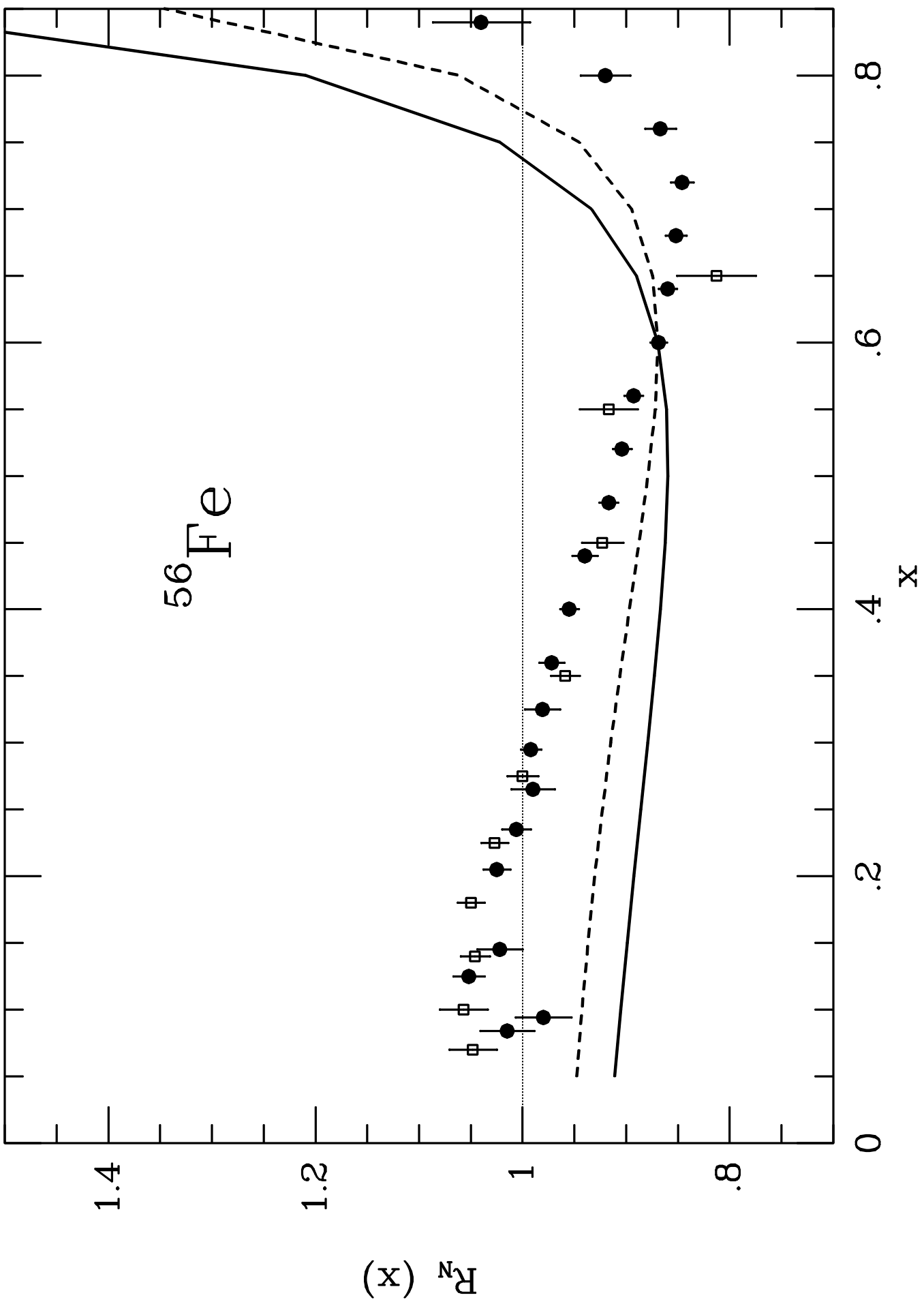
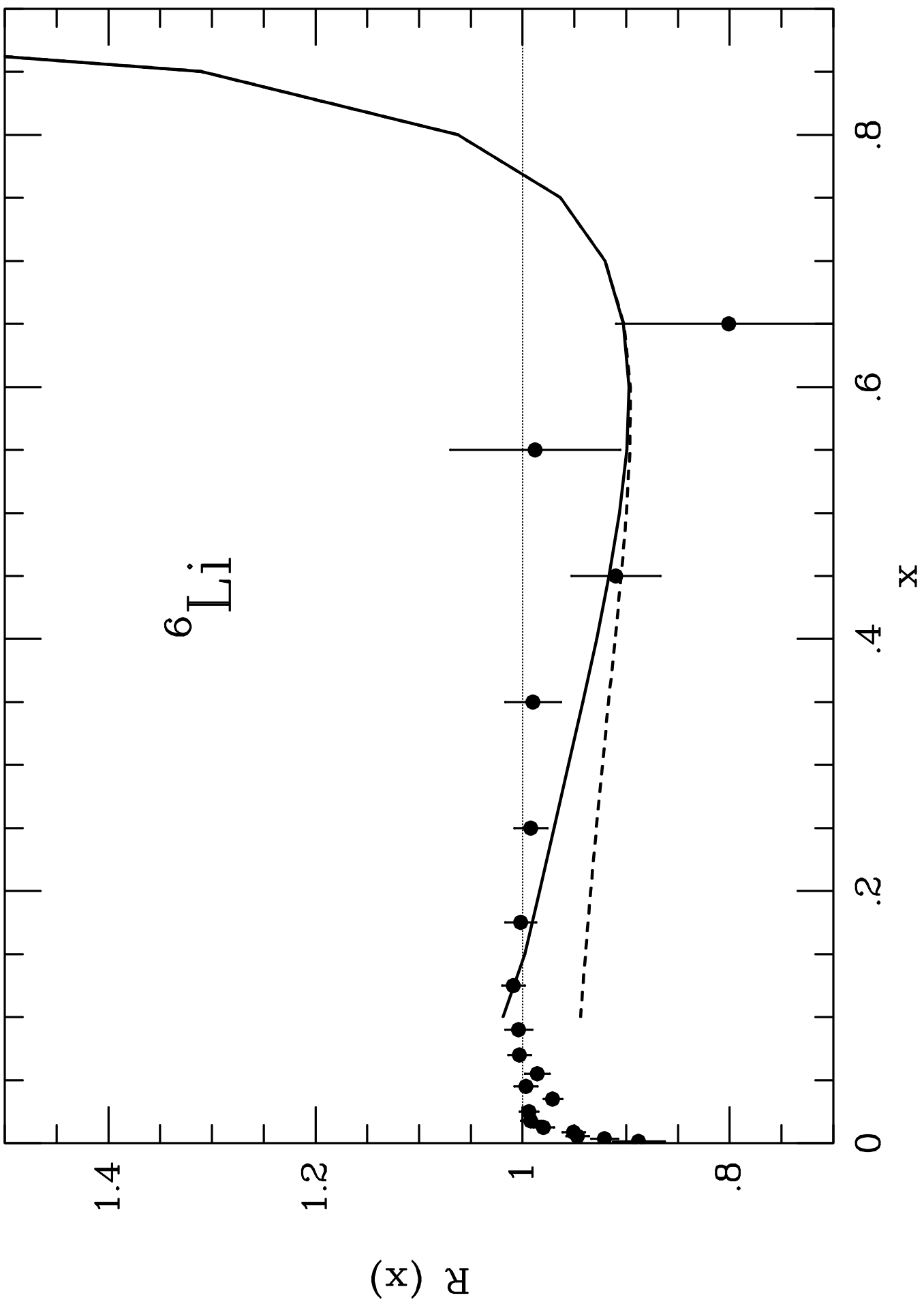
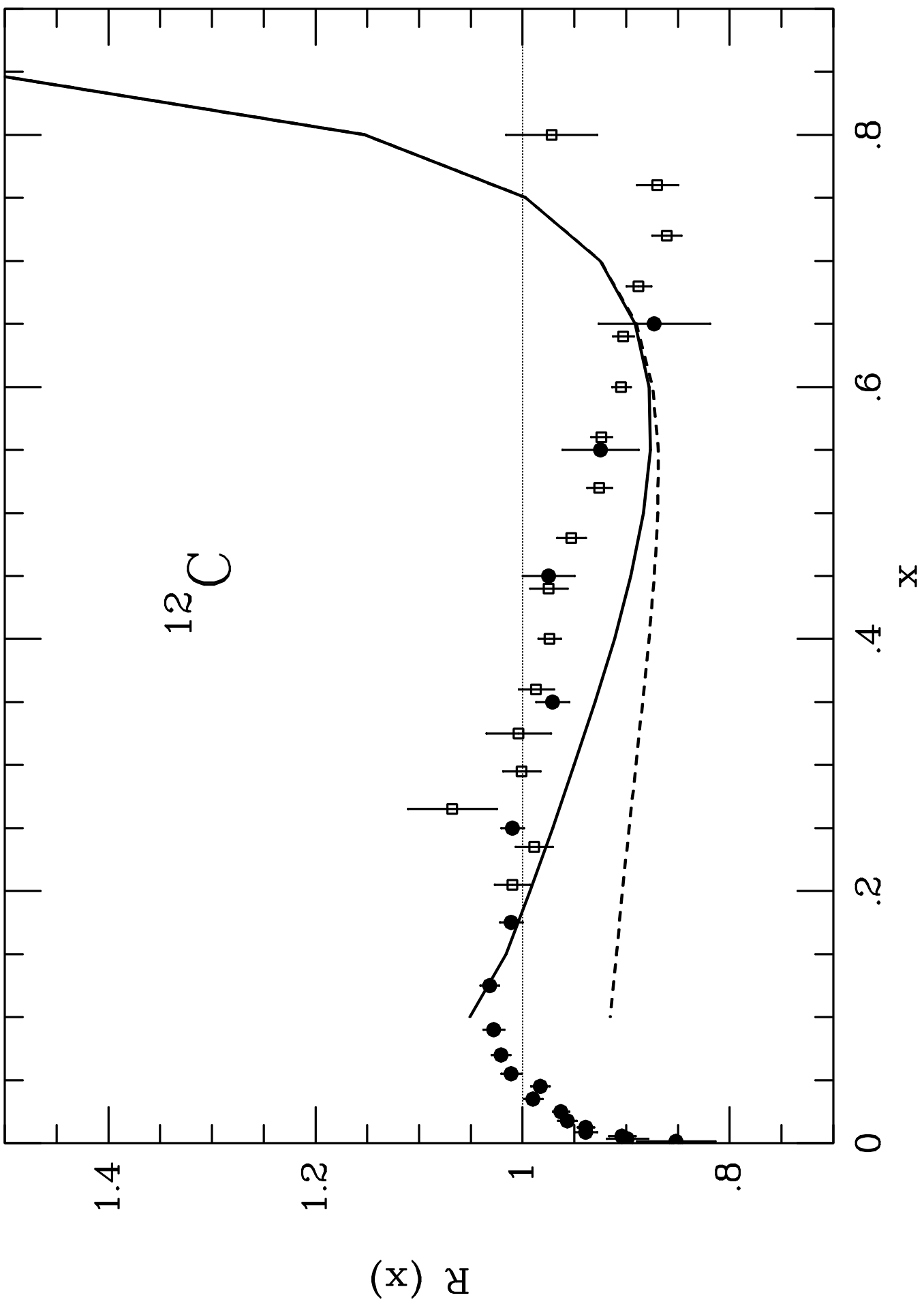


Fig. 6

^{56}Fe







DECAY MODES OF SIGMA AND LAMBDA HYPERNUCLEI

E. OSET, P. FERNÁNDEZ de CÓRDOBA

*Departamento de Física Teórica, and IFIC, Centro Mixto Universidad de Valencia – CSIC,
Facultad de Física, Burjassot (Valencia), Spain*

L.L. SALCEDO

*Center for Theoretical Physics, Laboratory for Nuclear Science, and Department of Physics,
Massachusetts Institute of Technology, Cambridge, MA 02139, USA*

and

R. BROCKMANN

Institut für Kernphysik der Universität Mainz, 6500 Mainz 1, Fed. Rep. Germany



NORTH-HOLLAND

DECAY MODES OF SIGMA AND LAMBDA HYPERNUCLEI*

E. OSET, P. FERNÁNDEZ de CÓRDOBA

*Departamento de Física Teórica, and IFIC, Centro Mixto Universidad de Valencia – CSIC, Facultad de Física,
Burjassot (Valencia), Spain*

L.L. SALCEDO**

*Center for Theoretical Physics, Laboratory for Nuclear Science, and Department of Physics, Massachusetts Institute of Technology,
Cambridge, MA 02139, USA*

and

R. BROCKMANN

Institut für Kernphysik der Universität Mainz, 6500 Mainz 1, Fed. Rep. Germany

Received August 1989

Contents:

1. Σ hypernuclei: introduction	81	5. Expression of the Σ self energy in terms of the Lindhard function	107
2. Formal derivation of the Σ width	84	6. Study of bound states of Σ hypernuclei	111
2.1. The $\Sigma N \rightarrow \Lambda N$ cross section and the Σ width	84	7. Λ decay in nuclei: introduction	119
2.2. The $\Lambda p \rightarrow \Sigma^0 p$ reaction	89	8. Formal derivation of the Λ width in nuclei	121
2.3. Pauli blocking effects in the Σ self-energy	89	8.1. The Λ free decay	121
3. Approaches proposed for narrow Σ states	92	8.2. Pauli blocking effects	122
3.1. The unstable bound states	92	8.3. Non-mesonic Λ decay	123
3.2. Pauli blocking	93	8.4. Proton and neutron induced Λ non-mesonic decay	125
3.3. Other approaches	94	8.5. Unified treatment of the mesonic and non-mesonic Λ decay	126
3.4. Summary	95	9. Shell model treatment of the Λ mesonic decay	133
4. The induced interaction approach	96	10. Non-mesonic decay: beyond one pion exchange	137
4.1. The nucleon self-energy in nuclear matter	96	11. Conclusions	140
4.2. Model for the $\Sigma N \rightarrow \Lambda N$ transition	99	Appendix. The Lindhard function	141
4.3. The $\Sigma N \rightarrow \Lambda N$ induced interaction	103	References	142
4.4. Approximate evaluation of the Σ width with the induced interaction	104		

* This work is supported in part by funds provided by the US Department of Energy (DOE) under contract #DE-AC02-76ER03069 and the Spanish CICYT.

** On leave from IFIC, Centro Mixto Universidad de Valencia – CSIC, Facultad de Física, Burjassot (Valencia), Spain. Present address: Departamento de Física Moderna, Facultad de Ciencias, E-18071 Granada, Spain.

Single orders for this issue

PHYSICS REPORTS (Review Section of Physics Letters) 188, No. 2 (1990) 79–145.

Copies of this issue may be obtained at the price given below. All orders should be sent directly to the Publisher. Orders must be accompanied by check.

Single issue price Dfl. 51.00, postage included.

Abstract:

A review is presented of the problem of Σ and Λ decay in nuclei. By means of handy, yet reliable approximations, an approach to Σ decay is developed which allows a clear insight into the different aspects of the problem. The role of nuclear polarization, due to the spin-isospin $\Sigma N \rightarrow \Lambda N$ interaction, in the reduction of the Σ widths is discussed. Many experimentally observable Σ hypernuclei are predicted by showing that their widths are narrower than the separation energies between levels. The mesonic and non-mesonic decays of Λ hypernuclei are analyzed. The non-mesonic width is fairly well reproduced by simplified models for the $\Lambda N \rightarrow NN$ weak transition, but quantities like the ratio of proton to neutron induced Λ decay are highly sensitive to the models used. On the other hand, the mesonic width is very sensitive to the pion-nucleus optical potential and can be used to discriminate between different potentials which are equally suited to describe low energy pion-nucleon scattering.

In memoriam

With great sorrow we learned about the sudden death of a respected colleague, Professor Hiroharu Bandō. His contribution to the hypernuclear field is outstanding and his passing away a great loss for all of us who had the pleasure to appreciate both the quality of his work and his personal charm. May his example stimulate us to continue his work with the same devotion and enthusiasm that he always showed.

1. Σ hypernuclei: introduction

The technique used to produce Λ hypernuclei in the (K^-, π^-) reaction [Br 75, 76] was used at CERN to produce Σ hypernuclei for the first time [Be 80]. The (K^-, π^-) reaction on ${}^9\text{Be}$ at $p_K = 720 \text{ MeV}/c$ with $\theta_\pi = 0^\circ$ was used, and two distinct peaks of width smaller than 8 MeV were found. The finding was unexpected because, unlike Λ particles that can only decay weakly inside the nucleus, the Σ particles can decay via strong interactions, through the channel $\Sigma N \rightarrow \Lambda N$, and the width was expected to be around $\Gamma \approx 25 \text{ MeV}$ [Ba 78].

Subsequently, (K^-, π^+) spectra were taken at BNL on ${}^6\text{Li}$ and ${}^{16}\text{O}$ with a kaon beam of 713 MeV/ c momentum [Pi 82] and several forward pion angles. The pion spectrum on ${}^6\text{Li}$ at $\theta = 3.7^\circ$ revealed two clear peaks, although three Gaussian peaks were assumed in the analysis, two of them with widths around 4.5 MeV. The structures are not evident at larger angles. On the other hand, the experiment on ${}^{16}\text{O}$ showed only a broad bump from which no narrow structure can be clearly extracted.

The CERN group developed a new kaon beam line in order to produce Σ particles in the nucleus with momentum close to zero (recoiless condition), for which a kaon momentum $p_K \approx 450 \text{ MeV}/c$ was chosen. Both the (K^-, π^-) and the (K^-, π^+) reactions on ${}^{12}\text{C}$ and ${}^{16}\text{O}$ were studied [Be 84, 85]. The results of the (K^-, π^+) spectrum can be seen in fig. 1.1. In the (K^-, π^+) ${}^{12}\text{C}$ spectrum a single peak in the continuum, with binding energy $B_\Sigma \approx -3 \text{ MeV}$, was identified as a Σ^- hypernuclear state, while in the (K^-, π^+) spectrum on ${}^{16}\text{O}$ two peaks, both in the continuum, were suggested around 280 MeV of excitation energy ($M_{HY} - M_A$) as corresponding to Σ^- hypernuclear states with widths around 5 MeV.

At KEK an experiment with stopped kaons was done with the (K^-, π^+) reaction on ${}^{12}\text{C}$ [Ya 85, 86]. Simultaneously a method to tag Σ^- hypernuclei was developed. The idea consists in detecting, together with the π^+ , the π^0 or π^- from the Λ decay after the $\Sigma N \rightarrow \Lambda N$ conversion. In this way, the continuum due to quasifree Σ^- production, where the Σ is not trapped but escapes, can be suppressed. Some peaks were detected and tentatively assigned to Σ^- hypernuclear states. However, the untagged experiment (inclusive pion spectrum) with more statistics [Ha 88a] did not show any clear narrow peak. Also, no significant enhancement of the cross section was observed around 279 MeV of excitation energy, where the peak in the kaon in-flight experiment was found [Be 84]. The experimental situation is hence a bit confusing due mostly to the lack of good statistics in the experiments.

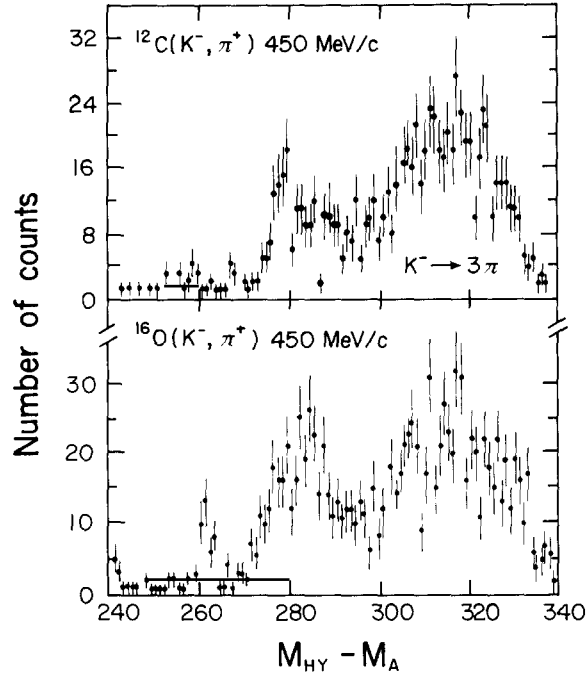


Fig. 1.1. (K^-, π^+) data at 0° on ^{12}C and ^{16}O from [Be 84, 85]. Masses are in MeV.

Before we proceed to study in detail the decay mechanism of a Σ in the nucleus and the different theoretical approaches, it is worthwhile to mention here some calculations which aim at reproducing the spectrum of the (K^-, π^+) reaction itself. Several of these calculations are available [MY 86, 88, Ha 87, Ko 87a, Ha 88c, a]. The first and the last use a Green function method, while the middle references use a DWIA with ΣN , ΛN as coupled channels. The results are similar in both approaches and peaks for bound states as well as resonances in the continuum can be found depending on the depth of the real Σ potential and the strength of the $\Sigma N \rightarrow \Lambda N$ conversion potential. We plot in fig. 1.2 the results of [Ko 87a] and compare them with the experimental results of [Be 84] and [Ha 88a] for the $^{12}\text{C}(K^-, \pi^+)$ reaction. As can be seen, the experimental results can be best fitted with a shallow potential ($|V| < 10$ MeV) and a $\Sigma N \rightarrow \Lambda N$ conversion potential of a similar strength. Other authors find deeper potentials, like $|V| \approx 20$ MeV in [Bo 82, Be 85], or $|V| \approx 30$ MeV from the analysis of Σ^- atoms in [Ba 78].

A very shallow potential would not produce bound states (ignoring the Coulomb force which would automatically bind the whole set of Σ^- atoms). On the other hand, as one can see in fig. 1.2d, the same shallow potential does not lead to any sharp resonance for kaons in flight at $p_K = 450$ MeV/c, in contradiction with the narrow resonance claimed in [Be 84]. We can also see that even with the set of parameters of fig. 1.2a leading to sharp structures in the kaon at rest experiment, the sharp peak claimed in [Be 84] is not reproduced and the theoretical results give rise to a smooth curve which passes through the experimental points in the Σ continuum. The sharp structure is not supported either by the kaons at rest experiment nor the theoretical results.

The situation is thus puzzling, with one of the few evident conclusions being the fact that more statistics and more experiments are needed to clarify the situation.

One should note that one can equally reproduce the experimental results of [Ha 88a] with other sets of parameters where narrow states appear, both for bound states or Σ 's in the continuum, however,

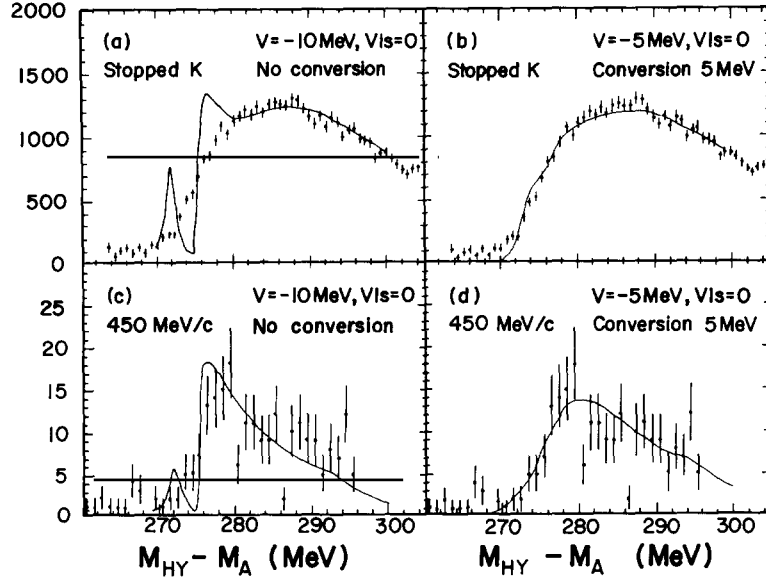


Fig. 1.2. In-flight ($p_k = 450$ MeV/c) and stopped pion spectra from [Be 84] and [Ha 88a] compared to the theoretical calculations of [Ko 87a] for the $^{12}\text{C}(K^-, \pi^+)$ reaction.

with little strength in the excitation function [Ha 88a, MY 88]. As noted in [Ha 88a] and [Ta 88] the data only allow one to determine combinations of the strength of the Σ and the conversion potentials, but not any of them separately. On the other hand the question of whether there are Σ bound states at all has a simple answer in one of the cases, the one of Σ^- states. Indeed, the Coulomb potential alone, irrespective of the strength of the short-range nuclear potential, is enough to bind Σ^- atomic states. Some of these states (the most bound) are such that the Σ wavefunction is essentially inside the nucleus, hence the name hypernuclei is more suited to them, although there is a gradual transition from these hypernuclear states to those more properly called Σ^- atoms [Ba 78], where the orbits are far away from the nucleus. These ideas have been recently exposed in [Ya 88] and [Ba 88a] and the states are called “Coulomb-assisted hybrid bound Σ^- states”. However, while in [Ya 88] the suggestion is made to look for such states in kaon experiments at rest, in [Ba 88a] the (π^-, K^+) reaction is proposed as an ideal process to produce Σ hypernuclear states.

The question of the observability of such states depends upon their width and the energy separation between the levels. If the width is larger than the level separation no sharp structures will be seen. On the other hand one has to take into account the strength by which each of these states is populated in a given reaction, since some states are more easily populated than others in certain reactions.

Although many Σ^- atomic states are known [Ba 78] there is a limitation to the observability of such states given by the detection method. The Σ^- (as in the case of π^- atoms) cascades down through atomic orbits and approaches the nucleus. The absorptive width increases in this process and when it exceeds the radiative width the Σ particle gets absorbed by the nucleus and no further level of smaller energy can be reached. However, such states exist and their observation would be most interesting to get a proper understanding of the dynamics of the Σ -nucleus interaction. No such states have been observed yet.

On the other hand, there is the possibility that there are bound states of Σ^0 or Σ^+ hypernuclei (all observed structures quoted above correspond to Σ energies in the continuum). An important boost to the problem from the experimental side has been given by the recent discovery at KEK of a bound state

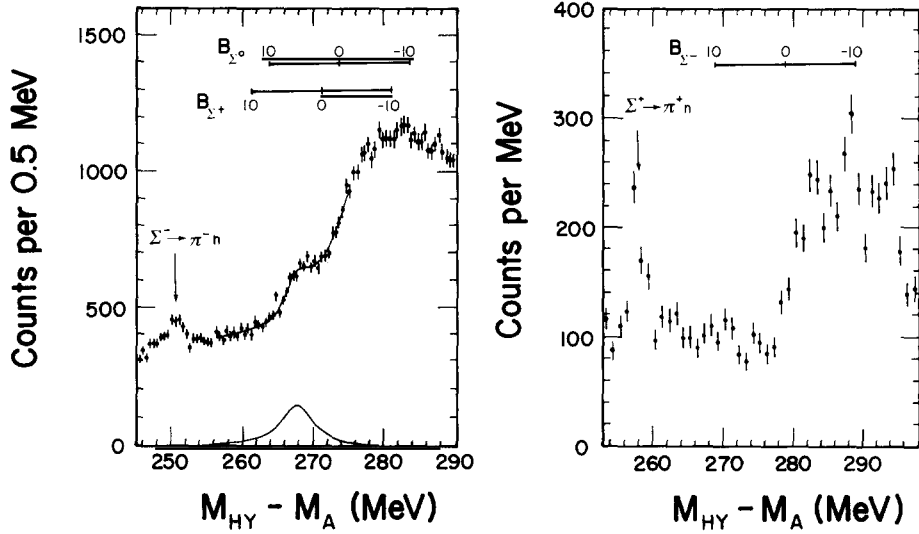


Fig. 1.3. ${}^4\text{He}$ (stopped K^- , π^-) data (left) and ${}^4\text{He}$ (stopped K^- , π^+) data (right) from [Ha 88b].

of the ${}^4_\Sigma\text{He}$ hypernucleus [HA 88b], suggested by the calculations of [Ak 86]. The (K^-, π^-) reaction on ${}^4\text{He}$ with stopped kaons gives rise to a significant bump in the pion spectrum, which is identified as a bound $\Sigma^{0,+}$ state with $B_\Sigma = 3.2$ MeV energy and a width of 4.6 MeV (see fig. 1.3). However no similar peak was found in the (K^-, π^+) reaction although the statistics is poorer.

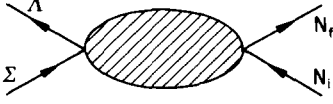
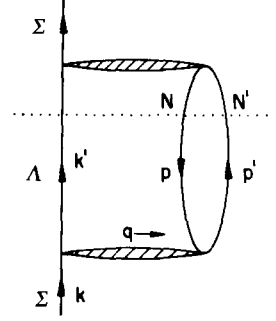
In spite of the limited experimental information available, the discovery of the sharp resonances stimulated much theoretical work, which is discussed in the following sections, aiming at understanding the origin of such narrow widths, since simple estimates provide widths between 20–30 MeV for the Σ hypernuclear states. An approach to the many-body problem based on the use of the induced interaction, which provides small widths for the bound hypernuclear states, is discussed in detail. The Σ^- atomic information is re-analyzed from this point of view and its information is used to obtain energies and widths of more bound Σ^- states of the hypernuclear type. One obtains many bound states in light and medium nuclei, where the widths are narrower than the separation between the levels. These results should stimulate further experimental work in the search for Σ hypernuclei.

2. Formal derivation of the Σ width

2.1. The $\Sigma N \rightarrow \Lambda N$ cross section and the Σ width

We are going to derive the Σ width in infinite nuclear matter from the $\Sigma N \rightarrow \Lambda N$ transition amplitude. We will see that the results are quite model independent and one can treat quite accurately the effect of the Pauli blocking. Let T be the transition amplitude in the $\Sigma N \rightarrow \Lambda N$ process depicted in fig. 2.1. We follow Bjorken–Drell conventions [BD 65] and thus the S matrix is given by

$$\langle f|S-1|i\rangle = -iT \frac{1}{(2\pi)^6} \sqrt{\frac{M}{E_{N_i}}} \sqrt{\frac{M}{E_{N_f}}} \sqrt{\frac{M_\Sigma}{E_\Sigma}} \sqrt{\frac{M_\Lambda}{E_\Lambda}} (2\pi)^4 \delta(p_\Sigma + p_{N_i} - p_\Lambda - p_{N_f}). \quad (2.1)$$


 Fig. 2.1. Feynman diagram for the $\Sigma N \rightarrow \Lambda N$ transition.

 Fig. 2.2. Many-body Feynman diagram for the Σ self-energy incorporating the $\Sigma N \rightarrow \Lambda N$ transition. The dotted line indicates the cut leading to $\text{Im } \Sigma^*$ when the particles cut by this line are placed on-shell in the integrations over the internal variables.

We can construct the Σ self-energy piece containing the $\Sigma N \rightarrow \Lambda N$ transition. This is depicted in fig. 2.2 as a standard many-body diagram. We shall call Σ^* the Σ self-energy, equivalent to the optical potential, and the width is then given by

$$\Gamma = -2 \text{Im } \Sigma^* . \quad (2.2)$$

This holds strictly if $\text{Re } \Sigma^*$ does not depend on the energy as an independent variable of the momentum, or equivalently, the residual interaction is small. We shall assume this here.

By following the standard Feynman rules [FW 71, Ma 76] we can readily evaluate Σ^* for the diagram of fig. 2.2. We obtain

$$\begin{aligned} -i\Sigma^*(k) = & (-) \int \frac{d^4 p}{(2\pi)^4} \int \frac{d^4 q}{(2\pi)^4} \frac{i n(\mathbf{p})}{p^0 - E_N(\mathbf{p}) - i\epsilon} \frac{i[1 - n(\mathbf{q} + \mathbf{p})]}{q^0 + p^0 - E_N(\mathbf{q} + \mathbf{p}) + i\epsilon} \\ & \times \frac{i}{k^0 - q^0 - E_\Lambda(\mathbf{k} - \mathbf{q}) + i\epsilon} \sum_{s_N, s_{N'}, t_N, t_{N'}, s_\Lambda} (-iT)(-iT) , \end{aligned} \quad (2.3)$$

where non-relativistic baryon propagators are used although relativistic energies are kept for convenience since we are dealing with particles with different masses. Thus, $k^0 = E_\Sigma(\mathbf{k})$ for a Σ on-shell and $E_i(\mathbf{p}) = (M_i^2 + \mathbf{p}^2)^{1/2}$. The first minus sign on the right-hand side of eq. (2.3) comes because of the nucleon loop, and s, t stand for the spin and isospin of the internal variables. We shall assume T real and independent of p^0 for the moment in eq. (2.3). The self-energy will be independent of the spin and isospin of the Σ in spin saturated symmetric nuclear matter. Hence let us concentrate on the Σ^- self-energy, in which case we only have the $\Sigma^- p \rightarrow \Lambda n$ reaction. We can then substitute the sum over spins and isospins of T^2 by $2\bar{\Sigma}\Sigma T^2$, where now we sum over spins of Λ, n (final state), and average over spins of Σ, p (initial state). Thus

$$\begin{aligned} \Sigma^*(k) = & \int \frac{d^4 p}{(2\pi)^4} \int \frac{d^4 q}{(2\pi)^4} \frac{n(\mathbf{p})}{p^0 - E_N(\mathbf{p}) - i\epsilon} \frac{[1 - n(\mathbf{q} + \mathbf{p})]}{q^0 + p^0 - E_N(\mathbf{q} + \mathbf{p}) + i\epsilon} \\ & \times \frac{1}{k^0 - q^0 - E_\Lambda(\mathbf{k} - \mathbf{q}) + i\epsilon} 2\bar{\Sigma}\Sigma T^2 . \end{aligned} \quad (2.4)$$

The p^0 integration can be performed readily and we have

$$\begin{aligned} \Sigma^*(k) = & i \int \frac{d^3 p}{(2\pi)^3} \int \frac{d^4 q}{(2\pi)^4} \frac{n(\mathbf{p})[1 - n(\mathbf{q} + \mathbf{p})]}{q^0 + E_N(\mathbf{p}) - E_N(\mathbf{q} + \mathbf{p}) + i\varepsilon} \\ & \times \frac{1}{k^0 - q^0 - E_\Lambda(\mathbf{k} - \mathbf{q}) + i\varepsilon} 2\bar{\Sigma} \Sigma T^2. \end{aligned} \quad (2.5)$$

The T matrix itself has a given analytical structure. If we think in the language of boson exchanges for the T matrix, it will contain terms like $(q^{02} - \mathbf{q}^2 - m_i^2 + i\varepsilon)^{-1}$, hence the poles of T lie in the second and fourth quadrant of the complex q^0 plane, as shown in fig. 2.3. The remaining analytical structure in the complex q^0 variable can be seen in fig. 2.3. This particular structure suggests that we perform a Wick rotation in order to do the q^0 integration. We have

$$\int_{-\infty}^{\infty} dq^0 + \int_C dq^0 + \int_{i\infty}^{-i\infty} dq^0 = 2\pi i R(k^0 - E_\Lambda) \theta(k^0 - E_\Lambda(\mathbf{k} - \mathbf{q})), \quad (2.6)$$

where C stands for the circles in the infinite in fig. 2.3 and $R(\cdot)$ is the residue of the integrand. Note that the pole of the particle-hole propagator is always in the fourth quadrant. Since the integral over C vanishes we have

$$\begin{aligned} \Sigma^*(k) = & i \int \frac{d^3 p}{(2\pi)^3} \int \frac{d^3 q}{(2\pi)^3} \int_{-i\infty}^{i\infty} dq^0 \frac{n(\mathbf{p})[1 - n(\mathbf{q} + \mathbf{p})]}{q^0 + E_N(\mathbf{p}) - E_N(\mathbf{q} + \mathbf{p})} \frac{1}{k^0 - q^0 - E_\Lambda(\mathbf{k} - \mathbf{q})} 2\bar{\Sigma} \Sigma T^2 \\ & + \int \frac{d^3 p}{(2\pi)^3} \int \frac{d^3 q}{(2\pi)^3} \frac{n(\mathbf{p})[1 - n(\mathbf{q} + \mathbf{p})]}{k^0 + E_N(\mathbf{p}) - E_\Lambda(\mathbf{k} - \mathbf{q}) - E_N(\mathbf{q} + \mathbf{p}) + i\varepsilon} \\ & \times \theta(k^0 - E_\Lambda(\mathbf{k} - \mathbf{q})) 2\bar{\Sigma} \Sigma T^2|_{q^0=k^0-E_\Lambda(\mathbf{k}-\mathbf{q})}. \end{aligned} \quad (2.7)$$

The first term in eq. (2.7) is a real background since the imaginary parts cancel when integrating over the positive and negative parts of the imaginary axis (note that T^2 is a real function which depends on

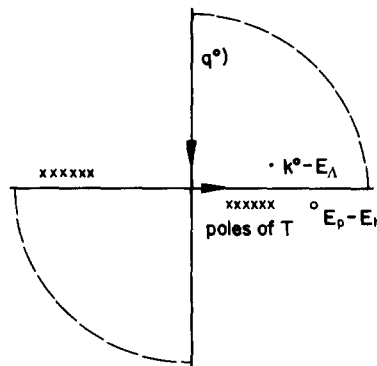


Fig. 2.3. Analytical structure of the integrand of eq. (2.5) in the complex variable q^0 . Shown in the figure is the path followed by the Wick rotation.

q^{02}). Thus only the second term contributes to the imaginary part and we obtain

$$\begin{aligned} \text{Im } \Sigma^*(k) = & - \int \frac{d^3 p}{(2\pi)^3} \int \frac{d^3 q}{(2\pi)^3} n(\mathbf{p}) [1 - n(\mathbf{q} + \mathbf{p})] \theta(k^0 - E_\Lambda(\mathbf{k} - \mathbf{q})) \\ & \times \pi \delta(k^0 + E_N(\mathbf{p}) - E_\Lambda(\mathbf{k} - \mathbf{q}) - E_N(\mathbf{q} + \mathbf{p})) 2 \bar{\Sigma} \Sigma T^2 \Big|_{q^0 = k^0 - E_\Lambda(\mathbf{k} - \mathbf{q})}. \end{aligned} \quad (2.8)$$

Note that the θ function is redundant because of the argument of the δ function. We can derive the same result for the imaginary part alone in a faster way by using Cutkowski's rules [IZ 80]. Indeed, the imaginary part of the diagram in fig. 2.2 comes when the particles cut by a horizontal line (dotted line in the figure) are placed on-shell in the four-dimensional integrations of eq. (2.4). Let us summarize Cutkowski's rules for the problem that we have: substitute in eq. (2.4) $\Sigma^*(k) \rightarrow 2i \text{Im } \Sigma^*(k)$, $G_0(p) \rightarrow \theta(p^0) 2i \text{Im } G_0$ and substitute T by T^* above the dotted line (we refer to it as the analytical cut). We then obtain the same eq. (2.8). However we obtain $|T|^2$ instead of T^2 , which is the general solution to account for the $\Sigma N \rightarrow \Lambda N$ decay mode of the Σ when T is complex and p^0 dependent.

Equation (2.8) allows now to relate $\text{Im } \Sigma^*$ to the $\Sigma N \rightarrow \Lambda N$ cross section. We have

$$\begin{aligned} \sigma(\Sigma N \rightarrow \Lambda N) = & \frac{1}{v_{\text{rel}}} \int \frac{d^3 k'}{(2\pi)^3} \int \frac{d^3 p'}{(2\pi)^3} \frac{M_\Sigma}{E_\Sigma(\mathbf{k})} \frac{M_\Lambda}{E_\Lambda(\mathbf{k}')} \frac{M}{E_N(\mathbf{p})} \frac{M}{E_N(\mathbf{p}')} \\ & \times \bar{\Sigma} \Sigma |T|^2 (2\pi)^4 \delta(p + k - p' - k'), \end{aligned} \quad (2.9)$$

where v_{rel} is the relative velocity of the ΣN system and M the nucleon mass.

Let us now make the usual non-relativistic approximations, $M_i/E_i \simeq 1$, change the variable $k' \rightarrow k - q$ and perform the p' integration. We obtain

$$\begin{aligned} \sigma(\Sigma N \rightarrow \Lambda N) = & \frac{1}{v_{\text{rel}}} \int \frac{d^3 q}{(2\pi)^3} \bar{\Sigma} \Sigma |T|^2 \\ & \times 2\pi \delta(E_\Sigma(\mathbf{k}) + E_N(\mathbf{p}) - E_N(\mathbf{p} + \mathbf{q}) - E_\Lambda(\mathbf{k} - \mathbf{q})), \end{aligned} \quad (2.10)$$

and hence eq. (2.8) can be rewritten as

$$\text{Im } \Sigma^*(k) = - \langle \sigma v_{\text{rel}} \rangle_{\text{av}} \rho_p / 2, \quad (2.11)$$

where ρ_p is the proton density and $\langle \sigma v_{\text{rel}} \rangle_{\text{av}}$ indicates the average of this quantity over the Fermi sea, including the Pauli blocking,

$$\begin{aligned} \langle \sigma v_{\text{rel}} \rangle_{\text{av}} = & \frac{1}{\rho_p / 2} \int \frac{d^3 p}{(2\pi)^3} n(\mathbf{p}) \int \frac{d^3 q}{(2\pi)^3} [1 - n(\mathbf{p} + \mathbf{q})] \\ & \times \bar{\Sigma} \Sigma |T(k, p; q)|^2 2\pi \delta(E_\Sigma(\mathbf{k}) + E_N(\mathbf{p}) - E_N(\mathbf{p} + \mathbf{q}) - E_\Lambda(\mathbf{k} - \mathbf{q})). \end{aligned} \quad (2.12)$$

Equation (2.11) is well known [GD 80, DR 81]. We have rederived it in a different way, using it as an excuse to introduce some techniques which will be used later on. The factor $M_\Sigma/E_\Sigma(\mathbf{k})$, for the

momenta involved in our problem, is of the order of 1%. For the ΛN final state the corresponding factors are more important. We keep these factors in the evaluation of σ in eq. (2.10).

Through eq. (2.2) we have then

$$\Gamma = \langle \sigma v_{\text{rel}} \rangle_{\text{av}} \rho_p . \quad (2.13)$$

Let us now make a connection with the experimental results for $\sigma(\Sigma N \rightarrow \Lambda N)$ in order to evaluate (2.13). By using $2v_{\text{rel}} E_{\Sigma}(\mathbf{k}) E_N(\mathbf{p}) = \lambda^{1/2}(s, M_{\Sigma}^2, M^2)$, with s the Mandelstam variable, $s = (p_{\Sigma} + p_N)^2$, and $\lambda(x, y, z) = x^2 + y^2 + z^2 - 2xy - 2yz - 2zx$, we have

$$\sigma(\Sigma N \rightarrow \Lambda N) = \frac{1}{4\pi^2} \frac{1}{s} M_{\Sigma} M_{\Lambda} M^2 \frac{\lambda^{1/2}(s, M_{\Lambda}^2, M^2)}{\lambda^{1/2}(s, M_{\Sigma}^2, M^2)} \int d\Omega \bar{\Sigma} \Sigma |T|^2 . \quad (2.14)$$

The low energy data for this reaction are found in [En 66] and range from $p_{\Sigma} = 110\text{--}160$ MeV/ c in the laboratory system.

We can investigate the energy dependence of the T matrix. For such purposes we divide the experimental cross section by the phase space (factor before the integral over $d\Omega$ in eq. (2.14)). The result of it is a remarkable constant value for $\int d\Omega \bar{\Sigma} \Sigma |T|^2$ for which a best χ^2 fit gives

$$M_{\Sigma} M_{\Lambda} \frac{1}{4\pi} \int d\Omega \bar{\Sigma} \Sigma |T|^2 \simeq 500 \text{ mb} . \quad (2.15)$$

In table 2.1 we show the results for σ and σv_{rel} obtained by using eqs. (2.14), (2.15) together with the experimental values for σ . The agreement with the experimental numbers is quite good as can be seen. On the other hand, because $\lambda^{1/2}(s, M_{\Lambda}^2, M^2)/s$ is rather constant in the region of interest to us, the value of σv_{rel} is also remarkably constant as can be seen in the table.

The values that we obtain for σv_{rel} agree also remarkably well with the empirical value that one obtains for this quantity from a best fit to the Σ^- atom data. From there one gets [Ba 78]

$$\begin{aligned} V_{\text{opt}}(r) &= -U(r) - iW(r) , \\ U(r) &= (28 \pm 3)\rho(r)/\rho_0 [\text{MeV}] , \quad W(r) = (15 \pm 2)\rho(r)/\rho_0 [\text{MeV}] . \end{aligned} \quad (2.16)$$

The results of the fit depend upon the value of the Σ magnetic moment. A reanalysis of the data in the

Table 2.1
Experimental data for the $\Sigma^- p \rightarrow \Lambda n$ reaction [En 66] together with the results with the assumption of eq. (2.15) for the T matrix.

p_{Σ} (MeV/ c)	σ_{exp} (mb)	σ_{fit} (mb)	$\sigma_{\text{fit}} v_{\text{rel}}$ (mb)
110	174 ± 47	186	17.1
120	178 ± 39	171	17.2
130	140 ± 28	158	17.2
140	164 ± 25	147	17.2
150	147 ± 19	138	17.3
160	124 ± 14	130	17.4

light of the more recent value for this quantity [He 83] only changes the results of the fit at the level of 3%, well within the experimental uncertainties [Ba 85]. Now, by equating $W(r)$ of eq. (2.16) to $-\text{Im } \Sigma^*(k)$ with $\rho_p = \rho/2$ in eq. (2.11), we find ($\rho_0 = 0.17 \text{ fm}^{-3}$):

$$\langle \sigma v_{\text{rel}} \rangle_{\text{av}} = (17.9 \pm 2.4) \text{ mb}, \quad (2.17)$$

the same value as quoted in [GD 80, Ga 81].

We should note that taking σv_{rel} constant, as seen in table 2.1, is a much better approximation to the experimental data than the formula quoted in [GD 80], $\sigma v = (\sigma v)_0 / (1 + \alpha v)$ with $(\sigma v)_0 = 65 \text{ mb}$ and $\alpha = 20$, coming from a fit to the theoretical values of [Na 73] for this reaction, which overshoots the experiment at low energies.

2.2. The $\Lambda p \rightarrow \Sigma^0 p$ reaction

We can write the cross section for this reaction analogously to eq. (2.14). We have

$$\sigma(\Lambda p \rightarrow \Sigma^0 p) = \frac{1}{4\pi^2} \frac{1}{s} M_\Sigma M_\Lambda M^2 \frac{\lambda^{1/2}(s, M_\Sigma^2, M^2)}{\lambda^{1/2}(s, M_\Lambda^2, M^2)} \int d\Omega \bar{\Sigma} \Sigma |T'|^2, \quad (2.18)$$

where now T' is the T matrix for the new reaction. Assuming isospin symmetry, a trivial isospin analysis of the $\Sigma^- p \rightarrow \Lambda n$ and $\Lambda p \rightarrow \Sigma^0 p$ reactions allows us to write

$$|T'|^2(\Lambda p \rightarrow \Sigma^0 p) = \frac{1}{2} |T|^2(\Sigma^- p \rightarrow \Lambda n), \quad (2.19)$$

and hence we can evaluate $\sigma(\Lambda p \rightarrow \Sigma^0 p)$ by means of (2.15). In this way we are relating the two cross sections through the principle of detailed balance and $SU(2)$ symmetry. We show the results in fig. 2.4 and compare them to the available experimental points in the low energy region [Ka 71, Ha 77]. The agreement with the data is quite good, although the experimental errors are rather large.

This is a new test of consistency of the fairness of the approximation of eq. (2.15). The results of fig. 2.4 indicate that the approximation of eq. (2.15) is fair for a range of energies beyond those of the experimental data for the $\Sigma N \rightarrow \Lambda N$ reaction of table 2.1.

2.3. Pauli blocking effects in the Σ self-energy

Equation (2.13) provides the Σ width with $\langle \sigma v_{\text{rel}} \rangle_{\text{av}}$ given by eq. (2.12). With respect to eq. (2.10), which provides the value of σv_{rel} for fixed initial state kinematics, eq. (2.12) involves an average over the initial nucleon momentum in the Fermi sea and contains the Pauli blocking factor $1 - n(\mathbf{p} + \mathbf{q})$. Let us evaluate the effect of this factor.

First, since we have to evaluate angular integrations in eq. (2.12) we must have some knowledge about the angular dependence of $T(k, p; q)$. Once again we rely upon the experimental data. In [En 66] one sees that the angular distribution averaged over the range of Σ momentum $100 \leq p_\Sigma \leq 170 \text{ MeV}/c$ is isotropic. If one selects the Σ momenta larger than $150 \text{ MeV}/c$ one can already see some forward peaking in the cross section indicating that the p -wave starts to contribute. This angular dependence is also consistent with the angular distributions in the $\Lambda p \rightarrow \Sigma^0 p$ reaction [Ka 71, Ha 77]. Since we are

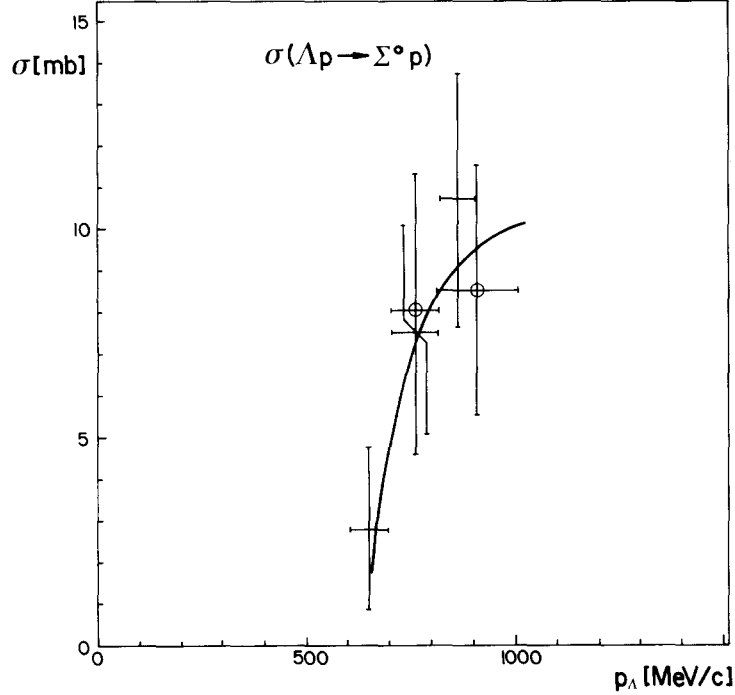


Fig. 2.4. Cross section of the $\Lambda p \rightarrow \Sigma^0 p$ reaction. Crosses from [Ka 71]; crosses with circle from [Ha 77]; solid curve: results using detailed balance, $SU(2)$ isospin symmetry and the assumption of eq. (2.15) for the $\Sigma^- p \rightarrow \Lambda n$ amplitude.

interested in low relative ΣN momentum it is a sufficiently good approximation to take $|T|^2$ independent of the angle for the purpose of illustrating the effect of the Pauli principle. In addition we shall use non-relativistic energies and take an angle average in the argument of the δ -function in (2.12). This allows one to carry out the \mathbf{p} integration with the Pauli blocking factor. One gets

$$4 \int \frac{d^3 p}{(2\pi)^3} n(\mathbf{p}) [1 - n(\mathbf{p} + \mathbf{q})] = \rho P_F(\mathbf{q}), \quad (2.20)$$

where $P_F(\mathbf{q})$ is given by

$$P_F(\mathbf{q}) = 1 - \theta(2 - \tilde{q}) \left(1 - \frac{3}{4} \tilde{q} + \frac{1}{16} \tilde{q}^3\right), \quad (2.21)$$

with $\tilde{q} = |\mathbf{q}|/k_F$. We further approximate $E_\Sigma(\mathbf{k}) - E_\Lambda(\mathbf{k}) = M_\Sigma + \mathbf{k}^2/2M_\Sigma - M_\Lambda - \mathbf{k}^2/2M_\Lambda \sim M_\Sigma - M_\Lambda$ and get the final result

$$\langle \sigma v_{\text{rel}} \rangle_{\text{av}} = \frac{1}{\pi} \tilde{M} \bar{q} \bar{\Sigma} \Sigma |T|^2 P_F(\bar{q}), \quad (2.22)$$

where \bar{q} is given by

$$\bar{q} = \sqrt{2\tilde{M}(M_\Sigma - M_\Lambda)}, \quad (2.23)$$

with \tilde{M} the reduced nucleon and lambda mass. Equation (2.22) allows for a factorization of the Pauli blocking effect and one gets for $\rho = \rho_0$ [$k_F = (3\pi^2\rho/2)^{1/3} = 268 \text{ MeV}/c$]

$$P_F(\bar{q}) = 0.73 . \quad (2.24)$$

This factor agrees with the value of 0.76 obtained in the nuclear matter calculations of [RD 79, DR 81]. It is also in agreement with the results of the exact treatment of Fermi motion and Pauli blocking that will be shown in section 5 when one makes use of the Lindhard function, which incorporates these features automatically.

It is also instructive to see that eq. (2.22), in the absence of the Pauli blocking factor, and using eq. (2.15) gives $\langle \sigma v_{\text{rel}} \rangle_{\text{av}} = 17.4 \text{ mb}$, in quite good agreement with the results of table 2.1, which shows the fairness of the approximations used to arrive at (2.22).

We can now make use of the local density approximation to evaluate the Σ^- width in the finite nucleus. We have

$$\Gamma = \int \Gamma(\rho(r)) |\varphi_{\Sigma}(r)|^2 d^3r , \quad (2.25)$$

where $\varphi_{\Sigma}(r)$ is the Σ^- wave function. Equation (2.25) would serve both in the case of Σ^- atoms or Σ^- hypernuclei. In the first case the effect of the Pauli blocking would be negligible while in the latter case it would be noticeable.

As an exercise we evaluate the width of a Σ^- in a $1s$ and a $1p$ state in ^{16}O , for which we assume the same wave function as for nucleons (we use harmonic oscillator wave functions with $\exp(-\alpha^2 r^2/2)$ for the radial part and $\alpha^2 = 0.316 \text{ fm}^{-2}$).

By taking eq. (2.13) for $\Gamma(\rho)$ and omitting the Pauli blocking factor in eq. (2.22) we obtain by means of (2.25)

$$\Gamma_{1s} = 19.4 \text{ MeV} , \quad \Gamma_{1p} = 13.6 \text{ MeV} . \quad (2.26)$$

If we include the effect of the Pauli blocking in eq. (2.22) we obtain the following results:

$$\Gamma_{1s} = 15.1 \text{ MeV} , \quad \Gamma_{1p} = 11.1 \text{ MeV} . \quad (2.27)$$

As we can see, the average over the nuclear distribution reduces the results of Γ to about one half of the nuclear matter estimate ($\Gamma \simeq 29 \text{ MeV}$, from (2.13)). Further inclusion of the Pauli blocking effect reduces the $1p$ width by about 18% and the $1s$ width by about 22%.

The values obtained here are similar to those found in [Ga 81] by using the optical potential of eq. (2.16) and solving directly the Schrödinger equation.

We can see that, even including the Pauli blocking effect, the widths for the bound states are larger than 10 MeV. The existence of experimental narrow structures has stimulated much theoretical work aimed at obtaining Σ hypernuclear states with $\Gamma \simeq 5 \text{ MeV}$.

The next section looks in some detail to the different approaches found in the literature attempting to explain the ‘‘abnormally small’’ Σ widths in the measured spectra.

3. Approaches proposed for narrow Σ states

In this section we give a critical review of the different approaches proposed to solve the puzzle of the Σ narrow widths.

3.1. The unstable bound states

Gal, Toker and Alexander [Ga 81] proposed the association of the narrow Σ states to the unstable bound states (UBS) of a complex potential. To understand the idea let us recall some of the analytical properties of the S matrix in a real potential. For an attractive potential $V = -U(r)$ the S matrix can develop in the complex k plane ($k^2/2m = E$) the poles depicted in fig. 3.1a. Poles on the positive imaginary axis correspond to bound states ($E < 0$). The pole in the fourth quadrant corresponds to a resonance ($2mE = k_R^2 - k_I^2 - 2i|k_R||k_I|$) at the pole $k = |k_R| - i|k_I|$). The empty circle on the negative imaginary axis corresponds to a virtual state, while the cross in the third quadrant corresponds to the “twin” pole of the resonant pole, which appears because of the reflection property $S(k) = (S(-k^*))^*$.

When one gradually introduces an imaginary part in the optical potential $\delta V = -iW(r)$, with $W(r) > 0$ (absorptive potential) the poles move in the direction of the arrows in the figure. Poles can now move in the second quadrant coming from bound states, virtual state poles or twin resonant poles as depicted in fig. 3.1b. The wave function for a pole in the second quadrant will be ($k = -|k_R| + i|k_I|$)

$$\frac{1}{r} e^{-iEt} e^{ikr} \rightarrow \frac{1}{r} e^{-i(k_R^2 - k_I^2)t/2m} e^{-|k_I||k_R|t/m} e^{-|k_R|r} e^{-|k_I|r}. \quad (3.1)$$

As can be seen all these states are bound, normalizable states (because of the $\exp(-|k_I|r)$ factor) and

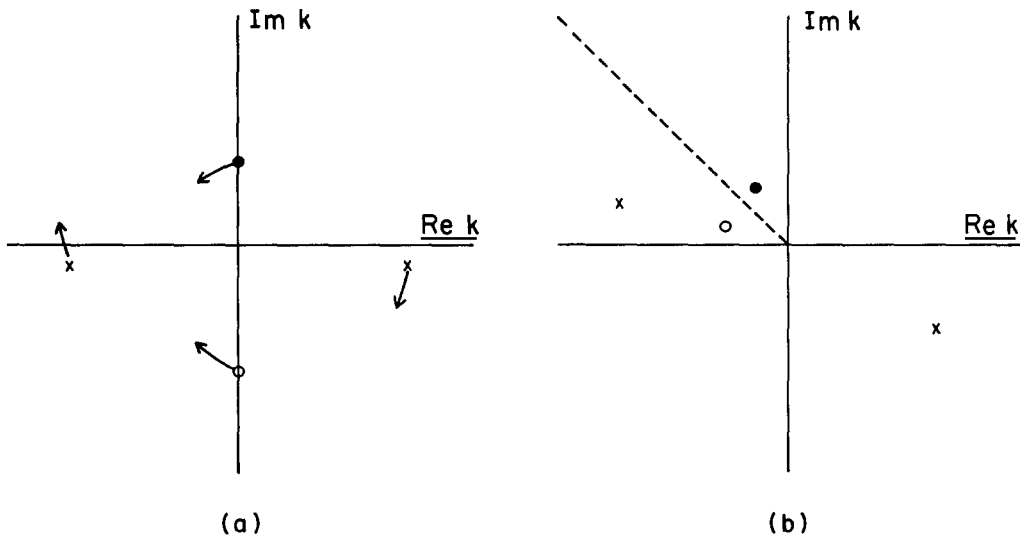


Fig. 3.1. Analytical structure of the S -matrix in the complex k plane. (a) Analytical structure for a real potential. The full dot corresponds to a bound state, the empty circle corresponds to a virtual state and the crosses correspond to a resonant state and its “twin” state. The arrows show the shift in the k plane of these states as a small absorptive part is added. (b) Analytical structure of $S(k)$ for an absorptive complex potential. The bisector which separates UBS embedded in the continuum (below) from ordinary (unstable) bound states (above) is shown.

unstable (because of the $\exp(-|k_I||k_R|t/m)$ factor). The first factor in the right-hand side of eq. (3.1) determines whether the energy of the state is positive or negative. We can see that below the bisector of the second quadrant ($|k_R| > |k_I|$) the energy is positive while above the bisector the energy is negative. The poles below the bisector are called in [Ga 81] unstable bound states embedded in the continuum (or UBS). Since $\Gamma = 2|k_I||k_R|/m$, some states with $|k_I|$ sufficiently small can have a small width. The appearance of such poles in the Σ hypernuclear problem is not unlikely since a small value of $|k_I|$ indicates a loosely bound Σ state with little overlap with the nucleus and consequently a small width. The appearance of these poles was thoroughly investigated in [Ga 81] by solving numerically the Schrödinger equation with a complex potential. In [Ba 83] it was also shown that if the range of the interaction is folded into the optical potential one obtains UBS states with sufficiently narrow widths for reasonable assumptions of the range of the interaction (~ 1 fm). While the p -states develop widths $\Gamma \leq 7$ MeV for $^{12}_{\Sigma}\text{C}$ or $^{16}_{\Sigma}\text{O}$ hypernuclei, the s -states, however, still have a large width, $\Gamma \geq 16$ MeV.

The interpretation of the narrow Σ states as UBS, however, faces a serious problem. One knows that in elastic scattering experiments the UBS are not observed. The question is whether they can show up in formation processes, like the reaction $K^-A \rightarrow \pi\Sigma A'$ used to produce the Σ hypernuclei. The question was studied by Morimatsu and Yazaki [MY 85] by analyzing the repercussion of the UBS poles in the reaction cross section. It was found there that while ordinary bound state poles or resonances show up clearly in the differential cross section $d^2\sigma/dE d\Omega$, with peaks in the cross section at the energy corresponding to the pole position and with the right width, the UBS have no repercussion in the cross section and no peaks nor enhancement of the cross section are found in the vicinity of the pole.

A more formal approach to the problem was made by Feshbach [Fe 85, 86]. He notes that because of the property of the S matrix, $S(k)S(-k) = 1$, a UBS pole of $S(k)$ at k_a implies that $S(-k_a)$ has a zero. However, $S(-k_a)$ is the observable quantity since $-k_a$ has a positive real part and corresponds to outgoing waves for an energy $E_a = k_a^2/2m$. Therefore, the probability of observing a peak at a neighboring real energy would be extremely small. The conclusion of all these authors is the same: "It is unlikely that the UBS correspond to the sharp Σ hypernuclear states".

A critical discussion of these papers is given in [Ga 86] with the suggestion that a coupled channels calculation, including explicitly the Λ channels, should be made in order to further clarify the situation.

3.2. Pauli blocking

The study done in section 2 has illustrated the role of the Pauli blocking in the $\Sigma N \rightarrow \Lambda N$ decay in nuclear matter and the nucleus. The effect of the Pauli blocking reducing the Σ width in nuclear matter and nuclei was recognized early [RD 79, DR 81, SW 81]. The calculations performed in these papers for nuclear matter lead to a quenching of Γ for $\rho \sim \rho_0$ of the order of 25%, in agreement with the estimate made in section 2. It looks thus clear that Pauli blocking by itself cannot produce a sizeable decrease in the Σ widths. However, Dąbrowski and Rozynek [DR 83] exploited the fact that the nucleon and hyperon self-energy depend on the momentum in order to further stress the quenching effect of the Pauli blocking.

The essence of the idea of these authors is the following: Because of the momentum dependence of the nucleon and hyperon self-energies, $\Sigma_i^*(\mathbf{k})$, the effective mass is decreased with respect to the free mass. As a consequence the momentum will be smaller for a given kinetic energy $p_i^2/2M_i^*$ and the values of the nucleon momentum allowed by the phase space coming from energy-momentum conservation will now be smaller, making the Pauli blocking more effective. The authors show that with

values of $M_i^*/M_i = 0.7$ for Σ , Λ and N , the quenching effect is rather sizeable and one can find widths of the order of 7–8 MeV for the $1s$ or $1p$ states of heavy hypernuclei.

One must, however, be cautious when using such arguments. Indeed, the effective mass is given by

$$\frac{m^*}{m} = \frac{1 - \partial \Sigma(k^0, \mathbf{k}) / \partial k^0}{1 + 2m \partial \Sigma(k^0, \mathbf{k}) / \partial k^2} \Big|_{k^0 = E(\mathbf{k})}, \quad (3.2)$$

where $\Sigma(k^0, \mathbf{k})$ is the particle self-energy as a function of the energy, k^0 , and the momentum, \mathbf{k} , considered as independent variables [Je 76, Ma 85].

Static theoretical approaches, like Hartree–Fock, give rise to effective masses smaller than one (in free mass units) because they do not provide any explicit k^0 dependence. Dynamical pictures like those in [Je 76, Ma 85, OP 81] give rise to an explicit k^0 dependence for the nucleons, by means of which one obtains a ratio of the effective nucleon mass to the free mass of the order of unity around the Fermi surface, in agreement with empirical determinations [Br 63] from the spacing of the nuclear energy levels.

Also, the assumption of equal effective masses for nucleons and the Σ and Λ hyperons requires some justification. Indeed, the G matrix calculations of [BN 82, YB 85, Bu 86, Mi 88] give Λ effective masses close to the free Λ mass.

Another reason for the extra quenching in [DR 83] at large densities comes from the dependence of $\sigma(\Sigma N \rightarrow NN)$ on the Σ momentum, which they take from the fit to the theoretical values of [Na 73]. As we discussed in section 2 this gives a faster fall with increasing Σ momentum than what is extracted from the experimental values. Hence, when taking into account the Pauli blocking, one would be stressing the large momentum components from the Fermi sea and this would reduce the value of σv , $\sigma v = (\sigma v)_0 / (1 + \alpha v)$, and accordingly the Σ width.

The arguments exposed here indicate that a reanalysis of the problem along the lines of [DR 83], but taking into account the considerations exposed here, would be most advisable.

3.3. Other approaches

The ideas of the two former points were exploited by Johnstone and Thomas [JT 83]. They start from a separable $YN \rightarrow Y'N$ interaction ($Y = \Sigma, \Lambda$) and solve coupled channel equations with some approximations, fitting some parameters in order to reproduce the experimental data. Pauli and binding effects are considered by assuming the Fermi momentum and the binding energy, B , constant for each nucleus. For $1s$ -states the combined effect of Pauli blocking and nuclear binding produces narrow widths ranging from 1.75 MeV in ${}^5_{\Sigma} \text{He}$ to 12.5 MeV in ${}^{16}_{\Sigma} \text{O}$. On the other hand, in the $1p$ -states of light hypernuclei, where the Pauli blocking is less effective, the strong absorptive potential is responsible for the appearance of UBS with widths ranging from 0.54 MeV in ${}^9_{\Sigma} \text{Be}$ to 4.04 MeV in ${}^{16}_{\Sigma} \text{O}$.

The consistency of the derived Σ -nucleus optical potential with the Σ^- atomic data is established in an approximate way by showing that for $k_F = 260$ MeV/ c and $B = 10$ MeV results are obtained which are compatible with the effective scattering length of Batty et al. [Ba 78]. However, the effective density felt by the Σ in the measured atoms is approximately $\rho \approx 0.1\rho_0$ or equivalently $k_F = 125$ MeV/ c . A look at fig. 5 of [JT 83] shows that with values of $k_F \approx 125$ MeV/ c the agreement of $\text{Im } \bar{a}_B$ with the empirical value of [Ba 78] would not be good. However, a calculation of Σ^- atom shifts and widths in the Johnstone–Thomas approach but with the Pauli blocking corresponding to the densities felt by the Σ^- should give us a more precise answer to this question than the simple extrapolation from the results of fig. 5 of [JT 83] which we have made.

Yamamoto and Bandō [YB 83] carry out similar calculations to those discussed in section 3.2. Their results for the Σ width depend upon assumptions made for the effective masses and nucleon and Λ potentials, but the features for the reduction of the width due to the Pauli blocking are similar to those discussed before.

Bogdanova and Markushin [BM 80, Bo 84a] also discuss the problem and show that under certain assumptions, amongst which having a constant $\Sigma N \rightarrow \Lambda N$ transition potential in coordinate space is the most relevant, they can reduce the Σ width. This choice of the potential reduces the width because of the approximate orthogonality of the Σ and Λ functions. A similar thing would then happen to the atomic widths, which would be sizeably decreased. By means of this approximation one would be transferring the problem of Σ hypernuclei to Σ^- atoms.

There is also a calculation by Kisslinger [Ki 80] where the Σ width is calculated starting from a $\Sigma N \rightarrow \Lambda N$ transition potential which contains only one pion exchange. A simplified ΣN wave function of the Hulthén type is used which is rather different from the one calculated in [DR 81, Dą 81]. As mentioned in [Ki 80] the results should be considered only as crude estimates, but they have the virtue of showing that considering short-range correlations in the evaluation of the Σ width is rather important.

A different idea based on SU(3) symmetry has been invoked to produce narrow widths in some light hypernuclear clusters involving a coherent admixture of Λ and Σ hyperons [DF 87].

Finally, we should not forget that on top of the conversion width, which we have discussed so far, there are the typical widths which we find in normal states of nuclei. On the one hand, the states with $l \neq 0$ of positive energy can have an escape width Γ^\uparrow . This is usually attributed to the fact that certain states pass through the centrifugal barrier. This has been noted in [MY 85, Au 87]. Note also that bound states, $E < 0$, and the UBS, which are also bound as seen in eq. (3.1), do not have escape width. On the other hand, there is a spreading width, Γ^\downarrow , which represents the spread of a single Σ nuclear state into the spectrum of surrounding nuclear excitations. Furthermore, we should also note that in the case of substitutional states (of the type Σ -nucleon hole) one would have to account for the width of the hole state in the nucleus (in Λ substitutional states the width of the nucleon hole accounts for most of the observed widths [Au 87]). On the other hand Γ^\uparrow and Γ^\downarrow for Σ hypernuclei have been investigated in [Au 87] and found to be of the order of several hundred keV, which would be about an order of magnitude smaller than the widths from the $\Sigma N \rightarrow \Lambda N$ conversion process which we have discussed in these sections.

3.4. Summary

The overview given in this section has illustrated the diversity of ideas people have tried in order to understand the problem of the Σ small widths. We have also discussed the problems met by the different approaches as well as the limitations due to the various approximations made. One of the few ideas which appear to be a constant in most approaches is the role of the Pauli exclusion principle, but there are different results about its relevance. Another idea which should have become clear is that we cannot separate the problem of the Σ hypernuclei from the one of the Σ atoms and that one must try to find a common solution to both.

The next section is devoted to a different approach where, apart from taking into account the Pauli blocking in an exact way, one exploits the properties of the induced interaction, by means of which one obtains a strong density dependence in the Σ self-energy which is consistent with the Σ^- atom data and also provides narrow widths for Σ hypernuclei.

4. The induced interaction approach

4.1. The nucleon self-energy in nuclear matter

Before we proceed to introduce the induced interaction it is worth making a little digression on some known features of the imaginary part of the nucleon optical potential and its density dependence. For that purpose we will rely upon the results of [Fa 83] obtained by means of the hypernetted chain approach, one of the most successful many-body schemes. We see the results in fig. 4.1 for $\rho = \rho_0$ and $\rho_0/2$ as a function of $E - E_F$, with E the nucleon energy and E_F the Fermi energy.

We can appreciate in the figure that for small energies $W_0(\rho_0/2)$ ($W_0 = -\text{Im } \Sigma^*$) is bigger than $W_0(\rho_0)$. At $E - E_F \approx 85$ MeV the two quantities have the same value and for higher energies $W_0(\rho_0)$ is already bigger than $W_0(\rho_0/2)$.

Let us try to understand this feature. We take again the second order diagram, equivalent to fig. 2.2, but with nucleon lines instead of Σ and Λ . This is depicted in fig. 4.2. We will now have the NN interaction, instead of the $\Sigma N \rightarrow \Lambda N$ interaction, for which we will take an amplitude T' . An equivalent procedure to the one that led us to eq. (2.8) will give us now for a particle state ($k^0 > E_F$)

$$\begin{aligned} \text{Im } \Sigma_N^*(k) = & - \int \frac{d^3p}{(2\pi)^3} \int \frac{d^3q}{(2\pi)^3} n(p)[1 - n(p+q)][1 - n(k-q)] \\ & \times \pi \delta(k^0 + E_N(p) - E_N(k-q) - E_N(q+p)) 4 \bar{\Sigma} \Sigma |T'|^2, \end{aligned} \quad (4.1)$$

where the novelties, apart from the change of Σ and Λ to nucleons, are the factor 4 in front of the sum and average of $|T'|^2$, because we wish to average over p and n , and the extra factor $[1 - n(k-q)]$, which takes care of the Pauli blocking of the second particle line (we should note that the hole part of this latter particle, proportional to $n(k-q)$, also contributes to $\text{Im } \Sigma_N^*(k)$ but only for external lines below the Fermi surface, which is not the case here). Now assuming again an average $|T'|^2$ and taking an average over the angle of p in the argument of the δ function (reasonable if $|k| \gg |p|$ as is approximately the case for $E - E_F = 85$ MeV) and using non-relativistic energies, we obtain the simplified result for an on-shell nucleon ($k^0 = M + k^2/2M$)

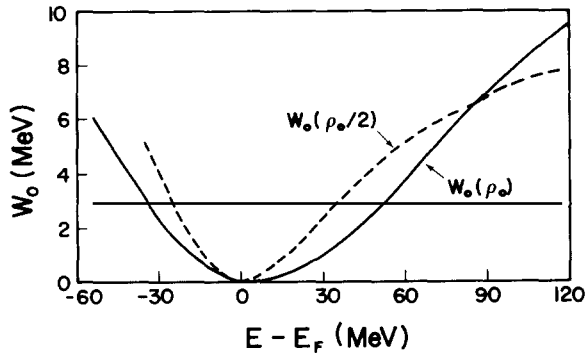


Fig. 4.1. The imaginary part of the optical potential for nucleons in nuclear matter at densities ρ_0 and $\rho_0/2$ from the hypernetted chain calculation of [Fa 83], as a function of the nucleon energy minus the Fermi energy.

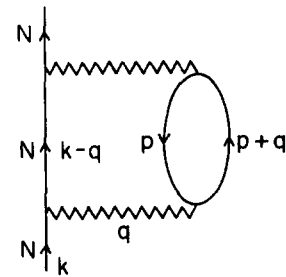


Fig. 4.2. Feynman diagram for the nucleon self-energy in nuclear matter.

$$\text{Im } \Sigma_N^*(k) \approx -\rho \frac{M}{|k|} \frac{\bar{\Sigma} \Sigma |T'|^2}{4\pi} \int_0^{(k^2 - k_F^2)^{1/2}} dq q P_F(q), \quad (4.2)$$

with $P_F(q)$ given by (2.21).

In the absence of the Pauli blocking factor for the two particle lines we would obtain

$$\text{Im } \Sigma_N^{*NP}(k) = -\rho \frac{M}{|k|} \frac{\bar{\Sigma} \Sigma |T'|^2}{4\pi} \int_0^{|k|} q dq = -\frac{1}{8\pi} k M \rho \bar{\Sigma} \Sigma |T'|^2. \quad (4.3)$$

When $(k^2 - k_F^2)^{1/2} < 2k_F$, as it is the case for $k^0 - E_F = 85$ MeV and $\rho = \rho_0, \rho_0/2$, eq. (4.2) can be written in analytical form as

$$\text{Im } \Sigma_N^*(k) = -\rho \frac{M}{|k|} \frac{\bar{\Sigma} \Sigma |T'|^2}{4\pi} k_F^2 \frac{1}{4} \tilde{q}_{\max}^3 \left(1 - \frac{1}{20} \tilde{q}_{\max}^2\right) \quad (4.4)$$

with

$$\tilde{q}_{\max} = \sqrt{(k/k_F)^2 - 1}. \quad (4.5)$$

By taking $E_F = M + k_F^2/2M$ we obtain the following results:

$$\frac{\text{Im } \Sigma_N^*(k)}{\text{Im } \Sigma_N^{*NP}(k)} = \begin{cases} 0.46, & \rho = \rho_0, \\ 0.60 & \rho = \rho_0/2, \end{cases} \quad k^0 - E_F = 85 \text{ MeV}. \quad (4.6)$$

We can observe that the Pauli blocking is more effective here than in the case of the Σ self-energy (note that the available energy for excitation $M_\Sigma - M_\Lambda \approx 82$ MeV is about the same as we have here). This reflects the fact that we have Pauli blocking in two nucleons rather than in one as we had before. On the other hand we can get the ratio of $\text{Im } \Sigma_N^*$ calculated at ρ_0 and $\rho_0/2$. We obtain

$$\frac{\text{Im } \Sigma_N^*(\rho_0)}{\text{Im } \Sigma_N^*(\rho_0/2)} = 1.6, \quad k^0 - E_F = 85 \text{ MeV}. \quad (4.7)$$

This result is bigger than the factor 1 from the calculation of [Fa 83] in fig. 4.1.

The results of fig. 4.1 can only be understood if there is a more effective, density dependent, quenching mechanism than the Pauli blocking alone. This mechanism should reduce $\text{Im } \Sigma_N^*(\rho_0)$ more effectively than $\text{Im } \Sigma_N^*(\rho_0/2)$ and then the ratio of eq. (4.7) could be 1, as the results of the figure. ($\bar{\Sigma} \Sigma |T'|^2$ would be slightly larger in the case of $\rho_0/2$ because this involves smaller momenta and the NN cross section is decreasing with energy in this range of energies. This increase is however of the order of 10%.)

Let us continue with the analogies with the Σ width. We can calculate absolute values of $\text{Im } \Sigma_N^*(k)$ by relating $\bar{\Sigma} \Sigma |T'|^2$ to the experimental cross section. With the normalization that we use we have

$$\bar{\Sigma} \Sigma |T'|^2 = \pi \frac{s}{M^4} \sigma_{NN}, \quad (4.8)$$

with $\sigma_{NN} \approx 25$ mb, 28 mb for $k^0 - E_F = 85$ MeV and $\rho = \rho_0, \rho_0/2$ respectively. In the case of identical particles in the final state there would be a symmetry factor in (4.1) and (4.8) but the relationship of $\text{Im } \Sigma^*$ to σ does not change.

Then eq. (4.4) gives us

$$\text{Im } \Sigma_N^*(k) = \begin{cases} -10.4 \text{ MeV}, & \rho = \rho_0, \\ -7.2 \text{ MeV}, & \rho = \rho_0/2, \end{cases} \quad k^0 - E_F = 85 \text{ MeV}. \quad (4.9)$$

These results should be compared with the value -6.5 MeV from the calculation of [Fa 83]. We can see again that an extra quenching is needed and that it is more effective in the case of $\rho = \rho_0$ than in the case of $\rho_0/2$.

At this point it is worth recalling the translation of the hypernetted chain approach to the Feynman diagrammatic many-body approach. The essence of the hypernetted chain approach consists in summing simultaneously the ladder and bubble diagrams depicted in fig. 4.3. That is, on one side the potential is iterated, as would be done with the Lippmann–Schwinger equation, but in nuclear matter in order to generate the G matrix. This gives rise to the effective interaction in the medium. Second, this effective interaction polarizes the medium by exciting ph excitations in an RPA series. The combination of both is the induced interaction [FW 71, Br 72]. It has the virtue of combining the dynamics at short distance, accounted for by the effective interaction, and at long distances (polarization phenomenon), which are taken care of by means of the iteration of the ph excitations induced by the effective interaction. In the scheme of [Fa 83] one can also include Δh excitations by means of the three-body forces.

Let us go back to the problem of the Σ width and start constructing a theoretical model for the $\Sigma N \rightarrow \Lambda N$ transition. We will follow [Na 77, 79] to construct a model based upon meson exchange to describe the amplitude for this transition.

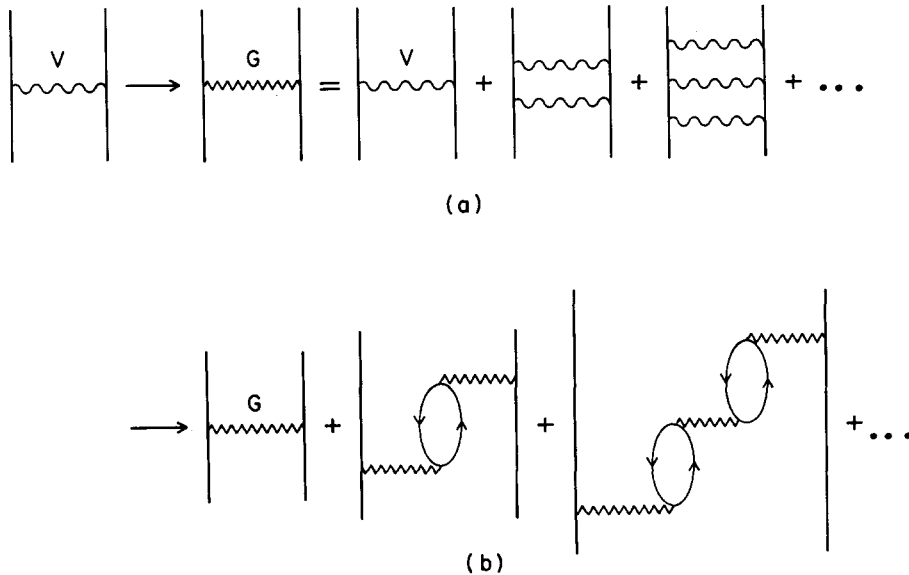


Fig. 4.3. Set of graphs included in the hypernetted chain approach to the NN interaction. (a) First the ladder series for the elementary interaction V is summed to give the G matrix or effective interaction. (b) Later the RPA series is summed to obtain the induced interaction.

4.2. Model for the $\Sigma N \rightarrow \Lambda N$ transition

Let us consider the $\Sigma N \rightarrow \Lambda N$ transition from the point of view of meson exchange as shown in fig. 4.4. Since Σ is a particle of isospin $T=1$ and Λ has isospin $T=0$ the exchanged meson has to have $T=1$. This leaves us with π and ρ exchange in the conventional meson exchange model. There is a possibility of having $\Sigma N \rightarrow \Lambda N$ mediated by kaon exchange but this contribution is rather small [BO 82] and we shall disregard it. We take a pseudoscalar coupling for the $\Sigma\Lambda\pi$ Hamiltonian,

$$\delta H_{\Sigma\Lambda\pi} = -i\bar{g}_{\Sigma\Lambda\pi}\bar{\psi}_{\Lambda}\gamma_5\psi_{\Sigma}\cdot\phi_{\pi} + \text{h.c.}, \quad (4.10)$$

where the scalar product $\psi_{\Sigma}\cdot\phi_{\pi}$ is over the isospin variables. For the $\Sigma\Lambda\rho$ coupling we take the conventional vector meson coupling,

$$\delta H_{\Sigma\Lambda\rho} = \bar{g}_{\Sigma\Lambda\rho}\bar{\psi}_{\Lambda}\gamma_{\mu}\psi_{\Sigma}\cdot\phi_{\rho}^{\mu} + \frac{\bar{f}_{\Sigma\Lambda\rho}}{4M}\bar{\psi}_{\Lambda}\sigma_{\mu\nu}\psi_{\Sigma}\cdot(\partial^{\mu}\phi_{\rho}^{\nu} - \partial^{\nu}\phi_{\rho}^{\mu}) + \text{h.c.} \quad (4.11)$$

The values for the coupling constants are [Na 77]

$$\bar{g}_{\Sigma\Lambda\pi}/\sqrt{4\pi} = 2.27, \quad \bar{g}_{\Sigma\Lambda\rho} = 0, \quad \bar{f}_{\Sigma\Lambda\rho}/\sqrt{4\pi} = 3.70. \quad (4.12)$$

The vertices corresponding to these Hamiltonians to be used in the Feynman rules are, in the non-relativistic reduction,

$$\delta\tilde{H}_{\Sigma\Lambda\pi} = i\frac{f_{\Sigma\Lambda\pi}}{\mu}\boldsymbol{\sigma}\cdot\mathbf{q}\hat{\psi}_{\Sigma}\cdot\hat{\phi}_{\pi}, \quad \delta\tilde{H}_{\Sigma\Lambda\rho} = i\frac{f_{\Sigma\Lambda\rho}}{m_{\rho}}(\boldsymbol{\sigma}\times\mathbf{q})\cdot\boldsymbol{\varepsilon}\hat{\psi}_{\Sigma}\cdot\hat{\phi}_{\rho}, \quad (4.13)$$

where $\hat{\psi}_{\Sigma}$ and $\hat{\phi}$ are the Σ and meson isospin unit vectors and μ is the pion mass. We can add the standard Yukawa $NN\pi$ coupling and the $NN\rho$ coupling,

$$\delta\tilde{H}_{NN\pi} = i\frac{f}{\mu}\boldsymbol{\sigma}\cdot\mathbf{q}\tau^{\lambda}, \quad \delta\tilde{H}_{NN\rho} = i\frac{f_{\rho}}{m_{\rho}}\boldsymbol{\sigma}\times\mathbf{q}\tau^{\lambda}, \quad (4.14)$$

and for later purposes the $N\Delta\pi$ and $N\Delta\rho$ couplings,

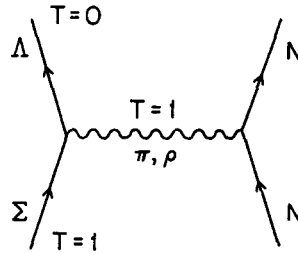


Fig. 4.4. Meson exchange mechanism for the $\Sigma N \rightarrow \Lambda N$ T matrix. π and ρ mesons are included.

$$\delta\tilde{H}_{N\Delta\pi} = i \frac{f^*}{\mu} \mathbf{S} \cdot \mathbf{q} T^\lambda, \quad \delta\tilde{H}_{N\Delta\rho} = i \frac{f_\rho^*}{m_\rho} \mathbf{S} \times \mathbf{q} T^\lambda, \quad (4.15)$$

where μ is the pion mass, τ^λ the ordinary Pauli matrices for the nucleons and \mathbf{S} , \mathbf{T} are the transition spin, isospin operators from S , $T = 1/2$ to $3/2$. They are defined by the easy relation (Wigner–Eckart theorem)

$$\langle 3/2 M_s | S_\nu^\dagger | 1/2 m_s \rangle = \mathcal{C}(1/2, 1, 3/2; m_s, \nu, M_s), \quad (4.16)$$

with ν the spherical component, which implies that the reduced matrix element $\langle 3/2 || S^\dagger || 1/2 \rangle$ is 1. The equivalent expression holds for the \mathbf{T} operator. One has also the usual closure property (and an equivalent one for \mathbf{T})

$$\sum_{M_s} S_i | 3/2 M_s \rangle \langle 3/2 M_s | S_j^\dagger = \delta_{ij} - \frac{1}{3} \sigma_i \sigma_j. \quad (4.17)$$

The coupling constants are now given by

$$\begin{aligned} f^2/4\pi &= 0.08, & f^{*2}/4\pi &= 0.36, & f_\rho^2/4\pi &= 9.56, & f_\rho^{*2}/f_\rho^2 &= f^{*2}/f^2, \\ f_{\Sigma\Lambda\pi}^2/4\pi &= 0.019, & f_{\Sigma\Lambda\rho}^2/4\pi &= 2.30. \end{aligned} \quad (4.18)$$

The value for f_ρ is taken from [Ma 87] and it has to be accompanied by the invariant form factor

$$F_\rho(q) = (\Lambda_\rho^2 - m_\rho^2)/(\Lambda_\rho^2 - q^2), \quad (4.19)$$

with $\Lambda_\rho = 1.4$ GeV. Equally, we take a form factor for the πNN vertex

$$F_\pi(q) = (\Lambda^2 - \mu^2)/(\Lambda^2 - q^2), \quad (4.20)$$

with $\Lambda = 1.3$ GeV [Ma 87]. The value of f_ρ in (4.18) is slightly increased with respect to [Ma 87] to match the data of [HP 75] at zero momentum transfer. The $\Sigma\Lambda\pi$ and $\Sigma\Lambda\rho$ couplings of [Na 77] have to be accompanied by a hard core at $r_c \approx 0.4$ fm although this cut-off is somewhat dependent on the channel [Na 77, DG 83]. The $\Sigma^- p \rightarrow \Lambda n$ transition potential is then given in momentum space by

$$V_{\Sigma N \rightarrow \Lambda N}(q) = V_\pi(q) + V_\rho(q), \quad (4.21)$$

with

$$\begin{aligned} V_\pi(q) &= \frac{f_{\Sigma\Lambda\pi}}{\mu} \frac{f}{\mu} \sqrt{2} \frac{q^2 F_\pi(q)}{q^{02} - q^2 - \mu^2} \hat{q}_i \hat{q}_j \sigma_i^{(1)} \sigma_j^{(2)}, \\ V_\rho(q) &= \frac{f_{\Sigma\Lambda\rho}}{m_\rho} \frac{f_\rho}{m_\rho} \sqrt{2} \frac{q^2 F_\rho(q)}{q^{02} - q^2 - m_\rho^2} (\delta_{ij} - \hat{q}_i \hat{q}_j) \sigma_i^{(1)} \sigma_j^{(2)}, \end{aligned} \quad (4.22)$$

where the hard core in coordinate space has still to be implemented. In (4.22), \hat{q}_i is $q_i/|\mathbf{q}|$.

We can observe that $V_\pi(q)$ is of a longitudinal type, $\hat{q}_i\hat{q}_j$, while $V_\rho(q)$ is of a transverse type ($\delta_{ij} - \hat{q}_i\hat{q}_j$). These two operators are mutually orthogonal. The normalization of the potential is such that $V(q) \rightarrow T$, defined in eq. (2.1) in the limit of the Born approximation.

With all these ingredients, we are now in a position to evaluate the G matrix. We could think that the hard core is produced by a strong repulsive spin-isospin independent force in the ΣN and ΛN channels and we can use the results of [BJ 79] to construct G . There we find that if the potential is split into a strong, V_S , and a weak part, V_W ,

$$V = V_S + V_W, \quad (4.23)$$

then the G matrix is given by

$$G = G_S + \Omega_S^\dagger V_W \Omega_S + \dots, \quad (4.24)$$

where G_S is the G matrix constructed with V_S alone and $\Omega_S^\dagger, \Omega_S$ are wave operators which in the case of a short-range repulsive V_S potential can be very well approximated by means of a local correlation function. We can apply these results to our case assuming V_W to be the $\Sigma N \rightarrow \Lambda N$ transition potential while V_S accounts for the interaction in the $\Sigma N \rightarrow \Sigma N$ or $\Lambda N \rightarrow \Lambda N$ channels which contain repulsive short range forces. Then, the second term of the r.h.s. of eq. (4.24) gives the effective $\Sigma N \rightarrow \Lambda N$ interaction which we shall use in the evaluation of the Σ width. The $\Sigma N \rightarrow \Lambda N$ effective interaction in our case is thus given by

$$G_{\Sigma N \rightarrow \Lambda N}(r) = g(r)V_{\Sigma N \rightarrow \Lambda N}(r), \quad (4.25)$$

with $g(r)$ a typical correlation function which vanishes as $r \rightarrow 0$ and goes to 1 as $r \rightarrow \infty$. This procedure is quite appropriate to the present case because it allows us to include the effect of the hard core used in the $\Sigma N \rightarrow \Lambda N$ transition potential in the analysis of [Na 73]. We shall use a practical correlation function

$$g(r) = 1 - j_0(q_c r), \quad (4.26)$$

by means of which one could get a fair reproduction of a realistic correlation function in the NN interaction with values $q_c \approx 780$ MeV/ c [OW 79]. The value of q_c should not necessarily be the same here given the different nature of the repulsive forces. In our case q_c should be indicative of the inverse of the hard core radius r_c of the analysis of [Na 73], $q_c \approx 500$ MeV/ c , but should depend on the density. On the other hand, in the limit of small densities we want the G matrix to be equal to the T matrix defined in eq. (2.1). Through the procedure exposed below we shall see that the T matrix is reproduced with $q_c = 475$ MeV/ c , i.e. with a hole in the correlation function slightly larger than the hard core radius. $G_{\Sigma N \rightarrow \Lambda N}$ in momentum space can be easily calculated analytically by means of the correlation function (4.26) and some angular averages, as was done in [OW 79]. One simply has to implement in the potential of (4.22) the change

$$q_i q_j D(q) F(q) \rightarrow q_i q_j D(q) F(q) - q_i q_j \tilde{D}(q) \tilde{F}(q) [1 + \frac{4}{3} q_c^2 \tilde{D}(q)] - \frac{1}{3} q_c^2 \tilde{D}(q) \tilde{F}(q) \delta_{ij}, \quad (4.27)$$

where $\tilde{D}(q)$ is the meson propagator $D(q)$ substituting \mathbf{q}^2 by $\mathbf{q}^2 + q_c^2$, and the same prescription for the function $F(q)$. $F(q)$ is supposed to be a smooth function of \mathbf{q}^2 , as is the case for the nucleon-meson

form factors. On the other hand, $|\mathbf{q}|/q_c$ is supposed to be small with respect to unity. Even in a case like ours where $|\mathbf{q}|/q_c \simeq 1/2$ the approximation of (4.27) holds at the level of 5%.

With this prescription we now obtain

$$G_{\Sigma N \rightarrow \Lambda N}(q) = \{G_l(q)\hat{q}_i\hat{q}_j + G_t(q)(\delta_{ij} - \hat{q}_i\hat{q}_j)\}\sigma_i^{(1)}\sigma_j^{(2)}, \quad (4.28)$$

where

$$\begin{aligned} G_l(q) &= \sqrt{2} \frac{f}{\mu} \frac{f_{\Sigma\Lambda\pi}}{\mu} \{q^2 D_\pi(q) F_\pi(q) - q^2 \tilde{D}_\pi(q) \tilde{F}_\pi(q) [1 + \frac{4}{3} q_c^2 \tilde{D}_\pi(q)] \\ &\quad - \frac{1}{3} q_c^2 \tilde{D}_\pi(q) \tilde{F}_\pi(q) - \frac{2}{3} q_c^2 \tilde{D}_\rho(q) \tilde{F}_\rho(q) C'_\rho\}, \\ G_t(q) &= \sqrt{2} \frac{f}{\mu} \frac{f_{\Sigma\Lambda\pi}}{\mu} \{q^2 D_\rho(q) F_\rho(q) C'_\rho - q^2 \tilde{D}_\rho(q) \tilde{F}_\rho(q) [1 + \frac{4}{3} q_c^2 \tilde{D}_\rho(q)] C'_\rho \\ &\quad - \frac{1}{3} q_c^2 \tilde{D}_\pi(q) \tilde{F}_\pi(q) - \frac{2}{3} q_c^2 \tilde{D}_\rho(q) \tilde{F}_\rho(q) C'_\rho\}, \end{aligned} \quad (4.29)$$

with

$$C'_\rho = \left(\frac{f_{\Sigma\Lambda\rho}}{m_\rho} \frac{f_\rho}{m_\rho} \right) / \left(\frac{f_{\Sigma\Lambda\pi}}{\mu} \frac{f}{\mu} \right) = 3.95. \quad (4.30)$$

As we said, at small densities this should coincide with the T matrix and hence we would have, using eq. (2.15),

$$\bar{\Sigma} \Sigma \langle |(G_l \hat{q}_i \hat{q}_j + G_t (\delta_{ij} - \hat{q}_i \hat{q}_j)) \sigma_i^{(1)} \sigma_j^{(2)}| \rangle^2 = G_l^2 + 2G_t^2 = \bar{\Sigma} \Sigma |T|^2 = 500 \text{ mb} / M_\Sigma M_\Lambda. \quad (4.31)$$

By using eqs. (4.29) we see that this is accomplished by choosing $q_c = 475 \text{ MeV}/c$, equivalent to a correlation hole slightly larger than the hard core radius. An average value of $|\mathbf{q}|$, given by eq. (2.23), together with $q^0 = q^2/2M$, is used in the evaluation of eq. (4.29).

There are some features to observe in eqs. (4.29) and (4.31). The first one is that $G_l^2 + 2G_t^2$ is smoothly dependent on $|\mathbf{q}|$. For values of $|\mathbf{q}| \sim 300 \text{ MeV}/c$ changes of 10% in $|\mathbf{q}|$ produce similar changes in $G_l^2 + 2G_t^2$. For small values of $|\mathbf{q}|$ this sum is about constant. This is thus consistent with our assumption of constant $\bar{\Sigma} \Sigma |T|^2$ in the regime of momenta of our problem, also supported by the experiment as shown in section 2.1. The other feature worth noting is that $G_l^2 + 2G_t^2$ is also smoothly dependent on q_c . Around $q_c = 475 \text{ MeV}/c$ changes of 10% in q_c bring about changes of 12% in the same direction in that sum. This is worth keeping in mind, because as we go to higher densities we expect the correlation hole to increase slightly, which would mean a corresponding decrease in q_c and a similar decrease in $G_l^2 + 2G_t^2$. As we go from $\rho = 0$ to $\rho = \rho_0$ we could expect an increase of the correlation hole of the order of 20–30% with respect to the large one already created by the hard core potential even at zero density. This would produce a similar decrease in $G_l^2 + 2G_t^2$ which we shall keep in mind for later purposes.

We should also mention here that changes in q_c barely affect the proportion of the transverse part of the interaction with respect to the total: an increase of q_c in 10% increases the ratio of $2G_t^2$ versus $G_l^2 + 2G_t^2$ by 4%.

Note also that because of the p -wave nature of the π and ρ couplings, the hard core has had the effect of introducing a large correction in G_i and G'_i , nearly constant, given by the last two terms in the brackets of eqs. (4.29). This would play the role of a Landau–Migdal g' parameter for this interaction. A similar derivation for the NN case was done in [OW 79]. The presence of these terms is what makes the G matrix so constant as a function of q . The other point worth mentioning is that in eq. (4.31) the transverse part $2G'_i$ contributes about 92% of the total $G_i^2 + 2G'_i$.

4.3. The $\Sigma N \rightarrow \Lambda N$ induced interaction

We have carried out the first part of the program in constructing the induced interaction. So far we have constructed the transition G matrix or effective interaction. The next step is to take into account the ph and Δh excitations to all orders in the RPA sense produced by the spin–isospin $\Sigma N \rightarrow \Lambda N$ interaction. This is depicted diagrammatically in fig. 4.5 for the particular case that we have here. Note that the first ph or Δh excitation is produced by $G_{\Sigma N \rightarrow \Lambda N}$, but after that, all the new excitations are produced by the NN or $N\Delta$ effective interactions. Since the interaction responsible for the $\Sigma N \rightarrow \Lambda N$ transition carries $T = 1$ in the spin channel, as can be seen in eq. (4.22), this will automatically select the spin–isospin channel of the NN or $N\Delta$ effective interactions between the ph or Δh excitations, for which we shall take the well-known form [Os 82]

$$G_{NN}^{s-i}(q) = \{V_i \hat{q}_i \hat{q}_j + V_t (\delta_{ij} - \hat{q}_i \hat{q}_j)\} \sigma_i^{(1)} \sigma_j^{(2)} \boldsymbol{\tau}^{(1)} \cdot \boldsymbol{\tau}^{(2)}, \quad (4.32)$$

and equivalent expressions for the $NN \rightarrow N\Delta$ transition or $N\Delta \rightarrow N\Delta$ interaction by changing $\boldsymbol{\sigma} \rightarrow \mathbf{S}$, $\boldsymbol{\tau} \rightarrow \mathbf{T}$ and f by f^* for each Δ involved. V_t and V_l are given by

$$V_l = \frac{f^2}{\mu^2} [q^2 D_\pi(q) F_\pi^2(q) + g'], \quad V_t = \frac{f^2}{\mu^2} [q^2 D_\rho(q) F_\rho^2(q) C_\rho + g'], \quad (4.33)$$

for the NN effective interaction, with $g' \approx 0.6$ and $C_\rho = (f_\rho^2/m_\rho^2)/(f^2/\mu^2) = 3.94$ with the form factor and coupling constants of eqs. (4.18) and (4.19).

The other ingredient needed to construct the induced interaction is the polarization contribution provided by the ph or Δh excitation depicted in fig. 4.6. This is done readily by means of the Lindhard function defined for the particle–hole excitation [FW 71]

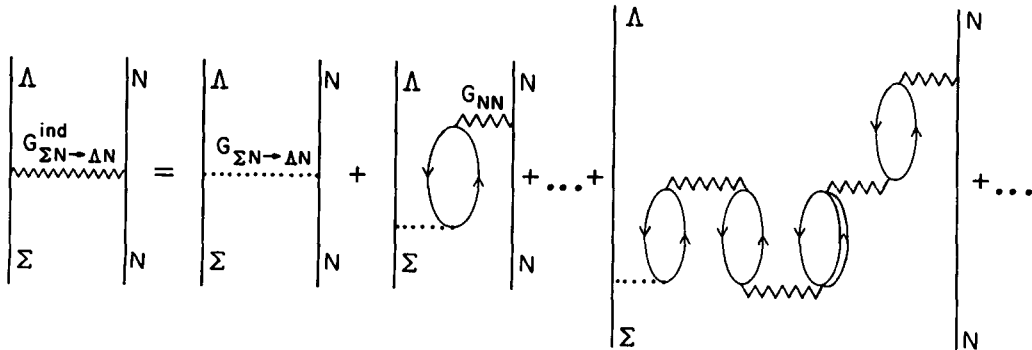
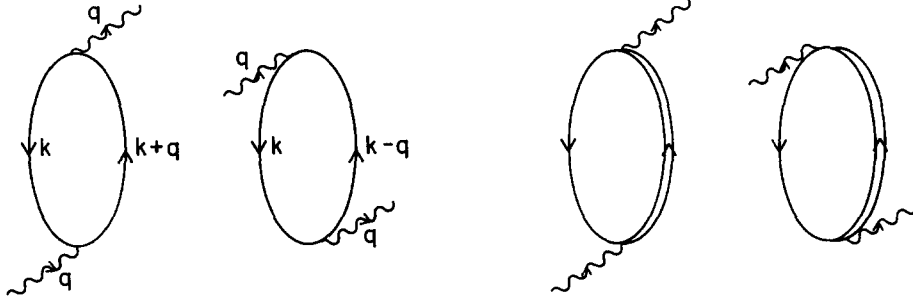


Fig. 4.5. RPA series for the induced $\Sigma N \rightarrow \Lambda N$ interaction of eq. (4.35). Both ph and Δh excitations are included [$U_{N,\Delta}(q)$], as well as the ph and Δh effective interaction ($V_{l,t}(q)$ in G_{NN}) between them. $G_{\Sigma N \rightarrow \Lambda N}$ is the $\Sigma N \rightarrow \Lambda N$ effective interaction.

Fig. 4.6. Feynman graphs included in $U_N(q)$ (left) and $U_\Delta(q)$ (right).

$$U_N(q) = 4 \int \frac{d^3k}{(2\pi)^3} \left\{ \frac{n(\mathbf{k})[1 - n(\mathbf{k} + \mathbf{q})]}{q^0 + \varepsilon(\mathbf{k}) - \varepsilon(\mathbf{k} + \mathbf{q}) + i\eta} + \frac{n(\mathbf{k})[1 - n(\mathbf{k} - \mathbf{q})]}{-q^0 + \varepsilon(\mathbf{k}) - \varepsilon(\mathbf{k} - \mathbf{q}) + i\eta} \right\}, \quad (4.34)$$

where $\varepsilon(\mathbf{k})$ stands now for the nucleon kinetic energy.

A similar expression is obtained for the Lindhard function $U_\Delta(q)$ of the Δh excitation by substituting the ph propagators by the Δh ones. Analytical expressions for $U_N(q)$ and $U_\Delta(q)$, also valid for complex values of q^0 , which will be needed later on, can be found in [OP 81]. More compact formulae for U_N and U_Δ can be found in the appendix. For simplicity in the formulae the ratio $(f^*/f)^2$ is incorporated also in $U_\Delta(q)$.

With the splitting of the interaction into longitudinal and transverse parts the sum implicit in fig. 4.5 can be done readily and it amounts to summing two independent geometrical series, one for the longitudinal part and another one for the transverse part, given the orthogonality of these two parts. We obtain

$$G^{\text{ind}}(q) = \left\{ \frac{G_l(q)}{1 - U(q)V_l(q)} \hat{q}_i \hat{q}_j + \frac{G_t(q)}{1 - U(q)V_t(q)} (\delta_{ij} - \hat{q}_i \hat{q}_j) \right\} \sigma_i^{(1)} \sigma_j^{(2)}, \quad (4.35)$$

where now

$$U(q) = U_N(q) + U_\Delta(q). \quad (4.36)$$

4.4. Approximate evaluation of the Σ width with the induced interaction

We shall now evaluate Γ by means of eq. (2.13) and the approximation of eq. (2.22) which was found to be quite good. We had

$$\Gamma = \langle \sigma v_{\text{rel}} \rangle_{\text{av}} \rho_p, \quad \langle \sigma v_{\text{rel}} \rangle_{\text{av}} \simeq \frac{1}{\pi} \tilde{M} \bar{q} \bar{\Sigma} \Sigma |T|^2 P_F(\bar{q}), \quad (4.37)$$

but now $\bar{\Sigma} \Sigma |T|^2$ will be changed to

$$\bar{\Sigma} \Sigma |T|^2 \rightarrow \frac{G_l^2}{|1 - UV_l|^2} + \frac{2G_t^2}{|1 - UV_t|^2}, \quad (4.38)$$

by means of which we can write Γ as a function of the density as

$$\Gamma(\rho) = \frac{1}{2\pi} \tilde{M} \bar{q} \rho_0 \left\{ \frac{G_t(\bar{q})^2}{|1 - U(\bar{q})V_t(\bar{q})|^2} + \frac{2G_l(\bar{q})^2}{|1 - U(\bar{q})V_l(\bar{q})|^2} \right\} P_F(\bar{q}) \frac{\rho}{\rho_0}, \quad (4.39)$$

where $\rho_p = \rho/2$ has been used again, with \tilde{M} the reduced nucleon and lambda mass and \bar{q} given by (2.23). The value of q^0 , neglecting the Fermi motion, is $\bar{q}^2/2M$ and we use that value in (4.39). However there is practically no dependence on q^0 in (4.39) for the small values of q^0 involved.

The essential assumption in eq. (4.39) is that one can also take an average of the renormalization effects produced by the induced interaction by evaluating them at the average value of q found in eq. (2.23). A more accurate evaluation will be done in the next section, but making this approximation is very useful for the purpose of illustration. The first advantage is that U_N and U_Δ have very easy forms. For $q^0 = \bar{q}^2/2M$ and $|q| > k_F$ as is the case here for $\rho < \rho_0$, we have

$$\begin{aligned} U_N &= \frac{Mk_F}{\pi^2} \left\{ -1 - \frac{1}{2\tilde{q}} [1 - \tilde{q}^2] \ln \left| \frac{\tilde{q} + 1}{\tilde{q} - 1} \right| \right\} - i \frac{Mk_F^2}{2\pi|q|}, \\ U_\Delta &\approx \frac{4}{9} \left(\frac{f^*}{f} \right)^2 \rho \left\{ \frac{1}{-\omega_R} + \frac{1}{-q^2/M - \omega_R} \right\}, \end{aligned} \quad (4.40)$$

with $\omega_R = M_\Delta - M$, $\tilde{q} = |q|/k_F$. For $|q| = 290$ MeV/c, $q^0 = 44.5$ MeV, $g' = 0.6$, and by means of an easy approximation to the real part of U_N in terms of ρ , we find

$$\begin{aligned} V_l &= -\frac{f^2}{\mu^2} 0.135, & V_t &= \frac{f^2}{\mu^2} 0.380, \\ U_N &\approx -0.790 \frac{\rho}{\rho_0} \left(1 + 0.260 \frac{\rho}{\rho_0} \right) - i 1.92 \left(\frac{\rho}{\rho_0} \right)^{2/3} [\mu^2], \\ U_\Delta &\approx -0.813 \frac{\rho}{\rho_0} [\mu^2]. \end{aligned} \quad (4.41)$$

Hence the renormalization factors are

$$\begin{aligned} \frac{1}{|1 - V_l U|^2} &= \frac{1}{[1 - 0.218\rho/\rho_0 - 0.028(\rho/\rho_0)^2]^2 + 0.067(\rho/\rho_0)^{4/3}}, \\ \frac{1}{|1 - V_t U|^2} &= \frac{1}{[1 + 0.612\rho/\rho_0 + 0.078(\rho/\rho_0)^2]^2 + 0.533(\rho/\rho_0)^{4/3}}. \end{aligned} \quad (4.42)$$

Inspection of these formulae tells us that the induced interaction introduces a large quenching in the transverse part and a more moderate enhancement in the longitudinal part. The net effect on the quantity $G_l^2 + 2G_t^2$ depends on the weight of the longitudinal and transverse parts in this expression. As we mentioned before, the longitudinal part G_l^2 gives only 8% of the total $G_l^2 + 2G_t^2$, while 92% of the contribution in that sum comes from the transverse part $2G_t^2$.

It is clear after this exposition that the net effect of the induced interaction will be to produce a quenching in Γ as a function of ρ .

We plot the numerical results of (4.39) in fig. 4.7. We can see that with respect to the straight line $\Gamma(\rho) = 29.4\rho/\rho_0$ [MeV] that we get in the absence of Pauli blocking and without the induced interaction (dashed straight line in the figure), the results for $\Gamma(\rho)$ including both effects show a dramatic density dependent quenching that reduces $\Gamma(\rho)$ by more than a factor 3 at $\rho = \rho_0$.

With the density dependence of this figure and by using eq. (2.25) we can now evaluate widths for Σ nuclear states. With the same assumptions as made there for the Σ wave functions we would find for the $1s$ and $1p$ Σ hypernuclear states the following widths:

$$\Gamma_{1s} = 7.0 \text{ MeV}, \quad \Gamma_{1p} = 5.9 \text{ MeV}. \quad (4.43)$$

One can see that the widths are appreciably changed (reduced by about a factor 2) with respect to the respective values with the Pauli blocking alone of eqs. (2.27), $\Gamma_{1s} = 15.1 \text{ MeV}$, $\Gamma_{1p} = 11.1 \text{ MeV}$.

The approximations made here have the virtue of showing us clearly the origin of the quenching in $\Gamma(\rho)$ as a function of the density.

We should also note that the quenching that we find is due to the NN or $N\Delta$ interaction, not to the $\Sigma N \rightarrow \Lambda N$ transition amplitude.

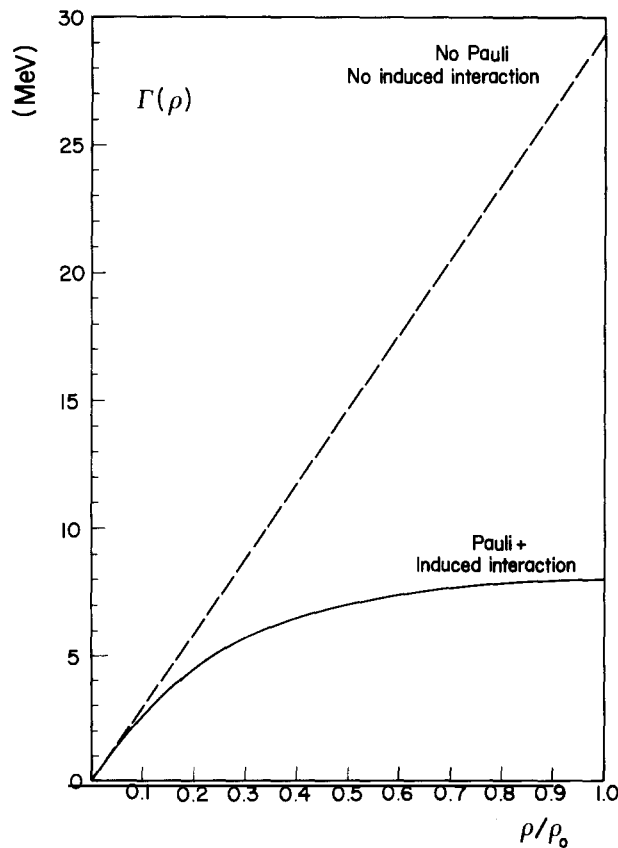


Fig. 4.7. Numerical results for the Σ width in nuclear matter as a function of ρ . Dashed line: results without Pauli blocking or induced interaction. Full line: results from eq. (4.39) with both Pauli blocking and induced interaction included.

We can look at the quenching of the $\Sigma N \rightarrow \Lambda N$ transition in a different way. We can say that the Σ decays into a Λ plus a ph excitation of the Gamow–Teller type (driven by the $\sigma\tau$ operator). The quenching observed here bears close resemblance to the quenching of the beta decay Gamow–Teller transitions in nuclei, which is very well established [Wi 73, 74, Br 78, AH 79, Os 82]. Even more related is the quenching observed in muon capture in nuclei [Ch 89], where the kinematics is more similar to the $\Sigma N \rightarrow \Lambda N$ transition. Indeed, the experimental value for the muon capture rates in medium and heavy nuclei are about a factor two smaller than the theoretical results in the impulse approximation. In this case about 85% of the capture rate comes from the Gamow–Teller term, $(g_A \sigma\tau)^2$, and this observation again is telling us that there is a substantial quenching of the Gamow–Teller operator. A study of the nuclear renormalization of the weak hadronic current in the muon capture problem, along the same lines as discussed in this section for the $\Sigma N \rightarrow \Lambda N$ transition, produces the necessary quenching, bringing the results in close agreement with experiment [Ch 89].

5. Expression of the Σ self-energy in terms of the Lindhard function

In this section we shall rewrite the Σ self-energy in terms of the Lindhard function without making the approximations of section 2 to derive the width. In addition, this allows one to calculate the real parts, too.

We start from eq. (2.5) and make use of the fact that $\bar{\Sigma} \Sigma T^2$ depends only on the momentum transfer in the model used in section 4. This allows us to carry out the integral over p since only the particle–hole propagator depends on it. By recalling eq. (4.34) for the Lindhard function we identify this integral with the first term of (4.34) (we shall use non-relativistic kinematics for the nucleon kinetic energies). However, the Lindhard function contains an additional term [second term in eq. (4.34)]. By including this term we are adding the diagram of fig. 5.1b to the one of fig. 5.1a already considered for the Σ self-energy. This additional diagram is a valid one, which only contributes to the real part of Σ^* and hence does not modify what we have said in the former sections about the Σ width. As a consequence we can now write eq. (2.5) as

$$\Sigma^*(k) = i \int \frac{d^4q}{(2\pi)^4} \frac{1}{4} U_N(q) \frac{1}{k^0 - q^0 - E_\Lambda(k - q) + i\eta} 2 \bar{\Sigma} \Sigma T^2. \quad (5.1)$$

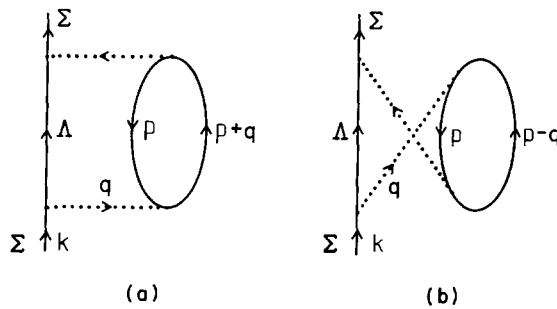


Fig. 5.1. Σ self-energy diagrams included in eq. (5.1). (a) Direct graph contributing to both $\text{Re } \Sigma^*$ and $\text{Im } \Sigma^*$, already considered in fig. 2.2. (b) New crossed graph contributing to $\text{Re } \Sigma^*$ only. The dotted lines stand for the effective $\Sigma N \rightarrow \Lambda N$ interaction.

The q^0 integral can now be performed in the same way as it was performed in section 2, by means of a Wick rotation. The analytical structure of the integrand is analogous to the one shown in fig. 2.3. Indeed the cuts of $U_N(q)$ appear in the same quadrants as those shown in the figure for T . Hence we can follow the same path as in fig. 2.3 to perform the q^0 integration and, analogously to eq. (2.7), we find

$$\begin{aligned} \Sigma^*(k) = & i \int \frac{d^3q}{(2\pi)^3} \int_{-i\infty}^{i\infty} dq^0 \frac{1}{4} U_N(q) \frac{1}{k^0 - q^0 - E_\Lambda(k-q)} 2\bar{\Sigma} \Sigma T^2 \\ & + \int \frac{d^3q}{(2\pi)^3} \frac{1}{4} U_N(q) \theta(q^0) 2\bar{\Sigma} \Sigma T^2 \Big|_{q^0=k^0-E_\Lambda(k-q)}, \end{aligned} \quad (5.2)$$

where the first term provides only a real background, while the second term gives rise to both a real and an imaginary part.

The width accounting for the Pauli blocking, which is now incorporated in $U_N(q)$, is given by

$$\Gamma^{(\text{lowest})}(k) = -2 \int \frac{d^3q}{(2\pi)^3} \frac{1}{4} \text{Im} U_N(q) \theta(q^0) 2\bar{\Sigma} \Sigma |T|^2 \Big|_{q^0=k^0-E_\Lambda(k-q)}, \quad (5.3)$$

where the superscript ‘‘lowest’’ indicates that we use the effective $\Sigma N \rightarrow \Lambda N$ interaction, instead of the induced interaction.

Equation (5.2) is evaluated numerically in [BO 82] without further approximations, by using the model of section 4 for the $\Sigma N \rightarrow \Lambda N$ transition. We can get back eqs. (2.13) together with (2.22) by making the approximation (assuming symmetric nuclear matter)

$$\theta(q^0) \text{Im} U_N(q) \simeq -\pi\rho\delta(q^0 - q^2/2M)P_F(q). \quad (5.4)$$

This approximation is obtained ignoring the Fermi motion. However, the results with this approximation are very similar to those with the exact evaluation of eq. (5.3). The integral in eq. (5.3) has a limited range in the q integration around the average value used in eq. (2.23), both because of the θ function and because $\text{Im} U_N(q)$ is zero beyond a certain value of $|q|$ for a given value of q^0 .

Inclusion of the induced interaction leads from fig. 5.1 to fig. 5.2. One can automatically include these effects by following similar steps to those in section 4.3. The result is the substitution in eq. (5.2) of

$$U_N \bar{\Sigma} \Sigma T^2 \equiv U_N(q) [G_i^2(q) + 2G_t^2(q)] \rightarrow \frac{G_i^2(q)U(q)}{1-U(q)V_i(q)} + \frac{2G_t^2(q)U(q)}{1-U(q)V_t(q)}, \quad (5.5)$$

with G_i , G_t given by (4.29), V_i , V_t by (4.33) and $U(q)$ by (4.36). In particular, by taking into account that

$$\text{Im} \frac{G_{i,t}^2(q)U(q)}{1-U(q)V_{i,t}(q)} = \frac{G_{i,t}^2(q) \text{Im}(U(q)[1-U^*(q)V_{i,t}(q)])}{|1-U(q)V_{i,t}(q)|^2} = \frac{G_{i,t}^2(q) \text{Im} U(q)}{|1-U(q)V_{i,t}(q)|^2} \quad (5.6)$$

because $V_{i,t}$ and $G_{i,t}$ are real, we obtain for the width

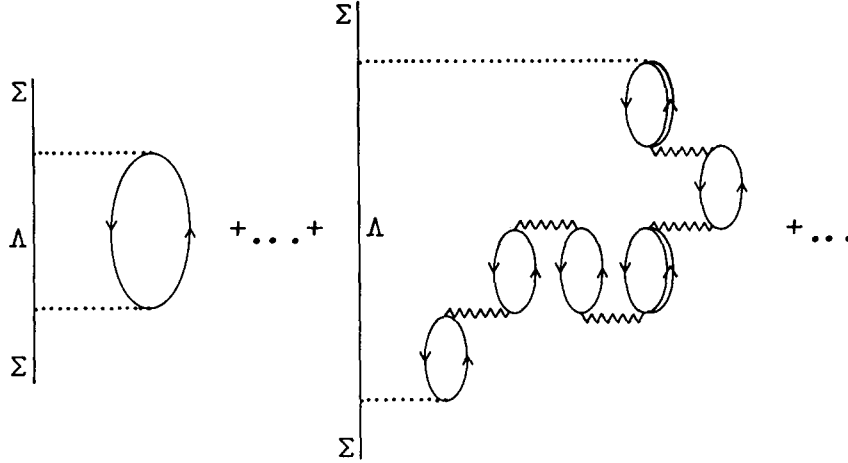


Fig. 5.2. Same as fig. 5.1 once the full induced interaction is included (eq. 5.7).

$$\Gamma(k) = - \int \frac{d^3q}{(2\pi)^3} \theta(k^0 - E_\Lambda(\mathbf{k} - \mathbf{q})) \left\{ \frac{G_t^2(q) \text{Im } U(q)}{|1 - U(q)V_t(q)|^2} + \frac{2G_t^2(q) \text{Im } U(q)}{|1 - U(q)V_t(q)|^2} \right\}_{q^0 = k^0 - E_\Lambda(\mathbf{k} - \mathbf{q})}, \quad (5.7)$$

where $\text{Im } U(q)$ can be substituted by $\text{Im } U_N(q)$ since $\text{Im } U_\Delta = 0$ in this range of energy-momentum. Once again, by means of the approximation of eq. (5.4) we reproduce the approximate formulae eqs. (4.37), (4.38) which we used in the former section.

We show in figs. 5.3, 5.4 the results of [BO 82]. The model used there is essentially the same as the one described in section 4 with minor differences: A form factor identical to the $NN\pi, NN\rho$ is used for the $\Sigma\Lambda\pi, \Sigma\Lambda\rho$ vertex and $q_c = 780 \text{ MeV}/c$. The combination of a weaker correlation function with the extra form factor has similar effects to the longer range correlation function used in section 4. In fig. 5.3 we show the results for $\text{Re } \Sigma^*$ in lowest order and with the induced interaction (“full” in the figure). We can observe that the real part is nearly linear in the nuclear density, and that the introduction of the induced interaction does not affect the results much.

In fig. 5.4 we show the results for Γ as a function of the density in lowest order and with the induced interaction. We can see that even in lowest order, $\Gamma(\rho)$ differs appreciably from a linear function in the nuclear density at densities $\rho \geq 0.5\rho_0$, illustrating the effect of the Pauli blocking. This different behavior of the real and imaginary parts reflects the fact that $\text{Re } U_N$, unlike $\text{Im } U_N$, is not affected by Pauli blocking [FW 71]. On the other hand the use of the induced interaction has as a consequence a drastic reduction of $\Gamma(\rho)$ at large densities. While at low densities, $\rho \sim 0.1\rho_0$, $\Gamma(\rho)$ is approximately linear in ρ , it deviates soon from a linear function and shows saturation properties at $\rho \sim 0.6\rho_0$ as a function of the density. These results are very similar to those which we obtained in the previous section and which are shown in fig. 4.7. The reasons for the quenching were discussed in detail in the previous section. One may wonder why one does not find the same quenching in the real part. The reason is that in $\text{Re } \Sigma^*$ the range of \mathbf{q} in the integration is not limited as in $\text{Im } \Sigma^*$. Larger values of $|\mathbf{q}|$ contribute now to the integral and with $U(q) \sim |\mathbf{q}|^{-2}$ at large $|\mathbf{q}|$ the effects of the renormalization of eq. (5.5) are smaller. On the other hand, one also has to consider that, while in $\text{Re } \Sigma^*$ the renormalization factor is $(1 - UV)^{-1}$, in $\text{Im } \Sigma^*$ it is $|1 - UV|^{-2}$, which makes the quenching more pronounced.

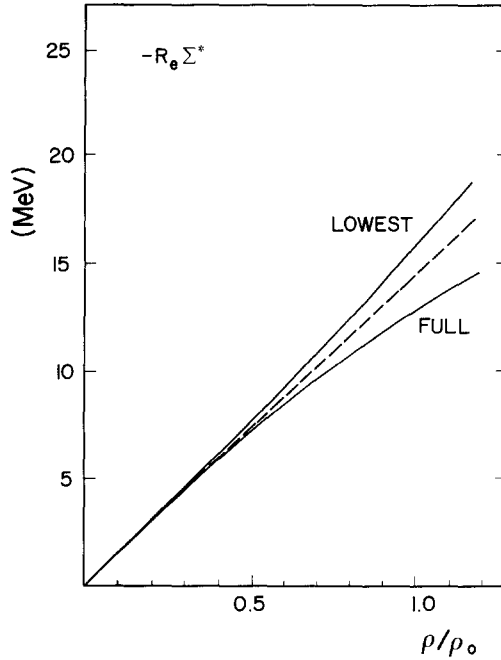


Fig. 5.3. Real part of the Σ self-energy in nuclear matter as a function of the density from [BO 82]. Straight line: linear extrapolation from $\rho = 0$. Line labeled as “lowest”: lowest order result from the mechanism of fig. 5.1. Line labeled as “full”: full induced interaction result from the mechanism of fig. 5.2.

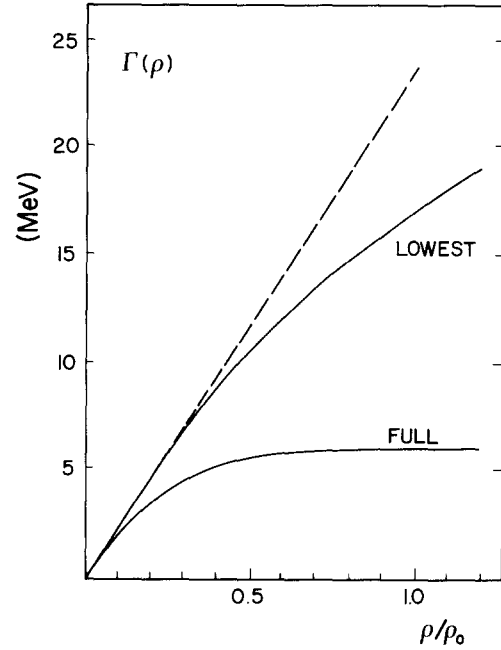


Fig. 5.4. Same as fig. 5.3 but for the Σ width.

We should note that a potential like the one in fig. 5.4 leads immediately to narrow hypernuclear states [BO 82]. In that reference the following widths were found for the ^{12}C and ^{16}O hypernuclei:

$$\begin{aligned}
 {}^{16}\text{O}: \quad & s \text{ state, } \Gamma = 4.95 \text{ MeV}; \quad p \text{ state, } \Gamma = 4.65 \text{ MeV}; \\
 {}^{12}\text{C}: \quad & s \text{ state, } \Gamma = 4.90 \text{ MeV}; \quad p \text{ state, } \Gamma = 4.48 \text{ MeV}.
 \end{aligned} \tag{5.8}$$

At the same time we can see that for low densities, a linear extrapolation of $\Gamma(\rho)$ from fig. 5.4 gives $\Gamma^{\text{ext}}(\rho) \sim 24 \rho/\rho_0$ [MeV], which should be compared with $2W(r)$ of eq. (2.16) from a best fit to Σ^- atoms. The theoretical results are about 15% below those quoted there. This tells us that with that potential, one can now get narrow widths for hypernuclear states and still be consistent with the Σ^- atomic data. This has been made more quantitative in [BO 84, 86], where a Schrödinger equation was solved numerically with the imaginary part of the optical potential given by the results of [BO 82] and a free real part.

In the next section we come back to this problem and use the data of Σ^- atoms to deduce $\text{Re } \Sigma^*$. With this function and the theoretical results for $\text{Im } \Sigma^*$, which are compatible with the experimental Σ^- atomic data, we make a thorough study of widths and energies of hypernuclear states in different nuclei. We should note that, while the imaginary part is well given by the model exposed above, $\text{Re } \Sigma^*$ could still get contributions from Hartree terms, which we have not calculated. However, the results of [BO 82] have the virtue of showing that $\text{Re } \Sigma^*$ is in any case approximately linear in the density and so

would be the Hartree pieces. Due to this, a parametrization of $\text{Re } \Sigma^*$ proportional to ρ seems most indicated.

6. Study of bound states of Σ hypernuclei

The results from sections 4 and 5 led us to the conclusion that the Σ optical potential has a real part approximately proportional to the nuclear density while the imaginary part has some saturation properties as a function of the density.

However, while we could evaluate the imaginary part of the Σ self-energy rather reliably, the real part, which was evaluated in [BO 82], is only a piece of the total real part of Σ^* , which would also come from other sources, mostly from Hartree pieces. The important finding of section 5 is that all these pieces are essentially linear in the nuclear density. In order to perform a systematic study of bound states with the Σ nuclear potential one needs the strength of the real part. The analysis of Σ^- atoms of [Ba 78] provides the real part $U(r) = 28 \rho/\rho_0$ [MeV], as quoted in eq. (2.16), twice as big as the real part associated with the diagram of fig. 2.2.

The low density limit of the optical potential in nuclear matter [Do 71, Hü 75] simply states that

$$\Sigma^* = \tilde{t}\rho, \quad (6.1)$$

where \tilde{t} is the $\Sigma N \rightarrow \Sigma N$ T matrix in the forward direction, averaged over spin and isospin of the nucleons. With the normalization of eq. (2.1)

$$\tilde{t} = \frac{1}{4} \sum_{s_N, t_N} \langle s_{\Sigma} s_N, t_{\Sigma} t_N | T_{\Sigma N \rightarrow \Sigma N} | s_{\Sigma} s_N, t_{\Sigma} t_N \rangle |_{\theta=0}. \quad (6.2)$$

The forward direction in \tilde{t} comes imposed because of the translational invariance of the infinite system, which forces momentum conservation. In a finite nucleus one has instead in momentum space [Ga 89]

$$\tilde{\Sigma}^*(\mathbf{k}, \mathbf{k}') = \tilde{t}(\mathbf{k}, \mathbf{k}') \tilde{\rho}(\mathbf{k} - \mathbf{k}'), \quad (6.3)$$

where

$$\tilde{\rho}(\mathbf{k} - \mathbf{k}') = \int d^3 r e^{i(\mathbf{k} - \mathbf{k}') \cdot \mathbf{r}} \rho(\mathbf{r}). \quad (6.4)$$

If the dependence of \tilde{t} on $(\mathbf{k}, \mathbf{k}')$ is through the momentum transfer $\mathbf{k} - \mathbf{k}'$, then one can perform the inverse Fourier transform in eq. (6.3) and one gets a convolution integral

$$\Sigma^*(\mathbf{r}) = \int d^3 r' \rho(\mathbf{r}') t(\mathbf{r} - \mathbf{r}'), \quad (6.5)$$

with

$$t(\mathbf{r}) = \int \frac{d^3 q}{(2\pi)^3} e^{-i\mathbf{q} \cdot \mathbf{r}} \tilde{t}(\mathbf{q}). \quad (6.6)$$

Hence, in the case when \tilde{t} depends only on the momentum transfer one gets a local optical potential constructed by convoluting the nuclear density with the range of the interaction $t(\mathbf{r})$. If the typical lengths in the system are large compared with the range of the interaction, then the interaction can be treated as local and one obtains the local density prescription

$$\Sigma^*(\mathbf{r}) = \tilde{t}(\mathbf{k}, \mathbf{k})\rho(\mathbf{r}). \quad (6.7)$$

That is, in order to obtain the self-energy, or optical potential, in a finite nucleus, simply replace $\rho \rightarrow \rho(\mathbf{r})$ in the expression of the self-energy in the infinite system. Alternatively, if the interaction is purely s -wave, its range is zero up to possible off-shell effects [Ga 89] and again the local density prescription of eq. (6.7) is appropriate.

The results of the analysis of [Na 73, 77, 79] indicate that at the energies involved in Σ^- atoms and Σ hypernuclei the processes $\Sigma N \rightarrow \Sigma N$ and $\Sigma N \rightarrow \Lambda N$ are largely dominated by the s -wave contribution. Hence the assumption of a zero range for the amplitude is a very good approximation, which allows one to extract the Σ optical potential in the low density limit from eq. (6.7).

In order to find \tilde{t} , a best fit to the Σ^- atom data is made in [Fe 89] by using the experimental charge distribution for each nucleus, corrected for the proton finite size. In order to do so, a two-parameter Fermi density is used for both, the charge distribution

$$\rho_e(\mathbf{r}) = \frac{\rho_{0,e}}{1 + e^{(r-R_e)/a_e}} \quad (6.8)$$

and the distribution of the centers

$$\rho(\mathbf{r}) = \frac{\rho_0}{1 + e^{(r-R)/a}}. \quad (6.9)$$

By imposing the conditions that must be fulfilled by the convolution [Sa 88a],

$$\rho_0 \approx \rho_{0,e}, \quad \langle r^2 \rangle + r_p^2 = \langle r^2 \rangle_e, \quad \int d^3r \rho(\mathbf{r}) = \int d^3r \rho_e(\mathbf{r}), \quad (6.10)$$

with r_p^2 the mean squared radius of the proton, and using the approximate formulae

$$\langle r^2 \rangle \approx \frac{3}{5}R^2 + \frac{7}{5}\pi^2 a^2, \quad \int d^3r \rho(\mathbf{r}) \approx \frac{4}{3}\pi\rho_0(R^3 + \pi^2 a^2 R), \quad (6.11)$$

one obtains with a good approximation^{*})

$$R \approx R_e + \frac{5r_p^2 R_e}{15R_e^2 + 7\pi^2 a_e^2}, \quad a \approx \left(\frac{R_e^3 + \pi^2 a_e^2 R - R^3}{\pi^2 R} \right)^{1/2}. \quad (6.12)$$

The value $r_p^2 = 0.69 \text{ fm}^2$ is used in the calculations. The best fit of [Fe 89] uses a high precision method to solve the Schrödinger equation with complex potentials [Lo 86] based on the method used for real

^{*}) There is a misprint in the formula for a in eq. (6.13) of [Sa 88a]. The denominator there should read $\pi^2 R$ as in eq. (6.12) above, instead of πR^2 .

potentials in [OS 85b] and a hybrid of the gradient and quadratic interpolation methods [Be 69] for the χ^2 fit. The usual nucleus finite size and vacuum polarization corrections to the Coulomb potential [Ba 70] are implemented.

By using the same notation as in eq. (2.16), the results of the best fit are (with $\rho_0 = 0.17$ fm)

$$\begin{aligned} V_{\text{opt}}(\mathbf{r}) &= -U(\mathbf{r}) - iW(\mathbf{r}), \\ U(\mathbf{r}) &= (31 \pm 4)\rho(\mathbf{r})/\rho_0 [\text{MeV}], \quad W(\mathbf{r}) = (15 \pm 2)\rho(\mathbf{r})/\rho_0 [\text{MeV}]. \end{aligned} \quad (6.13)$$

These results are in agreement with those of the best fit of [Ba 78]. The imaginary part is the same and the real part is 10% bigger here than in [Ba 78].

We should note that the strength of the potential depends strongly on the radii assumed for the nuclei. In [Ha 88a], the radius $R = 1.27A^{1/3}$ [fm] and diffuseness $a = 0.67$ fm in a two parameter Fermi distribution, as eq. (6.8), are used. By means of eqs. (6.10) and (6.11) this leads to a charge mean squared radius $\langle r^2 \rangle_e = 0.97A^{2/3} + 13.82a^2 + 0.69$ [fm²], which gives root mean square radii about 1 fm larger than the experimental results [Ja 74] for the nuclei of the Σ^- atomic states analyzed in [Ba 78]. With this density distribution the strength of the optical potential obtained providing the best fit for the Σ^- states is $U = 10\rho/\rho_0$ [MeV] and $W = 9\rho/\rho_0$ [MeV].

Although with this potential, and the assumed density distribution, one can describe the Σ^- data and other processes where the Σ might feel nuclear effective densities similar to those of the atoms, like the peripheral reaction (K^- , π^-) studied in [Ha 88a], it is clear that the potential of (6.13) and the one in [Ha 88a] would lead to very different values for the binding and widths of strongly bound Σ states, of the hypernuclear type. This illustrates the importance of taking the proper nuclear distributions in this problem.

Equation (6.13) with the value of 15 MeV for W agrees remarkably well with the low density limit prediction from the experimental results of the $\Sigma N \rightarrow \Lambda N$ reaction of eq. (2.13) and table 2.1. Together with the local density prescription, one had there

$$W \equiv \frac{1}{2} \langle \sigma v_{\text{rel}} \rangle_{\text{av}} \rho_0 / 2 = 14.6 \text{ MeV}, \quad (6.14)$$

versus 15 ± 2 from the fit, which provides a check of consistency for the local density prescription used here. The results of the real part, U , of eq. (6.13) are also consistent [Fe 89] with the analysis of [Na 73, 77, 79] for the $\Sigma^- N \rightarrow \Sigma^- N$ reaction.

In tables 6.1 and 6.2 we write down the theoretical values obtained for some selected Σ^- states. In table 6.1 the ‘‘atomic’’ states are computed, while table 6.2 contains the states of ‘‘hypernuclear’’ character, although obviously there is a gradual transition from one to the other. The results shown there are for the potential of eq. (6.13) and for the potential

$$U(\mathbf{r}) = 31\rho(\mathbf{r})/\rho_0 [\text{MeV}], \quad W(\mathbf{r}) = \frac{15}{5.2} \arctg(5.2 \rho(\mathbf{r})/\rho_0) [\text{MeV}], \quad (6.15)$$

where the form of $W(\mathbf{r})$ is chosen to reproduce the results of fig. 4.7 with an analytical formula. In table 6.1 one can observe a fair reproduction of the experimental data [Ba 78] of about the same quality with both the linear potential of eq. (6.13) or the saturating potential of eq. (6.15). However, for more strongly bound Σ^- states the difference in the shifts and specially in the widths become more apparent, particularly in the hypernuclear states as shown in tables 6.2, 6.3, and 6.4. In table 6.2 we show the

Table 6.1

Binding energies and widths for Σ^- atoms in different nuclei. In parentheses, below the binding energy, is the shift (Coulomb energy minus total energy). The results are shown with the linear potential of eq. (6.13) and with the saturating potential of eq. (6.15). The experimental points are from [Ba 78]. All numbers are in keV.

		5g		4f		3d	
		B (shift)	Γ	B (shift)	Γ	B (shift)	Γ
^{12}C	linear					115.726 (0.025)	0.043
	saturating					115.731 (0.030)	0.032
^{16}O	linear			118.468 (0.001)	4.1×10^{-4}	211.224 (0.306)	0.853
	saturating			118.468 (0.001)	3.4×10^{-4}	211.377 (0.459)	0.724
	experiment				$(10^{+17}_{-4}) \times 10^{-4}$	(0.32 \pm 0.23)	
^{24}Mg	linear	174.885	4.96×10^{-5}	273.596 (0.029)	0.049		
	saturating	174.885	4.4×10^{-5}	273.601 (0.034)	0.038		
	experiment		$(11 \pm 9) \times 10^{-5}$	(0.025 \pm 0.040)	< 0.07		
^{27}Al	linear	206.446	1.4×10^{-4}	323.004 (0.061)	0.119		
	saturating	206.446	1.2×10^{-4}	323.021 (0.078)	0.090		
	experiment		$(2.4 \pm 0.6) \times 10^{-4}$	(0.068 \pm 0.028)	0.043 \pm 0.075		
^{28}Si	linear	239.859	3.3×10^{-4}	375.335 (0.150)	0.274		
	saturating	239.859	2.8×10^{-4}	375.383 (0.167)	0.222		
	experiment		$(4.1 \pm 1.0) \times 10^{-4}$	(0.159 \pm 0.036)	(0.22 \pm 0.111)		
^{32}S	linear	315.110 (0.002)	1.99×10^{-3}	493.311 (0.373)	1.244		
	saturating	315.110 (0.002)	1.66×10^{-3}	493.630 (0.692)	1.199		
	experiment		$(1.5 \pm 0.8) \times 10^{-3}$	(0.36 \pm 0.22)	0.87 \pm 0.70		

energies and widths of the Σ^- hypernuclear states for several nuclei with both potentials. With the linear potential one finds $1s$ and $2p$ states (in the atomic nomenclature) with binding energies ranging from 14 MeV in ^{12}C to 28 MeV in ^{32}S for the $1s$ state and 4 MeV in ^{16}O to 16 MeV in ^{32}S for the $2p$ state. The interesting thing to observe there is that the widths range from 21 MeV in ^{12}C to 27 MeV in ^{32}S for the $1s$ state and from 14 MeV in ^{16}O to 23 MeV in ^{32}S for the $2p$ state. Since the widths are larger than the separation energies this would rule out the observation of these states. In order to facilitate the comparison between the tables, we follow the atomic nomenclature. Thus ^{16}O in the table indicates that we have a Σ^- orbiting an ^{16}O nucleus, irrespective of the atomic or hypernuclear character of the state. In tables 6.3 and 6.4 we also mean that we have a Σ^0 or a Σ^+ orbiting a certain nucleus.

The results with the saturating potential are rather different. The widths are reduced by about a factor 3 for light nuclei and about 3.5 for the most strongly bound states in medium nuclei. The widths range now from 4 MeV to 8 MeV for the $2p$ and $1s$ states of all the nuclei in table 6.2. The binding energies increase a bit with respect to the linear potential because the absorptive part of the potential ($\text{Im } \Sigma^*$) acts as a repulsive force and the saturation makes this repulsion less effective. As a

Table 6.2
Binding energies and widths of different Σ^- hypernuclear states in different nuclei calculated with the linear and the saturating potentials. All numbers are in keV.

		2s		2p		1s	
		B	Γ	B	Γ	B	Γ
^{12}C	linear					14213	20655
	saturating			1670	4100	14861	6873
^{16}O	linear			3900	14000	16572	20724
	saturating			5010	5400	17049	7043
^{24}Mg	linear			10030	18250	21717	23120
	saturating	2102	2012	10850	6530	22079	7360
^{27}Al	linear	1148	10700	13800	23310	27208	28895
	saturating	3674	3580	14700	7060	27636	7683
^{28}Si	linear	1380	9810	13300	20700	24716	24920
	saturating	3596	3470	14000	6890	25039	7504
^{32}S	linear	3622	13100	16040	22700	27581	26857
	saturating	5551	4560	16740	7140	27896	7628

consequence one can see now that the widths are smaller by a fair amount than the separation energies, which should make these states observable. To this structure of levels one would have to add the normal one of nuclear excitations, which could add difficulties to the interpretation of some states. In table 6.2 we have also shown a few 2s levels with similar characteristics as discussed above. As we go to heavier nuclei the widths of the most strongly bound states reach a saturation limit of about 7.5 MeV and a binding energy of around 28 MeV. When we go to even heavier nuclei more bound states of the hypernuclear type will appear and necessarily the separation energy becomes smaller. This simply tells us that for these nuclei the observability of the hypernuclear states would become gradually more difficult. On the other hand, by following the trend of the table, the 1s state of nuclei lighter than ^{12}C should also be clearly differentiable. The 2p state of lighter nuclei should be more difficult to distinguish. Indeed, in ^{12}C we can see that the half width is larger than the binding energy and hence the state would overlap with all the other “atomic” Σ^- states and the continuum.

In table 6.3 we show the results for a Σ^0 obtained using the same strong potentials but killing the Coulomb interaction. The features are similar to those for Σ^- states. However, the “atomic” states disappear and there are only a few bound states. We show in the table only the 1s and 2p states. For ^{12}C the 2p state disappears. The conclusions are similar: the binding energies are smaller than for the Σ^- states and the widths are of the same order of magnitude. With bigger separation energies than widths (with the saturating potential) the states should be observable.

Finally in table 6.4 we show the results for the Σ^+ states obtained by adding the repulsive Coulomb potential to the strong one. The widths obtained are similar but the bindings are reduced appreciably with respect to the Σ^- states. The 2p state of ^{24}Mg already disappears. The separation of the states is still larger than the widths and the states should be observable.

As we mentioned at the end of section 4.2, we should expect slightly smaller widths than those calculated here because the G matrix would be somewhat reduced as we go to higher densities with respect to the one used here.

Now we turn to the light systems, particularly the ^4_2He state of [Ha 88b]. As we mentioned in the Introduction, the width of the state was about 4.6 MeV and the binding 3.2 MeV if it corresponds to a Σ^+ or 6.2 MeV if it corresponds to a Σ^0 .

Table 6.3
Same as table 6.2 for Σ^0 states.

		2p		1s	
		B	Γ	B	Γ
^{12}C	linear			10466	20282
	saturating			11170	6781
^{16}O	linear			11972	20365
	saturating	1161	4988	12518	6958
^{24}Mg	linear	4264	17492	15418	22755
	saturating	5270	6296	15848	7294
^{27}Al	linear	7256	22562	20152	28517
	saturating	8372	6894	20649	7638
^{28}Si	linear	6617	19939	17527	24555
	saturating	7515	6708	17916	7447
^{32}S	linear	8549	21985	19514	26476
	saturating	9410	6982	19897	7579

Table 6.4
Same as table 6.2 for Σ^+ states.

		2p		1s	
		B	Γ	B	Γ
^{12}C	linear			6695	19864
	saturating			7512	6666
^{16}O	linear			7395	19958
	saturating			8029	6850
^{24}Mg	linear			9155	22331
	saturating			9672	7208
^{27}Al	linear	795	21697	13128	28087
	saturating	2149	6655	13715	7581
^{28}Si	linear	20	19088	10379	24126
	saturating	1146	6431	10857	7372
^{32}S	linear	1113	21133	11493	26028
	saturating	2196	6754	11969	7513

For very light nuclei one would have to consider, amongst other elements, that the number of neutrons and protons could be quite different and both the real and imaginary parts of the potential would be changed. Indeed, in the (K^-, π^-) reaction on ^4He we either form a $\Sigma^0 npp$ or a $\Sigma^+ pnn$ system. In the Σ^0 case the Σ^0 can be combined with either of the nucleons to produce ΛN . In the $\Sigma^+ pnn$ system the transition $\Sigma^+ n \rightarrow \Lambda p$ can take place. Because of isospin factors, the annihilation strength will be proportional to $2 \times \frac{2}{3}$ in the $\Sigma^+ pnn$ system versus $3 \times \frac{1}{3}$ in the $\Sigma^0 npp$. On the other hand, in the (K^-, π^+) reaction we will form the $\Sigma^- nnp$ system. Here the Σ^- can only be annihilated with the proton and its strength will be proportional to $1 \times \frac{2}{3}$. This counting, together with the value for $W(r)$, leads to the following values for $W(r)$ in the present case:

$$W(r) = 20\rho/\rho_0 [\text{MeV}] \quad \text{for } \Sigma^+ pnn, \quad (6.16a)$$

$$W(r) = 15\rho/\rho_0 [\text{MeV}] \quad \text{for } \Sigma^0 npp, \quad (6.16b)$$

$$W(r) = 10\rho/\rho_0 [\text{MeV}] \quad \text{for } \Sigma^- pnn, \quad (6.16c)$$

although only the first one, eq. (6.16a), has a firm basis since the two neutrons on which the Σ^+ annihilates saturate a spin shell. The real parts are difficult to assess from existing $\Sigma N \rightarrow \Sigma N$ models, given the difference in spin dependence between them (see, for instance, the $T = 3/2$, $S = 0, 1$ scattering lengths in the models of [Na 73, 77, 79]). In [Fe 89] a fit to the binding energy of the Σ^+ and Σ^0 states is conducted with $W(r)$ given by eqs. (6.16) and $U(r)$ free in order to get the proper binding. The Coloumb potential is added in all cases as in the former analysis. The fits are done with $W(r)$ from eqs. (6.16) and their saturating versions, as in eq. (6.15). The results can be summarized as follows:

(i) The $1s$ state of the $\Sigma^+ pnn$ system can be bound by about 3 MeV with the saturating potential and $U(r) \sim 45\rho/\rho_0$ [MeV], with a width $\Gamma \approx 5.6$ MeV. Trying to fit the binding energy with the linear potential requires $U(r)$ to be bigger than above and leads to widths of $\Gamma \approx 16$ MeV, which would be too big compared with experiment.

(ii) The $1s$ state of the $\Sigma^0 npp$ system can be bound by about 6 MeV with the saturating potential and $U(r) \sim 53\rho/\rho_0$ [MeV], with a width $\Gamma \approx 5$ MeV. Once again the linear potential would require a larger $U(r)$ and would give widths $\Gamma \approx 15$ MeV, too large compared with the experiment.

(iii) The $\Sigma^- nnp$ system would be bound by 3.2 MeV with $U(r) = 43\rho/\rho_0$ [MeV], with a width $\Gamma \approx 2.6$ MeV. The non-existence of a hypernuclear state (other than the Σ^- atomic states with $B < 100$ keV, for instance) would require $U(r) < 24\rho/\rho_0$ [MeV]. The $\Sigma^- nnp$ potential found in [Ha 89b] has indeed a very weak attraction compared to the Σ^+ or Σ^0 cases.

The interesting thing of this analysis is that, provided that enough attraction exists to bind a Σ^+ (or with more difficulty a Σ^0) with the binding observed in the experiment of [Ha 88b], the width has indeed the right magnitude provided that the saturating potential for $W(r)$ is used, but it would be too large if the linear potential is used. In the analysis of [Ak 86, Ha 89a, 89b], the authors find a bound state of $B = 2.3$ MeV and $\Gamma = 4.6$ MeV for the $T = 1/2$ combination of the Σ^+ , Σ^0 state, but none for the $T = 3/2$ state because of the very different Σ nuclear potentials in the two cases. Hence there is no bound state for the $\Sigma^- nnp$ system (excluding the tritium Σ^- atomic states, one must assume). On the other hand, the mechanism to reduce the width with respect to the results of an ordinary potential is based on the choice of the ΣN elementary potential. There a repulsive core of 5000 MeV is taken, but the authors also notice a weak dependence of χ^2 on the strength of the repulsive core in their best fit to the ΣN data. With this repulsive force, a corresponding repulsion at central densities is found for the $\Sigma(3N)$ system. This pushes the Σ wave function to the exterior of the nucleus, reduces the overlap with the nucleons and consequently reduces the Σ width. An analysis without the short range repulsion, leading to the same binding, provides $\Gamma \approx 8$ MeV.

It is clear that with the limited amount of data on the ΣN system it is difficult to assess the amount of repulsion at short distances (it is even difficult in the NN system with large amounts of information) but the analysis of [Ha 89a, 89b] shows that the presence of a repulsive core leads to smaller widths than with ordinary potentials for the Σ states of light nuclei. We have seen that the saturation in $\text{Im } \Sigma^*$ leads to the same results. What would then happen if in addition one had an appreciable hard core in the ΣN interaction? For very light nuclei this creates a central depletion in the Σ wave function and the Σ is pushed more to the surface of the nucleus. However, this is not the case in infinite nuclear matter and in medium and heavy nuclei, where the sizes are larger than the range of the elementary ΣN potential.

Indeed, the ingredient needed there to construct the Σ -nucleus optical potential is the $\Sigma N \tilde{t}$ matrix, not the elementary potential [see eq. (6.1)] and in the \tilde{t} matrix the effects of the repulsive core have already been incorporated. Since the \tilde{t} matrix information is available from experiment, one can do an accurate analysis of hypernuclear states in medium and heavy nuclei by using the experimental information, as we have done here, without the need of an extra analysis to deduce the ΣN elementary potential.

In light nuclei things are different as shown in [Ha 89a] and there is some residue of the short range ΣN repulsion in the pushing of the Σ towards the surface of the nucleus. If in addition one has the saturating effects in the imaginary part of the optical potential, these effects would be drastically reduced if the Σ is appreciably pushed outside the nucleus, since the saturation is density dependent. If the repulsion is smaller, the overlap of the Σ with the nucleus is larger and the saturation reduces the width. We can see that both mechanisms are compensatory and it is difficult to assess which can be the main reason for the narrow widths in light hypernuclei.

For medium and heavy nuclei, as we have discussed, the strong ΣN repulsion would have no repercussion in reducing the Σ width, but the saturation in the imaginary part of the optical potential does indeed reduce the widths, as we have seen throughout.

The approach of [Ha 89b] has been extended to heavy nuclei, where we can compare with our analysis. As mentioned before, in heavy nuclei the repulsive short range force should have no repercussion in the optical potential since the \tilde{t} matrix contains the information needed. With the same model of [Ha 89b] the Σ -nucleus optical potential for ^{208}Pb has been constructed in [Kh 89]. Since no quenching mechanism is introduced, except for the Pauli blocking, one should expect a potential like the one in eq. (6.13) with $W \approx 15\rho/\rho_0$ MeV reduced by about 25% at $\rho \approx \rho_0$ ($W \approx 11$ MeV at $\rho = \rho_0$). Instead, $W = 6$ MeV is obtained at central densities in [Kh 89]. In view of these discrepancies we think that it would be advisable to carry out further checks of consistency in the approach of [Ha 89b, Kh 89] to see what cross section the model provides for the $\Sigma N \rightarrow \Lambda N$ reaction and how it explains the data of Σ^- atoms, the checks of consistency that we have emphasized throughout this paper.

In finishing this section we would like to establish a connection with the situation in pionic atoms. It has long been known that some states in medium and heavy nuclei have shifts, and especially widths, in clear disagreement with standard optical potentials [Ko 79, 87b, Ol 85, Se 88]. One may wonder whether some mechanism similar to the one producing saturation in the optical potential could explain these anomalies. Actually, as noted in [Ta 84], such saturation properties should also appear in the p -wave part of the pion nucleus optical potential, because of the corresponding saturation properties in the imaginary part of the Δ self-energy [Ta 84, OS 87]. (Note that the $\Delta N \rightarrow NN$ interaction also requires the exchange of a $T = 1$ object.) The effects of this saturation in pionic atoms were checked in [Ta 84], with the observation that, while the bulk of states were unaffected, one obtained a small reduction of the $3d$ widths and a smaller increase in the $4f$ widths. The persistence of the pionic anomalies and the measurement of more anomalous states stimulated a reanalysis of the problem [Ni 89] along the lines of [Ta 84], but including isospin effects, a proper resonant structure in the p -wave part of the potential, different proton and neutron densities, etc. The result of it is a new fit to the pionic atoms, with much of the input theoretical, and still providing a much better fit than the standard Ericson-Ericson potential [EE 66] with all the parameters free. The most striking thing is the disappearance of the anomalies. At the same time it gives predictions for strongly bound states in heavy nuclei with widths about one half of those predicted with the standard potential [TY 88]. The measurements of such states in the (n, p) reactions, now running at TRIUMF [TY 88], or with other possible reactions such as $(\gamma, \pi^+\pi^-)$, $(\pi^-, \pi^+\pi^-)$ or $(e, e'\pi^-)$ with the final π^- bound, will be very useful to understand both the problem of the pionic anomalous atoms as well as the problem of the narrow Σ widths.

7. Λ decay in nuclei: introduction

Chrien in [Ch 87] distinguishes three periods in the history of Λ hypernuclei. The “early period” opened with the discovery of the first hypernucleus in a nuclear emulsion in 1952 [DP 53], and includes the studies of Λ hypernuclei carried out in emulsions in the decade following this discovery. A review of that work can be found in [Te 62]. The “middle ages” period contains the work done in the 60’s and 70’s and early 80’s with the (K^-, π^-) reaction. With a momentum of the kaons around 550 MeV/ c one transfers little momentum to the nucleus in the



reaction. In this way, one gives more chance to the Λ to be trapped by the nucleus, therefore increasing the production cross section. The reaction is most effective populating substitutional states, where the Λ replaces a neutron in the same orbit. However, since both K^- and π^- are strongly absorbed in the nucleus, this reaction populates specially the less strongly bound levels. Most of the work was carried out by collaborations at CERN and Brookhaven. Reviews of this work can be found in [Po 76, Ch 86, Sp 88]. The “modern era” would be signaled by the introduction of the associate production reaction (π^+, K^+) to produce Λ hypernuclei [Mi 85],



This reaction has the advantage that the K^+ is not much distorted in the nucleus and thus the reaction offers more possibilities to populate deeply bound states of the nucleus. The reaction has proved very successful to produce Λ bound states over the whole periodic table [Ch 88]. A typical spectrum is shown in fig. 7.1. The cross section for the elementary reaction $\pi^+ + n \rightarrow \Lambda + K^+$ peaks near 1050 MeV/ c . The corresponding momentum transfer for nuclear conversion of 1050 MeV/ c pions is about 350 MeV/ c at forward angles and is suited to populate states of high spin. Since the spin-flip amplitude is small, one populates the natural parity states where $l_n + l_\Lambda + J = \text{even}$. A theoretical study of these reactions has been carried out in [Do 80, BM 86].

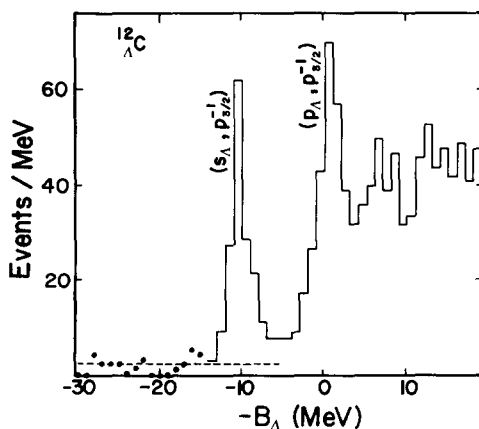


Fig. 7.1. ${}^{12}_\Lambda\text{C}$ production spectrum from the reaction ${}^{12}\text{C}(\pi^+, K^+){}^{12}_\Lambda\text{C}$. Data from [Ch 88].

With respect to the decay of Λ hypernuclei, unlike the case of Σ hypernuclei where the $\Sigma N \rightarrow \Lambda N$ channel allows the Σ to decay strongly in the nucleus, in the case of the Λ there is no other strange baryon with smaller mass than the Λ . Consequently, there is no strong reaction through which a Λ bound in the nucleus could decay. Energetically the $\Lambda N \rightarrow NN$ reaction is possible but it proceeds via weak interaction since $\Delta S = 1$. The weak channel of the Σ in the nucleus becomes negligible in the presence of the strong $\Sigma N \rightarrow \Lambda N$ decay mode. However, for the case of the Λ both the $\Lambda \rightarrow N\pi$ and the $\Lambda N \rightarrow NN$ decay modes involve weak interactions and might be of comparable strength. We refer to these channels as the mesonic and non-mesonic Λ decay channels, respectively.

Early calculations of the mesonic width for light hypernuclei were done by [Da 58, DL 59]. A peculiar thing about the mesonic decay is that, since there is little energy left in the $\Lambda \rightarrow N\pi$ decay, the nucleon carries little energy and there is a large overlap between this nucleon wave function and occupied states of the nucleus. As a consequence, the Pauli blocking is very effective in reducing the Λ mesonic width, which is considerably reduced in heavy nuclei with respect to the free Λ width.

The possibility of the non-mesonic decay was also realized early [CP 53] and received further attention in [RK 56, BD 63, Ad 67]. A series of emulsion and bubble chamber experiments [Mo 74] showed early that the non-mesonic channel dominated the Λ decay in the nuclei (see a selection of results in fig. 7.2). Similar measurements showed that the total Λ width in nuclei oscillates between one and three times the Λ free width [Ni 76, Ke 73, Bo 70, PS 69, Ke 70, PS 64] as can be seen in fig. 7.3, which already contains the result of the more recent experiment of [Gr 85].

Direct measurements of decay rates have proven difficult and had to await better kaon beams and improved experimental techniques as described in [Gr 85, Ba 86, Sa 88b]. The measurement of hypernuclei lifetimes in \bar{p} induced reactions has also proved feasible, although currently it is less precise than for other reactions [Po 88].

In coming chapters we discuss the theoretical framework to deal with the mesonic and non-mesonic Λ decay in nuclei and the different approaches used in the literature. As we shall see, the mesonic decay is quite sensitive to details of nuclear structure and to the pion properties inside nuclei. The non-mesonic decay seems more insensitive to the different ingredients in the $\Lambda N \rightarrow NN$ transition, but selected quantities like the ratio of proton to neutron induced Λ decay prove rather sensitive to these details and promises to be, in conjunction with other quantities, an important tool to investigate weak forces in nuclei.

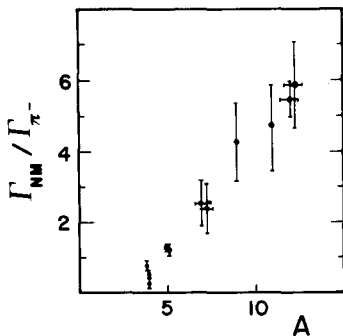


Fig. 7.2. Selected experimental data for $\Gamma_{nm}/\Gamma_{\pi^-}$ as a function of the mass number from [Mo 74].

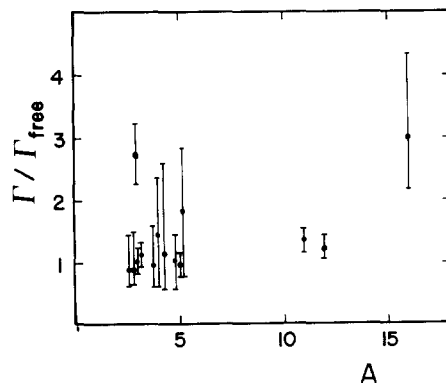


Fig. 7.3. Experimental data for $\Gamma_{total}/\Gamma_{free}$ from [Gr 85, Ni 76, Ke 73, Bo 70, PS 69, Ke 70, PS 64].

8. Formal derivation of the Λ width in nuclei

8.1. The Λ free decay

We start from an effective interaction Lagrangian which accounts for the $\Lambda \rightarrow \pi N$ weak decay given by

$$\mathcal{L}_{\pi\Lambda N} = G\mu^2 \bar{\psi}_N (A - B\gamma_5) \boldsymbol{\tau} \cdot \boldsymbol{\phi}_\pi \psi_\Lambda + \text{h.c.} , \quad (8.1)$$

with G the weak coupling constant,

$$(G\mu^2)^2/8\pi = 1.945 \times 10^{-15} , \quad (8.2)$$

and

$$A = 1.06 , \quad B = 7.10 . \quad (8.3)$$

In this equation we are artificially assuming the Λ to behave as the state $|1/2 \ -1/2\rangle$ of an isospin doublet with $T=1/2$. This, together with the inclusion of the $\boldsymbol{\tau}$ operator, is a practical way to implement the $\Delta T=1/2$ rule in this decay [MG 84], which tells us that the channel $\Lambda \rightarrow \pi^- p$ is twice more probable than the $\Lambda \rightarrow \pi^0 n$. Equation (8.1) contains an s -wave, parity violating part (A term) and a p -wave parity conserving part (B term).

We will first evaluate the free Λ width in a way that makes straightforward the evaluation of the Λ width in the nuclear medium. Once again we use the formula

$$\Gamma = -2 \text{Im} \Sigma^* \quad (8.4)$$

and look at the Λ self-energy from the diagrams of fig. 8.1.

We shall work with the non-relativistic reduction of eq. (8.1), which provides a vertex for $\Lambda \rightarrow N\pi$ with π momentum \mathbf{q} ,

$$\delta \tilde{H}_{\Lambda N \pi} = -G\mu^2 [S - (P/\mu) \boldsymbol{\sigma} \cdot \mathbf{q}] \tau^\lambda , \quad (8.5)$$

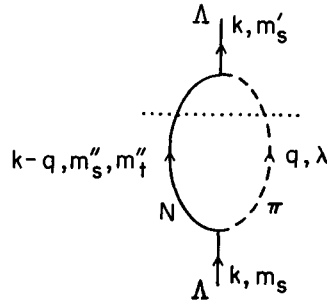


Fig. 8.1. Feynman graph for the free Λ self-energy of eq. (8.7). The $\Lambda \rightarrow \pi N$ "cut" is shown (dotted line).

with

$$S = A = 1.06, \quad P \equiv B\mu/2M = 0.527. \quad (8.6)$$

The Λ self-energy corresponding to the diagram of fig. 8.1 is given by

$$\begin{aligned} -i\Sigma^*(k) &= \int \frac{d^4q}{(2\pi)^4} (-i)^2 (G\mu^2)^2 \langle m'_s | S - (P/\mu) \boldsymbol{\sigma} \cdot \mathbf{q} | m''_s \rangle \langle m''_s | S - (P/\mu) \boldsymbol{\sigma} \cdot \mathbf{q} | m_s \rangle \\ &\quad \times \langle m_t = -\frac{1}{2} | \tau^\lambda | m'_t \rangle \langle m''_t | \tau^\lambda | m_t = -\frac{1}{2} \rangle \\ &\quad \times \frac{i}{k^0 - q^0 - E(\mathbf{k} - \mathbf{q}) + i\epsilon} \frac{i}{q^{02} - \mathbf{q}^2 - \mu^2 + i\epsilon}, \end{aligned} \quad (8.7)$$

with (k^0, \mathbf{k}) the four momentum of the Λ and $E(\mathbf{k} - \mathbf{q})$ the relativistic nucleon energy.

The q^0 integration in (8.7) is performed easily by closing the contour over the lower half of the q^0 complex plane and we obtain

$$\begin{aligned} \Sigma^*(k) &= 3(G\mu^2)^2 \int \frac{d^3q}{(2\pi)^3} \{ [S^2 + (P^2/\mu^2)q^2] \delta_{m_s, m'_s} - 2S(P/\mu) \langle m'_s | \boldsymbol{\sigma} \cdot \mathbf{q} | m_s \rangle \} \\ &\quad \times \frac{1}{2\omega(\mathbf{q})} \frac{1}{k^0 - \omega(\mathbf{q}) - E(\mathbf{k} - \mathbf{q}) + i\epsilon}, \end{aligned} \quad (8.8)$$

with $\omega(\mathbf{q})$ the pion energy.

We will not consider the term linear in $\boldsymbol{\sigma}$, which vanishes both for a Λ at rest and for a Λ in its ground state in the nucleus, which we shall study later on. A full relativistic treatment would show that this interference term between s - and p -waves vanishes identically in the integral of the free Λ self-energy.

By evaluating the imaginary part of eq. (8.8) and using (8.4) we obtain the free width for a Λ at rest,

$$\Gamma_{\text{free}} = 6(G\mu^2)^2 \frac{1}{4\pi} \frac{Mq_{\text{cm}}}{M_\Lambda} [S^2 + (P^2/\mu^2)q_{\text{cm}}^2], \quad q_{\text{cm}} = \frac{\lambda^{1/2}(M_\Lambda^2, M^2, \mu^2)}{2M_\Lambda}, \quad (8.9)$$

where the relativistic factor M/E has been implemented in eq. (8.8) for simplicity. This expression reproduces the Λ mean life of 2.63×10^{-10} s.

8.2. Pauli blocking effects

Before a more elaborate derivation is given in a coming section we show here an easy derivation of the Pauli effect.

In nuclear matter, provided that k^0 is bigger than $\mu + E(k_F)$, where k_F is the Fermi momentum, the Λ can also decay into a pion and a nucleon. One has to take the particle part of the nucleon propagator in eq. (8.7), forcing the nucleons to be above the Fermi surface. Hence the formula for the Λ decay into πN is given by eq. (8.8) including a multiplicative factor $1 - n(\mathbf{k} - \mathbf{q})$ in the integrand. If we assume the Λ to be at rest and enforce $k^0 = \omega(\mathbf{q}) + E(\mathbf{q})$, which makes zero the argument of the δ function in

Im Σ^* from eq. (8.8), one obtains $|\mathbf{q}| = 100 \text{ MeV}/c$. In normal nuclear matter the Fermi momentum is $k_F = 268 \text{ MeV}/c$ and hence the factor $1 - n(\mathbf{q})$ would be zero. Thus there would be no pionic decay of the Λ in normal nuclear matter.

In finite nuclei the situation is different and the mesonic decay is observed [Mo 74, DW 82, Gr 85]. Two reasons should be mentioned: In the first place the Λ in its ground state does not have zero momentum but it has a certain momentum distribution. This already favors the mesonic decay because it gives more chances to the nucleon to have larger momenta. The second reason is that the nucleus does not have a constant density, and as we approach the nuclear surface the local Fermi momentum becomes smaller, giving the Λ more chances to decay through the mesonic channel.

It is interesting to calculate the Λ mesonic width (Γ_m) as a function of the nuclear density with the procedure outlined before. We show the results in fig. 8.2 for two values of the pion mass, $\tilde{\mu} = \mu$ and $\tilde{\mu} = 0.9\mu$. The reason to show the calculations with two different pion masses is to show the sensitivity to this quantity. Since we know that the pion properties are strongly renormalized in nuclear matter, the results of fig. 8.2 tell us that this should be taken into account in order to have an accurate evaluation of the Λ mesonic width.

In fig. 8.2 we observe a great sensitivity of $\Gamma_m/\Gamma_{\text{free}}$ to the chosen value of the pion mass. At $\rho \approx 0.4\rho_0$ a decrease of 10% in the pion mass increases the mesonic width by a factor two and this factor increases up to infinity as the density approaches a certain value ($\rho \approx 0.48\rho_0$) where there is no more mesonic decay if $\tilde{\mu}$ is equal to the free pion mass. One can also observe in the figure that for $\tilde{\mu} = 0.9$, Γ_m is different from zero up to larger values of ρ than in the case $\tilde{\mu} = \mu$ ($\rho \sim 0.61\rho_0$ in this case).

8.3. Non-mesonic Λ decay

In electromagnetic interactions in nuclei we are used to dealing with exchange currents, the origin of which is shown diagrammatically in fig. 8.3. We start from the $\gamma N \rightarrow \pi N$ interaction, diagram 8.3a. Inside the nuclei, however, the pion can be produced in a virtual state and absorbed by a second nucleon. This is the essence of the electromagnetic exchange currents, the effects of which are well known in nuclear form factors and other reactions [Ar 85].

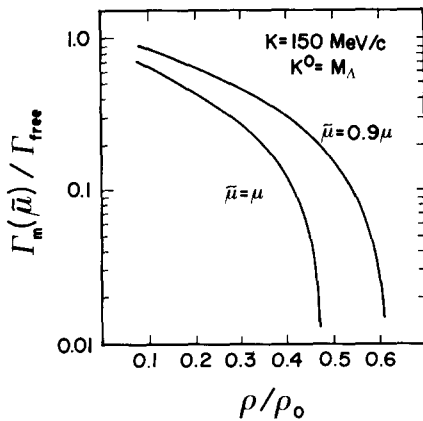


Fig. 8.2. $\Gamma_m/\Gamma_{\text{free}}$ in nuclear matter as a function of the nuclear density calculated for $k_A^0 = M_\Lambda$, $|\mathbf{k}_A| = 150 \text{ MeV}/c$. The results are shown for two different values of the pion mass, $\tilde{\mu} = 0.9\mu$ and $\tilde{\mu} = \mu$.

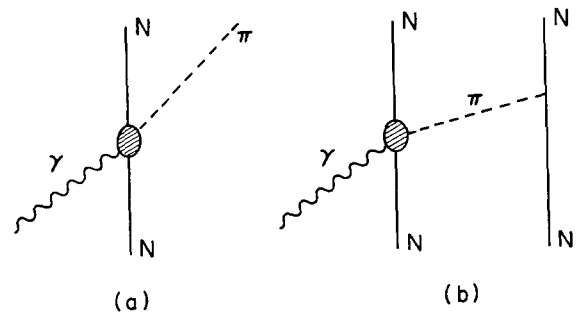


Fig. 8.3. (a) Pion photoproduction mechanism. (b) As (a) but the virtual pion is absorbed by one nucleon (meson exchange current).

This mechanism can immediately be extended to the weak Λ decay into πN . The pion can be produced in a virtual state and then be absorbed by a second nucleon. This is depicted in fig. 8.4. Diagram 8.4a gives rise to the Λ mesonic decay $\Lambda \rightarrow N\pi$, while diagram 8.4b gives rise to the non-mesonic decay, $\Lambda N \rightarrow NN$. The fact that the mesonic decay is so much reduced in a nucleus gives chances to the non-mesonic decay to be the dominant process, as is indeed the case.

In order to proceed to the evaluation of the non-mesonic width coming from diagram 8.4b we proceed as in the case of the Σ decay and evaluate the Λ self-energy corresponding to the diagram of fig. 8.5. By following the standard steps of the Feynman rules as in eq. (8.7), we obtain in terms of the Lindhard function of eq. (4.34) the following result:

$$\Sigma^*(k) = 3i(G\mu^2)^2 \int \frac{d^4q}{(2\pi)^4} [S^2 + (P/\mu)^2 q^2] G_0(k-q) D_0^2(q) F^4(q) \frac{f^2}{\mu^2} q^2 U_N(q), \quad (8.10)$$

with $G_0(k)$ the nucleon propagator,

$$G_0(k) = \frac{1 - n(k)}{k^0 - E(k) + i\varepsilon} + \frac{n(k)}{k^0 - E(k) - i\varepsilon}, \quad D_0(q) = \frac{1}{q^{02} - q^2 - \mu^2 + i\varepsilon}, \quad (8.11)$$

where we have assumed the same form factor, $F(q)$, for the $NN\pi$ and $N\Lambda\pi$ vertices. The q^0 integration can be performed now by means of a Wick rotation as we did to arrive at eq. (5.2) and hence we can write

$$\Gamma_{nm}^{(\text{lowest})}(k) = -6(G\mu^2)^2 \int \frac{d^3q}{(2\pi)^3} [S^2 + (P/\mu)^2 q^2] [1 - n(k-q)] \times \theta(q^0) D_0^2(q) F^4(q) \frac{f^2}{\mu^2} q^2 \text{Im} U_N(q) \Big|_{q^0 = k^0 - E(k-q)}, \quad (8.12)$$

which by means of the approximation of eq. (5.4) for $\text{Im} U_N(q)$ can be easily calculated and cast in the form of eq. (2.13),

$$\Gamma_{nm}^{(\text{lowest})}(k) = \langle \sigma v_{\text{rel}} \rangle_{\text{av}} \rho. \quad (8.13)$$

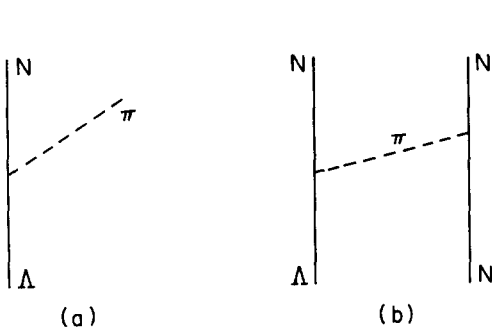


Fig. 8.4. (a) Mesonic decay of the Λ . (b) Non-mesonic decay mechanism mediated by pion exchange.

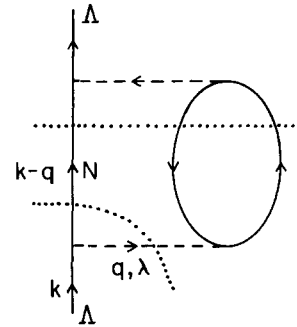


Fig. 8.5. Lowest order Λ self-energy graph. Dotted horizontal line: cut contributing to the Λ non-mesonic width. Curved dotted line: cut contributing to the Λ mesonic width.

Similar approximations to those leading to eq. (2.22) would allow us to write

$$\langle \sigma v_{\text{rel}} \rangle_{\text{av}} = \frac{1}{2\pi} M \bar{q} \bar{\Sigma} |T|^2 P_F(\bar{q}), \quad (8.14)$$

with \bar{q} given by

$$\bar{q} = \sqrt{M(M_A - M)}, \quad (8.15)$$

and

$$\bar{\Sigma} |T|^2 = 3(G\mu^2)^2 \bar{q}^2 [S^2 + (P^2/\mu^2) \bar{q}^2] (f^2/\mu^2) F^4(q) D_0^2(q), \quad (8.16)$$

where T is the $\Lambda N \rightarrow NN$ amplitude, $\bar{\Sigma}$ indicates the average over initial spin and isospin, and $q^0 = \bar{q}^2/2M$. Note that we have neglected the factor $1 - n(\mathbf{k} - \mathbf{q})$ since \bar{q} is about 400 MeV/c, hence bigger than the Fermi momentum, and the factor is inoperative for small values of \mathbf{k} . In the absence of any form factors, eq. (8.13) together with eqs. (8.14)–(8.16) provide at $\rho = \rho_0$, with and without the Pauli blocking, respectively [factor P_F of eq. (8.14)],

$$\frac{\Gamma_{nm}^{(\text{lowest})}}{\Gamma_{\text{free}}} = 4.04, \quad \frac{\Gamma_{nm}^{(\text{lowest})}}{\Gamma_{\text{free}}} = 4.41. \quad (8.17)$$

The first number compares very favorably with the value 4.1 of [MG 84], the value 4.3 of [OS 85a] and the value 3.89 of [Du 86a], all of them obtained with more elaborate calculations. The Pauli blocking factor here is $P_F(\bar{q}) = 0.92$, only 8% away from unity. The Pauli blocking effect is smaller here than in the case of $\Sigma N \rightarrow \Lambda N$ [$P_F = 0.73$ in eq. (2.24)]. The reason is that the momentum \bar{q} is larger here, 407 MeV/c versus 288 MeV/c in the $\Sigma N \rightarrow \Lambda N$ case. If the form factor is considered in (8.16), with $\Lambda = 1250$ MeV we obtain for the ratio $\Gamma_{nm}/\Gamma_{\text{free}} = 2.62$. In a coming section the effect of correlations is introduced reducing this number further.

8.4. Proton and neutron induced non-mesonic Λ decay

In the former analysis we have not distinguished between the $\Lambda p \rightarrow np$ and $\Lambda n \rightarrow nn$ reactions but have made an average over proton and neutron induced Λ decay, which was adequate for symmetric nuclear matter. However, for the model of π exchange Λ non-mesonic decay, a simple counting in the isospin factors provides this ratio. We can see in fig. 8.6 the different isospin combinations and we have added the exchange diagrams of the diagram in fig. 8.5. The different isospin factors are shown here in the order of upper Λ vertex, lower Λ vertex, upper N vertex, lower N vertex. In diagrams (a), (b) and (c) an extra minus sign appears because of the fermion loop. In addition, the spin sum in the exchange terms (c), (d) and (f) is a factor two smaller than in the direct terms. If in addition one sticks to the low density limit and a Λ at rest, which makes the set of propagators equal for the direct and exchange terms, we obtain

$$\frac{\Gamma_p}{\Gamma_n} = \frac{-1 - 4 - \frac{1}{2} \cdot 2 - \frac{1}{2} \cdot 2}{-1 + \frac{1}{2}} = 14. \quad (8.18)$$

the nucleus. In this way the mesonic cut in fig. 8.5 takes into account that the pion is renormalized in the nuclear medium, but only at lowest order since only a single ph excitation is included. As we have seen, the many body formalism tells us that the existence of a non-mesonic Λ decay channel has immediate repercussion on the mesonic Λ width.

However, when renormalizing a pion one must go beyond the lowest order and include the full RPA series. Equivalently one can say that one must consider the ph excitation as a piece of the pion self-energy that renormalizes the pion propagator. In addition, one should then include the Δh excitations, as well as an s -wave pion self-energy and second order corrections to the pion self-energy [Os 82].

The problem is similar to the one found in the evaluation of the Δ self-energy around resonance [OS 87], where one also finds a nuclear correction to the mesonic width and a non-mesonic decay channel corresponding to $\Delta N \rightarrow NN$ (see fig. 8.7a). When this information is used in the related pion-nucleus scattering problem, proceeding through Δh excitation, these two cuts give rise to corrections to the quasielastic scattering (lower cut in fig. 8.7b) and pion absorption (upper cut in fig. 8.7b), respectively.

A proper evaluation of the Λ width also requires a consideration of the different binding of nucleons and Λ . The Λ binding is incorporated in the Λ energy k^0 . The nucleon binding, for calculations done in infinite matter and implemented into finite nuclei through the local density approximation, is better taken into account by means of a local potential $V_N(r)$. The Thomas-Fermi approach is used in [OS 85a],

$$V_N(r) = -(2M)^{-1} \left[\frac{3}{2} \pi^2 \rho(r) \right]^{2/3}, \quad (8.19)$$

where $\rho(r)$ is taken as the empirical density for each nucleus. The nucleon propagator will now be

$$\begin{aligned} G(p) &= \frac{1 - n(p)}{p^0 - E(p) - V_N + i\epsilon} + \frac{n(p)}{p^0 - E(p) - V_N - i\epsilon} \\ &= \frac{1}{p^0 - E(p) - V_N + i\epsilon} + 2\pi i n(p) \delta(p^0 - E(p) - V_N). \end{aligned} \quad (8.20)$$

As mentioned before, in order to incorporate higher order terms of the pion renormalization we must consider the series of diagrams shown in fig. 8.8. The whole series can be summed by dressing the pion

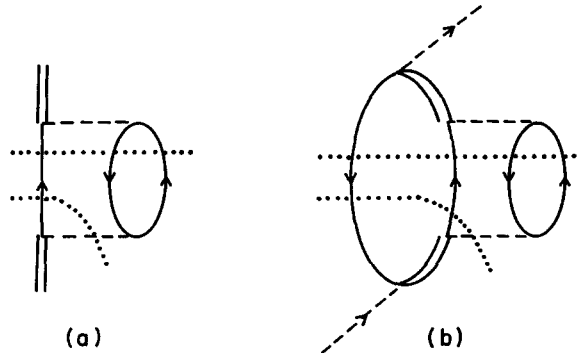


Fig. 8.7. (a) Δ self-energy graph showing the mesonic (curved dotted line) and non-mesonic (horizontal dotted line) decay modes. (b) Pion-nucleus scattering mechanism showing the absorption cut (horizontal dotted line) and a correction to the quasielastic scattering (curved dotted line).

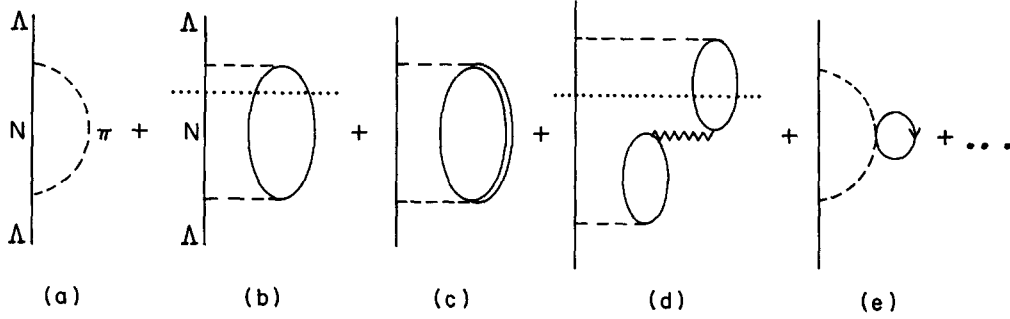


Fig. 8.8. Λ self-energy diagrams included in eq. (8.21). (a) Free self-energy graph. (b), (c) Insertion of p -wave pion self-energy at lowest order. (d) Generic RPA graph. (e) s -wave pion self-energy at lowest order.

with its self-energy in the pion propagator, where, in addition to the p -wave pion self-energy, the s -wave pion self-energy depicted in fig. 8.8e is also included. Hence we have

$$\Sigma^*(k) = 3i(G\mu^2)^2 \int \frac{d^4q}{(2\pi)^4} [S^2 + (P^2/\mu^2)q^2] G(k-q) D(q) F^2(q), \quad (8.21)$$

with $D(q)$ the renormalized pion propagator,

$$D(q) = \frac{1}{q^{02} - q^2 - \mu^2 - \Pi(q^0, \mathbf{q})}, \quad (8.22)$$

and $\Pi(q^0, \mathbf{q})$ the pion self-energy. In order to illustrate the physical content of eq. (8.21) we take the particle part of the nucleon propagator of (8.20) in eq. (8.21) and perform the q^0 integration by closing the contour in the lower half of the complex q^0 plane as shown in fig. 8.9. We get a contribution from the pole of the renormalized pion propagator $q^0 = \tilde{\omega}(\mathbf{q})$ such that

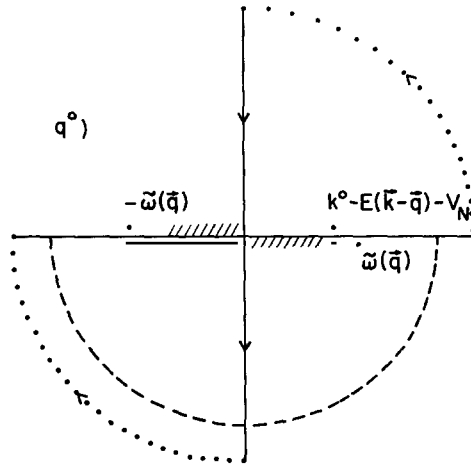


Fig. 8.9. Analytical structure of the integrand of eq. (8.21) in the complex q^0 plane. The renormalized pion propagator pole $\tilde{\omega}(\mathbf{q})$ is shown, as well as the two integration paths considered in the text. The dashed lines close to the real axis indicate the analytical cut from $\text{Im} \Pi(q^0, \mathbf{q})$ related to the non-mesonic Λ decay channel.

$$\tilde{\omega}(\mathbf{q})^2 - \mathbf{q}^2 - \mu^2 - \Pi(\tilde{\omega}(\mathbf{q}), \mathbf{q}) = 0, \quad (8.23)$$

plus the contribution from the continuous set of poles implicit in $\Pi(q^0, \mathbf{q})$ (analytical cut depicted by dashes in the figure) which give rise to $\text{Im } \Pi(q^0, \mathbf{q})$. After the q^0 integration is performed, the imaginary part of Σ^* will appear by taking $\text{Im } G(k - q)$ in the integrand and hence placing the intermediate nucleon on-shell. When this is done, the contribution coming from the pole $\tilde{\omega}(\mathbf{q})$ in the q^0 integration accounts for the mesonic decay width, while the contribution from the cut accounts for the non-mesonic decay width.

However, technically this is implemented more efficiently in a different way, which allows simultaneously for the consideration of the effect of nuclear correlations.

The series implicit in fig. 8.8 can be summed as

$$\begin{aligned} \Sigma^*(k) = & 3i(G\mu^2)^2 \int \frac{d^4q}{(2\pi)^4} G(k - q) [S^2 + (P^2/\mu^2)q_i q_i] F^2(q) \\ & \times \left\{ D_0(q) + \frac{f^2}{\mu^2} F^2(q) D_0^2(q) q_j q_m U(q) \left[\frac{\hat{q}_j \hat{q}_m}{1 - UV_j} + \frac{(\delta_{jm} - \hat{q}_j \hat{q}_m)}{1 - UV_j} \right] \right\}, \end{aligned} \quad (8.24)$$

where V_l, V_t are the ph and Δh effective longitudinal and transverse interactions given by (4.33). Such as it stands, in (8.24) only the longitudinal part in the square bracket contributes but this is not the case when correlations are introduced. The s -wave pion self-energy is added to the pion squared mass in the free pion propagator.

One can account for the effect of nuclear short-range correlations in the same way as in section 4.2. Then

$$\begin{aligned} (f/\mu) S F^2(q) D_0(q) q_j & \rightarrow V'_s \hat{q}_j, \\ (f/\mu) (P/\mu) F^2(q) D_0(q) q_i q_j & \rightarrow V'_l \hat{q}_i \hat{q}_j + V'_t (\delta_{ij} - \hat{q}_i \hat{q}_j), \end{aligned} \quad (8.25)$$

which in the approximation of [OS 85a] read

$$\begin{aligned} V'_s & \approx (f/\mu) S \{ F^2(q) D_0(q) - \tilde{F}^2(q) \tilde{D}_0(q) \} |q| \\ V'_l & \approx (f/\mu) (P/\mu) \{ F^2(q) D_0(q) q^2 + g'_\Lambda \}, \\ V'_t & \approx (f/\mu) (P/\mu) g'_\Lambda, \end{aligned} \quad (8.26)$$

with g'_Λ a quantity playing the same role as g' in the ph or Δh interaction for the p -wave $\Lambda N \rightarrow NN$ interaction. The same transformation must be done for the q_m and the $q_i q_m$ combinations in (8.24) and as a consequence we find

$$\Sigma^*(k) = 3i(G\mu^2)^2 \int \frac{d^4q}{(2\pi)^4} G(k - q) W(q), \quad (8.27)$$

$$\begin{aligned} W(q) = & [S^2 + (P^2/\mu^2)q^2] F^2(q) D_0(q) \\ & + \frac{V'_s{}^2(q) U(q)}{1 - U(q) V_l(q)} + \frac{V'_l{}^2(q) U(q)}{1 - U(q) V_l(q)} + \frac{2V'_t{}^2(q) U(q)}{1 - U(q) V_l(q)}. \end{aligned} \quad (8.28)$$

Given the analytical structure of the integrand of (8.27), we can perform the Wick rotation depicted in fig. 8.9 by a dotted line. Once more the integral along the imaginary axis does not contribute to $\text{Im } \Sigma^*$ and then we obtain

$$\Gamma(k, \rho) = -6(G\mu^2)^2 \int \frac{d^3q}{(2\pi)^3} [\theta(k^0 - E(\mathbf{k} - \mathbf{q}) - V_N) - n(\mathbf{k} - \mathbf{q})] \text{Im } W(q) \Big|_{q^0 = k^0 - E(\mathbf{k} - \mathbf{q}) - V_N}. \quad (8.29)$$

Now one must pay attention to the separation of the mesonic and non-mesonic channels. We have

$$\text{Im} \frac{V_n'^2 U}{1 - UV_m} = \text{Im} \frac{V_n'^2 U (1 - U^* V_m^*)}{|1 - UV_m|^2}, \quad (8.30)$$

where the indices n, m stand for s, l, t of eq. (8.28). The non-mesonic channel, as depicted in fig. 8.8 by the dotted line will come when the ph excitation is placed on-shell, or equivalently from $\text{Im } U_N$ in the numerator of eq. (8.30). Since the pion cannot be on-shell when $\text{Im } U_N \neq 0$ (a real pion cannot excite a ph excitation, or equivalently cannot be absorbed by one nucleon in nuclear matter), V_n', V_m , which eventually contain the free pion propagator, have no singularities when $\text{Im } U_N \neq 0$ and hence no imaginary part. Thus, the non-mesonic contribution comes from substituting

$$\text{Im} \frac{V_n'^2 U}{1 - UV_m} \rightarrow \frac{V_n'^2 \text{Im } U_N}{|1 - UV_m|^2}. \quad (8.31)$$

We have deliberately neglected $\text{Im } U_\Delta$ in the numerator since $\text{Im } U_\Delta$ comes from the Δ width into the πN channel. This would contribute to the Λ mesonic decay channel. The separation of the non-mesonic width from (8.29) is hence straightforward with the prescription of (8.31). On the other hand, one can evaluate the full width from eq. (8.29) and subtract from it the non-mesonic width in order to obtain the mesonic width. Although the expression (8.28) contains double poles from the $D_0(q^2)$ terms, one can easily see that these terms cancel and one is left with the evaluation of terms containing only single poles, the poles of the renormalized pion propagator of eq. (8.22).

The introduction of correlations in the $\Lambda N \rightarrow NN$ interaction introduces new elements in eq. (8.21), which contains only one pion exchange. This has some repercussion in the non-mesonic channel and in principle affects the mesonic channel also since pieces like the one in fig. 8.10 can now contribute to the

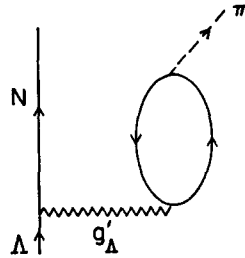


Fig. 8.10. One of the new Λ mesonic decay mechanisms introduced by the $\Lambda N \rightarrow NN$ short-range correlations.

mesonic Λ decay. Pieces like that are suggested also in [Mc 86]. Note that, in any case, the mesonic contribution comes from the poles of the renormalized pion propagator. This pole is not far away from the free pion pole and this means that $D_0(q)$ would be large at the renormalized pion pole and consequently the second terms of V'_s , V'_l in eq. (8.26) would only be small corrections. On the other hand, the term with V'_l does not contribute to the mesonic decay. This means that correlations in the $\Lambda N \rightarrow NN$ transition potential have a very small repercussion in the mesonic channel, a feature established numerically in [OS 85a].

In figs. 8.11 and 8.12 we show the results of [OS 85a] corresponding respectively to the lowest order (diagrams 8.8a,b) and the full induced interaction (all diagrams of fig. 8.8 except those with s -wave pion self-energy), both with correlations included. The results are shown for finite nuclei, where the local density approximation

$$\Gamma = \int |\phi_\Lambda(r)|^2 \Gamma(k, \rho(r)) d^3r \quad (8.32)$$

has been used with an average Λ momentum. The Λ wave function, its energy and the average momentum correspond to the $1s_{1/2}$ state of realistic Λ potentials [Bo 77, 79].

One observes that the effect of the full induced interaction on the non-mesonic width is a decrease of around 25% with respect to the lowest order results. The dependence of the results on g'_Λ is very weak once the induced interaction is used. The most outstanding feature of these results is, however, the dramatic increase of the mesonic width when the induced interaction is used, or equivalently when the pion propagator is properly renormalized. This should come as no surprise after the discussion in section 8.2. We saw there that the mesonic decay is very much reduced due to the Pauli exclusion principle. However, we also observed the sensitivity of the result to the value of the pion mass (fig. 8.2) and saw that the mesonic width increased remarkably as the pion mass decreased. The net effect of the pion self-energy is an attraction, at the energies involved in the $\Lambda \rightarrow N\pi$ decay, and hence we should expect a drastic increase in the mesonic width as is the case.

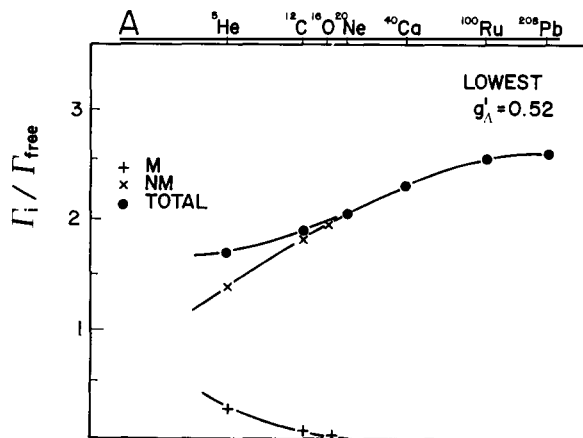


Fig. 8.11. Mesonic, non-mesonic and total Λ widths for several nuclei from [OS 85a]. The calculation does not include the induced interaction. The value of $g'_\Lambda = 0.52$ in eq. (8.26) is used.

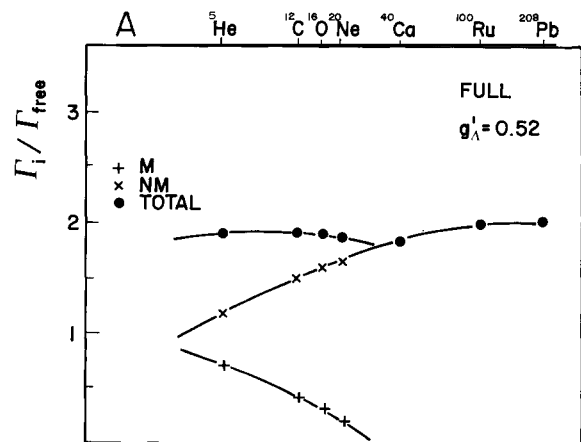


Fig. 8.12. Same as fig. 8.11 but with induced interaction included.

We can envisage this effect in a different way. For a given pion momentum the pion energy is now smaller than the corresponding one from a free pion [$\tilde{\omega}(\mathbf{q}) < \omega(\mathbf{q}) = (\mathbf{q}^2 + \mu^2)^{1/2}$]. Thus, energy conservation will give more energy to the nucleon, which will have more chances to overcome the Fermi energy. Also, the range of allowed values of \mathbf{q} will be larger, hence increasing the phase space for the mesonic decay. The pions from the Λ decay will leave the nucleus unless they are absorbed because their dispersion relation is such that $\tilde{\omega}(\mathbf{q}) > \mu$, and the pion energy is conserved through the nucleus. Similarly the nucleons, which are forced to have an energy over the local Fermi energy, will escape from the nucleus since

$$\mathcal{E}_N = V_N(\mathbf{r}) + \mathbf{k}^2(\mathbf{r})/2M > V_N(\mathbf{r}) + k_F^2(\mathbf{r})/2M = 0, \quad (8.33)$$

with \mathcal{E}_N the nonrelativistic total energy of the nucleon. The last equation in eq. (8.33) is the Thomas–Fermi condition.

Figure 8.13 shows the results of [OS 85a] when an average over the Λ momentum is taken for each nucleus, recoil corrections in the πNN , $\pi\Lambda N$ vertex are considered ($\boldsymbol{\sigma} \cdot \mathbf{q}_{\text{cm}}$ instead of $\boldsymbol{\sigma} \cdot \mathbf{q}$), and the lowest order s -wave pion self-energy is taken into account. The values for $\Gamma_{nm}/\Gamma_{\text{free}}$ range from around 1 for light nuclei to values around 2 for heavy nuclei. The values of $\Gamma_m/\Gamma_{\text{free}}$ range from 0.41 for ^{12}C to about 0.016 for $A \approx 200$.

Experimentally, we have

$$\Gamma^{16\text{O}}/\Gamma_{\text{free}} = 3 \pm 1 \quad (2.0) \text{ [Ni 76] ,}$$

$$\Gamma_{nm}^{12\text{C}}/\Gamma_{\text{free}} = 1.14 \pm 0.2 \quad (1.5) \text{ [Gr 85] ,}$$

$$\Gamma^{12\text{C}}/\Gamma_{\text{free}} = 1.25 \pm 0.18 \quad (1.9) \text{ [Gr 85] ,}$$

which would have to be compared with the numbers provided by the theory written in parentheses. The theoretical results for the non-mesonic channel, which accounts for most of the Λ decay width in ^{16}O , agree well with experiment. However, as we have mentioned before, the fact that the ratio of the p to n

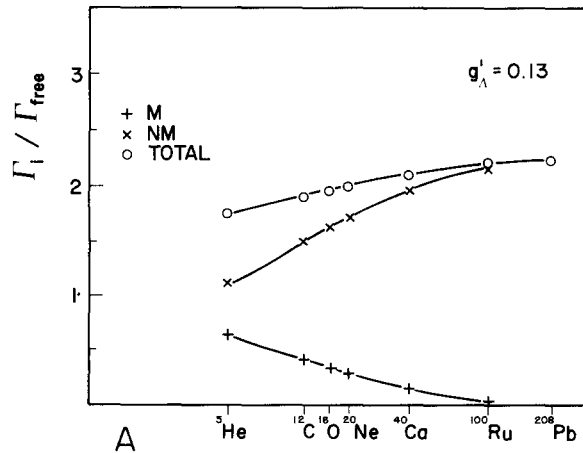


Fig. 8.13. Same as fig. 8.12 but with recoil corrections, averaged over momenta of the Λ in the nucleus and s -wave pion self-energy, included.

Table 8.1

Left: Theoretical results for Γ_m/Γ_{free} from [OS 85a, Os 86]. First row: unrenormalized pions. Second row: renormalized pion. Third row: as second row but with final state interaction. Right: Experimental results for $^{12}_\Lambda\text{C}$ with different assumptions for $\Gamma_\pi/\Gamma_{\pi^0}$ (see text).

Γ_m/Γ_{free}	^{12}C	^{16}O	^{20}Ne		
$\omega = \omega(\mathbf{q})$	0.075	0.033	0.01	[Mo 74]	{ [0.24–0.38]
				[Ju 72]	{ (0.34–0.53)
$\omega = \tilde{\omega}(\mathbf{q})$	0.41	0.37	0.30	[Gr 85]	{ [0.03–0.25]
$\omega = \tilde{\omega}(\mathbf{q}) + \text{fsi}$	0.29	0.26	0.21	[Sa 88a]	{ [0.40–0.85]
					{ (0.27–0.57)

induced Λ decay largely disagrees with the predictions of the π exchange model clearly indicates that there must be other important ingredients in the non-mesonic Λ decay.

With respect to the mesonic decay we write in table 8.1 the experimental results together with the theoretical values in different approximations. The first row contains the numbers obtained for Γ_m/Γ_{free} for free pions. The second row contains those obtained using renormalized pions. The third row contains the results with renormalized pions, reduced by 30% in order to account for pion absorption and charge exchange in the final state interaction of the pions [OS 86].

The experimental results for ^{12}C were obtained as follows. Those of [Gr 85] are from a direct experiment. Those of [Mo 74, Ju 72] are from an average of Γ_{nm}/Γ_π - around $A = 12$, $\Gamma_{nm}/\Gamma_\pi = 5.5 \pm 1.2$, by assuming $\Gamma_{\pi^-} \sim 2\Gamma_{\pi^0}$ and $\Gamma_{nm} = 1.14 \Gamma_{free}$ from [Gr 85]. Finally, those of [Sa 88b] were obtained from a direct measure of the branching ratio Γ_{π^0}/Γ multiplying the ratio by the value $\Gamma = 1.25 \Gamma_{free}$ from [Gr 85]. The numbers in parentheses correspond to the same data assuming that $\Gamma_{\pi^0} \sim \Gamma_{\pi^-}$, as follows from [Mo 88] due to shell model effects. We can observe that there are large discrepancies between different experiments, but (except for the one of [Gr 85]) they seem to support values of Γ_m/Γ_{free} much larger than the one obtained without the pion renormalization, 0.075, and more in agreement with the value obtained with a proper pion renormalization. The theoretical results also have intrinsic errors because of the approximations made in the pion self-energy where the second order pieces have been neglected.

The important message, however, is the large sensitivity of the mesonic width to the renormalized properties of the pion in the nuclear medium. Hence, when precise experimental measurements of the mesonic width are available they can be used to extract information about the pion–nucleus optical potential at low energies, for which there are large uncertainties, since pionic atoms and pion scattering at low energies do not determine the optical potential unequivocally.

9. Shell model treatment of the mesonic Λ decay

A detailed study of the mesonic Λ decay using explicit shell model wave functions for the nucleus was undertaken by Bandō and collaborators [BT 84]. The nucleon from the $\Lambda \rightarrow N\pi$ decay is allowed to go to any nuclear state except for the single particle occupied orbits of the nucleus. The expression for the Λ width when a closure sum is taken over the nucleon state is then given by eq. (8.9) multiplied by the suppression factor

$$S(\bar{q}) = 1 - \frac{1}{2} \sum_{nlj \in F} N_{nlj} \eta_{nlj}(\bar{q}), \quad (9.1)$$

$$\eta_{nlj}(\bar{q}) = |\langle \phi_{1s_{1/2}}^A(r) | j_l(\bar{q}r) | \phi_{nlj}^N(r) \rangle|^2,$$

with N_{nlj} the number of occupied particles in the (nlj) shell. The value of \bar{q} is trivially modified from the one in eq. (8.9) to account for the Λ and the average nucleon bindings. A more elaborate treatment, by summing explicitly over final nucleon states in a nuclear shell, is done in [It 88, Mo 88]. The results with the closure approximation and the explicit sum agree roughly in light and medium nuclei.

The calculation of the former section, based upon nuclear matter calculations and the local density approximation, incorporates, however, the binding of the nucleons and the Λ and should be compared to the explicit sum in the shell model. The results of the former section incorporating binding and Pauli blocking effects were [OS 85a] $\Gamma_m/\Gamma_{\text{free}} = 0.26, 0.075, 0.033$ for ${}^5_\Lambda\text{He}$, ${}^{12}_\Lambda\text{C}$, ${}^{17}_\Lambda\text{O}$, respectively, which compare very well with those of [It 88], 0.264, 0.093, 0.035, respectively.

The effects of the pion renormalization are studied in detail in [It 88, Ma 88, Mo 88]. However, the technical implementation is different to the one exposed in the former section. There the pion dispersion relation, $\tilde{\omega}(\mathbf{q})$, was changed at the local level and this modified the phase space locally. This had repercussions in the total mesonic decay width obtained by integrating over the nuclear volume. Here the phase space is calculated asymptotically, when the pion is far away from the nucleus, and thus a free pion dispersion relation is used in the evaluation. On the other hand, the effects of the renormalization are considered by means of the pion wave inside the nucleus, which is renormalized by the effect of the pion–nucleus optical potential. The transition matrix element from the Λ to the nucleon states is evaluated now by using the nuclear pion wave, with an asymptotic momentum \mathbf{k} and energy $(\mathbf{k}^2 + \mu^2)^{1/2}$, instead of a plane wave.

As noted in [OS 86] both methods are physically equivalent. The method of the local density approximation uses pion plane waves at any point, but the relationship of momentum and energy is different at any point, given by the solution of (8.23), which tells us that the pion energy accounts now for kinetic and potential energy provided by the pion–nucleus interaction. In the method of pion waves, the pion carries a constant energy, but as it goes deeper into the nucleus the pion wave picks up components of larger pion momentum. These larger pion momenta increase the mesonic width because, through momentum conservation, they force larger nucleon momenta, which have more chances to overcome the Fermi momentum. This was the argument used in the former section. Here we could argue alternatively that larger momentum components in the pion increase the nuclear transition matrix element, $\langle \psi_A | e^{i\mathbf{q}\cdot\mathbf{r}} | \psi_N \rangle$, from the Λ state to unoccupied nucleon states (at $\mathbf{q} = 0$, and for equal $1s_{1/2}$ wave function of Λ and nucleons, the transition matrix element to unoccupied states would be zero because of the orthogonality of the functions).

The nuclear matter with local density approximation method is a semiclassical approximation to the quantum mechanical approach of the pion wave method equivalent to having used the WKB approach to the quantum problem.

In table 9.1 we show the results of [It 88] for the mesonic width of different nuclei calculated with two different pion–nucleus optical potentials, MSU from [St 79] and WHIS from [Wh 86]. The ${}^5_\Lambda\text{He}$ case is compared with the experiment [Ba 88c, Sz 87]. Once again the experimental data seem to favor the results with renormalized pion waves. The approach of the local density approximation with renormalized pions using a shell model Λ wave function gives [Os 86] $\Gamma_m/\Gamma_{\text{free}} = 0.60$ versus the value 0.24 without pion renormalization. These values agree approximately with those of table 9.1 (0.47 with the

Table 9.1
 Calculated Γ_{π^0} , Γ_{π^-} and Γ_m from [It 88] with two different pion–nucleus optical potentials.
 MSU from [St 79] and WHIS from [Wh 86]. Experiment from [Ba 88a, Sz 87].

Hypernucleus		Γ_{π^0}	Γ_{π^-}	Γ_m
${}^5_{\Lambda}\text{He}$	Free	0.088	0.176	0.264
	MSU	0.154	0.318	0.472
	WHIS	0.108	0.223	0.331
	[exp]	$0.16^{+0.34}_{-0.21}$	0.43 ± 0.10	
${}^{13}_{\Lambda}\text{C}$	Free	0.031	0.062	0.093
	MSU	0.072	0.146	0.218
	WHIS	0.058	0.122	0.180
${}^{17}_{\Lambda}\text{O}$	Free	0.012	0.023	0.035
	MSU	0.032	0.065	0.097
	WHIS	0.022	0.050	0.072
${}^{41}_{\Lambda}\text{Ca}$	Free	0.002	0.004	0.006
	MSU	0.016	0.043	0.059
	WHIS	0.010	0.062	0.072

MSU pion optical potential and 0.26, respectively). As the nuclei become bigger there are more differences between the results of [OS 85a] and [It 88], as can be seen from a comparison of tables 8.1 and 9.1. These differences are essentially due to the different input for the optical potentials used in both approaches. In [OS 85a], as already mentioned, the second order repulsive s -wave part of the potential is missing and this stresses more the effect of the renormalization. The difference between the results in [It 88] using different optical potentials and those of [OS 85a] gives clear evidence of the sensitivity of the Λ mesonic width to the pion–nucleus optical potential. Therefore, this width, measured in many nuclei, can be used as a tool to select among different pion–nucleus optical potentials providing an equally good description of low energy pion–nucleus scattering.

The role of the ΛN correlations due to short range ΛN repulsion has been investigated in [Ku 85, Os 86]. In [Ku 85] an effective Λ potential in a ${}^4\text{He}$ cluster is constructed from the Dalitz hard core potential. This leads to a central repulsion in the ${}^5_{\Lambda}\text{He}$ nucleus and pushes the Λ wave function more to the surface than in ordinary shell model potentials. In [Os 86] the Λ wave function used for ${}^5_{\Lambda}\text{He}$ is constructed from variational methods using a two-body interaction and an additional ΛNN three-body force [Bo 84b]. One of the consequences of the short-range correlations is that because of the weaker ΛN attraction with respect to the NN force, the Λ wave function is pushed out considerably towards the surface of the nucleus. A measure of this effect is given by the r.m.s. radius. While for the nucleons of ${}^4\text{He}$ the r.m.s. radius is 1.5 fm, the r.m.s. radius for the Λ wave function is 2.97 fm [Bo 84b]. This value is still large compared with the value 2.2 fm for the Λ uncorrelated wave function that one gets from the usual Λ -nucleus potential $V_{\Lambda} \simeq -30 \rho(\mathbf{r})/\rho_0$.

The consequence of a Λ wave function with more overlap with the surface of the ${}^4\text{He}$ nucleus is an increase of the mesonic width because the Pauli blocking effect becomes less effective. The effects found in [Ku 85, Os 86] are very similar. One finds 40% increase in the mesonic width when using hypernuclear wave functions consistent with the short range ΛN repulsion. If in addition one considers the effect of the pion renormalization, the mesonic width gets further increased. However, as one can see in table 9.2, the results with the shell model wave function or the correlated one are very similar once the pion renormalization is included. On one hand the correlations push the wave function to the surface, reducing the effect of the Pauli blocking. On the other hand, if the Λ wave function is pushed

Table 9.2
 Calculated Γ_m/Γ_{free} from [Os 86] for $^3_\Lambda\text{He}$. Different combinations of unrenormalized and renormalized pions versus shell model and correlated Λ wave functions are shown.

Γ_m/Γ_{free}	Shell model wave function	Correlated wave function
Free pions	0.24	0.35
renormalized pions	0.60	0.54

to the surface, the effects of the pion renormalization are reduced. The two effects seem to approximately cancel in this nucleus, although it is not clear whether such cancellation would occur in heavier nuclei. For these nuclei we expect that the effect of the change in the Λ wave function diminishes, because even if the $1s_{1/2}$ Λ wave function is changed, it will be anyway buried inside the nucleus.

Another interesting question in the mesonic width is due to the peculiar features of the NN interaction, amongst them the short range repulsion, which have as a consequence a strong diversion from the shell model. The question of relevance here is the occupation number, which is not equal to unity for states with momentum below the Fermi momentum. Although the occupation number is different in different approaches, acceptable values range between 0.80 and 0.90 [Ma 85, FP 84, Ra 88]. This means that the Pauli blocking effect is only effective for about 80–90%. Thus, even for heavy nuclei we should expect a mesonic width of about $0.1 \Gamma_{free}$ or larger. Of course, one must take into account the absorption of the pions in their way out, but for low energy pions as we have here this does not drastically reduce the pion flux and the mesonic widths should be in the range of a few percent of the free width. Some calculations along this direction have been performed in [BT 85]. Assuming about 90% occupancy in the occupied states of the nucleus, the authors find $\Gamma_{\pi^-} \approx 2.5 \times 10^{-2} \Gamma_{free}$ for nuclei with $A \sim 100$. This compares favorably with the experimental numbers of $\Gamma_{\pi^-} \approx (1-3) \times 10^{-2} \Gamma_{free}$ obtained from the data $\Gamma_{nm}/\Gamma_{\pi^-} \sim 100-200$ for $A \sim 100$ [La 64] together with $\Gamma_{nm} \approx \Gamma_{tot} \approx (2-3) \Gamma_{free}$ as implied by existing data [Ni 76]. However a recent analysis of the problem has shown that the above argument, even if appealing, is incorrect [FO 90]. The reason is that the magnitude of relevance entering the evaluation of the Λ width is the spectral function, not the occupation number. The value $1 - n(\mathbf{k})$ is obtained by integrating the particle spectral function from the Fermi energy to infinity, and for $k < k_F$ this function is very smooth. The conservation of energy implicit in $\text{Im} \Sigma_\Lambda$ drastically reduces the interval of integration and one obtains a very small contribution, much smaller than the one obtained using the above intuitive arguments of the occupation number.

The point about pion absorption brings us to other considerations on the pion renormalization. In [It 88, Mo 88] the pion wave distorted with the pion–nucleus optical potential is used. The distortion of the pion wave has as a consequence the depletion of the pion flux due to pion absorption or quasielastic collisions. The use of these distorted pion waves is fine if one is studying a transition from the ground state of the hypernucleus to a particular discrete state of the final nucleus. But if one looks at the inclusive process of $\Lambda \rightarrow \pi N$ decay, i.e., without looking at the final nuclear state, then by eliminating in the theoretical counting all the events where a pion undergoes a quasielastic collision on its way out, one is not counting some of the events which will be observed experimentally, because even if the pion collides with one nucleon on its way out, the pion is still there and will contribute to the experimental mesonic Λ width. In other words, one should eliminate only the pions which are absorbed and not those which undergo quasielastic events. The problem is, however, that the pion optical potential has an imaginary part, which is responsible for both quasielastic scattering and absorption but does not tell us

how much strength corresponds to each channel. Fortunately, some theoretical schemes are now available which split the imaginary part of the optical potential in different parts corresponding to the probabilities of the different reaction channels, [OS 85a, Sa 88a, KT 88, GO 88], and elimination of the pions absorbed while keeping those which undergo quasielastic collisions is now possible.

An interesting feature of the shell model calculations [Mo 88] is that, for certain nuclei like ${}^{12}_\Lambda\text{C}$ or ${}^8_\Lambda\text{Be}$, Γ_{π^0} is slightly larger than Γ_{π^-} in spite of the ratio 1/2 that one should expect from the $\Delta T = 1/2$ rule in the absence of final state interaction of the pions. This can appear because in the π^0 decay some $T=0$ low lying states of ${}^8\text{Be}$ and ${}^{12}\text{C}$ are allowed to be reached, while these important transitions are missing in the π^- decay, which leads only to the high lying $T=1$ states (${}^8\text{B}$, ${}^{12}\text{N}$). The same situation but interchanging the role of the π^0 and π^- appears in ${}^8_\Lambda\text{Li}$ and ${}^{12}_\Lambda\text{B}$, where Γ_{π^-} is further enhanced with respect to Γ_{π^0} .

Another point noted in [Mo 88, Ba 88b] is the valuable information that one can extract from the analysis of the angular distributions and pion asymmetries in the mesonic decay of polarized hypernuclei [Ej 86, Fu 86]. Apart from sensitivity to nuclear structure details, this quantity also exhibits a strong sensitivity to the renormalization of pion waves and could be used, together with other quantities, to discriminate among different pion–nucleus optical potentials.

10. Non-mesonic decay: beyond one pion exchange

In section 8.3, we had a look at the non-mesonic Λ decay mediated by π exchange. Although the results obtained for the non-mesonic Λ width compare favorably with experiment, we could however see in section 8.4 that one pion exchange alone led to large discrepancies with the experimental values of the proton to neutron induced ratio.

A model with $\pi + \rho$ exchange is studied in detail in [MG 84]. The authors employ a number of different models to describe the ρ exchange, including a factorization model and one using $SU(6)$ symmetry. They also explore the role of the πNN and ρNN vertex functions and emphasize the uncertainties in the theoretical estimates of the ΛNM couplings for heavier mesons (M). Their results for the non-mesonic width depend strongly upon the choice of the relative phase between the π and ρ couplings. With destructive interference they get 0.1, versus 2.9 with constructive interference, for $\Gamma_{nm}/\Gamma_{\text{free}}$ in nuclear matter. The contribution from π exchange alone agrees with the results discussed before.

The same model is used to evaluate the non-mesonic width of the light hypernuclei ${}^5_\Lambda\text{He}$, ${}^4_\Lambda\text{He}$ and ${}^4_\Lambda\text{H}$ in [Ta 85]. Their results are summarized in table 10.1. The experimental results come from an old analysis of [BD 63], which rely upon the calculations of Γ_m of [DL 59]. Recent experiments [BS 86, Ba 88c, Sz 87] in ${}^5_\Lambda\text{He}$ give $0.44 \pm^{0.15}_{0.31}$. The high sensitivity of the results to the nucleus, shown in table

Table 10.1
Theoretical values of $\Gamma_{nm}/\Gamma_{\text{free}}$ from [Ta 85] for different $\Lambda N \rightarrow NN$ mechanisms. π : only pion exchange, $\pi + \rho$: π and ρ exchange with constructive interference. $\pi - \rho$: destructive interference. “exp”: results from the analysis of [BD 63].

Nucleus	π	$\pi + \rho$	$\pi - \rho$	“exp”
${}^5_\Lambda\text{He}$	0.144	0.450	0.033	0.41 ± 0.13
${}^4_\Lambda\text{He}$	0.126	0.369	0.038	0.14 ± 0.03
${}^4_\Lambda\text{H}$	0.013	0.013	0.013	0.29 ± 0.14

10.1, indicates that new measurements of the non-mesonic width along the lines of these latter experiments would be very interesting to investigate other ingredients of the $\Lambda N \rightarrow NN$ interaction beyond the $\pi + \rho$ model.

Along the same lines is the work [Na 88], where the author calculates the $\rho N \Lambda$ coupling by using a pole model and information from weak non-leptonic and radiative decays. The author obtains there $\Gamma_{nm}/\Gamma_{free} = 0.7$ for nuclear matter if vector meson dominance is assumed to calculate the ratio of the tensor to vector coupling constants in the ρNN vertex. If the empirical value of 6.6 from [HP 75] is used for this ratio he obtains $\Gamma_{nm}/\Gamma_{free} = 2.1$.

Another approach used in the literature is a hybrid model with nucleon and meson degrees of freedom for distances larger than $r_0 \approx 0.8-1.0$ fm and quark degrees of freedom for smaller distances [Ch 83, HK 86]. The contribution to the $\Lambda N \rightarrow NN$ process comes from pion exchange for distances beyond r_0 and from the weak Lagrangian at the quark level, corrected for the QCD induced renormalization. The approach attempts a more microscopic description of the process but has to face serious problems stemming from the unsolved problem of the strong renormalization of the non-leptonic weak transitions. Understanding the $\Delta T = 1/2$ dominance has long been a complex problem although very important progress has been made recently [Pi 88]. The Hamiltonian used in [Ch 83, HK 86] is an effective one derived from the weak quark Hamiltonian including the renormalization due to strong interactions. This is accomplished by means of renormalization group techniques based upon one-loop diagrams of W 's and gluons [GW 79]. This effective Hamiltonian does not satisfy the $\Delta T = 1/2$ rule. (The work of [Pi 88] has the virtue of showing the relevant role of higher QCD orders in the enhancement of the $\Delta T = 1/2$ contribution.) In addition, in the sharp division of the space into a quark sector and a nucleon and meson sector one has to rely for the calculations upon the concept of a six quark bag probability, somewhat imprecise from the physical point of view.

For the sake of comparison the authors also calculate the quark sector with the Cabibbo Lagrangian without strong renormalization and with a modified form of the [GW 79] Hamiltonian where the coefficients are chosen such as to impose the $\Delta T = 1/2$ rule. In table 10.2 we summarize the results of the most recent work of [HK 86], with improved results in the pionic contribution which was found to be negligible in [Ch 83].

We can see that the results of the quark sector are very sensitive to the strong renormalization and the way it is implemented. From the table one can observe a reduction factor $\Gamma_{nm}(\text{nuclear matter})/\Gamma_{nm}(^{12}_\Lambda\text{C}) = 2.34$ from nuclear matter to the nucleus of $^{12}_\Lambda\text{C}$ in the case of $\Delta T = 1/2$. This is in contrast to the value $2.0/1.5 = 1.33$ found in [OS 85a] and the value 1.42 quoted in [Du 86b]. One can also see in the table that for the $\Delta T = 1/2$ case, preferred in [HK 86], the pionic contribution is sizeable, since, when added coherently to the quark contribution, it increases the value of Γ_{nm} by a factor 4-5.

The most complete model for the non-mesonic Λ decay is the one of [To 90], although only

Table 10.2.

Theoretical values of $\Gamma_{nm}/\Gamma_{free}$ from [HK 86]. Quark: quark sector contribution. Total: quark plus pion exchange contributions. C: with Cabibbo Lagrangian for the quark sector. GW: with the effective Hamiltonian of [GW 79]. $\Delta T = 1/2$: with a modified version of the Hamiltonian to enforce the $\Delta T = 1/2$ rule.

$\Gamma_{nm}/\Gamma_{free}$	Nuclear Matter			$^{12}_\Lambda\text{C}$		
	C	GW	$\Delta T = 1/2$	C	GW	$\Delta T = 1/2$
quark	5.19	2.18	0.73	1.76	0.74	0.24
total	9.96	5.54	3.00	3.87	2.25	1.28

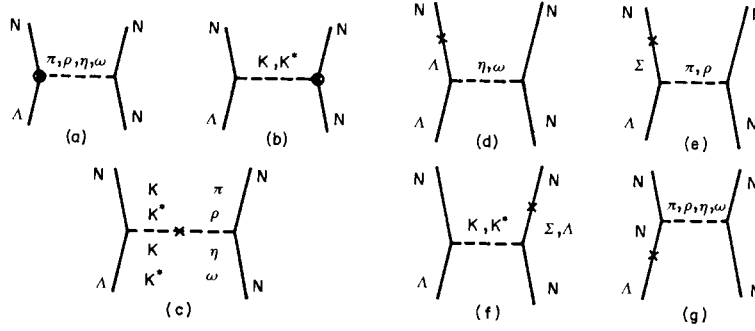


Fig. 10.1. Meson exchange diagrams used to evaluate the $\Lambda N \rightarrow NN$ transition potential in the model of [To 90, Du 86a, 86b].

preliminary results reported in conferences are available [Du 86a, b, c]. The model used there is the one depicted in fig. 10.1. It contains π , ρ , η , ω , K , K^* exchange. The full strangeness-changing weak interaction which is responsible for the transformation of a Λ hyperon into a nucleon is indicated by a encircled cross. The other vertices indicate strong interactions. In addition, diagrams where the meson exchange with strong interactions are followed or preceded by a weak transition meson \rightarrow meson or baryon \rightarrow baryon, are also considered (indicated by a cross).

By using $SU(6)_w$ symmetry and enforcing the empirical $\Delta T = 1/2$ rule they can obtain all the $\langle M' | H_w | M \rangle$ amplitudes from $\langle \pi | H_w | K \rangle$. Using PCAC, this latter quantity is related to the physical $K \rightarrow \pi\pi$ decay rate. In a similar way, by using PCAC, the baryon \rightarrow baryon amplitudes can be related to the Λ and Σ decay. The strong couplings are obtained by using $SU(3)$ symmetry, PCAC and the Goldberger–Treiman relation. In a similar way all parity conserving baryon–baryon–meson couplings can be related by $SU(6)_w$ symmetry and the $\Delta T = 1/2$ rule to the $\pi^- p \Lambda$ and $\pi^0 p \Sigma^+$ couplings. The results are evaluated in nuclear matter and summarized in table 10.3. The results for π exchange with and without correlations agree with [OS 85a]. Those with $\pi + \rho$ agree qualitatively with [MG 84] in the case of constructive interference. The inclusion of all other ingredients beyond π exchange reduces the width by only 30%, thus stressing the role of π exchange in non-mesonic Λ decay. However, the strength of the transition is split somewhat differently into partial waves when all the ingredients are considered and this has a special repercussion in the ratio of proton to neutron induced Λ decay.

An interesting critical review of all these approaches, complementary to the one here, can be found in [Mc 86].

The ratio of proton to neutron induced Λ decay is rather sensitive to details of the interaction. We already saw in section 8.4 that, by considering the direct and exchange terms in the interaction mediated by pion exchange, one obtained a value of 14 for that ratio, while, by considering the direct term only, one obtained a value of 5 for that ratio. However, the consideration of the exchange terms

Table 10.3
Theoretical values of $\Gamma_{nm}/\Gamma_{free}$ and $\Gamma_{\Lambda p \rightarrow np}/\Gamma_{\Lambda n \rightarrow nn}$ from the model of [To 90, Du 86a, b] for pion exchange, correlated pion exchange, $\pi + \rho$ exchange and full model.

	π no correlations	π correlations	$\pi + \rho$	$\pi, \rho, \eta,$ ω, K, K^*
$\Gamma_{nm}/\Gamma_{free}$	3.89	1.82	1.55	1.23
$\Gamma_{\Lambda p \rightarrow np}/\Gamma_{\Lambda n \rightarrow nn}$	11.2	16.6	13.1	2.9

only increased the width by 20%. In a similar way, this ratio is much more sensitive to the details of the interaction than the Λ width.

One of the most interesting results in [Du 86a] is the value of this ratio calculated for symmetric nuclear matter. It is summarized in table 10.3. We observe there that the results with π exchange, with or without correlations, provide values of 11.2 and 16.6, in qualitative agreement with the factor 14 obtained in section 8.4. These results are not much altered when the ρ contribution is added. However, the whole model provides a ratio of 2.9, quite different from the results provided by π or $\pi + \rho$ exchange. This result would be closer to the experimental values, ~ 2 [Mo 74] or ~ 1 [Gr 85].

The results of [Na 88] oscillate between 1.5 if vector meson dominance is assumed to construct the ρNN vertex, and 0.8 if the experimental value of the tensor coupling to vector coupling from [HP 75] is used. In any case these results differ substantially from those of [Du 86a] shown in table 10.3.

In [HK 88] the ratio is also evaluated in ${}^{12}_\Lambda\text{C}$. They obtain a ratio of 5.3 from the pionic contribution. This differs substantially from the factor 14 calculated in section 8.4 or from the results of [Du 86a] shown in table 10.3. However, it agrees with the factor 5 obtained in section 8.4 when the exchange terms are omitted. For the quark sector the ratio is $3/2$, obtained with a wave function product of single particle wave functions. With all these assumptions the value obtained for the ratio is 2.7. Other contributions from accounting for $\Lambda N \rightarrow \Sigma N \rightarrow NN$ intermediate contributions have been evaluated in [Ba 88d] and lead to an increase in the proton to neutron induced ratio.

The discussions in this section clearly tell us that the value of the non-mesonic width does not help much to discriminate between models, but selected quantities like the proton to neutron induced Λ decay ratio are very sensitive to details of the models. Another quantity equally sensitive to details of the model is the ratio of the parity violating to parity conserving contributions. This quantity changes from 0.14 with pion exchange to 0.90 in the full model of [Du 86a].

These findings should serve as a guideline for future experiments. On the other hand, when analyzing the data one must take proper care of the final state interaction because the nucleons leaving the nucleus can be different from those primarily involved in the $\Lambda N \rightarrow NN$ reaction.

11. Conclusions

We have made an exposition of the experimental and theoretical situation surrounding the decay modes and widths of Σ and Λ hypernuclei, with emphasis on a few particular points.

The Σ hypernuclear problem has been the subject of intense theoretical and experimental debate in the last few years. In this report we have made a special effort to expose in an easy, understandable way, the basic features of the problem. For that purpose we have developed a few useful approximations, which provide handy analytical formulas, yet very accurate, by means of which one can get a better understanding of the essence of the problem. The Pauli blocking effect was shown to play only a moderate role in reducing Σ widths. The major ingredient leading to narrow widths in Σ hypernuclei was shown to be the polarization of the medium by the spin-isospin interactions responsible for the $\Sigma N \rightarrow \Lambda N$ transition. This phenomenon produced a density dependent quenching of the imaginary part of the Σ self-energy, which had a very small repercussion in Σ^- atoms (low density regime) but produced Σ hypernuclear widths around three times smaller than those provided by a linear potential in the nuclear density extracted from the Σ^- atom data.

With a potential consistent with the Σ^- atom data, and incorporating the quenching effects from the polarization, a study of Σ hypernuclear states for several nuclei was carried out with predictions of

many $1s$, $2p$, $2s$ states, which should in principle be distinguishable experimentally since the widths are narrower than the separation energy between the levels. The case of the ${}^4_2\text{He}$ hypernucleus was also studied in the same context. The results are consistent with the experimental findings for this nucleus and with the non-observation of a similar state in the ${}^4\text{He}(K^-, \pi^+)$ reaction. However, it was also noted that in very light hypernuclei a strong ΣN repulsion at short distances also leads to narrower widths.

The relationship of the problem of narrow Σ widths with the one of pionic anomalous atoms was also discussed.

In Λ hypernuclei the two modes of decay, mesonic and non-mesonic have been investigated in the same many-body framework. We have also reviewed the work existing on the subject. The non-mesonic decay carries information on the $\Lambda N \rightarrow NN$ weak transition. Although many appropriate models yield values for the non-mesonic width in fair agreement with experiment, it was shown that this is not the case if one looks at selected magnitudes of the reaction like the ratio of proton to neutron induced Λ decay or the ratio of the parity conserving to parity violating parts.

In the mesonic decay the width is drastically reduced with respect to the free one because of the Pauli exclusion principle. An interesting feature is the high sensitivity of this width to the properties of the pions inside the nucleus or equivalently to the pion-nucleus optical potential. This makes the meson decay a useful tool to select among many possible optical potentials describing equally well the low energy pion-nucleus scattering.

With the limited amount of information available, the decay of Σ and Λ hypernuclei has posed a number of challenging questions and has shown that it contains very valuable information about magnitudes of much relevance in nuclear physics. The small amount of data available on these reactions and the difficulties to make rapid progress with the present experimental facilities call for a qualitative change in these facilities which would allow a steady development of this interesting field.

Acknowledgements

We would like to gratefully acknowledge discussions and comments from H. Bandō, P. Barnes, R. Bertini, C.B. Dover, J. Dubach, H. Feshbach, A. Gal, R. Hausmann, R.S. Hayano, K. Itonaga, O. Morimatsu, T. Motoba, V. Pandharipande, B. Povh, H. Toki, T. Walcher, W. Weise, T. Yamazaki and K. Yazaki.

Appendix. The Lindhard function

For complex values of q^0 , an evaluation of the integral in eq. (4.34) gives [FW 71, OP 81]

$$U_N(q) = \frac{3}{2} \rho \frac{M}{|q|k_F} \left[z + \frac{1}{2}(1 - z^2) \ln \left(\frac{z+1}{z-1} \right) + z' + \frac{1}{2}(1 - z'^2) \ln \left(\frac{z'+1}{z'-1} \right) \right], \quad (\text{A.1})$$

where k_F is the Fermi momentum and

$$z = \frac{M}{|q|k_F} \left(q^0 - \frac{q^2}{2M} \right), \quad z' = \frac{M}{|q|k_F} \left(-q^0 - \frac{q^2}{2M} \right). \quad (\text{A.2})$$

For real q^0 the prescription $q^0 \rightarrow q^0 + (q^0/|q^0|)i\epsilon$ should be used. The value of $\text{Re } U_N(q)$ is then given by eq. (A.1) but with absolute values in the arguments of the logarithms. The value of $\text{Im } U_N(q)$ is given by

$$\text{Im } U_N(q) = -\frac{3}{4}\pi\rho \frac{M}{|\mathbf{q}|k_F} [(1-z^2)\theta(1-|z|) - (1-z'^2)\theta(1-|z'|)] \frac{q^0}{|q^0|}. \quad (\text{A.3})$$

Similarly for $U_\Delta(q)$, making some approximations [OP 81], one obtains

$$U_\Delta(q) = \frac{2}{3} \left(\frac{f^*}{f}\right)^2 \rho \frac{M_\Delta}{|\mathbf{q}|k_F} \left[z_\Delta + \frac{1}{2}(1-z_\Delta^2) \ln\left(\frac{z_\Delta+1}{z_\Delta-1}\right) + z'_\Delta + \frac{1}{2}(1-z_\Delta'^2) \ln\left(\frac{z'_\Delta+1}{z'_\Delta-1}\right) \right], \quad (\text{A.4})$$

$$z_\Delta = \frac{M_\Delta}{|\mathbf{q}|k_F} \left(q^0 - \frac{\mathbf{q}^2}{2M_\Delta} - \omega_R + \frac{i}{2}\Gamma_\Delta(q^0, \mathbf{q}) \right),$$

$$z'_\Delta = \frac{M_\Delta}{|\mathbf{q}|k_F} \left(-q^0 - \frac{\mathbf{q}^2}{2M_\Delta} - \omega_R + \frac{i}{2}\Gamma_\Delta(-q^0, \mathbf{q}) \right), \quad (\text{A.5})$$

where $\omega_R = M_\Delta - M$ and Γ_Δ is the Δ width,

$$\Gamma_\Delta(q) = \frac{1}{3} \frac{1}{4\pi} \left(\frac{f^*}{\mu}\right)^2 \frac{q_{\text{cm}}^3}{\sqrt{s}} (M + \sqrt{M^2 + q_{\text{cm}}^2}) \theta(\sqrt{s} - M - \mu), \quad (\text{A.6})$$

$$s = M^2 + q^2 + 2q^0\sqrt{M^2 + \frac{3}{5}k_F^2}, \quad (\text{A.7})$$

$$q_{\text{cm}} = \lambda^{1/2}(s, M^2, \mu^2)/2\sqrt{s}, \quad (\text{A.8})$$

or $\Gamma_\Delta(q) = 0$ if q^0 is complex.

References

- [Ad67] J.B. Adams, Phys. Rev. 156 (1967) 1611.
- [Ak86] Y. Akaishi, Few-Body Systems Suppl. No. 1 (1986) 120.
- [Ar85] H. Arenhovel, in: New Vistas in Electro-Nuclear Physics, NATO ASI series B, Vol. 142, eds E.L. Tomusiak et al., p. 251.
- [AH79] A. Arima and H. Hyuga, in: Mesons in Nuclei, Vol. II, eds M. Rho and D.H. Wilkinson (North-Holland, Amsterdam, 1979).
- [Au87] N. Auerbach, Phys. Rev. C 35 (1987) 1798.
- [Ba70] G. Backenstoss, Annu. Rev. Nucl. Sci. 20 (1970) 467.
- [Ba78] C.J. Batty et al., Phys. Lett. B 74 (1978) 27.
- [Ba83] C.J. Batty, A. Gal and G. Toker, Nucl. Phys. A 402 (1983) 349.
- [Ba85] C.J. Batty, private communication.
- [Ba86] P.D. Barnes, Nucl. Phys. A 450 (1986) 43c.
- [Ba88a] H. Bandō, T. Motoba and J. Žofka, Z. Phys. A 330 (1988) 203.
- [Ba88b] H. Bandō, T. Motoba, M. Sotona and J. Žofka, Fukui Univ. preprint, FUMP-1988-8.
- [Ba88c] P.D. Barnes, Nucl. Phys. A 478 (1988) 127c.
- [Ba88d] H. Bandō, Y. Shono and H. Takaki, Int. J. Mod. Phys. A 3 (1988) 1581.
- [BD63] M.M. Block and R.H. Dalitz, Phys. Rev. Lett. 11 (1963) 96.
- [BD65] J.D. Bjorken and S.D. Drell, Relativistic Quantum Fields (McGraw-Hill, New York, 1965).
- [Be69] P.R. Bevington, Data Reduction and Analysis for the Physical Sciences (McGraw-Hill, New York, 1969).
- [Be80] R. Bertini et al., Phys. Lett. B 90 (1980) 375.

- [Be84] R. Bertini et al., Phys. Lett. B 136 (1984) 29.
 [Be85] R. Bertini et al., Phys. Lett. B 158 (1985) 19.
 [BJ79] G.E. Brown and A.D. Jackson, *The Nucleon-Nucleon Interaction* (North-Holland, Amsterdam, 1979).
 [BM80] L.N. Bogdanova and V.E. Markushin, JETP Lett. 32 (1980) 305.
 [BM86] H. Bandō and T. Motoba, Prog. Theor. Phys. 76 (1986) 1321.
 [BN82] H. Bandō and S. Nagata, Prog. Theor. Phys. 67 (1982) 522.
 [Bo70] G. Bohm et al., Nucl. Phys. B 23 (1970) 93.
 [Bo77] A. Bouyssy, Nucl. Phys. A 290 (1977) 324.
 [Bo79] A. Bouyssy, Phys. Lett. B 84 (1979) 41.
 [Bo84a] L.N. Bogdanova, Sov. J. Part. Nucl. 15 (1984) 361.
 [Bo84b] A.R. Bodmer, Q.U. Usmani and J. Carlson, Phys. Rev. C 29 (1984) 684.
 [BO82] R. Brockman and E. Oset, Phys. Lett. B 118 (1982) 33.
 [BO84] R. Brockman and E. Oset, in: *Nucleon Spectroscopy and Nuclear Interactions*, eds H. Ejiri and T. Fukuda (World Scientific, Singapore, 1984) p. 648.
 [BO86] R. Brockman and E. Oset, Nucl. Phys. A 450 (1986) 353c.
 [Br63] G.E. Brown, J.H. Gunn and P. Gould, Nucl. Phys. 46 (1963) 598.
 [Br72] G.E. Brown, *Many-Body Problems* (North Holland, Amsterdam, 1972).
 [Br75] W. Brückner et al., Phys. Lett. B 55 (1975) 107.
 [Br76] W. Brückner et al., Phys. Lett. B 62 (1976) 481.
 [Br78] B.A. Brown, W. Chung and B.H. Wildenthal, Phys. Rev. Lett. 40 (1978) 1631.
 [BS86] P.D. Barnes and J. J. Szymanski, in: *Proc. 1986 INS Intern. Symp. on Hypernuclear Physics*, eds H. Bandō, O. Hashimoto and K. Ogawa (INS, Tokyo) p. 136.
 [BT84] H. Bandō and H. Takaki, Prog. Theor. Phys. 72 (1984) 106.
 [BT85] H. Bandō and H. Takaki, Phys. Lett. B 150 (1985) 409.
 [Bu86] R. Buttgen, K. Holinde, B. Holzenkamp and J. Speth, in: *Intersections Between Particle and Nuclear Physics* (Lake Louise, 1986), ed. D.F. Geesaman AIP Conf. Proc. no. 150, p. 924.
 [Ch83] C.Y. Cheung, D.P. Heddle and L.S. Kisslinger, Phys. Rev. C 27 (1983) 335.
 [Ch86] R.E. Chrien, ed., *Proc. Intern. Sym. on Hypernuclear and Kaon Physics*, Nucl. Phys. A 450 (1986).
 [Ch87] R.E. Chrien, in: *Selected Problems of Modern Nuclear Physics*, Brookhaven preprint.
 [Ch88] R.E. Chrien, Nucl. Phys. A 478 (1988) 705c.
 [Ch89] H.C. Chiang, E. Oset and P. Fernández de Córdoba, University of Valencia preprint (1989).
 [CP53] W. Cheston and H. Primakoff, Phys. Rev. 92 (1953) 1537.
 [Da58] R.H. Dalitz, Phys. Rev. 112 (1958) 605.
 [Da72] R.H. Dalitz, R.C. Herndon and Y.C. Tang, Nucl. Phys. B 47 (1972) 109.
 [Dą81] J. Dąbrowski, Nukleonika 26 (1981) 1061.
 [DF87] C.B. Dover and H. Feshbach, Phys. Rev. Lett. 59 (1987) 2539.
 [DG83] C.B. Dover and A. Gal, Prog. Part. Nucl. Phys. 12 (1983) 171.
 [DL59] R.H. Dalitz and L. Liu, Phys. Rev. 116 (1959) 1312.
 [Do71] C.B. Dover, J. Hüfner and R.H. Lemmer, Ann. Phys. 66 (1971) 248.
 [Do80] C.B. Dover, L. Ludeking and G.E. Walker, Phys. Rev. C 22 (1980) 2073.
 [DP53] M. Danysz and J. Pniewski, Philos. Mag. 44 (1953) 348.
 [DR81] J. Dąbrowski and J. Rożynek, Phys. Rev. C 23 (1981) 1706.
 [DR83] J. Dąbrowski and J. Rożynek, Acta Phys. Polon. B 14 (1983) 439.
 [Du86a] J.F. Dubach, Nucl. Phys. A 450 (1986) 71c.
 [Du86b] J. Dubach, in: *Intersections of Particle and Nuclear Physics* (Lake Louise, 1986), ed. D.F. Geesaman, AIP Conf. Proc. no. 150.
 [Du86c] J. Dubach, in: *Proc. Intern. Conf. on Weak and Electromagnetic Interactions in Nuclei* (Heidelberg, 1986) ed. H.V. Klapdor, p. 576.
 [DW82] C.B. Dover and G.E. Walker, Phys. Rep. 89 (1982) 1.
 [EE66] M. Ericson and T.E.O. Ericson, Ann. Phys. 36 (1966) 323.
 [Ej86] H. Ejiri, T. Fukuda, T. Shibata, H. Bandō and K.I. Kubo, in: *Proc. 1986 INS Intern. Symp. on Hypernuclear Physics*, eds H. Bandō, O. Hashimoto and K. Ogawa (INS, Tokyo) p. 223.
 [En66] R. Engelmann, H. Filthuth, V. Hepp and E. Kluge, Phys. Lett. 21 (1966) 587.
 [Fa83] S. Fantoni, B.L. Friman and V.R. Pandharipande, Nucl. Phys. A 399 (1983) 51.
 [Fe85] H. Feshbach, Ann. Phys. 165 (1985) 398.
 [Fe86] H. Feshbach, Phys. Lett. B 168 (1986) 318.
 [Fe89] P. Fernández de Córdoba, E. Oset and L.L. Salcedo, University of Valencia preprint.
 [FO90] P. Fernández de Córdoba and E. Oset, University of Valencia preprint.
 [FP84] S. Fantoni and V.C. Pandharipande, Nucl. Phys. A 427 (1984) 473.
 [Fu86] T. Fukuda, H. Ejiri, T. Shibata, H. Bandō and T. Motoba, in: *Proc. 1986 INS Intern. Symp. on Hypernuclear Physics*, eds H. Bandō, O. Hashimoto and K. Ogawa (INS, Tokyo) p. 170.

- [FW71] A.L. Fetter and J.D. Walecka, *Quantum Theory of Many-Particle Systems* (McGraw-Hill, New York, 1971).
- [Ga81] A. Gal, G. Toker and Y. Alexander, *Ann. Phys.* 137 (1981) 341.
- [Ga86] A. Gal, in: *Proc. Intern. Symp. on Hypernuclear and Kaon Physics* (Brookhaven, 1985), ed. R.E. Chrien, *Nucl. Phys. A* 450 (1986) 343c.
- [Ga89] C. García-Recio, L.L. Salcedo and E. Oset, *Phys. Rev. C* 39 (1989) 595.
- [GD80] A. Gal and C.B. Dover, *Phys. Rev. Lett.* 44 (1980) 379.
- [GO88] C. García-Recio and E. Oset, *Phys. Rev. C* 40 (1989) 1308.
- [Gr85] R. Grace et al., *Phys. Rev. Lett.* 55 (1985) 1055.
- [GW79] F.J. Gilman and M. B. Wise, *Phys. Rev. D* 20 (1979) 2392.
- [Ha77] J.M. Haupton, J.A. Kadyk and G.H. Trilling, *Nucl. Phys. B* 125 (1977) 29.
- [Ha87] R. Hausmann, P.B. Siegel, W. Weise and M. Kohno, *Phys. Lett. B* 199 (1987) 17.
- [Ha88a] R.S. Hayano, *Nucl. Phys. A* 478 (1988) 113c.
- [Ha88b] R.S. Hayano et al., *Phys. Lett. B* 231 (1989) 355.
- [Ha88c] R. Hausmann, *Nucl. Phys. A* 479 (1988) 247.
- [Ha89a] T. Harada, S. Shinmura, Y. Akaishi and H. Tanaka, *Hokkaido University preprint* (1989).
- [Ha89b] T. Harada, S. Shinmura, Y. Akaishi and H. Tanaka, *Hokkaido University preprint* (1989).
- [He83] D. W. Herzog et al., *Phys. Rev. Lett.* 51 (1983) 1131.
- [HK86] D.P. Heddle and L.S. Kisslinger, *Phys. Rev. C* 33 (1986) 608.
- [HK88] D.P. Heddle and L.S. Kisslinger, *University of Illinois at Urbana preprint* (1988).
- [HP75] G. Höler and E. Pietarinen, *Nucl. Phys. B* 95 (1975) 210.
- [Hü75] J. Hüfner, *Phys. Rep.* 21 (1975) 1.
- [It88] K. Itonaga, T. Motoba and H. Bandō, *Z. Phys. A* 330 (1988) 209.
- [IZ80] C. Itzikson and J.B. Zuber, *Quantum Field Theory* (McGraw-Hill, New York, 1980).
- [Ja74] C.W. de Jager, H. de Vries and C. de Vries, *At. Data Nucl. Data Tables* 14 (1974) 479.
- [Je76] J.P. Jeukenne, A. Lejeune and C. Mahaux, *Phys. Rep.* 25 (1976) 83.
- [JT83] J.A. Johnstone and A.W. Thomas, *Nucl. Phys. A* 392 (1983) 409.
- [Ju72] M. Jelic et al., *Nucl. Phys. B* 47 (1972) 36.
- [Ka71] J.A. Kadyk et al., *Nucl. Phys. B* 27 (1971) 13.
- [Ke70] G. Keyes et al., *Phys. Rev. D* 1 (1970) 66.
- [Ke73] G. Keyes et al., *Nucl. Phys. B* 67 (1973) 269.
- [Kh89] Khin Swe Myint, S. Tadokoro and Y. Akaishi, *Hokkaido University preprint*, 1989.
- [Ki80] L.S. Kisslinger, *Phys. Rev. Lett.* 44 (1980) 968.
- [Ko79] J. Konijn et al., *Nucl. Phys. A* 326 (1979) 401.
- [Ko87a] M. Kohno, R. Hausmann, P. Siegel and W. Weise, *Nucl. Phys. A* 470 (1987) 609.
- [Ko87b] J. Konijn et al., *NIKHEF preprint*.
- [KT88] M. Kh. Khankhasaev and N.S. Topilskaya, *Phys. Lett. B* 217 (1989) 14.
- [Ku85] Y. Kurihara, Y. Akaishi and H. Tanaka, *Phys. Rev. C* 31 (1985) 971.
- [La64] J.P. Lagnaux et al., *Nucl. Phys.* 60 (1964) 97.
- [Lo86] M.J. López-Santodomingo, *Tesina de Licenciatura*, University of Valladolid.
- [Ma76] R.D. Mattuck, *A Guide to Feynman Diagrams in the Many-Body Problem* (McGraw-Hill, New York, 1976).
- [Ma85] C. Mahaux, P.F. Bortignon, R.A. Broglia and C.H. Dasso, *Phys. Rep.* 120 (1985) 1.
- [Ma87] R. Machleidt, K. Holinde and Ch. Elster, *Phys. Rep.* 149 (1987) 1.
- [Ma88] R. Mach, G. Žofka, K. Itonaga, T. Motoba and H. Bandō, *Fukui University preprint*.
- [Mc86] B.H.J. McKellar, in: *Proc. 1986 INS Intern. Symp. on Hypernuclear Physics*, eds H. Bandō, O. Hashimoto and K. Ogawa (INS, Tokyo) p. 146.
- [MG84] B.H.J. McKellar and B.F. Gibson, *Phys. Rev. C* 30 (1984) 322.
- [Mi85] E.C. Milner et al., *Phys. Rev. Lett.* 54 (1985) 1237.
- [Mi88] D.J. Millener, C.B. Dover and A. Gal, *Phys. Rev. C* 38 (1988) 2700.
- [Mo74] A. Montwill et al., *Nucl. Phys. A* 234 (1974) 413.
- [Mo88] T. Motoba, K. Itonaga and H. Bandō, *Nucl. Phys. A* 489 (1988) 683.
- [MY85] O. Morimatsu and K. Yazaki, *Nucl. Phys. A* 435 (1985) 727.
- [MY86] O. Morimatsu and K. Yazaki, in: *Proc. 1986 INS Intern. Symp. on Hypernuclear Physics*, eds H. Bandō, O. Hashimoto and K. Ogawa (INS, Tokyo) p. 50.
- [MY88] O. Morimatsu and K. Yazaki, *Nucl. Phys. A* 483 (1988) 493.
- [Na73] M.M. Nagels, T.A. Rijken and J.J. de Swart, *Ann. Phys.* 79 (1973) 338.
- [Na77] M.M. Nagels, T.A. Rijken and J.J. de Swart, *Phys. Rev. D* 15 (1977) 2547.
- [Na79] M.M. Nagels, T.A. Rijken and J.J. de Swart, *Phys. Rev. D* 20 (1979) 1633.
- [Na88] G. Nardulli, *Phys. Rev. C* 38 (1988) 832.
- [Ni76] K.J. Nield et al., *Phys. Rev. C* 13 (1976) 1263.

- [Ni89] J. Nieves, E. Oset and C. García-Recio, University of Valencia preprint (1989).
- [Ol85] A. Olin et al., Nucl. Phys. A 439 (1985) 589.
- [OP81] E. Oset and A. Palanques, Nucl. Phys. A 359 (1981) 289.
- [Os82] E. Oset, H. Toki and W. Weise, Phys. Rep. 83 (1982) 281.
- [Os85] E. Oset, L.L. Salcedo and D. Strottman, Phys. Lett. B 165 (1985) 13.
- [Os86] E. Oset, L.L. Salcedo and Q.N. Usmani, Nucl. Phys. A 450 (1986) 67c.
- [OS85a] E. Oset and L.L. Salcedo, Nucl. Phys. A 443 (1985) 704.
- [OS85b] E. Oset and L.L. Salcedo, J. Comput. Phys. 57 (1985) 361.
- [OS86] E. Oset and L.L. Salcedo, Nucl. Phys. A 450 (1986) 371c.
- [OS87] E. Oset and L.L. Salcedo, Nucl. Phys. A 468 (1987) 631.
- [OW79] E. Oset and W. Weise, Nucl. Phys. A 319 (1979) 477.
- [Pi82] H. Piekarczyk et al., Phys. Lett. B 110 (1982) 428.
- [Pi88] A. Pich, CERN preprint TH.5102/88 (1988).
- [Po76] B. Povh, Rep. Prog. Phys. 39 (1976) 823.
- [Po88] S. Polikanov, Nucl. Phys. A 478 (1988) 805c.
- [PS64] R.J. Prem and P.H. Steinberg, Phys. Rev. 136 (1964) B 1803.
- [PS69] R.E. Phillips and J. Schneps, Phys. Rev. 180 (1969) 1307.
- [Ra88] A. Ramos, Ph.D. thesis, University of Barcelona, Spain.
- [RD79] J. Rozynek and J. Dąbrowski, Phys. Rev. C 20 (1979) 1612.
- [RK56] M. Rutherford and R. Karplus, Phys. Rev. 102 (1956) 247.
- [Sa88a] L.L. Salcedo, E. Oset, M.J. Vicente and C. García-Recio, Nucl. Phys. A 484 (1988) 557.
- [Sa88b] A. Sakaguchi et al., Tokyo University preprint.
- [Se88] R. Seki, in: Pion Nucleus Physics: Future Directions and New Facilities at LAMPF (Los Alamos, 1988), eds R.J. Peterson and D. Strottman, AIP Conf. Proc. no. 163, p. 233.
- [Sp88] J. Speth, ed., Proc. Intern. Symp. on Strangeness in Hadronic Matter (Bad Honnef, 1987), Nucl. Phys. A 479 (1988).
- [St79] K. Stricker, H. McManus and J.A. Carr, Phys. Rev. C 19 (1979) 929.
- [SW81] W. Stepień-Ruzka and S. Wycech, Nucl. Phys. A 362 (1981) 1706.
- [Sz87] J.J. Szymansky, Ph.D. dissertation, Carnegie-Mellon University (1987).
- [Ta84] L. Tauscher, C. García-Recio and E. Oset, Nucl. Phys. A 415 (1984) 333.
- [Ta85] K. Takeuchi, H. Takaki and H. Bandō, Prog. Theor. Phys. 73 (1985) 841, Progr. Lett.
- [Ta88] H. Tamura et al., in: Proc. Intern. Symp. on Strangeness in Hadronic Matter (Bad Honnef, 1987), ed. J. Speth, Nucl. Phys. A 479 (1988) 161c.
- [Te62] V.L. Telegdi, Sci. Am. 206 (1962) 50.
- [To90] L. de la Torre, J.F. Donoghue, J. Dubach and B.R. Holstein, to be submitted.
- [TY88] H. Toki and T. Yamazaki, Phys. Lett. B 213 (1988) 129.
- [Wh86] C.S. Whisnant, Phys. Rev. C 34 (1986) 262.
- [Wi73] D.H. Wilkinson, Nucl. Phys. A 209 (1973) 470.
- [Wi74] D.H. Wilkinson, Nucl. Phys. A 225 (1974) 365.
- [Ya85] T. Yamazaki et al., Phys. Rev. Lett. 54 (1985) 102.
- [Ya86] T. Yamazaki et al., Nucl. Phys. A 450 (1986) 1c.
- [Ya88] T. Yamazaki, R.S. Hayano, O. Morimatsu and K. Yazaki, Phys. Lett. B 207 (1988) 393.
- [YB83] Y. Yamamoto and H. Bandō, Prog. Theor. Phys. 69 (1983) 1312.
- [YB85] Y. Yamamoto and H. Bandō, Prog. Theor. Phys. Suppl. 81 (1985) 9; Prog. Theor. Phys. 73 (1985) 905.

Proton and light ion induced charge exchange reactions in nuclei

This content has been downloaded from IOPscience. Please scroll down to see the full text.

1993 Phys. Scr. 48 101

(<http://iopscience.iop.org/1402-4896/48/1/017>)

View [the table of contents for this issue](#), or go to the [journal homepage](#) for more

Download details:

IP Address: 139.184.14.159

This content was downloaded on 02/10/2015 at 17:29

Please note that [terms and conditions apply](#).

Proton and Light Ion Induced Charge Exchange Reactions in Nuclei

E. Oset, P. Fernández de Córdoba, J. Nieves and M. J. Vicente-Vacas

Departamento de Física Teórica and IFIC, Centro Mixto Universidad de Valencia–CSIC, 46100 Burjassot, Valencia, Spain

Received October 15, 1992; accepted November 30, 1992

Abstract

We study the different channels which contribute to the charge exchange reactions of the type ($^3\text{He}, t$) (p, n) etc., in the region of excitation of the delta resonance. We show that the shift of the delta peak in nuclei is due to a collaboration of many processes: delta excitation in the projectile, quasi-elastic collisions, virtual pion absorption and coherent pion production. The first three processes are responsible for a considerable shift of strength but do not move the peak position, while the addition of the coherent channel produces finally the shift of the peak.

We concentrate first on the ($^3\text{He}, t$) reactions at 2 GeV kinetic energy of the ^3He where the Saclay data [1] show an appreciable shift of strength from the proton to the deuteron targets and an even more remarkable shift of the strength and the position of the peak for medium and heavy nuclei (see Fig. 1). We want to stress two features from this picture: On the first hand there is some shift in the deuteron target with respect to the $p(^3\text{He}, t)$ reaction. On the second one, in ^{12}C there is an appreciable amount of strength close to the maximum energy of the t , which corresponds to quasielastic collisions. With respect to the deuteron, since many body effects should be small in this inclusive cross section, the most natural assumption is that the ($^3\text{He}, t$) reaction on the neutron target is different to the one with the proton target and has its strength shifted towards higher t energies. With respect to the quasielastic peak one can see that a smooth extrapolation of this peak to lower t energies

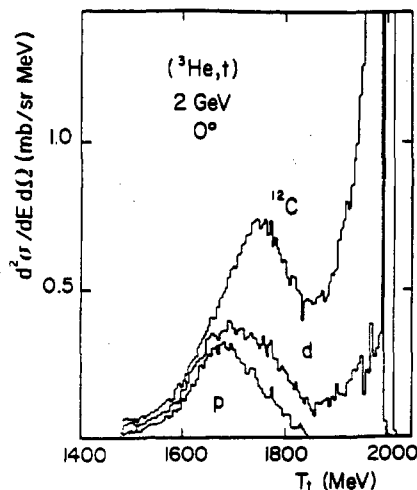


Fig. 1. Double differential cross section for ($^3\text{He}, t$) on different layer nuclei as a function of the t kinetic energy

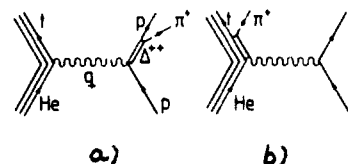


Fig. 2. (a) Delta excitation in the target; (b) Delta excitation in the projectile

necessarily has some strength below the delta peak. We have paid attention to these two issues.

The shift of strength in the deuteron was interpreted in Ref. [2] in terms of Δ excitation in the projectile. We show in Fig. 2(a) and (b) the mechanisms of delta excitation in the target (DET) and the projectile (DEP). The two mechanisms give rise to very different t energy shapes. Indeed in the DET process the Δ invariant mass is fixed in terms of the t four momentum while in the DEP mechanisms this invariant mass is not fixed and depends explicitly on the pion momentum which changes within the phase space. One has

$$\text{DET: } s_t = (p_{\text{He}} - p_t + p_N)^2$$

$$\text{DEP: } \sqrt{s_p} = [(p_t + p_\pi)^2]^{1/2} - 2M$$

which shows explicitly the dependence commented before. The values of s_p are such that the cross section peaks at higher t energies than the DET process. The weight of both mechanisms depends on the target and the type of reaction. We show in Table I the weight of these mechanisms based solely on the isospin counting.

As we can see, in the ($^3\text{He}, t$) reaction in the p target the DET mechanism dominates, however in the n target both DET and DEP mechanisms have the same weight and as a consequence there is a shift of strength in the neutron towards high t energies, and correspondingly in the deuteron when one sums the contributions of the p and n to the

Table I. Isospin coefficients

	Target	Projectile
$p(^3\text{He}, t)$	2	2/9
$n(^3\text{He}, t)$	2/3	2/3
$p(^3\text{He}, ^3\text{He})$	6/9	134/9
$n(^3\text{He}, ^3\text{He})$	6/9	86/9
$p(^4\text{He}, ^4\text{He})$	0	64/3
$n(^4\text{He}, ^4\text{He})$	0	64/3

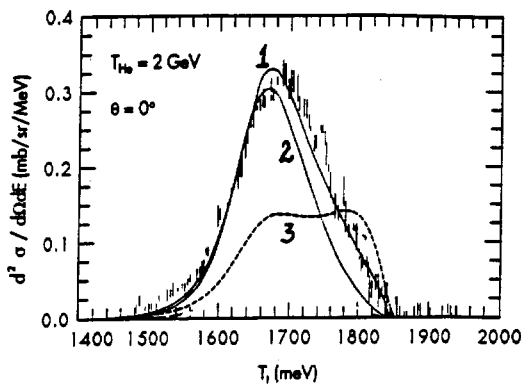


Fig. 3. Double differential cross section in the $p(\text{He}, t)p\pi^+$ reaction in the p lab system. (1) Results including the DET + DEP + s -wave mechanisms. (2) Results with the DET mechanism alone. (3) Results for the $n(\text{He}, t)N\pi$ reaction, including the DET + DEP + s -wave mechanisms

inclusive ($^3\text{He}, t$) reaction. In Table I we also show the isospin weight for other reactions, ($^3\text{He}, ^3\text{He}$) and ($^4\text{He}, ^4\text{He}$). Both of them are dominated by Δ excitation in the projectile. In particular in the ($^4\text{He}, ^4\text{He}$) reaction, for obvious reasons of isospin conservation, the DET mechanism is forbidden and there is only excitation in the projectile. Predictions for the ($^3\text{He}, ^3\text{He}$) reaction are done in Ref. [3] and measurements of the $p(^4\text{He}, ^4\text{He})$ reaction have been recently done [4], showing a cross section considerably larger than the one of the $p(^3\text{He}, t)$, in qualitative agreement with the expectations of Table I. Theoretical work under these lines is also in progress [5]. In Fig. 3 we show the predictions for the ($^3\text{He}, t$) cross section on the proton and the neutron and in Fig. 4 the predictions for the deuteron. As one can see, the shapes of the proton and neutron distributions are quite different and the deuteron distribution is fairly well reproduced.

Now we come to the second point and look at all channels which contribute to the inclusive ($^3\text{He}, t$) reaction on nuclei:

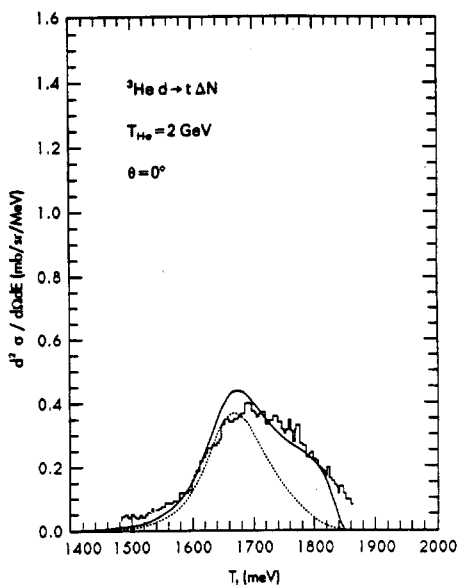


Fig. 4. Double differential cross section for ($^3\text{He}, t$) on deuteron target at fixed angle as a function of the t kinetic energy. Dotted curve: DEP mechanism alone. Solid curve: DET + DEP + s -wave

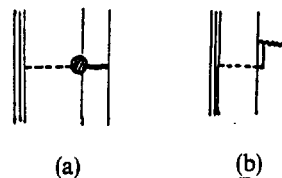
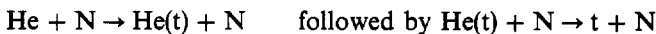
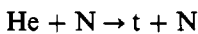


Fig. 5. Process of virtual pion absorption. (a) generic, (b) Δ dominated absorption piece

(1) Quasielastic collisions which include one step or two step processes:



where in the last process there is a quasielastic collision with breakup of the He or t in the first step and recombination in the second one.

(2) Pion production, for which the model of Fig. 2 is used including delta excitation in the target and the projectile. Two step processes in which a quasielastic collision appears before or after pion production are also considered. In all these processes the nucleons are ejected to the continuum or into ^{12}C excited states and the process accounts for incoherent pion production.

(3) Virtual pion absorption. These are processes of the type of Fig. 5(a) where the dashed circle represents the $\pi N \rightarrow \pi N$ amplitude which contains s - and p -waves. A particular case of the p -wave piece is shown in Fig. 5(b) corresponding to delta excitation followed by the non-mesonic Δ decay, $\Delta N \rightarrow NN$. It must be said, however, that at low virtual pion energies where this mechanism peaks, the mechanism of Fig. 5(b) only accounts for about one-third of the strength of the p -wave part, the rest coming from nucleon pole or crossed nucleon and delta pole terms and the interference with the diagram of Fig. 5(a). The pion in Fig. 5 is in practice substituted by the whole spin-isospin interaction, like in Fig. 2.

(4) Coherent pion production: This is a genuine nuclear channel which comes when the target nucleus is left in its ground state and the production amplitude is summed coherently over all the nucleons in the target. Diagrammatically it is shown in Fig. 6(a) where the pion with the shaded circle indicates the renormalized pion in the

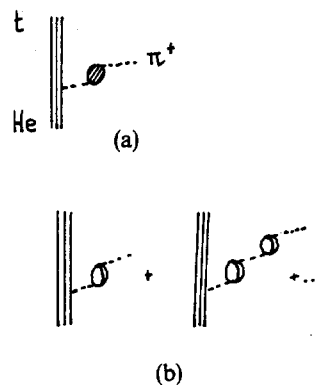


Fig. 6. Diagrams for coherent pion production. (a) generic, (b) detailed model in the delta resonance region

medium. In the resonance region where the Δh excitation dominates, the detailed picture would be given by Fig. 6(b), although, as commented, the exchanged pion lines are replaced by the spin-isospin interaction. The process, at least for forward or small t angles, requires necessarily the interaction of the pion with the nucleus, otherwise it does not proceed with a free pion alone, even if the ${}^3\text{He}$ and t are allowed to interact with the nucleus, as we do. The reason can be seen if one uses the Glauber eikonal approximation for the ${}^3\text{He}$ or t wavefunctions in the forward direction. The wavefunction picks up some transverse momentum components but the free longitudinal momenta are not modified. Hence the ${}^3\text{He} \rightarrow t + \pi^+$ transition is in this case as forbidden as if the ${}^3\text{He}$ or t did not interact with the nucleus. For all these reasons the process qualifies as virtual pion production followed by elastic scattering of this virtual pion with the nucleus till it becomes real. Hence the study of this channel is bound to offer valuable information about pion nucleus interaction, complementary to the one obtained from the scattering of real pions.

In Fig. 7 we show the contribution of all the channels discussed above. As we can see, the one step quasielastic fills the region of very high t energy while the two step quasielastic processes peak somewhat at lower t energies, as also does the virtual pion production. The incoherent pion production peaks at the same position as the elementary (${}^3\text{He}$, t) reaction on the p , something confirmed experimentally [6]. The most interesting feature, however, is that the peak of the coherent pion production is considerably shifted (about 70 MeV) with respect to the incoherent one. This feature is responsible for the ultimate shift of the peak in the total inclusive (${}^3\text{He}$, t) cross section. We can observe in the

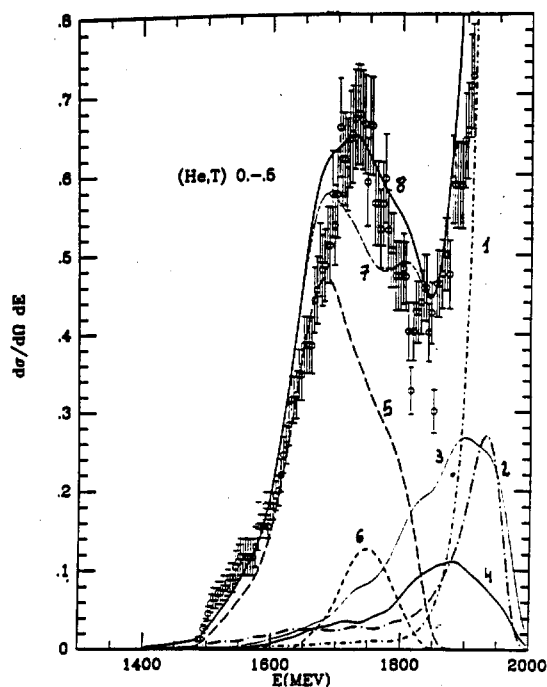


Fig. 7. Different contributions to the cross section for the (${}^3\text{He}$, t) inclusive reaction on ${}^{12}\text{C}$. (1) Quasielastic $\text{He} + \text{N} \rightarrow t + \text{N}$. (2) Two step quasielastic $\text{He} + \text{N} \rightarrow \text{He}(t) + \text{N}$ followed by $\text{He}(t) + \text{N}' \rightarrow t + \text{N}'$. (3) Two step quasielastic with intermediate $\text{He}(t)$ break up: $\text{He} + \text{N} \rightarrow \text{He}^*(t^*) + \text{N}$ followed by $\text{He}^*(t^*) + \text{N} \rightarrow t + \text{N}$. (4) Virtual pion production followed by pion absorption. (5) Incoherent pion production. (6) Coherent π^+ production. (7) Sum of incoherent processes 1-5. (8) Total: sum of coherent and incoherent processes

figure that the sum of all the incoherent channels shifts considerably the strength at higher t energies, but the position of the peak is not altered. When one then adds the coherent pion production cross section the peak is moved and one finds agreement with experiment. The reason for the shift of the coherent channel has to be seen in the effect of the nuclear form factor since the produced virtual pion and the detected real ones have the same energy but different momenta. At higher energies, for a given angle, $|q - q'|$ increases and the form factor decreases. The multiple scattering is also relevant, helping split the momentum transfer in several collisions and hence reducing the effect of the form factor, but at the same time producing and appreciable loss of flux into the pion quasielastic or absorption channels, as the pion energy increases.

Another feature of the coherent channel is that the pions are created in a very narrow cone around the direction of the (He , t) momentum transfer. This property and the fact that the nucleus recoil energy is very small, and well known if all pions come in the same direction, converts the coherent pion production in a tool to produce beams of highly monochromatic and unidirectional pions. Its potential practical use, similar to the tagging of highly monochromatic photons, should be investigated, once we know that the amount of pions produced is a sizeable fraction of the total number of pions (about one-third at the peak of the coherent channel).

We do not have a direct measurement of the coherent channel although preliminary partial data have been extracted from the Saturne measurements [7]. However, we can compare our results for coherent π^+ production in the analogous reaction (p , n) on ${}^{12}\text{C}$ with the data of Chiba *et al.* [8] when they separate the π^+ channel. Even here they have a background in this channel of neutral particles coming from $pn \rightarrow nn\pi^+$. We can see our results in Fig. 8 compared to the experiment. We have adopted our results to the experimental cuts and resolution. One observes that our coherent production peaks at the place of the experimental peak, which is appreciably shifted with respect to the peak of the incoherent pion production. On the other hand when our coherent pion production is subtracted from the experimental data one obtains a smooth background which looks very much like the cross section of the analogous

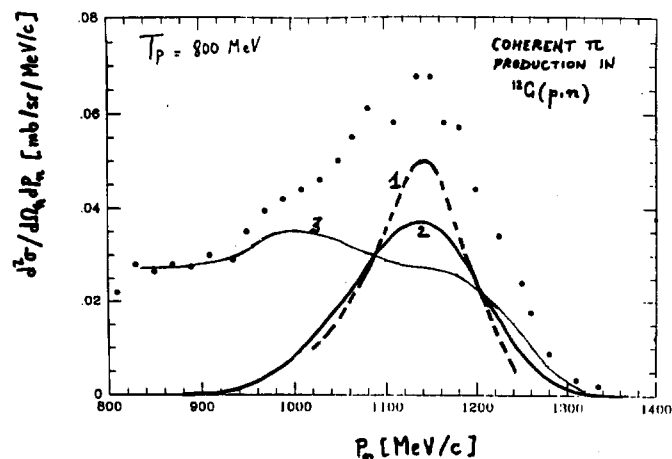


Fig. 8. (1) Coherent π^+ production with experimental cuts; (2) Idem with the folding with the experimental resolution; (3) Difference from experiment and the curve 2

${}^3\text{He} n \rightarrow t n \pi^+$ which is contained in the (${}^3\text{He}, t$) cross section on the neutron target of Fig. 3. The bigger weight at lower t energies (in the region of the Δ resonance) for the background of the $pn \rightarrow nn\pi^+$ reaction is understandable because of the absence of the (${}^3\text{He}, t$) transition form factor that reduces the cross section more strongly at lower t energies in this latter reaction.

As one can see, the information obtained from our theoretical analysis matches so far the available experimental information. However, experiments devoted to the measurements of the coherent channel should definitely be pursued.

Summarizing, the study done here has shown that the shift of the Δ peak in the (${}^3\text{He}, t$) [or (p, n)] reaction is due to a collaboration of many channels, amongst which the coherent pion production plays a crucial qualitative role as responsible for the shift of the peak position. This channel was implicitly included in the calculations of Refs [9, 10] and is the reason, in our opinion, of the shift found there, although other reasons were given in those papers.

Finally, the coherent pion production channel shows up as an interesting tool to learn about the pion nuclear interaction. Also, its properties as a source of highly monochromatic and unidirectional pions are bound to have some practical use in the future.

References

1. Contardo, D., Bedjidian, M., Grossiord, J. Y., Guichard, A., Haroutunian, R., Pizzi, J. R., Ellegaard, C., Gaarde, C., Larsen, J. S., Goodman, C., Bergqvist, I., Brockstedt, Carlen, L., Ekstrom, P., Bachelier, D., Boyard, J. L., Hennino, T., Jourdain, J. C., Roy-Stephan, M., Boivin, M. and Radvanyi, P., *Phys. Lett.* **B168**, 331 (1986).
2. Oset, E., Shiino, E. and Toki, H., *Phys. Lett.* **B224**, 249 (1989).
3. Fernández de Córdoba, P. and Oset, E., *Nucl. Phys.* **A544**, 793 (1992).
4. Morsch, H. P., Boivin, M., Jacobs, W., Plouin, F., Spang, W., Yonnet, J., Zupranski, P., Frascaria, R., Siebert, R., Warde, E., Didelez, J. P., Saghai, B. and Tegnér, P. E., *Phys. Rev. Lett.* **69**, 1336 (1992).
5. Fernández de Córdoba, P., Gareev, F. A., Oset, E., Ratis, Y. and Vicente-Vacas, M. J., (to be published).
6. Hennino, T., Ramstein, B., Bachelier, D., Bohlen, H. G., Boyard, J. L., Ellegaard, C., Gaarde, C., Gosset, J., Jourdain, J. C., Larsen, J. S., Lemaire, M. C., L'Hôte, D., Morsch, H. P., Österlund, M., Poitou, J., Radvanyi, P., Roy-Stephan, M., Sams, T., Sneppen, K., Valette, O. and Zupranski, P., *Phys. Lett.* **B283**, 42 (1992).
7. Gaarde, C., contribution to this Conference.
8. Chiba, J., Kobayashi, T., Nagae, T., Arai, I., Kato, N., Kitayama, H., Manabe, A., Tanaka, M., Tomizawa, K., Beatty, D., Edwards, G., Glaushausser, C., Kumbartzki, G. J., Ransome, R. D. and Baker, F. T., *Phys. Rev. Lett.* **67**, 1982 (1991).
9. Udagawa, T., Hong, S. H. and Osterfeld, F., *Phys. Lett.* **B245**, 1 (1990); Osterfeld, F., contribution to this Conference.
10. Delorme, J. and Guichon, P. A. M., *Phys. Lett.* **B263**, 157 (1991).

BB

FTUV/94-20
IFIC/94-18

FTUV 94-20
see 9420

A REVIEW ON MESONIC DECAY OF Λ HYPERNUCLEI

E. Oset¹⁾, P. Fernández de Córdoba²⁾, J. Nieves³⁾, A. Ramos⁴⁾
and L.L. Salcedo⁵⁾

1) *Departamento de Física Teórica and IFIC*

Centro Mixto Universidad de Valencia - CSIC, 46100 Burjassot (Valencia) Spain.

2) *Departamento de Matemática Aplicada; Universidad Politécnica de Valencia, Valencia, Spain.*

3) *Physics Department. The University Southampton, S09 5NH, United Kingdom.*

4) *Departament d'Estructura i Constituents de la Matèria.*

Universitat de Barcelona, 08028 Barcelona, Spain.

5) *Departamento de Física Moderna. Universidad de Granada, 18071 Granada, Spain.*

Contents.

1. A brief historical introduction.
2. Formal derivation of the Λ width in nuclei. The propagator method.
3. Finite nuclei approach to the mesonic width. The wave function method.
4. Equivalence of the propagator and wave function methods.
5. The mesonic width and the occupation number.
6. Results for the mesonic width.
7. The $2p2h$ induced decay around the pion branch.
8. Conclusions.



Abstract

A review of the present situation of the mesonic decay of Λ hypernuclei is done. The link between the propagator method and the one with wave functions and nuclear matrix elements is established. The lack of links between the mesonic decay and the nucleon occupation number in nuclear matter is also discussed, as well as the effect of the ΛN short range repulsion in the mesonic decay of light hypernuclei. The relevance of the $2p2h$ induced Λ decay channel is also discussed. Finally an overview of the potential use of the process, when systematic measurements over the periodic table are done, is presented at the end.

1 A brief historical introduction.

A paper devoted to the memory of our friend Hiroharu Bandō is the right place to recall some interesting events associated with him and the subject of this paper. In 1984 L.L. Salcedo was working in Valladolid for his Ph. D. on the decay of Λ hypernuclei and he surprised me (E.O.) with the results which indicated that the rate for pionic decay of heavy Λ hypernuclei was increased by about two orders of magnitude when a proper medium renormalization of the pion was done. At that time I was still not used to shake every one of the few times that Salcedo would open his mouth, so I told him to check again his program. He did so and came out with the same answer. This time I checked it myself and had to surrender to a reality that was difficult to swallow and worst, I had the feeling it would be difficult to sell. A paper was written and after a few useful corrections suggested by the referee the paper was published [1]. I should thank the generosity of the referee who, probably without believing the results, let it be published. I say that a posteriori because when my selling mission began I could not convince a single colleague of the soundness of the results. To make it short I recall the lapidary sentence of A. Gal: "I do not believe in any renormalization factor of 100".

With this predisposition from my colleagues I presented these results in the hypernuclear Conference at Brookhaven in 1985 [2]. I went there with clarifying and convincing arguments, with Feynman diagrams, with poles and cuts in the complex plane and Cutkosky rules to separate imaginary parts, and all this heavy artillery that should have crumbled the strongest walls. The result: a lost battle. The whole audience turned against me. Even my friends Gerry Brown and Torlif Ericson showed disbelief in their questions and comments at the end of the talk. But it was Torlif the one who opened my mind to what was happening: I was using an inappropriate language for that audience which was more used to the language of wave functions and matrix elements than to the one of propagators, selfenergies and cuts which I was using. And here came Bandō. I went to him and discussed with him. He was using this alternative language and he should be able to prove the same results using pionic wave functions in the nucleus and evaluating the proper matrix elements. He was the first person to take us seriously and he started to work with his colleagues Motoba and Itonaga on the issue. In ref. [2], after the experience with the audience and the discussions with Torlif, I wrote a section on "an alternative approach" sketching the way to follow using the language of wave functions and matrix elements, which was the one followed by Bandō and collaborators.

Their work has been very useful [3, 4, 5]. It not only confirmed the huge enhancement of the mesonic width found in [1], but produced detailed and quantitative results in many nuclei, taking into account shell effects, Q values and other details which go far beyond the nuclear matter and local density approach of ref. [1]. Since then the spectacular enhancement of the mesonic width has been universally accepted. Their predictions have been confirmed

by the new wave of experiments [6, 10].

I came to appreciate Bandō more with this incident. His quiet, flexible and gentle approach to the problems contrasted with my stern and temperamental one, and certainly proved to be much more efficient.

One of the interesting outputs of [3, 4, 5] is that the mesonic width is quite sensitive to the pion nucleus optical potential, for potentials which fit equally well the pion nucleus scattering data. This information is very useful and should serve as a check for different microscopic models of the pion nucleus interaction. The work done on the mesonic decay and its interconnection with the other Λ decay channels has also been essential to get a unified picture of the Λ decay in nuclei and has generated other interesting developments as we shall see below.

2 Formal derivation of the Λ width in nuclei. The propagator method.

The starting point is the $\Lambda \rightarrow \pi N$ Lagrangian, accounting for this weak process, which is given by

$$L_{\pi\Lambda N} = G\mu^2\bar{\psi}_N(A - B\gamma_5)\vec{\tau} \cdot \vec{\phi}_\pi\psi_\Lambda + h.c. \quad (1)$$

with

$$(G\mu^2)^2/8\pi = 1.94510^{-16}, \quad A = 1.06, \quad B = 7.10 \quad (2)$$

In eq. (1) the Λ is assumed to behave as the state $|1/2, -1/2\rangle$ of an isospin doublet with $T = 1/2$ and this imposes the $\Delta T = 1/2$ rule, which has as a consequence a strength double for the $\Lambda \rightarrow \pi^- p$ channel than for the $\Lambda \rightarrow \pi^0 n$ one. In eq. (1) the term A violates parity and the term B conserves it.

A practical way to evaluate the Λ width in nuclear matter and introduce the medium corrections is to start from the Λ selfenergy, Σ , associated to the diagram of fig. 1 and then use the relationship

$$\Gamma = -2Im\Sigma \quad (3)$$

The selfenergy is readily evaluated as

$$-i\Sigma(k) = 3(G\mu^2)^2 \int \frac{d^4q}{(2\pi)^4} G(k-q)D(q)[S^2 + (\frac{P}{\mu})^2 \vec{q}^2] \quad (4)$$

where G and D are the nucleon and pion propagators respectively and $P/\mu = B/2M$ with μ, M the pion and nucleon mass. By using the free nucleon and pion propagators, and making the typical nonrelativistic approximation $M/E = 1$, one obtains immediately the free Λ width [1, 11]

$$\Gamma_{free} \equiv \Gamma_{\Lambda} = 3(G\mu^2)^2 \int \frac{d^3q}{(2\pi)^3} \frac{1}{2\omega(\vec{q})} 2\pi\delta(E_{\Lambda} - \omega(\vec{q}) - E_N(\vec{k} - \vec{q})) \times [S^2 + (\frac{P}{\mu})^2 \vec{q}^2] \quad (5)$$

In a Fermi sea of nucleons, both the nucleon and pion propagators are changed

$$G(p) = \frac{1 - n(\vec{p})}{p^0 - E(\vec{p}) - V_N + i\epsilon} + \frac{n(\vec{p})}{p^0 - E(\vec{p}) - V_N - i\epsilon} \quad (6)$$

$$D(q) = \frac{1}{q^{02} - \vec{q}^2 - \mu^2 - \Pi(q^0, q)} \quad (7)$$

where V_N is the nucleon potential, $\Pi(q^0, q)$ is the pion selfenergy in the nuclear medium and $n(\vec{p})$ is the occupation number in the Fermi sea, $n(\vec{p}) = 1$ for $|\vec{p}| \leq k_F$, $n(\vec{p}) = 0$ for $|\vec{p}| > k_F$, with k_F the Fermi momentum. The practical way to perform the q^0 integral in eq.(4) is to perform a Wick rotation as shown in fig. 2, where the analytical structure of the integrand is shown. The shaded region accounts for the discontinuity of the pion propagator due to $Im \Pi$. The pole at $\tilde{\omega}(\vec{q})$ would correspond to a renormalized pion pole where

$$\tilde{\omega}(\vec{q})^2 - \vec{q}^2 - \mu^2 - \Pi(\tilde{\omega}(\vec{q}), q) = 0 \quad (8)$$

Missing in the figure is the pole of $G(k-q)$ corresponding to the second term in (6). This pole lies in the lower halfplane of the figure and would contribute in the Wick rotation only when it happens to be in the third quadrant, i.e., $k^0 - E(\vec{k} - \vec{q}) - V_N < 0$. But this corresponds to $(\vec{k} - \vec{q})$ very large where $n(\vec{k} - \vec{q}) = 0$ and hence this term does not contribute. Thus we obtain for the width [1, 11]

$$\Gamma(k) = -6(G\mu^2)^2 \int \frac{d^3q}{(2\pi)^3} [1 - n(\vec{k} - \vec{q})] \theta(k^0 - E(\vec{k} - \vec{q}) - V_N) \times [S^2 + (\frac{P}{\mu})^2 \vec{q}^2] Im \frac{1}{q^{02} - \vec{q}^2 - \mu^2 - \Pi(q^0, q)} \Big|_{q^0 = k^0 - E(\vec{k} - \vec{q}) - V_N} \quad (9)$$

In the discussion here we neglect the role of correlations and form factors, which are obviously important and are treated in all detail in [1, 11]. The simplified formalism will allow us to concentrate on the qualitative aspects of the reaction.

In the first place we observe the Pauli blocking factor, $1 - n$, in eq. (9). Since a Λ with $k = 0$ decays into a nucleon and pion with $q \simeq 100 MeV/c$, this momentum is smaller than the Fermi momentum for nuclear matter density,

$k_F = 270 MeV/c$, and the decay is forbidden by Pauli blocking, i.e., $1 - n(\vec{k} - \vec{q}) = 0$. The overlap of the Λ wave function with the nuclear surface in finite nuclei still allows the Λ decay since at some radius the local Fermi momentum will be smaller than $100 MeV/c$, and also because the momentum distribution of the Λ wave function helps a bit in allowing some nucleon momenta in the decay. Nevertheless the Λ mesonic width decreases drastically as a function of the mass number.

The language of propagators which we have used here is the most appropriate in order to provide a unified picture of the Λ nuclear decay. Indeed, eq. (9) contains not only the modified mesonic channel but also the nonmesonic one. This can be seen diagrammatically by expanding the pion propagator and taking a ph and Δh excitation to account for the pion selfenergy, Π . This is depicted in fig. 3. The imaginary part of a selfenergy diagram is obtained when the set of intermediates states cut by a horizontal line are placed simultaneously on shell in the intermediate integration. In fig. 3 we observe a source corresponding to placing on shell a nucleon and the ph of the pion selfenergy. This corresponds to a channel where there are no pions and only nucleons in the final state. The physical process which has occurred is $\Lambda N \rightarrow NN$ and this is the nonmesonic channel. Technically it would be obtained by substituting in eq. (9)

$$Im \frac{1}{q^{02} - \vec{q}^2 - \mu^2 - \Pi} \rightarrow \frac{Im \Pi_{ph}}{|q^{02} - \vec{q}^2 - \mu^2 - \Pi|^2} \quad (10)$$

where Π_{ph} is the pion selfenergy due to the $1p1h$ excitation. There is no overlap between $Im \Pi_{ph}(q^0, q)$ and the pion pole in the propagator of eq. (9) and thus the separation is clear.

The mesonic channel would correspond to a different cut, the one where the N and the π are placed on shell. This is shown diagrammatically in fig. 4. The terms in fig. 4b, and further iterations contained in (9), lead to a renormalization of the mesonic width, and an appreciable one, as it was shown in ref [1].

Technically the mesonic width can be calculated from the total width, eq. (9), subtracting the nonmesonic width, or equivalently by obtaining the pion pole contribution in eq. (4) from the renormalized pion pole given in eq. (8).

The qualitative reason on why the mesonic width is so drastically changed is given in [1, 11]: The attractive character of the pion selfenergy leads to a larger pion momentum for the same pion energy and thus, to a larger nucleon momentum by momentum conservation. Thus, the nucleon has more chances to have a momentum bigger than the Fermi momentum, therefore increasing the mesonic width.

The width in finite nuclei is obtained in [1] via the local density approximation

$$\Gamma = \int d^3r |\phi_{\Lambda}(\vec{r})|^2 \Gamma(k, \rho(\vec{r})) \quad (11)$$

where ϕ_Λ is the Λ wave function. A further average over the momentum distribution of the Λ wave function is also done in [1].

3 Finite nuclei approach to the mesonic width. The wave function method.

This approach was sketched in [2] and carried out in detail in [3]. The mesonic width is given, in analogy to eq. (5) by

$$\begin{aligned} \Gamma^{(\alpha)} = & \frac{1}{2} C^{(\alpha)} (G\mu^2)^2 \sum_{N \notin F} \int \frac{d^3 q}{(2\pi)^3} \frac{1}{2\omega(\vec{q})} 2\pi \delta(E_\Lambda - \omega(\vec{q}) - E_N) \\ & \times \left\{ S^2 \left| \int d^3 x \phi_\Lambda(\vec{x}) \phi_\pi^{(-)}(\vec{q}, \vec{x})^* \phi_N^*(\vec{x}) \right|^2 \right. \\ & \left. + \left(\frac{P}{\mu} \right)^2 \left| \int d^3 x \phi_\Lambda(\vec{x}) \vec{\nabla} \phi_\pi^{(-)}(\vec{q}, \vec{x})^* \phi_N^*(\vec{x}) \right|^2 \right\} \end{aligned} \quad (12)$$

where ϕ_N is the wave function of the nucleon states and $\phi_\pi^{(-)*}$ corresponds to an outgoing solution of the Klein Gordon equation normalized to a plane wave asymptotically ($e^{-i\vec{q}\vec{r}}$). The index α stands now for $\pi^- p$ or $\pi^0 n$ decay, with $C^{(p)} = 4, C^{(n)} = 2$, which one separates here since due to shell effects these channels can depart drastically from the elementary $\Delta T = 1/2$ rule.

The sum in eq. (12) runs only over non occupied nucleon states in the shell model. On the other hand the effects of using for $\phi_\pi^{(-)*}$ a solution of the Klein Gordon equation with a proper optical potential (or pion selfenergy, $\Pi = 2\omega V_{opt}, V_c$ Coulomb potential), i.e.,

$$[-\vec{\nabla}^2 + \mu^2 + 2\omega V_{opt}(\vec{x})] \phi_\pi^{(-)}(\vec{q}, \vec{x})^* = [\omega - V_c(\vec{x})]^2 \phi_\pi^{(-)}(\vec{q}, \vec{x})^* \quad (13)$$

[Instead of a plane wave are rather drastic and increase the mesonic width in about two orders of magnitude in heavy nuclei [3, 5], in qualitative agreement with the nuclear matter results of ref. [1].

The arguments for the renormalization are expressed now in the alternative language as follows: the attraction caused by the pion selfenergy increases the pion momenta in the pion wave function. As a consequence the matrix element of the Λ wave function (in a $1s_{1/2}$ ground state of the Λ nucleus potential) and the nucleon wave function is considerably enhanced. Note that if the Λ and N potentials were the same, the Λ and $N \notin F$ states are orthogonal and the matrix elements of (12) would be zero for $q = 0$. The matrix elements thus necessarily increase with \vec{q} , for the moderately small values of \vec{q} involved in the present process. In the two languages the physical consequences are the same: an increased probability of reaching the unoccupied states and thus an enhancement of the mesonic width.

4 Equivalence of the propagator and wave function methods.

The discussion above has shown that the physical and numerical results of the pion renormalization are the same. Yet, technically the two approaches look different. In this section we establish the equivalence of the two methods and the approximations implicit in them.

Let us start from the pion propagator in finite nuclei written in coordinate space

$$D(\vec{x}, \vec{y}, \omega) = \sum_n \frac{\varphi_n(\vec{x}) \varphi_n^*(\vec{y})}{\omega^2 - \epsilon_n^2 + i\eta} \quad (14)$$

where $\varphi_n(\vec{x})$ are the pion wave functions in the nucleus and ϵ_n their corresponding energies. Ignoring pionic bound states, which do not play a role in our problem, we can identify the pionic wave functions by the asymptotic momentum \vec{q} . Hence their energy is given by $\omega(\vec{q}) = (\vec{q}^2 + \mu^2)^{1/2}$. The sum over the index n is then replaced by an integral over \vec{q} as given below

$$D_\pi(\vec{x}_1, \vec{x}_2, E_\pi) = \int \frac{d^3 q}{(2\pi)^3} \frac{\phi_\pi(\vec{q}, \vec{x}_1) \phi_\pi^*(\vec{q}, \vec{x}_2)}{E_\pi^2 - \omega(\vec{q})^2 + i\eta} \quad (15)$$

For simplicity in the derivation we shall take the s -wave part of the width (the one providing the largest contribution) and will not distinguish between π^0 or π^- decay. Hence, from eq. (12) we obtain

$$\begin{aligned} \Gamma_S = & 3(G\mu^2)^2 S^2 \sum_{N \notin F} \int \frac{d^3 q}{(2\pi)^3} \frac{1}{2\omega(\vec{q})} 2\pi \delta(E_\Lambda - E_N - \omega(\vec{q})) \\ & \times \left| \int d^3 x \phi_\Lambda(\vec{x}) \phi_\pi^*(\vec{q}, \vec{x}) \phi_N^*(\vec{x}) \right|^2 \end{aligned} \quad (16)$$

which can be rewritten as

$$\begin{aligned} \Gamma_S = & 3(G\mu^2)^2 S^2 \sum_{N \notin F} \int d^3 x_1 \int d^3 x_2 \phi_\Lambda^*(\vec{x}_1) \phi_\Lambda(\vec{x}_2) \\ & \times \phi_N(\vec{x}_1) \phi_N^*(\vec{x}_2) \int \frac{d^3 q}{(2\pi)^3} \frac{1}{2\omega(\vec{q})} 2\pi \delta(E_\Lambda - E_N - \omega(\vec{q})) \\ & \phi_\pi(\vec{q}, \vec{x}_1) \phi_\pi^*(\vec{q}, \vec{x}_2) \end{aligned} \quad (17)$$

or by virtue of eq. (15) as

$$\begin{aligned} \Gamma_S = & 3(G\mu^2)^2 S^2 \sum_{N \notin F} \int d^3 x_1 d^3 x_2 \phi_\Lambda^*(\vec{x}_1) \phi_N(\vec{x}_1) (-2) \\ & \times \text{Im } D_\pi(\vec{x}_1, \vec{x}_2; E_\pi = E_\Lambda - E_N) \theta(E_\Lambda - E_N) \phi_\Lambda(\vec{x}_2) \phi_N^*(\vec{x}_2) \end{aligned} \quad (18)$$

Now, in order to connect with eqs. (9) and (11) one makes a local density approximation. In the first step one evaluates Γ for a slab of infinite nuclear matter and in the second step one replaces the width in the infinite slab by an integral over the nuclear volume assuming slabs of matter in each d^3r of the nucleus with local density $\rho(\vec{r})$ and with a probability of finding the Λ particle given by $|\phi_\Lambda(\vec{r})|^2$. This last step is implemented by means of eq. (11). Hence we should see how we reproduce now eq. (9) when we assume in eq. (18) a slab of infinite nuclear matter. For this purpose we have to substitute for the nucleon sector

$$\begin{aligned} N &\rightarrow \vec{p} \\ \sum_{N \notin F} &\rightarrow V \int \frac{d^3p}{(2\pi)^3} (1 - n(\vec{p})) \\ \phi_N(\vec{x}) &\rightarrow \frac{1}{\sqrt{V}} e^{i\vec{p}\vec{x}} \\ E_N &\rightarrow E(\vec{p}) - V_N \end{aligned} \quad (19)$$

and for the Λ wave function

$$\phi_\Lambda(\vec{x}) \rightarrow \frac{1}{\sqrt{V}} e^{i\vec{k}\vec{x}} \quad (20)$$

Now in the infinite slab of nuclear matter the pion propagator of eq. (15) is substituted by

$$D_\pi(\vec{x}_1, \vec{x}_2, E_\pi) \rightarrow \int \frac{d^3q}{(2\pi)^3} \frac{e^{i\vec{q}(\vec{x}_1 - \vec{x}_2)}}{E_\pi^2 - \omega(\vec{q})^2 - \Pi(E_\pi, \vec{q})} \quad (21)$$

where $\Pi(E_\pi, \vec{q})$ is the pion selfenergy, which is a function of ρ . Note that for values of \vec{x}_1, \vec{x}_2 far away from the nucleus eqs. (15) and (21) are equivalent since there $\rho = 0$ and Π (in the local density approximation) will be zero. At other densities, Π will be different of zero and the integral of eq. (21) gives rise to other momentum components, modulating the plane wave of the numerator and providing a kind of WKB approximation to the wave functions of the numerator of eq. (15). The local density approximation gives rise to a variable local momentum and hence a distorted pion wave.

By substituting eqs. (19), (20), (21) in eq. (18) we obtain:

$$\begin{aligned} \Gamma_S &= -6(G\mu^2)^2 S^2 \int \frac{d^3p}{(2\pi)^3} \int \frac{d^3q}{(2\pi)^3} (1 - n(\vec{p})) \text{Im} D_\pi(q) \theta(q^0) \Big|_{q^0 = E_\Lambda - E(\vec{k} - \vec{q}) - V_N} \\ &\times \int d^3x_1 d^3x_2 \frac{1}{V} e^{i\vec{p}(\vec{x}_1 - \vec{x}_2)} e^{i\vec{q}(\vec{x}_1 - \vec{x}_2)} e^{-i\vec{k}(\vec{x}_1 - \vec{x}_2)} \end{aligned} \quad (22)$$

with $D_\pi(q)$ given by eq. (7). Finally, by means of the relationship $(2\pi)^3 \delta^3(0) = \int d^3x = V$ we can cast eq. (22) as

$$\Gamma_S = -6(G\mu^2)^2 S^2 \int \frac{d^3q}{(2\pi)^3} (1 - n(\vec{k} - \vec{q})) \text{Im} D_\pi(q) \theta(q^0) \Big|_{q^0 = E_\Lambda - E(\vec{k} - \vec{q}) - V_N} \quad (23)$$

which coincides with the s -wave contribution to Γ from eq. (9). This establishes the equivalence between the two methods within the local density approximation which we have done in the case of the propagator method.

5 The mesonic width and the occupation number.

We have seen that Pauli blocking is the major factor in the small mesonic width of heavy Λ hypernuclei. It was suggested that because real interacting nuclei have the "occupied" states partly unoccupied, the mesonic width should be enhanced with respect to a calculation with fully occupied Fermi levels [14]. In the nuclear matter approach of section 2 this is easily visualized by recalling a realistic picture of the occupation number of the Fermi sea [15], which is depicted in fig. 5. For the states below the Fermi energy the level of occupancy is of the order of 85% and by assuming that in the Λ decay the nucleons can occupy the 15% vacancy of these states we would guess that the mesonic width would stabilize at the level of about 10% of the free width for heavy nuclei (taking into account pion absorption in the way out of the pions). If this were the case the mesonic width could serve as a measure of the occupation number in the Fermi sea. The argument is very appealing and intuitive, however, it is incorrect and leads to an overestimate of the width in about three orders of magnitude in heavy nuclei.

The detailed discussion of this problem was done in ref. [16]. The fallacy in the argumentation lies in the fact that

$$\frac{1 - n_1(\vec{k})}{k^0 - E(\vec{k}) + i\epsilon} + \frac{n_1(\vec{k})}{k^0 - E(\vec{k}) - i\epsilon} \quad (24)$$

where $n_1(\vec{k})$ is the realistic occupation number in nuclear matter, is not an improvement over the propagator in eq. (6). The realistic N propagator for an interacting Fermi sea is given in terms of the spectral functions by

$$G(k^0, k) = \int_{-\infty}^{\mu} d\omega \frac{S_h(\omega, k)}{k^0 - \omega - i\epsilon} + \int_{\mu}^{\infty} d\omega \frac{S_p(\omega, k)}{k^0 - \omega + i\epsilon} \quad (25)$$

with μ the chemical potential.

When performing the calculations of the mesonic width with this N propagator one obtains the factor

$$\int_{\mu}^{\infty} d\omega S_p(\omega, \vec{k} - \vec{q}) 2\pi\delta(k^0 - \omega - \omega(\vec{q})) \quad (26)$$

replacing the factor

$$[1 - n(\vec{k} - \vec{q})] 2\pi\delta(k^0 - E(\vec{k} - \vec{q}) - \omega(\vec{q})) \quad (27)$$

in eq. (5), when the Pauli blocking factor of eq. (9) is implemented. Eqs. (26), (27) bare some intuitive resemblance because

$$\int_{\mu}^{\infty} d\omega S_p(\omega, \vec{k} - \vec{q}) = 1 - \int_{-\infty}^{\mu} d\omega S_h(\omega, \vec{k} - \vec{q}) = 1 - n_1(\vec{k} - \vec{q}) \quad (28)$$

However, in the presence of the δ function of eq. (26), the integral of eq. (28) cannot be factored out because the δ function in eq. (26) has ω in the argument. Furthermore because of restrictions of the phase space (energy and momentum conservation) the range of values of ω allowed are very small compared to the range (μ, ∞) needed in eq. (28) to obtain $1 - n_1(\vec{k} - \vec{q})$ of the interacting Fermi sea. In physical terms we can interpret it in the following way: the occupation number $n_1(\vec{k} - \vec{q})$ is an integral for all the energies of the nucleon, ω , of the probability of finding a nucleon with momentum $\vec{k} - \vec{q}$ and an energy ω , which is given by the spectral function $S_h(\omega, \vec{k} - \vec{q})$. However, in a physical decay process we have conservation of energy and momentum and hence there are severe restrictions to the values of the energies that the nucleon can have. This is why the occupation number $n_1(\vec{k} - \vec{q})$ cannot be factored out.

The actual calculations carried out in ref. [16] showed that for light and medium nuclei the use of the spectral representation for the nucleon propagator, eq. (25), instead of the one of the noninteracting Fermi sea, eq. (6), has negligible consequences in the mesonic width (of the order of 6% corrections in ^{16}O). The corrections can be of the order of 50% in heavy nuclei, but in all cases, when the pionic renormalization is taken into account, one can disregard these effects.

These findings have been of relevance in showing similar problems in the study of other physical processes, like in the contribution of the pion cloud to K^+ nucleus scattering where one can show [17] that one cannot relate the effect of the pion cloud to the pion excess number in the nucleus as assumed in refs. [18, 19].

6 Results for the mesonic width.

In refs. [3, 4, 5] one can find abundant results in different nuclei which are rather realistic. These results have been recently improved [13] by a more accurate description of the energy balance in the particular reactions, taking into account transitions to the bound and continuum N states and using a

pion nucleus optical potential which has been derived theoretically and leads to a good description of the data of pionic atoms and to elastic, reaction and absorption cross sections in the scattering processes [20]. The potential allows the separation of its imaginary part into two terms related to pion absorption and quasielastic scattering. In [13] the pion quasielastic events are not removed from the pion flux, as it corresponds to the actual experimental observation, while the use of a full distortion of the pion with the total optical potential, as done in [3, 4, 5], inevitably removes the pion quasielastic events, together with the pion absorption events. Though conceptually important, this refinement turns out to be of little practical relevance in the present problem given the small energy that the pions carry and the very small phase space for quasielastic collisions [13]. However, other considerations, particularly the energy balance in the reactions makes the widths in heavy nuclei for π^- -decay about one order of magnitude smaller than those of ref. [5].

In fig. 6 we show the prediction of ref. [13] for different nuclei and for π^0 and π^- decay, with plane waves and the renormalized pion wave function. The drastic effects of the pion renormalization are seen there and are a bit smaller than in former works because the energy balance makes the pions come out with smaller energies than in the previous approaches and the attractive effects of the p -wave part of the optical potential are then diminished.

Of particular relevance are the results in ^{12}C . One obtains the following

	$\Gamma_{\pi^0}/\Gamma_{\Lambda}$	$\Gamma_{\pi^-}/\Gamma_{\Lambda}$	$\Gamma_{\pi^0}/\Gamma_{\pi^-}$
[13]	0.159	0.086	1.86
[5]	0.13	0.098	1.32
exp	0.217 ± 0.084 [10]	$0.052 \pm_{-0.036}^{0.063}$	

Although with large errors the experimental results confirm these striking theoretical predictions which show a large violation of the $\Delta T = 1/2$ in nuclei ($\Gamma_{\pi^0}/\Gamma_{\pi^-}$ should be 0.5 under this rule) due mostly to nuclear shell effects.

Another interesting finding is seen in very light nuclei. The mesonic width of $^5_{\Lambda}He$ has attracted particular attention. There, in addition to the pion renormalization, the repulsive character of the ΛN interaction and the relatively weaker medium range attraction, compared to the NN interaction, has as an effect the pushing of the Λ to the surface of the nucleus, weakening the Pauli blocking effect and thus enhancing the mesonic decay [21, 22]. The experimental numbers clearly favour potentials with a repulsive ΛN core. One should note that such a repulsion automatically appears in quark based models of the ΛN interaction. A recent study of the $^5_{\Lambda}He$ decay using a quark model based hypernuclear wave function [23] leads to the following results

	$\Gamma_{\pi^-}/\Gamma_{\Lambda}$	$\Gamma_{\pi^0}/\Gamma_{\Lambda}$	$\Gamma_{tot}/\Gamma_{\Lambda}$
[23]	0.431	0.239	0.670
exp	0.44 ± 0.11 [9]	0.18 ± 0.20 [9]	$0.59 \pm_{-0.11}^{0.44}$

These theoretical results are also in good agreement with those of ref. [24] when a Λ wave function from the modified YNG ΛN interaction of ref. [25], which has a strong repulsion at short distances, is used.

7 The $2p2h$ induced decay around the pion branch.

One of the interesting findings concerning the pionic decay was done in ref. [26]. The idea of this work, expressed in a different way, is the following: A real pion in a nuclear medium has a large width because of the coupling to $2p2h$ components which lead to pion absorption. This means that the strength of the pion is spread in a wide region, unlike a free pion which has all its strength accumulated in one point (one energy for a certain value of q). The decay leading to the emission of one pion is drastically reduced in nuclei because of Pauli blocking. However, one extreme of the pion distribution in the nucleus could be saved from Pauli blocking, because we can have a smaller energy for the pion and correspondingly more energy for the nucleon, and thus this part of the nuclear pion spectrum could participate in the Λ decay. Technically we could say that the strength of a free pion, which is accumulated in a δ function, becomes now a Breit Wigner distribution and part of the tail will correspond to a Pauli unblocked situation. Since the width of the Breit Wigner distribution at low pion energies is mostly due to pion absorption through $2p2h$ emission, the new mode would be observed as three particle emission from $\Lambda NN \rightarrow NNN$. This is depicted in fig. 7.

In order to see this analytically we go back to eq. (9). $\Gamma(k)$ is related to $Im D(q)$. Assume we have

$$\Pi(q^0, q) = \Pi_{ph} + \Pi_{\Delta h} \quad (29)$$

as done in [1]. Then

$$Im D(q) = \frac{Im \Pi_{ph} + Im \Pi_{\Delta h}}{|q^{02} - \vec{q}^2 - \mu^2 - \Pi|^2} \quad (30)$$

Around the pion pole, when the denominator in (30) vanishes, $Im \Pi_{\Delta h}$ is extremely small because there is little phase space for pion quasielastic collisions and the Δ is far off shell. In addition, there $Im \Pi_{ph} = 0$ because a real pion cannot be absorbed by just one nucleon in nuclear matter. As a consequence we have a δ like distribution which corresponds to a pion in the medium, renormalized by a real pion selfenergy $Re \Pi \simeq \Pi_{ph} + \Pi_{\Delta h}$. Now, if in addition we consider the $2p2h$ part of the pion selfenergy leading to pion absorption we would have

$$\Pi(q^0, q) = \Pi_{ph} + \Pi_{\Delta h} + \Pi_{2p2h} \quad (31)$$

and now $Im \Pi_{2p2h} \neq 0$ for (q^0, q) close to on shell pions. As a consequence we will have around the pion pole the following strength of the pion propagator

$$Im D(q) \simeq \frac{Im \Pi_{2p2h}}{(q^{02} - \vec{q}^2 - \mu^2 - \Pi_{ph} - \Pi_{\Delta h} - Re \Pi_{2p2h})^2 + (Im \Pi_{2p2h})^2} \quad (32)$$

This is like a Breit-Wigner distribution in q^0 , except for the fact that Π_{2p2h} depends explicitly on the variable q^0 (and q).

Since now there is overlap between $Im \Pi_{2p2h}$ and the pion pole one has to be cautious in the separation of the pionic width and the one associated to $2p2h$ emission. In ref [26] the calculations were done in infinite nuclear matter at normal nuclear matter density where the mesonic decay channel is forbidden. Hence, all the strength from eq. (9) with $Im D(q)$ from eq. (32) was attributed to the $2p2h$ channel. In finite nuclei, where there is some mesonic decay allowed, eq. (9) with the distribution of eq. (32) accounts simultaneously for the mesonic and $2p2h$ excitation channel. The separation of the two channels can be done by calculating the contribution of the pion pole and associating it to pion emission, and then associating to the $2p2h$ excitation channel, the difference between the width calculated with eqs. (9), (32) and the width from the pion pole contribution. The pion pole contribution is calculated by means of eq. (9) substituting $Im D(q)$ by $-\pi\delta(q^{02} - \vec{q}^2 - \mu^2 - Re \Pi(q^0, q))$. This is the way followed in ref. [27]. In addition a more realistic input for Π_{2p2h} is used in [27] taking care properly of the phase space available for the $2p2h$ excitation.

The results of [27] indicate that $\Gamma_{2p2h}/\Gamma_{\Lambda} \simeq 0.30$ for different nuclei from ^{12}C up to ^{208}Pb . In ref. [26] this ratio had a value around 0.60 for values of the g'_{Λ} parameter compatible with those used in [27].

Even with smaller values for $\Gamma_{2p2h}/\Gamma_{\Lambda}$ than those of ref. [26], the existence of this channel has important repercussions in the number of neutrons and protons emitted in the Λ decay process, a piece of information which is used to determine the ratio of proton to neutron induced Λ decay in the nonmesonic channel. It is clear that in view of the new results one cannot associate all n or p emerging from the experiment to the primary $\Lambda n \rightarrow nn$ or $\Lambda p \rightarrow np$ reactions and hence a reanalysis of the experimental data is needed. This analysis requires the consideration of the Λ nonmesonic decay channel, which we have not addressed here, hence the reader is addressed to this paper [27] for further details.

Up to now the experiments for Λ decay have focused on two channels, the mesonic and the non mesonic. In view of the former results and the fact that the $2p2h$ channel has a bigger strength than the mesonic one from nuclei like ^{16}O up, it would be very interesting to conduct experimental searches for this channel too.

8 Conclusions.

We have made a review of the present situation concerning the mesonic decay of Λ hypernuclei. We have established the formal link between the propagator method, where the huge enhancement of the pionic decay width was first reported, and the finite nuclei approach with wave functions and matrix elements. Shell effects and precise values of the nuclear binding energies are also important in the mesonic width and they are best taken into account in the finite nuclei approach. The intuitive and appealing, but fallacious, link between the nucleon occupation number and the mesonic width has also been discussed, which has served to unveil rough approximations used in other processes to link the pion excess number with contributions of the nuclear meson cloud to some physical observables, like K^+ nucleus scattering. We have also discussed the relevance of the short range ΛN repulsion in the mesonic width of light hypernuclei and showed how the repulsion provided by quark models of the ΛN interaction can naturally account for the present experimental widths. Finally we have discussed the Λ decay induced by pairs of nucleons through the tail of the pion distribution in the nucleus, which "cheats" the Pauli blocking and leads to a three nucleon decay channel, $\Lambda NN \rightarrow NNN$.

With the limited amount of experimental data available on the mesonic channel, the amount of physical information obtained is remarkable. There is support for strong ΛN repulsion at short distances providing indirect support for quark models of the ΛN interaction; the process provides us with the most striking renormalization effect due to the pion nucleus interaction. Furthermore, the "cheating" of Pauli blocking by the $2p2h$ induced decay can provide good information on the coupling of the pion to these nuclear components, a very valuable complement to real pion absorption, etc. The sensitivity of the Λ decay to the pion nucleus optical potential can also serve as a tool to choose between different theoretical descriptions of the complex mechanisms of pion nucleus interaction. The decay channel into π^0 can be an excellent instrument to learn about π^0 nucleus interaction, and so on.

It is clear that a systematic experimental search in many nuclei of the mesonic decay channel and its related $2p2h$ induced decay mode will provide us with very valuable information to unravel the intricacies of the pion nucleus interaction or the elementary properties of the ΛN interaction, as well as proper nuclear structure details of the Λ hypernuclei themselves.

This work has been partially supported by CICYT contract no. AEN 93-1205, PB92-0927, PB 92-0761. One of us, J. N. wishes to acknowledge financial support from the European Union.

References

- [1] E. Oset and L.L. Salcedo, Nucl. Phys. A443 (1985) 704.
- [2] E. Oset and L.L. Salcedo, Nucl. Phys. A450 (1986) 371c.
- [3] K. Itonaga, T. Motoba and H. Bandō, Z. Phys. A330 (1988) 209.
- [4] T. Motoba, K. Itonaga and H. Bandō, Nucl. Phys. A489 (1988) 683.
- [5] T. Motoba, Nucl. Phys. A527 (1991) 485c; Few Body Systems, Suppl. 5 (1992) 386; Proc. Int. Sym. on Hypernuclear and Strange Particle Physics, Shimoda, 1991 [Nucl. Phys. A547 (1992) 115c].
- [6] R. Grace et al., Phys. Rev. Lett. 55 (1985) 1055.
- [7] A. Sakaguchi et al., Nuovo Cimento 102A (1989) 511.
- [8] P.D. Barnes, Nucl. Phys. A450 (1986) 43c; A478 (1988) 127c.
- [9] J.J. Szymanski et al., Phys. Rev. C43 (1991) 849.
- [10] A. Sakaguchi et al., Phys. Rev. C43 (1991) 73.
- [11] E. Oset, P. Fernández de Córdoba, L.L. Salcedo and R. Brockmann, Phys. Reports 188 (1990) 79.
- [12] R.J. Glauber, Lectures in Theoretical Physics, Interscience, New York, 1959, Vol. 1, pp. 315-414.
- [13] J. Nieves and E. Oset, Phys. Rev. C47 (1993) 1478.
- [14] H. Bandō and H. Takaki, Phys. Lett. B150 (1985) 409.
- [15] S. Fantoni and V.R. Pandharipande, Nucl. Phys. A427 (1984) 473.
- [16] P. Fernández de Córdoba and E. Oset, Nucl. Phys. A528 (1991) 736.
- [17] C. García-Recio, J. Nieves and E. Oset, University of Granada preprint 1994.
- [18] S.V. Akulinichev, Phys. Rev. Lett. 68 (1992) 290.
- [19] M.F. Jiang and D.S. Koltum, Phys. Rev. C46 (1992) 2462.
- [20] J. Nieves, E. Oset and C. García-Recio, Nucl. Phys. A554 (1993) 509; *ibid* pag. 554.
- [21] Y. Kurihara, Y. Akaishi and H. Tanaka, Phys. Rev. C31 (1985) 971.
- [22] E. Oset, L.L. Salcedo and Q.N. Usmani, Nucl. Phys. A450 (1986) 67c.

- [23] U. Straub, J. Nieves, A. Faessler and E. Oset. Nucl. Phys. A556 (1993) 531.
- [24] T. Motoba, H. Bandō, T. Fukuda and J. Žofka, Nucl. Phys. A534 (1991) 597.
- [25] Y. Yamamoto and H. Bandō, Prog. Theor. Phys. 73 (1985) 905; Prog. Theor. Phys. Suppl. no. 81 (1985) ch. II.
- [26] W.M. Alberico, A. de Pace, M. Ericson and A. Molinari, Phys. Lett. B256 (1991) 134.
- [27] A. Ramos, E. Oset and L.L. Salcedo, University of Barcelona preprint.

Figure captions.

Fig. 1 Feynman graph for the free Λ self-energy of eqs. (4), (5). The $\Lambda \rightarrow \pi N$ “cut” is shown (dotted line).

Fig. 2. Analytical structure of the integrand of eq. (4) in the complex q^0 plane with the nucleon and pion propagators of eqs. (6), (7). The renormalized pion propagator pole $\tilde{\omega}(q)$ is shown. The dashed lines close to the real axis indicate the analytical cut from $Im \Pi(q^0, q)$ related to the nonmesonic Λ decay channel.

Fig. 3 Λ self-energy diagrams included in eq. (4) with the nucleon and pion propagators of eqs. (6), (7). (a) Free self-energy graph. (b), (c) Insertion of p -wave pion self-energy at lowest order. (d) Generic RPA graph from the expansion of the pion propagator in powers of the pion selfenergy. (e) s -wave pion self-energy at lowest order. The cuts represent the nonmesonic decay channel.

Fig. 4. Free and lowest order Λ self-energy graph. The dotted cuts represent the mesonic decay channel.

Fig. 5. Schematic representation of the nucleon occupation number for an interacting Fermi sea.

Fig. 6. Pionic decay rate for π^0 and π^- as a function of the mass number (of the host nucleus, ^{16}O , ^{40}Ca , ^{90}Zr , ^{138}Ba , and ^{208}Pb). The two lower lines show the calculation with plane waves for the pion and the two upper lines the results with pion distorted waves.

Fig. 7. Schematic representation of the Λ decay coupling to $2p2h$ components through virtual (close to real) pion absorption.

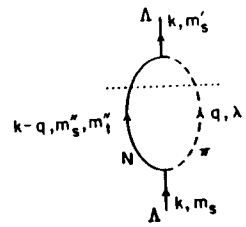


fig. 1

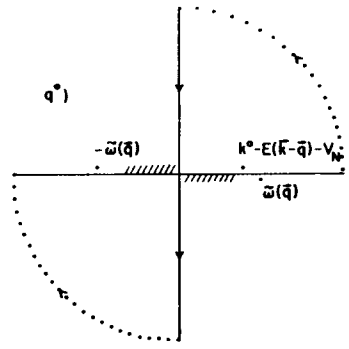


fig. 2

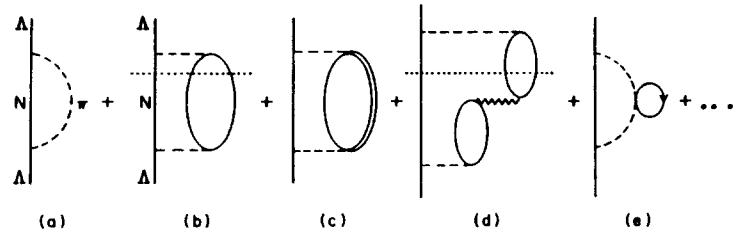


fig. 3

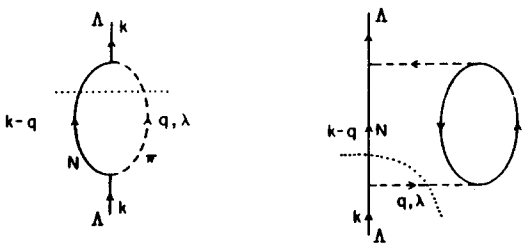


fig. 4

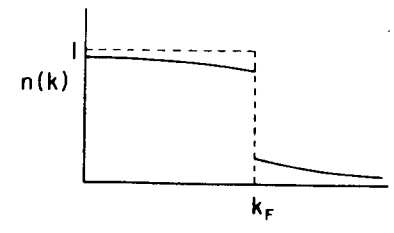


fig. 5

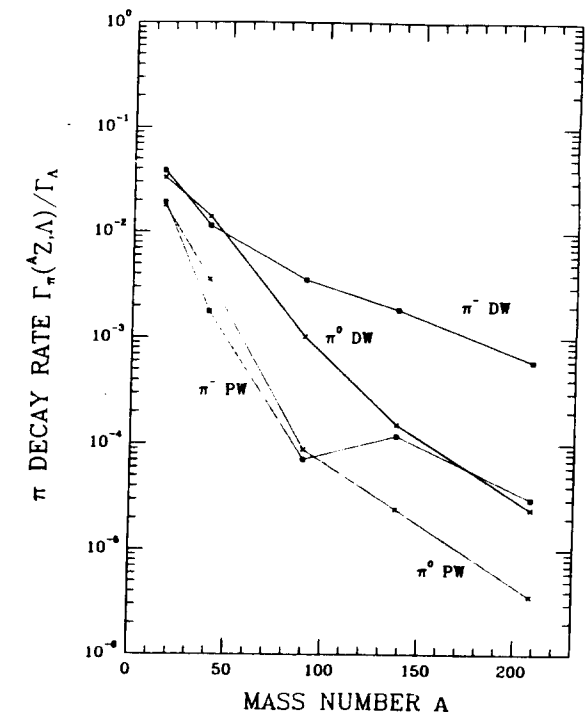
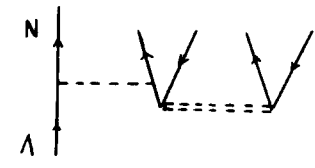


fig. 6



A code to calculate (high order) Bessel functions based on the continued fractions method

Yu.L. Ratis¹ and P. Fernández de Córdoba

*Departamento de Física Teórica and IFIC, Centro Mixto Universidad de Valencia – CSIC,
46100 Burjassot (Valencia), Spain*

Received 26 June 1992; in revised form 5 February 1993

We have developed a fast code to calculate Bessel functions of integer and fractional order based on the continued fractions method. This algorithm is specially useful in the case of Bessel functions of high order because it does not require any recalculation using normalization relations.

PROGRAM SUMMARY

Title of program: BESSEL, SPHERICAL

Catalogue number: ACNL

Program obtainable from: CPC Program Library, Queen's University of Belfast, N. Ireland (see application form in this issue)

Licensing provisions: none

Computer: VAX 6410; *Installation:* Instituto de Física Corpuscular (IFIC), Burjassot (Valencia)

Operating system: VAX/VMS

Programming language used: FORTRAN 77

Memory required to execute with typical data: 12 kB

No. of bits in a word: 32

No. of lines in distributed program, including test data, etc.: 382

Keywords: high order Bessel functions, continued fractions method.

Nature of the physical problem

We include two codes in order to evaluate: (a) Bessel functions of fractional order (subroutine SPHERICAL); (b) Bessel functions of integer order (subroutine BESSEL).

Method of solution

We have developed a fast code to calculate Bessel functions of integer and fractional order based on the continued fractions method. This algorithm is specially useful in the case of Bessel functions of high order because it does not require any recalculation using normalization relations.

Restrictions on the complexity of the problem

We can use our algorithm for different order Bessel functions taking into account that the maximum order N_{\max} that we can reach with our method, for a fixed real positive value of z , is provided by the maximum real number defined in our machine: N_{\max} will be the maximum n for which $Y_n(z)$ is less than the maximum real number of our machine. (See section 4 of the Long Write-Up.)

Typical running time

See Long Write-Up, section 3.

Correspondence to: Yu.L. Ratis, Departamento de Física Teórica and IFIC, Centro Mixto Universidad de Valencia – CSIC, 46100 Burjassot (Valencia), Spain.

¹ Permanent address: Samara Aviation Institute, Moskovskoe Avenue, 34, 443019, Samara, Russia.

LONG WRITE-UP

1. Introduction

The usual methods to calculate Bessel functions take into account normalization relations [1]. In this paper we introduce an algorithm and corresponding computer code to evaluate regular and irregular Bessel functions without any re-calculation through normalization relations. Furthermore, the method maintains the stability of each recurrence relation, i.e. we use forward recurrence relations for the Bessel functions (BFs) of the second kind and backward ones [2] for the BFs of the first kind.

In fact the algorithm uses forward recurrence relations to generate irregular BFs and takes into account the continued fraction method to evaluate high order regular BFs. From these values we can generate regular BFs applying backward recurrence relations. Because of this structure (in which we do not use any normalization relation), the algorithm is specially useful for calculating high order BFs. The code evaluates simultaneously regular and irregular BFs; in the following sections we show in detail the algorithm for the cases of BFs of fractional and integer orders.

The code has direct application in a wide variety of problems where high order BFs are necessary: in the evaluation of Lommel's functions of two variables [5,6] (very often used in wave and light guides), in application codes where very high order Hankel functions (which include regular and irregular BFs) appear, and in scattering theory when one can encounter problems where large values of the impact parameter (i.e. large values of angular momentum) are involved (and where Glauber's approach is not very appropriate).

2. Bessel functions of fractional order

We are interested in presenting a code to generate the spherical Bessel functions (SBFs) of the first and second kinds.

In this paper we use the standard Abramowitz and Stegun [3] notation and we introduce the SBFs of the first kind, $j_n(z) = \sqrt{\pi/2z} J_{n+1/2}(z)$, and the SBFs of the second kind, $y_n(z) = \sqrt{\pi/2z} Y_{n+1/2}(z)$, as particular solutions of the differential equation:

$$z^2 \omega''(z) + 2z \omega'(z) + [z^2 - n(n+1)] \omega(z) = 0 \quad (n = 0, \pm 1, \pm 2, \dots). \quad (1)$$

In the code we calculate simultaneously the SBFs of all orders below Nmax, i.e. we generate the set

$$SB(z) \equiv \{j_n(z), y_n(z); n = 0, 1, 2, 3, \dots, Nmax\}. \quad (2)$$

The algorithm is organized in the following way:

- Evaluate all the SBFs of the second kind, $\{y_n(z), n = 0, 1, 2, \dots, Nmax\}$, taking into account the known values of $y_0(z) = -\cos(z)/z$ and $y_1(z) = -\sin(z)/z - \cos(z)/z^2$ and using the forward recurrence relation

$$y_{n+1}(z) = \frac{(2n+1)}{z} y_n(z) - y_{n-1}(z). \quad (3)$$

-Use the continued fractions method [3] to evaluate the ratio

$$\begin{aligned} H(z) &\equiv \frac{j_{Nmax}(z)}{j_{Nmax-1}(z)} = \frac{J_{Nmax+1/2}(z)}{J_{Nmax-1/2}(z)} \\ &= \frac{1}{2(Nmax + \frac{1}{2})z^{-1} -} \frac{1}{2(Nmax + \frac{3}{2})z^{-1} -} \frac{1}{2(Nmax + \frac{5}{2})z^{-1} -} \dots \end{aligned} \quad (4)$$

We implement this method in our code by using Steed's algorithm [4].

– Calculate the upper order SBFs of the first kind, $j_{N_{\max}}(z)$, using the already known values $y_{N_{\max}}(z)$ and $y_{N_{\max}-1}(z)$, the ratio $H(z)$ and the value for the Wronskian of the SBFs:

$$W\{j_{N_{\max}}(z), y_{N_{\max}}(z)\} \equiv j_{N_{\max}}(z) y_{N_{\max}-1}(z) - j_{N_{\max}-1}(z) y_{N_{\max}}(z) = z^{-2}. \quad (5)$$

Using (5) we can write

$$j_{N_{\max}-1}(z) = \frac{1}{z^2(H(z) y_{N_{\max}-1}(z) - y_{N_{\max}}(z))} \quad (6)$$

and then

$$j_{N_{\max}}(z) = H(z) j_{N_{\max}-1}(z). \quad (7)$$

Notice that we have calculated not only $j_{N_{\max}}(z)$ but also $j_{N_{\max}-1}(z)$.

– Evaluate all the SBFs of the first kind, $\{j_n(z), n = 0, 1, 2, \dots, N_{\max}\}$, taking into account the calculated values of $j_{N_{\max}}(z)$ and $j_{N_{\max}-1}(z)$ and using the backward recurrence relation:

$$j_{n-1}(z) = \frac{(2n+1)}{z} j_n(z) - j_{n+1}(z). \quad (8)$$

3. Bessel functions of integer order

We require a code to generate the Bessel functions of the first and second kinds. (We restrict attention to real values of the argument z). As in the previous section we use the standard Abramowitz and Stegun notation and introduce the BFs of the first kind, $J_n(z)$, and the BFs of the second kind, $Y_n(z)$, as particular solutions of the differential equation:

$$z^2 \omega''(z) + z \omega'(z) + (z^2 - n^2) \omega(z) = 0. \quad (9)$$

In the code we calculate simultaneously the BFs of all order below N_{\max} , i.e. we generate the set

$$B(z) = \{J_n(z), Y_n(z); n = 0, 1, 2, 3, \dots, N_{\max}\}. \quad (10)$$

The algorithm is organized in the following way:

– Evaluate $Y_0(z)$ and $Y_1(z)$ using the ascending series [3]

$$Y_n(z) = -\frac{\left(\frac{1}{2}z\right)^{-n}}{\pi} \sum_{k=0}^{n-1} \frac{(n-k-1)!}{k!} \left(\frac{1}{4}z^2\right)^k + \frac{2}{\pi} \ln\left(\frac{1}{2}z\right) J_n(z) - \frac{\left(\frac{1}{2}z\right)^n}{\pi} \sum_{k=0}^{\infty} \{\Psi(k+1) + \Psi(n+k+1)\} \frac{\left(-\frac{1}{4}z^2\right)^k}{k!(n+k)!}, \quad (11)$$

where

$$J_n(z) = \left(\frac{1}{2}z\right)^n \sum_{k=0}^{\infty} \frac{\left(-\frac{1}{4}z^2\right)^k}{k!(n+k)!} \quad (12)$$

and $\Psi(\cdot)$ is defined by

$$\Psi(n) = -\gamma + \sum_{k=1}^{n-1} k^{-1}, \quad (13)$$

with γ being Euler's constant.

In the particular case of $Y_0(z)$ we can write

$$Y_0(z) = \frac{2}{\pi} \left[\ln\left(\frac{1}{2}z\right) + \gamma \right] J_0(z) + \frac{2}{\pi} \left(\frac{\frac{1}{4}z^2}{(1!)^2} - \left(1 + \frac{1}{2}\right) \frac{\left(\frac{1}{4}z^2\right)^2}{(2!)^2} + \left(1 + \frac{1}{2} + \frac{1}{3}\right) \frac{\left(\frac{1}{4}z^2\right)^3}{(3!)^2} - \dots \right), \quad (14)$$

where

$$J_0(z) = 1 - \frac{\frac{1}{4}z^2}{(1!)^2} + \frac{\left(\frac{1}{4}z^2\right)^2}{(2!)^2} - \frac{\left(\frac{1}{4}z^2\right)^3}{(3!)^2} + \dots \quad (15)$$

For the case $z \rightarrow \infty$ ($z > 10$) we use the Hankel asymptotic expansions for $Y_0(z)$ and $Y_1(z)$ and we write

$$Y_n(z) = \sqrt{\frac{2}{\pi z}} [P(n, z) \sin \chi + Q(n, z) \cos \chi], \quad (16)$$

where

$$P(n, z) \sim \sum_{k=0}^{\infty} \frac{(-)^k (n, 2k)}{(2z)^{2k}}, \quad (17)$$

$$Q(n, z) \sim \sum_{k=0}^{\infty} \frac{(-)^k (n, 2k+1)}{(2z)^{2k+1}}, \quad (18)$$

with (n, k) , the Hankel symbol,

$$(n, k) = \frac{\Gamma\left(\frac{1}{2} + n + k\right)}{k! \Gamma\left(\frac{1}{2} + n - k\right)} \quad (19)$$

and χ given by

$$\chi = z - \left(\frac{1}{2}n + \frac{1}{4}\right)\pi. \quad (20)$$

– Evaluate all the BFs of the second kind, $\{Y_n(z), n = 0, 1, 2, \dots, N_{\max}\}$, taking into account the calculated values of $Y_0(z)$ and $Y_1(z)$ and using the forward recurrence relation

$$Y_{n+1}(z) = \frac{2n}{z} Y_n(z) - Y_{n-1}(z). \quad (21)$$

– Use the continued fractions method to evaluate the ratio

$$H(z) = \frac{J_{N_{\max}}(z)}{J_{N_{\max}-1}(z)} = \frac{1}{2N_{\max} z^{-1} -} \frac{1}{2(N_{\max} + 1) z^{-1} -} \frac{1}{2(N_{\max} + 2) z^{-1} -} \dots \quad (22)$$

We implement this method in our code again, using Steed's algorithm [4].

– Calculate the upper order BFs of the first kind, $J_{N_{\max}}(z)$, using the already known values of $Y_{N_{\max}}(z)$ and $Y_{N_{\max}-1}(z)$, the ratio $H(z)$ and the value for the Wronskian of the BFs [3]:

$$W\{J_{N_{\max}-1}(z), Y_{N_{\max}-1}(z)\} \equiv J_{N_{\max}}(z) Y_{N_{\max}-1}(z) - J_{N_{\max}-1}(z) Y_{N_{\max}}(z) = \frac{2}{\pi z}. \quad (23)$$

As in the previous section we can write

$$J_{N_{\max}}(z) = \frac{2}{\pi z (Y_{N_{\max}-1}(z) - Y_{N_{\max}}(z)/H(z))} \quad (24)$$

and then

$$J_{N_{\max}-1}(z) = J_{N_{\max}}(z)/H(z). \quad (25)$$

Notice again that we calculate not only $J_{N_{\max}}(z)$ but also $J_{N_{\max}-1}(z)$.

– Evaluate all the BFs of the first kind, $\{J_n(z), n = 0, 1, 2, \dots, N_{\max}\}$, taking into account the calculated values of $J_{N_{\max}}(z)$ and $J_{N_{\max}-1}(z)$ and using the backward recurrence relation

$$J_{n-1}(z) = \frac{2n}{z} J_n(z) - J_{n+1}(z). \quad (26)$$

We would like to point out that $J_0(z)$ and $J_1(z)$ can be used as checks on the accuracy of the procedure.

We have compared our algorithm with a standard one (subroutine MMBSJN of the IMSL library) by calculating different order BFs with arguments in the range $10^{-36} < z < 10^3$ and getting a relative error of $\sim 10^{-9}$ in the values supplied by both methods if we use a typical value $\text{EPS} \sim 10^{-12}$ to control the accuracy in the continued fraction method (see subroutine BESSEL in the next section). We have studied our algorithm for different order BFs taking into account that the maximum order N_{\max} that we can reach with our method, for a fixed z , is provided by the maximum real number defined in our machine: N_{\max} will be the maximum n for which $Y_n(z)$ is less than the maximum real number of our machine. We have analyzed also the computer times calculating a wide range of BFs of different orders and arguments concluding that we can calculate simultaneously the set $B(z) = \{J_n(z), Y_n(z); n = 0, 1, 2, 3, \dots, N_{\max}\}$ approximately in the same CPU time in which the MMBSJN calculates only the BFs of the first kind $\{J_n(z); n = 0, 1, 2, 3, \dots, N_{\max}\}$. At this point we would like to mention that approximately 95% of the total CPU time in our method is consumed in the implementation of Steed's algorithm.

4. Subprogram specification

In this section we introduce the two versions of the code that we have analyzed: (a) subroutine SPHERICAL: To evaluate Bessel functions of fractional order; (b) subroutine BESSEL: to evaluate Bessel functions of integer order.

The calling sequences for the subroutines are:

CALL SPHERICAL (Z, NMAX, BJ, BY, EPS, NUEVO) and
CALL BESSEL (Z, NMAX, BJ, BY, EPS, NUEVO)

where the arguments have the following meaning:

SUBROUTINE SPHERICAL(Z, NMAX, BJ, BY, EPS, NUEVO)

INPUT:

Z: argument of the Bessel functions.

NMAX: maximum order of the Bessel functions. We shall get Bessel functions of all the orders below MIN(NMAX, NUEVO). NUEVO is defined below.

EPS: control of the accuracy in the continued fraction method.

OUTPUT:

BJ(L + 1): spherical Bessel function of the first kind of order L. We shall keep these values in an array.

BY(L + 1): spherical Bessel function of the second kind of order L. We shall keep these values in an array.

NUEVO: maximum order of Bessel functions calculated when BY(NMAX + 1,Z) is larger than 10^{**36}

NOTE:

This version of the code is for all real positive z and Nmax less than 500.

SUBROUTINE BESSEL (Z,NMAX,BJ,BY,EPS,NUEVO)

INPUT:

Z: argument of the Bessel functions.

NMAX: maximum order of the Bessel functions. We shall get Bessel functions of all the orders below MIN(NMAX,NUEVO). NUEVO is defined below.

EPS: control of the accuracy in the continued fraction method.

OUTPUT:

BJ(L + 1): Bessel function of the first kind of order L. We shall keep these values in an array.

BY(L + 1): Bessel function of the second kind of order L. We shall keep these values in an array.

NUEVO: Maximum order of Bessel functions calculated when BY (NMAX + 1,Z) is larger than 10^{**36}

NOTE:

This version of the code is for all real positive z and Nmax less than 500.

5. Test run

The subroutines have been extensively tested and we present at the end of this paper a simple test program (with the corresponding output). (We can also call (in the program TEST) the subroutine SPHERICAL instead of the Bessel one keeping the same structure in the program TEST).

6. Conclusions

We have analyzed a method which is especially useful and efficient for the calculation of high order BFs and which is apparently numerically stable. The most appealing feature of this algorithm is that it does not require any recalculation using normalization relations. The basis for the code is the use of the

continued fraction method to relate (high order) irregular BFs to regular BFs of the same order. This code has direct application in a wide variety of problems where high order BFs are necessary, as indicated in the introduction above.

Acknowledgements

We would like to acknowledge useful discussions with P.P. Korovin from Samara Aviation Institute and M.J. Vicente-Vacas from University of Valencia. This work has been partly supported by a CICYT and S. Petersburg University grant (2-61-14-31). One of us, P.F.C., wishes to acknowledge the support of a fellowship from the Consejo Superior de Investigaciones Científicas.

References

- [1] Y.L. Luke, *Mathematical Functions and their approximations*, (Academic, New York, 1975).
- [2] J.C.P. Miller, *Bessel Functions, Part II, Functions of Positive Integer Order*, *Mathematical Tables*, Vol. 10 (Cambridge Univ. Press, Cambridge, 1952).
- [3] M. Abramowitz and I.A. Stegun, eds, *Handbook of Mathematical Functions* (Dover, New York, 1972).
- [4] A.R. Barnett, D.H. Feng, J.W. Steed and L.J.B. Goldfarb, Coulomb wave functions for all real η and ρ , *Comput. Phys. Commun.* 8 (1974) 377.
- [5] Y.L. Luke, *Integrals of Bessel functions* (McGraw-Hill, New York, 1962).
- [6] C.N. Watson, *Theory of Bessel Functions* (Cambridge Univ. Press, Cambridge, 1962).

TEST PROGRAM

```

PROGRAM TEST

IMPLICIT REAL*8 (A-H,O-Z)
DIMENSION BJ(501),BY(501)

CCCCCCCCCCCCCCCCCCCCCCCCCCCCCCCCCCCCCCCCCCCCCCCCCCCCCCCCCCCC
C      INPUT                                C
CCCCCCCCCCCCCCCCCCCCCCCCCCCCCCCCCCCCCCCCCCCCCCCCCCCCCCCCCCCC

WRITE(6,*) 'THE VALUE OF Z IS?'
READ(5,*) Z
WRITE(6,*) 'THE VALUE OF NMAX IS?'
READ(5,*) NMAX
WRITE(6,*) 'THE VALUE OF EPS IS?'
READ(5,*) EPS
WRITE(6,*) 'WHICH ORDER OF BF DO YOU WANT TO PRINT?'
READ(5,*) L

CCCCCCCCCCCCCCCCCCCCCCCCCCCCCCCCCCCCCCCCCCCCCCCCCCCCCCCCCCCC
C      CALLING SEQUENCE                      C
CCCCCCCCCCCCCCCCCCCCCCCCCCCCCCCCCCCCCCCCCCCCCCCCCCCCCCCCCCCC

CALL BESSEL (Z,NMAX,BJ,BY,EPS,NUEVO)

CCCCCCCCCCCCCCCCCCCCCCCCCCCCCCCCCCCCCCCCCCCCCCCCCCCCCCCCCCCC
C      OUTPUT                                C
CCCCCCCCCCCCCCCCCCCCCCCCCCCCCCCCCCCCCCCCCCCCCCCCCCCCCCCCCCCC

WRITE(6,*) 'Z=',Z
WRITE(6,*) 'NMAX=',NMAX
WRITE(6,*) 'EPS=',EPS
WRITE(6,*) 'NUEVO=',NUEVO

CCCCCCCCCCCCCCCCCCCCCCCCCCCCCCCCCCCCCCCCCCCCCCCCCCCCCCCCCCCC
C      NOTICE THAT WE GET THE BESSEL FUNCTIONS OF          C
C      THE FIRST AND SECOND KIND OF ALL THE ORDERS BELOW    C
C      THE MINIMUM OF "NMAX" AND "NUEVO"                    C
CCCCCCCCCCCCCCCCCCCCCCCCCCCCCCCCCCCCCCCCCCCCCCCCCCCCCCCCCCCC

WRITE(6,*) 'WE WANT TO PRINT THE BFS OF ORDER =',L
WRITE(6,*) 'THE BF OF THE FIRST KIND OF ORDER L IS=', BJ(L+1)
WRITE(6,*) 'THE BF OF THE SECOND KIND OF ORDER L IS=', BY(L+1)

STOP
END

```

TEST RUN OUTPUT

```

Z=      5.000000000000000
NMAX=   500
EPS=    1.000000000000000E-09
NUEVO=  20
WE WANT TO PRINT THE BESSEL FUNCTIONS OF ORDER = 0
THE BF OF THE FIRST KIND OF ORDER L IS= -0.1775967713143383
THE BF OF THE SECOND KIND OF ORDER L IS= -0.3085176252490338

```



ELSEVIER

Computer Physics Communications 105 (1997) 263-272

Computer Physics
Communications

A code to evaluate modified Bessel functions based on the continued fraction method

J. Segura^{a,b,c}, P. Fernández de Córdoba^c, Yu.L. Ratis^d

^a Max Planck Institut für Physik, Werner Heisenberg Institut, München, Germany

^b Departamento de Ingeniería de Sistemas y Comunicaciones, Escuela Politécnica Superior, U. de Alicante, Ap. de Correos 99, 03080-Alicante, Spain¹

^c Departamento de Matemática Aplicada, Universidad Politécnica de Valencia, Valencia, Spain

^d Samara Aviation Institute, Samara, Russian Federation

Received 1 August 1996; revised 21 May 1997

Abstract

We present an algorithm to evaluate the modified Bessel functions I_ν and K_ν of integral and half-integral order based on the calculation of the continued fraction for the I'_ν 's, the Wronskian and the application of forward recurrence relations for the K'_ν 's and backward recurrence for the I'_ν 's. The main feature of the algorithm is that it does not require recalculations using normalization relations nor trial values to start the recurrences; the code evaluates in each step (already normalized) Bessel functions. The accuracy of the method (10^{-16} for half-integral order and better than 2×10^{-7} for integral order in our code) is limited only by the precision in the initial values for the recurrence and the maximum order available for a given value of the argument is restricted only by the maximum real number available in the computer. © 1997 Elsevier Science B.V.

PACS: 02.60.Gf; 02.30.Gp

Keywords: Modified Bessel functions; Integral and semi-integral orders; Continued fraction

PROGRAM SUMMARY

Title of program: BESSIMIN, BESSIMSE

Catalogue identifier: ADGM

Program obtainable from: CPC Program Library, Queen's University of Belfast, N. Ireland

Licensing provisions: none

Computer for which the program is designed and others on which

it is operable:

Computers: VAX 6410, HP 712/60; Installations: Instituto de Física Corpuscular (IFIC), C/ Doctor Moliner, 50 . E-46100 Burjassot (Valencia), Spain

Operating systems under which the program has been tested: VAX/VMS, UNIX

Programming language used: Fortran 77

No. of bits in a word: 32

¹ Postal Address; e-mail: jsegura@disc.ua.es

No. of bytes in distributed program, including test data, etc.:
59940

Distribution format: ASCII

Keywords: Modified Bessel functions, integral and semi-integral orders, continued fraction

Nature of the physical problem

We include two codes in order to evaluate:

(1) Modified Spherical Bessel functions (subroutine BESSIMSE).

(2) Modified Bessel functions of integral order (subroutine BESSIMIN).

Both codes evaluate Modified Bessel functions from the lower (positive) orders to a maximum order NMAX in a same run.

Method of solution

We have developed a fast code to calculate modified Bessel functions of integral and half-integral order based on continued fractions. This algorithm is specially useful in the case of Bessel functions of high order because it does not require any recalculation using normalization relations.

Restrictions on the complexity of the problem

The maximum order that can be reached with our method, for a fixed real positive value of x , is provided by the maximum real number defined in the machine. The maximum x is limited by the same kind of restriction; however, the overflow problem for high x can be eliminated by factoring out e^x for the K 's and e^{-x} for the I 's (see Section 5).

Typical running time

See Section 5.

LONG WRITE-UP

1. Introduction

The numerical codes to evaluate Bessel functions usually take into account normalization relations [1]. However, in Ref. [2] an algorithm based on the continued fraction method has been proposed, which allows to compute Bessel functions without any recalculation through normalization relations; besides, the method maintains the stability of each recurrence relation. Ref. [3] presents an algorithm, based also on continued fractions, to evaluate Modified Bessel functions (MBF) for a fixed fractional order; we present two codes (for integral or semi-integral order) which evaluate simultaneously the modified Bessel functions I_ν and K_ν from the lower (positive) orders to a maximum order (NMAX) in the same run. The algorithm takes advantage of forward recurrence relations to generate the K_ν 's and, after taking into account the continued fraction (CF) and the Wronskian to evaluate high-order I_ν 's, backward recurrence relations to calculate the I_ν 's. Because of its structure, these codes are specially useful to calculate high-order MBFs; the highest order available for a given value of the argument is limited only by the maximum real number available in the computer.

2. Modified Bessel functions of half-integral order

We are interested in presenting a code to generate the Modified Spherical Bessel Functions (MSBFs) of the first and second kinds for real and positive values of the argument. These functions are particular solutions of the differential equation

$$x^2 \omega''(x) + 2x \omega'(x) - [x^2 + n(n+1)] \omega(x) = 0, \quad n = 0, \pm 1, \pm 2, \dots \quad (1)$$

We define the Modified Spherical Bessel functions of the first kind (see [1] Eqs. (10.2.1–4)),

$$i_n(x) = \sqrt{\frac{1}{2}\pi/x} I_{n+1/2}(x), \quad (2)$$

of the second kind,

$$i_{-n}(x) = \sqrt{\frac{1}{2}\pi/x} I_{-n-1/2}(x), \tag{3}$$

and of the third kind,

$$k_n(x) = \sqrt{\frac{1}{2}\pi/x} K_{n+1/2} = \frac{1}{2}\pi(-1)^{n+1}(i_n(x) - i_{-n}(x)), \tag{4}$$

which are particular solutions of Eq. (1).

The pairs $i_n(x)$, $i_{-n}(x)$ and $i_n(x)$, $k_n(x)$ are linearly independent solutions for every n . We will calculate $i_n(x)$ and $k_n(x)$; the i_{-n} will be related to them through Eq. (4).

In this code we calculate simultaneously the MSBFs of all orders below N_{\max} , i.e. we generate the set

$$\text{MSB}(x) \equiv \{i_n(x), k_n(x); n = 0, 1, 2, 3, \dots, N_{\max}\}. \tag{5}$$

The algorithm is organized in the following way:

- We evaluate all the k 's $\{k_n(x), n = 0, 1, 2, \dots, N_{\max}\}$, taking into account the known values of $k_0(x) = \frac{1}{2}\pi e^{-x}/x$ and $k_1(x) = \frac{1}{2}\pi e^{-x}(1/x + 1/x^2)$ and using the forward recurrence relation

$$k_{n+1}(x) = \frac{(2n+1)}{x} k_n(x) + k_{n-1}(x). \tag{6}$$

- We use the continued fraction method to evaluate the ratio

$$\begin{aligned} H(x) &\equiv \frac{i_{N_{\max}}(x)}{i_{N_{\max}-1}(x)} = \frac{I_{N_{\max}+1/2}(x)}{I_{N_{\max}-1/2}(x)} \\ &= \frac{1}{2(N_{\max} + \frac{1}{2})x^{-1} +} \frac{1}{2(N_{\max} + \frac{3}{2})x^{-1} +} \frac{1}{2(N_{\max} + \frac{5}{2})x^{-1} +} \dots \end{aligned} \tag{7}$$

Notice that a similar expression appears for the ratio of the spherical Bessel functions $J_{N+1/2}(x)/J_{N-1/2}(x)$ except for the change of sign preceding each fraction [2,1]; this change can be easily traced out from the change of sign in the recurrence relation for the i_n 's with respect to the recurrence relation for the j_n 's. We implement the calculation of this continued fraction by using Steed's algorithm [4].

- We calculate the upper order $i_{N_{\max}}(x)$, using the already known values $k_{N_{\max}}(x)$ and $k_{N_{\max}-1}(x)$, the ratio $H(x)$ and the value for the Wronskian,

$$W\{k_{N_{\max}}(x), i_{N_{\max}}(x)\} \equiv i_{N_{\max}}(x)k_{N_{\max}-1}(x) + i_{N_{\max}-1}(x)k_{N_{\max}}(x) = \frac{1}{2}\pi x^{-2}. \tag{8}$$

Using (8), we can write

$$i_{N_{\max}-1}(x) = \frac{\pi/2}{x^2(H(x)k_{N_{\max}-1}(x) + k_{N_{\max}}(x))} \tag{9}$$

and then

$$i_{N_{\max}}(x) = H(x)i_{N_{\max}-1}(x). \tag{10}$$

- We evaluate all the MSBFs of the first kind, $\{i_n(x), n = 0, 1, 2, \dots, N_{\max}\}$, taking into account the calculated values of $i_{N_{\max}}(x)$ and $i_{N_{\max}-1}(x)$ and using the backward recurrence relation,

$$i_{n-1}(x) = \frac{(2n+1)}{x} i_n(x) + i_{n+1}(x). \tag{11}$$

3. Modified Bessel functions of integral order

We require a code to generate the modified Bessel functions $I_n(x)$ and $K_n(x)$. We use the standard Abramowitz and Stegun notation (Eqs. 9.6.1–4) and we introduce the MBFs $I_n(x)$ and $K_n(x)$ as particular solutions of the differential equation

$$x^2\omega''(x) + x\omega'(x) - (x^2 + n^2)\omega(x) = 0. \quad (12)$$

In this code we calculate simultaneously the MBFs of all order below Nmax, i.e. we generate the set

$$MB(x) = \{I_n(x), K_n(x); n = 0, 1, 2, 3, \dots, N_{\max}\}. \quad (13)$$

The algorithm is organized in the following way:

- We evaluate $K_0(x)$ and $K_1(x)$ using the polynomial approximations from [1] (Eqs. 9.8.1–8). In the code, these expansions have been rearranged to minimize the number of required operations [3].
- We evaluate all the MBFs $\{K_n(x), n = 0, 1, 2, \dots, N_{\max}\}$, taking into account the calculated values of $K_0(x)$ and $K_1(x)$ and using the forward recurrence relation

$$K_{n+1}(x) = \frac{2n}{x}K_n(x) + K_{n-1}(x). \quad (14)$$

- We use the continued fraction method to evaluate the ratio

$$H(x) = \frac{I_{N_{\max}}(x)}{I_{N_{\max}-1}(x)} = \frac{1}{2N_{\max}x^{-1} + \frac{1}{2(N_{\max}+1)x^{-1} + \frac{1}{2(N_{\max}+2)x^{-1} + \dots}}. \quad (15)$$

We implement this method in our code again, using Steed's algorithm [4].

- We calculate the upper order MBFs of the first kind, $I_{N_{\max}}(x)$, using the already known values of $K_{N_{\max}}(x)$ and $K_{N_{\max}-1}(x)$, the ratio $H(x)$ and the value for the Wronskian of the MBFs [1],

$$W\{K_{N_{\max}-1}(x), I_{N_{\max}-1}(x)\} \equiv I_{N_{\max}}(x)K_{N_{\max}-1}(x) + I_{N_{\max}-1}(x)K_{N_{\max}}(x) = 1/x. \quad (16)$$

As in the previous section, we can write

$$I_{N_{\max}}(x) = \frac{1}{x(K_{N_{\max}-1}(x) + K_{N_{\max}}(x)/H(x))} \quad (17)$$

and then

$$I_{N_{\max}-1}(x) = I_{N_{\max}}(x)/H(x). \quad (18)$$

Notice again that we calculate not only $I_{N_{\max}}(x)$ but also $I_{N_{\max}-1}(x)$.

- We evaluate all the MBFs $\{I_n(x), n = 0, 1, 2, \dots, N_{\max}\}$, taking into account the calculated values of $I_{N_{\max}}(x)$ and $I_{N_{\max}-1}(x)$ and using the backward recurrence relation

$$I_{n-1}(x) = \frac{2n}{x}I_n(x) + I_{n+1}(x). \quad (19)$$

4. Subprogram specification

In this section we introduce the two versions of the code that we have analyzed:

- (a) Subroutine BESSIMSE: to evaluate modified Bessel functions of fractional order;
- (b) Subroutine BESSIMIN: to evaluate modified Bessel functions of integral order.

The calling sequences for the subroutines are CALL BESSIMSE (X,NMAX,BI,BK,NUEVO) and CALL BESSIMIN (X,NMAX,BI,BK,NUEVO), where the arguments have the following meaning:

SUBROUTINE BESSIMSE (X,NMAX,BI,BK,NUEVO)

INPUT:

X: Argument of the Bessel functions.

NMAX: Maximum order of the Bessel functions: We shall get Bessel functions of all the orders below MIN(NMAX,NUEVO). NUEVO is defined below.

EPS: Control of the accuracy in the continued fraction method.

OUTPUT:

BI(L+1): Modified Spherical Bessel function i_L . We keep these values in an array.

BK(L+1): Modified Spherical Bessel function k_L . We keep these values in an array.

NUEVO: Maximum order of Bessel functions calculated when BK (NMAX+1,X) is larger than $10^{**}EXPMA$.

CALLS:

SLIMIT(X,EXPMA,MODE,NMAX,NUEVO): Prevents overflows by evaluating the maximum order that can be calculated (NUEVO). The program then evaluates Bessel functions only to this order when NMAX > NUEVO. This subroutine is optional.

NOTES: This version of the code is for real positive X and Nmax less than 2000.

The integer parameter MODE can be used to factor out $e^{\pm x}$ from the MBFs to prevent overflows for high X. MODE=1 when factorization is carried and MODE=0 in the other case. EPS= 10^{-16} and EXPMA=300 in this version of the code.

SUBROUTINE BESSIMIN (X,NMAX,BI,BK,NUEVO)

INPUT:

X: Argument of the Bessel functions

NMAX: Maximum order of the Bessel functions. We shall get Bessel functions of all the orders below MIN(NMAX,NUEVO). NUEVO is defined below.

EPS: Control of the accuracy in the continued fraction method.

OUTPUT:

BI(L+1): Modified Bessel function I_L . We shall keep these values in an array.

BK(L+1): Modified Bessel function K_L . We shall keep these values in an array.

NUEVO: Maximum order of Bessel functions calculated when BY (NMAX+1,X) is larger than $10^{**}EXPMA$.

CALLS:

LIMIT(X,EXPMA,MODE,NMAX,NUEVO): Prevents overflows by evaluating the maximum order that can be calculated (NUEVO). The program then evaluates Bessel functions only to this order when NMAX > NUEVO. This subroutine is optional.

BESSIM01(X,MODE,XK0,XK1): Evaluates $K(0)$ and $K(1)$.

NOTES:

This version of the code is for real positive X and Nmax less than 2000.

The integer parameter MODE can be used to factor out $e^{\pm x}$ from the MBFs to prevent overflows for high X. MODE=1 when factorization is carried and MODE=0 in the other case. EPS= 10^{-8} and EXPMA=300 in this version of the code.

5. Main features of the code; comparison with other programs

We have compared our algorithm with standard ones (Numerical Recipes `bessi` and `bessik` in double-precision) by calculating different order MBFs with arguments in a wide range of values. The numerical recipes program `bessi` calculates the MBFs I_n for integral order using Miller's algorithm. The program `bessik` calculates the modified Bessel functions I_ν , K_ν for fractional order. In our code we calculate simultaneously all modified Bessel functions (I_ν , K_ν) up to a given order NMAX (limited by the overflow/underflow number of the machine) for integral or half-integral order, while the N.R. program `bessi` calculates just one fixed integral order I_n and `bessik` computes both I_ν , K_ν and its derivatives for a fixed (real) order. Both N.R. codes `bessi` and `bessik`, differently from our codes, apply the backward recurrence relation for unnormalized I_ν 's; to obtain normalized values from these codes one should then renormalize each of the results obtained from the recurrence; our codes always use normalized results. It is important to take into account these different features when comparing the codes.

In our code NMAX should be chosen to be the maximum order we want to calculate; since the recurrence relations are applied forward for K 's, starting from correct, normalized, values and backwards for I 's (as has to be), there is no need to start the backward recurrence with higher orders than that of the desired result, as happens in Miller's algorithm [1] where the higher order has to be estimated according to the required accuracy; then, choosing EPS for the continued fraction lower than the precision in the calculation of K_0 and K_1 (or k_0 , k_1), the precision achieved by our algorithm is just given by the accuracy in the starting values for the K recurrence. The algorithm is stable and keeps the same relative errors for each evaluated MBF; in our version of the code the precision is better than 2×10^{-7} for integral order and 10^{-16} for half-integral order. We have checked the precision of our codes by comparing with a double-precision version of the code `bessik`. In case one needs more precision for the integral case, then one should adopt a more accurate expansion for K_0 , and K_1 ; SLATEC subroutines `dbesk0`, `dbesk1` and `dbesk0e`, `dbesk1e` (the last two for exponentially scaled functions) do this work.

Our algorithm proves to be, most of the times, faster than the two codes from the N.R. (or at least equivalent) for the calculation of a fixed given order; recalling that, besides, our code stores all the Bessel function I_n and K_n (or i_n and k_n) up to this maximum order we have to conclude that, in many situations, our codes will be more convenient. Our code `bessimin` is in fact faster than `bessi` for all values of x and n we show in Table 1 (except when $n < x$). On the other hand, `bessik` becomes comparable to our code, for a same value of n (see table) for large enough values of x but our code calculates all K_ν 's and I_ν 's up to the higher order.

Besides, one should note that our codes reduce the possibility of overflows since no test values for the recurrence and no normalization have to be carried. In each step, the codes generate the correct answers.

Table 1 compares the code `bessimin` (integral order) with `bessi` and `bessik` from Numerical Recipes. EPS has been fixed to 10^{-8} both in `bessimin` and `bessik`; and the dimension of the arrays in `bessimin` and `bessimse` is fixed to 501. Both codes work in MODE 0 in this case. Together with the relative errors for the I_n 's and K_n 's compared to the results tabulated in [1], we show the relative CPU (rel. CPU(i)) time spent for each program, taking our code as reference; positive values show our code is faster for such x and n . We do not use the subroutines LIMIT and SLIMIT in this case to make a fair comparison with N.R. routines (they do not limit the maximum order); however, these subroutines spend little time, specially when the higher order required lies below the overflow capability of the computer, and can be kept without much loss.

The comparison between `bessimse` and `bessik` in CPU time for a precision of 10^{-16} is also presented in the table; the difference in CPU (rel. CPU(s)) becomes similar except for small x . Numerical results coincide with all digits to those tabulated in [1], and so we do not show the accuracy in this case with respect to this reference. It is again important to note that our code evaluates all the MBFs up to the higher calculated order.

Both the range of x and the maximum order that can be reached depend on the overflow number of the machine. The values from the table were obtained using a VAX 6410 machine; the overflow number is 10^{36} . For such restrictive bound, in MODE 0, the range goes from $n \sim 20$ for $x \sim 1$ to $n \sim 180$ at $x = 86$ (maximum

Table 1
Comparison in % CPU time between *bessimin* and *bessimse* and the Numerical Recipes codes

Program	x	$n = \text{NMAX}$	accur. (J)	accur. (K)	rel. CPU(i)	rel. CPU(s)
<i>bessimin</i>	1.0	20	8×10^{-8}	10^{-7}		
<i>bessi</i>	1.0	20	2×10^{-7}		+55%	
<i>bessik</i>	1.0	20	10^{-8}	10^{-8}	+85%	+165%
<i>bessimin</i>	2.0	30	1.5×10^{-8}	1.4×10^{-8}		
<i>bessi</i>	2.0	30	5×10^{-8}		+55%	
<i>bessik</i>	2.0	30	5×10^{-8}	2×10^{-8}	+135%	+25%
<i>bessimin</i>	5.0	40	2×10^{-9}	3×10^{-9}		
<i>bessi</i>	5.0	40	6×10^{-7}		+70%	
<i>bessik</i>	5.0	40	10^{-8}	10^{-8}	+70%	+20%
<i>bessimin</i>	50	10	10^{-9}	10^{-9}		
<i>bessi</i>	50	10	2×10^{-8}		-30%	
<i>bessik</i>	50	10	10^{-8}	3×10^{-8}	+25%	+15%
<i>bessimin</i>	50	100	10^{-9}	10^{-9}		
<i>bessi</i>	50	100	4×10^{-7}		+50%	
<i>bessik</i>	50	100	10^{-8}	6×10^{-8}	+15%	+5%

Rel. CPU(i) accounts for the relative CPU time in the evaluation of integral order; rel. CPU(s) is the relative CPU time for semi-integral order. Positive results show our code is faster.

$x = 86 \simeq \log(10^{36})$; in MODE 1 the maximum order is $n \sim 20$ for $x \sim 1$ and $n \sim 500$ for $x \sim 1500$; there is no limitation for x in this case. Using a less restrictive and more usual overflow number $\sim 10^{300}$ x ranges from 0 to 740 in MODE 0 and n from 150 to 1500, respectively; in MODE 1 $n \sim 150$ for $x \sim 1$ and $n \sim 1500$ for $x \sim 1500$. The maximum order that can be evaluated increases in all cases with increasing x .

When the evaluation of high orders is required then one should use subroutines LIMIT and SLIMIT to obtain the maximum order and to prevent overflows.

6. Test run

We present at the end of the paper, as a last check, a test program which calculates integral and semi-integral MBFs, together with the corresponding output, for several values of x ; five different Bessel functions are shown (with only one call for each x). The test program evaluates, for every value of the argument, I_ν and K_ν for the higher order that can be evaluated together with an intermediate order and I_0 (i_0). Parameters: MODE=0; EPS=1.d-16 for BESSIMSE; MODE=1, EPS=1.d-8 for BESSIMIN. DIMENSION of the arrays = 2001. Subroutines LIMIT and SLIMIT are used.

7. Conclusions

We have analyzed an efficient method for the calculation of MBFs of integral and half integral order which is numerically stable. The most appealing feature of this algorithm is that it does not require any recalculation using normalization relations thus giving in each step of the recurrences the correct values for the the K'_ν 's (I'_ν 's). The codes prove to be generally faster than the previous codes for the evaluation of a fixed order; taking into account that our codes calculate the complete set $\{I_n, K_n, n = 0, 1, \dots, \text{NMAX}\}$ (or $\{i_n, k_n, n = 0, 1, \dots, \text{NMAX}\}$) in each run we conclude it will be convenient in many situations. The basis for the code is the use of the continued fraction for the I'_ν 's and the Wronskian to relate (high order) K_ν 's to I_ν 's of the same (high) order.

Acknowledgements

J. Segura wishes to acknowledge the support from *Ramón Areces* Foundation for his post-doctoral fellowship and also wishes to acknowledge the hospitality from the *Departamento de Matemática Aplicada* de la Universidad Politécnica de Valencia during his visit, where the final part of this paper was developed. J.S. thanks the Instituto de Física Corpuscular (I.F.I.C.-Valencia) for the technical support and A. Gil for carefully reading the manuscript.

References

- [1] M. Abramowitz and I.A. Stegun, eds., *Handbook of Mathematical Functions* (Dover, New York, 1972) ch. 9 and 10.
- [2] Y.L. Ratis, P. Fernández de Córdoba, *Comput. Phys. Commun.* 76 (1993) 381–388.
- [3] W.H. Press, S.A. Teukolski, W.T. Vetterling and B.P. Flannery, *Numerical Recipes in Fortran* (Cambridge Univ. Press, Cambridge, 1992), ch. 6, pp. 229–233, 239–243.
- [4] A.R. Barnett, D.H. Feng, J.W. Steed and L.J.B. Goldfarb, *Coulomb Wave Functions for all real η and ρ* , *Comput. Phys. Commun.* 8 (1974) 377–395.

TEST PROGRAM

```
PROGRAM test
IMPLICIT REAL*8 (a-h,o-z)
DIMENSION bi(2001),bk(2001)
WRITE(4,29)'SEMI-INTEGRAL ORDER,NMAX=1000,MODE 0'
Nmax=1000
WRITE(4,30)
WRITE(4,31)'x','n','i(n)','k(n)','i(0)'
DO x=1,5
  CALL bessimse(x,Nmax,bi,bk,nuevo)
  l=nuevo+1
  WRITE(4,32) x, l-1, bi(l),bk(l),bi(l)
  l=21
  WRITE(4,32) x, l-1, bi(l),bk(l),bi(l)
ENDDO
Nmax=2000
WRITE(4,30)
WRITE(4,30),'INT. ORDER, NMAX=2000, MODE 1'
WRITE(4,30)
WRITE(4,31)'x','n','I(n)','K(n)','I(0)'
DO ix=0,3,1
  x=10.D0**ix
  CALL bessimin(x,Nmax,bi,bk,nuevo)
  l=nuevo+1
  WRITE(4,33) x, l-1,bi(l),bk(l),bi(l)
  l=101
  WRITE(4,33) x, l-1,bi(l),bk(l),bi(l)
ENDDO
29 FORMAT (A37)
30 FORMAT (A30)
31 FORMAT (4X,A1,3X,A1,(10X,A4),2(12X,A4))
32 FORMAT (F6.0,I4,1x,3D17.11)
33 FORMAT (F6.0,I4,1x,3D16.9)
END
```

TEST RUN OUTPUT

SEMI-INTEGRAL ORDER, NMAX=1000, MODE 0

x	n	i(n)	k(n)	i(0)
1.	145	.20485572398-296	.26349266337+295	.11752011936D+01
1.	20	.77151475651D-25	.49599176332D+24	.11752011936D+01
2.	166	.76680319953-299	.30756038851+297	.18134302039D+01
2.	20	.83767284780D-19	.22759868192D+18	.18134302039D+01
3.	181	.13646759897-300	.10568251190+299	.33392916425D+01
3.	20	.29516512906D-15	.42809295308D+14	.33392916425D+01
4.	193	.11908645436-301	.85191012661+299	.68224792993D+01
4.	20	.10091688321D-12	.93149579165D+11	.68224792993D+01
5.	202	.48511791184-300	.15985093824+298	.14840642116D+02
5.	20	.97082664411D-11	.76674462354D+09	.14840642116D+02

INT. ORDER, NMAX=2000, MODE 1

x	n	I(n)	K(n)	I(0)
1.	146	.351583052-298	.974045018+296	.465759631D+00
1.	100	.311729062-188	.160387677+187	.465759631D+00
10.	236	.363365299-298	.582539011+296	.127833337D+00
10.	100	.491383506D-92	.101248485D+91	.127833337D+00
100.	476	.975988178-302	.105327086+300	.399443796D-01
100.	100	.172668628D-21	.204757366D+20	.399443796D-01
1000.	1235	.101219640-302	.310853068+300	.126172404D-01
1000.	100	.851558757D-04	.584244656D+01	.126172404D-01

Limiting properties of the radial distribution function in electronic liquids

To cite this article: I M Tkachenko 1996 *J. Phys. A: Math. Gen.* **29** 2599

View the [article online](#) for updates and enhancements.

You may also like

- [Numerical modeling of thermodynamic parameters for mixtures with a few-parameter equation of state of their components](#)
K K Maevskii
- [Relativistic transformation of thermodynamic parameters and refined Saha equation](#)
Xin Hao, Shaofan Liu and Liu Zhao
- [Thermodynamic geometry of Kaniadakis statistics](#)
Hossein Mehri-Dehnavi and Hosein Mohammadzadeh

Limiting properties of the radial distribution function in electronic liquids

I M Tkachenko†, P Fernández de Córdoba and M Urrea

Departamento de Matemática Aplicada, Universidad Politécnica de Valencia, Aptdo. 22012, E-46071 Valencia, Spain

Received 2 October 1995

Abstract. The static dielectric function of electronic liquids is studied in a wide range of thermodynamic parameters. The local-field correction to the RPA permeability is modelled to satisfy the compressibility sum rule and the short-wavelength exact relation to the zero-separation value of the radial distribution function. The latter is determined by a self-consistency procedure and is shown to verify all known asymptotic conditions.

1. Introduction

A natural approach to the investigation of static correlations in strongly coupled, specifically, inertial fusion plasmas, is based on the separation of electronic and ionic components of the system, so that the interionic interactions are assumed to be screened by the electronic static dielectric function $\varepsilon_e(k)$. In dense systems the latter should be treated beyond the random-phase approximation (RPA), i.e. the calculation of $\varepsilon_e(k)$ involves the electronic static local field correction (LFC) $G_e(k) = G_e(k, \omega = 0)$,

$$\varepsilon_e(k) = 1 + \frac{Q(k, 0)}{1 - G_e(k)Q(k, 0)} \quad (1)$$

where $Q(k, 0)$ is the product $\phi(k)\Pi_e^0(k, \omega)$ at $\omega = 0$, and $\Pi_e^0(k, \omega)$ is the electronic polarization operator in the RPA, $\phi(k) = 4\pi e^2/k^2$.

There exist various approaches to the computation of the LFC $G_e(k)$ (see, e.g. [1]), but mostly they are applicable in specific realms of the system phase diagram. The most notable and far-reaching approach is the modified-convolution approximation (MCA) model suggested by Ichimaru and his co-workers [1]. We present a simple alternative model which is to serve as a basis for future studies of various properties of strongly coupled systems.

The aim of this paper is to propose and check a self-consistent method of calculation of $G_e(k)$ based on its limiting properties and adjusted to the Monte Carlo (MC) data on the one-component plasma (OCP) equation of state (EOS) [2, 3]. Preliminary results obtained within this approach were published elsewhere [4].

2. The model

The interpolating formula for the electronic LFC suggested in [3, 4]

$$G_e(k) = \frac{k^2}{ak_F^2 + bk^2} \quad (2)$$

† E-mail address: imtk@pleiades.upv.es

incorporates both long- and short-wavelength asymptotic values of $G_e(k)$, $k_F = (3\pi^2 n)^{1/3}$ is the Fermi wavenumber.

In particular,

$$b^{-1} = \lim_{k \rightarrow \infty} G_e(k). \quad (3)$$

The short-range behaviour of $G_e(k)$ in the low-temperature limit has been studied in the papers of Shaw [5] and Kimball [6] (see also [7, 8]). Namely, it has been shown that if $T \rightarrow 0$ in hydrogen-like systems,

$$b^{-1} = 1 - g_e(0) \quad (4)$$

where $g_e(r)$ is the usual electronic radial distribution function. This result is based on the famous ‘cusp’ condition

$$\left(\frac{\partial g}{\partial r} \right)_{r=0} = \frac{1}{a_B} g_e(0) \quad (5)$$

which can be obtained from the s-solution of the two-particle Schrödinger equation at $r = 0$, where a_B is the Bohr radius (see, e.g. [6]).

On the other hand, since $G_e(k \rightarrow \infty)$ involves only the short-range properties of the system, one expects the asymptotic value

$$G_e(\infty) = \lim_{k \rightarrow \infty} G_e(k) \quad (6)$$

to be finite and the relation

$$1 - g_e(0) = \lim_{k \rightarrow \infty} G_e(k) \quad (7)$$

to hold at arbitrary values of temperature T .

The relation (7) stems from the asymptotic value [6]

$$\left(\frac{\partial g(r)}{\partial r} \right)_{r=0} = \frac{3\pi}{8k_F^3} \lim_{k \rightarrow \infty} (k^4(1 - S_e(k))) \quad (8)$$

where

$$S_e(k) = 1 + \int dr e^{ikr} (g_e(r) - 1) \quad (9)$$

or of electrons.

The long-wavelength behaviour of the latter was studied by Kimball [6, 7] at $T = 0$:

$$1 - S_e(k) = \frac{8k_F^3}{3\pi a_B k^4} (1 - G_e(\infty)) + O\left(\frac{1}{k^6}\right). \quad (10)$$

At $T \neq 0$ the same asymptotic formula (10) also follows from the fluctuation–dissipation theorem,

$$S_e(k) = -\frac{\hbar}{\pi n \phi(k)} \int_0^{+\infty} \coth\left(\frac{\beta \hbar \omega}{2}\right) \text{Im}(\varepsilon_e^{-1}(k, \omega)) d\omega \quad (11)$$

and the static-LFC approximation for the dynamic electronic dielectric function,

$$\varepsilon_e(k, \omega) = 1 + \frac{Q(k, \omega)}{1 - G_e(k)Q(k, \omega)}. \quad (12)$$

In equation (11) \hbar is the Planck constant and β^{-1} is the system temperature T in energy units.

The imaginary part of $\Pi_e^0(k, \omega)$ is exponentially small as $k \rightarrow \infty$ [9], and $\text{Im } \varepsilon_e^{-1}(k, \omega)$ can be substituted by

$$-\frac{\pi}{1 - G_e(\infty)} \delta(1 + (1 - G_e(\infty))\text{Re}Q(k \rightarrow \infty, \omega)) \quad (13)$$

($\delta(z)$ is the Dirac δ -function), while the asymptotic form of $\text{Re}Q(k \rightarrow \infty, \omega)$ is just [9]

$$-(\chi_0^2/3) z^{-2} (u^2 - z^2)^{-1}. \quad (14)$$

Here the Lindhardt notations are introduced:

$$\chi_0^{-2} = \pi k_F a_B \quad z = k/2k_F \quad u = (m\omega)/(\hbar k k_F) \quad (15)$$

where m is the electronic mass.

The expansion (10) has been confirmed by our computations (see further on) with a very high precision.

Returning to the interpolation form (2) for the LFC, one notices that the long-wavelength behaviour of $G_e(k \rightarrow 0) \approx a^{-1}(k/k_F)^2$ is responsible for the screening of a static impurity in the plasma. On the other hand, the parameter a is determined by the system thermodynamic properties via the compressibility sum rule,

$$a^{-1} = \left(\frac{k_F}{k_D}\right)^2 \lim_{k \rightarrow 0} \left(\frac{k_D^2 G_e(k)}{k^2}\right) = \left(\frac{k_F}{k_D}\right)^2 \left(1 - \beta \left(\frac{\partial P}{\partial n}\right)_\beta\right) \quad (16)$$

where $k_D^2 = 4\pi n e^2 \beta$ is the Debye radius and P is the pressure.

The most recent MC data on the OCP EOS [2]

$$P = \frac{n}{\beta} + \frac{\beta U}{3} \equiv \frac{n}{\beta} + \frac{nf(\Gamma)}{3} \quad (17)$$

(U is the system interaction energy and $\Gamma = \beta e^2(4\pi n/3)^{1/3}$) were utilized in this paper with

$$f(\Gamma) = A\Gamma + B + C\Gamma^{-1/3} + D\Gamma^{1/3} \quad (18)$$

and $A = -0.899\,374\,9$, $B = -0.224\,469\,9$, $C = -0.017\,874\,7$, $D = 0.517\,575\,3$.

The interpolation form (17) valid in a very wide region of values of Γ , $0 \leq \Gamma \leq 200$, brought us to a simple algebraic expression for the a parameter,

$$a = -(12\pi^2)^{-1/3} \left(\frac{A}{9} + \frac{B}{12}\Gamma^{-1} + \frac{2C}{27}\Gamma^{-4/3} + \frac{5D}{54}\Gamma^{-2/3}\right)^{-1}. \quad (19)$$

No quantum effects are included in the EOS (17) and, hence, there is discrepancy between (19) (and, thus, equation (2) too) and our desire to apply it to electron liquids under ‘quantum’ thermodynamic conditions.

To diminish the influence of this inconsistency, the parameter $g_e(0)$ (and b of (2)) was determined by a precise self-consistent procedure. In effect, the value of $g_e(0)$ (which itself has a profound physical meaning [1]) was computed via a simultaneous solution of two integral equations,

$$S_e(z) = \sum_{l=-l_1}^{l_1} \frac{\mathcal{P}_e(z, l)}{\varepsilon_e(z, l)} \quad (20)$$

$$g_e(0) = 1 + 12 \int_0^\infty (S_e(z) - 1)z^2 dz. \quad (21)$$

In equation (20) the summation is over the Matsubara frequencies, $v_l = (\pi\Theta l)/(2z)$, and

$$\varepsilon_e(z, l) = 1 + \frac{\Gamma}{(12\pi^2)^{1/3}} \frac{\mathcal{P}_e(z, l)}{z^2} \quad (22)$$

as usually, $\Theta = 2m/(\beta\hbar^2 k_F^2)$, the l_1 -parameter was determined by the numerical precision.

$\mathcal{P}_e(z, l)$ in equation (20) is the dimensionless polarization operator $\Pi_e(k, \omega)$ with the LFC,

$$\mathcal{P}_e(z, l) = \mathcal{P}_e^0(z, l) \left(1 - \frac{\Gamma}{(12\pi^2)^{1/3}} \frac{G_e(z)\mathcal{P}_e^0(z, l)}{z^2} \right)^{-1} \quad (23)$$

$$G_e(z) = \left(b + \frac{a}{(2z)^2} \right)^{-1} \quad b = (1 - g_e(0))^{-1}. \quad (24)$$

The RPA dimensionless polarization operator $\mathcal{P}_e^0(z, l)$ can be calculated (for each value of density and temperature, z and l) by simple integration,

$$\mathcal{P}_e^0(z, l) = \frac{3\Theta}{4z} \int_0^\infty \frac{y dy}{e^{y^2/\Theta-\eta}} \ln \left| \frac{z + y + iv_l}{z - y + iv_l} \right| \quad (25)$$

while the chemical potential η is determined by the normalization condition

$$\int_0^\infty \frac{t^{1/2} dt}{e^{(t-\eta)} + 1} = \frac{2}{3} \Theta^{-3/2}. \quad (26)$$

We studied the asymptotic behaviour of the model parameter $g_e(0)$ and compared (where possible) our results with those of [1], etc.

The self-consistency procedure, equations (20), (21), proved to be numerically stable, and the resulting values of $g_e(0)$ were independent of the initiation points. The latter did influence the number of iterations slightly, which varied (for the data given below) between 2 and 5 to ensure the absolute error in the determination of $g_e(0)$ was between 10^{-2} and 10^{-3} .

3. Results and conclusions

The results of the above self-consistent procedure to evaluate the zero-separation value of the electronic radial distribution function $g_e(0)$ are provided in figure 1. Some additional points are also given in table 1, where, in particular, we present the values of $g_e(0)$ for

Table 1. The zero-separation value of the electronic pair correlation function $g_e(0)$ for various values of electronic density and temperature. The values of $g_e^Y(0)$ (last column) are calculated according to (27) [11]. The values of the parameters Γ , Θ and r_s are given for reference.

n_e (10^{24} cm $^{-3}$)	T (10^5 K)	Γ	Θ	r_s	$g_e(0)$	$g_e^Y(0)$
0.2579	1.715	1.0	1.0	1.84	0.026	0.1635
1.6100	6.315	0.5	1.08	1.00	0.1262	0.2661
2.063	3.429	1.0	0.5	0.92	0.1633	0.2792
1.611	1.579	2.0	0.27	1.00	0.1903	0.2662
2.517×10^1	1.579×10^1	0.5	0.4342	0.40	0.3198	0.3856
2.579×10^2	1.715×10^1	1.0	0.1	0.18	0.4376	0.4430
2.579×10^5	1.715×10^3	0.1	0.1	0.02	0.4919	0.4939
2.160×10^3	3×10^3	0.01	4.24	0.09	0.6960	0.4709
1.250	2.5×10^2	0.01	50.00	1.09	0.9850	0.2525

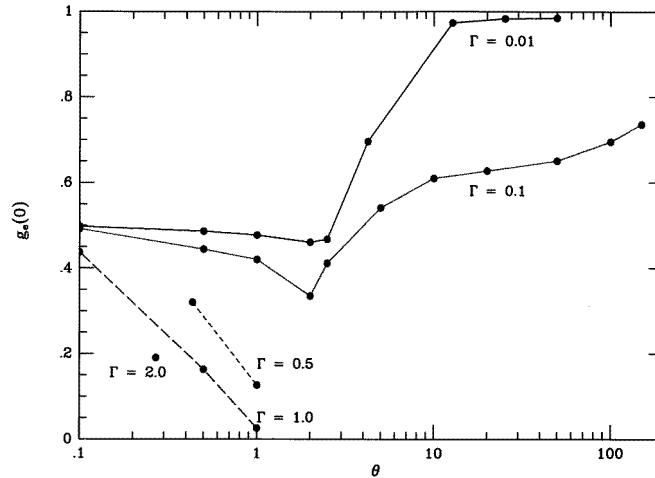


Figure 1. The zero-separation value of the pair correlation function $g_e(r)$ in the electron liquid as a function of the degeneracy parameter Θ and for $\Gamma = 2.0$ (one point), $\Gamma = 1.0$ (long broken), $\Gamma = 0.5$ (short broken), $\Gamma = 0.1$ (dotted) and $\Gamma = 0.01$ (full). Points represent the results of the present model, the lines are drawn to distinguish different values of the coupling parameter Γ .

the electronic density $n_e = 1.60 \times 10^{24} \text{ cm}^{-3}$ and temperature $T = 1.579 \times 10^5 \text{ K}$ and $T = 6.315 \times 10^5 \text{ K}$, i.e. $r_s = 1.0$ and $\Theta = 0.27$ and $\Theta = 1.0$, respectively, r_s being, as usually, the Wigner–Seitz radius in the units of a_B , $r_s = \Gamma\Theta/0.543$. These values are the only ones for which we could carry out the comparison with the results published by Tanaka *et al* [10]. The values of $g_e(0)$ (0.1903 and 0.1262) coincide with the data of [10] corresponding to the approximation, when the electron–ion LFC was set to be zero. This coincidence is not astonishing, since here we virtually consider the one-component electronic system.

The self-consistency procedure also permitted us to calculate the static structure factor of electrons, these results are provided in figure 2 for three characteristic pairs of values of the parameters Γ , Θ and $g_e(0)$ (see table 1).

For the sake of comparison we also present in table 1 the corresponding values of $g_e(0)$ calculated according to the formula, obtained by Yasuhara [11] through a resummation of the electron–electron ladder diagrams,

$$g_e(0) = [q/I_1(q)]^2/8 \quad (27)$$

where $q \simeq 1.629\sqrt{r_s}$ and $I_1(q)$ is the first-order modified Bessel function.

Notice, that though we do not include spin effects (bearing in mind that they would manifest themselves only in magnetized Coulomb systems) it is obvious that $g_e(r=0) \neq 0$ only for two electrons with opposite spins. Thus, within the Hartree–Fock approximation when the exchange effects prevail over those of the Coulomb interaction, the value of $g_e(0)$ is just $\frac{1}{2}$. This high-degeneracy limiting value is actually the asymptotic value of $g_e(0)$ resulting from our calculations as $\Theta \rightarrow 0$, and the smaller Γ , the quicker $g_e(0)$ approaches the quantum ideal-gas value $g_e^{HF}(0) = \frac{1}{2}$.

On the other hand, as Θ grows, the system becomes more and more classical from the statistical point of view, when no spin effects could manifest themselves. And if, in addition, the Coulomb interaction is relatively small ($\Gamma \simeq 0.01$), the value of $g_e(0)$ approaches the

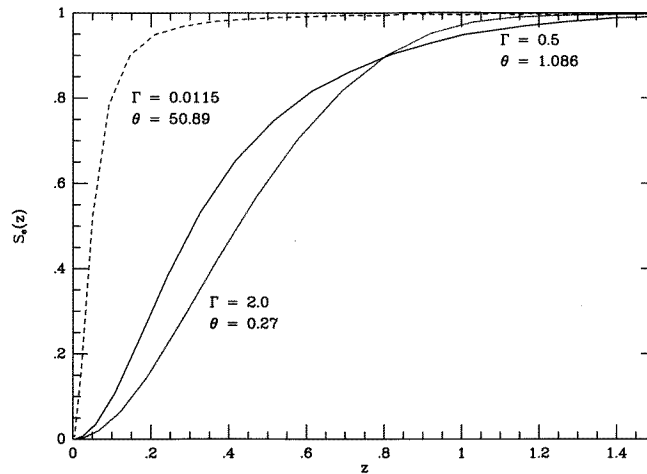


Figure 2. The self-consistent electronic static structure factor $S_e(z)$ ($z = k/(2k_F)$) for three characteristic pairs of values of density and temperature: $\Gamma = 0.01$, $\Theta = 50.0$ (broken curve); $\Gamma = 0.5$, $\Theta = 1.0$ (full curve); $\Gamma = 2.0$, $\Theta = 0.27$ (dotted curve). For other parameters, see table 1.

classical ideal-gas limiting value of 1 already at $\Theta \simeq 10$. In systems with stronger Coulomb interactions ($\Gamma \simeq 0.1$) this asymptotic value is reached at higher values of $\Theta > 150$.

In weakly coupled electron liquids with $\Gamma \gtrsim 0.5$ the exchange effects resulting in attraction of electrons with antiparallel spins are compensated for by the Coulomb repulsion, and in such systems the value of $g_e(0)$ decreases significantly with growing Γ . Strong Coulomb coupling ($\Gamma \gtrsim 1$) can (asymptotically) reduce the value of $g_e(0)$ to zero (pure Coulomb repulsion). In our model it appears that the exchange contribution to $g_e(0)$ is underestimated, so that this reduction already occurs at about $r_s \simeq 1.84$, which is 22% higher than the value stemming from the high-density expansion of the Yasuhara's formula [11], $q = 2$.

In conclusion, the dielectric formalism is applied to the description of electron one-component liquids and a simple model expression for the electronic local-field correction satisfying the compressibility sum rule and the exact short-wavelength limiting ('cusp') condition is studied. The long-wavelength behaviour of the LFC is adjusted to the MC-fitted equation of state. The model parameter $g_e(0)$ (the zero-separation value of the electronic radial distribution function) is obtained by the self-consistency procedure in a wide range of thermodynamic parameters and is shown to possess physically reasonable limiting properties.

Nevertheless, further studies of $g_e(0)$ might be carried out to include low-temperature [12] and dynamic effects.

In addition, to improve the physical self-consistency of our approach, one needs the quantal EOS, either theoretical or numerical (obtained, e.g. within a quantum-statistical variant of the MC method).

The static LFC determined here is expected to become a reliable tool in the determination of static and thermodynamic characteristics of dense Coulomb systems at intermediate and high values of temperature. Their dynamic and kinetic properties can be studied within an alternative approach to those pointed out by Sturm in his recent paper [13], and based on the construction of the plasma dynamic dielectric function by the method of frequency moments using all known exact relations and sum rules (see [4, 14] and references therein).

Acknowledgments

One of the authors (IMT) is grateful to Dr J Ortner for valuable discussions. The work was partially financed by the Institució Valenciana d'Estudis i Investigació (IVEI) (grant no 024-94).

References

- [1] Ichimaru S 1994 *Statistical Plasma Physics* vol II *Condensed Plasmas* (New York: Addison-Wesley)
- [2] Stringfellow G S, de Witt H E and Slattery W L S 1990 *Phys. Rev. A* **41** 1105
- [3] Tkachenko I M 1989 *Europhys. Lett.* **9** 351
Djurić Z *et al* 1991 *Phys. Lett.* **155A** 415
- [4] Adamjan S V, Tkachenko I M, Muñoz-Cobo González J L and Verdú Martín G 1993 *Phys. Rev. E* **48** 2067
- [5] Shaw R W 1970 *J. Phys. C: Solid State Phys.* **3** 1140
- [6] Kimball J C 1973 *Phys. Rev. A* **7** 1648
- [7] Kimball J C 1976 *Phys. Rev. B* **14** 2371
- [8] Ichimaru S 1982 *Rev. Mod. Phys.* **54** 1017
- [9] Arista N R and Brandt W 1984 *Phys. Rev. A* **29** 1471
- [10] Tanaka S, Yan X-Z and Ichimaru S 1990 *Phys. Rev. A* **41** 5616, see also [1]
- [11] Yasuhara H 1972 *Solid State Commun.* **11** 1481
- [12] Utsumi K and Ichimaru S 1982 *Phys. Rev. A* **26** 603
- [13] Sturm K 1995 *Phys. Rev. B* **52** 8028
- [14] Ortner J, Rylyuk V M and Tkachenko I M 1994 *Phys. Rev. E* **50** 4937

Transport properties of strongly coupled plasmas

I. M. Tkachenko* and P. Fernández de Córdoba

Department of Applied Mathematics, Polytechnic University of Valencia, Valencia E-46022, Spain

(Received 12 May 1997; revised manuscript received 16 October 1997)

A self-consistent field theory is proposed of transport properties of strongly coupled, fully ionized, multi-component plasmas. The results are compared with those of simulation and experimental studies [for molecular-dynamics one-component plasmas see J. P. Hansen *et al.*, Phys. Rev. A **23**, 2041 (1981); for capillary discharges see J. F. Benage, Jr. *et al.*, Phys. Rev. E **49**, 4391 (1994); for vaporization of copper wires in water see A. W. DeSilva (private communication)]. Like in previously considered cases [V. M. Adamyan *et al.*, J. Phys. D **27**, 927 (1994), and references therein], the agreement is good or reasonable; the approach possesses no adjustable parameters. [S1063-651X(98)06302-8]

PACS number(s): 52.25.Fi

I. INTRODUCTION

Recently, there has been an increasing amount of work both theoretical and experimental, on electrical conductivity of strongly coupled Coulomb systems. The experimental studies have been carried out by measuring the resistivity of a plasma channel produced by strong electrical (capillary) discharges in dense materials such as polyurethane [1] and copper [2,3].

Recent experimental data, especially those of DeSilva and Kunze and DeSilva, have invited a number of researchers to compare their theoretical predictions with these data; see [4,5] and also [6].

These theoretical approaches either are based, like [7], on generalizations of the Ziman formula for resistivity of metals (see also [8]) or, as in [9], construct appropriate interpolation formulas between the Ziman and Spitzer theories [8]. One should also take into consideration the semiempirical results of [10].

More references can be found in the review article by Iakubov [11], where it was also pointed out that there was no theoretical approach capable of describing all experimental data, despite its ambiguity. In an early work [12] a correlation-function expression for the collision frequency was found and shown to reduce to the Ziman and Lenard-Balescu results in the appropriate limits. The realm of validity of this expression is limited by the possibility of applying and solving the hypernetted-chain equations.

In this paper we want to show that the theory of transport coefficients of dense cold plasmas based on the concept of self-consistent field and the generalized random-phase approximation (RPA) also possesses correct low- and high-density limiting properties and is in reasonable, taking into account a low level of precision of resistivity measurements, agreement with all available experimental data. This theory considers only fully ionized plasmas and has not yet been extended to the description of data corresponding to alleged Mott phase transition conditions.

II. MODEL

We consider dense relatively cold plasmas with temperature T of about $T \geq 10^4$ K and electronic number density $n_e \geq 10^{21}$ cm $^{-3}$ [13]. Under such conditions all characteristic lengths such as the Wigner-Seitz radius $d = (3/4\pi n_e)^{1/3}$, the electronic Debye radius $\lambda_{De} = (4\pi n_e e^2 \beta)^{1/2}$ ($\beta^{-1} = k_B T$, k_B is the Boltzmann constant), and the de Broglie wavelength $\lambda = \pi \hbar (2\beta/m)^{1/2}$ (\hbar is the Planck constant) are of the same order of a few atomic units and the Debye correction to the ionization energy becomes comparable to the (hydrogen) ionization energy itself. Thus, at least the valent atomic electrons become collectivized and one cannot distinguish between charged and neutral components of the plasma.

The basic idea considered in the present approach is that of self-consistent field: Each electron (carrier) moves in a self-consistent field generated by all other free charges in the system. The finite values of the transport coefficients result from the electron's scattering on the self-consistent field fluctuations.

This approach was outlined and applied in [13]. This work was based on the paper [14] by Edwards, which related the Lorentz-model expression for the fully ionized plasma electrical conductivity to the strict quantum-statistical calculation involving the Green's-function formalism with the self-consistent field potential.

III. THEORY

The starting point for the conductivity calculation is the quantum-mechanical expression

$$\sigma = \text{Re} \frac{\partial}{\partial F} j_x(\vec{r}, t) \Big|_{F=0}, \quad (1)$$

where $\vec{j}(\vec{r}, t)$ is the averaged current density generated in the system by an external electric field $\vec{F}(F, 0, 0)$. We presume that

$$F(\vec{r}, t) = F \exp(\delta t), \quad (2)$$

with $\delta > 0, \delta \rightarrow 0^+$. This specific time dependence of the field is introduced to avoid coherent currents inducted at the switch-on moment $t = -\infty$. Thus

*Electronic address: imtk@iqn.upv.es

$$j_x(\vec{r}, t) = \text{Tr} \hat{\rho}(t) \left\{ -\frac{i\hbar e}{2m} \left[\Psi^\dagger(\vec{r}, -\infty) \frac{\partial}{\partial x} \Psi(\vec{r}, -\infty) - \frac{\partial}{\partial x} \Psi^\dagger(\vec{r}, -\infty) \Psi(\vec{r}, -\infty) \right] \right\}, \quad (3)$$

where only the density matrix operator $\hat{\rho}(t)$ depends on the external field (2), so that

$$\left[\frac{\partial \hat{\rho}(t)}{\partial F} \right]_{F=0} = \frac{ie}{\hbar} \int_0^\infty e^{-\delta s} ds \times \int_\Omega x [\Psi^\dagger(\vec{r}, s) \Psi(\vec{r}, s), \hat{\rho}(-\infty)] d\vec{r}. \quad (4)$$

[$(-e)$ and m are the electronic charge and mass.] Here

$$-eF e^{-\delta t} \int_\Omega x \Psi^\dagger(\vec{r}, s) \Psi(\vec{r}, s) d\vec{r}$$

is the interaction contribution to the system Hamiltonian $H(t)$ and

$$\begin{aligned} \hat{\rho}(-\infty) &= \exp\{-\beta[H(-\infty) - \phi]\}, \\ \exp(-\beta\phi) &= \text{Tr} \exp[-\beta H(-\infty)], \end{aligned} \quad (5)$$

ϕ being the system free energy of Helmholtz and Ω the system volume. Thus,

$$\begin{aligned} \sigma &= \frac{e^2}{2m} \text{Re} \int_0^\infty e^{-\delta s} ds \int_\Omega d\vec{r}' x' \text{Tr} \hat{\rho}(-\infty) \\ &\times \left[\Psi^\dagger(\vec{r}, -\infty) \frac{\partial}{\partial x} \Psi(\vec{r}, -\infty) - \frac{\partial}{\partial x} \Psi^\dagger(\vec{r}, -\infty) \right. \\ &\left. \times \Psi(\vec{r}, -\infty), \Psi^\dagger(\vec{r}', s) \Psi(\vec{r}', s) \right]. \end{aligned} \quad (6)$$

The second-quantized wave function $\Psi(\vec{r}, t)$ is expressible in terms of the one-electron wave function $\psi_\nu(\vec{r})$ of the one-electron free Hamiltonian H_0 ,

$$H_0 \psi_\nu(\vec{r}) = \varepsilon_\nu \psi_\nu(\vec{r}), \quad (7)$$

$$\Psi(\vec{r}, s) = \sum_\nu a_\nu \exp\left(-\frac{i}{\hbar} \varepsilon_\nu s\right) \psi_\nu(\vec{r}), \quad (8)$$

a_ν being the corresponding annihilation operator, for which we have the averaged commutator

$$\text{Tr} \hat{\rho}(-\infty) [a_\mu^\dagger, a_\mu, a_\nu^\dagger, a_\nu] = \delta_{\mu\nu} \delta_{\mu'\nu'} [w_\nu - w_\mu], \quad (9)$$

where

$$w_\nu = w(\varepsilon_\nu) = \{\exp[\beta(\varepsilon_\nu - \mu)] + 1\}^{-1}$$

is the Fermi-Dirac distribution, μ being the electronic subsystem chemical potential.

The trace in Eq. (6) can thus be simplified to get

$$\begin{aligned} \sigma &= \frac{e^2}{2m} \text{Re} \int_0^\infty \int_0^\infty d\varepsilon_1 d\varepsilon_2 \int_\Omega d\vec{r}' x' \\ &\times \left\langle G(\vec{r}, \vec{r}'; \varepsilon_1) \frac{\partial}{\partial x} G(\vec{r}, \vec{r}'; \varepsilon_2) \right. \\ &\left. - G(\vec{r}, \vec{r}'; \varepsilon_2) \frac{\partial}{\partial x} G(\vec{r}, \vec{r}'; \varepsilon_1) \right\rangle \frac{\hbar[w(\varepsilon_1) - w(\varepsilon_2)]}{i(\varepsilon_1 - \varepsilon_2 - i\hbar\delta)}. \end{aligned} \quad (10)$$

Here

$$G(\vec{r}, \vec{r}'; \varepsilon) = \sum_\nu \psi_\nu^\dagger(\vec{r}) \psi_\nu(\vec{r}') \delta(\varepsilon_\nu - \varepsilon)$$

is the electronic Green's function of the Schrödinger equation involving the self-consistent field $V(\vec{r})$:

$$-\frac{\hbar^2}{2m} \Delta G + eV(\vec{r})G = \varepsilon G + \delta(\vec{r} - \vec{r}'),$$

$$G(\vec{r}, \vec{r}'; \varepsilon) = G(\vec{r}', \vec{r}; \varepsilon). \quad (11)$$

Averaging in Eq. (10) is to be carried out over the self-consistent field fluctuations. The symmetry properties of the Green's function lead to

$$\begin{aligned} \sigma &= \frac{\pi e^2 \hbar^3}{m^2} \text{Re} \int_0^\infty d\varepsilon \frac{d\omega(\varepsilon)}{d\varepsilon} \int_\Omega d\vec{r}' \\ &\times \left\langle \frac{\partial G(\vec{r}, \vec{r}'; \varepsilon)}{\partial x'} \frac{\partial G(\vec{r}, \vec{r}'; \varepsilon)}{\partial x} \right\rangle. \end{aligned} \quad (12)$$

An important advantage of formula (12) for σ is that it is analogous to the expression that describes the interaction of electrons with quantized electromagnetic field and there already exists the diagrammatic perturbation theory technique of calculation of the right-hand side of Eq. (12). In addition, the present problem lacks the divergence difficulties characteristic of quantum electrodynamics and various approximate methods of the quantum field theory can be applied to evaluate Eq. (12) without complications.

There is an important difference between Eqs. (1) and (3), on the one hand, and Eq. (12), on the other. The latter permits one to carry out the self-consistent field averaging procedure before the coordinate integration.

Edwards [14], who previously obtained Eq. (12), developed and applied to it a diagrammatic technique analogous to that of the quantum field theory. He showed that if the interaction operator \hat{I} could be introduced by the equation

$$\langle GG \rangle = \langle G \rangle \langle G \rangle + \langle G \rangle \langle G \rangle \hat{I} \langle GG \rangle \quad (13)$$

and estimated within a perturbation theory, the *free* Green's function

$$G_0(\vec{r}, \vec{r}'; \varepsilon) = \frac{m}{2\pi^2 \hbar^2} \frac{\sin(k|\vec{r} - \vec{r}'|)}{|\vec{r} - \vec{r}'|} \quad (14)$$

[here $k=(2m\varepsilon/\hbar^2)^{1/2}$] in the presence of the self-consistent field $V(\vec{r})$ fluctuations should be substituted by

$$\langle G(\vec{r}, \vec{r}'; \varepsilon) \rangle = \frac{m}{2\pi^2 \hbar^2} \frac{\sin(k|\vec{r}-\vec{r}'|)}{|\vec{r}-\vec{r}'|} \exp\left(-\frac{|\vec{r}'-\vec{r}|}{\gamma(\varepsilon)}\right), \quad (15)$$

where $\gamma(\varepsilon)$ is the electronic mean free path. Then integration in Eq. (12) yields

$$\sigma = -\frac{2me^2}{3\pi^2 \hbar^3} \int_0^\infty E \frac{dw(E)}{dE} \gamma(E) dE. \quad (16)$$

Since, as in the kinetic theory,

$$\gamma(E) = (2E/m)^{1/2} \tau(E), \quad (17)$$

$\tau(E)$ being the mean relaxation time, Eq. (16) coincides with the Lorentz formula

$$\sigma = -\frac{4e^2}{3m} \int_0^\infty E dE \frac{dw(E)}{dE} \rho(E) \tau(E), \quad (18)$$

where $\rho(E) = (2m^3 E)^{1/2} / 2\pi^2 \hbar^3$ is the density of one-electron states in the energy space. Generally speaking, the mean free path $\gamma(E)$ or the mean relaxation time $\tau(E)$ of Eq. (18) is determined by the exact pairwise scattering cross section. Notice also that the averaging over the self-consistent field thermal fluctuations includes *configurations* for which the conductivity is infinite. We attribute to such contributions of $V(\vec{r})$ a negligible statistical weight.

IV. CALCULATION OF CONDUCTIVITY

It was shown in [14] that Eq. (15) for the averaged one-electron Green's function $\langle G \rangle$ is a result of summation of infinite series in powers of the pairwise-interaction transport cross section. That is why, though we substitute the latter by its first Born approximation and thus neglect a good deal of diagrammatic contributions to $\langle G \rangle$ [13], we can consider Coulomb systems with relatively strong interactions. Thus we express the inverse mean relaxation time in terms of the self-consistent field correlation function

$$\tau^{-1}(E) = \frac{me^2}{4\pi(2mE)^{3/2}} \int_0^Q q^3 dq \int_{-\infty}^\infty \langle |\hat{V}(\vec{q}, \omega)|^2 \rangle d\omega. \quad (19)$$

Here $Q = (8mE/\hbar^2)^{1/2}$, the momentum $\hbar Q$ being the maximum possible variation of the electronic momentum as a result of the scattering process, and

$$\hat{V}(\vec{q}, \omega) = \frac{4\pi e}{q^2 \varepsilon(q, \omega)} \sum_a \kappa_a(q) \hat{\rho}_a(\vec{q}, \omega) \quad (20)$$

is the field potential operator complete Fourier transform, $\hat{\rho}_a(\vec{q}, \omega)$ being the a -species density operator in (\vec{q}, ω) space and $\varepsilon^{-1}(q, \omega)$ the plasma dynamic screening function. The system is presumed to contain electrons (e) and p ionic species (i_1, i_2, \dots, i_p) characterized by their respective form factors $\kappa_a(q)$, $a = e, i_1, i_2, \dots, i_p$, which describe the inter-

nal charge distribution of the species a , $\kappa_e = -1$, and $\kappa_i(0) = Z_i$, the charge number of ions i . The field potential correlation function thus equals

$$\langle |\hat{V}(\vec{q}, \omega)|^2 \rangle = \left(\frac{4\pi e}{q^2 \varepsilon(q, \omega)} \right)^2 \sum_{a,b} \kappa_a(q) \kappa_b(q) S_{ab}(\vec{q}, \omega). \quad (21)$$

The dynamic structure factor of the species a and b ,

$$S_{ab}(\vec{q}, \omega) = \langle \hat{\rho}_a^*(\vec{q}, \omega) \hat{\rho}_b(\vec{q}, \omega) \rangle, \quad (22)$$

is related, by the fluctuation dissipation theorem [15]

$$S_{ab}(\vec{q}, \omega) = \frac{\hbar}{2\pi} \coth(\beta \hbar \omega / 2) \text{Im} X_{ab}(\vec{q}, \omega), \quad (23)$$

to the partial density-response (Green's) function

$$X_{ab}(\vec{q}, \omega) = \Pi_a(q, \omega) \delta_{ab} - \Pi_a(q, \omega) \Pi_b(q, \omega) J^{ab}(\vec{q}, \omega), \quad (24)$$

$$J^{ab}(\vec{q}, \omega) = \frac{4\pi e^2}{q^2} \frac{\kappa_a(q) \kappa_b(q)}{\varepsilon(q, \omega)} \quad (25)$$

being the full vertex part and $\Pi_a(q, \omega)$ the a -species polarization operators, which also determine the dielectric function in Eq. (20) and

$$\varepsilon(q, \omega) = 1 + \frac{4\pi e^2}{q^2} \sum_a \kappa_a^2(q) \Pi_a(q, \omega). \quad (26)$$

Substitution of Eqs. (21)–(25) into Eq. (19) and integration [15] yields

$$\tau^{-1}(E) = \frac{4\pi m e^4}{\beta(2mE)^{3/2}} \int_0^Q \frac{dq}{q} \sum_{a,l} \frac{\kappa_a^2(q) \Pi_a(q, l)}{\varepsilon^3(q, l)}. \quad (27)$$

(A corresponding expression from [16] is valid for hydrogen plasmas only.) Here the l summation is spread over the poles

$$\Omega_l = 2\pi l / \beta \hbar \quad (l = 0, \pm 1, \pm 2, \dots) \quad (28)$$

of $\coth(\beta \hbar z / 2)$ on the imaginary z -axis, i.e., over the Matsubara frequencies [17], and $\Pi_a(q, l)$ are the real parts of the $\Pi_a(q, \omega)$ operators at $\omega = i\Omega_l$. Equation (27) together with Eq. (18), forms a general algorithm of conductivity calculation, as soon as specific approximate expressions are used for the density-response functions and the polarization operators.

In our computations we evaluated the real part $\Pi_a(q, l)$ of the a -species polarization operator beyond the standard RPA, using the temperature-dependent static local-field correction $G_e(q)$ [18,16,19] parametrized to satisfy both the compressibility sum rule [with the electronic subsystem compressibility determined from the one-component plasma excess interaction energy determined by the Monte Carlo (MC) simulation [20]] and the long-wavelength limiting condition of Kimball [21]

$$G_e(q) = G_e(z) = [b + a/(2z)^2]^{-1}. \quad (29)$$

Here $b = [1 - g_e(0)]^{-1}$ and a was estimated as in [19]:

$$a = -(12\pi^2)^{-1/3} \left(\frac{A}{9} + \frac{B}{12} \Gamma^{-1} + \frac{2C}{27} \Gamma^{-4/3} + \frac{5D}{54} \Gamma^{-2/3} \right)^{-1}. \quad (30)$$

Here $\Gamma = \beta e^2 (4\pi n_e/3)^{1/3}$ measures the rate of Coulomb coupling in the system, $z = q/k_F$, $k_F = (3\pi^2 n_e)^{1/3}$ is the Fermi wave vector, and $A = -0.899\,374\,9$, $B = -0.224\,469\,9$, $C = -0.017\,874\,7$, $D = -0.517\,575\,3$, [20].

The model parameter $g_e(0)$, which is the zero-separation value of the electronic radial distribution function was determined by a self-consistent procedure: It was computed via a simultaneous solution of two integral equations

$$S_e(z) = \sum_{l=-l_1}^{l_1} \frac{P_e(z,l)}{\varepsilon_e(z,l)}, \quad (31)$$

$$g_e(0) = 1 + 12 \int_0^\infty (S_e(z) - 1) z^2 dz. \quad (32)$$

In Eq. (31) the summation is spread over the Matsubara dimensionless frequencies

$$v_l = \pi l / 2Dz; \quad (33)$$

$$\varepsilon_e(z,l) = 1 + \frac{\Gamma}{(12\pi^2)^{1/3}} \frac{P_e(z,l)}{z^2} \quad (34)$$

is the electronic dielectric function; the value of l_1 in Eq. (31) was determined by the numerical precision.

Here $D = \theta^{-1} = \beta \hbar^2 k_F^2 / 2m$ is another dimensionless parameter measuring the plasma degeneracy rate; notice that the Brueckner parameter

$$r_s = \Gamma \theta / 0.543. \quad (35)$$

$P_e(z,l)$ in Eq. (31) is the dimensionless polarization operator $\Pi_e(q,l) = \Pi_e(q, i\Omega_l)$ with the local-field correction included:

$$P_e(z,l) = P_e^0(z,l) \left(1 - \frac{\Gamma}{(12\pi^2)^{1/3}} \frac{G_e(z) P_e^0(z,l)}{z^2} \right)^{-1}. \quad (36)$$

The RPA dimensionless polarization operator $P_e^0(z,l)$ can be calculated (for each value of density and temperature, z and l) by simple integration [22],

$$P_e^0(z,l) = \frac{3\theta}{4z} \int_0^\infty \frac{y dy}{e^{y^{2/\theta} - \eta} + 1} \ln \left| \frac{z+y+iv_l}{z-y+iv_l} \right|, \quad (37)$$

while the dimensionless chemical potential $\eta = \beta\mu$ is determined by the normalization condition

$$\int_0^\infty \frac{t^{1/2}}{e^{(t-\eta)} + 1} = \frac{2}{3} \theta^{-3/2}. \quad (38)$$

Thus we used in Eq. (27)

$$\Pi_e(q,l) = n_e \beta P_e^0(z,l) \quad (39)$$

for the electronic polarization operator and [8]

$$\Pi_i(z,l) = \beta n \delta_{l,0} \left(1 - \frac{\Gamma}{(12\pi^2)^{1/3}} \frac{G_i(z)}{z^2} \right)^{-1} \quad (40)$$

with

$$G_i(z) = \{b[\varepsilon_e(z,l)] + a/(2z)^2\}^{-1}, \quad (41)$$

for the ionic one ($\delta_{l,m}$ is the Kronecker delta symbol) and thus obtained a closed expression for the conductivity coefficient. Notice that the influence of the value of $g_e(0)$ proved to be quite small; see, nevertheless, Sec. VII A.

V. LIMITING CASES

Despite the approximations made to obtain our expression for the plasma conductivity, it possesses correct limiting forms corresponding to the cases of dilute gas plasma and metal-density Coulomb systems. In particular, if we omit the electronic contribution in Eq. (27) and neglect the screening effects (i.e., set $\varepsilon(q,l) = 1$) and the momentum dependence of the ionic form factors, the sum on the right-hand side of Eq. (27) becomes a constant

$$\beta \sum_i Z_i^2 n_i.$$

If further we presume E to be equal to the mean kinetic energy of an electron, we retrieve from Eq. (27) the Coulomb logarithm, and Eq. (18) with $w(E)$ substituted by the Boltzmann distribution takes the form of the Spitzer formula without corrections due to electron-electron interactions [23]. We have estimated the relative weight of this last correction. In particular, in the dilute plasma regime, we calculated the conductivity contribution due to scattering on ions only. Hydrogenlike plasmas were considered in these computations with $n_e = Zn_i$ and the screening function was substituted by its long-range static limiting form

$$\varepsilon(q,\omega) \rightarrow (1 + q^2/k_s^2)^{-1}$$

with the screening length k_s^{-1} chosen to be either the electronic Debye radius $k_1^{-1} = (4\pi n_e e^2 \beta)^{-1/2}$ or the complete Debye radius $k_2^{-1} = [4\pi(1+Z)n_e e^2 \beta]^{-1/2}$. Thus we employed instead of the relaxation time of Eq. (27) the limiting expression

$$\tau_s^{-1}(E) = \frac{4\pi m Z^2 e^4 n_i}{(2mE)^{3/2}} \int_0^Q \frac{q^5 dq}{(q^2 + k_s^2)^3}. \quad (42)$$

These estimates are provided in Table I, labeled σ_1 and σ_2 , along with the results of our complete calculations, labeled σ and obtained as explained in Sec. VII C. It is seen that the electron-electron interactions are responsible for up to 45% of the resistivity value.

On the other hand, if we consider the low-temperature limiting case ($\beta^{-1} \rightarrow 0$), the Fermi-Dirac distribution derivative in Eq. (18) turns into $-\delta(E - E_F)$ with $E_F = \hbar^2 k_F^2 / 2m$ and Q becomes equal to $2k_F$, so that we immediately regain the Ziman specific resistance formula [24].

Notice that no special effort was done *ab initio* to guarantee the correct limiting behavior of our model. Neverthe-

TABLE I. Relative contributions to the plasma conductivity σ of Table III, σ_s ($s=1,2$), are calculated according to Eq. (18) but with $\tau_s(E)$ from Eq. (40) with $k_1 = \sqrt{4\pi n_e e^2 \beta}$ and $k_2 = \sqrt{4\pi(1+Z)n_e e^2 \beta}$, respectively. T, n_e are the temperature and electronic number density in copper and Ze is the effective ion charge.

T (kK)	$n_e \times 10^{-21}$ (cm $^{-3}$)	Z	$\sigma \times 10^{-4}$ (S/m)	$\sigma_1 \times 10^{-4}$ (S/m)	$\sigma_2 \times 10^{-4}$ (S/m)
20	3.18	1.3	2.12	3.13	4.07
20	7.69	1.2	2.94	4.55	6.34
30	4.07	1.6	3.03	4.02	5.21
30	6.03	1.6	3.42	4.47	5.97
40	4.33	2.0	3.66	4.37	5.72

less, further studies of the limiting behavior of our model and a comparison with other general expressions for the collision frequency (e.g., [12]) or for the conductivity itself (see [25]) are to be carried out.

In general, the difference between our expression and that of Ziman (widely used lately to calculate conductivity [4–6]) is that we include the energy-dependent relaxation time [Eq. (27)] and the Ziman formula takes it at $E = E_F$. In addition, we have the electron-electron interaction included explicitly via the structure factor $S_{ee}(q, \omega)$.

The $\sigma(T)$ dependence at constant density (see [16]) is characterized by a minimum corresponding to a transition from the low-temperature regime with decreasing (with growing T) conductivity characteristic for metals and liquid metals (Ziman regime) to that of increasing conductivity at higher temperatures, characteristic for dilute plasmas (Spitzer regime). Thermodynamic conditions were specified in [16] corresponding to the domain of values of the electronic concentration and the plasma temperature (in hydrogen plasmas) where our expression asymptotically approaches the Spitzer regime with $\sigma_{Sp}(T) \propto T^{3/2}$.

Finally, relative contributions due to various factors in Eq. (27) were also estimated. We found that at least for $T=20$ kK and $n_e \geq 10^{21}$ cm $^{-3}$ (conditions considered earlier in [13]), the value of conductivity calculated with the sum in Eq. (27) substituted by

$$[\Pi_e(q,0) + Z^2 \Pi_i(q,0)]/\varepsilon(q,0)$$

(as in [13]) was about 50% higher than the complete calculation results given in Tables I and III.

VI. OTHER TRANSPORT COEFFICIENTS

If the initial state of plasma is not far from that of thermodynamic equilibrium, the generalized transport equations for the mean current density \vec{J} and for the thermal flux \vec{Q} can be written as [26]

$$\vec{J} = e^2 K_0 \vec{F} + T^{-1} e K_1 (-\vec{\nabla} T), \quad (43)$$

$$\vec{Q} = e K_1 \vec{F} + T^{-1} K_2 (-\vec{\nabla} T). \quad (44)$$

T is the plasma temperature and no magnetic effects are taken into account. The transport coefficients K_i ($i=0,1,2$) in Eqs. (43) and (44) satisfy the Onsager relations [26] and within the same approximation instead of Eq. (18) we have

$$K_i = -\frac{4}{3m} \int_0^\infty E \rho(E) \tau(E) \frac{dw(E)}{dE} (E - \mu)^i dE, \quad (45)$$

where μ is the electronic subsystem chemical potential and $\tau(E)$ is the same relaxation time defined by Eq. (27). The transport coefficient K_0 determines the static conductivity

$$\sigma = e^2 K_0, \quad (46)$$

while the static thermal conductivity

$$\kappa = \frac{1}{T} (K_2 - K_1^2/K_0) \quad (47)$$

and the thermal electromotive potential

$$\alpha = K_1 (eTK_0)^{-1}. \quad (48)$$

In the case of complete degeneracy of the electronic subsystem the conductivities κ and σ are related by the Wiedemann-Franz law

$$\frac{\kappa}{\sigma} = \frac{\pi^2}{3} \left(\frac{k_B}{e} \right)^2 T. \quad (49)$$

If the degeneracy is incomplete, like in our case, there appear temperature-dependent corrections to Eq. (49). Nevertheless, we will see that these corrections under the conditions we consider are quite small.

VII. RESULTS AND CONCLUSIONS

Extensive studies of electrical and thermal conductivities in a wide range of variation of temperature and electronic density in hydrogenlike plasmas (with $n_e = Zn_i$) were carried out in [16,27,28]. Here we report our results on the conductivities obtained for the conditions corresponding to (i) model Coulomb plasmas [29], (ii) capillary discharges in polyurethane [1], and (iii) copper plasmas obtained by vaporizing copper wire in a water bath [3].

A. Microscopic simulation of hydrogen plasma

Fully ionized strongly coupled hydrogen plasmas were simulated using the method of molecular dynamics (MD) in well-known studies by Hansen and McDonald [29]. Quantum effects were taken into account in these simulations through the use of effective pair potentials; at short distances these differed significantly from the bare Coulomb potential. Reasonable agreement with the conductivity results of [29]

TABLE II. σ_L^* are the results of the extrapolation procedure according to Eq. (50) and σ_D^* were calculated in terms of the diffusion coefficients as explained in Sec. VII A. σ_{Cp}^* are the results of the present work computed using the Coulomb potential and σ_{pp}^* represent our results calculated with the model pseudopotential suggested in [31] and employed in [29]; σ_{BRD}^* stands for the results of [12].

$n_e \times 10^{-24}$ (cm $^{-3}$)	$T \times 10^{-5}$ (K)	Γ	r_s	σ_L^*	σ_D^*	σ_{Cp}^*	σ_{pp}^*	σ_{BRD}^*
1.611	1.579	2.0	1.00	1.1	0.60	0.59	1.20	3.72
1.610	6.315	0.5	1.00	2.15	0.86	1.00	1.40	2.13
25.170	15.79	0.5	0.40	3.6	1.47	1.80	2.70	4.13

was obtained in [12] (see Table II, where the results are presented for the dimensionless conductivity $\sigma^* = \sigma/\omega_{pe}$ ($\omega_{pe} = (4\pi n_e e^2/m)^{1/2}$ being the electronic plasma frequency). The *dynamical* results of [29] were successfully considered in [30].

The static conductivity of model plasmas was obtained in [29] on the basis of the Nernst-Einstein law in terms of electronic and ionic diffusion coefficients directly estimated by MD simulations:

$$\sigma_D = \beta n_e e^2 (D_i + D_e). \quad (50)$$

In addition, σ was determined, at least for $\Gamma=2$ and $r_s=1$, through the electric current autocorrelation function in the relaxation time approximation [29].

Notice that the simulation data for $\Gamma=2$ and $r_s=1$ were obtained in [29] by MD calculations; in this case the value σ_D^* was calculated as

$$\sigma_D^* = \frac{3\Gamma}{4\pi} \left(\frac{m}{M} \right) D_i^* + D_e^*, \quad (51)$$

D_e^* and D_i^* being the dimensionless diffusion coefficients determined in [29]. Other results were found in [29] by extrapolation. In these cases D_i^* was set equal to zero (not determined in [29]); M is the proton mass.

The value of σ_L^* was obtained in [29] by a limiting procedure over the dynamic conductivity $\sigma(k, \omega)$,

$$\sigma_L = \lim_{\omega \rightarrow 0} \lim_{k \rightarrow 0} \text{Re} \sigma(k, \omega), \quad (52)$$

and thus related via the fluctuation-dissipation theorem to the dynamic *charge-charge* structure factor. The limiting value of Eq. (50) could be found in [29] only by extrapolation of long-wavelength MD data (see Table IV of [29]). The point with $\Gamma=2.0$ was the only point really simulated in [29]. The other two points were obtained in this work using an extrapolation procedure; its precision is unknown to us. We would rather not consider $\sigma_L^* = \sigma_L/\omega_{pe}$ (characterized in [29] as the *true* value) to be much more reliable than σ_D^* .

We computed the conductivity of strongly coupled hydrogen plasma for all three cases considered in [29] and using the static local field correction of Eq. (29). The calculations were carried out for both the Coulomb interaction and the model pseudopotential suggested by Deutsch and co-workers in [31] and employed in [29]. In the case of Coulomb interactions the relaxation time was calculated according to Eq. (27) with $\kappa_a^2(q) = 1, a = e, i$; see the σ_{Cp}^* data in Table II.

The model pseudopotential of [31,29] is determined by the interacting particles charge numbers and their reduced masses. The species form factors cannot be introduced, so that Eq. (21) should be modified:

$$\langle |\hat{V}(\vec{q}, \omega)|^2 \rangle = \left(\frac{4\pi e}{q^2 \varepsilon(q, \omega)} \right)^2 \sum_{a,b} Y_{ab}(q) S_{ab}(\vec{q}, \omega), \quad (53)$$

where

$$Y_{ab}(q) = Y_{ba}(q) = Z_a Z_b [1 + (q\lambda_{ab})^2]^{-1}, \quad (54)$$

$$\varepsilon(q, \omega) = 1 + \frac{4\pi e^2}{q^2} \sum_a Y_{aa}^2(q) \Pi_a(q, \omega), \quad (55)$$

and

$$\lambda_{ab} = \left[\frac{\hbar\beta}{2\pi} (m_a^{-1} + m_b^{-1}) \right]^{1/2}, \quad (56)$$

m_a and Z_a being the a species mass and charge number. In hydrogen plasmas $m_e = m$ and $m_i = M$, while $Z_e = -1$ and $Z_i = 1$.

The pseudoparticles screened interaction energy is equal to $4\pi e^2 Y_{ab}/q^2 \varepsilon(q, \omega)$ and the relaxation time expression of Eq. (27) becomes more complicated:

$$\tau_{pp}^{-1}(E) = \frac{4\pi m e^4}{\beta(2mE)^{3/2}} \int_0^Q \frac{dq}{q} \sum_l [Y_{ee}^2 \Pi_e + Y_{ii}^2 \Pi_i + 2(Y_{ee} Y_{ii} - Y_{ei}^2) \Pi_e \Pi_i] / \varepsilon^3(q, l). \quad (57)$$

The results of our computations with all these changes included, labeled σ_{pp}^* , are also provided in Table II. We cannot overestimate the fact that σ_{pp}^* virtually coincides with the *true* conductivity value σ_L^* at $\Gamma=2.0$. More simulation results on both transport and dynamic plasma properties are needed to decide whether, and to what extent, the behavior of the classical pseudoparticles with the pseudopotential of [31,29] imitates that of the true quantum system. We conclude that overall satisfactory agreement with available plasma-simulation data is achieved.

B. Capillary discharge in polyurethane

Dense strongly coupled plasmas were created in a well-diagnosed uniform discharge in polyurethane with density 1.265×10^{-2} g/cm 3 and temperatures in the 25–30 eV range

TABLE III. σ are the results of the present work, the experimental values σ^{exp} are by DeSilva [3], T and ρ are the temperature and mass density of copper, Ze is the effective ion charge, and f is the dimensionless Wiedemann-Franz ratio (59).

T (kK)	ρ (g/cm ³)	Z	Γ	θ	$\sigma^{exp} \times 10^{-4}$ (S/m)	$\sigma \times 10^{-4}$ (S/m)	f
20	0.7930	1.5	2.97	1.020	5.1	10.50	0.99
10	2.4550	2.3	10.12	0.167	32.1	21.00	0.99
14	1.2036	1.7	5.15	0.460	9.5	11.95	0.98
20	0.1557	1.2	1.62	3.240	2.2	4.12	1.11
26	0.0580	1.4	0.94	7.340	3.9	3.44	1.11
30	0.0400	1.6	0.75	9.930	4.8	3.42	1.11
40	0.0230	2.0	0.51	16.50	5.8	3.66	1.10
10	1.3546	1.7	7.51	0.304	8.3	11.27	0.99
14	0.3500	1.1	2.95	1.401	1.3	4.90	1.05
20	0.0260	1.3	0.92	10.13	2.0	2.12	1.11
10	2.2616	2.2	9.70	0.182	27.1	19.10	0.99
14	0.9704	1.5	4.60	0.577	6.4	9.86	0.99
16	0.1323	1.1	1.87	3.060	1.2	3.27	1.11
20	0.0680	1.2	1.62	5.630	2.2	2.94	1.11
30	0.0270	1.6	0.66	12.61	4.4	3.03	1.11

[1]. These results were compared in [1] with several dense plasma theories [32,33,12,34] and showed to be in a significant disagreement.

Preliminary experiments of this type were reported in [35–37]. Reasonable agreement with these data was obtained in [16], especially at $T=17$ – 18 eV [37], but within the hydrogen model.

An effective average ionic charge number $Z=2.3$ was obtained in [1] presuming Saha equilibrium. This permitted us to carry out the calculation of the electrical conductivity of a multiply ionized two-component plasma in the range $n_e=(4.8-5.2)\times 10^{21}$ cm⁻³ and $T=(2.5-4.0)\times 10^5$ K. The same local field correction as in Sec. VII A was employed with $g_e(0)=0$ (see [19] and above).

The experimental data of [1] (provided graphically for the resistivity) range between 2.0×10^5 and 3.3×10^5 (Ω m)⁻¹. Our results varied between 3.3×10^5 (Ω m)⁻¹ (for $n_e=5.2\times 10^{21}$ cm⁻³ and $T=2.5\times 10^5$ K) and about 10^6 (Ω m)⁻¹ (for $n_e=4.8\times 10^{21}$ cm⁻³ and $T=4.0\times 10^5$ K), taking the value of $\sigma=5.0\times 10^5$ (Ω m)⁻¹ at about 3×10^5 K and $n_e=5\times 10^{21}$ cm⁻³. This last value is characteristic for the results of *dense plasma theories* [32,33,12,34] referred to in [1]. Notice that the lowest conductivity value reached by these theories is about 4.2×10^5 (Ω m)⁻¹ [1] and also that under these specific conditions, i.e., at $\Gamma=0.18$ – 0.12 , the dimensionless (normalized to the plasma frequency) computed plasma conductivity can be fitted to a simple potential function of the coupling parameter Γ only:

$$\sigma^*(\Gamma) = u/\Gamma^v \quad (58)$$

with $u=1.70\times 10^{-2}$ and $v=2.27$.

C. Discharges in water

We have also carried out a broad comparison with the conductivity data measured by vaporizing copper wires in a water bath [3]. Plasma densities observed ranged from about 2.5 g/cm³ down to 0.025 g/cm³ and temperatures varied be-

tween 10 and 30 kK. The ionization state used by DeSilva and in our computations was taken from the Fermi-Thomas model by More [38]. The plasma coupling and degeneracy parameters ranged from $\Gamma=0.66$ to $\Gamma=10.12$ and $\theta=0.167$ to $\theta=16.5$, respectively; see Table III.

We considered three shots of data of [3] and calculated both electrical and thermal conductivities. The results are provided in Table III, where f is the dimensionless Wiedemann-Franz ratio

$$f = \frac{3}{\pi^2} (\kappa e^2 / \sigma k_B^2 T). \quad (59)$$

First of all, we observe a good level of verification of the Wiedemann-Franz law: We neglected the ionic transport. A reasonable 30% agreement is observed in the majority of points, especially at higher densities. A factor of 2–3 disagreement detected at 14–16 kK and low densities is attributable to the possible onset at the conductor-dielectric phase transition: The copper plasma begins to undergo a transformation from the fully ionized state corresponding to our model into the partially ionized state where charge-atom interactions are to be taken into account. The SESAME code “is increasingly inaccurate with the onset of strong Coulomb interaction” [39] and cannot include the possible Mott-type phase transition. The precision level of this code is not known. In addition, the experimental measurements are quite difficult [2,3] and we believe that an overall precision of the experimental data of [3] is of the order of 30–100 %.

Notice once more that no adjustable parameters were used in our computations. The only input data were the plasma temperature (T) and density (ρ) (provided by the SESAME code; see [3]) and the precalculated charge number Z (see above).

Calculations were carried out for different values of the local-field correction static parameter $g_e(0)$, ranging according to its definition between zero and unity. No appreciable dependence on the value of $g_e(0)$ was detected; further cal-

culations were carried out with $g_e(0)$ set to be zero. Thus the only *experimental* data our results are based on is the computer fit to the one-component plasma interaction energy obtained by MC simulations [20].

In conclusion, a theory of transport coefficients of fully ionized strongly coupled plasmas, based on the self-consistent field concept and having no adjustable parameters, is presented. The self-consistent field theory suggested in [13], outlined in detail, modified, and applied here to various model and real plasmas, is not based on the solution of kinetic equations. In particular, we do not have to introduce into our expression the order of 2 correction [40] (see also [12,7,8]) that takes into account higher-order Sonine polyno-

mials contributions to the solution of the kinetic equation. The theory is applicable to multiple-component (non-hydrogen-like) plasmas with variable ionization states, and is shown to possess correct low-density (Spitzer) and metal-density (Ziman) limiting forms.

ACKNOWLEDGMENTS

The authors are grateful to A. W. DeSilva for providing his numerical data on conductivity and ionization state and also to V. M. Adamyman, W. Ebeling, J. Ortner, and A. A. Mihajlov for valuable discussions.

-
- [1] J. F. Benage, Jr. *et al.*, Phys. Rev. E **49**, 4391 (1994).
 [2] A. W. DeSilva and H. J. Kunze, Phys. Rev. E **49**, 4448 (1994).
 [3] A. W. DeSilva, in *Physics of Strongly Coupled Plasmas*, edited by W. D. Kraeft and M. Schlanges (World Scientific, Singapore, 1995), p. 216 and private communication.
 [4] J. K. Yuan, Y. S. Sun, and S. T. Zhang, Phys. Rev. E **53**, 1059 (1996).
 [5] E. Nardi, Phys. Rev. E **54**, 1899 (1996).
 [6] H. Reinholz, R. Redmer, and S. Nagel, Phys. Rev. E **52**, 5368 (1995).
 [7] S. Ichimaru and S. Tanaka, Phys. Rev. A **32**, 1790 (1985).
 [8] S. Ichimaru, *Statistical Plasma Physics* (Addison-Wesley, Reading, MA, 1991), Vol. II.
 [9] G. Röpke and R. Redmer, Phys. Rev. A **39**, 907 (1989).
 [10] W. Ebeling *et al.*, *Thermophysical Properties of Hot Dense Plasmas* (Teubner Verlagsgesellschaft, Stuttgart, 1991), pp. 210–212.
 [11] I. T. Iakubov, Usp. Fiz. Nauk **163**, 35 (1993) (in Russian).
 [12] D. B. Boercker, F. Rogers, and H. E. DeWitt, Phys. Rev. A **25**, 1623 (1982).
 [13] V. M. Adamyman *et al.*, Teplofiz. Vys. Temp. **18**, 230 (1980) [High Temp. **18**, 186 (1980)].
 [14] S. F. Edwards, Philos. Mag. **3**, 1020 (1958).
 [15] S. Ichimaru, *Statistical Plasma Physics* (Addison-Wesley, Reading, MA, 1992), Vol. I.
 [16] Z. Djurić, A. A. Mihajlov, V. A. Nastasyuk, M. Popović, and I. M. Tkachenko, Phys. Lett. A **155**, 415 (1991).
 [17] A. A. Abrikosov, L. P. Gor'kov, and I. E. Dzyaloshinskii, *Quantum Field Methods in Statistical Physics* (GIFML, Moscow, 1962).
 [18] I. M. Tkachenko, Europhys. Lett. **9**, 351 (1989).
 [19] I. M. Tkachenko, P. Fernández de Córdoba, and M. Urrea, J. Phys. A **29**, 2599 (1996).
 [20] G. S. Stringfellow, H. E. de Witt, and W. L. S. Slattery, Phys. Rev. A **41**, 1105 (1990).
 [21] J. C. Kimball, Phys. Rev. A **7**, 1648 (1973); Phys. Rev. B **14**, 2371 (1976).
 [22] N. R. Arista and W. Brandt, Phys. Rev. A **29**, 1471 (1983).
 [23] L. Spitzer, Jr., *Physics of Fully Ionized Gases* (Interscience, New York, 1962).
 [24] J. M. Ziman, *Theory of Solids* (Cambridge University Press, London, 1972).
 [25] R. Redmer, Phys. Rep. **282**, 35 (1997).
 [26] See, e.g., A. R. Hochstim, *Kinetic Processes in Gases and Plasma* (Academic, New York, 1969), Chap. 6.
 [27] V. M. Adamyman, Z. Djurić, A. M. Ermolaev, A. A. Mihajlov, and I. M. Tkachenko, J. Phys. D **27**, 111 (1994).
 [28] V. M. Adamyman, Z. Djurić, A. M. Ermolaev, A. A. Mihajlov, and I. M. Tkachenko, J. Phys. D **27**, 927 (1994).
 [29] J. P. Hansen and I. R. McDonald, Phys. Rev. A **23**, 2041 (1981).
 [30] S. V. Adamyman, I. M. Tkachenko, J. L. Muñoz-Cobo González, and G. Verdú Martín, Phys. Rev. E **48**, 2067 (1993).
 [31] C. Deutsch, Phys. Lett. **60A**, 317 (1977); C. Deutsch, M. M. Gombert, and H. Minoo, *ibid.* **66A**, 381 (1978); **72A**, 481 (1979).
 [32] R. Cauble and W. Rozmus, J. Plasma Phys. **37**, 405 (1987).
 [33] G. A. Rinker, Phys. Rev. B **31**, 4207 (1985).
 [34] S. Ichimaru, S. Mitake, S. Tanaka, and X.-Z. Yan, Phys. Rev. A **32**, 1768 (1985).
 [35] R. L. Shepherd, D. R. Kania, and L. A. Jones, Phys. Rev. Lett. **61**, 1278 (1988).
 [36] R. L. Shepherd *et al.*, in *Strongly Coupled Plasma Physics*, edited by S. Ichimaru (Yamada Science Foundation, 1990), p. 437.
 [37] J. F. Benage *et al.*, *Strongly Coupled Plasma Physics* (Ref. [36]), p. 429.
 [38] R. M. More, in *Physics of Laser Plasma*, edited by A. M. Rubenchik and S. Witkowski, Handbook of Plasma Physics Vol. 3 (Elsevier, Amsterdam, 1991), Chap. 2, p. 70; R. M. More, Adv. At. Mol. Phys. **21**, 305 (1985).
 [39] K. S. Trainor, J. Appl. Phys. **54**, 2372 (1983).
 [40] R. H. Williams and H. E. DeWitt, Phys. Fluids **12**, 2326 (1969).